Advances in Mathematical Physics

Dynamical Processes and Systems of Fractional Order

Guest Editors: Ming Li, Carlo Cattani,
Massimo Scalia, S. C. Lim, and Wen-Sheng Chen

Dynamical Processes and Systems of Fractional Order

Advances in Mathematical Physics

Dynamical Processes and Systems of Fractional Order

Guest Editors: Ming Li, Carlo Cattani, Massimo Scalia, S. C. Lim, and Wen-Sheng Chen

Editorial Board

Contents

Hindawi Publishing Corporation
Advances in Mathematical Physics
Volume 2014, Article ID 272493, 2 pages
http://dx.doi.org/10.1155/2014/272493

Editorial
Dynamical Processes and Systems of Fractional Order

Ming Li,[1] Carlo Cattani,[2] Massimo Scalia,[3] S. C. Lim,[4] and Wen-Sheng Chen[5]

[1] *Institute of Systems Science, East China Normal University, Shanghai 200241, China*
[2] *Department of Mathematics, University of Salerno, Via Ponte Don Melillo, 84084 Fisciano, Italy*
[3] *Department of Mathematics, University of Rome, la Sapienza Piazzale Aldo Moro, 00185 Rome, Italy*
[4] *Faculty of Engineering, Multimedia University, 63100 Cyberjaya, Selanger, Malaysia*
[5] *College of Mathematics and Computational Science, Shenzhen University, Shenzhen 518160, China*

Correspondence should be addressed to Ming Li; ming_lihk@yahoo.com

Received 28 January 2014; Accepted 28 January 2014; Published 2 March 2014

Processes and systems of fractional order recently attract research interests. This special issue collects 18 papers with respect to dynamical processes and systems of fractional order, their computations, and their applications.

Fractional-order models and problems are the main focus of this issue. The recent progress in calculus and symbolic computation has open new frontiers in Engineering applications, in Physics, and in Technology, thus enabling facing challenging problems such as nonlinear problems, scale depending problems, noninteger dimensional problems, and nondifferentiable functions. In different fields of research, there is an urgent demand for fractals; for instance, new materials with extreme mechanical behavior or traffic optimization problems in communications can be suitably investigated by using fractal theory and beyond. Fractal theory, originally based on the analysis of functions with strange behaviors like the self-similar functions or the recursively defined unsmooth paths, which fill in the plane, was developing in the last decade by handling more complex fractal-like phenomena in science, nature, and biology. For instance, fractals in science were studied in signals, communications, and fractures in materials. Fractals in nature arise along the coast line, geomorphology, and tree branches. Fractals in biology were observed and studied in the heath beats, blood vessels, brain activity, and DNA. There follows that nearly every phenomenon in nature, when observed at a suitable scale or investigated by a scientific model, looks like a fractal and the corresponding model is fractional.

M. Li and W. Zhao's paper entitled "*Solving Abel's type integral equation with Mikusinski's operator of fractional order*" gives a novel explanation of the integral equation of Abel's type from the point of view of Mikusinski's operational calculus. Y.-M. Wang's paper "*Maximum norm error estimates of ADI methods for a two-dimensional fractional subdiffusion equation*" discusses two alternating direction implicit finite difference methods for solving a two-dimensional fractional subdiffusion equation, providing an explicit error estimate for each of the two methods in the discrete maximum norm. J.-S. Duan's paper "*The periodic solution of fractional oscillation equation with periodic input*" exhibits that their results are similar to the case of a damped oscillation with a periodic input in the integer-order case. In addition, the paper introduces the fractional resonance frequency. The paper by X.-M. Yang and Z.-L. Deng that is in the title "*A point source identification problem for a time fractional diffusion equation*" develops an effective numerical algorithm to recover both the intensities and locations of unknown point sources from final measurements when an inverse source identification problem for a time fractional diffusion equation is considered.

The paper by M. H. Heydari et al. is entitled "*Chebyshev wavelets method for solution of nonlinear fractional integrodifferential equations in a large interval*." It develops an efficient Chebyshev wavelets method for solving a class of nonlinear fractional integrodifferential equations in a large interval and presents a new technique for computing nonlinear terms in equations of such type. L. Liu's paper entitled "*Interval wavelet numerical method on Fokker-Planck equations for nonlinear random system*" proposes an interval wavelet numerical method for nonlinear random systems using interval

Shannon-Gabor wavelet interpolation operator. Two types of equations, namely, a Fokker-Planck-Kolmogorov equation for nonlinear oscillators and a time fractional Fokker-Planck equation, are taken as examples to illustrate the effectiveness and efficiency of the proposed method. S.-L. Mei and D.-H. Zhu's paper entitled "*Interval Shannon wavelet collocation method for fractional Fokker-Planck equation*" presents a method of an adaptive interval interpolation wavelet.

The paper by H. S. Alkhaldi et al., entitled "*Vibration control of fractionally-damped beam subjected to a moving vehicle and attached to fractionally-damped multiabsorbers*," presents promising results in mechanics and theoretic physics with respect to the dynamic response of Bernoulli-Euler homogeneous isotropic fractionally damped simply supported beam. The paper by S. Wen et al., which is entitled "*The study of fractional order controller with SLAM in the humanoid robot*," presents a fractional-order PI controller with SLAM method. The proposed method was used in the simulation of navigation of NAO humanoid robot from Aldebaran.

Z. Wang and L. Yan's paper "*The S-transform of sub-fBm and an application to a class of linear subfractional BSDEs*" studies be a subfractional Brownian motion with index $0 < H < 1$. M. Li's paper entitled "*Power spectrum of generalized fractional Gaussian noise*" gives the Fourier transform of the generalized fractional Gaussian noise (GfGn). By GfGn, one means that the autocorrelation function of GfGn is equipped with fractional lag. Hence, it is a kind of noise equipped with two indexes, the Hurst parameter $0 < H < 1$ and the index of fractional lag that is less than or equals 1 but greater than 0.

Z. Liao's paper with the title "*Low-dosed X-ray computed tomography imaging by regularized fully spatial fractional-order Perona-Malik diffusion*" proposes a new fractional-order Perona-Malik Diffusion (FOPMD) algorithm for noise suppressing. The algorithm has the advantages of both regularization and FOPMD. It has good abilities in singularities preserving while suppressing noise. S. Hu's paper entitled "*External fractional-order gradient vector Perona-Malik diffusion For sinogram restoration of low-dosed X-ray computed tomography*" presents a novel fractional-order diffusion scheme, named external fractional-order gradient vector Perona-Malik diffusion, which has advantage in avoiding artifacts, dark resulting images, and speckle effect. The paper by W.-S. Chen et al. is entitled "*Geometric distribution weight information modeled using radial basis function with fractional order for linear discriminant analysis method*." It introduces the radial basis function (RBF) with fractional order to model the geometric distribution weight information of the training samples and proposes a novel geometric distribution weight information-based Fisher discriminant criterion. The paper by B. Chen et al. entitled "*A fast region-based segmentation model with Gaussian kernel of fractional order*" proposed the Gaussian kernel of fractional order for image processing. The paper by J. Yang et al. "*Extraction of affine invariant features using fractal*" presents an approach for extracting affine invariant features based on fractal for object classification.

The paper by W. Huang et al., in the title of "*Distance-based routing strategy for traffic transport in spatial networks*," proposes a novel distance-based routing strategy in spatial scale-free networks. X. Sun and J. Liu's paper "*Weak convergence for a class of stochastic fractional equations driven by fractional noise*" gives the analysis of the issue about the weak convergence of a class of stochastic fractional equations with the excitation of fractional Gaussian noise.

Acknowledgments

We are grateful to the authors of the special issue for their contributions and the reviewers for their valuable comments on the submissions. Ming Li acknowledges the supports for his work in part by the National Natural Science Foundation of China under the Project Grant nos. 61272402, 61070214, and 60873264 and by the Macau Science and Technology Development Fund under Grant nos. 061/2011/A3, 009/2010/A1, and 021/2009/A1.

Ming Li
Carlo Cattani
Massimo Scalia
S. C. Lim
Wen-Sheng Chen

Hindawi Publishing Corporation
Advances in Mathematical Physics
Volume 2014, Article ID 479873, 10 pages
http://dx.doi.org/10.1155/2014/479873

Research Article

Weak Convergence for a Class of Stochastic Fractional Equations Driven by Fractional Noise

Xichao Sun[1] and Junfeng Liu[2]

[1] *Department of Mathematics and Physics, Bengbu College, 1866 Caoshan Road, Bengbu, Anhui 233030, China*
[2] *School of Mathematics and Statistics, Nanjing Audit University, 86 West Yu Shan Road, Pukou, Nanjing 211815, China*

Correspondence should be addressed to Xichao Sun; sunxichao626@126.com

Received 21 September 2013; Revised 27 December 2013; Accepted 27 December 2013; Published 12 February 2014

Academic Editor: Ming Li

We consider a class of stochastic fractional equations driven by fractional noise on $(t,x) \in [0,T] \times [0,1]$ $\partial u/\partial t = D_\delta^\alpha u + f(t,x,u) + \partial^2 B^H(t,x)/\partial t\, \partial x$, with Dirichlet boundary conditions. We formally replace the random perturbation by a family of sequences based on Kac-Stroock processes in the plane, which approximate the fractional noise in some sense. Under some conditions, we show that the real-valued mild solution of the stochastic fractional heat equation perturbed by this family of noises converges in law, in the space $\mathscr{C}([0,T] \times [0,1])$ of continuous functions, to the solution of the stochastic fractional heat equation driven by fractional noise.

1. Introduction

In recent years, there has been considerable interest in studying fractional equations due to interesting properties and applications in various scientific areas including image analysis, risk management, and statistical mechanics (see Droniou and Imbert [1] and Uchaikin and Zolotarev [2] for a survey of applications). Much effort has been devoted to apply the fractional calculus to mathematical problems in science and engineering. For example, Chen et al. [3] and Li et al. [4] studied the fractional-order networks and Li [5] investigated fractal time series. More works on the fields can be found in [6–12] and the references therein. Stochastic partial differential equation involving fractional Laplacian operator (which is an integrodifferential operator) has been studied by many authors. For example, Mueller [13] and Wu [14] proved the existence of a solution of stochastic fractional heat and Burgers equation perturbed by a stable noise, respectively. Other related references are Chang and Lee [15], Truman and Wu [16], Liu et al. [17], Wu [18], and the references therein.

On the other hand, weak convergence to Brownian motion, fractional Brownian motion, and related stochastic processes have been considered extensively since the work of Taqqu [19] and Delgado and Jolis [20]. Recently, many researchers are interested in studying weak convergence of stochastic differential equation. Some surveys could be found in Bardina et al. [21], Boufoussi and Hajji [22], and Mellall and Ouknine [23]. Bardina et al. [21] studied the convergence in law, in the space $\mathscr{C}([0,t] \times [0,1])$ of continuous functions, of the solution of

$$\frac{\partial X_n}{\partial t}(t,x) - \frac{\partial^2 X_n}{\partial x^2}(t,x) = \theta_n(t,x), \tag{1}$$

with vanishing initial data and Dirichlet boundary conditions, towards the solution of

$$\frac{\partial X}{\partial t}(t,x) - \frac{\partial^2 X}{\partial x^2}(t,x) = \dot{W}(t,x), \tag{2}$$

where $(t,x) \in [0,T] \times [0,1]$ and θ_n is a noisy input which converges to white noise $\dot{W}$. Mellall and Ouknine [23] considered the quasilinear stochastic heat equation on $[0,1]$

$$\frac{\partial u}{\partial t}(t,x) - \frac{\partial^2 u}{\partial x^2}(t,x) = b(u(t,x)) + \frac{\partial^2 B^H(t,x)}{\partial t\, \partial x}, \tag{3}$$

with Dirichlet boundary conditions

$$u(t,0) = u(t,1) = 0, \quad t \in [0,T], \tag{4}$$

and initial condition $u(0,x) = u_0(x)$, $x \in [0,1]$, where $\partial^2 B^H(t,x)/\partial t \partial x$ is a fractional noise with Hurst parameter $H \in (1/2,1)$.

Motivated by these works, we consider the weak convergence for the following stochastic fractional heat equation driven by fractional noise on $(t,x) \in [0,T] \times [0,1]$:

$$\frac{\partial u}{\partial t} = D_\delta^\alpha u + f(t,x,u) + \frac{\partial^2 B^H(t,x)}{\partial t\, \partial x}, \qquad u(t,0) = u(t,1) = 0, \tag{5}$$

where D_δ^α is the fractional Laplacian operator with respect to the spatial variable, to be defined in Section 2 which was recently introduced by Debbi [24] and Debbi and Dozzi [25], and $B^H(t,x)$ is a fractional noise on $[0,T] \times [0,1]$ with Hurst index $H > 1/2$ defined on a complete probability space $\{\Omega, \mathscr{F}, \{\mathscr{F}_t\}_{t\geq 0}, P\}$. Actually, we understand (5) in the sense of Walsh [26], and so one can present a mild formulation of (5) as follows:

$$\begin{aligned} u(t,x) = {} & \int_0^1 G_{\alpha,\delta}(t, x-y)\, u_0(y)\, dy \\ & + \int_0^t \int_0^1 G_{\alpha,\delta}(t-s, x-y)\, f(s,y,u(s,y))\, dy\, ds \\ & + \int_0^t \int_0^1 G_{\alpha,\delta}(t-s, x-y)\, B^H(ds,dy), \end{aligned} \tag{6}$$

where $G_{\alpha,\delta}(\cdot,*)$ denotes the Green function associated with (5).

The rest of this paper is organized as follows. In Section 2, we begin by making some notation and by recalling some basic preliminaries which will be needed later. In Section 3, we will prove weak limit theorems for (5) in space $\mathscr{C}([0,t] \times [0,1])$. Most of the estimates of this paper contain unspecified constants. An unspecified positive and finite constant will be denoted by C, which may not be the same in each occurrence. Sometimes we will emphasize the dependence of these constants upon parameters.

2. Preliminaries

In this section, we briefly recall some basic definitions of fractional noise and Green function.

2.1. Fractional Noise. For each $t \in [0,T]$, let $\mathscr{F}_t^H$ be the σ-field generated by the random variables $\{B^H(t,A),\ t \in [0,T],\ A \in \mathscr{B}[0,1]\}$ and the sets of probability zero, and denote by $\mathscr{P}$ the σ-field of progressively measurable subsets of $[0,T] \times \Omega$.

We denote by $\mathscr{E}$ the set of step functions on $[0,T] \times [0,1]$. Let $\mathscr{H}$ be the Hilbert space defined as the closure of $\mathscr{E}$ with respect to the scalar product

$$\left\langle \mathbb{1}_{[0,t]\times A}, \mathbb{1}_{[0,s]\times B} \right\rangle_{\mathscr{H}} = |A \cap B|\, R_H(t,s), \tag{7}$$

where covariance kernel $R_H(t,s) = (1/2)[t^{2H} + s^{2H} - |t-s|^{2H}]$ and $|A|$ denotes the Lebesgue measure of the set A.

According to Nualart and Ouknine [27], the mapping $\mathbb{1}_{[0,t]\times A} \to B^H(t,A)$ can be extended to an isometry between $\mathscr{H}$ and the Gaussian space $H_1(B^H)$ associated with B^H and denoted by

$$\varphi \longmapsto B^H(\varphi) := \int_{[0,t]\times A} \varphi(s,y)\, B^H(ds,dy). \tag{8}$$

Define the linear operator $K_H^* : \mathscr{E} \mapsto L^2([0,T])$ by

$$\begin{aligned} K_H^*(\varphi)(s,x) = {} & K_H(T,s)\, \varphi(s,x) \\ & + \int_s^T (\varphi(r,x) - \varphi(s,x))\, \frac{\partial K_H}{\partial r}(r,s)\, dr, \end{aligned} \tag{9}$$

where K_H is the square integrable kernel given by

$$K_H(t,s) := \begin{cases} c_H (t-s)^{H-1/2} + C_H s^{1/2-H} \\ \quad \times \displaystyle\int_s^t (u-s)^{H-3/2} \left(1 - \left(\frac{s}{u}\right)^{1/2-H}\right) du, & 0 < s \leq t, \\ 0, & \text{otherwise}, \end{cases} \tag{10}$$

with $c_H = (2H\Gamma(3/2-H)/\Gamma(H+1/2)\Gamma(2-2H))^{1/2}$, and one can get

$$\frac{\partial K_H}{\partial t}(t,s) = c_H \left(\frac{1}{2} - H\right) \left(\frac{t}{s}\right)^{H-1/2} (t-s)^{H-3/2}. \tag{11}$$

Moreover, the kernel K_H satisfies the following property:

$$\int_0^{s\wedge t} K_H(t,r)\, K_H(s,r)\, dr = R_H(t,s), \tag{12}$$

$R_H(t,s)$ being the covariance kernel of the fractional Brownian motion. Then, for any pair of step functions φ and ψ in $\mathscr{E}$ we have

$$\left\langle K_H^*(\varphi), K_H^*(\psi) \right\rangle_{L^2([0,T]\times[0,1])} = \langle \varphi, \psi \rangle_{\mathscr{H}}, \tag{13}$$

because

$$\left(K_H^* 1_{[0,t]\times A}\right)(s,x) = K_H(t,s)\, 1_{[0,t]\times A}(s,x). \tag{14}$$

As a consequence, the operator K_H^* provides an isometry between the Hilbert space $\mathscr{H}$ and $L^2([0,T] \times [0,1])$. Hence, the Gaussian family $\{W(t,A),\ t \in [0,T],\ A \in \mathscr{B}[0,1]\}$ defined by

$$W(t,A) = B^H\left(\left(K_H^*\right)^{-1}\left(1_{[0,t]\times A}\right)\right) \tag{15}$$

is a space-time white noise, and the process B^H has an integral representation of the form

$$B^H(t,x) = \int_0^t \int_0^x K_H(t,s)\, W(ds,dy). \tag{16}$$

Now, we can present a mild formulation of (5) as follows:

$$u(t,x) = \int_0^1 G_{\alpha,\delta}(t,x-y)\,u_0(y)\,dy + \int_0^t\int_0^1 G_{\alpha,\delta}(t-s,x-y)\,f(s,y,u(s,y))\,dy\,ds + \int_0^t\int_0^1 K_H^* G_{\alpha,\delta}(t-s,x-y)\,W(ds,dy). \tag{17}$$

That is, the last term of (6) is equal to

$$\int_0^t\int_0^1 G_{\alpha,\delta}(t-s,x-y)\,B^H(ds,dy) = \int_0^t\int_0^1 K_H^* G_{\alpha,\delta}(t-s,x-y)\,W(ds,dy). \tag{18}$$

2.2. Green Function. In this subsection, we will introduce the nonlocal factional differential operator D_δ^α defined via its Fourier transform $\mathcal{F}$ by

$$\mathcal{F}(D_\delta^\alpha\varphi)(\xi) = -|\xi|^\alpha \exp\left(-i\delta\frac{\pi}{2}\operatorname{sgn}(\xi)\right)\mathcal{F}(\varphi)(\xi). \tag{19}$$

In this paper, we will assume that $|\delta| \le \min\{\alpha-[\alpha]_2, 2+[\alpha]_2-\alpha\}$, $i = 1,\dots,d$, $[\alpha]_2$, is the largest even integer less or equal to α (even part of α), and $\delta \in 2\mathbb{N}+1$.

The operator D_δ^α is a closed, densely defined operator on $L^2(\mathbb{R})$ and it is the infinitesimal generator of a semigroup which is in general not symmetric and not a contraction. This operator is a generalization of various well-known operators, such as the Laplacian operator (when $\alpha = 2$), the inverse of the generalized Riesz-Feller potential (when $\alpha > 2$), and the Riemann-Liouville differential operator (when $|\delta| = 2+[\alpha]_2$ or $|\delta| = \alpha-[\alpha]$). It is self-adjoint only when $\delta = 0$ and, in this case, it coincides with the fractional power of the Laplacian. We refer the readers to Debbi [24], Debbi and Dozzi [25], and Komatsu [28] for more details about this operator.

According to Komatsu [28], D_δ^α can be represented for $1 < \alpha < 2$ by

$$D_\delta^\alpha\varphi(x) = \int_{\mathbb{R}} \frac{\varphi(x+y)-\varphi(x)-y\varphi'(x)}{|y|^{1+\alpha}} \times\left(\kappa_-^\delta 1_{(-\infty,0)}(y) + \kappa_+^\delta 1_{(-0,+\infty)}(y)\right)dy \tag{20}$$

and for $0 < \alpha < 1$ by

$$D_\delta^\alpha\varphi(x) = \int_{\mathbb{R}} \frac{\varphi(x+y)-\varphi(x)}{|y|^{1+\alpha}} \times\left(\kappa_-^\delta 1_{(-\infty,0)}(y) + \kappa_+^\delta 1_{(-0,+\infty)}(y)\right)dy, \tag{21}$$

where κ_-^δ and κ_+^δ are two nonnegative constants satisfying $\kappa_-^\delta + \kappa_+^\delta > 0$ and φ is a smooth function for which the integral exists, and φ' is its derivative. This representation identifies it as the infinitesimal generator for a nonsymmetric α-stable Lévy process.

Let $G_{\alpha,\delta}(t,x)$ be the fundamental solution of the following Cauchy problem:

$$\frac{\partial u}{\partial t}(t,x) = D_\delta^\alpha(t,x), \qquad u(0,x) = \delta_0(x), \quad t > 0,\ x \in \mathbb{R}, \tag{22}$$

where $\delta_0(\cdot)$ is the Dirac distribution. By Fourier transform, we see that $G_{\alpha,\delta}(t,x)$ is given by

$$G_{\alpha,\delta}(t,x) = \frac{1}{2\pi}\int_{\mathbb{R}} \exp\left(-izx - t|z|^\alpha \exp\left(-i\delta\frac{\pi}{2}\operatorname{sgn}(z)\right)\right)dz. \tag{23}$$

The relevant parameters α, called the index of stability, and δ (related to the asymmetry), improperly referred to as the skewness, are real numbers satisfying $|\delta| \le \min\{\alpha-[\alpha]_2, 2+[\alpha]_2-\alpha\}$, and $\delta = 0$ when $\delta \in 2\mathbb{N}+1$.

Let us list some known facts on $G_{\alpha,\delta}(t,x)$ which will be used later on (see, e.g., Debbi [24] and Debbi and Dozzi [25]).

Lemma 1. *Let $\alpha \in (0,\infty)/\{\mathbb{N}\}$; one has the following:*

(1) *the function $G_{\alpha,\delta}(t,\cdot)$ is not in general symmetric relatively to x and it is not everywhere positive;*

(2) *for any $s,t \in (0,\infty)$ and $x \in \mathbb{R}$,*

$$\frac{\partial^n}{\partial x^n}G_{\alpha,\delta}(t,x) = (s)^{-(n+1)/\alpha}G_{\alpha,\delta}\left(s^{-1}t, s^{-1/\alpha}x\right), \tag{24}$$

or equivalently,

$$\frac{\partial^n}{\partial x^n}G_{\alpha,\delta}(t,x) = (t)^{-(n+1)/\alpha}G_{\alpha,\delta}\left(1,(t)^{-1/\alpha}x\right); \tag{25}$$

(3) $G_{\alpha,\delta}(s,\cdot) * G_{\alpha,\delta}(t,\cdot) = G_{\alpha,\delta}(s+t,\cdot)$ *for any $s,t \in (0,\infty)$;*

(4) *For $n \ge 1$, there exist some constants C and $C_n > 0$ such that, for all $x \in \mathbb{R}$,*

$$|G_{\alpha,\delta}(1,x)| \le C\frac{1}{1+|x|^{1+\alpha}}, \qquad \left|\frac{\partial^n}{\partial x^n}G_{\alpha,\delta}(1,x)\right| \le C_n\frac{|x|^{\alpha+n-1}}{\left(1+|x|^{\alpha+n}\right)^2}; \tag{26}$$

(5) $\int_0^T\int_{\mathbb{R}} |G_{\alpha,\delta}(t,x)|^\lambda dt\,dx < \infty$ *if and only if $1/\alpha < \lambda < \alpha$.*

3. Main Results and Its Proof

Our aim is to prove that the mild solution of (5), given by (17), can be approximated in law in the space $\mathscr{C}([0,t]\times[0,1])$ by the processes

$$\begin{aligned} u_n(t,x) &= \int_0^1 G_{\alpha,\delta}(t,x-y)\,u_0(y)\,dy \\ &\quad + \int_0^t\int_0^1 G_{\alpha,\delta}(t-s,x-y)\,f(s,y,u_n(s,y))\,dy\,ds \\ &\quad + \int_0^t\int_0^1 K_H^* G_{\alpha,\delta}(t-s,x-y)\,\theta_n(s,y)\,dy\,ds, \end{aligned} \tag{27}$$

where $\{\theta_n(t,x)\}_{n\in\mathbb{N}}$ is a weak approximation of a Brownian sheet; that is, $\{\theta_n(t,x)\}_{n\in\mathbb{N}}$, $(t,x)\in[0,T]\times[0,1]$ is a family of Kac-Stroock processes in the plane which is square integral a.s., defined by

$$\theta_n(t,x) = n\sqrt{tx}(-1)^{N_n(t,x)}, \quad n\in\mathbb{N}, \tag{28}$$

$N_n(t,x) = N(\sqrt{n}t,\sqrt{n}x)$ and $\{N(t,x),(t,x)\in[0,T]\times[0,1]\}$ is a standard Poisson process in plane.

Theorem 2. *Let $\{\theta_n(t,x),(t,x)\in[0,T]\times[0,1]\}$, $n\in\mathbb{N}$, be the Kac-Stroock processes in the plane. Assume that $u_0:[0,1]\to\mathbb{R}$ is a continuous function and f satisfies the following linear growth conditions:*

$$\left|f(t,x,u)\right| \le C(1+|u|) \tag{29}$$

and uniformly Lipschitz conditions

$$\left|f(t,x,u)-f(t,x,u)\right| \le C|u-v|. \tag{30}$$

Then, the family of stochastic processes $\{u_n,n\in\mathbb{N}\}$ defined by (27) *converges in law, as n tends to infinity, in the space $\mathscr{C}([0,T]\times[0,1])$, to the mild solution u of* (5)*, given by* (17)*.*

In order to prove Theorem 2, we will focus on the linear problem, which is amount to establish the convergence in law, in the space $\mathscr{C}([0,T]\times[0,1])$, of the solutions of

$$\frac{\partial X_n}{\partial t} - \frac{\partial^2 X_n}{\partial x^2} = \frac{\partial^2 B_n^H}{\partial t\,\partial x}, \tag{31}$$

with vanishing initial data and Dirichlet boundary conditions, toward the solution of

$$\frac{\partial X}{\partial t} - \frac{\partial^2 X}{\partial x^2} = \frac{\partial^2 B^H}{\partial t\,\partial x}, \tag{32}$$

where the solutions of (31) and (32) are, respectively, given by

$$X_n(t,x) = \int_0^t\int_0^1 K_H^* G_{\alpha,\delta}(t-s,x-y)\,\theta_n(s,y)\,dy\,ds, \tag{33}$$

$$X(t,x) = \int_0^t\int_0^1 K_H^* G_{\alpha,\delta}(t-s,x-y)\,W(ds,dy). \tag{34}$$

In the following, we need two results which can be found in Bardina et al. [21]. The first one leads to the tightness in $\mathscr{C}([0,T]\times[0,1])$ of a family.

Lemma 3. *Let $\{X_n,n\in\mathbb{N}\}$ be a family of random variables taking values in $\mathscr{C}([0,T]\times[0,1])$. The family of the laws of $\{X_n,n\in\mathbb{N}\}$ is tight, if there exist $p',p>0,\delta>2$, and a constant C such that*

$$\sup_{n\ge1} E\left|X_n(0,0)\right|^{p'} < \infty, \tag{35}$$

and, for every $t,t'\in[0,T]$ and $x,x'\in[0,1]$,

$$\sup_{n\ge1} E\left|X_n(t',x') - X_n(t,x)\right|^p < C\left(\left|x'-x\right|+\left|t'-t\right|\right)^\delta. \tag{36}$$

The second one is a technical lemma.

Lemma 4. *Denote by $\theta_n(t,x)$ the Kac-Stroock kernels; for any even $n\in\mathbb{N}$, there exists a constant C_n, such that, for any $t_1,t_2\in[0,T]$ and $x_1,x_2\in[0,1]$ satisfying $0<t_1<t_2<2t_1$ and $0<x_1<x_2<2x_1$, one can get*

$$\begin{aligned} &\sup_{n\ge1} E\left[\left(\int_{t_1}^{t_2}\int_{x_1}^{x_2} f(s,x)\,\theta_n(s,x)\,dx\,ds\right)^n\right] \\ &\qquad \le C_n\left(\int_{t_1}^{t_2}\int_{x_1}^{x_2} f^2(s,x)\,dx\,ds\right)^{n/2}, \end{aligned} \tag{37}$$

for any $f(s,x)\in L^2([0,T]\times[0,1])$.

Proposition 5. *The family of processes $\{X_n,n\in\mathbb{N}\}$ is tight in $\mathscr{C}([0,T]\times[0,1])$.*

Proof. We first estimate the moment of order m of the quantity

$$\begin{aligned} &X_n(t',x') - X_n(t,x) \\ &\quad = \int_0^{t'}\int_0^1 K_H^* G_{\alpha,\delta}(t'-s,x'-y)\,\theta_n(s,y)\,dy\,ds \\ &\qquad - \int_0^t\int_0^1 K_H^* G_{\alpha,\delta}(t-s,x-y)\,\theta_n(s,y)\,dy\,ds, \end{aligned} \tag{38}$$

which is equal to

$$\begin{aligned} &\int_0^t\int_0^1 K_H^*\left(G_{\alpha,\delta}(t'-s,x'-y)\right. \\ &\qquad \left. - G_{\alpha,\delta}(t'-s,x-y)\right)\theta_n(s,y)\,dy\,ds \\ &\quad + \int_0^t\int_0^1 K_H^*\left(G_{\alpha,\delta}(t'-s,x-y)\right. \\ &\qquad \left. - G_{\alpha,\delta}(t-s,x-y)\right)\theta_n(s,y)\,dy\,ds \\ &\quad + \int_t^{t'}\int_0^1 K_H^* G_{\alpha,\delta}(t'-s,x'-y)\,\theta_n(s,y)\,dy\,ds. \end{aligned} \tag{39}$$

By Lemma 4, one can get

$$\begin{aligned}
&\sup_{n\geq 1} E\left|X_n\left(t',x'\right)-X_n(t,x)\right|^m \\
&\quad\leq C_m\left[\int_0^t\int_0^1\left[K_H^*\left(G_{\alpha,\delta}\left(t'-s,x'-y\right)\right.\right.\right. \\
&\qquad\left.\left.\left.-G_{\alpha,\delta}\left(t'-s,x-y\right)\right)\right]^2 dy\,ds\right]^{m/2} \\
&\quad + C_m\left[\int_0^t\int_0^1\left[K_H^*\left(G_{\alpha,\delta}\left(t'-s,x-y\right)\right.\right.\right. \\
&\qquad\left.\left.\left.-G_{\alpha,\delta}\left(t-s,x-y\right)\right)\right]^2 dy\,ds\right]^{m/2} \\
&\quad + C_m\left[\int_t^{t'}\int_0^1\left(K_H^* G_{\alpha,\delta}\left(t'-s,x'-y\right)\right)^2 dy\,ds\right]^{m/2} \\
&\quad = C_m\left(I+II+III\right).
\end{aligned} \tag{40}$$

Using the continuous embedding established in [27]

$$L^{1/H}([0,T]\times[0,1])\subset\mathscr{H}, \tag{41}$$

we obtain

$$\begin{aligned}
I &= \left[\int_0^t\int_0^1\left[K_H^*\left(G_{\alpha,\delta}\left(t'-s,x'-y\right)\right.\right.\right. \\
&\qquad\left.\left.\left.-G_{\alpha,\delta}\left(t'-s,x-y\right)\right)\right]^2 dy\,ds\right]^{m/2} \\
&\leq C_H\left[\int_0^t\int_0^1\left(G_{\alpha,\delta}\left(t'-s,x'-y\right)\right.\right. \\
&\qquad\left.\left.-G_{\alpha,\delta}\left(t'-s,x-y\right)\right)^{1/H} dy\,ds\right]^{mH} \\
&= C_H\left\|G_{\alpha,\delta}\left(t'-\cdot,x'-*\right)\right. \\
&\qquad\left.-G_{\alpha,\delta}(t'-\cdot,x-*)\right\|^m_{L^{1/H}([0,T]\times[0,1])} \\
&= C_H\left\|\left|G_{\alpha,\delta}\left(t'-\cdot,x'-*\right)-G_{\alpha,\delta}\left(t'-\cdot,x-*\right)\right|^\theta\right. \\
&\qquad\cdot\left|G_{\alpha,\delta}\left(t'-\cdot,x'-*\right)\right. \\
&\qquad\left.\left.-G_{\alpha,\delta}\left(t'-\cdot,x-*\right)\right|^{1-\theta}\right\|^m_{L^{1/H}([0,T]\times[0,1])} \\
&\leq C_H\left[\left\|\left|G_{\alpha,\delta}\left(t'-\cdot,x'-*\right)-G_{\alpha,\delta}\left(t'-\cdot,x-*\right)\right|^\theta\right.\right. \\
&\qquad\cdot\left|G_{\alpha,\delta}\left(t'-\cdot,x'-*\right)\right|^{1-\theta}\Big\|^m_{L^{1/H}([0,T]\times[0,1])} \\
&\qquad+\left\|\left|G_{\alpha,\delta}\left(t'-\cdot,x'-*\right)-G_{\alpha,\delta}\left(t'-\cdot,x-*\right)\right|^\theta\right. \\
&\qquad\left.\left.\cdot\left|G_{\alpha,\delta}\left(t'-\cdot,x-*\right)\right|^{1-\theta}\right\|^m_{L^{1/H}([0,T]\times[0,1])}\right] \\
&= C_H\left(I_1+I_2\right).
\end{aligned} \tag{42}$$

Let $\theta\in(0,\min\{1,(\alpha+1)H-1\})$. Thanks to the mean-value theorem, one can get

$$\begin{aligned}
I_1 &= \left\|\left|x'-x\right|^\theta\left|\frac{\partial}{\partial x}G_{\alpha,\delta}\left(t'-\cdot,\xi-*\right)\right|^\theta\right. \\
&\qquad\left.\times\left|G_{\alpha,\delta}(t'-\cdot,x'-*)\right|^{1-\theta}\right\|^m_{L^{1/H}([0,T]\times[0,1])} \\
&= \left(\left|x'-x\right|^{\theta/H}\int_0^T\int_0^1\left|\frac{\partial}{\partial x}G_{\alpha,\delta}\left(t'-s,\xi-y\right)\right|^{\theta/H}\right. \\
&\qquad\left.\times\left|G_{\alpha,\delta}\left(t'-s,x'-y\right)\right|^{(1-\theta)/H} dy\,ds\right)^{mH}, \\
&\int_0^1\left|\frac{\partial}{\partial x}G_{\alpha,\delta}\left(t'-s,\xi-y\right)\right|^{\theta/H} \\
&\qquad\times\left|G_{\alpha,\delta}\left(t'-s,x'-y\right)\right|^{(1-\theta)/H} dy \\
&\leq \int_{\mathbb{R}}\left|\frac{\partial}{\partial x}G_{\alpha,\delta}\left(t'-s,\xi-y\right)\right|^{\theta/H} \\
&\qquad\times\left|G_{\alpha,\delta}\left(t'-s,x'-y\right)\right|^{(1-\theta)/H} dy \\
&= \left(t'-s\right)^{1/\alpha-(1+\theta)/\alpha H}\int_{\mathbb{R}}\left|\frac{\partial}{\partial x}G_{\alpha,\delta}\left(1,\xi-y\right)\right|^{\theta/H} \\
&\qquad\times\left|G_{\alpha,\delta}\left(1,y\right)\right|^{(1-\theta)/H} dy \\
&\leq C_{H,\theta}\left(t'-s\right)^{1/\alpha-(1+\theta)/\alpha H}.
\end{aligned} \tag{43}$$

Therefore, if $1/\alpha-(1+\theta)/\alpha H+1>0$, that is, $\theta<(\alpha+1)H-1$, then

$$I_1\leq C_{T,H,\theta}\left|x'-x\right|^{m\theta}. \tag{44}$$

Similarly, one can get

$$I_2\leq C_{T,H,\theta}\left|x'-x\right|^{m\theta}. \tag{45}$$

Hence

$$I\leq C_{T,H,\theta}\left|x'-x\right|^{m\theta}. \tag{46}$$

Now we are in the position to deal with II. Consider

$$\begin{aligned}
II &= \left[\int_0^t\int_0^1 \left[K_H^*\left(G_{\alpha,\delta}\left(t'-s,x-y\right)\right.\right.\right.\\
&\qquad \left.\left.\left.-G_{\alpha,\delta}\left(t-s,x-y\right)\right)\right]^2 dy\,ds\right]^{m/2}\\
&\le C_H\left[\int_0^t\int_0^1 \left(G_{\alpha,\delta}\left(t'-s,x-y\right)\right.\right.\\
&\qquad \left.\left.-G_{\alpha,\delta}(t-s,x-y)\right)^{1/H} dy\,ds\right]^{mH}\\
&= C_H \left\|G_{\alpha,\delta}\left(t'-\cdot,x-*\right)\right.\\
&\qquad \left.-G_{\alpha,\delta}\left(t-\cdot,x-*\right)\right\|^m_{L^{1/H}([0,T]\times[0,1])}\\
&= C_H \left\|\left|G_{\alpha,\delta}\left(t'-\cdot,x-*\right)-G_{\alpha,\delta}\left(t-\cdot,x-*\right)\right|^{\mu}\right.\\
&\qquad \cdot\left|G_{\alpha,\delta}\left(t'-\cdot,x-*\right)\right.\\
&\qquad \left.\left.-G_{\alpha,\delta}\left(t-\cdot,x-*\right)\right|^{1-\mu}\right\|^m_{L^{1/H}([0,T]\times[0,1])}\\
&\le C_H\left[\left\|\left|G_{\alpha,\delta}\left(t'-\cdot,x-*\right)-G_{\alpha,\delta}\left(t-\cdot,x-*\right)\right|^{\mu}\right.\right.\\
&\qquad \left.\cdot\left|G_{\alpha,\delta}\left(t'-\cdot,x-*\right)\right|^{1-\mu}\right\|^m_{L^{1/H}([0,T]\times[0,1])}\\
&\qquad +\left\|\left|G_{\alpha,\delta}\left(t'-\cdot,x-*\right)-G_{\alpha,\delta}\left(t-\cdot,x-*\right)\right|^{\mu}\right.\\
&\qquad \left.\left.\cdot\left|G_{\alpha,\delta}\left(t-\cdot,x-*\right)\right|^{1-\mu}\right\|^m_{L^{1/H}([0,T]\times[0,1])}\right]\\
&= C_H\left(II_1+II_2\right).
\end{aligned} \tag{47}$$

By mean-value theorem, it holds that

$$\begin{aligned}
II_1 &= \left\|\left|t'-t\right|^{\mu}\left|\frac{\partial}{\partial t}G_{\alpha,\delta}\left(\eta-\cdot,x-*\right)\right|^{\mu}\right.\\
&\qquad \left.\cdot\left|G_{\alpha,\delta}\left(t'-\cdot,x-*\right)\right|^{1-\mu}\right\|^m_{L^{1/H}([0,T]\times[0,1])}\\
&= \left(\int_0^T\int_0^1 \left|t'-t\right|^{\mu/H}\left|\frac{\partial}{\partial t}G_{\alpha,\delta}\left(\eta-s,x-y\right)\right|^{\mu/H}\right.\\
&\qquad \left.\cdot\left|G_{\alpha,\delta}\left(t'-s,x-y\right)\right|^{(1-\mu)/H} dy\,ds\right)^{mH}.
\end{aligned} \tag{48}$$

Noting that

$$G_{\alpha,\delta}(t,x) = t^{-1/\alpha}G_{\alpha,\delta}\left(1,t^{-1/\alpha}x\right), \tag{49}$$

one can get

$$\begin{aligned}
&\frac{\partial}{\partial t}G_{\alpha,\delta}(t,x)\\
&\quad = \left(-\frac{1}{\alpha}\right)t^{-1-1/\alpha}G_{\alpha,\delta}\left(1,t^{-1/\alpha}x\right)\\
&\qquad +\left(-\frac{1}{\alpha}\right)t^{-1-2/\alpha}\left[x\frac{\partial}{\partial z}G_{\alpha,\delta}(1,z)\left|_{z=t^{-1/\alpha}x}\right.\right].
\end{aligned} \tag{50}$$

Then

$$\begin{aligned}
&\int_0^1\left|\frac{\partial}{\partial t}\mathcal{G}_{\alpha,\delta}\left(\eta-s,x-y\right)\right|^{\mu/H}\\
&\qquad \cdot\left|\mathcal{G}_{\alpha,\delta}\left(t'-s,x-y\right)\right|^{(1-\mu)/H}dy\\
&\quad \le \int_R\left|\frac{\partial}{\partial t}\mathcal{G}_{\alpha,\delta}\left(\eta-s,x-y\right)\right|^{\mu/H}\\
&\qquad \cdot\left|\mathcal{G}_{\alpha,\delta}\left(t'-s,x-y\right)\right|^{(1-\mu)/H}dy\\
&\quad \le \int_R\left|\left(-\frac{1}{\alpha}\right)(\eta-s)^{-1-1/\alpha}G_{\alpha,\delta}\left(1,(\eta-s)^{-1/\alpha}(x-y)\right)\right.\\
&\qquad +\left(\frac{1}{\alpha}\right)(\eta-2)^{-1-2/\alpha}\\
&\qquad \left.\times\left[(x-y)\frac{\partial}{\partial z}G_{\alpha,\delta}(1,z)\left|_{z=(\eta-s)^{-1/\alpha}(x-y)}\right.\right]\right|^{\mu/H}\\
&\qquad \cdot\left|\mathcal{G}_{\alpha,\delta}\left(t'-s,x-y\right)\right|^{(1-\mu)/H}dy\\
&\quad \le C_{\alpha,\delta,H}\left[(t-s)^{-(\alpha\mu+1)/H\alpha+1/\alpha}\right.\\
&\qquad \left.+(t-s)^{-(\alpha\mu+\mu+1)/H\alpha+1/\alpha}\right].
\end{aligned} \tag{51}$$

Therefore, if $\mu\in(0,((\alpha+1)H-1)/\alpha)$, we have

$$II_1 \le C_{\alpha,\delta,H,T,\mu}\left|t'-t\right|^{m\mu}. \tag{52}$$

Similarly,

$$II_2 \le C_{\alpha,\delta,H,T,\mu}\left|t'-t\right|^{m\mu}. \tag{53}$$

Thus, we have

$$II \le C_{T,H,\theta}\left|t'-t\right|^{m\mu}. \tag{54}$$

Now we deal with III; similar to the proof of I, we get

$$\begin{aligned}
III &= \left[\int_t^{t'}\int_0^1\left(K_H^*G_{\alpha,\delta}\left(t'-s,x'-y\right)\right)^2 dyds\right]^{m/2}\\
&\le C_{\alpha,\delta,H}\left[\int_t^{t'}\int_0^1\left|G_{\alpha,\delta}\left(t'-s,x'-y\right)\right|^{1/H}dyds\right]^{mH}\\
&\le C_{\alpha,\delta,H}\left[\int_t^{t'}\left(t'-t\right)^{-1/H\alpha+1/\alpha}\right.\\
&\qquad \left.\times\left(\int_0^1\left|G_{\alpha,\delta}(1,z)\right|^{1/H}dz\right)ds\right]^{mH}\\
&\le C_{\alpha,\delta,H}\left|t'-t\right|^{m(((\alpha+1)H-1)/\alpha)}.
\end{aligned} \tag{55}$$

Together with (40)–(55), one can get

$$\begin{aligned}
&\sup_{n\ge1}E\left|X_n\left(t',x'\right)-X_n(t,x)\right|^m\\
&\qquad \le C\left[\left|t'-t\right|^{m\mu}+\left|x'-x\right|^{m\theta}\right].
\end{aligned} \tag{56}$$

By Lemma 3, the proof can be completed. □

Proposition 6. *The family of processes* $\{X_n, n \in \mathbb{N}\}$ *defined by* (33) *converges to the process* X *given by* (34)*, in the sense of finite-dimensional distributions, as* n *tends to infinity, in the space* $\mathscr{C}([0,T]\times[0,1])$.

Proof. We claim that, for any $a_1,\dots,a_m \in \mathbb{R}$ and $(t_1,x_1),\dots,(t_m,x_m) \in [0,T]\times[0,1]$, the law of linear combination

$$\sum_{j=1}^{m} a_j X_n\left(t_j,x_j\right) \tag{57}$$

converges weakly to the law of a random variable defined by

$$\sum_{j=1}^{m} a_j X\left(t_j,x_j\right). \tag{58}$$

This will be done by proving the convergence of the corresponding characteristic functions; that is,

$$E\left[\exp\left\{i\xi\sum_{j=1}^{m} a_j X_n\left(t_j,x_j\right)\right\}\right] \longrightarrow E\left[\exp\left\{i\xi\sum_{j=1}^{m} a_j X\left(t_j,x_j\right)\right\}\right]. \tag{59}$$

Since for any fixed $(t,x)\in[0,T]\times[0,1]$, $K_H^* G_{\alpha,\delta}(t-s,x-y) \in L^2([0,T]\times[0,1])$, then for any $(t_j,x_j)\in[0,T]\times[0,1]$, $j\in\{1,2,\dots,m\}$, there exists a sequence $(K_H^* G_{\alpha,\delta}(t_j-s,x_j-y))_k$ of simple functions such that $(K_H^* G_{\alpha,\delta}(t_j-s,x_j-y))_k$ converges to $K_H^* G_{\alpha,\delta}(t_j-s,x_j-y)$ in $L^2([0,T]\times[0,1])$ as $k\to\infty$.

To simplify notation, we define

$$\begin{aligned} X_n^{j,k} &= \int_0^t\int_0^1 \left(K_H^* G_{\alpha,\delta}\left(t_j-s,x_j-y\right)\right)_k \theta_n(s,y)\,dy\,ds,\\ X^{j,k} &= \int_0^t\int_0^1 \left(K_H^* G_{\alpha,\delta}\left(t_j-s,x_j-y\right)\right)_k W(ds,dy). \end{aligned} \tag{60}$$

Then

$$\left|E\left[\exp\left\{i\xi\sum_{j=1}^{m} a_j X_n\left(t_j,x_j\right)\right\}\right] -E\left[\exp\left\{i\xi\sum_{j=1}^{m} a_j X\left(t_j,x_j\right)\right\}\right]\right| \le V + VI + VII, \tag{61}$$

where

$$\begin{aligned} V &= \left|E\left[\exp\left\{i\xi\sum_{j=1}^{m} a_j X_n\left(t_j,x_j\right)\right\}\right] -E\left[\exp\left\{i\xi\sum_{j=1}^{m} a_j X_n^{j,k}\right\}\right]\right|,\\ VI &= \left|E\left[\exp\left\{i\xi\sum_{j=1}^{m} a_j X_n^{j,k}\right\}\right] -E\left[\exp\left\{i\xi\sum_{j=1}^{m} a_j X^{j,k}\right\}\right]\right|,\\ VII &= \left|E\left[\exp\left\{i\xi\sum_{j=1}^{m} a_j X^{j,k}\right\}\right] -E\left[\exp\left\{i\xi\sum_{j=1}^{m} a_j X\left(t_j,x_j\right)\right\}\right]\right|. \end{aligned} \tag{62}$$

We will proceed to prove (59) in three steps.

Step 1. By the mean-value theorem, there exists a constant $C>0$ such that

$$\begin{aligned} V &\le C\max_{1\le j\le m}\left\{E\left|X_n\left(t_j,x_j\right)-X_n^{j,k}\right|\right\}\\ &= C\max_{1\le j\le m}\left\{E\left|\int_0^T\int_0^1 \left[K_H^* G_{\alpha,\delta}\left(t_j-s,x_j-y\right) -\left(K_H^* G_{\alpha,\delta}\left(t_j-s,x_j-y\right)\right)_k\right] \times\ \theta_n(s,y)\,dy\,ds\right|\right\}. \end{aligned} \tag{63}$$

Using the same method as the proof of Lemma 4, by Hölder inequality we can get

$$\begin{aligned} &E\left|\int_0^T\int_0^1 \left[K_H^* G_{\alpha,\delta}\left(t_j-s,x_j-y\right) -\left(K_H^* G_{\alpha,\delta}\left(t_j-s,x_j-y\right)\right)_k\right]\theta_n(s,y)\,dy\,ds\right|\\ &\le C\left(\int_0^T\int_0^1 \left[K_H^* G_{\alpha,\delta}\left(t_j-s,x_j-y\right) -\left(K_H^* G_{\alpha,\delta}\left(t_j-s,x_j-y\right)\right)_k\right]^2 dy\,ds\right)^{1/2}. \end{aligned} \tag{64}$$

So V uniformly converges to 0 with respect to n.

Step 2. We proceed to deal with VI. Using the mean-value theorem again,

$$\begin{aligned} VI &\le C \max_{1\le j\le m} \left\{ E\left| X_n^{j,k} - X^{j,k} \right| \right\} \\ &= C \max_{1\le j\le m} \left\{ E \left| \int_0^T \int_0^1 \left(K_H^* G_{\alpha,\delta}\left(t_j - s, x_j - y\right)\right)_k \right.\right. \\ &\qquad \times \theta_n(s,y)\, dy\, ds \\ &\qquad - \int_0^T \int_0^1 \left(K_H^* G_{\alpha,\delta}\left(t_j - s, x_j - y\right)\right)_k \\ &\qquad \left.\left. \times\ W(ds,dy) \right| \right\}. \end{aligned} \tag{65}$$

Thanks to Donsker's theorem, as $n \to \infty$, the laws of processes

$$\int_0^T \int_0^1 \left(K_H^* G_{\alpha,\delta}\left(t_j - s, x_j - y\right)\right)_k \theta_n(s,y)\, dy\, ds \tag{66}$$

converge weakly to the law of

$$\int_0^T \int_0^1 \left(K_H^* G_{\alpha,\delta}\left(t_j - s, x_j - y\right)\right)_k W(ds,dy), \tag{67}$$

since $(K_H^* G_{\alpha,\delta}(t_j - s, x_j - y))_k$ is a simple function. So we can get $VI \to 0$, as $n \to \infty$.

Step 3. Finally we deal with VII. Using the mean-value theorem again, one can get

$$\begin{aligned} VII &\le C \max_{1\le j\le m} \left\{ E\left| X^{j,k} - X\left(t_j, x_j\right)\right| \right\} \\ &= C \max_{1\le j\le m} \left\{ E \left| \int_0^T \int_0^1 \left(K_H^* G_{\alpha,\delta}\left(t_j - s, x_j - y\right)\right)_k \right.\right. \\ &\qquad \times W(ds,dy) \\ &\qquad - \int_0^T \int_0^1 K_H^* G_{\alpha,\delta}\left(t_j - s, x_j - y\right) \\ &\qquad \left.\left. \times W(ds,dy) \right| \right\}. \end{aligned} \tag{68}$$

Then by the Hölder inequality and the variance for a stochastic integral, we get

$$\begin{aligned} &E \left| \int_0^T \int_0^1 \left(K_H^* G_{\alpha,\delta}\left(t_j - s, x_j - y\right)\right)_k W(ds,dy) \right. \\ &\qquad \left. - \int_0^T \int_0^1 K_H^* G_{\alpha,\delta}\left(t_j - s, x_j - y\right) W(ds,dy) \right| \\ &\le \left(\int_0^T \int_0^1 \left[\left(K_H^* G_{\alpha,\delta}\left(t_j - s, x_j - y\right)\right)_k \right.\right. \\ &\qquad \left.\left. - K_H^* G_{\alpha,\delta}\left(t_j - s, x_j - y\right) \right]^2 dy\, ds \right)^{1/2}. \end{aligned} \tag{69}$$

So, $VII \to 0$, for all $1 \le j \le m$, as $n \to \infty$. Our proof is completed. □

As a consequence of the last two properties, we can state the following.

Theorem 7. *The family of processes $\{X_n, n \in \mathbb{N}\}$ defined by* (33) *converges in law, as n tends to infinity, in the space $\mathscr{C}([0,T]\times[0,1])$, to the process X defined by* (34).

Now, we can give the proof of Theorem 2.

Proof of Theorem 2. Let us recall first the mild solution of (5), which is given by

$$\begin{aligned} u(t,x) &= \int_0^1 G_{\alpha,\delta}(t, x-y)\, u_0(y)\, dy \\ &\quad + \int_0^t \int_0^1 G_{\alpha,\delta}(t-s, x-y)\, f(s,y,u(s,y))\, dy\, ds \\ &\quad + \int_0^t \int_0^1 K_H^* G_{\alpha,\delta}(t-s, x-y)\, W(ds,dy), \end{aligned} \tag{70}$$

and the approximation sequence toward the mild solution of (5), which fulfils

$$\begin{aligned} u_n(t,x) &= \int_0^1 G_{\alpha,\delta}(t, x-y)\, u_0(y)\, dy \\ &\quad + \int_0^t \int_0^1 G_{\alpha,\delta}(t-s, x-y)\, f(s,y,u_n(s,y))\, dy\, ds \\ &\quad + \int_0^t \int_0^1 K_H^* G_{\alpha,\delta}(t-s, x-y)\, \theta_n(s,y)\, dy\, ds, \end{aligned} \tag{71}$$

where $\{\theta_n(t,x), (t,x) \in [0,T]\times[0,1]\}$, $n \in \mathbb{N}$, stand for the Kac-Stroock process which is square integrable a.s.

Moreover, the approximating sequence u_n has continuous paths a.s., for all $n \in \mathbb{N}$ which can be obtained by using the properties of the Green function, the fact that $\theta_n \in L^2([0,T]\times[0,1])$ a.s., together with a Gronwall-type argument.

On the other hand, consider the following function:

$$\begin{aligned} \psi : \mathscr{C}([0,T]\times[0,1]) &\longrightarrow \mathscr{C}([0,T]\times[0,1]), \\ \eta &\longrightarrow z_\eta, \end{aligned} \tag{72}$$

where $\eta : [0,T]\times[0,1] \to \mathbb{R}$ is a continuous function, and

$$\begin{aligned} z_\eta(t,x) &= \int_0^1 G_{\alpha,\delta}(t, x-y)\, u_0(y)\, dy \\ &\quad + \int_0^t \int_0^1 G_{\alpha,\delta}(t-s, x-y)\, f(s,y,u_n(s,y))\, dy\, ds \\ &\quad + \eta(t,x). \end{aligned} \tag{73}$$

Then it can be proved that this last function admits a unique continuous solution. Now, according to Theorem 3.5 in Bardina et al. [21], the function ψ is continuous. Considering

$$X_n(t,x) = \int_0^t \int_0^1 K_H^* G_{\alpha,\delta}(t-s, x-y)\, \theta_n(s,y)\, dy\, ds,$$
$$X(t,x) = \int_0^t \int_0^1 K_H^* G_{\alpha,\delta}(t-s, x-y)\, W(ds, dy), \tag{74}$$

one can get that X_n converges in law in $\mathcal{C}([0,T]\times[0,1])$ to X, as n goes to infinity. On the other hand, we have that $u_n = \psi(X_n)$ and $u = \psi(X)$, and hence the continuity of ψ implies the convergence in law of u_n to u in $\mathcal{C}([0,T]\times[0,1])$. □

Conflict of Interests

The authors declare that there is no conflict of interests regarding the publication of this paper.

Acknowledgments

The authors would like to express their sincere gratitude to the editor and the anonymous referees for their valuable comments and error corrections. Xichao Sun is partially supported by Natural Science Foundation of Anhui Province: Stochastic differential equation driven by fractional noise and its application in finance (no. 1408085QA10), Natural Science Foundation of Anhui Province (no. 1408085QA09), and Key Natural Science Foundation of Anhui Education Commission (no. KJ2013A183). Junfeng Liu is partially supported by Mathematical Tianyuan Foundation of China (no. 11226198).

References

[1] J. Droniou and C. Imbert, "Fractal first order partial differential equations," *Archive for Rational Mechanics and Analysis*, vol. 182, pp. 229–261, 2004.

[2] V. V. Uchaikin and V. M. Zolotarev, *Chance and Stability, Stable Distributions and Their Applications*, Modern Probability and Statistics, 1999.

[3] L. Chen, Y. Chai, R. Wu, J. Sun, and T. Ma, "Cluster synchronization in fractional-order complex dynamical networks," *Physics Letters A*, vol. 376, no. 35, pp. 2381–2388, 2010.

[4] M. Li, W. Zhao, and C. Cattani, "Delay bound: fractal traffic passes through network servers," *Mathematical Problems in Engineering*, vol. 2013, Article ID 157636, 15 pages, 2013.

[5] M. Li, "Fractal time series—a tutorial review," *Mathematical Problems in Engineering*, vol. 2010, Article ID 157264, 26 pages, 2010.

[6] S. Cohen and A. Lindner, "A central limit theorem for the sample autocorrelations of a Lévy driven continuous time moving average process," *Journal of Statistical Planning and Inference*, vol. 143, no. 8, pp. 1295–1306, 2013.

[7] K. Jaczak-Borkowska, "Generalized BSDEs driven by fractional Brownian motion," *Statistics and Probability Letters*, vol. 83, no. 3, pp. 805–811, 2013.

[8] M. Besal and C. Rovira, "Stochastic Volterra equations driven by fractional Brownian motion with Hurst parameter $H > 1/2$," *Stochastics and Dynamics*, vol. 12, no. 4, pp. 1–24, 2012.

[9] D. T. Nguyen, "Mackey-Glass equation driven by fractional Brownian motion," *Physica A*, vol. 391, no. 22, pp. 5465–5472, 2012.

[10] Y. S. Mishura and S. V. Posashkova, "Stochastic differential equations driven by a Wiener process and fractional Brownian motion: convergence in Besov space with respect to a parameter," *Computers and Mathematics with Applications*, vol. 62, no. 3, pp. 1166–1180, 2011.

[11] M. Li and W. Zhao, "Quantitatively investigating locally weak stationarity of modified multifractional Gaussian noise," *Physica A*, vol. 391, no. 24, pp. 6268–6278, 2012.

[12] M. Li, Y. Q. Chen, J. Y. Li, and W. Zhao, "Hölder scales of sea level," *Mathematical Problems in Engineering*, vol. 2012, Article ID 863707, 22 pages, 2012.

[13] C. Mueller, "The heat equation with Lévy noise 1," *Stochastic Processes and Their Applications*, vol. 74, no. 1, pp. 67–82, 1998.

[14] J. Wu, "Fractal Burgers equation with stable Lévy noise," in *Proceedings of the 7th International Conference SPDE and Applications*, January 2004.

[15] T. Chang and K. Lee, "On a stochastic partial differential equation with a fractional Laplacian operator," *Stochastic Processes and Their Applications*, vol. 122, no. 9, pp. 3288–3311, 2012.

[16] A. Truman and J. Wu, "Fractal Burgers equation driven by Lévy noises," in *Stochastic Partial Differential Equations and Applications*, G. da Prato and L. Tubaro, Eds., vol. 245 of *Lecture Notes in Pure and Applied Mathematics*, pp. 295–310, Chapman Hall/CRC Taylor, 2006.

[17] J. Liu, L. Yan, and Y. Cang, "On a jump-type stochastic fractional partial differential equation with fractional noises," *Nonlinear Analysis: Theory, Methods & Applications*, vol. 75, no. 16, pp. 6060–6070, 2012.

[18] D. Wu, "On the solution process for a stochastic fractional partial differential equation driven by space-time white noise," *Statistics and Probability Letters*, vol. 81, no. 8, pp. 1161–1172, 2011.

[19] M. S. Taqqu, "Weak convergence to fractional brownian motion and to the rosenblatt process," *Zeitschrift für Wahrscheinlichkeitstheorie und Verwandte Gebiete*, vol. 31, no. 4, pp. 287–302, 1975.

[20] R. Delgado and M. Jolis, "Weak approximation for a class of Gaussian processes," *Journal of Applied Probability*, vol. 37, no. 2, pp. 400–407, 2000.

[21] X. Bardina, M. Jolis, and L. Quer-Sardanyons, "Weak convergence for the stochastic heat equation driven by Gaussian white noise," *Electronic Journal of Probability*, vol. 15, pp. 1267–1295, 2010.

[22] B. Boufoussi and S. Hajji, "An approximation result for a quasi-linear stochastic heat equation," *Statistics and Probability Letters*, vol. 80, no. 17-18, pp. 1369–1377, 2010.

[23] T. E. Mellall and Y. Ouknine, "Weak convergence for qualinear stochastic heat equation driven by a fractional noise with Hurst parameter $H \in ((1/2), 1)$," *Stochastics and Dynamics*, vol. 13, no. 3, pp. 1–13, 2013.

[24] L. Debbi, "On some properties of a high order. Fractional differential operator which is not in general selfadjoint," *Applied Mathematical Sciences*, vol. 1, pp. 1325–1339, 2007.

[25] L. Debbi and M. Dozzi, "On the solutions of nonlinear stochastic fractional partial differential equations in one spatial dimension," *Stochastic Processes and Their Applications*, vol. 115, no. 11, pp. 1764–1781, 2005.

[26] J. B. Walsh, "An introduction to stochastic partial differential equations," in *École d'Été de Probabilités de Saint Flour XIV—1984*, vol. 1180 of *Lecture Notes in Mathematics*, pp. 266–439, Springer, Berlin, Germany, 1986.

[27] D. Nualart and Y. Ouknine, "Regularization of quasilinear heat equation by a fractional noise," *Stochastics and Dynamics*, vol. 4, no. 2, pp. 201–221, 2004.

[28] T. Komatsu, "On the martingale problem for generators of stable processes with perturbations," *Osaka Journal of Mathematics*, vol. 21, pp. 113–132, 1984.

Hindawi Publishing Corporation
Advances in Mathematical Physics
Volume 2014, Article ID 741351, 8 pages
http://dx.doi.org/10.1155/2014/741351

Research Article

The Study of Fractional Order Controller with SLAM in the Humanoid Robot

Shuhuan Wen,[1] Xiao Chen,[1] Yongsheng Zhao,[2] Ahmad B. Rad,[3] Kamal Mohammed Othman,[3] and Ethan Zhang[3]

[1] *Key Lab of Industrial Computer Control Engineering of Hebei Province, Yanshan University, Qinhuangdao 066004, China*
[2] *Machanical Engineering, Yanshan University, Qinhuangdao 066004, China*
[3] *School of Engineering Sciences, Simon Fraser University, 250-13450, 102 Avenue, Surrey, BC, Canada V3T 0A3*

Correspondence should be addressed to Yongsheng Zhao; yszhao@ysu.edu.cn

Received 26 September 2013; Revised 15 November 2013; Accepted 17 November 2013; Published 28 January 2014

Academic Editor: Ming Li

We present a fractional order PI controller (FOPI) with SLAM method, and the proposed method is used in the simulation of navigation of NAO humanoid robot from Aldebaran. We can discretize the transfer function by the Al-Alaoui generating function and then get the FOPI controller by Power Series Expansion (PSE). FOPI can be used as a correction part to reduce the accumulated error of SLAM. In the FOPI controller, the parameters (K_p, K_i, and α) need to be tuned to obtain the best performance. Finally, we compare the results of position without controller and with PI controller, FOPI controller. The simulations show that the FOPI controller can reduce the error between the real position and estimated position. The proposed method is efficient and reliable for NAO navigation.

1. Introduction

More than 95% of the control loops are of PI/PID type in process control, but only a few of control loops work well [1]. There are some problems in PI/PID control, such as bad tuning, incorrect implementation techniques, some restrictions and limitations, and actuator and sensor problems.

Using the notion of fractional order, it may be a step closer to the real world life, because many real physical systems are well characterized by fractional order differential equations [2]. So a considerable amount of research in fractional order dynamic systems and controllers was published in scientific and engineering literature in the last few years. Modern examples of applications are bioengineering [3], physics [4], chaos theory [5], viscoelasticity [6], and many others (see, e.g., [7]). Fractional order controllers can be expressed by fractional order differential equations. Fractional order controllers have been used in industrial applications [8] and various fields such as power electronics [9], system identification [10], robotic manipulators, irrigation canal control [11], mechatronics systems [12], and heat diffusion systems [13]. In addition, the stability is an essential property of systems, for example, for the stability of conventional systems of integer order and for fractional systems. So the stability issues for fractional order have been solved [2, 14–19].

In this paper, we will study fractional order PI (FOPI) controller combined with SLAM in the navigation of humanoid robot because of the limitation of PI controller. In the FOPI controller, the parameters (K_p, K_i, and α) need to be tuned based on some design specifications. The results will be compared without controller and with PI controller, fractional order PI controller.

The rest of this paper is organized as follows: the FOPI controller used in the NAO robot navigation control is presented in Section 2, the background knowledge of SLAM and the NAO robot are described in Section 3, and the simulation results and conclusion are given in Sections 4 and 5, respectively.

2. Fractional Order PI Controller

2.1. Fractional Calculus. The fractional order $PI^{\lambda}D^{\mu}$ was proposed as a generalization of the PID controller [20]. A general fundamental operator is denoted as follows:

$$ {}_aD_t^{\alpha} = \begin{cases} \dfrac{d^{\alpha}}{dt^{\alpha}} & \mathrm{Re}(\alpha) > 0 \\ 1 & \mathrm{Re}(\alpha) = 0 \\ \displaystyle\int_a^t (d\tau)^{-\alpha}, & \mathrm{Re}(\alpha) < 0, \end{cases} \tag{1} $$

where a and t are the limit of the operation, α is the fractional order, which can be any complex number, and τ is the variable of integration.

Commonly, there are three methods to define the fractional calculus [21].

2.1.1. Grünwald-Letnikov Definition. Consider

$$ {}_aD_t^{\alpha} f(t) = \lim_{h \to 0} \frac{1}{h^{\alpha}} \sum_{j=0}^{[(t-a)/h]} (-1)^j \binom{\alpha}{j} f(t - jh), \tag{2} $$

where $\binom{\alpha}{j} = \Gamma(\alpha+1)/\Gamma(j+1)\Gamma(\alpha-j+1) = \alpha!/j!(\alpha-j)!$ is the binomial coefficient, $[\cdot]$ is the integer part, h is the calculation of step length, and $\Gamma(\bullet)$ is gamma function.

2.1.2. Riemann-Liouville Definition. Consider

$$ {}_aD_t^{\alpha} f(t) = \frac{1}{\Gamma(n-\alpha)} \frac{d^n}{dt^n} \int_a^t \frac{f(\tau)}{(t-\tau)^{\alpha-n+1}} d\tau, \quad (n-1 < \alpha < n). \tag{3} $$

2.1.3. Caputo Definition. Consider

$$ {}_aD_t^{\alpha} f(t) = \frac{1}{\Gamma(n-\alpha)} \int_a^t \frac{f^{(n)}(\tau)}{(t-\tau)^{\alpha-n+1}} d\tau, \quad (n-1 < \alpha < n). \tag{4} $$

For zero initial conditions and lower limit $a = 0$, the Laplace transform of fractional derivatives is

$$ L\left\{ {}_0D_t^{\alpha} f(t) \right\} = s^{\alpha} F(s). \tag{5} $$

2.2. Fractional Order Controller. From the definition, it is shown that the fractional order differential is different from the integer order differential. It is not to obtain the limit values at the point, but it is related to the function values from the initial time to this point time. So the fractional order PI has memory.

The typical n-term linear fractional order differential equation as is follows:

$$ \begin{aligned} &a_n D^{\beta_n} y(t) + a_{n-1} D^{\beta_{n-1}} y(t) + \cdots a_1 D^{\beta_1} y(t) + a_0 D^{\beta_0} y(t) \\ &\quad = b_n D^{\alpha_n} u(t) + b_{n-1} D^{\alpha_{n-1}} u(t) + \cdots b_1 D^{\alpha_1} u(t) \\ &\qquad + b_0 D^{\alpha_0} u(t), \end{aligned} \tag{6} $$

where α_k and β_k are arbitrary real numbers. Assuming $\alpha_k > \alpha_{k-1} > \cdots \alpha_0 > 0$, $\beta_k > \beta_{k-1} > \cdots \beta_0 > 0$ because of no loss of generality.

Assume (6) meets the zero initial condition; we can get the continuous fractional order transfer function by using Laplace transform technique:

$$ G(s) = \frac{Y(s)}{U(s)} = \frac{b_m s^{\beta_m} + b_{m-1} s^{\beta_{m-1}} + \cdots + b_0 s^{\beta_0}}{a_n s^{\alpha_n} + a_{n-1} s^{\alpha_n - 1} + \cdots + a_0 s^{\alpha_0}}. \tag{7} $$

For the discrete fractional order control system, the equation z transform is available:

$$ \begin{aligned} G(z) &= \frac{Y(z)}{U(z)} \\ &= \left(b_m \left(w\left(z^{-1}\right) \right)^{\beta_m} + b_{m-1} \left(w\left(z^{-1}\right) \right)^{\beta_{m-1}} + \cdots \right. \\ &\qquad \left. + b_0 \left(w\left(z^{-1}\right) \right)^{\beta_0} \right) \\ &\qquad \times \left(a_n \left(w\left(z^{-1}\right) \right)^{\alpha_n} + a_{n-1} \left(w\left(z^{-1}\right) \right)^{\alpha_{n-1}} + \cdots \right. \\ &\qquad \left. + a_0 \left(w\left(z^{-1}\right) \right)^{\alpha_0} \right)^{-1}, \end{aligned} \tag{8} $$

where $w(z^{-1})$ is the transform function from s domain to z domain.

In general, the discretization of continuous fractional order differentiator/integrator $s^{\pm\gamma}$ ($\gamma \in R$) can be expressed as $s^{\pm\gamma} \approx (w(z^{-1}))^{\pm\gamma}$. So the generating function and its expansion determine both the form of the approximation and the coefficients [22]. We can get different generating function because of different calculation method. As a generating function, $w(z^{-1})$, the following formula can be used in general:

$$ w\left(z^{-1}\right) = \left(\frac{1}{\mu T} \frac{1 - z^{-1}}{\gamma + (1-\gamma) z^{-1}} \right), \tag{9} $$

where μ and γ denote the gain and phase tuning parameters, respectively, and T is the sampling period. For example, when $\mu = 1$ and $\gamma = \{0, 1/2, 7/8, 1, 3/2\}$, the generating function (9) becomes the forward Euler, the Tustin, the Al-Alaoui, the backward Euler, and the implicit Adams rules, respectively [23]. We will consider the Al-Alaoui generating function of the form

$$ \left(w\left(z^{-1}\right) \right)^{\pm\gamma} = \left(\frac{8}{7T} \frac{1 - z^{-1}}{1 + (z^{-1}/7)} \right)^{\pm\gamma}. \tag{10} $$

The discretization formal for GL formula (2) is given after performing the PSE (Power Series Expansion) of $(1 - z^{-1})^{\pm\gamma}$. By using the short memory principle [24], the discrete equivalent of the fractional order integrodifferential operator $(w(z^{-1}))^{\pm\gamma}$ is given by

$$ \left(w\left(z^{-1}\right) \right)^{\pm\gamma} = T^{\mp\gamma} z^{-[L/T]} \sum_{j=0}^{[L/T]} (-1)^j \binom{\pm\gamma}{j} z^{[L/T]-j}, \tag{11} $$

where T is the sampling period, L is the memory length, and $(-1)^j \binom{\pm\gamma}{j}$ are binomial coefficients $c_j^{(r)}$ $(j = 0, 1, \ldots)$, $c_0^{(r)} = 1$, and $c_j^{(r)} = (1 - (1 + (\pm\gamma))/j)c_{j-1}^{(\gamma)}$.

We use the FOPI controller, and its transfer function can be expressed as

$$G(s) = \frac{U(s)}{E(s)} = K_p + \frac{K_i}{s^\alpha} = \frac{K_p s^\alpha + K_i}{s^\alpha}. \tag{12}$$

With the Al-Alaoui operation, we can obtain

$$\begin{aligned} G(s) = \frac{U(s)}{E(s)} &= \frac{K_p(8/7T)^\alpha \left(P_p/Q_q\right) + K_i}{(8/7T)^\alpha \left(P_p/Q_q\right)} \\ &= \frac{K_p(8/7T)^\alpha P_p + K_i Q_q}{(8/7T)^\alpha P_p}. \end{aligned} \tag{13}$$

The third order expansion by using PSE method is

$$\begin{aligned} G(s) = \frac{U(s)}{E(s)} &= \left(K_p K^\alpha \left(p_3 z^{-3} + p_2 z^{-2} + p_1 z^{-1} + 1\right)\right. \\ &\quad \left. + K_i \left(q_3 z^{-3} + q_2 z^{-2} + q_1 z^{-1} + 1\right)\right) \\ &\quad \times \left(K^\alpha \left(p_3 z^{-3} + p_2 z^{-2} + p_1 z^{-1} + 1\right)\right)^{-1}, \end{aligned} \tag{14}$$

where

$$\begin{aligned} &p_1 = -\alpha, \quad p_2 = \frac{\alpha^2 - \alpha}{2}, \quad p_3 = \frac{-\alpha^3 + 3\alpha^2 - 2\alpha}{6}, \\ &q_1 = \frac{\alpha}{7}, \quad q_2 = \frac{\alpha^2 - \alpha}{98}, \quad q_3 = \frac{\alpha^3 - 3\alpha^2 + 2\alpha}{2058}, \\ &K^\alpha = \left(\frac{8}{7T}\right)^\alpha. \end{aligned} \tag{15}$$

Equation (14) can be given by

$$\begin{aligned} G(s) = &\left(\left(K_p K^\alpha p_3 + K_i q_3\right) z^{-3} + \left(K_p K^\alpha p_2 + K_i q_2\right) z^{-2}\right. \\ &\left. + \left(K_p K^\alpha p_1 + K_i q_1\right) z^{-1} + \left(K_i + K_p K^\alpha\right)\right) \\ &\times \left(K^\alpha \left(p_3 z^{-3} + p_2 z^{-2} + p_1 z^{-1} + 1\right)\right)^{-1}. \end{aligned} \tag{16}$$

And it can be expressed as

$$\begin{aligned} &U(z) K^\alpha \left(p_3 z^{-3} + p_2 z^{-2} + p_1 z^{-1} + 1\right) \\ &= E(z) \left[\left(K_p K^\alpha p_3 + K_i q_3\right) z^{-3} + \left(K_p K^\alpha p_2 + K_i q_2\right) z^{-2}\right. \\ &\quad \left. + \left(K_p K^\alpha p_1 + K_i q_1\right) z^{-1} + \left(K_i + K_p K^\alpha\right)\right]. \end{aligned} \tag{17}$$

So we can get

$$\begin{aligned} u(t) = &\left(K_p p_3 + K_i q_3 K^\alpha\right) e(t-3) \\ &+ \left(K_p p_2 + K_i q_2 K^\alpha\right) e(t-2) \\ &+ \left(K_p p_1 + K_i q_1 K^\alpha\right) e(t-1) \\ &+ \left(K_p + K_i K^\alpha\right) e(t) \\ &- p_1 u(t-1) - p_2 u(t-2) - p_3 u(t-3). \end{aligned} \tag{18}$$

3. Background of SLAM and NAO Humanoid Robot

The simultaneous localization and mapping (SLAM) is a process by which a robot can build a map of an environment and at the same time use this map to deduce its location. In SLAM, both the trajectory of the platform and the location of all landmarks are estimated online without the need for any a priori knowledge of location [25, 26]. EKF-SLAM is very well known to navigation problems. The main steps of SLAM include robot motion prediction, new landmarks initialization, and known landmarks correction.

The observation model is

$$y = h(x) + v, \tag{19}$$

where x is robot state vector and landmark states, $h(x)$ is the observation function, and v is the measurement noise.

The covariance matrix is

$$P = FPF' + Q, \tag{20}$$

where F is Jacobian matrix and Q is the Gaussian noise.

The EKF correction step is written as

$$\begin{aligned} z &= y - h\left(x'\right), \\ Z &= HPx^T + R, \end{aligned} \tag{21}$$

where z is the innovation's mean, x' is the observation position of the robot, H is Jacobian matrix, and R is the covariance matrix of the measurement noise.

Kalman gain K is $K = PH^T Z$.

The update position of the robot is

$$x' = x' + Kz. \tag{22}$$

The correction covariance matrix is

$$P = P - KZK^T. \tag{23}$$

NAO is a new biped robot recently developed by French company Aldebaran-Robotics. This humanoid robot had been designed purposely to look approachable. With a height of 0.57 meters and weight of about 4.5 kilogram, NAO has the appealing appearance of a human toddler [27]. Based on NAO robot, the FOPI controller as the correction part is used in the SLAM simulation of NAO navigation in this paper.

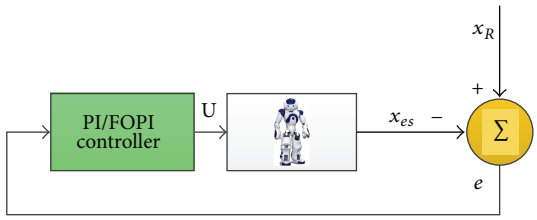

Figure 1: The correction part, where x_R is the real position and x_{es} is the EKF-estimated position.

4. Simulation Result

4.1. Control System Model. When NAO robot moves in 2D space, the motion is mainly influenced by three variables, namely, the robot current position, the control variable, and the disturbance variable. Therefore, it is very important to reduce the accumulated error for robot and effectively overcome the negative influence of disturbance variable.

NAO will deviate from a set target because there is no correction part to compensate noise of the sensors. When the control U is a fixed value, the real position and estimated position of the NAO will be largely different. So we use controller as the correction part to reduce the error. The correction part is based on the return error of the real position and estimated position of NAO. The outline of this correction part is presented in Figure 1.

4.2. Algorithm Performance Index. Because the NAO in SLAM mainly produces two kinds of errors, so the average error index of robot position, the average error index of landmarks, and the average variance index of robot position are proposed to test the performance of the controller. The average error index of robot position is the average different value between the real position and the estimated position. When NAO moves in s steps, the definition $\overline{e}$ is expressed by

$$\overline{e} = \frac{\sum_{i=1}^{s} e}{s}, \tag{24}$$

where e is the error of x_R and x_{es} and s is the number of steps.

If the number of landmarks is n and le is the error of the real landmarks and estimated landmarks, the average error index of landmarks $\overline{le}$ is defined as follows:

$$\overline{le} = \frac{\sum_{i=1}^{n} le}{n}. \tag{25}$$

According to (24) and (25), we can see that the smaller the average error, the better the control effect. But it could not judge the stability of the control system from the single average error index. So we define the average variance that shows the distribution degree of error. The average variance σ is defined as follows:

$$\sigma = \frac{\sum_{i=1}^{s} (e - \overline{e})^2}{s}. \tag{26}$$

The smaller the average variance, that is, every step error of NAO is close to the average error, the better the stability of the control.

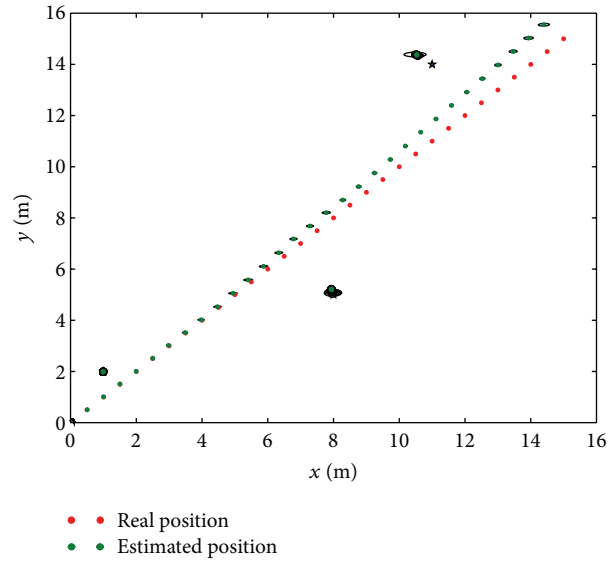

Figure 2: The simulation motion result of NAO in SLAM with the fixed U.

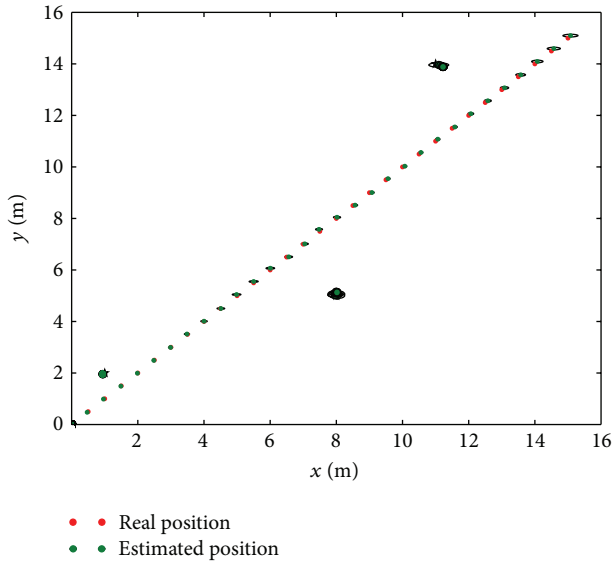

Figure 3: The simulation motion result of NAO in SLAM with PI controller.

4.3. Control Algorithm Comparison. Figures 2 and 3 show the simulation result of SLAM with the fixed U and PI controller, respectively. The three stars are the landmarks. The red points and green points are the real position and the estimated position, respectively. The circles on the green points are the covariance of the robot. The circles become smaller when the robot is near the landmark. The green circles are the estimated landmarks.

In this paper, if not specified, abscissa represents steps, and ordinate represents the error. Figure 4 shows the error of the different K_p with PI controller in EKF-SLAM. When $K_p < 0.7$, the PI controller cannot effectively adjust the control variable according to the error. And when $0.7 < K_p < 1$,

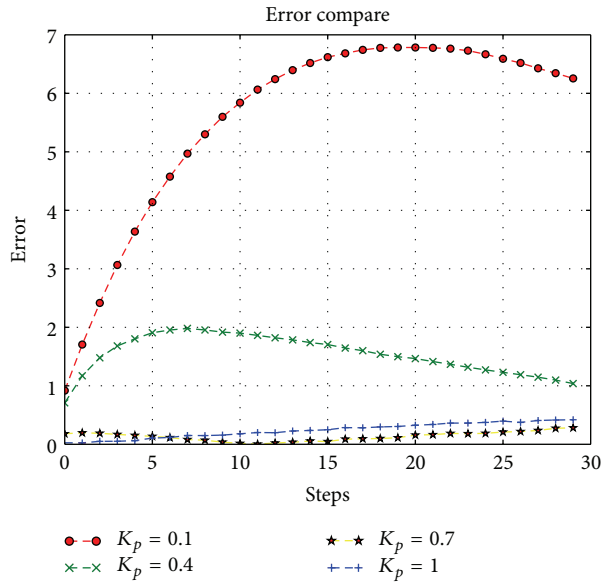

Figure 4: The error of the different K_p with PI controller.

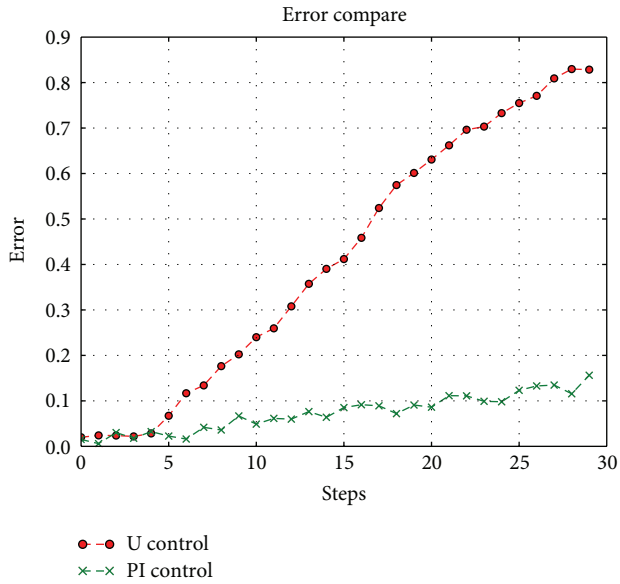

Figure 5: The comparison of the error with fixed U and PI controller.

the control variable generated from PI controller can basically make the estimated position trace to the real position. But when K_p is too large, the PI control variable cannot keep stable, so we cannot follow the estimated position of robot.

Figure 5 shows the comparison of the errors with fixed U and PI controller. It can be seen that the error with PI controller is far less than the one with the fixed U. However, when the steps of the robot motion increase, the error generated from PI controller also gradually increases. So PI controller cannot efficiently reduce the accumulated error of the robot with the increasing steps. Therefore, we use FOPI controller to decrease the error in the motion process. There are three parameters (K_p, K_i, and α) to be tuned.

Table 1: The average error index and variance index of robot position with PI/FOPI controller.

Controller	PI	FOPI
$\bar{e}$	0.074	0.015
σ	0.014	0.00005

Table 2: The average error of the real landmarks and estimated landmarks with PI/FOPI controller.

Controller	PI	FOPI
$\overline{le}$	0.167	0.083

From Figure 6, we can know that the scope of K_p is 0.7–0.9, K_i is about 0.2, and α is the value of about 0.1. In Figure 6(c), if the parameter α increases, the result of controller will become bad. But when α is too small, the effect of integral is not obvious, so the value of α is about 0.1. In the permitted range of proportional coefficient K_p and integral coefficient K_i, the FOPI error influenced by the changing of K_p or K_i will not be a linear increasing trend, and its curve will move up or down with the increasing K_p or K_i. There is a fundamental difference between FOPI controller and PI controller. The error in FOPI controller has oscillation trend, which reflects that FOPI has a better control performance.

Based on the analysis of the parameters, this paper selects the optimal parameters ($K_p = 0.7$, $K_i = 0.2$, and $\alpha = 0.1$) of FOPI controller. The simulation of motion result of EKF-SLAM with FOPI controller is given in Figure 7. We can conclude that FOPI control can keep stable and get a better dynamics performance. The NAO robot's estimated position has almost completely been close to the real position.

Figure 8 is the comparison between the optimal parameters of FOPI controller ($K_p = 0.7$, $K_i = 0.2$, and $\alpha = 0.1$) and PI controller ($K_p = 0.9$, $K_i = 0.02$). We compare them with the fixed U. The results verify the validity of FOPI controller. The average error and average variance are listed in Table 1. When NAO moves 0.5 each step, we can get that the error rate has got to 14% with PI controller and the error rate to approximately 3% with FOPI controller from Table 1. According to the index, it is shown that FOPI controller has better stability and higher accuracy. In addition, the average errors of the real landmarks and estimated landmarks with PI and FOPI controller are given in Table 2. We get the errors between the real landmarks and estimated landmarks based on the coordinates [1, 2, 5, 8, 11, 14]. In order to ensure the accuracy of simulation, we do the simulation 30 times, respectively, and get the $\overline{le}$ in Table 2. We can see that the errors between the real landmarks and estimated landmarks based on FOPI controller with EKF-SLAM are much smaller than PI controller.

From the above figures and tables we can see that the pros and cons of three control methods are very obvious. FOPI controller is superior to PI controller, and PI controller is better than the fixed U control. The error of the robot movement with FOPI controller gradually tends to zero with the increasing steps. Moreover, the error of FOPI controller will not gradually increase and remain oscillation trend

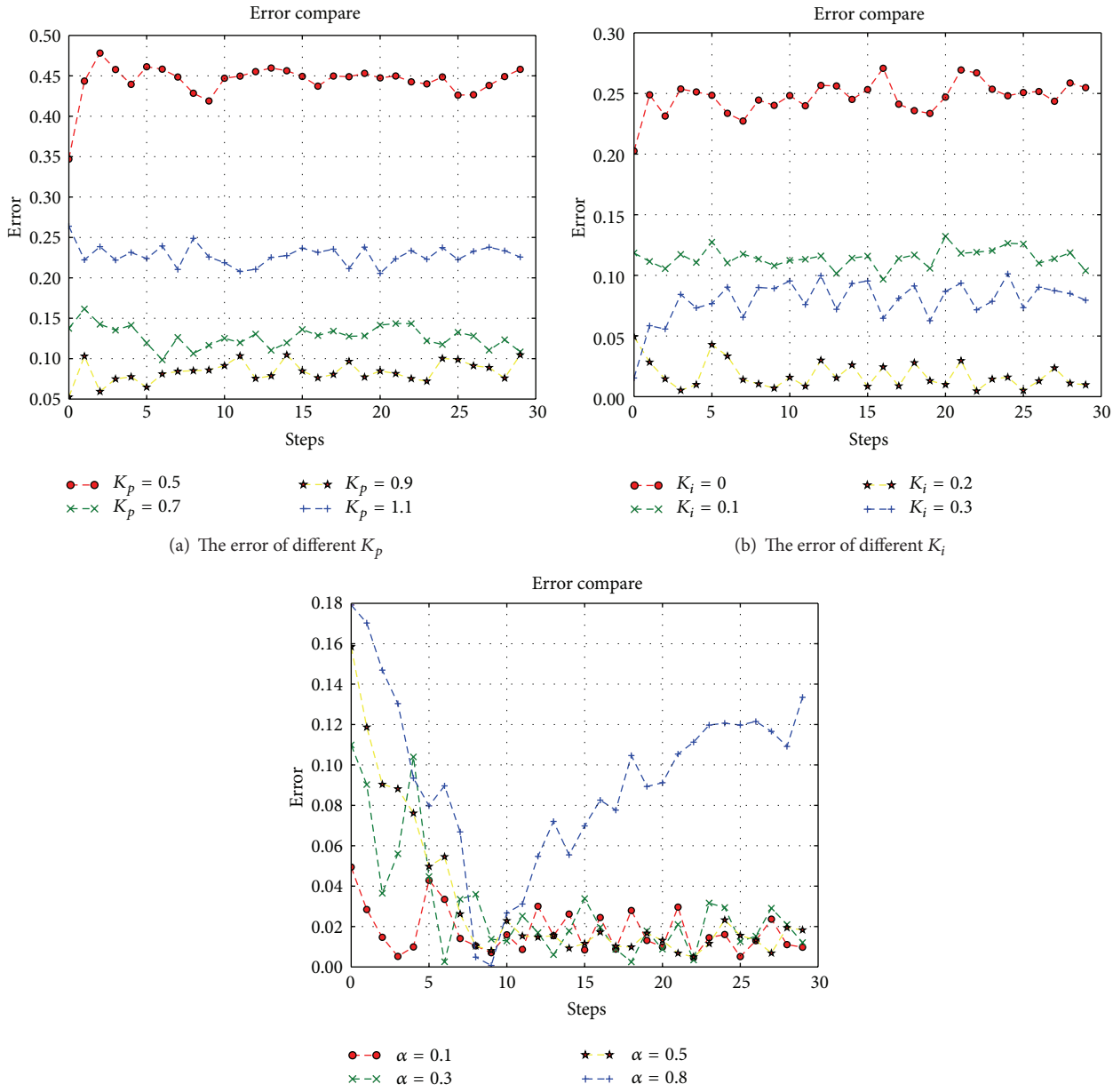

(a) The error of different K_p

(b) The error of different K_i

(c) The error of different α

FIGURE 6: The effect of three parameters (K_p, K_i, and α) of FOPI controller.

within a certain number of steps. It is shown that FOPI has a better performance than PI.

5. Conclusion

In this paper, FOPI controller with EKF-SLAM is proposed. FOPI can be applied as a correction part. FOPI controller with EKF-SLAM can effectively reduce the accumulated error. The simulation shows that the FOPI controller is better than PI controller in NAO robot. The feasibility of FOPI is valid for the error of robot position and the error of landmarks. The feasibility of the proposed algorithm is validated by simulation results. In the future work, we can apply FOPI controller with SLAM to NAO platform and do the experiment in order to finish the navigation indoors environment. In addition, it is worth studying how to generalize the two-dimensional EKF-SLAM problem to the multidimensional EKF-SLAM problem.

Conflict of Interests

The authors declare that there is no conflict of interests regarding the publication of this paper.

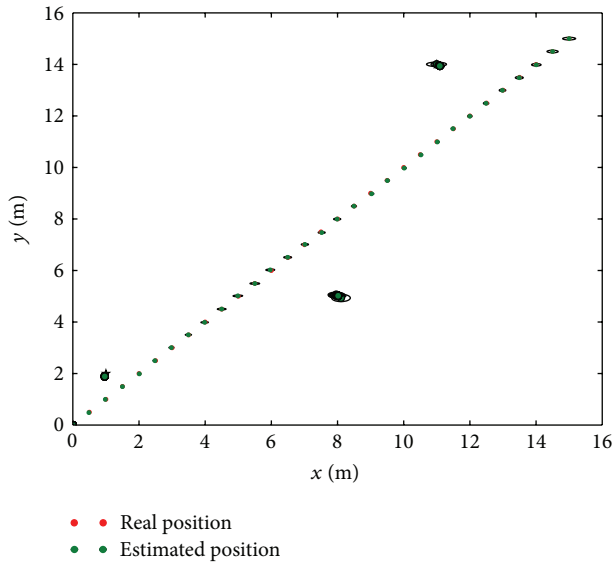

Figure 7: The simulation motion result of SLAM with FOPI controller.

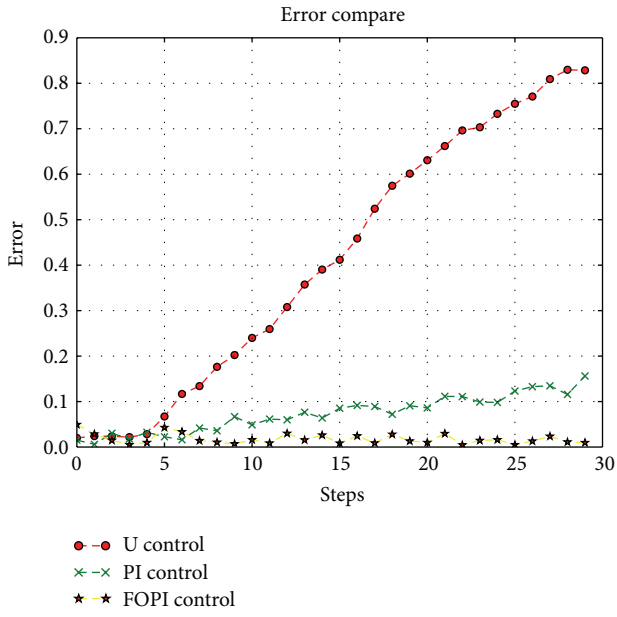

Figure 8: The comparison of the error with fixed U/PI/FOPI controller.

Acknowledgments

The work was partly supported by the National Natural Science Foundation of China (NSFC) under the Project Grant no. 51275439 and the 973 Plan under the Project no. 2013CB733003, and the Natural Science Foundation of Hebei Province of China under the project no. F2014203095.

References

[1] K. J. Astrom and T. Hagglund, *Advanced PID Control*, ISA, USA, 2006.

[2] Z. Jiao and Y. Q. Chen, "Stability of fractional-order linear time-invariant systems with multiple noncommensurate orders," *Computers & Mathematics with Applications*, vol. 64, no. 10, pp. 3053–3058, 2012.

[3] R. L. Magin, *Fractional Calculus in Bioengineering*, Begell House, 2006.

[4] R. Hilfer, *Applications of Fractional Calculus in Physics*, World Scientific, Singapore, 2000.

[5] I. Petráš, *Fractional-Order Nonlinear Systems: Modeling, Analysis and Simulation*, Springer, New York, NY, USA, 2011.

[6] F. Mainardi, *Fractional Calculus and Waves in Linear Viscoelasticity: An Introduction to Mathematical Models*, Imperial College Press, London, UK, 2010.

[7] J. Sabatier, O. P. Agrawal, and J. A. TenreiroMachado, Eds., *Advances in Fractional Calculus: Theoretical Developments and Applications in Physics and Engineering*, Springer, 2007.

[8] B. M. Vinagre, C. A. Monje, A. J. Caldern, and J. I. Surez, "Fractional PID controllers for industry application: a brief introduction," *Journal of Vibration and Control*, vol. 13, no. 9-10, pp. 1419–1429, 2007.

[9] A. J. Calderón, B. M. Vinagre, and V. Feliu, "Fractional order control strategies for power electronic buck converters," *Signal Processing*, vol. 86, no. 10, pp. 2803–2819, 2006.

[10] M. Schlegel and M. Cech, "Fractal system identification for robust control-the moment approach," in *Proceedings of the 5th International Carpathian Control Conference*, pp. 1–6, AGH-UST, Krakaw, Poland, May 2004.

[11] V. Feliu-Batlle, R. R. Pérez, and L. S. Rodríguez, "Fractional robust control of main irrigation canals with variable dynamic parameters," *Control Engineering Practice*, vol. 15, no. 6, pp. 673–686, 2007.

[12] F. Hongmei, S. Yu, and Z. Xiaobin, "Research on fractional order controller in servo press control system," in *Proceedings of the IEEE International Conference on Mechatronics and Automation (ICMA '07)*, pp. 2934–2938, August 2007.

[13] I. S. Jesus and J. A. Tenreiro Machado, "Fractional control of heat diffusion systems," *Nonlinear Dynamics*, vol. 54, no. 3, pp. 263–282, 2008.

[14] M. Li, S. C. Lim, C. Cattani, and M. Scalia, "Characteristic roots of a class of fractional oscillators," *Advances in High Energy Physics*, vol. 2013, Article ID 853925, 7 pages, 2013.

[15] M. Li, "Approximating ideal filters by systems of fractional order," *Computational and Mathematical Methods in Medicine*, vol. 2012, Article ID 365054, 6 pages, 2012.

[16] M. Li, S. C. Lim, and S. Chen, "Exact solution of impulse response to a class of fractional oscillators and its stability," *Mathematical Problems in Engineering*, vol. 2011, Article ID 657839, 9 pages, 2011.

[17] H. Hejazi, T. Moroney, and F. Liu, "Stability and convergence of a finite volume method for the space fractional advection-dispersion equation," *Journal of Computational and Applied Mathematics*, vol. 255, pp. 684–697, 2014.

[18] J. Sabatier and C. Farges, "On stability of commensurate fractional order systems," *International Journal of Bifurcation and Chaos*, vol. 22, no. 4, Article ID 1250084, 8 pages, 2012.

[19] J.-G. Lu, Y. Chen, and W. Chen, "Robust asymptotical stability of fractional-order linear systems with structured perturbations," *Computers & Mathematics with Applications*, vol. 66, no. 5, pp. 873–882, 2013.

[20] I. Podlubny, "Fractional-order systems and $PI^{\lambda}D^{\mu}$-controllers," *IEEE Transactions on Automatic Control*, vol. 44, no. 1, pp. 208–214, 1999.

[21] I. Podlubny, *Fractional Differential Equations*, Academic Press, San Diego, Calif, USA, 1999.

[22] Ch. Lubich, "Discretized fractional calculus," *SIAM Journal on Mathematical Analysis*, vol. 17, no. 3, pp. 704–719, 1986.

[23] I. Petras, "An adaptive fractional-order controller," in *Proceedings of the 14th IEEE International Carpathian Control Conference (ICCC '13)*, pp. 297–2301, Rytro, Poland, May 2013.

[24] I. Podlubny, "Fractional-order systems and fractional order controllers," Technical Report UEF-03-94, Slovak Academy of Sciences. Institute of Experimental Physics, Department of Control Engineering. Faculty of Mining, University of Technology, Kosice, Slovak Republic, 1994.

[25] H. Durrant-Whyte and T. Bailey, "Simultaneous localization and mapping. Part I: the essential algorithms," *IEEE Robotics and Automation Magazine*, vol. 13, no. 2, pp. 99–108, 2006.

[26] T. Bailey and H. Durrant-Whyte, "Simultaneous localization and mapping (SLAM). Part II: state of the art," *IEEE Robotics and Automation Magazine*, vol. 13, no. 3, pp. 108–117, 2006.

[27] S. Shamsuddin, L. I. Ismail, H. Yussof et al., "Humanoid robot NAO: review of control and motion exploration," in *Proceedings of the IEEE International Conference on Control System, Computing and Engineering (ICCSCE '11)*, pp. 511–5516, Penang, Malaysia, November 2011.

Hindawi Publishing Corporation
Advances in Mathematical Physics
Volume 2013, Article ID 232160, 12 pages
http://dx.doi.org/10.1155/2013/232160

Research Article

Vibration Control of Fractionally-Damped Beam Subjected to a Moving Vehicle and Attached to Fractionally-Damped Multiabsorbers

Hashem S. Alkhaldi,[1] Ibrahim M. Abu-Alshaikh,[1] and Anas N. Al-Rabadi[2]

[1] *Mechanical Engineering Department, The University of Jordan, Amman 11942, Jordan*
[2] *Computer Engineering Department, The University of Jordan, Amman 11942, Jordan*

Correspondence should be addressed to Anas N. Al-Rabadi; a.alrabadi@ju.edu.jo

Received 8 September 2013; Accepted 6 November 2013

Academic Editor: Ming Li

This paper presents the dynamic response of Bernoulli-Euler homogeneous isotropic fractionally-damped simply-supported beam. The beam is attached to multi single-degree-of-freedom (SDOF) fractionally-damped systems, and it is subjected to a vehicle moving with a constant velocity. The damping characteristics of the beam and SDOF systems are described in terms of fractional derivatives. Three coupled second-order fractional differential equations are produced and then they are solved by combining the Laplace transform with the decomposition method. The obtained numerical results show that the dynamic response decreases as (a) the number of absorbers attached to the beam increases and (b) the damping-ratios of used absorbers and beam increase. However, there are some critical values of fractional derivatives which are different from unity at which the beam has less dynamic response than that obtained for the full-order derivatives model. Furthermore, the obtained results show very good agreements with special case studies that were published in the literature.

1. Introduction

Many physical problems were adequately described by differential equations of fractional order. The list of these problems is long and the areas of applications are broad. Polymeric damping, fluid mechanics, and the theory of viscoelasticity [1–8] are some of these applications. The solution in the closed form to a class of SDOF fractional oscillators subjected to an impulse response is investigated [9]. Relationship between fractional oscillator processes and the corresponding fractional Brownian motion processes is well established in research. However, the increment process of fractional Brownian motion can be described by a random function with long-range dependence fractional Gaussian noise model [10]. A fractal time series is taken as the solution of differential equation of a fractional order, or a response of a fractional system, or a fractional filter driven with a white noise in the domain of stochastic processes [11, 12]. A general approach for approximating ideal filters that are based on fractional calculus from the point of view of systems of fractional order was introduced [13, 14]. A new direct operational inversion method is introduced for solving coupled linear systems of ordinary fractional differential equations, where the obtained solutions are expressed explicitly in terms of multivariate Mittag-Leffler functions [9, 15, 16]. The solutions of fractional Langevin equation of two different orders which are known as the fractional Ornstein-Uhlenbeck processes, based on Weyl and Riemann-Liouville fractional derivatives were obtained [9, 17]. Power-laws-type data may further, in earthquake and wind engineering applications, be governed by stochastically differential equations of fractional order [18, 19]. Analysis of signals generated by fractional-order process and applications of such model in a wide range of physical, mechanical, and biological systems are discussed in [20]. However, as noted from the literature, a clear physical interpretation of the fractional derivative has been elusive. Good examples are (1) transverse vibration of homogeneous beams whose damping behavior is described by a fractional derivative of predefined

constant orders was an important subject of matter [11, 21–24]; (2) diffusion process where fractional differential equations have been employed to describe an anomalous diffusion regime including both subdiffusion and superdiffusion [25]; and (3) many linear viscoelastic damping materials exhibit a macroscopic constitutive behavior which has been the subject of many investigations involving fractional order derivative [26]. However, in the fractional-derivative model of viscoelastic materials over extended ranges of time and frequency, the deformation work corresponding to springs and losses corresponding to dashpots (described by fractional derivatives) have both energy types (stored and dissipated) at any point of the utilized materials [27, 28].

The dynamic response characteristics of beams resulting from the passage of different moving load systems, and with the existence of dampers and oscillators, have been studied within many applications. Some of the applications consist of the vibrations existing in bridges, aircraft carriers, and railroad tracks due to moving vehicles, and vibrations existing in pipeline systems due to fluid flows [29–31]. One of the main objectives of studying such problems is to minimize or to suppress the dynamic response characteristics or vibration levels of beams when subjected to different load systems. The simplest and most economical way to achieve this objective is by having different lumped appendages attached to the beam at different locations. In investigating the dynamic response of beams, if the travelling force is constant, then the time-dependent coefficients can be obtained in analytical forms [32] which make it easy to find a solution to any particular problem. However, in many cases, it is not just the response of the beam (which is a function of the spatial variable and time and depends on several parameters such as beam characteristics, the magnitude of the force, its velocity, number of appendages attached to the beam, and their locations) that the designer is interested in. However, it has long been observed that, as a structure is subjected to moving loads, the induced dynamic deflection and stress can be significantly higher than those observed in the static case [33]. In this regard, the majority of the literature has been devoted to the study of the so-called moving force [34], moving mass [35–38], moving oscillator problems [39–41], and multiple moving oscillators [42].

The vibration of a beam excited by a moving unmaintained oscillator is discussed in [43]. In this study, for certain values of system parameters and travelling speeds of the moving oscillator, separation of the oscillator from the beam can occur frequently and even more than once during the travel of the load [43]. The problem of an oscillator traversing on an elastically-supported continuum is studied, whereas the flexibility in the boundaries of the continuum is modeled by linear-transverse springs [33]. Green functions formulation to analyze the free vibration of a linear undamped beam subjected to grounded SDOF oscillators appendages at different discrete points is used [44], where researchers compared their results with the approximate solution obtained by Galarkin's method.

Searching the relevant literature shows only few papers dealing with the vibration of beams with constant values for the fractional damping behavior [23, 24, 45]. However, in this study, the fractional damping behaviors of the beam and absorbers are taken with arbitrary orders. Therefore, this study is important for the following key reasons: the damping behavior of the dynamic response of the beam can be analyzed over a continuous wide range by means of fractional-derivative parameters. Moreover, the fractional derivative damping behavior may better converge to realistic experimental models than the well-known first order damping model. Hence, the fractional derivative model may precisely prescribe a nonlinear damping behavior than other existing damping models.

In this paper, a homogeneous isotropic Euler beam with different appendages attached at different locations subjected to a uniformly moving vehicle is investigated. The solution to the handled problem is based on decomposing the generalized transverse displacements of the beam, attached oscillators, and the moving vehicle into infinite series components. Then, the generalized displacements are recursively solved by in the Laplace transform domain. The solutions in this work mainly focus on the following characteristics: the maximum response of the beam for a given velocity of the vehicle, the maximum response over all possible velocities and the velocity at which it occurs, the optimal beam and absorbers fractional-damping characteristics, and the effect of the number of attached absorbers.

2. Formulation of the Problem

Transverse vibration of Bernoulli-Euler homogeneous isotropic fractionally-damped simply-supported beam is investigated. The beam is assumed to be subjected to a vehicle moving from left-to-right with a constant velocity (v). The governing equation of the beam under investigation, whose damping characteristics are described by a fractional derivative of order β, can be written as

$$EI\frac{\partial^4 w(x,t)}{\partial x^4} + C\frac{\partial^\beta w(x,t)}{\partial t^\beta} + \mu\frac{\partial^2 w(x,t)}{\partial t^2} = -m_v(\ddot{q}-g)\,\delta(x-vt)\,H\left(\frac{L}{v}-t\right) - \sum_{i=1}^{N}\widehat{M}_i\ddot{\widehat{z}}_i(t)\,\delta(x-d_i), \quad x\in(0,L), t>0, \tag{1a}$$

$$\text{BC's: } w(0,t)=0,\quad w(L,t)=0,\quad w_{xx}(0,t)=0,\quad w_{xx}(L,t)=0, \tag{1b}$$

$$\text{IC's: } w(x,0)=0,\qquad \frac{dw(x,0)}{dt}=0, \tag{1c}$$

where $H(\cdot)$ refers to the unit step Heaviside function and $\delta(\cdot)$ refers to the Kronecker delta function. The equations corresponding to the N-SDOF absorbers that are appendaged to the beam are given as

$$\widehat{M}_i\ddot{\widehat{z}}_i(t) = \widehat{K}_i\left[w(d_i,t)-\widehat{z}_i(t)\right] + \widehat{C}_i\frac{d^\gamma\left[w(d_i,t)-\widehat{z}_i(t)\right]}{dt^\gamma}, \quad t>0, \tag{2a}$$

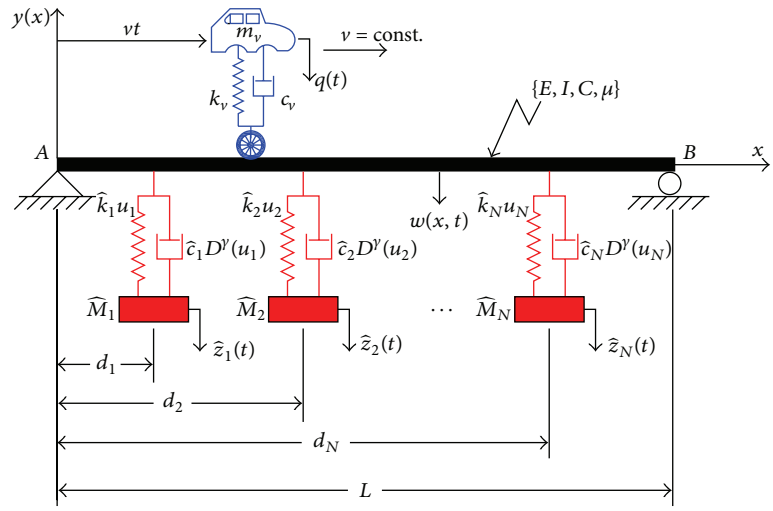

FIGURE 1: A Simply-supported beam attached to N-absorbers and subjected to a moving vehicle with a constant speed.

$$\text{IC's: } \widehat{z}_i(0) = 0, \quad \frac{d\widehat{z}_i(0)}{dt} = 0. \tag{2b}$$

The equations corresponding to the moving vehicle can be expressed as

$$m_v\left(\ddot{q}(t) - g\right) = k_v\left[w(vt,t) - q(t)\right] + c_v\frac{d\left[w(vt,t) - q(t)\right]}{dt}, \quad 0 < t < \frac{v}{L}, \tag{3a}$$

$$\text{IC's: } q(0) = 0, \quad \frac{dq(0)}{dt} = 0, \tag{3b}$$

where the beam is assumed to be initially at rest and $\{L, E, I, \mu, C\}$ are the length, modulus of elasticity, moment of inertia of cross-sectional area (A), mass per unit length, and the coefficient of external damping of the beam, respectively. Furthermore, these values are assumed to be constants. The N-rigid-body SDOF fractionally-damped absorbers of order γ, masses $\widehat{M}_i$, stiffnesses $\widehat{K}_i$, and damping constants $\widehat{C}_i$ are attached to the beam, as shown in Figure 1 (for $i = 1, 2, \ldots, N$). These elements are located at distances d_i measured from the left-end of the beam. However, the parameters $\{m_v, k_v, c_v\}$ refer to mass, stiffness, and damping constants of the vehicle, respectively. Furthermore, the set $\{w(x,t), \widehat{z}_i(t), q(t)\}$ represents the beam transverse deflection at location (x) and time (t), the transverse dynamic displacements of the masses $\widehat{M}_i$, and vehicle's transverse displacement, respectively.

Equations that are similar to (1a), (1b), (1c), (2a), (2b), (3a), and (3b) are presented in [42], but with the conventional first order derivative damping behaviors. The fractional derivatives of order β or γ, presented in (1a) and (2a), may be defined in many ways [47]. Among these are the two most frequently encountered, the Riemann-Liouville and Caputo fractional derivatives of order β which are defined by the following convolution integrals, respectively:

$$\frac{\partial^\beta w(x,t)}{\partial t^\beta} = \frac{1}{\Gamma(k-\beta)}\frac{\partial^k}{\partial t^k}\int_0^t \frac{w(x,u)}{(t-u)^{\beta+1-k}}du, \tag{4a}$$

$$\frac{\partial^\beta w(x,t)}{\partial t^\beta} = \frac{1}{\Gamma(k-\beta)}\int_0^t \frac{1}{(t-u)^{\beta+1-k}}\frac{\partial^k w(x,u)}{\partial u^k}du, \tag{4b}$$

where k is a positive integer such that $(k-1 \le \beta < k)$.

In modal form, the transverse deflection of the simply-supported beam can be written as [31, 32]:

$$w(x,t) = \sum_{n=1}^{\infty} Y_n(t)\, X_n(x), \tag{5}$$

where $Y_n(t)$ is the generalized displacement or the modal response of the beam and $X_n(x)$ are the normal modes of the undamped free vibration of the simply-supported beam written as [46]

$$X_n(x) = \sin(\kappa_n x), \tag{6}$$

where $(\kappa_n = n\pi/L)$ is the frequency parameter associated with the simply-supported beam. Equation (6) should satisfy the following fourth-order partial differential equation:

$$EI\frac{\partial^4 X_n(x)}{\partial x^4}Y_n(t) + \mu\frac{\partial^2 Y_n(t)}{\partial t^2}X_n(x) = 0. \tag{7}$$

Substituting (5) into (1a), (2a), and (3a) leads to the following coupled-system of fractional differential equations:

$$\begin{aligned} EI\sum_{n=1}^{\infty} Y_n(t)\frac{d^4 X_n(x)}{dx^4} + C\sum_{n=1}^{\infty}\frac{d^\beta Y_n(t)}{dt^\beta}X_n(x) \\ + \mu\sum_{n=1}^{\infty}\frac{d^2 Y_n(t)}{dt^2}X_n(x) \\ = -m_v\left(\ddot{q} - g\right)\delta(x - vt)\, H\left(\frac{L}{v} - t\right) \\ - \sum_{i=1}^{N}\widehat{M}_i\ddot{\widehat{z}}_i(t)\,\delta\left(x - d_i\right), \end{aligned} \tag{8a}$$

$$\widehat{M}_i\ddot{\widehat{z}}_i(t) = -\left(\widehat{K}_i\widehat{z}_i(t) + \widehat{C}_i\frac{d^\gamma\widehat{z}_i(t)}{dt^\gamma}\right) + \sum_{r=1}^{\infty}\left(\widehat{K}_iY_r(t)X_r(d_i) + \widehat{C}_i\frac{d^\gamma Y_r(t)}{dt^\gamma}X_r(d_i)\right), \tag{8b}$$

$$m_v\ddot{q}(t) = m_vg - \left(k_vq(t) + c_v\frac{dq(t)}{dt}\right) + \sum_{p=1}^{\infty}\left(k_vY_p(t)X_p(vt) + c_v\frac{dY_p(t)}{dt}X_p(vt)\right). \tag{8c}$$

Multiplying (8a) by $X_m(x)$ and integrating over the domain $(0 \le x \le L)$ yields

$$\begin{aligned}&\sum_{n=1}^{\infty}\int_0^L EIY_n(t)\frac{d^4X_n(x)}{dx^4}X_m(x)\,dx + \sum_{n=1}^{\infty}\int_0^L\frac{d^\beta Y_n(t)}{dt^\beta}CX_n(x)X_m(x)\,dx + \sum_{n=1}^{\infty}\int_0^L\frac{d^2Y_n(t)}{dt^2}\mu X_n(x)X_m(x)\,dx \\ &= -\int_0^L m_v(\ddot{q}-g)X_m(x)\delta(x-vt)H\left(\frac{L}{v}-t\right)dx - \sum_{i=1}^{N}\int_0^L\widehat{M}_i\ddot{\widehat{z}}_i(t)X_m(x)\delta(x-d_i)\,dx.\end{aligned} \tag{9}$$

The dynamic response of the beam represented by (1a) is analyzed after projecting the 4th order partial derivative into a complete orthogonal basis. For the present problem, the eigenfunctions of the linear operator representing the simply-supported beam without appendages given in (6) can be used. These eigenfunctions should satisfy the following orthogonality conditions [32, 42]:

$$\int_0^L\mu X_n(x)X_m(x)\,dx = \frac{\mu L}{2}\delta_{nm}, \tag{10a}$$

$$\int_0^L\left(EIX_n''(x)\right)''X_m(x)\,dx = \frac{EIn^4\pi^4}{2L^3}\delta_{nm}, \quad \text{for } n,m = 1,2,3,\ldots. \tag{10b}$$

By considering these orthogonality conditions, the differential equation of the nth mode of the generalized beam-displacement, (9), can be rewritten as

$$\sum_{n=1}^{\infty}Y_n(t)\frac{EIn^4\pi^4}{2L^3}\delta_{nm} + \sum_{n=1}^{\infty}\frac{d^\beta Y_n(t)}{dt^\beta}\frac{CL}{2}\delta_{nm} + \sum_{n=1}^{\infty}\frac{d^2Y_n(t)}{dt^2}\frac{\mu L}{2}\delta_{nm} = -m_v(\ddot{q}-g)X_m(vt)H\left(\frac{L}{v}-t\right) - \sum_{i=1}^{N}\widehat{M}_i\ddot{\widehat{z}}_i(t)X_m(d_i). \tag{11}$$

Substituting (6) into (8a), (8b), (8c), and (11) and noting that $(m = n)$ lead to the following coupled system of fractional differential equations:

$$\frac{d^2Y_n(t)}{dt^2} + 2\omega_n\zeta_n\frac{d^\beta Y_n(t)}{dt^\beta} + \omega_n^2Y_n(t) = -\eta_1\left(m_v(\ddot{q}-g)\sin(\Omega_nt)H\left(\frac{L}{v}-t\right) + \sum_{i=1}^{N}\widehat{M}_i\ddot{\widehat{z}}_i(t)\sin\left(\frac{\Omega_nd_i}{v}\right)\right), \tag{12a}$$

$$\ddot{\widehat{z}}_i(t) = -\left(\widehat{\omega}_i^2\widehat{z}_i(t) + 2\widehat{\omega}_i\widehat{\zeta}_i\frac{d^\gamma\widehat{z}_i(t)}{dt^\gamma}\right) + \sum_{r=1}^{\infty}\left[\widehat{\omega}_i^2Y_r(t)\sin\left(\frac{\Omega_rd_i}{v}\right) + \frac{d^\gamma Y_r(t)}{dt^\gamma}2\widehat{\omega}_i\widehat{\zeta}_i\sin\left(\frac{\Omega_rd_i}{v}\right)\right], \tag{12b}$$

$$\ddot{q}(t) = g - \left(\omega_v^2q(t) + 2\omega_v\zeta_v\frac{dq(t)}{dt}\right) + \sum_{p=1}^{\infty}\left(\omega_v^2Y_p(t)\sin(\Omega_pt) + 2\omega_v\zeta_v\frac{dY_p(t)}{dt}\sin(\Omega_pt)\right), \tag{12c}$$

where

$$\omega_n = \kappa_n^2\sqrt{\frac{EI}{\mu}}, \quad \zeta_n = \frac{C}{2\mu\omega_n}, \quad \widehat{\zeta}_i = \frac{\widehat{C}_i}{2\widehat{M}_i\omega_i}, \quad \zeta_v = \frac{c_v}{2m_v\omega_v}, \quad \omega_v = \sqrt{\frac{k_v}{m_v}}, \quad \widehat{\omega}_i = \sqrt{\frac{\widehat{K}_i}{\widehat{M}_i}}, \quad \Omega_n = \frac{n\pi v}{L} \tag{13}$$

are the undamped natural circular frequency (ω_n), beam damping ratio (ζ_n), ith oscillator damping ratio ($\widehat{\zeta}_i$), vehicle damping ratio (ζ_v), the natural frequency of the vehicle (ω_v), the natural frequency of the ith oscillator ($\widehat{\omega}_i$), and the load frequency (Ω_n), respectively, where ($\eta_1 = 2/\mu L$).

To find the solution of the system in (12a), (12b), and (12c), associated with the boundary and initial conditions given in (1b), (1c), (2b), and (3b), the dependent variables $Y_n(t)$, $\widehat{z}_i(t)$, and $q(t)$ can be decomposed into the following infinite series:

$$Y_n(t) = \sum_{k=0}^{\infty} Y_n^k(t) = Y_n^0(t) + Y_n^1(t) + Y_n^2(t) + \cdots, \quad (14a)$$

$$\widehat{z}_i(t) = \sum_{k=0}^{\infty} \widehat{z}_i^k(t) = \widehat{z}_i^0(t) + \widehat{z}_i^1(t) + \widehat{z}_i^2(t) + \cdots, \quad (14b)$$

$$q(t) = \sum_{k=0}^{\infty} q^k(t) = q^0(t) + q^1(t) + q^2(t) + \cdots, \quad (14c)$$

where $Y_n^k(t)$, $\widehat{z}_i^k(t)$, and $q^k(t)$ for $(k = 0, 1, 2, \ldots)$ are the components of $Y_n(t)$, $\widehat{z}_i(t)$, and $q(t)$, respectively. The components of $Y_n(t)$, $\widehat{z}_i(t)$, and $q(t)$ can be determined recursively, by substituting (14a), (14b), and (14c) into (12a), (12b), and (12c), from the following equations:

$$\frac{d^2Y_n^0(t)}{dt^2} + \omega_n^2 Y_n^0(t) = \eta_1 m_v g \sin(\Omega_n t) H\left(\frac{L}{v} - t\right), \quad (15a)$$

$$\frac{d^2 z_i^0(t)}{dt^2} = \sum_{r=1}^{\infty} \sin\left(\frac{\Omega_r d_i}{v}\right)\left[\widehat{\omega}_i^2 Y_r^0(t) + \frac{d^{\gamma}Y_r^0(t)}{dt^{\gamma}} 2\widehat{\omega}_i\widehat{\zeta}_i\right], \quad (15b)$$

$$\frac{d^2q^0(t)}{dt^2} = g + \sum_{p=1}^{\infty} \sin(\Omega_p t)\left(\omega_v^2 Y_p^0(t) + 2\omega_v\zeta_v\frac{dY_p^0(t)}{dt}\right), \quad (15c)$$

$$\frac{d^2Y_n^{k+1}(t)}{dt^2} + \omega_n^2 Y_n^{k+1}(t) = -2\omega_n\zeta_n\frac{d^{\beta}Y_n^k(t)}{dt^{\beta}} - \eta_1\left(m_v\frac{d^2q^k(t)}{dt^2}\sin(\Omega_n t) H\left(\frac{L}{v} - t\right) + \sum_{i=1}^{N}\widehat{M}_i\frac{d^2z_i^k(t)}{dt^2}\sin\left(\frac{\Omega_n d_i}{v}\right)\right), \quad (15d)$$

$$\frac{d^2z_i^{k+1}(t)}{dt^2} = -\left(\widehat{\omega}_i^2 z_n^k(t) + 2\widehat{\omega}_i\widehat{\zeta}_i\frac{d^{\gamma}z_n^k(t)}{dt^{\gamma}}\right) + \sum_{r=1}^{\infty}\sin\left(\frac{\Omega_r d_i}{v}\right)\left[\widehat{\omega}_i^2 Y_r^{k+1}(t) + \frac{d^{\gamma}Y_r^{k+1}(t)}{dt^{\gamma}}2\widehat{\omega}_i\widehat{\zeta}_i\right], \quad (15e)$$

$$\frac{d^2q^{k+1}(t)}{dt^2} = -\left(\omega_v^2 q^k(t) + 2\omega_v\zeta_v\frac{dq^k(t)}{dt}\right) + \sum_{p=1}^{\infty}\sin(\Omega_p t)\left(\omega_v^2 Y_p^{k+1}(t) + 2\omega_v\zeta_v\frac{dY_p^{k+1}(t)}{dt}\right), \quad (15f)$$

for $k \geq 0$. Now, using the Laplace transform for the Caputo fractional derivative which is defined in (4b) as [47]

$$\ell\left(\frac{d^{\beta}Y_n^k(t)}{dt^{\beta}}\right) = s^{\beta}y_n^k(s) - \sum_{j=0}^{m-1} s^{\beta-j-1}\left(y_n^k\right)^j(0), \quad \text{for } m-1 < \beta \leq m, \quad (16)$$

the Laplace transforms of (14a), (14b), (14c), (15a), (15b), (15c), (15d), (15e), and (15f), with the related homogeneous initial conditions, can be rewritten as

$$y_n(s) = \sum_{k=0}^{\infty} y_n^k(s), \quad (17a)$$

$$Z_i(s) = \sum_{k=0}^{\infty} Z_i^k(s), \quad (17b)$$

$$Q(s) = \sum_{k=0}^{\infty} Q^k(s), \quad (17c)$$

where

$$y_n^0(s) = \frac{\eta_1 m_v g}{(s^2 + \omega_n^2)}\ell\left(\sin(\Omega_n t) H\left(\frac{L}{v} - t\right)\right), \quad (18a)$$

$$Z_i^0(s) = \sum_{r=1}^{\infty}\sin\left(\frac{\Omega_r d_i}{v}\right)\left(\frac{\widehat{\omega}_i^2 + 2\widehat{\omega}_i\widehat{\zeta}_i s^{\gamma}}{s^2}\right)y_r^0(s), \quad (18b)$$

$$Q^0(s) = \frac{g}{s^3} + \sum_{p=1}^{\infty}\left(\frac{\omega_v^2\ell\left(\sin(\Omega_p t)Y_p^0(t)\right)}{s^2} + \frac{2\omega_v\zeta_v\ell\left(\sin(\Omega_p t)\left(dY_p^0(t)/dt\right)\right)}{s^2}\right), \quad (18c)$$

$$y_n^{k+1}(s) = -\frac{2\omega_n\zeta_n s^{\beta}}{(s^2 + \omega_n^2)} - \eta_1\left(\frac{m_v\ell\left(d^2q^k(t)/dt^2\sin(\Omega_n t) H(L/v - t)\right)}{(s^2 + \omega_n^2)} + \sum_{i=1}^{N}\frac{\widehat{M}_i s^2 Z_i^k(s)\sin(\Omega_n d_i/v)}{(s^2 + \omega_n^2)}\right), \quad (18d)$$

$$Z_i^{k+1}(s) = -\left(\widehat{\omega}_i^2 \frac{Z_i^k(s)}{s^2} + 2\widehat{\omega}_i\widehat{\zeta}_i \frac{s^\gamma Z_i^k(s)}{s^2}\right) + \sum_{r=1}^{\infty} \sin\left(\frac{\Omega_r d_i}{v}\right)\left[\widehat{\omega}_i^2 \frac{y_r^{k+1}(s)}{s^2} + 2\widehat{\omega}_i\widehat{\zeta}_i \frac{s^\gamma y_r^{k+1}(s)}{s^2}\right], \tag{18e}$$

$$Q^{k+1}(s) = -\left(\frac{\omega_v^2 Q^k(s)}{s^2} + \frac{2sQ^k(s)\,\omega_v\zeta_v}{s^2}\right) + \sum_{p=1}^{\infty}\left(\frac{\omega_v^2 \ell\left(\sin\left(\Omega_p t\right) Y_p^{k+1}(t)\right)}{s^2} + \frac{2\omega_v\zeta_v \ell\left(\sin\left(\Omega_p t\right)\left(dY_p^{k+1}(t)/dt\right)\right)}{s^2}\right), \tag{18f}$$

for $k \geq 0$ and $(i = 1, 2, \ldots, N)$, where N is the number of the SDOF fractionally-damped absorbers attached to the beam. In the above equations $\ell(\cdot)$designates the Laplace transform of $(\cdot)$ where $(\ell(\widehat{z}_i(t)) = Z_i(s)$, $\ell(Y_n(t)) = y_n(s)$ and $(\ell(q(t)) = Q(s)$. Nevertheless, the explicit forms of (18a), (18b), (18c), (18d), and (18e) for $k \geq 0$ are rather long and complex. However, when the damping effect is fractional, these equations contain the well-known hepergeometric function defined as [48]

$$\text{hypergeom}\left([n_1], [d_1, d_2], z\right) = \sum_{k=0}^{\infty} \frac{z^k\left(\Gamma\left(n_1 + k\right)/\Gamma\left(n_1\right)\right)}{k!\left(\prod_{j=1}^{2}\left(\Gamma\left(d_j + k\right)/\Gamma\left(d_j\right)\right)\right)}. \tag{19}$$

The term-by-term inversion of (18a), (18b), (18c), (18d), and (18e) with (14a), (14b), and (14c) represents the corresponding solution of the handled problem. However, many problems can be treated as special cases of (18a), (18b), (18c), (18d), and (18e); the absorbers can be neglected by assuming that $(\widehat{\omega}_i = 0)$ and the moving vehicle can be treated as a moving load by assuming ($\zeta_v = 1$ and $k_v = 1$) or by replacing the Heaviside step function by unity, where (in this case) the gravity acceleration (g) is further replaced by the intensity of the moving load.

3. Results and Discussion

In this Section, two examples are given to verify the validity of the formal technique used in this paper. Moreover, three more important case studies are introduced to show the effect of fractional-damping behaviors for both of the beam and the SDOF absorbers and the effect of the number of SDOF absorbers attached to the beam (N). In all case studies, the dynamic response of the beam is mainly governed by the fundamental mode $(n = 1)$ of the beam because this mode has the significant effect on the beam dynamic response.

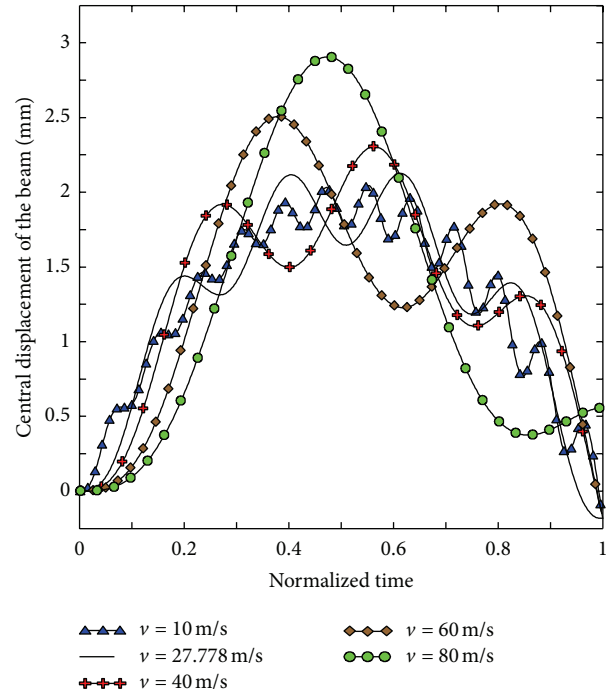

Figure 2: The dynamic response of an elastic beam at mid-span for many load speeds.

3.1. Verification Problem I. This example verifies the validity of the technique used in this paper. In this example, an undamped beam with a moving oscillator is investigated [49]. The parameters adopted for the beam under investigation are given in Table 1. The displacement response for the beam versus the normalized time is shown in Figure 2; that is, when $(t = 0)$ the load enters the beam from left-hand side $(x = 0)$ and when $(t = L/v)$ the moving load system leaves the right-hand side of the beam $(x = L)$. The curves of Figure 2 show the dynamic mid-span displacement response of the beam for the five cases of traveling velocities: $v = 10$ m/s, $v = 27.778$ m/s, $v = 40$ m/s, $v = 60$ m/s, and $v = 80$ m/s, respectively.

In this example, it is shown that the dynamic displacement response increases as the traveling speed increase. This follows from the fact that the energy content of the elastic beam increases when the speed increases. Furthermore, Figure 2 shows that the amplitude of the displacement response for the force and mass moving systems increases as speed increases. The maximum displacement when $v = 27.778$ m/s is ($w_{\max} = 2.17453$ m/s) which satisfies the results obtained by Duhamel integral [32] and is almost the same as that presented in [49].

3.2. Verification Problem II. This verification problem presents a damped beam attached to a single absorber and subjected to a moving load of intensity 9.81 N; that is, the moving vehicle of unit mass approaches to the moving load ($k_v = 0$ N/m, $\zeta_v = 1$ Ns/m, $m_v = 1$ kg). The data presented in [50, 51] are used for solving this problem, see Table 1. In this problem, the response of an initially stationary beam subjected to a moving load with a constant velocity is

Table 1: Material and geometrical properties of beam, vehicle, and absorbers.

Problem	Properties
Verification problem I in Section 3.1	$L = 25\,\text{m}$, $E = 82.7\,\text{GPa}$, $I = 9.2\,\text{m}^4$, $\mu = 2303\,\text{kg/m}$, $m_v = 5750\,\text{kg}$, $k_v = 1595000\,\text{N/m}$, $c_v = 0\,\text{Ns/m}$, $\widehat{K}_i = 0\,\text{N/m}$, $\widehat{\omega}_i = 0\,\text{rad/s}$.
Verification problem II in Section 3.2	$\beta = 1, \gamma = 1, N = 1$: $\{d_1 = L/2(\text{m})\}$, $(i = 1, 2, \ldots, N)$ $N = 2$: $\begin{Bmatrix} d_1 = \left(\frac{L}{2} - \delta\right)\text{m} \\ d_2 = \left(\frac{L}{2} + \delta\right)\text{m} \end{Bmatrix}$, $N = 3$: $\begin{Bmatrix} d_1 = \left(\frac{L}{2} - \delta\right)\text{m} \\ d_2 = \left(\frac{L}{2}\right)\text{m} \\ d_3 = \left(\frac{L}{2} + \delta\right)\text{m} \end{Bmatrix}$, $\delta = 0.02\,\text{m}$. $k_v = 0.0\,\text{N/m}$, $\zeta_v = 0.1$, $m_v = 1\,\text{kg}$.
Problem in Section 3.4	$N = 1$, $d_1 = (L/2)\text{m}$, $v = 25\,\text{m/s}$, $m_v = 1\,\text{kg}$, $k_v = 700\,\text{N/m}$, $\zeta_v = 0.1, \zeta = 0.15$.
Problem in Section 3.5	$\beta = 1.245$, $\gamma = 1.19$, $k_v = 700.0\,\text{N/m}$, $\zeta_v = 0.1$, $m_v = 1\,\text{kg}$, $N = 1$: $\left\{d_1 = \frac{L}{2}(\text{m})\right\}$, $N = 2$: $\begin{Bmatrix} d_1 = \left(\frac{L}{2} - \delta\right)\text{m} \\ d_2 = \left(\frac{L}{2} + \delta\right)\text{m} \end{Bmatrix}$, $N = 3$: $\begin{Bmatrix} d_1 = \left(\frac{L}{2} - \delta\right)\text{m} \\ d_2 = \left(\frac{L}{2}\right)\text{m} \\ d_3 = \left(\frac{L}{2} + \delta\right)\text{m} \end{Bmatrix}$, $\delta = 0.02\,\text{m}$.
For all problems (except verification Problem I)	$L = 4\,\text{m}$, $E = 206.8\,\text{GPa}$, $\rho = 7820\,\text{kg/m}^3$, $A = 0.03 \times 0.03\,\text{m}^2$, $\widehat{M}_i = 1.4076\,\text{kg}$, $\widehat{K}_i = 877.767\,\text{N/m}$, $\widehat{\zeta}_i = 0.1846356$ for $i = 1, 2, \ldots, N$.

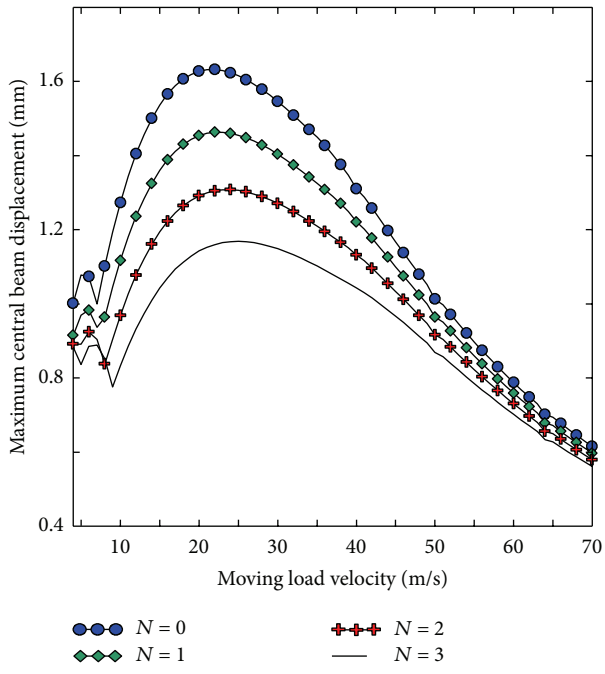

Figure 3: The maximum displacement of the beam at mid-span versus the velocity of the moving load for $\zeta = 0$.

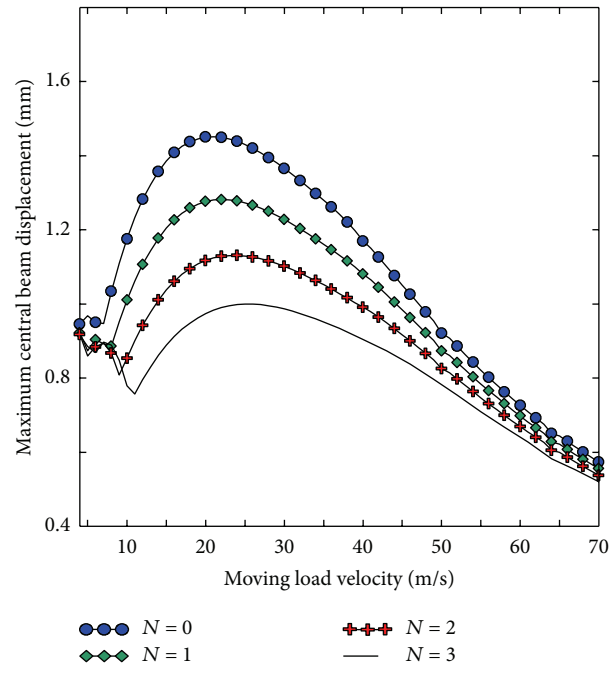

Figure 4: The maximum displacement of the beam at mid-span versus the velocity of the moving load for $\zeta = 0.075$.

considered. The beam is assumed to be free or appendaged to one, two, or three absorbers ($N = 0, 1, 2, 3$) and ($i = 1, \ldots, N$) at different locations of the beam, see Figures 3, 4, and 5.

In this problem, ($N = 0$) refers to a beam without any appendages; that is, all parametric properties of the oscillators are null. The case for ($N = 1$) was studied in [51] as a two-SDOF system, while in [50], it was analyzed using the Euler-Bernoulli theory. In [50], the Galerkin-Bubnov variation method is used to solve the beam problem with only one absorber attached at the mid-span of the beam. The order of the fractional derivative for both of the beam and the oscillator is assumed to be unity; that is, $\beta = \gamma = 1$.

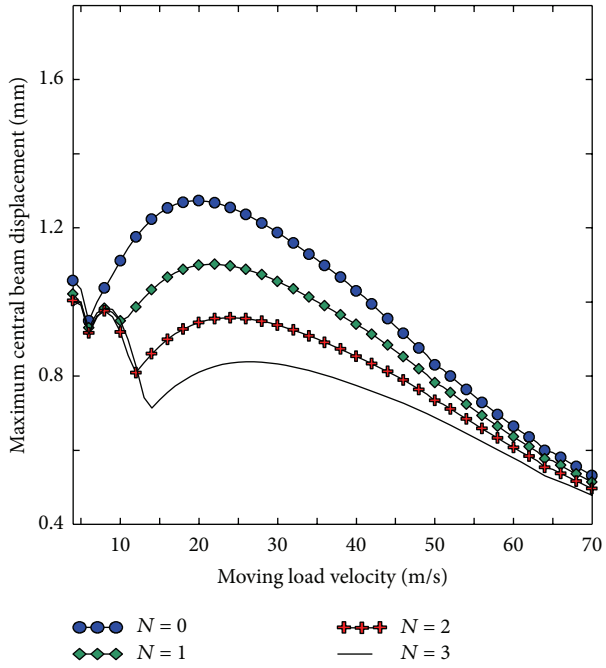

Figure 5: The maximum displacement of the beam at mid-span versus the velocity of the moving load for $\zeta = 0.15$.

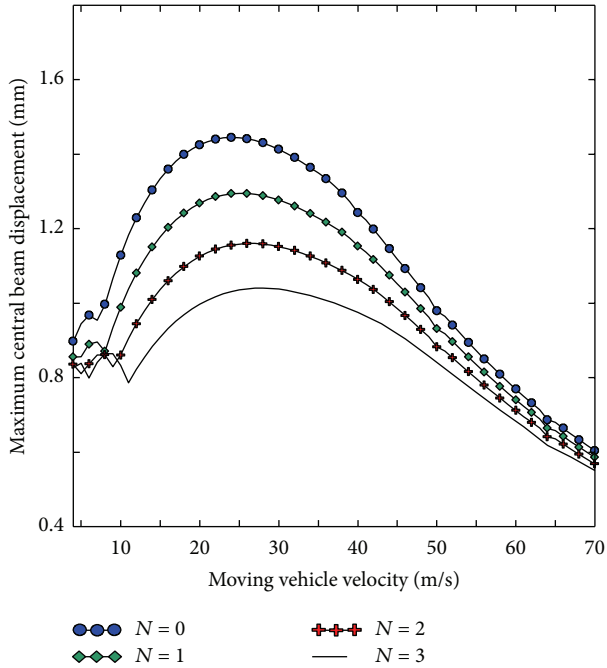

Figure 6: The maximum displacement of the beam at mid-span versus the velocity of the moving vehicle for $\zeta = 0$.

Figures 3–5 show the maximum response of the beam at the mid-span versus the velocity of the moving load for three different values of the beam damping ratio; that is, $\zeta = 0$, $\zeta = 0.075$, and $\zeta = 0.15$, respectively. The upper two curves in Figure 3 fit precisely the published results in [50, 51]. The curve for ($N = 0$) in Figure 3 fits exactly the well-known exact solution which is obtained by the Duhamel integral [32]. Furthermore, we note from Figures 3–5 that, as both the number of absorbers which are attached to the beam and as the damping beam-ratio increases, the dynamic response decreases. This is clearly seen from the lowest curve in Figure 5 where $N = 3$ and $\zeta = 0.15$.

3.3. Optimization of the Vehicle Dynamic Response. The moving load problem that was solved in Section 3.2 is solved here for the more general case of a moving vehicle ($k_v = 700$ N/m, $\zeta_v = 0.1$, $m_v = 1$ kg). Figures 6, 7, and 8 illustrate the maximum response of the beam at the mid-span versus the velocity of the moving vehicle for three different values of the damping ratio of the beam; that is, $\zeta = 0$, $\zeta = 0.075$, and $\zeta = 0.15$, respectively. Moreover, Figure 9 shows the maximum central beam displacement versus the velocity of the moving vehicle for different numbers of absorbers ($N = 1, 2$). The curves in these figures show that the maximum central displacement of the beam decreases as the number of absorbers, beam damping ratio, and vehicle velocity increase. By comparing Figures 3–5 obtained for a moving load with Figures 6–8 obtained for a moving vehicle, it is clearly seen that the maximum displacement of the beam decreases for the moving vehicle case and this is due to the effect of the damping ratio of the vehicle. Moreover, the

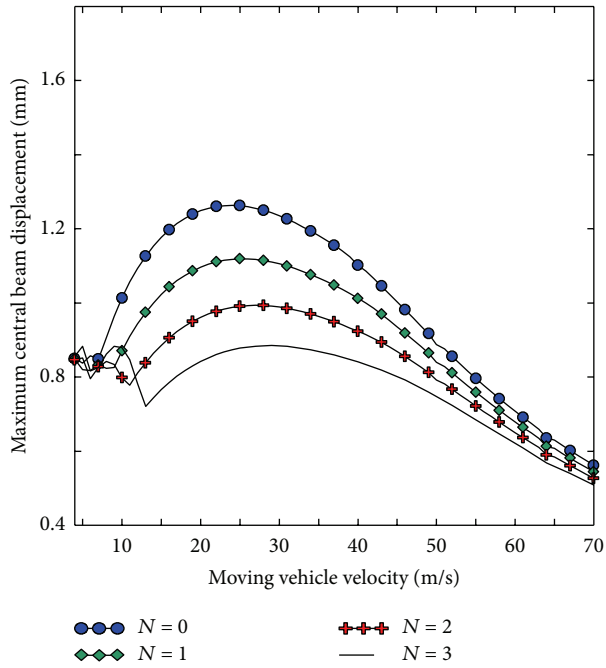

Figure 7: The maximum displacement of the beam at mid-span versus the velocity of the moving vehicle for $\zeta = 0.075$.

critical mean velocity of the moving vehicle at which the maximum displacement occurs is $v = 25$ m/s, see Figures 6–8.

3.4. Optimization of the Fractional Derivatives. In this Section, one example is analyzed to show the effect of the order

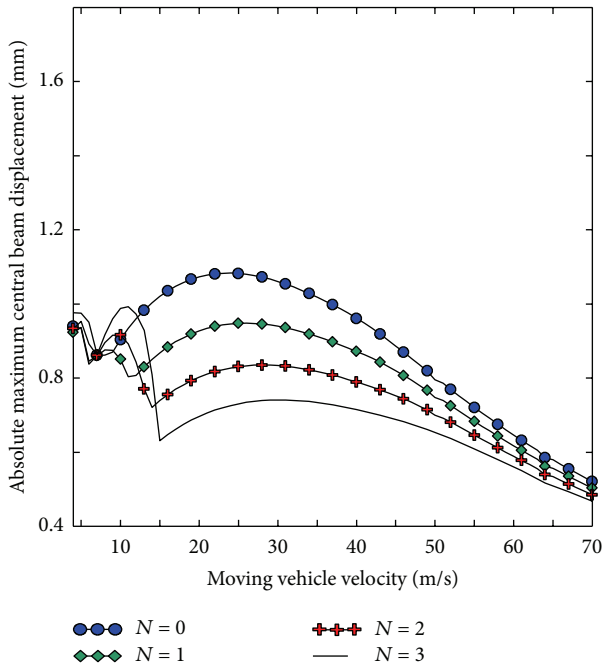

FIGURE 8: The maximum displacement of the beam at mid-span versus the velocity of the moving vehicle for $\zeta = 0.15$.

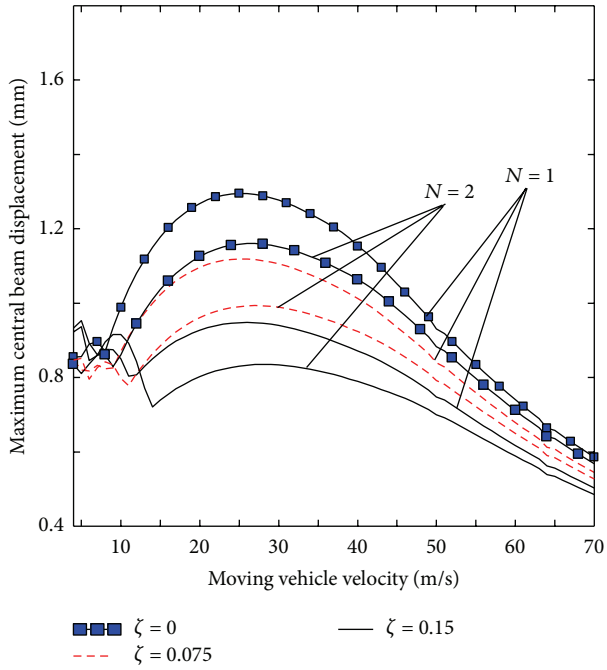

FIGURE 9: The maximum displacement of the beam at mid-span versus the velocity of the moving vehicle with one and two ($N = 1, 2$) absorbers attached.

of fractional derivatives for both of the beam and absorbers ($0 < \gamma < 2$, $0 < \beta < 2$). The 3D surface shown in Figure 10 (for the data given in Table 1) represents the variation of the maximum deflection of the beam at the mid-span (where the absorber is attached) with the beam fractional derivative (β) and the fractional derivative of the absorber (γ). The obtained surface in Figure 10 leads to very interesting critical values of β and γ. From this surface, the optimal values obtained are $\beta = 1.245$ and $\gamma = 1.190$, at which the minimum beam deflection occurs. This reduction is due to the effect of the damper added to the vehicle. The optimal values obtained from the surface shown in Figure 10 further show the physical meaning of fractional derivative, which is equivalent to increasing the damping characteristics of the beam.

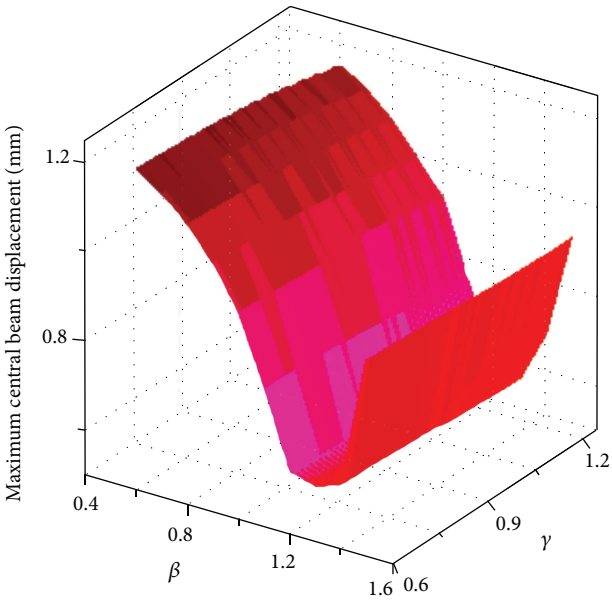

FIGURE 10: The maximum central deflection of the beam against the order of the beam's fractional derivative and the fractional derivative of the absorber (β, γ).

3.5. Optimization of the Number of Fractionally-Damped Oscillators. In this section, the optimal values that were obtained in Sections 3.3 and 3.4 ($\beta = 1.245$, $\gamma = 1.19$, $v = 25$ m/s) are used to determine the dynamic response of the beam attached to many SDOF systems. The other parameters considered in this example are shown in Table 1. Figures 11, 12, 13, and 14 show the dynamic response of the beam for various values of beam damping ratio ($\zeta = 0$, $\zeta = 0.075$, $\zeta = 0.15$), respectively. The effects of the beam damping ratio and the number of oscillators are clearly observed from the curves in Figures 11–14.

The effect of the previously obtained optimal values is observed clearly when both Figures 5 and 8 are compared with Figure 13. The percent relative reduction in the maximum central deflection (when the beam subjected to a moving load is compared to that subjected to a moving vehicle) is computed for ($N = 0$, $N = 1$, $N = 2$, and $N = 3$) as (14.5%, 13.85%, 12.74%, and 11.63%), respectively, see Figures 5 and 8, while the percent relative reduction in the maximum central deflection when Figure 8 ($\beta = 1$ and $\gamma = 1$) is compared with Figure 13 ($\beta = 1.245$ and $\gamma = 1.19$) of the beams subjected to a moving vehicle is computed for ($N = 0$,

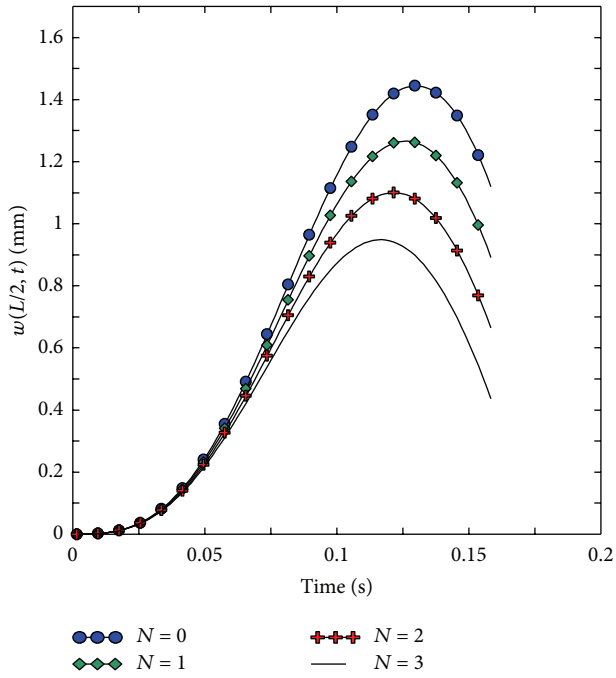

Figure 11: The dynamic response ($w(L/2,t)$) for the beam with $\zeta = 0$, subjected to a moving vehicle and attached to many absorbers.

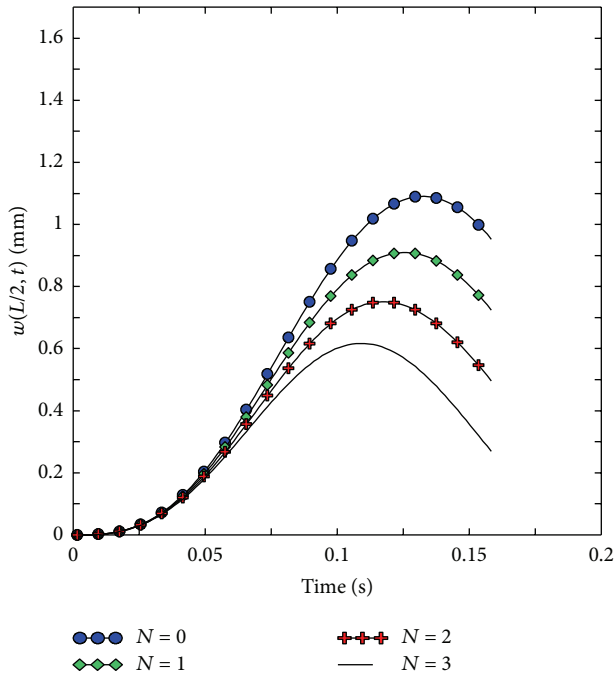

Figure 12: The dynamic response ($w(L/2,t)$) for the beam with $\zeta = 0.075$, subjected to a moving vehicle and attached to many absorbers.

$N = 1$, $N = 2$, and $N = 3$) as (27.58%, 41.27%, 48.99%, and 54.54%), respectively, see Figures 8 and 13. This reduction in the dynamic response of the beam is due to the effect of the damping of the beam, fractional damping, number of absorbers, and the vehicle-damping. However, the influence of the order of fractional derivatives, beam damping ratio,

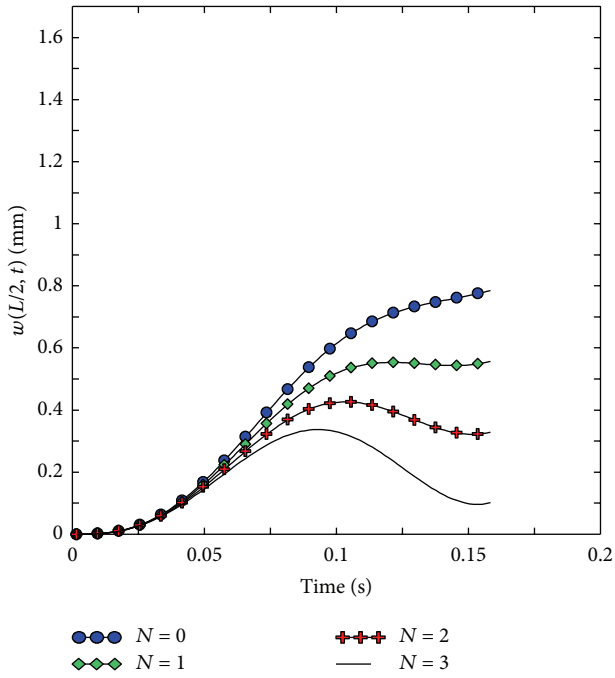

Figure 13: The dynamic response ($w(L/2,t)$) for the beam with $\zeta = 0.15$, subjected to a moving vehicle attached to many absorbers.

oscillators damping ratios, and the number of the attached oscillators on the beam dynamic response is clearly observed.

Figure 14 shows the dynamic response of the beam versus time for both of the moving load and vehicle for the beam damping ratio ($\zeta = 0.15$) for which ($N = 0$, $N = 1$, $N = 2$, $N = 3$). The fractional derivatives for both the beam and absorbers are taken as $\beta = 1.245$ and $\gamma = 1.19$, respectively. The effect of these optimal values on the beam response is clearly observed. The reduction in the dynamic response of the beam is due to the effect of the damping of the beam, fractional damping, number of attached absorbers, and the vehicle-damping.

4. Conclusions and Future Work

In this paper, an analytical model is introduced to solve the transverse vibration of Bernoulli-Euler beam attached to N-SDOF absorbers with damping characteristics that are described in terms of fractional derivatives. The damping characteristics of the beam and absorbers are assumed to be of fractional-order derivatives. The method employed uses the Laplace transform with decomposing the displacement into infinite series to find the solution. However, the solution may be written in a closed form for some special cases; otherwise, it may be truncated and produced by using appropriate mathematical software such as Maple.

The numerical results obtained in this paper, illustrate that (1) the dynamic response decreases as the number of absorbers attached to the beam increases, (2) as both the damping-ratios of absorbers and beam increase, the dynamic response decreases, (3) the type of load further affects the

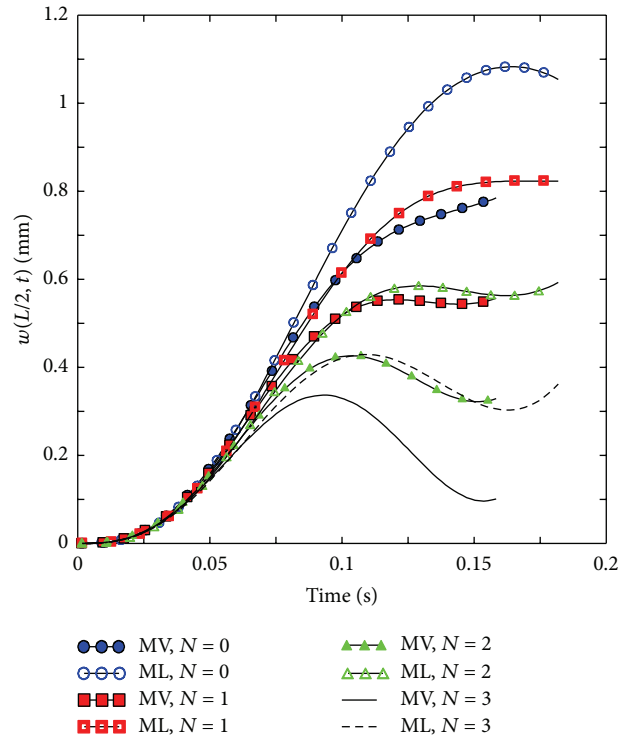

FIGURE 14: The dynamic response ($w(L/2, t)$) for the beam with $\zeta = 0.15$, attached to many absorbers for moving vehicle (MV) and moving load (ML).

dynamic response of the beam; hence, a moving vehicle reduces the response due to its damping property, and (4) there are some critical values of β and γ at which the beam has less deflection than that which is obtained from the full-order derivative models (i.e., $\beta = 1$ and $\gamma = 1$).

Finally, even though the fractional derivative model provides better damping models of fractionally-damped structures and materials, a limited number of papers have been presented in this field. This is probably due to the fact that the underlying mathematics of the fractional derivative models are sophisticated and not well-developed. Hence, developments in this field will lead to the development of the applications of fractional derivative models in several other engineering problems.

The approach of the fractional derivative damping, used in this paper, will allow researchers to choose suitable mathematical models that may better converge to realistic experimental models than the well-known conventional first-order damping models. Hence, the fractional derivative models may precisely represent a nonlinear damping behavior better than other existing damping models.

Future work will involve the following items for the application of the fractional calculus-based approach that is used in this paper within: (1) quantum and nano computing systems [52], (2) nanobeams, materials and medical applications [52–54], (3) fractal-based formulations to the microquasistatic thermoviscoelastic creep for rough surfaces in contact [55], and (4) other beam configurations for various types of nonlinearities, damping characteristics, and moving vehicles.

References

[1] R. L. Bagley and P. J. Torvik, "On the appearance of the fractional derivative in the behavior of real materials," *Journal of Applied Mechanics*, vol. 51, no. 2, pp. 294–298, 1984.

[2] R. L. Bagley and P. J. Torvik, "On the fractional calculus model of viscoelastic behavior," *Journal of Rheology*, vol. 30, no. 1, pp. 133–155, 1986.

[3] E. G. Bakhoum and C. Toma, "Transient aspects of wave propagation connected with spatial coherence," *Mathematical Problems in Engineering*, vol. 2013, Article ID 691257, 5 pages, 2013.

[4] C. Koh and J. M. Kelly, "Application of fractional derivatives to seismic analysis of base- isolated models," *Earthquake Engineering & Structural Dynamics*, vol. 19, no. 2, pp. 229–241, 1990.

[5] N. Makris and M. C. Constantinou, "Fractional-derivative Maxwell model for viscous dampers," *Journal of Structural Engineering*, vol. 117, no. 9, pp. 2708–2724, 1991.

[6] T. Pritz, "Five-parameter fractional derivative model for polymeric damping materials," *Journal of Sound and Vibration*, vol. 265, no. 5, pp. 935–952, 2003.

[7] H. Qi and M. Xu, "Unsteady flow of viscoelastic fluid with fractional Maxwell model in a channel," *Mechanics Research Communications*, vol. 34, no. 2, pp. 210–212, 2007.

[8] N. Shimizu and W. Zhang, "Fractional calculus approach to dynamic problems of viscoelastic materials," *JSME International Journal C*, vol. 42, no. 4, pp. 825–837, 1999.

[9] M. Li, S. C. Lim, and S. Y. Chen, "Exact solution of impulse response to a class of fractional oscillators and its stability," *Mathematical Problems in Engineering*, vol. 2011, Article ID 657839, 9 pages, 2011.

[10] M. Li, C. Cattani, and S. Y. Chen, "Viewing sea level by a one-dimensional random function with long memory," *Mathematical Problems in Engineering*, vol. 2011, Article ID 654284, 13 pages, 2011.

[11] M. Li, "Fractal time series: a tutorial review," *Mathematical Problems in Engineering*, vol. 2010, Article ID 157264, 26 pages, 2010.

[12] M. Li and W. Zhao, "Representation of a stochastic traffic bound," *IEEE Transactions on Parallel and Distributed Systems*, vol. 21, no. 9, pp. 1368–1372, 2010.

[13] M. Li, "Approximating ideal filters by systems of fractional order," *Computational and Mathematical Methods in Medicine*, vol. 2012, Article ID 365054, 6 pages, 2012.

[14] M. Li, Y. Q. Chen, J. Y. Li, and W. Zhao, "Hölder scales of sea level," *Mathematical Problems in Engineering*, vol. 2012, Article ID 863707, 22 pages, 2012.

[15] M. Li, S. C. Lim, C. Cattani, and M. Scalia, "Characteristic roots of a class of fractional oscillators," *Advances in High Energy Physics*, vol. 2013, Article ID 853925, 7 pages, 2013.

[16] C. Toma, "Wavelets-computational aspects of sterian-realistic approach to uncertainty principle in high energy physics-A transient approach," *Advances in High Energy Physics*, vol. 2013, Article ID 735452, 6 pages, 2013.

[17] M. Li and W. Zhao, "On 1/f noise," *Mathematical Problems in Engineering*, vol. 2012, Article ID 673648, 23 pages, 2012.

[18] M. Li and W. Zhao, "Visiting power laws in cyber-physical networking systems," *Mathematical Problems in Engineering*, vol. 2012, Article ID 302786, 13 pages, 2012.

[19] M. Li, W. Zhao, and C. Cattani, "Delay bound: fractal traffic passes through servers," *Mathematical Problems in Engineering*, vol. 2013, Article ID 157636, 15 pages, 2013.

[20] H. Sheng, Y. Q. Chen, and T. S. Qiu, *Fractional Processes and Fractional Order Signal Processing*, Springer, 2012.

[21] R. Abu-Mallouh, I. Abu-Alshaikh, H. S. Zibdeh, and K. Ramadan, "Response of fractionally damped beams with general boundary conditions subjected to moving loads," *Shock and Vibration*, vol. 19, no. 3, pp. 333–347, 2012.

[22] B. N. N. Achar, J. W. Hanneken, and T. Clarke, "Damping characteristics of a fractional oscillator," *Physica A*, vol. 339, no. 3-4, pp. 311–319, 2004.

[23] O. P. Agrawal, "Analytical solution for stochastic response of a fractionally damped beam," *Journal of Vibration and Acoustics*, vol. 126, no. 4, pp. 561–566, 2004.

[24] S. S. Ray, B. P. Poddar, and R. K. Bera, "Analytical solution of a dynamic system containing fractional derivative of order one-half by adomian decomposition method," *Journal of Applied Mechanics*, vol. 72, no. 2, pp. 290–295, 2005.

[25] K. S. Fa, "A falling body problem through the air in view of the fractional derivative approach," *Physica A*, vol. 350, no. 2–4, pp. 199–206, 2005.

[26] A. Chatterjee, "Statistical origins of fractional derivatives in viscoelasticity," *Journal of Sound and Vibration*, vol. 284, no. 3–5, pp. 1239–1245, 2005.

[27] E. Goldfain, "Fractional dynamics and the Standard Model for particle physics," *Communications in Nonlinear Science and Numerical Simulation*, vol. 13, no. 7, pp. 1397–1404, 2008.

[28] A. Hernández-Jiménez, J. Hernández-Santiago, A. Macias-García, and J. Sánchez-González, "Relaxation modulus in PMMA and PTFE fitting by fractional Maxwell model," *Polymer Testing*, vol. 21, no. 3, pp. 325–331, 2002.

[29] E. Savin, "Dynamic amplification factor and response spectrum for the evaluation of vibrations of beams under successive moving loads," *Journal of Sound and Vibration*, vol. 248, no. 2, pp. 267–288, 2001.

[30] Y. B. Yang and C. W. Lin, "Vehicle-bridge interaction dynamics and potential applications," *Journal of Sound and Vibration*, vol. 284, no. 1-2, pp. 205–226, 2005.

[31] H. S. Zibdeh and R. Rackwitz, "Moving loads on beams with general boundary conditions," *Journal of Sound and Vibration*, vol. 195, no. 1, pp. 85–102, 1996.

[32] L. Fryba, *Vibration of Solids and Structures under Moving Loads*, Noordhoff International Publishing, Groningen, The Netherlands, 1972.

[33] Y. Chen, C. A. Tan, and L. A. Bergman, "Effects of boundary flexibility on the vibration of a continuum with a moving oscillator," *Journal of Vibration and Acoustics, Transactions of the ASME*, vol. 124, no. 4, pp. 552–560, 2002.

[34] M. Olsson, "On the fundamental moving load problem," *Journal of Sound and Vibration*, vol. 145, no. 2, pp. 299–307, 1991.

[35] M. A. Foda and Z. Abduljabbar, "A dynamic green function formulation for the response of a beam structure to a moving mass," *Journal of Sound and Vibration*, vol. 210, no. 3, pp. 295–306, 1998.

[36] H. P. Lee, "Dynamic response of a beam with a moving mass," *Journal of Sound and Vibration*, vol. 191, no. 2, pp. 289–294, 1996.

[37] G. Michaltsos, D. Sophianopoulos, and A. N. Kounadis, "The effect of a moving mass and other parameters on the dynamic response of a simply supported beam," *Journal of Sound and Vibration*, vol. 191, no. 3, pp. 357–362, 1996.

[38] S. Sadiku and H. H. E. Leipholz, "On the dynamics of elastic systems with moving concentrated masses," *Ingenieur-Archiv*, vol. 57, no. 3, pp. 223–242, 1987.

[39] A. V. Pesterev and L. A. Bergman, "An improved series expansion of the solution to the moving oscillator problem," *Journal of Vibration and Acoustics*, vol. 122, no. 1, pp. 54–61, 2000.

[40] B. Yang, C. A. Tan, and L. A. Bergman, "Direct numerical procedure for solution of moving oscillator problems," *Journal of Engineering Mechanics*, vol. 126, no. 6, pp. 462–469, 2000.

[41] Y. B. Yang and Y. S. Wu, "A versatile element for analyzing vehicle-bridge interaction response," *Engineering Structures*, vol. 23, pp. 452–469, 2001.

[42] F. Samani, F. Pellicano, and A. Masoumi, "Performance of nonlinear vibration absorbers for beams under moving vehicles," ENOC 2011, Rome, Italy, July 2011.

[43] D. Stăncioiu, H. Ouyang, and J. E. Mottershead, "Vibration of a beam excited by a moving oscillator considering separation and reattachment," *Journal of Sound and Vibration*, vol. 310, no. 4-5, pp. 1128–1140, 2008.

[44] J. W. Nicholson and L. A. Bergman, "Free vibration of combined dynamical systems," *ASCE Journal of Engineering Mechanics*, vol. 112, no. 1, pp. 1–13, 1986.

[45] Z.-F. Liang and X.-Y. Tang, "Analytical solution of fractionally damped beam by Adomian decomposition method," *Applied Mathematics and Mechanics*, vol. 28, no. 2, pp. 219–228, 2007.

[46] M. A. Hilal and H. S. Zibdeh, "Vibration analysis of beams with general boundary conditions traversed by a moving force," *Journal of Sound and Vibration*, vol. 229, no. 2, pp. 377–388, 2000.

[47] I. Podlubny, *Fractional Differential Equations*, Academic Press, San Diego, Calif, USA, 1999.

[48] Y. L. Luke, *The Special Functions and Their Approximations*, Academic Press, New York, NY, USA, 1969.

[49] G. Venkatesan, *Dynamic behavior of bridge structure under moving load [Ph.D. thesis]*, University of Oklahoma, 2009.

[50] F. S. Samani and F. Pellicano, "Vibration reduction on beams subjected to moving loads using linear and nonlinear dynamic absorbers," *Journal of Sound and Vibration*, vol. 325, no. 4-5, pp. 742–754, 2009.

[51] J.-J. Wu, "Study on the inertia effect of helical spring of the absorber on suppressing the dynamic responses of a beam subjected to a moving load," *Journal of Sound and Vibration*, vol. 297, no. 3–5, pp. 981–999, 2006.

[52] A. N. Al-Rabadi, "Carbon nanotube (CNT) multiplexers, circuits, and actuators," *United States Patent and Trademark Office (USPTO)*, Patent no. US 7, 508, 039 B2, March 2009.

[53] C. Cattani and A. Ciancio, "Separable transition density in the hybrid model for tumor-immune system competition," *Computational and Mathematical Methods in Medicine*, vol. 2012, Article ID 610124, 6 pages, 2012.

[54] C. Cattani, A. Ciancio, and B. Lods, "On a mathematical model of immune competition," *Applied Mathematics Letters*, vol. 19, no. 7, pp. 678–683, 2006.

[55] O. M. Abuzeid, A. N. Al-Rabadi, and H. S. Alkhaldi, "Recent advancements in fractal geometric-based nonlinear time series solutions to the micro-quasistatic thermoviscoelastic creep for rough surfaces in contact," *Mathematical Problems in Engineering*, vol. 2011, Article ID 691270, 29 pages, 2011.

Hindawi Publishing Corporation
Advances in Mathematical Physics
Volume 2013, Article ID 485273, 8 pages
http://dx.doi.org/10.1155/2013/485273

Research Article

A Point Source Identification Problem for a Time Fractional Diffusion Equation

Xiao-Mei Yang[1] and Zhi-Liang Deng[2]

[1] *School of Mathematics, Southwest Jiaotong University, Chengdu 610031, China*
[2] *School of Mathematical Sciences, University of Electronic Science and Technology of China, Chengdu 610054, China*

Correspondence should be addressed to Xiao-Mei Yang; yangxiaomath@home.swjtu.edu.cn

Received 19 September 2013; Revised 20 October 2013; Accepted 21 October 2013

Academic Editor: Ming Li

An inverse source identification problem for a time fractional diffusion equation is discussed. The unknown heat source is supposed to be space dependent only. Based on the use of Green's function, an effective numerical algorithm is developed to recover both the intensities and locations of unknown point sources from final measurements. Numerical results indicate that the proposed method is efficient and accurate.

1. Introduction

Let Ω be a bounded domain in $\mathbb{R}^2$ and let $\partial\Omega$ be the boundary of Ω. Consider the following time fractional diffusion process:

$$\begin{aligned} {}_0D_t^\gamma u(x,t) - \mathscr{L}u(x,t) &= f(x), \quad x \in \Omega,\ t \in (0,T), \\ u(x,0) &= 0, \quad x \in \Omega, \\ \mathscr{B}u(x,t) := \mu u(x,t) + \beta \frac{\partial u}{\partial \nu} &= 0, \quad x \in \partial\Omega,\ t \in (0,T), \end{aligned} \tag{1}$$

where $\mathscr{L}$ is the uniformly elliptic operator, ν is the outward normal at the boundary $\partial\Omega$, and μ, β are known constants which are not simultaneously zero. Here, ${}_0D_t^\gamma$ stands for the Caputo fractional derivative operator of order $0 < \gamma \leq 1$ defined by

$${}_0D_t^\gamma \psi(t) := \begin{cases} \dfrac{1}{\Gamma(1-\gamma)} \displaystyle\int_0^t \frac{\psi'(s)}{(t-s)^\gamma} ds, & 0 < \gamma < 1 \\ \psi'(t), & \gamma = 1, \end{cases} \tag{2}$$

where $\Gamma(\cdot)$ is the standard Γ-function and the prime denotes the general derivative.

From the last few decades, fractional calculus grabbed great attention of not only mathematicians and engineers but also many scientists from all fields (e.g., see [1–4]). Fractional diffusion equations describe anomalous diffusions on fractals (physical objects of fractional dimension, like some amorphous semiconductors or strongly porous materials; see [5, 6] and references therein). Indeed, fractional derivatives provide an excellent tool for the description of memory and hereditary properties of various materials and processes. This is the main superiority of fractional derivatives in comparison with classical integer-order models, in which such effects are in fact neglected. For the detailed theory and application of fractional calculus, one can refer to [1–4] and references therein. Not only have differential equations of fractional order attracted people's attention, but also theories and applications related to physics and geometry of fractal dimension have been well studied (e.g., [7–11]).

If the initial condition is nonhomogeneous, that is, $u(x,0) = \varphi(x)$, we are always able to simplify the system (1) into two components; that is, $u = v + w$, where v solves the homogeneous equation with nonhomogeneous initial condition and w satisfies the nonhomogeneous equation with homogeneous initial condition. As we know, the initial value/boundary value problem associated with v is well-posed and there exist many works on such forward problem, for example, [12, 13]. In the following, instead of nonhomogeneous initial condition, we only focus on the system (1) with homogeneous initial condition. Ordinarily, when f is

a known function, we are asked to determine the solution function $u(x,t)$ so as to satisfy (1). So posed, this is a direct problem. However, the source term f is not always known and has to be computed from some additional data. The additional information is mainly the following: the interior/boundary transient measurement values and the final measurement values. Here, we suppose that the measured data are given in final time $t = T$ as $u(x,T) + \epsilon * \text{rand}$ (ϵ is the noise level).

For most classical partial differential equations, the identification and reconstruction of source functions from the final data or the partial boundary data are an inverse problem with many applications (e.g., [14]). A number of articles address the solvability problem of source term identification. For parabolic-type differential equation, please see [15–26]. For elliptic-type differential equation, one can refer to [27–29], though the source identification problem has been well discussed in the classic framework, yet, to the best of the authors' knowledge, there are rare researches in the aspect of the source identification problem associated with fractional differential equation in spite of the physical and practical importance. As indicated in [30–33], the source identification problem associated with the time fractional diffusion equation is also ill-posed. That means the solution does not depend continuously on the given data and any small perturbation in the given data may cause large change to the solution. In [33], when additional data is given on the partial boundary, the uniqueness in identifying a source term independent of time t is established for one-dimensional time fractional diffusion equation. In [30], if the final time temperature distribution is known, the existence and uniqueness results are proved. Murio and Mejía [31] propose a mollification regularization technique to reconstruct the unknown forcing term $f(x,t)$. In this paper, we aim to deal with the special case that the sources and measurements are both point like. The main focus will be placed on the recovery of both intensities and locations of the unknown point source term. For this, we propose a method based on the use of Green's function to solve the inverse source identification problems.

The outline of the paper is as follows. In Section 2, we provide a brief sketch on the considered identification problem. The reconstruction method by Green's function is then given in Section 3. Numerical implementation of the proposed method is provided in Section 4. In Section 5, we summarize the results.

2. Statement of the Problem

In this paper, we deal with the special case that the source function $f(x)$ is of the form

$$f(x) = \sum_{1}^{M} \lambda_j \delta\left(x - \theta_j\right), \quad j = 1, 2, \ldots, M, \tag{3}$$

where θ_j denotes the location of the point source and λ_j is the intensity associated with each point source at θ_j. Thereby, the temperature distribution $u = u(x,t)$ inside the domain Ω is generated by $f(x)$ satisfying

$$\begin{aligned} {}_0D_t^{\gamma} u(x,t) - \mathscr{L}u(x,t) &= \sum_{j=1}^{M} \lambda_j \delta\left(x - \theta_j\right), \quad x \in \Omega, \\ &\qquad t \in (0,T), \\ u(x,0) &= 0, \quad x \in \Omega, \\ \mathscr{B}u(x,t) := \mu u(x,t) + \beta \frac{\partial u}{\partial \nu} &= 0, \quad x \in \partial\Omega, \\ &\qquad t \in (0,T), \end{aligned} \tag{4}$$

where $\delta(\cdot)$ is the Dirac delta function. Meanwhile, let N be a natural number and let $\{x_i\}_{i=1}^{N}$ be a group of points in Ω. Here, the points x_i, $i = 1, \ldots, N$, scattered in Ω are the collocation points. Our goal is to determine the strength sources λ_j and the locations θ_j from user-input estimated position and the set of final measurement data

$$u^{\epsilon}(x_i, T) := u_{i,T} + v_i, \quad x_i \in \Omega, \ i = 1, 2, \ldots, N, \tag{5}$$

where $(v_i)_{i=1}^{N}$ denotes the Gaussian variable with mean zero and variance ϵ. This magnitude ϵ also represents the level of noises.

Let us first suppose that the locations of the point sources $\{\theta_j\}$ are given. Under this assumption, we come to the problem of the recovery of the intensity λ_j associated with the point sources θ_j from the N distinct final collocation data $u^{\epsilon}(x_i, T)$. This recovery problem is ill-posed, which prompts us to use some regularization methods.

Consequently, we assume that the locations of the point sources θ_j are not known but an initial guess location $\overline{\theta}_j$ is given for each unknown point source. Moreover, we make the assumption that each point source belongs to a distinct ball inside the domain; that is,

$$\begin{aligned} \theta_j &\in B\left(\overline{\theta}_j, \rho_j\right) \cap \Omega, \quad j = 1, 2, \ldots, M, \\ B\left(\overline{\theta}_j, \rho_j\right) &\cap B\left(\overline{\theta}_k, \rho_k\right) = \emptyset, \quad 1 \le j < k \le M, \end{aligned} \tag{6}$$

where $B(\theta, \rho)$ denotes the ball centered at θ with radius ρ. It should be pointed that if two or more point sources are concentrated in a sufficient small domain, the proposed method in the following section will treat them as one point source.

3. Methodology Based on Green's Function

In this section, we discuss the identification method based on Green's function. Green's function $G(x,t;\theta)$ can be defined as

the solution of the following equations:

$$
\begin{aligned}
{}_0D_t^{\gamma}G(x,t;\theta) - \mathscr{L}G(x,t;\theta) &= \delta(x-\theta), \quad x,\theta \in \Omega, \\
&\qquad t \in (0,T), \\
G(x,0;\theta) &= 0, \quad x,\theta \in \Omega, \\
\mathscr{B}G(x,t;\theta) := \mu G(x,t;\theta) + \beta\frac{\partial G}{\partial \nu} &= 0, \quad x,\theta \in \partial\Omega, \\
&\qquad t \in (0,T).
\end{aligned}
\tag{7}
$$

By applying Laplace transform technique, we have that

$$
G(x,t;\theta) = \sum_{n=1}^{\infty} t^{\gamma} E_{\gamma,\gamma+1}\left(-\lambda_n^2 t^{\gamma}\right)\varphi_n(\theta)\varphi_n(x), \tag{8}
$$

where φ_n is the nth orthonormal eigenfunction and λ_n is the corresponding eigenvalue to the Sturm-Liouville problem

$$
\begin{aligned}
\mathscr{L}\varphi + \lambda_n^2\varphi &= 0, \\
\mu\varphi + \beta\frac{\partial\varphi}{\partial\nu} &= 0,
\end{aligned}
\tag{9}
$$

and $E_{\gamma,\zeta}(z)$ is the Mittag-Leffler function defined by

$$
E_{\gamma,\zeta}(z) = \sum_{k=0}^{\infty}\frac{z^k}{\Gamma(\gamma k + \zeta)}. \tag{10}
$$

For the details of Mittag-Leffler function, one can refer to [2].

Utilizing Green's function, we then can write the solution of (4) as

$$
u(x,t) = \sum_{j=1}^{M}\lambda_j G\left(x,t;\theta_j\right). \tag{11}
$$

Therefore, when the locations $\{\theta_j\}$ of point sources are known, once we obtain the final time measurement data specified in (5), we can solve the following linear algebraic equation:

$$
\sum_{j=1}^{M}\lambda_j G\left(x_i,T;\theta_j\right) = u_{i,T}^{\varepsilon}, \quad i = 1,2,\ldots,N \tag{12}
$$

to get the unknown values of the intensities λ_j. Moreover, denoting $\lambda = (\lambda_j)$ and $\varpi = (u_{i,T}^{\varepsilon})$, (12) can be rewritten as the following matrix form:

$$
A\lambda = \varpi, \tag{13}
$$

where A is an $N \times M$ matrix:

$$
A_{ij} = G\left(x_i,T;\theta_j\right). \tag{14}
$$

Taking $N = M$, then the system of (13) contains N linear equations with N unknowns. Subsequently, if the matrix A is invertible, one simply has

$$
\lambda = A^{-1}\varpi. \tag{15}
$$

However, due to the ill-posedness of the source identification problem, the system of (13) is ill-conditioned, and hence a direct solution, as given by (15), will be either impossible or will produce very inaccurate results. To obtain stable solutions to these kinds of ill-conditioning systems, various regularization techniques have been studied and applied extensively [34]. Here, a standard Tikhonov regularization technique is adopted to find the approximation solution of the matrix equation (13). By λ_α, we denote the Tikhonov regularized solution defined to be the minimal element of the following least square problem:

$$
\min_{\lambda} J_\alpha(\lambda) := \min_{\lambda}\|A\lambda - \varpi\|^2 + \alpha^2\|\lambda\|^2, \tag{16}
$$

where $\alpha > 0$ is the regularization parameter and $\|\cdot\|$ denotes the usual Euclidean norm. It is well known [34] that the minimal element of J_α can be written as

$$
\lambda_\alpha = \left(A^*A + \alpha^2 I\right)^{-1}A^*\varpi, \tag{17}
$$

where A^* denotes the conjugate transposed matrix of A and I denotes the identity matrix.

Next, assume that the locations $\{\theta_j\}$ of the point sources are also unknown. In such case, we will get a nonlinear system. The nonlinear system is not suitable or difficult for direct numerical computation. In order to eliminate the difficulty in implementing the numerical computation, we propose in the following to linearize the nonlinear system.

For the estimate locations $\{\overline{\theta}_j\}$, we define the following union set

$$
\Theta := \bigcup_{j=1}^{M} B\left(\overline{\theta}_j,\rho_j\right)\cap\Omega \tag{18}
$$

and suppose that it contains all exact positions of the point sources with proper radius ρ_j. To linearize the nonlinear system, we take some additional collocation points $\{\xi_l\}_{l=1}^n$ from the set Θ. Assume that $\{\xi_l\}_{l=1}^n$ are uniformly distributed in Θ. On each point ξ_l, we put in a point source with intensity τ_l. Suppose that the temperature distribution generated by the n point sources $\{\xi_l\}_{l=1}^n$ is equal to that generated by the M point sources $\{\theta_j\}_{j=1}^M$. Subsequently, we have

$$
\begin{aligned}
{}_0D_t^{\gamma}u(x,t) - \mathscr{L}u(x,t) &= \sum_{l=1}^{n}\tau_l\delta\left(x-\xi_l\right), \\
&\qquad x \in \Omega,\ t \in (0,T), \\
u(x,0) &= 0, \quad x \in \Omega, \\
\mu u(x,t) + \beta\frac{\partial u}{\partial\nu} &= 0, \quad x \in \partial\Omega,\ t \in (0,T),
\end{aligned}
\tag{19}
$$

with additional data (5), where τ_l is the intensity at the location ξ_l. By using the above proposed method to solve (19) with (5), the intensity τ_l of each point source ξ_l can then be obtained approximately. Next, we transform the intensities $\{\tau_l\} \subset B(\overline{\theta}_j,\rho_j)\cap\Omega$ back to a single source point as follows:

the jth unknown source intensity λ_j associated with each ball $B(\overline{\theta}_j, \rho_j) \cap \Omega$ is approximated by $\widetilde{\lambda}_j$ as

$$\widetilde{\lambda}_j := \sum_{l:\xi_l \in B(\overline{\theta}_j, \rho_j) \cap \Omega} \tau_l, \quad j = 1, 2, \ldots, M. \tag{20}$$

With the approximation intensity in hand, we can start to look at how to find the locations of the point sources. For every point source θ_j, we use the weight sum of the location coordinate ξ_l in the ball $B(\overline{\theta}_j, \rho_j)$ to approximate the exact location. More specifically, the approximation location $\widetilde{\theta}_j$ corresponding to the intensity λ_j is defined by

$$\widetilde{\theta}_j := \frac{1}{\widetilde{\lambda}_j} \sum_{l:\xi_l \in B(\overline{\theta}_j, \rho_j) \cap \Omega} \tau_l \xi_l, \quad j = 1, 2, \ldots, M. \tag{21}$$

4. Numerical Examples

In this section, some numerical examples are given to verify the effectiveness of the method proposed in Section 3. In our computation, we use the MATLAB code developed by Hansen [35, 36] for solving the ill-conditioned system (13). To compare the accuracy of the approximation, we use the root mean square (RMS) which is defined as

$$\mathrm{RMS} = \sqrt{\frac{1}{M} \sum_{j=1}^{M} \left(\widetilde{\lambda}_{\alpha,j} - \lambda_j\right)^2}. \tag{22}$$

The noisy data $u^\epsilon(x_i, T)$ at measurement points x_i is obtained by adding random noise to the exact data $u(x_i, T)$ by

$$u^\epsilon(x_i, T) = u(x_i, T) + \epsilon \mathrm{rand}(i) \tag{23}$$

for $x_i \in \Omega$, where rand(i) is a random number between $[-1, 1]$. The measurement points $\{x_i\}$ are equally distributed in Ω. In addition, as we know, for ill-posed problem, the regularization parameter α plays an important role and hence has to be chosen appropriately. In theory, α depends on some *a priori* knowledge of exact solution and noise level ϵ [34]. However, in practice, the *a priori* knowledge and noise level may not always be known. Therefore, to compensate this lack of information for the noise level, it is necessary for us to consider some error-free parameter choice rules. Here, we adopt the L-curve criterion [35–37] to choose the regularization parameter.

Example 1. Consider the following heat conduction problem on a semi-infinite stripe domain $\Omega = \{(x, y) \mid 0 \le x \le l, y \ge 0\}$:

$$\begin{aligned} u_t(x, y, t) - \Delta u &= f(x, y), \quad 0 < x < l, \\ &\quad y > 0, \ t \in (0, T), \\ u(x, y, 0) &= 0, \quad 0 \le x \le l, \ y \ge 0, \\ u|_{x=0} &= u|_{x=l} = 0, \quad y \ge 0, \\ u|_{y=0} &= 0, \quad 0 \le x \le l. \end{aligned} \tag{24}$$

Green's function is given by

$$\begin{aligned} G(x, y, t; \xi, \eta) = {} & \frac{2}{l\sqrt{\pi t}} e^{-(y^2+\eta^2)/4t} \sinh \frac{y\eta}{2t} \\ & \times \sum_{n=1}^{\infty} e^{-n^2\pi^2 t/l^2} \sin \frac{n\pi\xi}{l} \sin \frac{n\pi x}{l} H(t), \end{aligned} \tag{25}$$

where $H(\cdot)$ is the Heaviside function. Without loss of generality, we take $l = 1$.

In this test, we consider the case that the source function (3) contains five source points $\{\theta_j\}_{j=1}^5$. The input source locations $\overline{\theta}_j$ are randomly chosen such that

$$\left|\overline{\theta}_j - \theta_j\right| < \overline{\rho}_j, \quad \text{for } j = 1, 2, 3, 4, 5, \tag{26}$$

where $\overline{\rho}_j$ are sufficient small to ensure $\overline{\theta}_j \in \Omega$. The value of the parameters $\{\rho_j\}_{j=1}^5$ in (18) used in this computations is 0.1. When the noisy data are given in the final time $T = 1$, we demonstrate the numerical performance under two noise levels: $\epsilon = 0.01$ and $\epsilon = 0.001$. The computations are performed by using a total of Q trial centers in each ball. We report the numerical results under different Q in Tables 1 and 2. The displayed results show that the total number Q of trial centers plays no role in the convergence of the scheme. Only a small number of trial centers are sufficient to approximate the unknown source function. Therefore, we only consider the case when 100 trial centers are taken in each ball in subsequent examples.

Example 2. In this example, we consider the following inverse identification problem on a square domain $\Omega = [0, 1] \times [0, 1]$ for $0 < \gamma < 1$:

$$\begin{aligned} {}_0D_t^\gamma u(x, y, t) - \Delta u &= f(x, y), \quad (x, y) \in \Omega, \ t \in (0, T), \\ u(x, y, 0) &= 0, \quad (x, y) \in \Omega, \\ u(x, y, t) &= 0, \quad (x, y) \in \partial\Omega, \ t \in (0, T). \end{aligned} \tag{27}$$

By virtue of Laplace's transform [2, 38], one can derive the corresponding Green's function

$$\begin{aligned} G(x, y, t; \xi, \eta) = {} & 4 \sum_{n=1}^{\infty} t^\gamma E_{\gamma,\gamma+1}\left(-n^2\pi^2 t^\gamma\right) \sin(n\pi x) \\ & \times \sin(n\pi y) \sin(n\pi\xi) \sin(n\pi\eta). \end{aligned} \tag{28}$$

Firstly, we see the robustness of the proposed algorithm about the parameter γ. For $\epsilon = 0.01, 0.001$, $\rho_j = 0.1$, and $T = 1$, we report the RMS in Table 3 under different γ for three point sources located at

$$(0.3, 0.3), \ (0.5, 0.7), \ (0.7, 0.3) \tag{29}$$

with intensities 1, 3, and 5. The corresponding approximation locations are given in Tables 4 and 5. The displayed results

Table 1: Example 1: numerical comparison for $\epsilon = 0.01$ and $M = 5$.

Exact	λ_j	11	1	21	−5	−7
	θ_j	(0.5, 1)	(0.5, 5)	(0.5, 10)	(0.5, 15)	(0.5, 25)
$Q = 25$	$\widetilde{\lambda}_j$	11.6978	1.0539	22.0974	−5.1806	−7.3625
	$\widetilde{\theta}_j$	(0.5196, 0.9876)	(0.5349, 4.9513)	(0.5173, 10.0002)	(0.5059, 14.9989)	(0.5129, 25.0005)
$Q = 100$	$\widetilde{\lambda}_j$	11.7866	0.9881	22.1760	−5.1460	−7.3026
	$\widetilde{\theta}_j$	(0.5226, 0.9925)	(0.5196, 4.9688)	(0.5188, 10.0002)	(0.5059, 15.0016)	(0.5102, 25.0001)
$Q = 256$	$\widetilde{\lambda}_j$	11.4531	1.0006	22.1702	−5.1226	−7.1781
	$\widetilde{\theta}_j$	(0.5136, 0.9929)	(0.5219, 4.9689)	(0.5190, 10.0005)	(0.5027, 15.0023)	(0.5046, 24.9995)
$Q = 400$	$\widetilde{\lambda}_j$	11.6968	1.0962	22.1453	−5.0899	−7.1799
	$\widetilde{\theta}_j$	(0.5213, 0.9977)	(0.5521, 4.9829)	(0.5186, 10.0005)	(0.5009, 15.0027)	(0.5047, 25.0008)
$Q = 625$	$\widetilde{\lambda}_j$	11.9726	1.0230	22.0421	−5.1289	−7.1438
	$\widetilde{\theta}_j$	(0.5274, 0.9951)	(0.5309, 5.0000)	(0.5171, 10.0004)	(0.5033, 15.0033)	(0.5028, 24.9993)
$Q = 900$	$\widetilde{\lambda}_j$	11.5229	1.0794	22.3220	−4.9636	−7.1709
	$\widetilde{\theta}_j$	(0.5163, 0.9975)	(0.5477, 4.9907)	(0.5209, 10.0004)	(0.4919, 15.0005)	(0.5035, 25.0000)

Table 2: Example 1: numerical comparison for $\epsilon = 0.001$ and $M = 5$.

Exact	λ_j	5	7	2	5	7
	θ_j	(0.3, 1)	(0.6, 5)	(0.5, 10)	(0.7, 15)	(0.2, 25)
$Q = 25$	$\widetilde{\lambda}_j$	4.9670	7.3015	1.8876	5.1820	6.9783
	$\widetilde{\theta}_j$	(0.3016, 1.0113)	(0.6133, 5.0007)	(0.4816, 10.0010)	(0.7097, 14.9972)	(0.1985, 24.9974)
$Q = 100$	$\widetilde{\lambda}_j$	4.9553	7.1001	1.9929	5.0736	6.9830
	$\widetilde{\theta}_j$	(0.3009, 1.0117)	(0.6057, 4.9999)	(0.4993, 10.0079)	(0.7061, 15.0017)	(0.1982, 24.9966)
$Q = 256$	$\widetilde{\lambda}_j$	4.9891	7.0950	2.0070	4.9055	6.7970
	$\widetilde{\theta}_j$	(0.3041, 1.0112)	(0.6054, 4.9992)	(0.5018, 10.0075)	(0.7003, 15.0016)	(0.2031, 25.0043)
$Q = 400$	$\widetilde{\lambda}_j$	4.9690	7.0538	1.9133	4.9015	6.7483
	$\widetilde{\theta}_j$	(0.3020, 1.0114)	(0.6041, 4.9998)	(0.4859, 10.0036)	(0.7002, 15.0014)	(0.2032, 25.0023)
$Q = 625$	$\widetilde{\lambda}_j$	4.9678	7.0433	1.9759	4.9636	6.6110
	$\widetilde{\theta}_j$	(0.3022, 1.0115)	(0.6036, 5.0003)	(0.4966, 10.0061)	(0.7025, 15.0035)	(0.2078, 25.0015)
$Q = 900$	$\widetilde{\lambda}_j$	4.9803	7.0981	2.0104	5.0513	6.6630
	$\widetilde{\theta}_j$	(0.3030, 1.0103)	(0.6052, 4.9991)	(0.5019, 10.0072)	(0.7047, 15.0059)	(0.2065, 25.0024)

Table 3: Example 2: RMS under different ϵ and γ for $M = 3$.

ϵ	γ									
	0.0909	0.1818	0.2727	0.3636	0.4545	0.5455	0.6364	0.7273	0.8182	0.9091
0.01	0.0231	0.0121	0.0388	0.0266	0.0137	0.0250	0.0184	0.0233	0.0822	0.0589
0.001	0.0083	0.0045	0.0088	0.0080	0.0089	0.0114	0.0099	0.0091	0.0096	0.0070

Table 4: Example 2: the approximation locations for (0.3, 0.3), (0.5, 0.7), and (0.7, 0.3).

ϵ	γ				
	0.0909	0.1818	0.2727	0.3636	0.4545
0.01	(0.2986, 0.2844) (0.5017, 0.7031) (0.7023, 0.2998)	(0.2983, 0.2987) (0.5013, 0.6993) (0.7018, 0.3014)	(0.3053, 0.3013) (0.5022, 0.6979) (0.7030, 0.3061)	(0.2951, 0.2875) (0.5005, 0.7029) (0.7036, 0.3016)	(0.3035, 0.3049) (0.5009, 0.6985) (0.7022, 0.3030)
0.001	(0.3002, 0.2937) (0.5010, 0.7010) (0.7024, 0.3018)	(0.3031, 0.2956) (0.5002, 0.7002) (0.7016, 0.3016)	(0.3019, 0.2951) (0.5006, 0.7003) (0.7020, 0.3017)	(0.3021, 0.2950) (0.5006, 0.7003) (0.7021, 0.3019)	(0.2996, 0.2947) (0.5008, 0.7008) (0.7024, 0.3018)

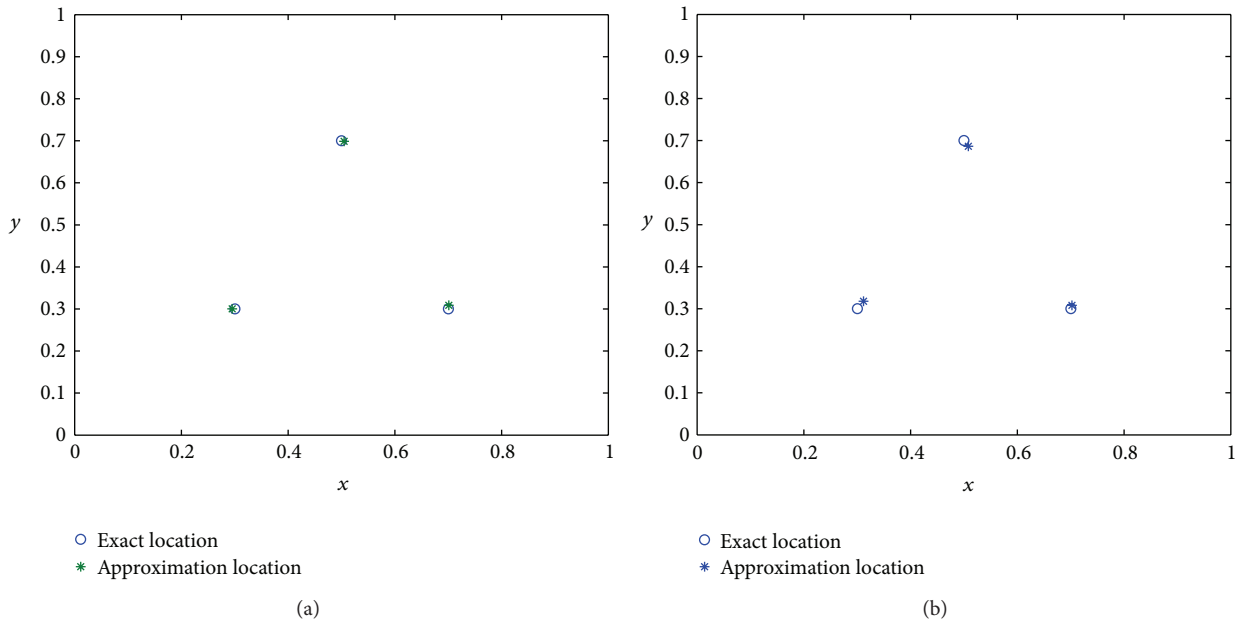

Figure 1: Approximation for $\epsilon = 0.1$ with $T = 0.1$ (a), 1 (b).

Table 5: Example 2: the approximation locations for (0.3, 0.3), (0.5, 0.7), and (0.7, 0.3).

ϵ	γ				
	0.5455	0.6364	0.7273	0.8182	0.9091
0.01	(0.3029, 0.2955)	(0.3003, 0.3007)	(0.3083, 0.3026)	(0.2957, 0.2992)	(0.2830, 0.2881)
	(0.5021, 0.7004)	(0.5007, 0.6983)	(0.4974, 0.6976)	(0.5050, 0.6980)	(0.4980, 0.7038)
	(0.7029, 0.3036)	(0.7010, 0.3029)	(0.6995, 0.3008)	(0.7018, 0.3088)	(0.7056, 0.3000)
0.001	(0.3011, 0.2940)	(0.3029, 0.2946)	(0.3017, 0.2943)	(0.2992, 0.2954)	(0.3023, 0.2972)
	(0.5010, 0.7006)	(0.5006, 0.7002)	(0.5009, 0.7006)	(0.5004, 0.7008)	(0.5005, 0.6996)
	(0.7025, 0.3022)	(0.7021, 0.3021)	(0.7021, 0.3017)	(0.7026, 0.3019)	(0.7021, 0.3024)

Table 6: Example 2: numerical comparison for $\epsilon = 0.01$ using different T.

Exact	λ_j	1	3	5
	θ_j	(0.3, 0.3)	(0.5, 0.7)	(0.7, 0.3)
$T = 0.1$	$\widetilde{\lambda}_j$	1.0108	3.0096	5.0584
	$\widetilde{\theta}_j$	(0.2886, 0.2917)	(0.5007, 0.7032)	(0.7043, 0.3034)
$T = 1$	$\widetilde{\lambda}_j$	1.0039	3.0035	4.8805
	$\widetilde{\theta}_j$	(0.3265, 0.3068)	(0.4966, 0.6984)	(0.6993, 0.3001)
$T = 2$	$\widetilde{\lambda}_j$	0.8916	2.9666	5.0708
	$\widetilde{\theta}_j$	(0.2959, 0.2993)	(0.5046, 0.6980)	(0.7004, 0.3093)
$T = 5$	$\widetilde{\lambda}_j$	0.8560	2.9201	5.1635
	$\widetilde{\theta}_j$	(0.2805, 0.3130)	(0.5134, 0.6938)	(0.7026, 0.3100)

show that the change of the parameter γ has little effect on the numerical computations, which reflects that the proposed method is robust about γ. On the other hand, one can see that, for smaller noise level ϵ, we obtain better numerical effect.

Secondly, we also consider the effect of the final time T on the numerical precision. Fixing $\gamma = 0.5$ and choosing parameter $\rho_j = 0.1$, we report the numerical results in Table 6, from which one can see that the accuracy of the approximation decreases with respect to the increase of the number of T. Such phenomenon can be explained by the nature of ill-posed inverse source identification problem.

Finally, using the previous point source, we plot the exact and approximation locations of source points in Figure 1 for $\epsilon = 0.1$ and $T = 0.1, 1$. The computational intensities are 0.9326, 2.9555, and 5.1065 for $T = 0.1$ and 1.4365, 1.9797, and 5.8621 for $T = 1$, respectively. It can be seen that even for

high noise level $\epsilon = 0.1$, the proposed method produces an acceptable numerical approximation.

5. Conclusion

Based on the use of Green's function, we propose in this paper an effective numerical method to recover both the intensities and locations of point sources for a time fractional diffusion process. Some numerical results show that the proposed algorithm provides an accurate and reliable scheme.

Acknowledgments

This work is supported by the Fundamental Research Funds for the Central Universities (SWJTU11BR078, ZYGX2011J104) and the NSF of China (no. 11226040).

References

[1] A. A. Kilbas, H. M. Srivastava, and J. J. Trujillo, *Theory and Applications of Fractional Differential Equations*, vol. 204 of *North-Holland Mathematics Studies*, Elsevier Science, Amsterdam, The Netherlands, 2006.

[2] I. Podlubny, *Fractional Differential Equations*, vol. 198 of *Mathematics in Science and Engineering*, Academic Press, San Diego, Calif, USA, 1999.

[3] J. Sabatier, O. P. Agrawal, and J. A. T. Machado, *Advances in Fractional Calculus: Theoretical Developments and Applications in Physics and Engineering*, Springer, Dordrecht, The Netherlands, 2007.

[4] S. G. Samko, A. A. Kilbas, and O. I. Marichev, *Fractional Integrals and Derivatives*, Gordon and Breach Science, Yverdon, Switzerland, 1993.

[5] V. V. Anh and N. N. Leonenko, "Spectral analysis of fractional kinetic equations with random data," *Journal of Statistical Physics*, vol. 104, no. 5-6, pp. 1349–1387, 2001.

[6] R. Metzler and J. Klafter, "The random walk's guide to anomalous diffusion: a fractional dynamics approach," *Physics Reports*, vol. 339, no. 1, p. 77, 2000.

[7] C. Cattani, A. Ciancio, and B. Lods, "On a mathematical model of immune competition," *Applied Mathematics Letters*, vol. 19, no. 7, pp. 678–683, 2006.

[8] M. Li, "Fractal time series—a tutorial review," *Mathematical Problems in Engineering*, vol. 2010, Article ID 157264, 26 pages, 2010.

[9] M. Li, Y. Q. Chen, J. Y. Li, and W. Zhao, "Holder scales of sea level," *Mathematical Problems in Engineering*, vol. 2012, Article ID 863707, 22 pages, 2012.

[10] M. Li, W. Zhao, and C. Cattani, "Delay bound: fractal traffic passes through servers," *Mathematical Problems in Engineering*, vol. 2013, Article ID 157636, 15 pages, 2013.

[11] M. Li and W. Zhao, "On $1/f$ noise," *Mathematical Problems in Engineering*, vol. 2012, Article ID 673648, 23 pages, 2012.

[12] M. M. Khader, "On the numerical solutions for the fractional diffusion equation," *Communications in Nonlinear Science and Numerical Simulation*, vol. 16, no. 6, pp. 2535–2542, 2011.

[13] Y. Luchko, "Some uniqueness and existence results for the initial-boundary-value problems for the generalized time-fractional diffusion equation," *Computers & Mathematics with Applications*, vol. 59, no. 5, pp. 1766–1772, 2010.

[14] V. Isakov, *Inverse Problems for Partial Differential Equations*, vol. 127 of *Applied Mathematical Sciences*, Springer, New York, NY, USA, 1998.

[15] E. C. Baran and A. G. Fatullayev, "Determination of an unknown source parameter in two-dimensional heat equation," *Applied Mathematics and Computation*, vol. 159, no. 3, pp. 881–886, 2004.

[16] A. de Cezaro and B. T. Johansson, "A note on uniqueness in the identification of a spacewise dependent source anddiffusion coefficient for the heat equation," http://arxiv.org/abs/1210.7346.

[17] A. de Cezaro and F. T. de Cezaro, "Uniqueness and regularization for unknown spacewise lower-order coefficient and source for the heat type equation," http://arxiv.org/abs/1210.7348.

[18] S. D'haeyer, B. T. Johansson, and M. Slodička, "Reconstruction of a spacewise-dependent heat source in a time-dependent heat diffusion process," *IMA Journal of Applied Mathematics*, 2012.

[19] V. Isakov, "Inverse parabolic problems with the final overdetermination," *Communications on Pure and Applied Mathematics*, vol. 44, no. 2, pp. 185–209, 1991.

[20] T. Johansson and D. Lesnic, "Determination of a spacewise dependent heat source," *Journal of Computational and Applied Mathematics*, vol. 209, no. 1, pp. 66–80, 2007.

[21] B. T. Johansson and D. Lesnic, "A procedure for determining a spacewise dependent heat source and the initial temperature," *Applicable Analysis*, vol. 87, no. 3, pp. 265–276, 2008.

[22] I. A. Kaliev and M. M. Sabitova, "Problems of the determination of the temperature and density of heat sources from the initial and final temperatures," *Journal of Applied and Industrial Mathematics*, vol. 4, no. 3, pp. 332–339, 2010.

[23] G. A. Kriegsmann and W. E. Olmstead, "Source identification for the heat equation," *Applied Mathematics Letters*, vol. 1, no. 3, pp. 241–245, 1988.

[24] W. Rundell, "The determination of a parabolic equation from initial and final data," *Proceedings of the American Mathematical Society*, vol. 99, no. 4, pp. 637–642, 1987.

[25] L. Yan, C.-L. Fu, and F.-L. Yang, "The method of fundamental solutions for the inverse heat source problem," *Engineering Analysis with Boundary Elements*, vol. 32, no. 3, pp. 216–222, 2008.

[26] L. Yan, F.-L. Yang, and C.-L. Fu, "A meshless method for solving an inverse spacewise-dependent heat source problem," *Journal of Computational Physics*, vol. 228, no. 1, pp. 123–136, 2009.

[27] Y. C. Hon, M. Li, and Y. A. Melnikov, "Inverse source identification by Green's function," *Engineering Analysis with Boundary Elements*, vol. 34, no. 4, pp. 352–358, 2010.

[28] N. F. M. Martins, "An iterative shape reconstruction of source functions in a potential problem using the MFS," *Inverse Problems in Science and Engineering*, vol. 20, no. 8, pp. 1175–1193, 2012.

[29] L. Ling, Y. C. Hon, and M. Yamamoto, "Inverse source identification for Poisson equation," *Inverse Problems in Science and Engineering*, vol. 13, no. 4, pp. 433–447, 2005.

[30] M. Kirane and S. A. Malik, "Determination of an unknown source term and the temperature distribution for the linear heat equation involving fractional derivative in time," *Applied Mathematics and Computation*, vol. 218, no. 1, pp. 163–170, 2011.

[31] D. A. Murio and C. E. Mejía, "Source terms identification for time fractional diffusion equation," *Revista Colombiana de Matemáticas*, vol. 42, no. 1, pp. 25–46, 2008.

[32] J. G. Wang, Y. B. Zhou, and T. Wei, "Two regularization methods to identify a space-dependent source for the time-fractional

diffusion equation," *Applied Numerical Mathematics*, vol. 68, pp. 39–57, 2013.

[33] Y. Zhang and X. Xu, "Inverse source problem for a fractional diffusion equation," *Inverse Problems*, vol. 27, no. 3, Article ID 035010, 12 pages, 2011.

[34] H. W. Engl, M. Hanke, and A. Neubauer, *Regularization of Inverse Problems*, vol. 375 of *Mathematics and its Applications*, Kluwer Academic, Dordrecht, The Netherlands, 1996.

[35] P. C. Hansen, *Rank-Deficient and Discrete Ill-Posed Problems*, SIAM Monographs on Mathematical Modeling and Computation, Society for Industrial and Applied Mathematics, Philadelphia, Pa, USA, 1998.

[36] P. C. Hansen, "Regularization tools: a Matlab package for analysis and solution of discrete ill-posed problems," *Numerical Algorithms*, vol. 6, no. 1-2, pp. 1–35, 1994.

[37] P. C. Hansen and D. P. O'Leary, "The use of the *L*-curve in the regularization of discrete ill-posed problems," *SIAM Journal on Scientific Computing*, vol. 14, no. 6, pp. 1487–1503, 1993.

[38] R. Gorenflo and F. Mainardi, "Fractional calculus: integral and differential equations of fractional order," in *Fractals and Fractional Calculus in Continuum Mechanics*, A. Carpinteri and F. Mainardi, Eds., pp. 223–276, Springer, New York, NY, USA, 1997.

Hindawi Publishing Corporation
Advances in Mathematical Physics
Volume 2013, Article ID 821820, 12 pages
http://dx.doi.org/10.1155/2013/821820

Research Article

Interval Shannon Wavelet Collocation Method for Fractional Fokker-Planck Equation

Shu-Li Mei and De-Hai Zhu

College of Information and Electrical Engineering, China Agricultural University, Beijing 100083, China

Correspondence should be addressed to Shu-Li Mei; meishuli@163.com

Received 4 September 2013; Revised 5 October 2013; Accepted 6 October 2013

Academic Editor: Ming Li

Metzler et al. introduced a fractional Fokker-Planck equation (FFPE) describing a subdiffusive behavior of a particle under the combined influence of external nonlinear force field and a Boltzmann thermal heat bath. In this paper, we present an interval Shannon wavelet numerical method for the FFPE. In this method, a new concept named "dynamic interval wavelet" is proposed to solve the problem that the numerical solution of the fractional PDE is usually sensitive to boundary conditions. Comparing with the traditional wavelet defined in the interval, the Newton interpolator is employed instead of the Lagrange interpolation operator, so, the extrapolation points in the interval wavelet can be chosen dynamically to restrict the boundary effect without increase of the calculation amount. In order to avoid unlimited increasing of the extrapolation points, both the error tolerance and the condition number are taken as indicators for the dynamic choice of the extrapolation points. Then, combining with the finite difference technology, a new numerical method for the time fractional partial differential equation is constructed. A simple Fokker-Planck equation is taken as an example to illustrate the effectiveness by comparing with the Grunwald-Letnikov central difference approximation (GL-CDA).

1. Introduction

Due to the fact that $1/f$ signal gains the increasing interests in the field of biomedical signal processing and engineering systems [1], the differential equations of fractional order appear more and more frequently in various research areas and engineering applications [2, 3]. As a matter of fact, the applications of fractional differential equations and their corresponding time series have been developed in various fields of sciences and technologies [4, 5] in recent years, ranging from computer science to physics [6, 7]. An effective and easy-to-use method for solving such equations is needed. However, known methods have certain disadvantages. Methods, described in detail in [3] for fractional differential equations of rational order, do not work in the case of arbitrary real order. On the other hand, there is an iteration method described in [8], which allows solution of fractional differential equations of arbitrary real order but it works effectively only for relatively simple equations, in addition to the series method. Up to now, most studies on the numerical methods for the fractional PDEs concentrate on the finite difference methods. Li [9] proposed an analytical method taking the fractal time series as the solution to a differential equation of fractional order or a response of a fractional system or a fractional filter driven with a white noise in the domain of stochastic processes and gave the exact solution of impulse response to a class of fractional oscillators [10]. According to this idea, Li and his coresearchers solved many problems in science and technology [11–14]. In addition, Wavelet numerical method is another way to get the solution of the fractional PDEs. In fact, the wavelet transform theory has been widely used in numerical analysis such as PDEs-based image processing [15–17], option pricing model [18], integrodifferential operators [19–23], and other nonlinear PDEs [24–28]. The wavelet functions possess many excellent numerical properties, such as orthogonality, interpolation, smoothness, and compact support, which are helpful in improving numerical accuracy and efficiency. In recent decades, many wavelets which have compact support, smoothness, and other properties have

been constructed. Among these wavelets, Shannon wavelet is paid little attention in applications as it does not possess compact support property although it possesses orthogonality, smooth continuity, and analytical expression. Cattani studied the properties of the Shannon wavelet function, which possesses many advantages such as orthogonality, continuous and differentiable. It also has the advantage over the Hermite DAF in that it is an interpolating function, producing matrix equations that have the potential to be relatively sparse. In addition, the second order approximation of a C^2-function, based on Shannon wavelet functions, is given [29]. The approximation is compared with the wavelet reconstruction formula and the error of approximation is explicitly computed [30].

A perceived disadvantage of the Shannon scaling function is that it tends to zero quite slowly as $|x| \to \infty$. A direct consequence of this is that when calculating the derivatives, a large number of the nodal values will contribute significantly. It is for this reason that Hoffman et al. [31] have suggested using the Shannon-Gabor wavelet, which introduces the Gaussian window function to improve the compact support property of Shannon wavelet function in required precision range. However, the presence of the Gaussian window destroys the orthogonal properties possessed by the Shannon wavelet, effectively worsening the approximation to a Dirac delta function.

Comparing with the common PDEs, the solutions of the fractional PDEs are more sensitive to the boundary condition. Using the wavelet transform defined in infinite domain to solve the engineering problems in finite interval, the wavelet transform coefficients at the boundary are usually very large. It will bring server boundary effect which affects the calculation accuracy and efficiency. Vasilyev and Paolucci [32] construct an interval wavelet using external wavelets, which can decrease the boundary effect to some extent. Based on the same principle, a more general construction method for the interval interpolation wavelet [33, 34] was given in the framework of generalized variational principle and has been widely used in many areas [35–37]. But the choice of parameter L (that is the amount of the external collocation points) was not discussed in detail. It just points out that the value of L should be taken between 1 and 3 based on experience. In fact, the value of L depends on the smoothness and derivative of the approximated function at boundary points. That is, if the approximated function is the solution of the diffusion PDEs with respect to the time parameter, the value of L should be taken dynamically. In addition, we should take into account that the impact of the external collocation points to the condition number of the system of the discretized algebraic equations. So, it is necessary to construct a dynamic interval wavelet in solving the PDEs with dynamic boundary conditions such as the fractional PDEs.

In this paper, a dynamic interval Shannon wavelet collocation method for the fractional FPDs is proposed. In this method, the relation between the parameter L and the wavelet approximation error was discussed based on the interpolation error theory, and an adaptive choice procedure on L was constructed. Therefore, the so-called dynamic interval Shannon wavelet is constructed. Next, based on the Grünwald-Letnikov definition of the fractional order derivative, we construct a Shannon wavelet numerical method for the fraction Fokker-Planck equation.

2. Fractional Fokker-Planck Equation

The fractional Fokker-Planck equation has been used in many physical transport problems which take place under the influence of an external force field [2, 38].

In the presence of an external force field $F(x) = -v'(x)$, the evolution of a test particle is usually described in terms of the Fokker-Planck equation (FPE)

$$\frac{\partial u(x,t)}{\partial t} = {}_0D_t^{1-\alpha}\left[\frac{\partial}{\partial x}\frac{v'(x)}{m\eta_\alpha} + K_\alpha\frac{\partial^2}{\partial x^2}\right]u(x,t), \quad a \le x \le b,\ 0 \le t \le T, \tag{1}$$

which defines the probability $u(x,t)$ of finding the particle at a certain position x at a given time t. m denotes the mass of the diffusing particle, $K_\alpha > 0$ denotes the generalized diffusion coefficient with dimension $[K_\alpha] = \mathrm{cm}^2\mathrm{sec}^{-\alpha}$, and η_α is the generalized friction coefficient with dimension $[\eta_\alpha] = \mathrm{sec}^{\alpha-2}$. The corresponding initial condition is

$$u(x,0) = \varphi(x), \quad a \le x \le b, \tag{2}$$

and the boundary conditions are

$$u(a,t) = p_1(t), \quad u(b,t) = p_2(t), \quad 0 < t \le T. \tag{3}$$

Equation (1) uses the Riemann-Liouville fractional derivative of order $1-\alpha$, defined by

$${}_0D_t^{1-\alpha}u(x,t) = \frac{1}{\Gamma(\alpha)}\frac{\partial}{\partial t}\int_0^1 \frac{u(x,\eta)}{(t-\eta)^{1-\alpha}}d\eta, \quad 0 \le \alpha < 1, \tag{4}$$

where $\Gamma(\alpha)$ is the gamma function.

According to the properties of the Riemann-Liouville fractional derivative, it is easy to know that, if $(x,t) \in C_{x,t}^{2,1}([a,b]\times[0,T])$, (1) can be rewritten as follows:

$$D_t^\alpha u(x,t) - \frac{u(x,0)\,t^{-\alpha}}{\Gamma(1-\alpha)} = \left[\frac{\partial}{\partial x}\frac{v'(x)}{m\eta_\alpha} + K_\alpha\frac{\partial^2}{\partial x^2}\right]u(x,t), \quad a \le x \le b,\ 0 \le t \le T. \tag{5}$$

Metzler et al. [2] proposed three implicit approximations for solving (5) as follows.

(1) The Grünwald-Letnikov expansion and the backward Euler implicit approximation (GL-BDIA)

$$\tau^{-\alpha}\left[u_i^n+\sum_{k=1}^{n-1}g_k u_i^{n-k}-\sum_{k=0}^{n-1}g_k u_i^0\right]=\frac{f_i u_i^n-f_{i-1}u_{i-1}^n}{h}+K_\alpha\frac{u_{i+1}^n-2u_i^n+u_{i-1}^n}{h^2},\quad i=1,2,\ldots,M-1$$

$$u_i^0=\varphi(x_i),\quad 1\le i\le M$$
$$u_0^n=p_1(t_n),\quad u_M^n=p_2(t_n),\quad n\ge 1,$$
$$g_k=\left(1-\frac{1+\alpha}{k}\right)g_{k-1},\qquad g_0=1,$$
$$f_i=f(x_i)=\frac{\nu'(x_i)}{m\eta_\alpha},\tag{6}$$

where $h=(b-a)/M$, $\tau=T/N$, $x_i=a+ih$, and $t_n=n\tau$. M and N are positive integers. The local truncation error is $O(\tau+h)$.

(2) L_1-approximation and the central difference implicit approximation (L_1-CDIA)

$$\frac{\tau^{-\alpha}}{\Gamma(2-\alpha)}\left[u_i^n+\sum_{k=1}^{n-1}(a_{n-k-1}-a_{n-k})u_i^k-a_{n-1}u_i^0\right]=\frac{f_{i+1}u_{i+1}^n-f_{i-1}u_{i-1}^n}{2h}+K_\alpha\frac{u_{i+1}^n-2u_i^n+u_{i-1}^n}{h^2}\quad i=1,2,\ldots,M-1$$

$$u_i^0=\varphi(x_i),\quad 1\le i\le M,$$
$$u_0^n=p_1(t_n),\quad u_M^n=p_2(t_n),\quad n\ge 1$$
$$a_k=(k+1)^{1-\alpha}-k^{1-\alpha},$$
$$f_i=f(x_i)=\frac{\nu'(x_i)}{m\eta_\alpha}.\tag{7}$$

The local truncation error is $O(\tau^{2-\alpha}+h^2)$.

(3) L_1-approximation and the backward difference implicit approximation (L_1-BDIA)

$$\frac{\tau^{-\alpha}}{\Gamma(2-\alpha)}\left[u_i^n+\sum_{k=1}^{n-1}(a_{n-k-1}-a_{n-k})u_i^k-a_{n-1}u_i^0\right]=\frac{f_i u_i^n-f_{i-1}u_{i-1}^n}{h}+K_\alpha\frac{u_{i+1}^n-2u_i^n+u_{i-1}^n}{h^2}\quad i=1,2,\ldots,M-1$$

$$u_i^0=\varphi(x_i),\quad 1\le i\le M$$
$$u_0^n=p_1(t_n),\quad u_M^n=p_2(t_n),\quad n\ge 1$$
$$f_i=f(x_i)=\frac{\nu'(x_i)}{m\eta_\alpha},$$
$$a_k=(k+1)^{1-\alpha}-k^{1-\alpha}.\tag{8}$$

The local truncation error is $O(\tau^{2-\alpha}+h)$.

In fact, (6)–(2) are not perfect approximation as the boundary effect is not taken into account. So, it will introduce boundary effect in solving the PDEs with the Nuemann boundary conditions. It is well known that the finite difference method is equivalent to the Faber-Schauder wavelet collocation method, so the construction method of the dynamic interval wavelet introduced in this paper can also be used to deal with the boundary problem in the finite difference method.

According to the Shannon sample theory, it can improve the calculation precision that combining the Grünwald-Letnikov expansion or L_1-approximation of the fractional derivative in (5) with the Shannon scaling function as the weight function instead of the various difference operators as follows:

$$\frac{\tau^{-\alpha}}{\Gamma(2-\alpha)}\left[u_i^n+\sum_{k=1}^{n-1}(a_{n-k-1}-a_{n-k})u_i^k-a_{n-1}u_i^0\right]=\sum_{i=0}^{2^J}\left[f_i u_i w'(x)+K_\alpha u_i w''(x)\right]$$

$i=1,2,\ldots,2^J$, consider J is the positive integer.

$$u_i^0=\varphi(x_i),\quad 1\le i\le M$$
$$u_0^n=p_1(t_n),\quad u_M^n=p_2(t_n),\quad n\ge 1$$
$$f_i=f(x_i)=\frac{\nu'(x_i)}{m\eta_\alpha}$$
$$a_k=(k+1)^{1-\alpha}-k^{1-\alpha}.\tag{9}$$

3. Construction of the Interval Interpolation Wavelet

3.1. Shannon Wavelet and Shannon-Gabor Wavelet. The representation of Shannon wavelet is based upon approximating the Dirac delta function as a band-limited function and is given by

$$\phi(x)=\frac{\sin(\pi x)}{\pi x}\tag{10}$$

and the Shannon-Gabor scaling function is defined as [17]

$$G(x)=\frac{\sin(\pi x)}{\pi x}\exp\left(-\frac{x^2}{2\sigma^2}\right),\quad \sigma>0,\tag{11}$$

where σ is the window size.

Consider a one-dimensional function $f(x)$, $x\in[a,b]$. A discrete point sequence of the variable x is defined as

$$x_n = a + \frac{b-a}{2^j} \cdot n, \quad j \in \mathbf{Z},\ n = 0, 1, 2, \ldots, 2^j, \tag{12}$$

and the corresponding discrete point sequence of the scaling function $\phi(x)$ and $G(x)$ can be defined, respectively, as

$$\begin{aligned} \phi_{j,n}(x) &= \phi_j(x - x_n) = \frac{\sin\left(2^j\pi/(b-a)\right)(x-x_n)}{\left(2^j\pi/(b-a)\right)(x-x_n)}, \\ G_{j,n}(x) &= G_j(x - x_n) = \frac{\sin\left(2^j\pi/(b-a)\right)(x-x_n)}{\left(2^j\pi/(b-a)\right)(x-x_n)} \\ &\quad \times \exp\left(-\frac{2^{2^j-1}(x-x_n)^2}{r^2(b-a)^2}\right), \end{aligned} \tag{13}$$

where $r = 2^j\sigma/(b-a)$.

The first and second order derivatives of $\phi_j(x - x_n)$ at the discrete point x_k are

$$\begin{aligned} \phi_j'(x_k - x_n) &= \begin{cases} 0, & k = n, \\ \dfrac{2^j \cos[\pi(k-n)]}{(k-n)(b-a)}, & k \neq n, \end{cases} \\ \phi_j''(x_k - x_n) &= \begin{cases} -\dfrac{\pi^2}{3\left((b-a)/2^j\right)^2}, & k = n, \\ -\dfrac{2\cos[\pi(k-n)]}{\left((b-a)/2^j\right)^2(k-n)^2}, & k \neq n. \end{cases} \end{aligned} \tag{14}$$

And the first and second order derivatives of $G_j(x - x_n)$ at the discrete point x_k are

$$\begin{aligned} G_j'(x_k - x_n) &= \begin{cases} 0, & k = n \\ \dfrac{2^j \cos[\pi(k-n)] \exp\left[-(k-n)^2/2r^2\right]}{(k-n)(b-a)}, & k \neq n \end{cases} \\ G_j''(x_k - x_n) &= \begin{cases} -\dfrac{3 + \pi^2 r^2}{3r^2\left((b-a)/2^j\right)^2}, & k = n \\ -\dfrac{2\cos[\pi(k-n)] \exp\left[-(k-n)^2/2r^2\right]}{\left((b-a)/2^j\right)^2}\left[\dfrac{1}{(k-n)^2} + \dfrac{1}{r^2}\right], & k \neq n. \end{cases} \end{aligned} \tag{15}$$

In fact, there is no difference between the construction method of the Interval Shannon wavelet and the interval Shannon-Gabor wavelet. So, we just take one uniform symbol $w(x)$ as the representation of the Shannon wavelet and the Shannon-Gabor wavelet in the following.

3.2. Interval Interpolation Wavelet. According to the definition of the interval wavelet, the interval interpolation basis functions can be expressed as:

$$w_{jk}(x) = \begin{cases} \phi\left(2^j x - k\right) + \displaystyle\sum_{n=-L+1}^{-1} a_{nk}\phi\left(2^j x - n\right), & k = 0, \ldots, L \\ \phi\left(2^j x - k\right), & k = L+1, \ldots, 2^j - L - 1 \\ \phi\left(2^j x - k\right) + \displaystyle\sum_{n=2^j+1}^{2^j+L-1} b_{nk}\phi\left(2^j x - n\right), & k = 2^j - L, \ldots, 2^j, \end{cases} \tag{16}$$

where,

$$\begin{aligned} a_{nk} &= \prod_{i=L-1, i\neq k}^{-1} \frac{x_{j,n} - x_{j,i}}{x_{j,k} - x_{j,i}}, \qquad b_{nk} = \prod_{i=2^j+1, i\neq k}^{2^j+1+L} \frac{x_{j,n} - x_{j,i}}{x_{j,k} - x_{j,i}} \\ x_{j,k} &= k\frac{x_{\max} - x_{\min}}{2^j}, \quad k \in \mathbb{Z}, \end{aligned} \tag{17}$$

where L is the amount of the external collocation points, the amount of discrete points in the definition domain is $2^j + 1$ ($j \in \mathbb{Z}$), and $[x_{\min}, x_{\max}]$ is the definition domain of the approximated function.

Equations (16) and (17) show that the interval wavelet is derived from the domain extension. The supplementary discrete points in the extended domain are called external points. The value of the approximated function at the external points can be obtained by Lagrange extrapolation method. Using the interval wavelet to approximate a function, the boundary effect can be left in the supplementary domain; that is, the boundary effect is eliminated in the definition domain.

According to (16) and (17), the interval wavelet approximant of the function $f(x)$ $x \in [x_{\min}, x_{\max}]$ can be expressed as

$$f_j(x) = \sum f_j(x_n)\, w_j\left(2^j x - n\right), \qquad x_n = x_{\min} + n\frac{x_{\max} - x_{\min}}{2^j}. \tag{18}$$

$f_j(x_n)$ is the given value at the discrete point x_n. At the external points, $f_j(x_n)$ can be obtained by extrapolation; that is

$$f_j(x_n) = \begin{cases} \sum_{k=0}^{L-1}\left(f_j(x_k)\prod_{i=0,i\neq k}^{L-1}\frac{x_n - x_i}{x_k - x_i}\right), & n = -1,\ldots,-L \\ \sum_{k=2^j-L+1}^{2^j}\left(f_j(x_k)\prod_{i=2^j-L+1,k\neq i}^{2^j}\frac{x_n - x_i}{x_k - x_i}\right), & n = 2^j+1,\ldots,2^j+L. \end{cases} \tag{19}$$

So the interval wavelet approximant of $f(x)$ can be rewritten as

$$\begin{aligned} f_j(x) = {} & \sum_{n=-L}^{-1}\left(\sum_{k=0}^{L-1} f_j(x_k)\prod_{i=0}^{L-1}\frac{x_n - x_i}{x_k - x_i}\right)\omega\left(2^j x - n\right) \\ & + \sum_{n=0}^{2^j} f_j(x_k)\,\omega\left(2^j x - n\right) \\ & + \sum_{n=2^j+1}^{2^j+L}\left(\sum_{k=2^j-L}^{2^j} f_j(x_k)\prod_{i=2^j-L}^{2^j}\frac{x_n - x_i}{x_k - x_i}\right)\omega\left(2^j x - n\right). \end{aligned} \tag{20}$$

Let

$$LS_L(x_n) = \sum_{k=0}^{L-1} f_j(x_k)\prod_{i=0}^{L-1}\frac{x_n - x_i}{x_k - x_i}, \qquad LE_L(x_n) = \sum_{k=2^j-L}^{2^j} f_j(x_k)\prod_{i=2^j-L}^{2^j}\frac{x_n - x_i}{x_k - x_i}, \tag{21}$$

then

$$\begin{aligned} f_j(x) = {} & \sum_{n=-L}^{-1} LS_L(x_n)\,\omega\left(2^j x - n\right) \\ & + \sum_{n=0}^{2^j} f_j(x_k)\,\omega\left(2^j x - n\right) \\ & + \sum_{n=2^j+1}^{2^j+L} LE_L(x_n)\,\omega\left(2^j x - n\right). \end{aligned} \tag{22}$$

$LS_L(x_n)$ and $LE_L(x_n)$ correspond to the left and the right external points, respectively. They are obtained by Lagrange extrapolation using the internal collocation points near the boundary. So, the interval wavelet's influence on the boundary effect can be attributed to Lagrange extrapolation. It should be pointed out that we did not care about the reliability of the extrapolation. The only function of the extrapolation is enlarging the definition domain of the given function which can avoid the boundary effect occurred in the domain. Therefore, we can discuss the choice of L by means of Lagrange inner-and extrapolation error polynomial as follows:

$$R_L(x) = \frac{f^{(L+1)}(\xi)}{(L+1)!}\prod_{i=0}^{L}(x - x_i), \text{ for some } \xi \text{ between } x, x_0, \ldots, x_L. \tag{23}$$

Equation (23) indicates that the approximation error is both related to the smoothness and the gradient of the original function near the boundary. Setting different L can satisfy the error tolerance.

3.3. Adaptive Interval Interpolation Wavelet. The interval interpolation wavelet is often used to solve the diffusion PDEs with Neumann boundary conditions. The smoothness and gradient of the PDE's solution usually vary with the time parameter. If the parameter L is a constant, we have to take a bigger value in order to obtain results with higher calculation precision. But the bigger L usually introduces the famous Gibbs phenomena into the numerical solution, which usually results in the algorithm becoming invalid. In addition, the bigger L will bring much more calculation. To keep higher numerical precision and save calculation, the best way is to design a procedure that L can vary with the curve's smoothness and gradient dynamically.

In this dynamic procedure, the error estimation equation (23) can be taken as the criterion about L. But in most cases, we cannot know the smoothness and the derivative's order of the original function. This can be solved by substituting the difference coefficient for the derivative. This is coincident with the Newton interpolation equation which is equivalent with Lagrange interpolation equation. In addition, the Lagrange interpolation algorithm has no inheritance which is the key feature of Newton interpolation. So, the basis function has to be calculated repeatedly as interpolation points are added into the calculation, which increases the computation complexity greatly. In contracst to the Lagrange method, the advantage of Newton interpolation method is that the Newton divided difference form is employed, which can produce a mathematically equivalent result by using recurrence relations, which reduces the number of compute operation, especially the multiplication. So it is convenient using the Newton interpolation method to construct the dynamic procedure.

3.3.1. Newton Interpolation. The expression of Newton interpolation can be written as

$$\begin{aligned} N_n(x) = {} & f(x_0) + (x - x_0) f(x_0, x_1) \\ & + (x - x_0)(x - x_1) f(x_0, x_1, x_2) + \cdots \\ & + (x - x_0)(x - x_1) \cdots (x - x_{n-1}) \\ & \times f(x_0, x_1, \ldots, x_n). \end{aligned} \tag{24}$$

Substituting the Newton interpolation instead of the Lagrange interpolation into (22) can be rewritten as

$$\begin{aligned} f_j(x) = {} & \sum_{n=-L}^{-1} (NS_L(x_n))\, \omega\left(2^j x - n\right) \\ & + \sum_{n=0}^{2^j} f_j(x_n)\, \omega\left(2^j x - n\right) \\ & + \sum_{n=2^j+1}^{2^j+L} (NE_L(x_n))\, \omega\left(2^j x - n\right), \end{aligned} \tag{25}$$

where

$$\begin{aligned} NS_L(x_n) = {} & f(x_0) + (x_n - x_0) f(x_0, x_1) \\ & + (x_n - x_0)(x_n - x_1) f(x_0, x_1, x_2) + \cdots \\ & + (x_n - x_0)(x_n - x_1) \cdots (x_n - x_{L-1}) \\ & \times f(x_0, x_1, \ldots, x_L), \\ NS_R(x_n) = {} & f(x_{2^j}) + (x_n - x_{2^j}) f(x_{2^j}, x_{2^j-1}) \\ & + (x_n - x_{2^j})(x_n - x_{2^j-1}) \\ & \times f(x_{2^j}, x_{2^j-1}, x_{2^j-2}) + \cdots \\ & + (x_n - x_{2^j})(x_n - x_{2^j-1}) \cdots (x_n - x_{2^j-L}) \\ & \times f(x_{2^j}, x_{2^j-1}, \ldots, x_{2^j-L}). \end{aligned} \tag{26}$$

3.3.2. Relation between the Newton Interpolation Error and the Choice of L. It is well known that the Newton interpolation is equivalent to the Lagrange interpolation. The corresponding error estimation can be expressed as

$$R_n(x) = (x - x_0)(x - x_1) \cdots (x - x_n) f(x, x_0, \ldots, x_n). \tag{27}$$

And the simplest criterion to terminate the dynamic choice on L is $|R_n(x)| \le T_a$ (T_a is the absolute error tolerance). Obviously, it is difficult to define T_a which should meet with the precision requirement of all approximated curves. In fact, the difference coefficient $f(x, x_0, \ldots, x_n)$ can be used directly as the criterion; that is

$$\left| f(x, x_0, \ldots, x_n) \right| < \varepsilon. \tag{28}$$

As mentioned above, once the curves with lower order smoothness are approximated by higher order polynomial expression, the errors will become bigger on the contrary. In fact, even if the L is infinite, the computational precision cannot be satisfied except by increasing computational complexity. To avoid this, we design the termination procedure of dynamic choice about L as follows:

If $f(x_0, x_1) < T_a$, then $L = 1$

else if $f(x_0, x_1, x_2) < T_a$ or $f(x_0, x_1, x_2) < f(x_0, x_1)$, then $L = 2$

else if $f(x_0, x_1, x_2, x_3) < T_a$ or $f(x_0, x_1, x_2, x_3) < f(x_0, x_1, x_2)$, then $L = 3$

...

3.3.3. L and the Condition Number of the System of Algebraic Equations. In the field of numerical analysis, the condition number of a function with respect to an argument measures how much the output value of the function can change for a small change in the input argument. This is used to measure how sensitive a function is to changes or errors in the input and how much error in the output results from an error in the input. It is no doubt that the choice of L can change the condition number of the system of algebraic equations discretized by the wavelet interpolation operator or the finite difference method. Therefore, the choice of L should take the condition number into account. In fact, if the condition number $\mathrm{cond}(A) = 10^k$, then you may lose up to k digits of accuracy on top of what would be lost to the numerical method due to loss of precision from arithmetic methods [24]. According to the general rule of thumb, the choice should follow the rule as follows:

$$\frac{\mathrm{Cond}(A_{L+1})}{\mathrm{Cond}(A_L)} < 10. \tag{29}$$

3.3.4. Relation between L and Computation Complexity. The computational complexity of interpolation calculation is not proportional to the increasing points. The former is mainly up to the computation amount of $(x - x_0)(x - x_1) \cdots (x - x_n)$ and the derivative operations. Obviously, according to (5), the increase in computational complexity is $O(L^3)$ when the number of extension points L increases by 1. But the computational complexity of adaptively increasing collocation points is related to the different wavelet functions. For the wavelet with compact support property such as Daubechies wavelet and Shannon wavelet, the value of L is impossible to be infinite. For Haar wavelet which has no smoothness property, L can be taken as 0 at most since it need not to be extended. For Faber-Schauder wavelet, L can be taken as 1 at most. For Daubechies wavelet, L can be taken as different values according to the order of vanishing moments, but it must be finite. For the wavelets without compact support property, L can take value dynamically, such as Shannon wavelet. The computational complexity of increasing points is mainly up to the wavelet function of itself.

4. Numerical Results and Discussion

Fractional Fokker-Planck equation is a typical fractional PDE, which is often used to describe a subdiffusive behavior of a particle under the combined influence of external nonlinear force field, and a Boltzmann thermal heat bath. This section considers the accuracy and efficiency of the proposed method for a fractional Fokker-Planck equation. Comparisons are made with results obtained with Chen's finite difference approximations and the exact analytic solution.

It has been pointed out that the finite difference approximation formats proposed in [2] are not perfect as they do not take the boundary problems into account. In this section, we take the Grünwald-Letnikov expansion and the central difference implicit approximation (GL-CDIA) to solve the example. That is,

$$\begin{aligned}
&\tau^{-\alpha}\left[u_i^n+\sum_{k=1}^{n-1}g_k u_i^{n-k}-\sum_{k=0}^{n-1}g_k u_i^0\right]\\
&\quad=\frac{f_{i+1}u_{i+1}^n-f_{i-1}u_{i-1}^n}{2h}+K_\alpha\frac{u_{i+1}^n-2u_i^n+u_{i-1}^n}{h^2},\\
&\qquad\qquad i=1,2,\ldots,M-1,\\
&\tau^{-\alpha}\left[u_0^n+\sum_{k=1}^{n-1}g_k u_0^{n-k}-\sum_{k=0}^{n-1}g_k u_0^0\right]\\
&\quad=\frac{4f_1u_1^n-3f_0u_0^n-f_2u_2^n}{2h}+K_\alpha\frac{u_0^n-2u_1^n+u_2^n}{h^2},\\
&\tau^{-\alpha}\left[u_M^n+\sum_{k=1}^{n-1}g_k u_M^{n-k}-\sum_{k=0}^{n-1}g_k u_M^0\right]\\
&\quad=\frac{f_{M-2}u_{M-2}^n-4f_{M-1}u_{M-1}^n+3f_Mu_M^n}{2h}\\
&\qquad+K_\alpha\frac{u_{M-2}^n-2u_{M-1}^n+u_M^n}{h^2},\\
&\qquad u_i^0=\varphi(x_i),\quad 1\le i\le M,\\
&u_0^n=p_1(t_n),\quad u_M^n=p_2(t_n),\quad n\ge 1,\\
&\qquad g_k=\left(1-\frac{1+\alpha}{k}\right)g_{k-1},\quad g_0=1\\
&\qquad f_i=f(x_i)=\frac{\nu'(x_i)}{m\eta_\alpha}.
\end{aligned}\tag{30}$$

According to the wavelet collocation method, the fractional Fokker-Planck equation can be approximately represented as

$$\begin{aligned}
&\tau^{-\alpha}\left[u_j(x_i,t_n)+\sum_{k=1}^{n-1}g_k u_j(x_i,t_{n-k})\right.\\
&\qquad\left.-\sum_{k=0}^{n-1}g_k u_j(x_i,t_0)\right]\\
&\quad=f'(x_i)\,u_j(x_i,t_n)\\
&\qquad+\sum_{m=0}^{2^j}u_j(x_m,t_n)\\
&\qquad\qquad\times\left[w'(x_i-x_m)+K_\alpha w''(x_i-x_m)\right],
\end{aligned}\tag{31}$$

where $i=0,1,2,\ldots 2^j$. Let

$$\begin{aligned}
V_j^n&=\left(u_j(x_0,t_n),u_j(x_1,t_n),\ldots,u_j(x_{2^j},t_n)\right)^T,\\
F&=\operatorname{diag}\left(f'(x_0),f'(x_1),\ldots,f'(x_{2^j})\right),\\
W_1&=\begin{bmatrix}
w'(x_0-x_0) & w'(x_0-x_1) & \cdots & w'(x_0-x_{2^j})\\
w'(x_1-x_0) & w'(x_1-x_1) & \cdots & w'(x_1-x_{2^j})\\
\vdots & \vdots & \ddots & \vdots\\
w'(x_{2^j}-x_0) & w'(x_{2^j}-x_1) & \cdots & w'(x_{2^j}-x_{2^j})
\end{bmatrix},\\
W_2&=\begin{bmatrix}
w''(x_0-x_0) & w''(x_0-x_1) & \cdots & w''(x_0-x_{2^j})\\
w''(x_1-x_0) & w''(x_1-x_1) & \cdots & w''(x_1-x_{2^j})\\
\vdots & \vdots & \ddots & \vdots\\
w''(x_{2^j}-x_0) & w''(x_{2^j}-x_1) & \cdots & w''(x_{2^j}-x_{2^j})
\end{bmatrix}.
\end{aligned}\tag{32}$$

Then the system of (31) can be expressed as the matrix format:

$$\begin{aligned}
&\left(W_1+K_\alpha W_2+F-\tau^{-\alpha}I\right)V_j^n\\
&\qquad=\sum_{k=1}^{n-1}g_kV_j^{n-k}-\sum_{k=0}^{n-1}g_kV_j^0.
\end{aligned}\tag{33}$$

Next, we will discuss the precision of the method proposed in this paper with numerical experience. Consider the Fokker-Planck equation as follows:

$$\begin{aligned}
\frac{\partial u(x,t)}{\partial t}&={}_0\mathbf{D}_t^{1-\alpha}\left[\frac{\partial}{\partial x}(-1)+\frac{\partial^2}{\partial x^2}\right]u(x,t),\\
&\qquad 0\le x\le 1,t>0,
\end{aligned}\tag{34}$$

with the initial condition

$$u(x,0)=x(1-x),\quad 0\le x\le 1\tag{35}$$

and the boundary conditions

$$\begin{aligned}
u(0,t)&=-\frac{3t^\alpha}{\Gamma(1+\alpha)}-\frac{2t^{2\alpha}}{\Gamma(1+2\alpha)},\quad t>0,\\
u(1,t)&=-\frac{t^\alpha}{\Gamma(1+\alpha)}-\frac{2t^{2\alpha}}{\Gamma(1+2\alpha)},\quad t>0.
\end{aligned}\tag{36}$$

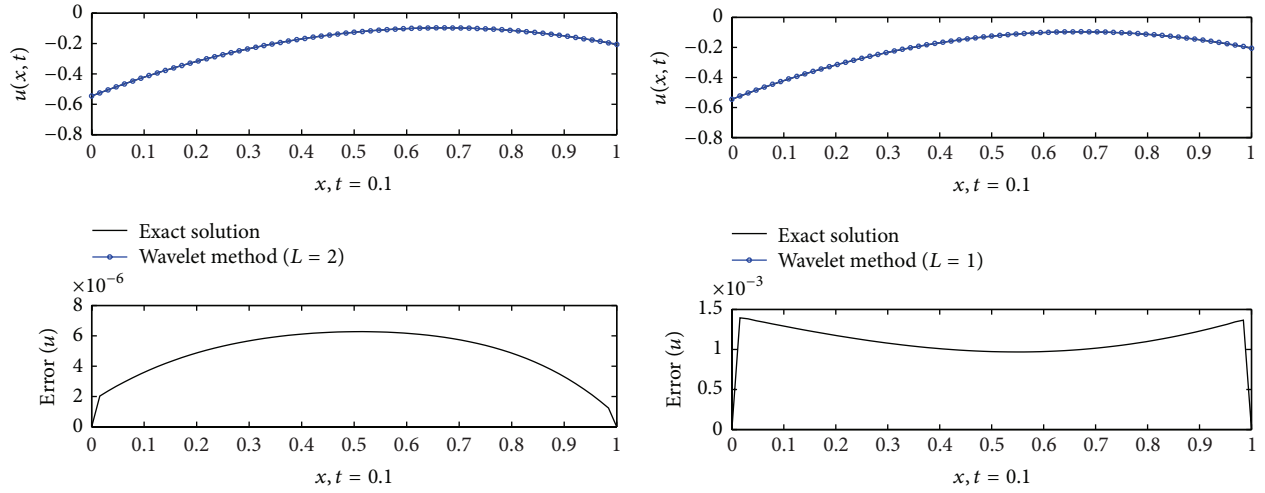

(a) $j = 6, L = 2$, condition number is 76.7074, $e_1 = 6.2776 \times 10^{-6}$, and $e_2 = 4.9985 \times 10^{-6}$

(b) $j = 6, L = 1$, condition number is 31.2950, $e_1 = 1.4 \times 10^{-3}$, and $e_2 = 1.1 \times 10^{-3}$

FIGURE 1: Wavelet collocation method with constant L ($\alpha = 0.8$).

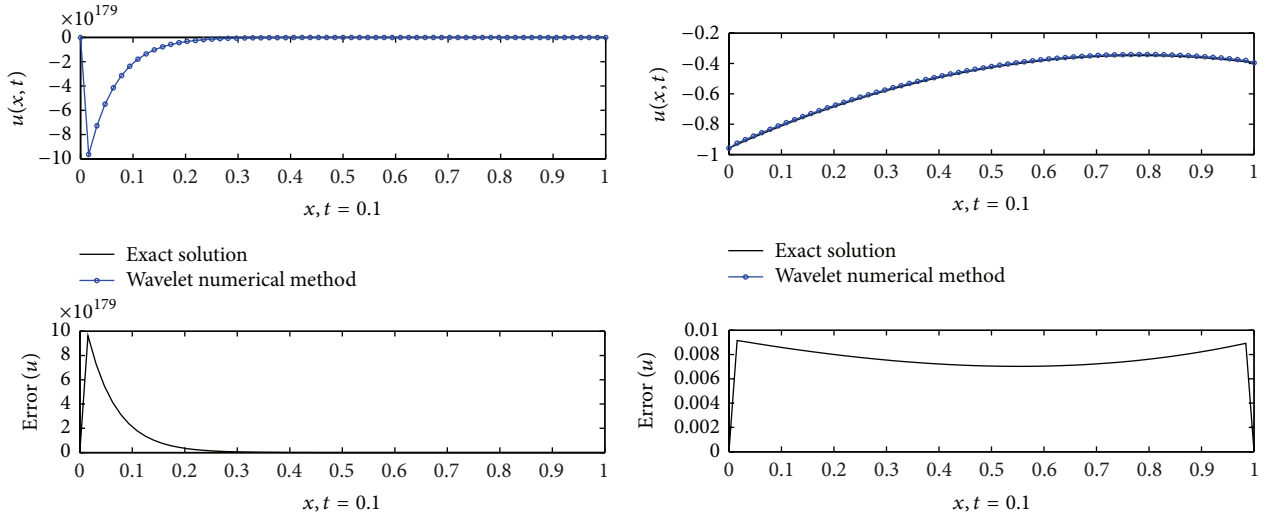

(a) $j = 6, L = 2$, and $\tau = 0.0001$

(b) $j = 6, L = 1$, and $\tau = 0.0001$

FIGURE 2: Wavelet collocation method with constant L ($\alpha = 0.6$).

The exact analytic solution is

$$u(x,t) = x(1-x) + (2x-3)\frac{t^{\alpha}}{\Gamma(1+\alpha)} - \frac{2t^{2\alpha}}{\Gamma(1+2\alpha)}. \quad (37)$$

All the comparisons in this section are made qualitatively by comparing the calculation precision in the same time step and space mesh grid size. The first measure of error e_1 is given by

$$e_1 = \left\| V_j^n - V_{\text{exact}}^n \right\|_{\infty}, \quad (38)$$

which provides a measure of the accuracy of the solution near the boundary. The second measure of error e_2 is given by

$$e_2 = \sqrt{\frac{1}{2^j+1}\sum_{i=0}^{2^j}\left(u(x_i) - u_{\text{exact}}(x_i)\right)^2}, \quad (39)$$

which provides a general measure of the accuracy of the solution over the main body of the distribution and was often used to investigate the accuracy of the FEM.

The comparisons between the static interval Shannon-Gabor wavelets with $L = 1$ and $L = 2$ are showen in Figure 1. The boundary effect of the interval wavelet with $L = 2$ (Figure 1(a)) is almost eliminated compared

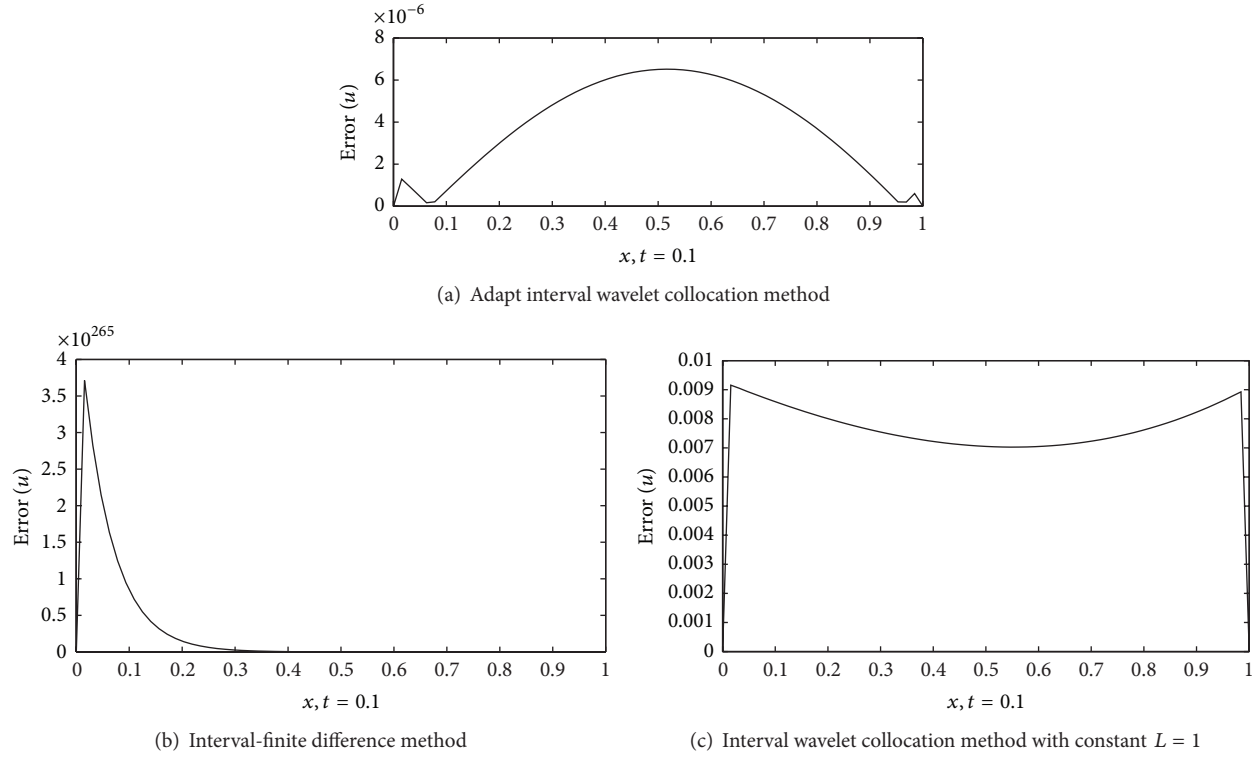

(a) Adapt interval wavelet collocation method

(b) Interval-finite difference method

(c) Interval wavelet collocation method with constant $L = 1$

Figure 3: Numerical errors comparison among the dynamic, static interval wavelet method and the finite difference method ($j = 6, \alpha = 0.6$).

Table 1: Condition number of the Fokker-Planck equation.

j	α	$\tau = 0.0001$			$\tau = 0.00001$		
		Interval FDM	Interval wavelet		Interval FDM	Interval wavelet	
			$L = 1$	$L = 2$		$L = 1$	$L = 2$
4	0.8	1.9730	2.5810	2.9399	1.1364	1.2461	1.2738
	0.6	11.3319	11.8703	20.8760	2.6645	3.5347	4.3019
	0.4	198.8737	91.0582	365.5470	43.4632	31.2993	80.5876
5	0.8	6.2479	7.8009	11.6382	1.5798	2.0236	2.2010
	0.6	83.0421	52.1757	160.0987	10.9216	12.0887	20.8948
	0.4	1912.4	476.7221	3632.5	380.6050	152.3718	727.8708
6	0.8	39.1651	31.2950	76.7074	39.1651	5.2458	6.9255
	0.6	764.3693	255.2801	1476.4	79.4793	51.7012	155.2663
	0.4	19847.0000	2574.7	37997	3769.1	790.3041	7238.0
7	0.8	340.7877	145.7761	663.4654	19.8525	19.3224	38.9722
	0.6	7757.6000	1333.9	14931	730.3466	249.7668	1416.8
	0.4	214660.0000	14202	415100	39724	4266.4	76386

to $L = 1$ (Figure 1(b)). FFPE is a 2-order PDEs with respect to x, so $L \geq 2$ is the necessary condition for the interval wavelet satisfying the requirement of FFPE. We also noticed that the condition number of FFPE from the Table 1 that the condition number of $L = 2$ increases more rapid than $L = 1$ with the increase of j and the decrease of α. It has been mentioned in Section 2 that the larger condition number can decrease the calculation precision greatly. This also can be illustrated in Figure 2. The condition number in Figure 2(a) is greatly larger than in Figure 2(b), although the

Table 2: Influence of α on the numerical precision ($t = 0.0001$, $T = 0.1$).

j	α	e_1			e_2		
		Interval FDM	Interval WCM ($L = 2$)	Dynamic interval WCM	Interval FDM	Interval WCM ($L = 2$)	Dynamic interval WCM
4	0.8	5.5367×10^{-6}	8.1588×10^{-5}	5.5920×10^{-6}	4.1037×10^{-6}	5.8298×10^{-5}	4.1514×10^{-6}
	0.6	5.7907×10^{-6}	4.1158×10^{-4}	7.1813×10^{-6}	4.2424×10^{-6}	2.9468×10^{-4}	5.5971×10^{-6}
	0.4	3.5309×10^{-6}	9.1673×10^{-4}	3.7967×10^{-5}	2.6232×10^{-6}	6.3692×10^{-4}	2.1348×10^{-5}
5	0.8	5.5551×10^{-6}	8.2118×10^{-5}	5.8424×10^{-6}	4.1718×10^{-6}	5.9148×10^{-5}	4.4649×10^{-6}
	0.6	5.7760×10^{-6}	4.0932×10^{-4}	8.9707×10^{-6}	4.2907×10^{-6}	2.9753×10^{-4}	7.5330×10^{-6}
	0.4	6.5910×10^{264}	0.3971	0.0585	inf	0.1195	0.0491
6	0.8	5.5563×10^{-6}	8.1965×10^{-5}	1.3154×10^{-5}	4.2041×10^{-6}	5.9517×10^{-5}	8.6913×10^{-6}
	0.6	3.7124×10^{265}	0.0554	0.0096	inf	0.0105	0.0076
	0.4	inf	1.2637×10^{3}	0.0588	inf	375.3305	0.0499
7	0.8	3.4932×10^{243}	0.0031	0.0019	inf	3.8313×10^{-4}	1.2937×10^{-4}
	0.6	inf	216.5596	23.7361	inf	40.0263	9.3964
	0.4	inf	1.4462×10^{6}	327.6987	inf	4.2662×10^{5}	21.7694

Table 3: Dynamic L and the iteration times at the same L value ($j = 6$, $T = 0.1$, and $\tau = 0.0001$).

L	3	1	2	3	2
Iteration times	11	14	4	3	968

approximation of $L = 2$ is better than $L = 1$. The former has failed to solve FFPE obviously. In fact, this explained the reason why we construct the dynamic interval wavelet.

The numerical errors comparisons among the dynamic, static interval wavelet method and the interval finite difference method are showen in Figure 3. The result also can be illustrated in Table 2.

The robustness of the dynamic interval wavelet collocation method (DIWCM) is the best compared to the interval FDM and the static interval WCM, as it avoids both of the larger condition number and the error of the approximation simultaneity. The varied process of L is showen in Table 3. It shows that the value of L is fixed at $L = 2$ after a short time of vibration. This reflects the properties of the FFPE to some extent.

In addition, it also has to be noticed that we can get the higher precision solution with the interval finite difference method (FDM) as the amount of the collocation points decreases (Figure 4). It is well known that increasing the collocation points can impove the approximation although it can increase the condition number in FFPE. In fact, it profits from the smoothness of the solution, which would not work in solving the nonlinear problems.

All above numerical experiments are done with the Shannon-Gabor wavelet. It is well known that the presence of the Gaussian window destroys the orthogonal properties possessed by the Shannon wavelet, effectively worsening the approximation efficiency to a Dirac delta function. Comparing with the Shannon wavelet collocation method (Figure 5), the Shannon-Gabor wavelet numerical method has higher precision and more complicated calculation amount. But it is showen in Figure 5 that dynamic interpolation wavelet construction scheme can be applied to both of the Shannon-Gabor wavelet and the Shannon wavelet. As a matter of fact, the dynamic scheme is designed for the interpolation wavelet, which has no connection with certain concrete wavelet function.

5. Conclusions

In solving the fractional Fokker-Planck equations, there are two factors related to the choice of L. The first factor is the condition number, which relates to the parameters α, j and the time step τ. The larger L can decrease the calculation precision greatly. Another factor is the approximation of the function and its derivatives, especially near the boundary. Using the interval wavelet with constant L to solve the fraction Fokker-Planck equations cannot eliminate the boundary effect completely as the condition number is sensitive to the parameter α. With regard to the accuracy and time complexity of the solution in comparison with those obtained with other algorithms, the dynamic interval wavelet on L constructed in this paper is more reasonable. The numerical experiments illustrate that it is necessary to construct the dynamic interval wavelet collocation method for the fractional PDEs.

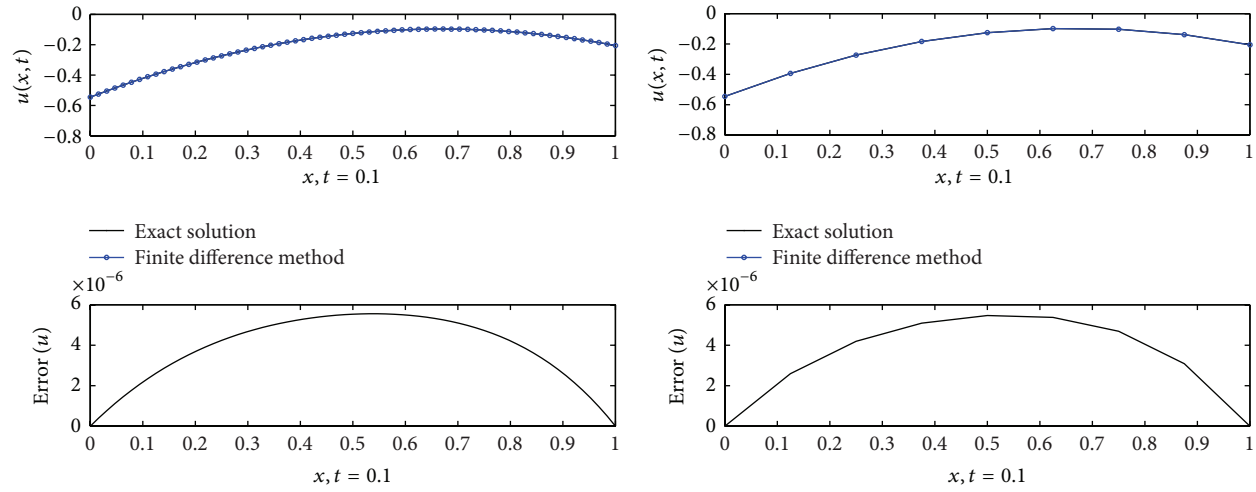

(a) $j = 6$, $e_1 = 5.5563 \times 10^{-6}$, $e_2 = 4.2041 \times 10^{-6}$, and condition number is 39.1651

(b) $j = 3$, $e_1 = 5.4691 \times 10^{-6}$, $e_2 = 3.9526 \times 10^{-6}$, and condition number is 1.2202

FIGURE 4: Finite-difference method ($\alpha = 0.8$).

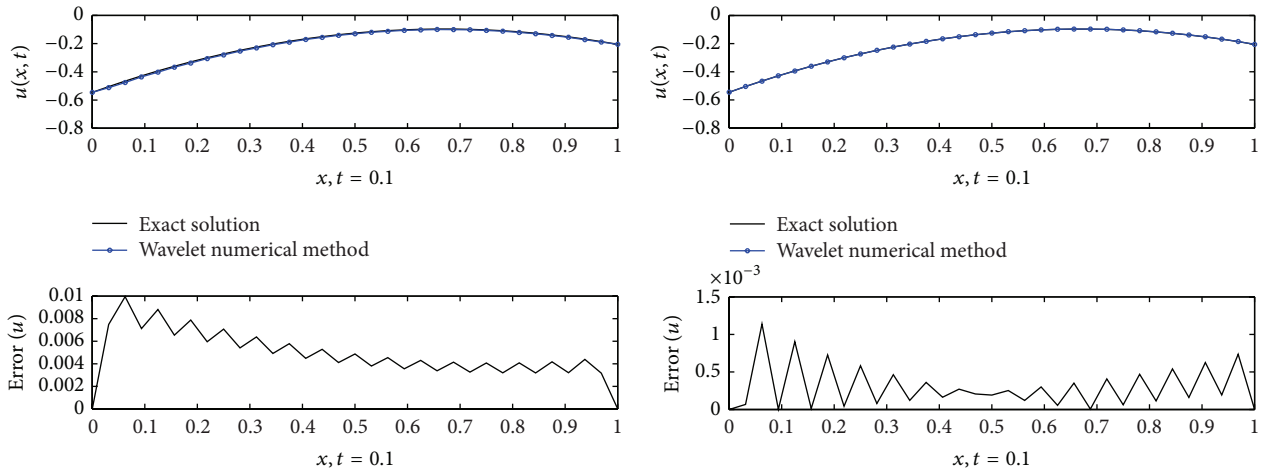

(a) Static interval Shannon wavelet collocation method, $j = 5$, and $e_1 = 9.95023 \times 10^{-3}$, $e_2 = 5.23917 \times 10^{-3}$

(b) Dynamic interval Shannon wavelet collocation method, $j = 5$, $e_1 = 1.1392 \times 10^{-3}$, and $e_2 = 4.0893 \times 10^{-4}$

FIGURE 5: Comparison between the static and dynamic interval Shannon wavelet collocation method ($\alpha = 0.8$).

Acknowledgments

This work is supported by the National Natural Science Foundation of China (no. 41171337) and the National High Technology Research and Development Program of China (no. 2006AA10Z235).

References

[1] M. Li and W. Zhao, "On $1/f$ noise," *Mathematical Problems in Engineering*, vol. 2012, Article ID 673648, 23 pages, 2012.

[2] R. Metzler, E. Barkai, and J. Klafter, "Anomalous diffusion and relaxation close to thermal equilibrium: a fractional fokker-planck equation approach," *Physical Review Letters*, vol. 82, no. 18, pp. 3563–3567, 1999.

[3] S. Chen, F. Liu, P. Zhuang, and V. Anh, "Finite difference approximations for the fractional fokker-planck equation," *Applied Mathematical Modelling*, vol. 33, no. 1, pp. 256–273, 2009.

[4] E. G. Bakhoum and C. Toma, "Modeling transitions in complex systems by multiplicative effect of temporal patterns extracted from signal flows," *Mathematical Problems in Engineering*, vol. 2012, Article ID 409856, 11 pages, 2012.

[5] C. Toma, "Advanced signal processing and command synthesis for memory-limited complex systems," *Mathematical Problems in Engineering*, vol. 2012, Article ID 927821, 13 pages, 2012.

[6] E. G. Bakhoum and C. Toma, "Transient aspects of wave propagation connected with spatial coherence," *Mathematical Problems in Engineering*, vol. 2013, Article ID 691257, 5 pages, 2013.

[7] S. X. Hu, Z. W. Liao, and W. F. Chen, "Sinogram restoration for low-dosed x-ray computed tomography using fractional-order perona-malik diffusion," *Mathematical Problems in Engineering*, vol. 2012, Article ID 391050, 13 pages, 2012.

[8] J. H. He, "Asymptotic methods for solitary solutions and compactons," *Abstract and Applied Analysis*, vol. 2012, Article ID 916793, 130 pages, 2012.

[9] M. Li, "Fractal time series—a tutorial review," *Mathematical Problems in Engineering*, vol. 2010, Article ID 157264, 26 pages, 2010.

[10] M. Li, S. C. Lim, and S. Y. Chen, "Exact solution of impulse response to a class of fractional oscillators and its stability," *Mathematical Problems in Engineering*, vol. 2011, Article ID 657839, 9 pages, 2011.

[11] M. Li, "Approximating ideal filters by systems of fractional order," *Computational and Mathematical Methods in Medicine*, vol. 2012, Article ID 365054, 6 pages, 2012.

[12] M. Li and W. Zhao, "Solving Abel's type integral equation with Mikusinski's operator of fractional order," *Advances in Mathematical Physics*, vol. 2013, Article ID 806984, 4 pages, 2013.

[13] M. Li, C. Cattani, and S. Y. Chen, "Viewing sea level by a one-dimensional random function with long memory," *Mathematical Problems in Engineering*, vol. 2011, Article ID 654284, 13 pages, 2011.

[14] M. Li and W. Zhao, "Visiting power laws in cyber-physical networking systems," *Mathematical Problems in Engineering*, vol. 2012, Article ID 302786, 13 pages, 2012.

[15] I. Daubechies and G. Teschke, "Variational image restoration by means of wavelets: simultaneous decomposition, deblurring, and denoising," *Applied and Computational Harmonic Analysis*, vol. 19, no. 1, pp. 1–16, 2005.

[16] S. L. Mei, "Construction of target controllable image segmentation model based on homotopy perturbation technology," *Abstract and Applied Analysis*, vol. 2013, Article ID 131207, 8 pages, 2013.

[17] S.-L. Mei, "HPM-based dynamic wavelet transform and its application in image denoising," *Mathematical Problem in Engineering*, vol. 2013, Article ID 309418, 10 pages, 2013.

[18] H. Yan, "Adaptive wavelet precise integration method for nonlinear black-scholes model based on variational iteration method," *Abstract and Applied Analysis*, vol. 2013, Article ID 735919, 6 pages, 2013.

[19] L. W. Liu, "Interval wavelet numerical method on fokker-planck equations for nonlinear random system," *Advances in Mathematical Physics*, vol. 2013, Article ID 651357, 7 pages, 2013.

[20] C. Cattani and A. Ciancio, "Separable transition density in the hybrid model for tumor-immune system competition," *Computational and Mathematical Methods in Medicine*, vol. 2012, Article ID 610124, 6 pages, 2012.

[21] C. Cattani, A. Ciancio, and B. Lods, "On a mathematical model of immune competition," *Applied Mathematics Letters*, vol. 19, no. 7, pp. 678–683, 2006.

[22] C. Cattani, "Fractional calculus and shannon wavelet," *Mathematical Problems in Engineering*, vol. 2012, Article ID 502812, 26 pages, 2012.

[23] C. Cattani, "Shannon wavelets for the solution of integro-differential equations," *Mathematical Problems in Engineering*, vol. 2010, Article ID 408418, 22 pages, 2010.

[24] R. Y. Xing, "Wavelet-based homotopy analysis method for nonlinear matrix system and its application in Burgers equation," *Mathematical Problems in Engineering*, vol. 2013, Article ID 982810, 7 pages, 2013.

[25] S.-L. Pang, "Wavelet numerical method for nonlinear random system," *Transactions of the Chinese Society of Agricultural Machinery*, vol. 38, no. 3, pp. 168–170, 2007.

[26] S. M. Bibic, "Harmonic wavelet analysis—connection coefficients for nonlinear PDE," *UPB Scientific Bulletin, Series A*, vol. 73, no. 1, pp. 27–36, 2011.

[27] M. Bieri, "A sparse composite collocation finite element method for elliptic SPDEs," *SIAM Journal on Numerical Analysis*, vol. 49, no. 6, pp. 2277–2301, 2011.

[28] N. A. Libre, A. Emdadi, E. J. Kansa, M. Shekarchi, and M. Rahimian, "A fast adaptive wavelet scheme in RBF collocation for nearly singular potential PDEs," *Computer Modeling in Engineering and Sciences*, vol. 38, no. 3, pp. 263–284, 2008.

[29] C. Cattani, "Second order shannon wavelet approximation of C^2-functions," *UPB Scientific Bulletin, Series A*, vol. 73, no. 3, pp. 73–84, 2011.

[30] C. Cattani and L. M. S. Ruiz, "Discrete differential operators in multidimensional haar wavelet spaces," *International Journal of Mathematics and Mathematical Sciences*, vol. 2004, no. 44, pp. 2347–2355, 2004.

[31] D. K. Hoffman, G. W. Wei, D. S. Zhang, and D. J. Kouri, "Shannon-Gabor wavelet distributed approximating functional," *Chemical Physics Letters*, vol. 287, no. 1-2, pp. 119–124, 1998.

[32] O. V. Vasilyev and S. Paolucci, "A dynamically adaptive multilevel wavelet collocation method for solving partial differential equations in a finite domain," *Journal of Computational Physics*, vol. 125, no. 2, pp. 498–512, 1996.

[33] S. L. Mei, H. L. Lv, and Q. Ma, "Construction of interval wavelet based on restricted variational principle and its application for solving differential equations," *Mathematical Problems in Engineering*, vol. 2008, Article ID 629253, 14 pages, 2008.

[34] S. L. Mei, C. J. Du, and S. W. Zhang, "Asymptotic numerical method for multi-degree-of-freedom nonlinear dynamic systems," *Chaos, Solitons and Fractals*, vol. 35, no. 3, pp. 536–542, 2008.

[35] S. L. Mei, Q. S. Lu, S. W. Zhang, and L. Jin, "Adaptive interval wavelet precise integration method for partial differential equations," *Applied Mathematics and Mechanics*, vol. 26, no. 3, pp. 364–371, 2005.

[36] S. L. Mei, C. J. Du, and S. W. Zhang, "Linearized perturbation method for stochastic analysis of a rill erosion model," *Applied Mathematics and Computation*, vol. 200, no. 1, pp. 289–296, 2008.

[37] S.-L. Mei, "HAM-based adaptive multi-scale meshless method for Burgers equation," *Journal of Applied Mathematics*, vol. 2013, Article ID 248246, 10 pages.

[38] T. D. Frank, "Autocorrelation functions of nonlinear fokker-planck equations," *European Physical Journal B*, vol. 37, no. 2, pp. 139–142, 2004.

Hindawi Publishing Corporation
Advances in Mathematical Physics
Volume 2013, Article ID 371868, 9 pages
http://dx.doi.org/10.1155/2013/371868

Research Article

Low-Dosed X-Ray Computed Tomography Imaging by Regularized Fully Spatial Fractional-Order Perona-Malik Diffusion

Zhiwu Liao

School of Computer Science, Sichuan Normal University, Chengdu, Sichuan 610101, China

Correspondence should be addressed to Zhiwu Liao; liaozhiwu@163.com

Received 19 September 2013; Accepted 2 November 2013

Academic Editor: Ming Li

Existing fractional-order Perona-Malik Diffusion (FOPMD) algorithms used in noise suppressing suffer from undesired artifacts and speckle effect, which hamper FOPMD used in low-dosed X-ray computed tomography (LDCT) imaging. In this paper, we propose a new FOPMD method for low-dose computed tomography (LDCT) imaging, which is called regularized fully spatial FOPMD (RFS-FOPMD), whose numerical scheme is also given based on Grünwald-Letnikov derivative (G-L derivative). Here, fully spatial FOPMD represents all the integer-order derivatives (IODs) in the right hand of Perona-Malik Diffusion (PMD) which are replaced by fractional-order derivatives (FODs). Since the new scheme has advantages of both regularization and FOPMD, it has good abilities in singularities preserving while suppressing noise. Some real sinogram of LDCT are used to compare the different performances not only for some classical but also for some state-of-art diffusion schemes. These schemes include PMD, regularized PMD (RPMD), and FOPMD in (Hu et al. 2012). Experimental results show that besides good ability in edge preserving, the new scheme also has good stability for iteration number and can avoid artifacts and speckle effect with suitable parameters.

1. Introduction

Perona-Malik diffusion (PMD) proposed in 1990 is a popular technique in image denoising and it is defined as [1]

$$\frac{\partial u(x,y,t)}{\partial t} = \operatorname{div}\left[c\left(\left\|\nabla u(x,y,t)\right\|\right)\nabla u(x,y,t)\right], \quad (1)$$

where $u(x,y,0)$ is the initial gray scale image, $u(x,y,t)$ is the smoothed gray scale image at time t, ∇ denotes the gradient, $\operatorname{div}(\cdot)$ is the divergence operator, and $c(\cdot)$ is the diffusion coefficient.

In 1992, Catté et al. indicated that PMD is ill-posed and they propose a new well-posed method named regularized Perona-Malik diffusion (RPMD), by replacing the gradient ∇u in diffusion coefficients by the smoothed version $G_\sigma \cdot \nabla u$ [2]. Thus, the RPMD can be represented as

$$\frac{\partial u(x,y,t)}{\partial t} = \operatorname{div}\left[c\left(\left\|G_{\sigma_1} \cdot \nabla u(x,y,t)\right\|\right)\nabla u(x,y,t)\right]. \quad (2)$$

Here G_{σ_1} is defined as:

$$G_{\sigma_1} = \frac{1}{C} e^{-((x^2+y^2)/\sigma_1^2)} \quad (3)$$

which is a Gaussian function and C is a constant.

In order to eliminate undesired "staircase" of PMD and RPMD, high-order PDEs (typically fourth-order PDEs) for image restoration have been introduced in [3, 4]. Though these methods can eliminate the staircase effect efficiently, they often leave the image with isolated black and white speckles (so-called speckle effect) [5].

Recently, fractional-order PMD (FOPMD) has been studied in image denoising [5–14], whose fractional order is α, $0 \le \alpha \le 2$, which is a "natural interpolation" between PMD and fourth-order PDEs. Therefore, it has the benefits of both of PMD and high order PDEs.

Bai and Feng proposed a FSFOD method for image denoising with Euler-Lagrange equations of a cost functional and using Fourier-domain to compute the fractional

derivative [5]. Jun and Zhihui develop a class of fractional-order multiscale variational model using G-L definition of fractional-order derivative and propose an efficient condition of the convergence of the model [6].

We also reported an experimental study that used FOPMD for sinogram restoration of low-dosed computed tomography (LDCT) based on fully spatial FOPMD using G-L definition [8]. In [8], we observe that FOPMD experiments with different fractional orders show different diffusion behaviors, which leads us to study FOPMD further.

In a most recent study, Hu proposed a new FOPMD by diffusing only on external gradient vector and reported good performance in LDCT imaging [9].

Although above FOPMD have reported on good performance of preserving edges, suppressing staircase and speckle effects, the resulting images of these FOPMD methods still have some artifacts and speckle effect which hamper them to be used in LDCT imaging.

Minimizing the radiation exposure to patients has been one of the major efforts in modern clinical X-ray CT radiology [15–17]. However, the presentation of strong noise degrades the quality of LDCT images dramatically and decreases the accuracy of diagnosis.

Filtering noise from clinical scans is a challenging task, since these scans contain many structures with different shapes, sizes, and contrasts, which should be preserved for making correct diagnosis. In addition, LDCT imaging also requires no artifacts and speckle effect to emerge while denoising because artifacts also increase chances of misdiagnosis. Many strategies have been proposed to reduce noises, but few of them discuss how to avoid artifacts and speckle effect [8, 18–28].

The artifacts of existing FOPMD methods used for LDCT imaging are generated by strong noises of LDCT sinogram, which leads to falsely located positions of edges. Thus, the resulting images produce some undesired weak edges, which form the artifacts.

Therefore, one valid method to suppress artifacts and speckle effect of existing FOPMD methods is by smoothing the fractional-order gradient (FOG) in the diffusion coefficients to avoid error-detected edges of the noisy LDCT.

Following the above discussion, we propose a regularized FOPMD, named regularized fully spatial FOPMD (RFS-FOPMD), by replacing FOG of diffusion coefficients with its smoothing counterparts while keeping "external" FOD unchanged. Here "fully spatial" represents all the derivatives of right-hand side of PMD equation and "external" indicates the spatial derivatives except for the derivatives used in diffusion coefficients. Since locations of edges can be detected correctly by our new scheme, FOPMD can preserve edges well and avoid artifacts.

The arrangement of this paper is as follows: in Section 2, the EFOGV-PMD is introduced, and then the the numerical scheme is given in Section 3, the experiment results are shown and discussed in Section 4, the final part is the conclusions and acknowledgments.

2. Regularized Fully Spatial Fractional-Order Perona-Malik Diffusion

In this paper, we use G-L definition defined as follows [29, 30]:

$$D^{\alpha} g(x) = \lim_{h \to 0^{+}} \frac{\sum_{k \geq 0} (-1)^{k} C_{k}^{\alpha} g(x - kh)}{h^{\alpha}}, \quad \alpha > 0, \tag{4}$$

where $g(x)$ is a real function, $\alpha > 0$ is a real number, $C_k^{\alpha} = \Gamma(\alpha + 1)/[\Gamma(k + 1)\Gamma(\alpha - k + 1)]$ is the generalized binomial coefficient, and $\Gamma(\cdot)$ denotes the gamma function.

Isotropic diffusion will damage the image features such as edges, lines, and textures. To avoid the damage, the smoothing has to be adaptively controlled by the amount of smoothing or the direction of smoothing. A classic example of adaptive smoothing is the anisotropic diffusion scheme proposed by Perona and Malik [1], in which the smoothing process is formulated by a partial differential equation (PDE). PMD is formulated in (1).

However, PMD methods suffer from their "staircase" effects. Therefore, FOPMD is proposed to suppress the staircase of PMD.

The fractional-order gradient vector with α order is defined as

$$\nabla^{\alpha} u(x, y, t) = \left[\nabla_{x}^{\alpha} u(x, y, t), \nabla_{y}^{\alpha} u(x, y, t) \right], \tag{5}$$

where α is a positive real, $\nabla_x^{\alpha} u(x, y, t)$ represents the partial fractional-order derivative of $u(x, y, t)$ with respect to the variable x whose order is α, and $\nabla_y^{\alpha} u(x, y, t)$ represents the partial fractional-order derivative of $u(x, y, t)$ with respect to the variable y whose order is α.

According to [8], FOPMD is defined as

$$\frac{\partial u(x, y, t)}{\partial t} = \operatorname{div}^{\alpha} \left[c\left(\left\| \nabla^{\alpha} u(x, y, t) \right\| \right) \nabla^{\alpha} u(x, y, t) \right], \tag{6}$$

where $\operatorname{div}^{\alpha}$ denotes the α-order divergence. For the vector $\nabla^{\beta} v = [v_x^{\beta}, v_y^{\beta}]$ where v_x^{β}, v_y^{β} represent the partial fractional-order derivative of $u(x, y, t)$ with whose order is β respect to the variable x and y respectively, its α-order divergence is defined as:

$$\operatorname{div}^{\alpha} \nabla^{\beta} v = v_{x}^{\beta+\alpha} + v_{y}^{\beta+\alpha}. \tag{7}$$

However, FOPMD defined by (3) will produce some artifacts for sinogram restoration of LDCT, which increases the probability of error diagnosis. In order to avoid artifacts produced in sinogram restoration of LDCT using FOPMD, we propose a new diffusion model, named regularized fully spatial fractional-order PMD (RFS-FOPMD), where "fully spatial" indicates all derivatives of the right-hand side of (6). That is, the FOD in diffusion coefficient is replaced by its smoothed version.

Therefore, the RFS-FOPMD is given by

$$\frac{\partial u(x, y, t)}{\partial t} = \operatorname{div}^{\alpha} \left[c\left(\left\| G_{\sigma_1} \cdot \nabla^{\alpha} u(x, y, t) \right\| \right) \nabla^{\alpha} u(x, y, t) \right] \tag{8}$$

with the observed image as the initial condition and G_{σ_1} is defined in (3).

When $\alpha = 1$, (6) is precisely the PMD and (8) is precisely the RPMD; when $\alpha = 2$, (6) is precisely the fourth-order anisotropic diffusion equation. In this paper, we are interested in $0.5 \le \alpha \le 1.5$ since Bai and Feng in [5] suggest that $\alpha = 1.5$ in their model has the best performance.

3. The Numerical Scheme

An image U will be a 2-dimensional matrix of size $N \times N$. In order to get the aim of anisotropic diffusion along different directions and because the discrete α-order gradient $\nabla^\alpha u$ is an 8-dimensional vector

$$\begin{aligned}\nabla^\alpha \mathbf{u}(\mathbf{i},\mathbf{j}) &= \left(\nabla_0^\alpha u(i,j), \nabla_1^\alpha u(i,j), \nabla_2^\alpha u(i,j), \nabla_3^\alpha u(i,j),\right. \\ &\quad \left.\nabla_4^\alpha u(i,j), \nabla_5^\alpha u(i,j), \nabla_6^\alpha u(i,j), \nabla_7^\alpha u(i,j)\right)^T,\end{aligned} \tag{9}$$

where T represents the transpose of the vector and $\nabla^\alpha u_k(i,j)$, $k = 0, \ldots, 7$ are defined as

$$\begin{aligned}
\nabla_0^\alpha u(i,j) &= \sum_{k=0}^{K-1} (-1)^k C_k^\alpha u(i, j+k-(K-1)),\\
\nabla_1^\alpha u(i,j) &= \sum_{k=0}^{K-1} (-1)^k C_k^\alpha u(i-k+(K-1), j+k-(K-1)),\\
\nabla_2^\alpha u(i,j) &= \sum_{k=0}^{K-1} (-1)^k C_k^\alpha u(i-k+(K-1), j),\\
\nabla_3^\alpha u(i,j) &= \sum_{k=0}^{K-1} (-1)^k C_k^\alpha u(i-k+(K-1), j-k+(K-1)),\\
\nabla_4^\alpha u(i,j) &= \sum_{k=0}^{K-1} (-1)^k C_k^\alpha u(i, j-k+(K-1)),\\
\nabla_5^\alpha u(i,j) &= \sum_{k=0}^{K-1} (-1)^k C_k^\alpha u(i+k-(K-1), j-k+(K-1)),\\
\nabla_6^\alpha u(i,j) &= \sum_{k=0}^{K-1} (-1)^k C_k^\alpha u(i+k-(K-1), j),\\
\nabla_7^\alpha u(i,j) &= \sum_{k=0}^{K-1} (-1)^k C_k^\alpha u(i+k-(K-1), j+k-(K-1)).
\end{aligned} \tag{10}$$

Thus,

$$\begin{aligned}\nabla^{2\alpha} \mathbf{u}(\mathbf{i},\mathbf{j}) &= \left(\nabla_0^{2\alpha} u(i,j), \nabla_1^{2\alpha} u(i,j), \nabla_2^{2\alpha} u(i,j), \nabla_3^{2\alpha} u(i,j),\right. \\ &\quad \left.\nabla_4^{2\alpha} u(i,j), \nabla_5^{2\alpha} u(i,j), \nabla_6^{2\alpha} u(i,j), \nabla_7^{2\alpha} u(i,j)\right)^T,\end{aligned} \tag{11}$$

where T represents the transpose of the vector. From (4), we have

$$\begin{aligned}
\nabla_0^{2\alpha} u(i,j) &= \sum_{k=0}^{K-1} (-1)^k C_k^{2\alpha} u(i, j+k-(K-1)),\\
\nabla_1^{2\alpha} u(i,j) &= \sum_{k=0}^{K-1} (-1)^k C_k^{2\alpha} u(i-k+(K-1), j+k-(K-1)),\\
\nabla_2^{2\alpha} u(i,j) &= \sum_{k=0}^{K-1} (-1)^k C_k^{2\alpha} u(i-k+(K-1), j),\\
\nabla_3^{2\alpha} u(i,j) &= \sum_{k=0}^{K-1} (-1)^k C_k^{2\alpha} u(i-k+(K-1), j-k+(K-1)),\\
\nabla_4^{2\alpha} u(i,j) &= \sum_{k=0}^{K-1} (-1)^k C_k^{2\alpha} u(i, j-k+(K-1)),\\
\nabla_5^{2\alpha} u(i,j) &= \sum_{k=0}^{K-1} (-1)^k C_k^{2\alpha} u(i+k-(K-1), j-k+(K-1)),\\
\nabla_6^{2\alpha} u(i,j) &= \sum_{k=0}^{K-1} (-1)^k C_k^{2\alpha} u(i+k-(K-1), j),\\
\nabla_7^{2\alpha} u(i,j) &= \sum_{k=0}^{K-1} (-1)^k C_k^{2\alpha} u(i+k-(K-1), j+k-(K-1)).
\end{aligned} \tag{12}$$

Let

$$\mathbf{g} = (g_0, g_1, g_2, g_3, g_4, g_5, g_6, g_7)^T, \tag{13}$$

where T represents the transpose of the vector and g_k, $k = 0, \ldots, 7$ are defined as

$$g_k = \frac{g\left(\left\|G_{\sigma_1} \cdot \nabla_k^\alpha u(i,j)\right\|\right)}{\sum_{n=0}^{7} g\left(\left\|G_{\sigma_1} \cdot \nabla_n^\alpha u(i,j)\right\|\right)}, \quad k = 0, 1, \ldots, 7, \tag{14}$$

where $\nabla_k^\alpha u(i,j), k = 0, \ldots 7$ defined in (9) are the components of vector $\nabla^\alpha \mathbf{u}(\mathbf{i},\mathbf{j})$ and $\sum_{n=0}^{7} g(\|G_{\sigma_1} \cdot \nabla_n^\alpha u(i,j)\|)$ is the normalized constant, g is the decreasing function of absolute value of $\nabla_k^\alpha u(i,j)$, $k = 0, \ldots 7$, and $g(\|\nabla_k^\alpha u(x,y,t)\|)$ is defined as

$$g\left(\left\|\nabla_k^\alpha u(x,y,t)\right\|\right) = e^{-\left(\left\|\nabla_k^\alpha u(x,y,t)\right\|/\sigma\right)^2}, \quad k = 0, \ldots, 7 \tag{15}$$

or

$$g\left(\left\|\nabla_k^\alpha u(x,y,t)\right\|\right) = \frac{1}{1 + \left(\left\|\nabla_k^\alpha u(x,y,t)\right\|/\sigma\right)^2}, \quad k = 0, \ldots, 7, \tag{16}$$

where $\|\cdot\|$ is the module of the fractional-order vector and the constant σ controls the sensitivity to edges.

The new FOPMD based on G-L fractional-order derivative is defined as

$$\frac{\partial u(i,j,t)}{\partial t} = \operatorname{div}^{\alpha}\begin{pmatrix} g_0\nabla_0^{\alpha}u(i,j,t) \\ g_1\nabla_1^{\alpha}u(i,j,t) \\ g_2\nabla_2^{\alpha}u(i,j,t) \\ g_3\nabla_3^{\alpha}u(i,j,t) \\ g_4\nabla_4^{\alpha}u(i,j,t) \\ g_5\nabla_5^{\alpha}u(i,j,t) \\ g_6\nabla_6^{\alpha}u(i,j,t) \\ g_7\nabla_7^{\alpha}u(i,j,t) \end{pmatrix}, \tag{17}$$

where $g_k, k = 0,\ldots,7$ defined in (14) are the components of $\mathbf{g}$ in (13).

The above equation can be represented as

$$\frac{\partial u(i,j,t)}{\partial t} = \sum_{k=0}^{7} g_k \nabla_k^{2\alpha} u(i,j,t), \tag{18}$$

where $\sum_{k=0}^{7} g_k = 1$ and $\nabla_k^{2\alpha}u(i,j,t)$ can be computed according to (8).

Thus, the explicit form for solving (18) is

$$u(i,j,t+1) = u(i,j,t) + \lambda\sum_{k=0}^{7} g_k \nabla_k^{2\alpha} u(i,j,t), \tag{19}$$

where $u(i,j,t+1)$ is the gray level of (i,j) at time $t+1$ and λ is the integration constant ($0 \le \lambda \le 1/7$).

To summarize, our sinogram restoration approach is done in the following steps:

(1) let the input sinogram be U and set $t = 1$, $U_t = U$, input iterative numbers n, Gaussian deviations σ_1 of regularized Gaussian kernel in (3), fractional order α, integration constant λ in (19), gradient modulus threshold σ that controls the conduction used in (15) or (16), and choose (15) or (16) as diffusion coefficients;

(2) compute α-order gradient vector $\nabla^{\alpha}\mathbf{u}$ using (9);

(3) compute diffusion coefficients vector $\mathbf{g}$ using (13)–(16);

(4) compute 2α-order gradient vector $\nabla^{2\alpha}\mathbf{u}$ using (11);

(5) compute U_{t+1} using (19), and set $t = t+1$, if $t = n$, output sinogram U_t; else goto step 2;

(6) return back-project sinogram U_t into the image I.

4. Experiments and Discussion

The main objective for LDCT imaging is to delete the noise and avoid artifacts while preserving anatomy details for the back-projection images.

Two abdominal CT images of a 58-year-old man and two abdominal CT images of a 62-year-old woman with different doses were scanned from a 16-multi detector-row CT unit (Somatom Sensation 16; Siemens Medical Solutions) using 120 kVp and 5 mm slice thickness. Other remaining scanning parameters are gantry rotation time, 0.5 second; detector configuration (number of detector rows section thickness), 16×1.5 mm; table feed per gantry rotation, 24 mm; pitch, 1 : 1, and reconstruction method, back projection (FBP) algorithm with the soft-tissue convolution kernel "B30f." Different CT doses were controlled by using two different fixed tube currents 60 mAs and 150 mAs (60 mA or 150 mAs) for LDCT and standard-dose CT (SDCT) protocols, resp.). The CT dose index volume (CTDIvol) for LDCT images and SDCT images is in positive linear correlation to the tube current and is calculated to be approximately ranging between 15.32 mGy and 3.16 mGy [28] (see Figures 1(a)–1(d)).

In order to compare our method with classical PM and other state-of-art FOPMD methods, three compared methods: PMD [1], regularized PMD (RPM) [2], and FOPMD are proposed in [8]. According to the numerical scheme of PMD and RPMD, they used half-point central difference discretization scheme, while FOPMD in [8] and RFS-FOPMD use integer-point unilateral difference discretization scheme.

In order to ensure that the comparison is put on a fair level, the common used parameters are set to the same value. The common used parameters for four methods include gradient modulus threshold σ that controls the conduction, integration constant λ, and iteration number t. Due to numerical stability, λ is set to its maximum value 1/100 and σ is set to 30 to reduce iteration number.

The iteration number t is very important in all comparison methods. That is, big t will make smooth image while small t will still leave a lot of noise. In order to study the performance of four compared methods with different iteration numbers t and other fixed parameters, t is set to 20, 50, and 100, respectively.

The standard deviation of smoothed Gaussian kernel for the image σ_1 used for RPMD is set to 1 since, in [2], the authors suggest that σ_1 should be a small number.

On sinogram space, FOPMD with $\alpha = 0.5$, $\alpha = 0.8$ and $\alpha = 1.2$ is carried on two image collections.

Since bigger iteration number leads to smoother denoised results sometimes, it also leads to dark processed images by posing too big integration constant λ. In order to observe the behaviors of big iteration number clearly, Figure 1 sets iteration number $t = 100$. Comparing all the original SDCT images in Figures 1(a) and 1(c), LDCT images Figures 1(b) and 1(d) were severely degraded by nonstationary noise. All denoised images in Figure 1 can suppress most of noises. Particular, FOPMD and RFS-FOPMD can provide very satisfied images with little noise and preserving all useful anatomy structures. However, denoised images of PMD and RPMD are oversmooth, which lost a lot of details.

In order to test the consistency of the definitions of different integer order or fractional order, we set fractional-order $\alpha = 1$, in which a two fractional-order PMD should have same forms and they also correspond to the order of PMD and RPMD (see Figures 1(e)–1(l)). Observing Figures

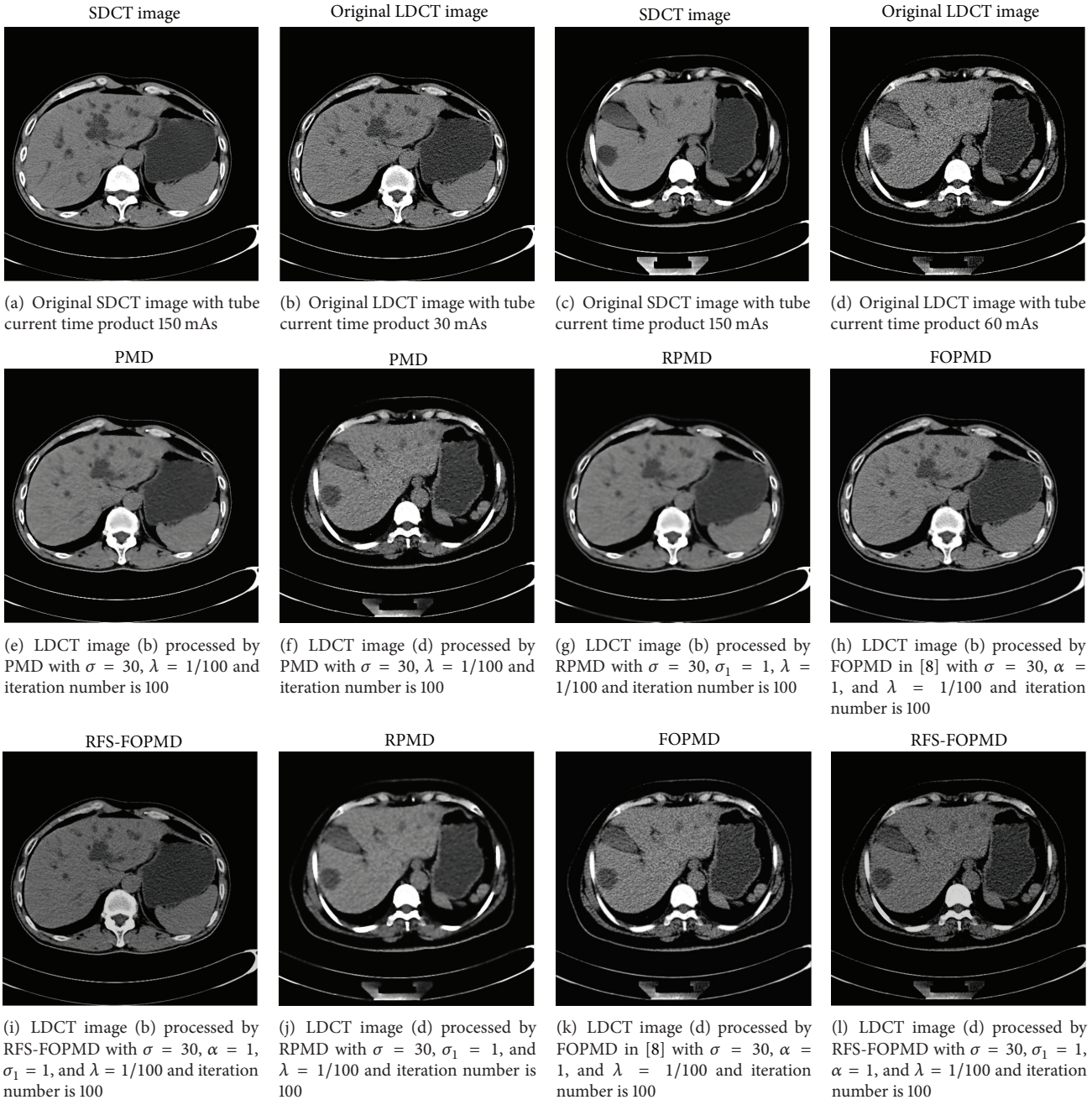

(a) Original SDCT image with tube current time product 150 mAs

(b) Original LDCT image with tube current time product 30 mAs

(c) Original SDCT image with tube current time product 150 mAs

(d) Original LDCT image with tube current time product 60 mAs

(e) LDCT image (b) processed by PMD with $\sigma = 30$, $\lambda = 1/100$ and iteration number is 100

(f) LDCT image (d) processed by PMD with $\sigma = 30$, $\lambda = 1/100$ and iteration number is 100

(g) LDCT image (b) processed by RPMD with $\sigma = 30$, $\sigma_1 = 1$, $\lambda = 1/100$ and iteration number is 100

(h) LDCT image (b) processed by FOPMD in [8] with $\sigma = 30$, $\alpha = 1$, and $\lambda = 1/100$ and iteration number is 100

(i) LDCT image (b) processed by RFS-FOPMD with $\sigma = 30$, $\alpha = 1$, $\sigma_1 = 1$, and $\lambda = 1/100$ and iteration number is 100

(j) LDCT image (d) processed by RPMD with $\sigma = 30$, $\sigma_1 = 1$, and $\lambda = 1/100$ and iteration number is 100

(k) LDCT image (d) processed by FOPMD in [8] with $\sigma = 30$, $\alpha = 1$, and $\lambda = 1/100$ and iteration number is 100

(l) LDCT image (d) processed by RFS-FOPMD with $\sigma = 30$, $\sigma_1 = 1$, $\alpha = 1$, and $\lambda = 1/100$ and iteration number is 100

Figure 1: Original SDCT and LDCT images ((a)–(d)), LDCT images processed by PMD, RPMD, FOPMD, and RFS-FOPMD with fractional order $\alpha = 1$ and iteration number is set to 100.

1(h) and 1(i), 1(k) and 1(l), we can find that the denoised images are identical, which demonstrate that the fractional-order definitions between [8] and RFS-FOPMD are identical when $\alpha = 1$.

However, the resulting images of PMD and RPMD are quite different to the images denoised by FOPMD and RFS-FOPMD. That is, the images processed by PMD and RPMD are smoother than the images processed by FOPMD and RFS-FOPMD. Just as introduced in the previous paragraph, different discretization schemes lead to this interesting result.

Since two FOMD schemes provide more satisfied results, we only compare two FOPMD methods with different fractional orders (see Figure 2) and different iteration numbers (see Figure 3).

In order to compare denoised results of two FOPMD schemes with different fractional orders, two original LDCT images in Figures 1(b) and 1(d) are used with iteration number $t = 100$ and fractional-order $\alpha = 0.5$, $\alpha = 0.8$, and $\alpha = 1.2$. From the second and the fourth rows of Figure 2, we can conclude that the resulting images of RFS-FOPMD are very

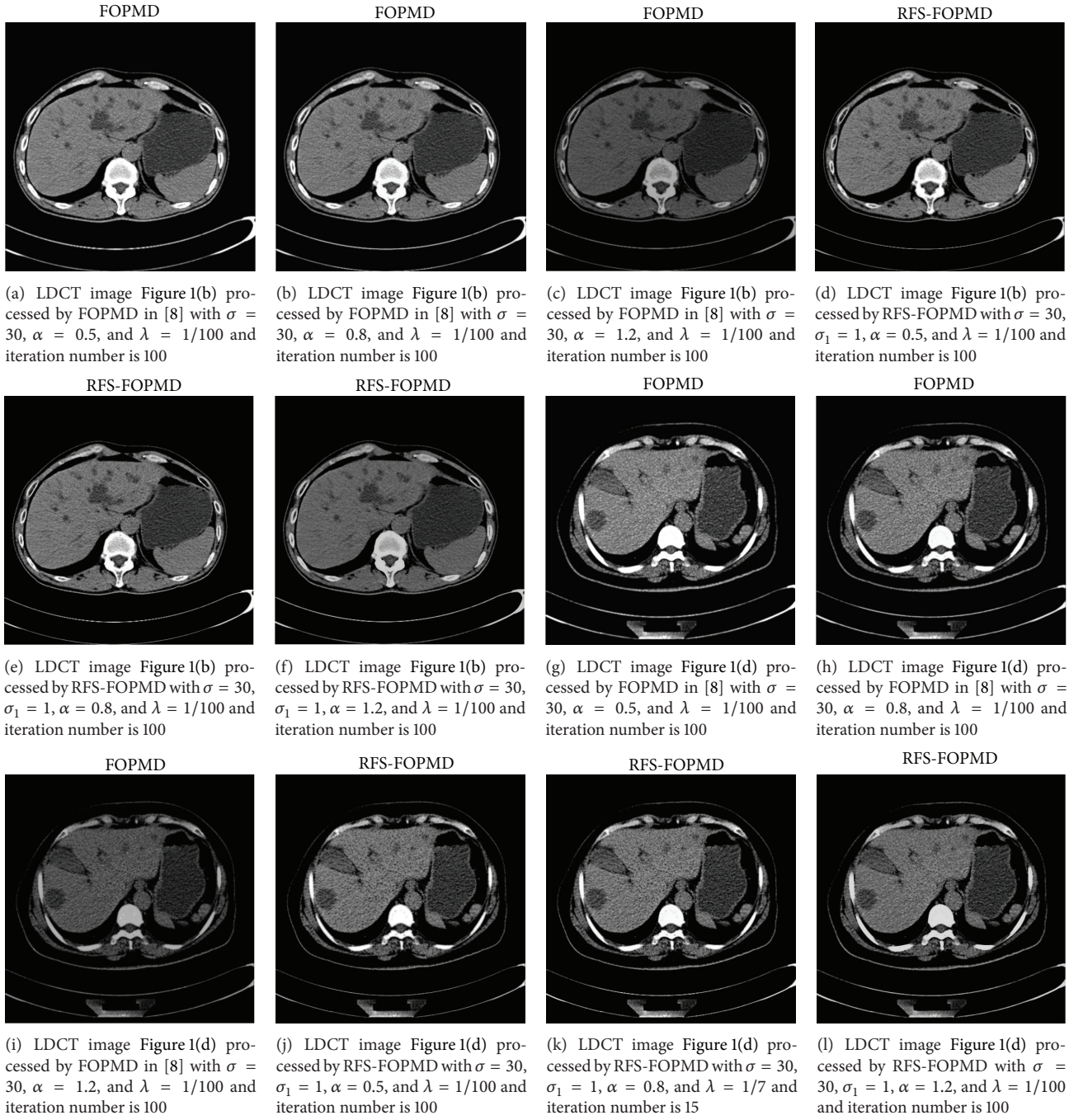

(a) LDCT image Figure 1(b) processed by FOPMD in [8] with $\sigma = 30$, $\alpha = 0.5$, and $\lambda = 1/100$ and iteration number is 100

(b) LDCT image Figure 1(b) processed by FOPMD in [8] with $\sigma = 30$, $\alpha = 0.8$, and $\lambda = 1/100$ and iteration number is 100

(c) LDCT image Figure 1(b) processed by FOPMD in [8] with $\sigma = 30$, $\alpha = 1.2$, and $\lambda = 1/100$ and iteration number is 100

(d) LDCT image Figure 1(b) processed by RFS-FOPMD with $\sigma = 30$, $\sigma_1 = 1$, $\alpha = 0.5$, and $\lambda = 1/100$ and iteration number is 100

(e) LDCT image Figure 1(b) processed by RFS-FOPMD with $\sigma = 30$, $\sigma_1 = 1$, $\alpha = 0.8$, and $\lambda = 1/100$ and iteration number is 100

(f) LDCT image Figure 1(b) processed by RFS-FOPMD with $\sigma = 30$, $\sigma_1 = 1$, $\alpha = 1.2$, and $\lambda = 1/100$ and iteration number is 100

(g) LDCT image Figure 1(d) processed by FOPMD in [8] with $\sigma = 30$, $\alpha = 0.5$, and $\lambda = 1/100$ and iteration number is 100

(h) LDCT image Figure 1(d) processed by FOPMD in [8] with $\sigma = 30$, $\alpha = 0.8$, and $\lambda = 1/100$ and iteration number is 100

(i) LDCT image Figure 1(d) processed by FOPMD in [8] with $\sigma = 30$, $\alpha = 1.2$, and $\lambda = 1/100$ and iteration number is 100

(j) LDCT image Figure 1(d) processed by RFS-FOPMD with $\sigma = 30$, $\sigma_1 = 1$, $\alpha = 0.5$, and $\lambda = 1/100$ and iteration number is 100

(k) LDCT image Figure 1(d) processed by RFS-FOPMD with $\sigma = 30$, $\sigma_1 = 1$, $\alpha = 0.8$, and $\lambda = 1/7$ and iteration number is 15

(l) LDCT image Figure 1(d) processed by RFS-FOPMD with $\sigma = 30$, $\sigma_1 = 1$, $\alpha = 1.2$, and $\lambda = 1/100$ and iteration number is 100

Figure 2: LDCT images (Figures 1(b) and 1(d)) processed by FOPMD and RFS-FOPMD with different fractional orders and iteration number is set to 100. The first column: $\alpha = 0.5$; the second column: $\alpha = 0.8$, and the third column: $\alpha = 1.2$. The first row: Figure 1(b) processed by FOPMD; the second row: Figure 1(b) processed by RFS-FOPMD; the third row: Figure 1(d) processed by FOPMD, and the fourth row: Figure 1(d) processed by RFS-FOPMD.

satisfied and they become smoother when α becomes bigger, which is coherent with our intuition, for example, bigger fractional-order smoother resulting images.

However, denoised images in Figures 2(a) and 2(g) with $\alpha = 0.5$ using FOPMD in [8] have many artifacts, which are small black circles in two images. Although big fractional-order FOPMD proposed in [8] will decrease the artifacts, its denoised images in Figures 2(c) and 2(i) are very dark comparing with the original LDCT images in Figures 1(b) and 1(d). Images in Figures 2(c) and 2(i) also have some isolated artificial white points, which are called speckle effect. It is obvious that resulting images in Figures 2(b) and 2(h) with $\alpha = 0.8$ processed by FOPMD in [8] have the best performance in three image series with different α.

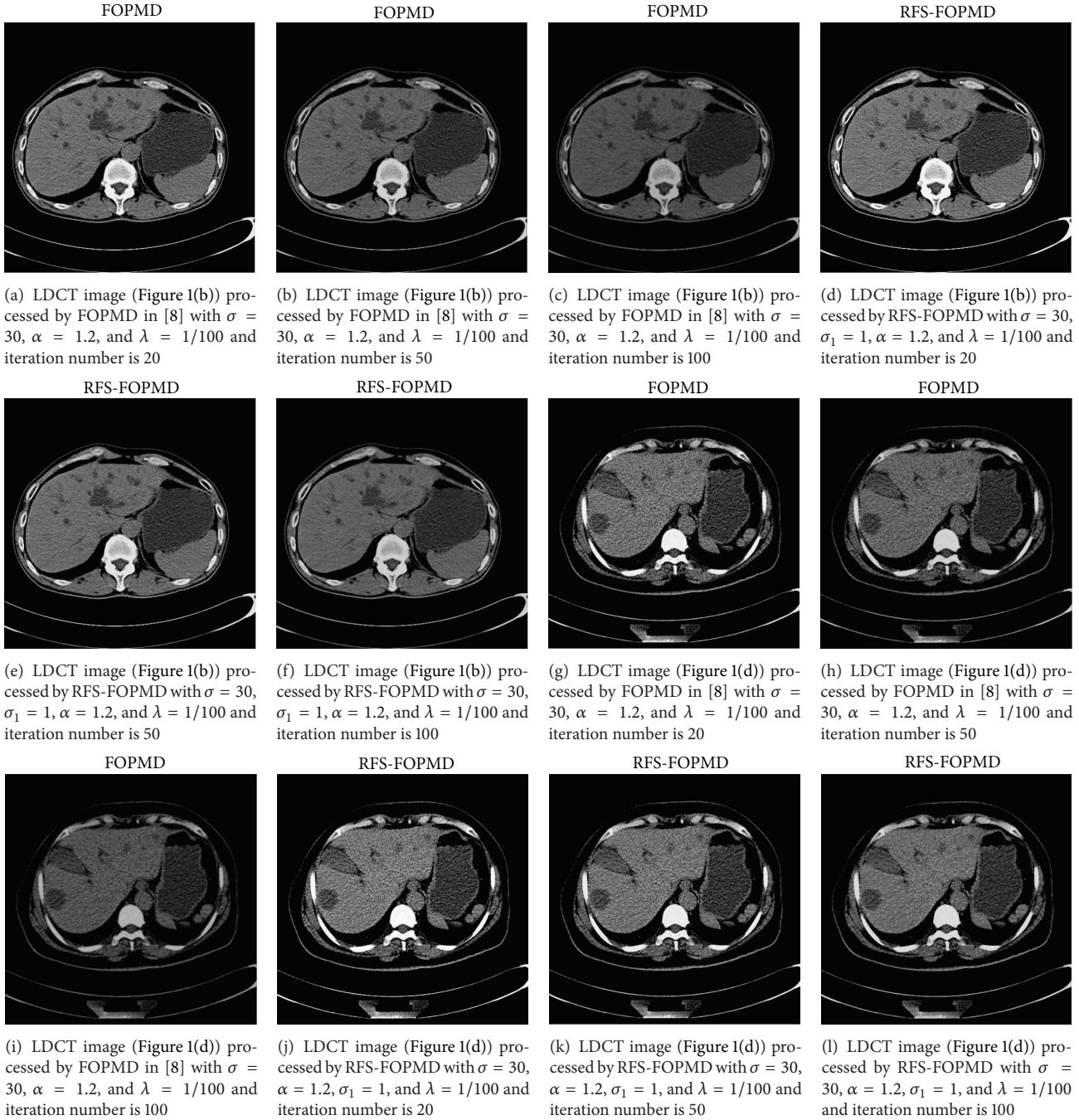

(a) LDCT image (Figure 1(b)) processed by FOPMD in [8] with $\sigma = 30$, $\alpha = 1.2$, and $\lambda = 1/100$ and iteration number is 20

(b) LDCT image (Figure 1(b)) processed by FOPMD in [8] with $\sigma = 30$, $\alpha = 1.2$, and $\lambda = 1/100$ and iteration number is 50

(c) LDCT image (Figure 1(b)) processed by FOPMD in [8] with $\sigma = 30$, $\alpha = 1.2$, and $\lambda = 1/100$ and iteration number is 100

(d) LDCT image (Figure 1(b)) processed by RFS-FOPMD with $\sigma = 30$, $\sigma_1 = 1$, $\alpha = 1.2$, and $\lambda = 1/100$ and iteration number is 20

(e) LDCT image (Figure 1(b)) processed by RFS-FOPMD with $\sigma = 30$, $\sigma_1 = 1$, $\alpha = 1.2$, and $\lambda = 1/100$ and iteration number is 50

(f) LDCT image (Figure 1(b)) processed by RFS-FOPMD with $\sigma = 30$, $\sigma_1 = 1$, $\alpha = 1.2$, and $\lambda = 1/100$ and iteration number is 100

(g) LDCT image (Figure 1(d)) processed by FOPMD in [8] with $\sigma = 30$, $\alpha = 1.2$, and $\lambda = 1/100$ and iteration number is 20

(h) LDCT image (Figure 1(d)) processed by FOPMD in [8] with $\sigma = 30$, $\alpha = 1.2$, and $\lambda = 1/100$ and iteration number is 50

(i) LDCT image (Figure 1(d)) processed by FOPMD in [8] with $\sigma = 30$, $\alpha = 1.2$, and $\lambda = 1/100$ and iteration number is 100

(j) LDCT image (Figure 1(d)) processed by RFS-FOPMD with $\sigma = 30$, $\alpha = 1.2$, $\sigma_1 = 1$, and $\lambda = 1/100$ and iteration number is 20

(k) LDCT image (Figure 1(d)) processed by RFS-FOPMD with $\sigma = 30$, $\alpha = 1.2$, $\sigma_1 = 1$, and $\lambda = 1/100$ and iteration number is 50

(l) LDCT image (Figure 1(d)) processed by RFS-FOPMD with $\sigma = 30$, $\alpha = 1.2$, $\sigma_1 = 1$, and $\lambda = 1/100$ and iteration number is 100

Figure 3: LDCT images (Figures 1(b) and 1(d)) processed by FOPMD and RFS-FOPMD with different iteration numbers and the fractional-order $\alpha = 1.2$. The first column: iteration number is 20; the second column: iteration number is 50 and the third column: iteration number is 100. The first row: Figure 1(b) processed by FOPMD; the second row: Figure 1(b) processed by RFS-FOPMD; the third row: Figure 1(d) processed by FOPMD and the fourth row: Figure 1(d) processed by RFS-FOPMD.

Generally, artifacts in denoised images are oscillations near edges, caused by that the low-passed filtering is not processed correctly near the real edges. That is, some smooth regions near edges are regarded falsely as edges, which makes these error edges preserved. Therefore, improving accuracy of edge detection is a good choice for improving the performance of FOPMD in [8]. In this paper, we use regularization for FOPMD in [8] to locate edges correctly.

Intuitively, processed images with bigger iteration number correspond to smoother images. In order to check the influence of iteration numbers for FOPMD in [8] and RFS-FOPMD, processed image series of two original LDCT images, Figures 1(b) and 1(d) with different iteration numbers 20, 50, and 100 are shown in Figure 3.

The resulting images in the first and the third rows of Figure 3 are the processed images using FOPMD in [8].

Comparing with original LDCT images in Figures 1(b) and 1(d), all resulting images with different iteration numbers have less noise. In addition, the smoother images can be obtained as the iteration number becomes bigger. However, the most undesired default for FOPMD in [8] is that resulting images become dark as the iteration number becomes big. Moreover, except for Figure 3(g), the resulting images in the third row have some isolated white points, which are the speckle effect.

The resulting images in the second and the fourth rows of Figure 3 show that RFS-FOPMD with different iteration numbers is very satisfied and it becomes smoother when the iteration number becomes bigger, which is coherent with our intuition. Another attractive nature for RFS-FOPMD about iteration is that the smoothing shown in these images is very slow. That is, the resulting images Figures 3(d) and 3(j) with iteration number 20 are slightly different to the images Figures 3(f) and 3(l) with iteration number 100. This nature shows that RFS-FOPMD has good stability. Therefore, it is not sensitive to iteration number.

All existing FOPMD methods at least suffer from speckle effect from the resulting images of these images. Fortunately, RFS-FOPMD can avoid artifacts, dark images, and speckle effect partly, which ensure its applications in sinogram restoration. More important for the new scheme is its stability, which makes it not sensitive to the iteration number.

5. Conclusions

In this paper, we propose a new FOPMD, RFS-FOPMD, for LDCT sinogram imaging based on G-L fractional-order derivative definition. RFS-FOPMD not only has good ability in preserving edges while denoising, but it also can avoid artifacts, dark images, and speckle effects of FOPMD in [8] and other existing FOPMD schemes partly by improving the performance of edges locating by regularization, which ensures that RFS-FOPMD can be used for sinogram restoration of LDCT. Of more importance, RFS-FOPMD has good stability for iteration numbers, which makes it not sensitive to the iteration number choice.

Acknowledgments

This paper is supported by the National Natural Science Foundation of China (no. 60873102), Major State Basic Research Development Program (no. 2010CB732501), and Open Foundation of Visual Computing and Virtual Reality Key Laboratory of Sichuan Province (no. J2010N03). This work was supported by a Grant from the National High Technology Research and Development Program of China (no. 2009AA12Z140).

References

[1] P. Perona and J. Malik, "Scale-space and edge detection using anisotropic diffusion," *IEEE Transactions on Pattern Analysis and Machine Intelligence*, vol. 12, no. 7, pp. 629–639, 1990.

[2] F. Catté, P.-L. Lions, J.-M. Morel, and T. Coll, "Image selective smoothing and edge detection by nonlinear diffusion," *SIAM Journal on Numerical Analysis*, vol. 29, no. 1, pp. 182–193, 1992.

[3] Y.-L. You and M. Kaveh, "Fourth-order partial differential equations for noise removal," *IEEE Transactions on Image Processing*, vol. 9, no. 10, pp. 1723–1730, 2000.

[4] T. Chan, A. Marquina, and P. Mulet, "High-order total variation-based image restoration," *SIAM Journal on Scientific Computing*, vol. 22, no. 2, pp. 503–516, 2000.

[5] J. Bai and X.-C. Feng, "Fractional-order anisotropic diffusion for image denoising," *IEEE Transactions on Image Processing*, vol. 16, no. 10, pp. 2492–2502, 2007.

[6] Z. Jun and W. Zhihui, "A class of fractional-order multi-scale variational models and alternating projection algorithm for image denoising," *Applied Mathematical Modelling*, vol. 35, no. 5, pp. 2516–2528, 2011.

[7] M. Janev, S. Pilipović, T. Atanacković, R. Obradović, and N. Ralević, "Fully fractional anisotropic diffusion for image denoising," *Mathematical and Computer Modelling*, vol. 54, no. 1-2, pp. 729–741, 2011.

[8] S. Hu, Z. Liao, and W. Chen, "Sinogram restoration for low-dosed X-ray computed tomography using fractional-order Perona-Malik diffusion," *Mathematical Problems in Engineering*, vol. 2012, Article ID 391050, 13 pages, 2012.

[9] S. Hu, "External fractional-order gradient vector Perona-Malik diffusion for sinogram restoration of low-dosed X-ray computed tomography," *Advances in Mathematical Physics*, vol. 2013, Article ID 516919, 14 pages, 2013.

[10] C. Cattani, A. Ciancio, and B. Lods, "On a mathematical model of immune competition," *Applied Mathematics Letters*, vol. 19, no. 7, pp. 678–683, 2006.

[11] C. Cattani and A. Ciancio, "Separable transition density in the hybrid model for tumor-immune system competition," *Computational and Mathematical Methods in Medicine*, vol. 2012, Article ID 610124, 6 pages, 2012.

[12] M. Li, Y. Q. Chen, J. Y. Li, and W. Zhao, "Hölder scales of sea level," *Mathematical Problems in Engineering*, vol. 2012, Article ID 863707, 22 pages, 2012.

[13] M. Li, W. Zhao, and C. Cattani, "Delay bound: fractal traffic passes through servers," *Mathematical Problems in Engineering*, vol. 2013, Article ID 157636, 15 pages, 2013.

[14] M. Li and W. Zhao, "On $1/f$ noise," *Mathematical Problems in Engineering*, vol. 2012, Article ID 673648, 23 pages, 2012.

[15] D. J. Brenner and E. J. Hall, "Computed tomography—an increasing source of radiation exposure," *The New England Journal of Medicine*, vol. 357, no. 22, pp. 2277–2284, 2007.

[16] L. Yu, "Radiation dose reduction in computed tomography: techniques and future perspective," *Imaging in Medicine*, vol. 1, no. 1, pp. 65–84, 2009.

[17] J. Weidemann, G. Stamm, M. Galanski, and M. Keberle, "Comparison of the image quality of various fixed and dose modulated protocols for soft tissue neck CT on a GE Lightspeed scanner," *European Journal of Radiology*, vol. 69, no. 3, pp. 473–477, 2009.

[18] M. K. Kalra, M. M. Maher, M. A. Blake et al., "Detection and characterization of lesions on low-radiation-dose abdominal CT images postprocessed with noise reduction filters," *Radiology*, vol. 232, no. 3, pp. 791–797, 2004.

[19] J. C. Giraldo, Z. S. Kelm, L. S. Guimaraes et al., "Comparative study of two image space noise reduction methods for computed tomography: bilateral filter and nonlocal means," in *Proceedings of the Conference Proceedings IEEE Engineering in Medicine and Biology Society*, vol. 1, pp. 3529–3532, 2009.

[20] A. Manduca, L. Yu, J. D. Trzasko et al., "Projection space denoising with bilateral filtering and CT noise modeling for dose reduction in CT," *Medical Physics*, vol. 36, no. 11, pp. 4911–4919, 2009.

[21] N. Mail, D. J. Moseley, J. H. Siewerdsen, and D. A. Jaffray, "The influence of bowtie filtration on cone-beam CT image quality," *Medical Physics*, vol. 36, no. 1, pp. 22–32, 2009.

[22] Z. Liao, S. Hu, and W. Chen, "Determining neighborhoods of image pixels automatically for adaptive image denoising using nonlinear time series analysis," *Mathematical Problems in Engineering*, vol. 2010, Article ID 914564, 14 pages, 2010.

[23] H. Lu, I.-T. Hsiao, X. Li, and Z. Liang, "Noise properties of low-dose CT projections and noise treatment by scale transformations," in *Proceedings of the IEEE Nuclear Science Symposium Conference Record*, pp. 1662–1666, November 2001.

[24] J. Xu and B. M. W. Tsui, "Electronic noise modeling in statistical iterative reconstruction," *IEEE Transactions on Image Processing*, vol. 18, no. 6, pp. 1228–1238, 2009.

[25] I. A. Elbakri and J. A. Fessler, "Statistical image reconstruction for polyenergetic X-ray computed tomography," *IEEE Transactions on Medical Imaging*, vol. 21, no. 2, pp. 89–99, 2002.

[26] J. Wang, H. Lu, J. Wen, and Z. Liang, "Multiscale penalized weighted least-squares sinogram restoration for low-dose X-ray computed tomography," *IEEE Transactions on Biomedical Engineering*, vol. 55, no. 3, pp. 1022–1031, 2008.

[27] J. Wang, T. Li, H. Lu, and Z. Liang, "Penalized weighted least-squares approach to sinogram noise reduction and image reconstruction for low-dose X-ray computed tomography," *IEEE Transactions on Medical Imaging*, vol. 25, no. 10, pp. 1272–1283, 2006.

[28] Y. Chen, W. Chen, X. Yin et al., "Improving low-dose abdominal CT images by weighted intensity averaging over large-scale neighborhoods," *European Journal of Radiology*, vol. 80, no. 2, pp. e42–e49, 2011.

[29] M. D. Ortigueira and F. Coito, "From differences to derivatives," *Fractional Calculus and Applied Analysis*, vol. 7, no. 4, pp. 459–471, 2004.

[30] K. B. Oldham and J. Spanier, *The Fractional Calculus*, Academic Press, New York, NY, USA, 1974.

Hindawi Publishing Corporation
Advances in Mathematical Physics
Volume 2013, Article ID 516919, 10 pages
http://dx.doi.org/10.1155/2013/516919

Research Article

External Fractional-Order Gradient Vector Perona-Malik Diffusion for Sinogram Restoration of Low-Dosed X-Ray Computed Tomography

Shaoxiang Hu

School of Automation Engineering, University of Electronic Science and Technology of China, Chengdu, Sichuan 611731, China

Correspondence should be addressed to Shaoxiang Hu; hushaox@126.com

Received 11 September 2013; Accepted 20 September 2013

Academic Editor: Ming Li

Existing fractional-order Perona-Malik Diffusion (FOPMD) algorithms are defined as fully spatial fractional-order derivatives (FSFODs). However, we argue that FSFOD is not the best way for diffusion since different parts of spatial derivative play different roles in Perona-Malik diffusion (PMD) and derivative orders should be decided according to their roles. Therefore, we adopt a novel fractional-order diffusion scheme, named external fractional-order gradient vector Perona-Malik diffusion (EFOGV-PMD), by only replacing integer-order derivatives of "external" gradient vector to their fractional-order counterparts while keeping integer-order derivatives of gradient vector for diffusion coefficients since the ability of edge indicator for 1-order derivative is demonstrated both in theory and applications. Here "external" indicates the spatial derivatives except for the derivatives used in diffusion coefficients. In order to demonstrate the power of the proposed scheme, some real sinograms of low-dosed computed tomography (LDCT) are used to compare the different performances. These schemes include PMD, regularized PMD (RPMD), and FOPMD. Experimental results show that the new scheme has good ability in edge preserving, is convergent quickly, has good stability for iteration number, and can avoid artifacts, dark resulting images, and speckle effect.

1. Introduction

Since the work of Perona-Malik in 1990, Perona-Malik diffusion (PMD) becomes a popular technique in image denoising and it is defined as [1]

$$\frac{\partial u(x,y,t)}{\partial t} = \operatorname{div}\left[c\left(\left\|\nabla u(x,y,t)\right\|\right)\nabla u(x,y,t)\right], \quad (1)$$

where $u(x, y, 0)$ is the initial gray scale image, $u(x, y, t)$ is the smoothed gray scale image at time t, ∇ denotes the gradient, $\operatorname{div}(\cdot)$ is the divergence operator and $c(\cdot)$ is the diffusion coefficient. $c(\cdot)$ controls the rate of diffusion and it is usually chosen as a monotonically decreasing function of the module of the image gradient.

The key idea of PMD is to smooth the homogenous regions with small $\|\nabla u(x, y, t)\|$ while near singularities with big $\|\nabla u(x, y, t)\|$, PMD only smoothes along the perpendicsular direction of the gradient. This idea is based on that the 1-order gradient module can be used as singularities locator. Thus the order of gradient vector in diffusion coefficients should be kept as 1. It is the start point of EFOGV-PMD proposed in this paper.

In 1992, Catté et al. indicate that PMD is ill posed and they propose a new well-posed method named regularized Perona-Malik Diffusion (RPMD) by modifying the module of the image gradient in diffusion coefficients to the module of the gradient convoluted with a Gaussian kernel [2].

Although PMD methods have been demonstrated to be able to achieve a good trade-off between noise removal and edge preservation, the resulting image in the presence of the noise often suffers from its "staircase" look. In order to eliminate undesired "staircase" effect, high-order PDEs (typically fourth-order PDEs) for image restoration have been introduced in [3–5]. Though these methods can eliminate the staircase effect efficiently, they often leave the image with isolated black and white speckles (so-called "speckle effect") [6].

Recently, fractional-order PMD (FOPMD) has been studied in image denoising [6–9]. The fractional derivative can be seen as the generalization of the integer-order derivative [10–13]. FOPMD whose fractional-order is α, $0 \le \alpha \le 2$ is a "natural interpolation" between PMD and fourth-order PDEs. Therefore, it has the benefits of both of PMD and high-order PDEs.

Bai and Feng proposed a FSFOD method for image denoising with Euler-Lagrange equations of a cost functional and using Fourier domain to compute the fractional derivative [6]. The numerical results showed that both of the staircase effect and the speckle effect can be eliminated effectively.

Zhang and Wei develop a class of fractional-order multiscale variational model using G-L definition of fractional-order derivative and propose an efficient condition of the convergence for the model [7].

Janev et al. propose a new FOPMD scheme by extending classical spatial derivatives to spatial as well as time fractional derivatives based on R-L derivative [8].

We also reported an experimental study used FOPMD for sinogram restoration of low-dosed computed tomography (LDCT) based on fully spatial FOPMD using G-L definition [9]. In [9], we observe that FOPMD experiments with different fractional-orders show different diffusion behaviors, which lead us to study FOPMD further.

All above new schemes adopt ESFOD schmes. Although they have reported on good performance in preserving edges, suppressing staircase, and speckle effects, the resulting images of these FOPMD methods still have some artifacts and speckle effect which hamper them to be used in LDCT imaging.

Minimizing the radiation exposure to patients has been one of the major efforts in modern clinical X-ray CT radiology [14–16]. However, the presentation of strong noise degrades the quality of LDCT images dramatically and decreases the accuracy of diagnosis.

Filtering noise from clinical scans is a challenging task, since these scans contain artifacts and consist of many structures with different shape, size, and contrast, which should be preserved for making correct diagnosis. In addition, LDCT imaging also requires there are not artifacts to arise while denoising because artifacts also increase chances of mistakes and misdiagnosis. Many strategies have been proposed to reduce noises, but less of them discuss how to avoid artifacts [9, 17–27].

The artifacts of existing FOPMD methods for resulting images are generated by locating error positions of edges. Thus the resulting images produce some undesired weak edges, which form the artifacts.

The basic reason for locating edge positions falsely is that fractional-order gradient module cannot be used for edge indicator. That is, edge locations can be located as big leaps of 1-order derivatives while fractional-order derivatives do not have this nature. Thus keeping 1-order derivative to be edge indicator of diffusion coefficients is a better choice compared to existing fully spatial FOPMD.

Following above discussion, we adopt a novel fractional-order diffusion scheme, named external fractional-order gradient vector Perona-Malik Diffusion PMD (EFOGV-PMD), by only replacing integer-order derivatives of external gradient vector to their fractional-order counterparts while keeping 1-order derivatives for diffusion coefficients. Here "external" indicates the spatial derivatives except for the derivatives used in diffusion coefficients. Since locations of edges can be detected correctly by our new scheme, FOPMD can preserve edges well and avoid artifacts.

The arrangement of this paper is as follows: In Section 2, the EFOGV-PMD is introduced, and then the the numerical scheme is given in Section 3, the experiment results are shown and discussed in Section 4, and the final part is the conclusions and acknowledgements.

2. External Fractional-Order Gradient Vector Perona-Malik Diffusion

The fractional-order derivative can be computed in a number of ways. The most famous of these definitions are the R-L and Grunwald-Letnikov definitions. In this paper, we use G-L definition defined as follows:

$$D^{\alpha} g(x) = \lim_{h \to 0^{+}} \frac{\sum_{k \ge 0} (-1)^{k} C_{k}^{\alpha} g(x - kh)}{h^{\alpha}}, \quad \alpha > 0, \tag{2}$$

where $g(x)$ is a real function, $\alpha > 0$ is a real number, $C_k^{\alpha} = \Gamma(\alpha + 1)/[\Gamma(k + 1)\Gamma(\alpha - k + 1)]$ is the generalized binomial coefficient and $\Gamma(\cdot)$ denotes the Gamma function.

Isotropic diffusion will damage image features such as edges, lines, and textures. To avoid the damage, smoothing has to be adaptively controlled by the amount of smoothing or the direction of smoothing. A classic example of adaptive smoothing is the anisotropic diffusion scheme proposed by Perona and Malik [1], in which the smoothing process is formulated by a partial differential equation (PDE). PMD is formulated on (1).

However, PMD methods suffer from their "staircase" effects. Therefore, FOPMD is proposed to suppress the staircase of PMD.

The fractional-order gradient vector with α order is defined as

$$\nabla^{\alpha} u(x, y, t) = \left[\nabla_{x}^{\alpha} u(x, y, t), \nabla_{y}^{\alpha} u(x, y, t)\right], \tag{3}$$

where α is a positive real, $\nabla_x^{\alpha} u(x, y, t)$ represents the partial fractional-order derivative of $u(x, y, t)$ with respect to the variable x whose order is α, and $\nabla_y^{\alpha} u(x, y, t)$ represents the partial fractional-order derivative of $u(x, y, t)$ with respect to the variable y whose order is α.

According to [9], FOPMD is defined as

$$\frac{\partial u(x, y, t)}{\partial t} = \operatorname{div}^{\alpha}\left[c\left(\left\|\nabla^{\alpha} u(x, y, t)\right\|\right) \nabla^{\alpha} u(x, y, t)\right], \tag{4}$$

where $\operatorname{div}^{\alpha}$ denotes the α-order divergence. For the vector $\nabla^{\beta} v = [v_x^{\beta}, v_y^{\beta}]$ where v_x^{β}, v_y^{β} represent the partial fractional-order derivative of $u(x, y, t)$ with whose order is β respect to the variable x and y respectively, its α-order divergence is defined as

$$\operatorname{div}^{\alpha} \nabla^{\beta} v = v_{x}^{\beta+\alpha} + v_{y}^{\beta+\alpha}. \tag{5}$$

However, FOPMD defined on (4) will produce some artifacts for sinogram restoration of LDCT, which increases the probability of error diagnosis. In order to avoid artifacts produced in sinogram restoration of LDCT using FOPMD, we propose a new diffusion model, named external fractional-order gradient vector of PMD (EFOGV-PMD) where "external" indicates the gradient vector of PMD except for the gradient vector of diffusion coefficients. That is, the orders of derivatives for spatial gradient vectors on different positions are different, the order of gradient vector used in diffusion coefficients is 1 while order of external gradient vector is a positive real α.

Therefore, the EFOGV-PMD is given by

$$\frac{\partial u(x,y,t)}{\partial t} = \operatorname{div}^{\alpha}\left[c\left(\left\|\nabla u(x,y,t)\right\|\right)\nabla^{\alpha}u(x,y,t)\right] \tag{6}$$

with the observed image as the initial condition.

When $\alpha = 1$, (6) is precisely the PMD; when $\alpha = 2$, (13) is precisely the fourth-order anisotropic diffusion equation. In this paper, we are interested in $0.5 \le \alpha \le 1.5$ since Bai and Feng in [6] suggest that $\alpha = 1.5$ in their model has the best performance.

3. The Numerical Scheme

An image U will be a 2-dimensional matrix of size $N \times N$. In order to get the aim of anisotropic diffusion along different directions and the discrete 1-order gradient $\mathbf{\nabla u}$ is an 8-dimensional vector:

$$\begin{aligned}\mathbf{\nabla u}(\mathbf{i},\mathbf{j}) = {} & \left(\nabla_0 u(i,j), \nabla_1 u(i,j), \nabla_2 u(i,j), \nabla_3 u(i,j),\right.\\ & \left.\nabla_4 u(i,j), \nabla_5 u(i,j), \nabla_6 u(i,j), \nabla_7 u(i,j)\right)^T,\end{aligned} \tag{7}$$

where T represents the transpose of the vector and $\nabla u_k(i,j)$, $k = 0,\ldots,7$ are defined as

$$\begin{aligned}\nabla_0 u(i,j) &= u(i,j+1) - u(i,j),\\ \nabla_1 u(i,j) &= u(i-1,j+1) - u(i,j),\\ \nabla_2 u(i,j) &= u(i-1,j) - u(i,j),\\ \nabla_3 u(i,j) &= u(i-1,j-1) - u(i,j),\\ \nabla_4 u(i,j) &= u(i,j-1) - u(i,j),\\ \nabla_5 u(i,j) &= u(i+1,j-1) - u(i,j),\\ \nabla_6 u(i,j) &= u(i+1,j) - u(i,j),\\ \nabla_7 u(i,j) &= u(i+1,j+1) - u(i,j).\end{aligned} \tag{8}$$

Thus

$$\begin{aligned}&\mathbf{\nabla^{2\alpha} u}(\mathbf{i},\mathbf{j})\\ &= \left(\nabla_0^{2\alpha} u(i,j), \nabla_1^{2\alpha} u(i,j), \nabla_2^{2\alpha} u(i,j), \nabla_3^{2\alpha} u(i,j),\right.\\ &\quad \left.\nabla_4^{2\alpha} u(i,j), \nabla_5^{2\alpha} u(i,j), \nabla_6^{2\alpha} u(i,j), \nabla_7^{2\alpha} u(i,j)\right)^T,\end{aligned} \tag{9}$$

where T represents the transpose of the vector. From (14) we have

$$\begin{aligned}\nabla_0^{2\alpha} u(i,j) &= \sum_{k=0}^{K-1}(-1)^k C_k^{2\alpha} u(i, j+k-(K-1))\\ \nabla_1^{2\alpha} u(i,j) &= \sum_{k=0}^{K-1}(-1)^k C_k^{2\alpha} u\\ &\qquad \times (i-k+(K-1), j+k-(K-1))\\ \nabla_2^{2\alpha} u(i,j) &= \sum_{k=0}^{K-1}(-1)^k C_k^{2\alpha} u(i-k+(K-1), j)\\ \nabla_3^{2\alpha} u(i,j) &= \sum_{k=0}^{K-1}(-1)^k C_k^{2\alpha} u\\ &\qquad \times (i-k+(K-1), j-k+(K-1))\\ \nabla_4^{2\alpha} u(i,j) &= \sum_{k=0}^{K-1}(-1)^k C_k^{2\alpha} u(i, j-k+(K-1))\\ \nabla_5^{2\alpha} u(i,j) &= \sum_{k=0}^{K-1}(-1)^k C_k^{2\alpha} u\\ &\qquad \times (i+k-(K-1), j-k+(K-1))\\ \nabla_6^{2\alpha} u(i,j) &= \sum_{k=0}^{K-1}(-1)^k C_k^{2\alpha} u(i+k-(K-1), j)\\ \nabla_7^{2\alpha} u(i,j) &= \sum_{k=0}^{K-1}(-1)^k C_k^{2\alpha} u\\ &\qquad \times (i+k-(K-1), j+k-(K-1)).\end{aligned} \tag{10}$$

Let

$$\mathbf{g} = \left(g_0, g_1, g_2, g_3, g_4, g_5, g_6, g_7\right)^T, \tag{11}$$

where T represents the transpose of the vector and g_k, $k = 0,\ldots,7$ is defined as

$$g_k = \frac{g\left(\left\|\nabla_k u(i,j)\right\|\right)}{\sum_{n=0}^{7} g\left(\left\|\nabla_n u(i,j)\right\|\right)}, \quad k = 0,1,\ldots,7, \tag{12}$$

where $\nabla_k u(i,j)$, $k = 0,\ldots 7$ defined in (7) are the components of vector $\mathbf{\nabla u}(\mathbf{i},\mathbf{j})$, $\sum_{n=0}^{7} g(\|\nabla_n u(i,j)\|)$ is the normalized constant, and g is the decreasing function of absolute value of $\nabla_k u(i,j)$, $k = 0,\ldots 7$. In [1], $g(\|\nabla u_k(x,y,t)\|)$ is defined as

$$g\left(\left\|\nabla u_k(x,y,t)\right\|\right) = e^{-(\|\nabla u_k(x,y,t)\|/\sigma)^2}, \quad k = 0,\ldots,7 \tag{13}$$

or

$$g\left(\left\|\nabla u_k(x,y,t)\right\|\right) = \frac{1}{1+\left(\|\nabla u_k(x,y,t)\|/\sigma\right)^2}, \quad k = 0,\ldots,7, \tag{14}$$

where $\|\cdot\|$ is the module of the vector, and the constant σ controls the sensitivity to edges.

The new FOPMD based on G-L fractional-order derivative is defined as

$$\frac{\partial u(i,j,t)}{\partial t} = \operatorname{div}^{\alpha}\begin{pmatrix} g_0\nabla_0^{\alpha}u(i,j,t) \\ g_1\nabla_1^{\alpha}u(i,j,t) \\ g_2\nabla_2^{\alpha}u(i,j,t) \\ g_3\nabla_3^{\alpha}u(i,j,t) \\ g_4\nabla_4^{\alpha}u(i,j,t) \\ g_5\nabla_5^{\alpha}u(i,j,t) \\ g_6\nabla_6^{\alpha}u(i,j,t) \\ g_7\nabla_7^{\alpha}u(i,j,t) \end{pmatrix}, \tag{15}$$

where $g_k, k = 0, \ldots, 7$ defined in (11) are the components of $\mathbf{g}$ in (11).

The above equation can be represented as

$$\frac{\partial u(i,j,t)}{\partial t} = \sum_{k=0}^{7} g_k \nabla_k^{2\alpha} u(i,j,t), \tag{16}$$

where $\sum_{k=0}^{7} g_k = 1$ and $\nabla_k^{2\alpha}u(i,j,t)$ can be computed according to (9).

Thus the explicit form for solving (16) is

$$u(i,j,t+1) = u(i,j,t) + \lambda \sum_{k=0}^{7} g_k \nabla_k^{2\alpha} u(i,j,t), \tag{17}$$

where $u(i,j,t+1)$ is the gray level of (i,j) at time $t+1$ and λ is the integration constant ($0 \le \lambda \le 1/7$). Usually, due to numerical stability, λ is set to its maximum value.

To summarize, our sinogram restoration approach is done in the following steps.

(1) Let the input sinogram be U and set $t = 1$, $U_t = U$, input iterative number n, fractional-order α, integration constant λ in (17), and gradient modulus threshold σ that controls the conduction used in (13) or (14) and choose (13) or (14) as diffusion coefficients.

(2) Compute 1-order gradient vector $\nabla\mathbf{u}$ using (7).

(3) Compute diffusion coefficients vector $\mathbf{g}$ using (11)–(14).

(4) Compute 2α-order gradient vector $\nabla^{2\alpha}\mathbf{u}$ using (9).

(5) Compute U_{t+1} using (17), and set $t = t+1$, if $t = n$, output sinogram U_t; else goto step 2.

(6) Back-project sinogram U_t into the image I.

4. Experiments and Discussion

The main objective for sinogram restoration of LDCT is to delete the noise and avoid artifacts while preserving anatomy details for the back-projection images.

Two abdominal CT images of a 58-year-old man and two abdominal CT images of a 62-year-old woman with different doses were scanned from a 16 multidetector row CT unit (Somatom sensation 16; Siemens Medical Solutions) using 120 kVp and 5 mm slice thickness. Other remaining scanning parameters are gantry rotation time, 0.5 second; detector configuration (number of detector rows section thickness), 16×1.5 mm; table feed per gantry rotation, 24 mm; and pitch, 1 : 1 and reconstruction method, back projection (FBP) algorithm with the soft-tissue convolution kernel "B30f". Different CT doses were controlled by using two different fixed tube currents 60 mAs and 150 mAs (60 mA or 150 mAs) for LDCT and standard-dose CT (SDCT) protocols, respectively. The CT dose index volume (CTDIvol) for LDCT images and SDCT images is in positive linear correlation with the tube current and is calculated to be approximately ranged between 15.32 mGy to 3.16 mGy [27] (see Figures 1(a)–1(d)).

In order to compare our method with classical PM and other state-of-the art FOPMD methods, three compared methods are PMD [1], regularized PMD (RPM) [2], and FOPMD proposed in [9]. Since PMD has been discussed in detail in Section 1. We will briefly introduce other two methods.

It is well known that PMD is an ill-posed equation but RPMD [2] is a well-posed equation, which is defined as

$$\frac{\partial u(x,y,t)}{\partial t} = \operatorname{div}\left(g\left(\left\|G_{\sigma_1} \cdot \nabla u(x,y,t)\right\|\right)\nabla u(x,y,t)\right) \tag{18}$$

Here G_{σ_1} is defined as

$$G_{\sigma_1} = \frac{1}{C} e^{-(x^2+y^2)/\sigma_1^2} \tag{19}$$

is a Gaussian function and C is a constant. The diffusion coefficients $g(\cdot)$ are defined in (13) or (14). That is, the gradient vector in diffusion coefficients is convoluted by a Gaussian kernel to suppressing unsteadiness in image. Both PMD and RPMD use half-point central difference discretization scheme.

The FOPMD proposed in [9] is defined in (4), which is a FSFOD using G-L definition. Both FOPMD in [9] and EFOGV-PMD use integer-point unilateral difference discretization scheme.

In order to ensure that comparison is put on a fair level, the common used parameters are set to the same value. The commonly used parameters for four methods include gradient modulus threshold σ that controls the conduction, integration constant λ ($0 \le \lambda \le 1/7$), and iteration number t. Due to numerical stability, λ is set to its maximum value $1/7$ and σ is set to 30 to reduce iteration number.

The iteration number t is very important in PMD. That is, big t will make smooth image while small t will still leave much noise. In order to study the performance of four compared methods with different iteration number t and fixed other parameters, t is set to 3, 8, and 15, respectively.

The standard deviation of smoothed Gaussian kernel for the image σ_1 used for RPMD is set to 1 since in [2], the authors suggest that σ_1 should be a small number.

On sinogram space, FOPMD with $\alpha = 0.5$, $\alpha = 0.8$, and $\alpha = 1.2$ is carried on two image collections.

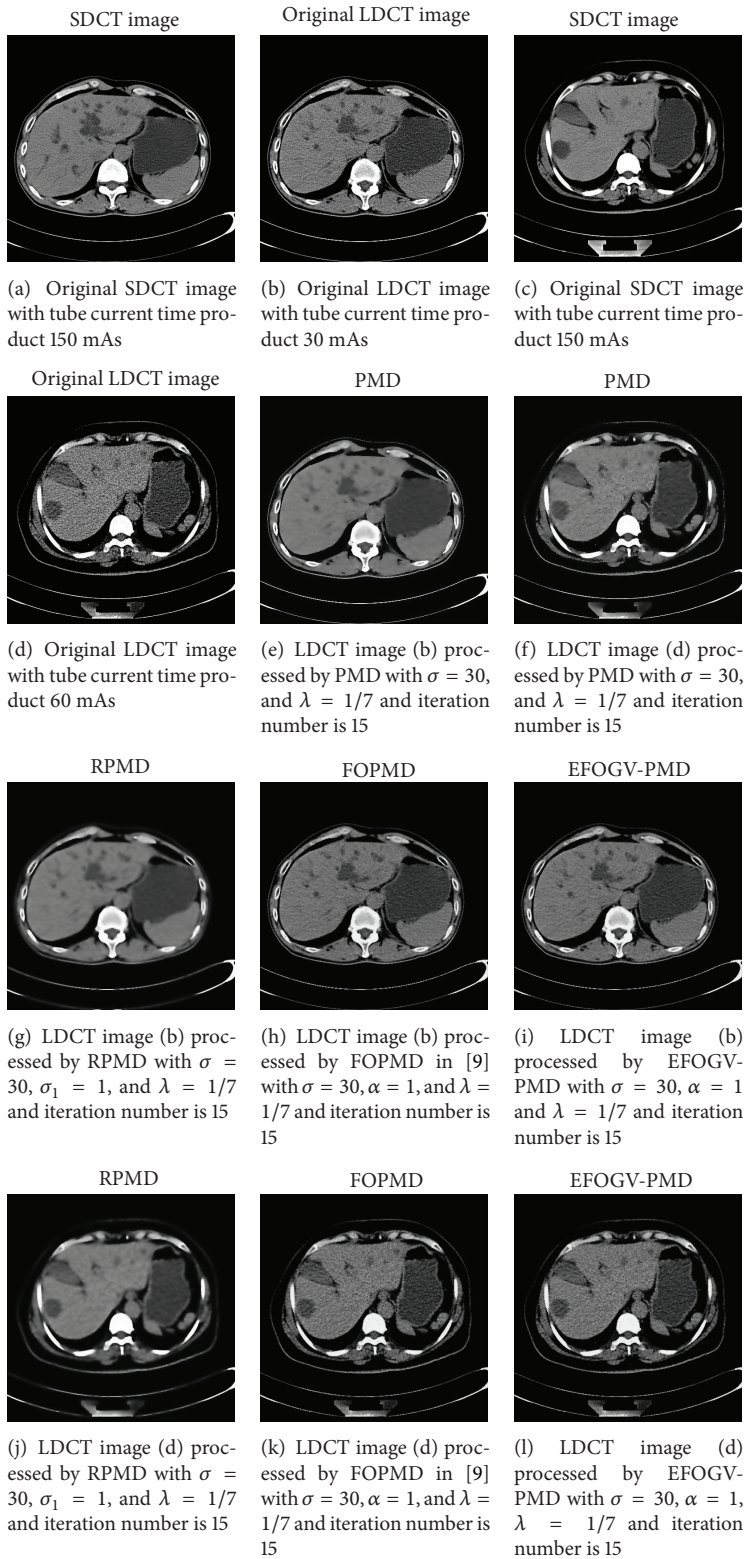

(a) Original SDCT image with tube current time product 150 mAs

(b) Original LDCT image with tube current time product 30 mAs

(c) Original SDCT image with tube current time product 150 mAs

(d) Original LDCT image with tube current time product 60 mAs

(e) LDCT image (b) processed by PMD with $\sigma = 30$, and $\lambda = 1/7$ and iteration number is 15

(f) LDCT image (d) processed by PMD with $\sigma = 30$, and $\lambda = 1/7$ and iteration number is 15

(g) LDCT image (b) processed by RPMD with $\sigma = 30$, $\sigma_1 = 1$, and $\lambda = 1/7$ and iteration number is 15

(h) LDCT image (b) processed by FOPMD in [9] with $\sigma = 30, \alpha = 1$, and $\lambda = 1/7$ and iteration number is 15

(i) LDCT image (b) processed by EFOGV-PMD with $\sigma = 30$, $\alpha = 1$ and $\lambda = 1/7$ and iteration number is 15

(j) LDCT image (d) processed by RPMD with $\sigma = 30$, $\sigma_1 = 1$, and $\lambda = 1/7$ and iteration number is 15

(k) LDCT image (d) processed by FOPMD in [9] with $\sigma = 30, \alpha = 1$, and $\lambda = 1/7$ and iteration number is 15

(l) LDCT image (d) processed by EFOGV-PMD with $\sigma = 30$, $\alpha = 1$, $\lambda = 1/7$ and iteration number is 15

Figure 1: Original SDCT and LDCT images ((a)–(d)), LDCT images processed by PMD, RPMD, FOPMD and EFOGV-PMD with fractional-order $\alpha = 1$ and iteration number is 15.

Since bigger iteration number leads to smoother denoised results, in order to observe the behaviors of big iteration number clearly, Figure 1 sets iteration number $t = 15$. Comparing all the original SDCT images in Figures 1(a) and 1(c), LDCT images in Figures 1(b) and 1(d) were severely degraded by nonstationary noise. All denoised images in Figure 1 can suppress most of noises. In particular, FOPMD and EFOGV-PMD can provide very satisfied images with having little noise and preserving all useful anatomy structures. However, denoised images of PMD and RPMD are oversmooth, which lost a lot of details.

In order to test the consistency of the definitions of different integer order or fractional order, we set fractional-order $\alpha = 1$, in which two fractional-order PMD should have same forms and they also correspond to the order of PMD and RPMD (see Figures 1(e)–1(l)). Observing Figures 1(h), 1(i), 1(k), and 1(l), we can find that the denoised images are identical, which demonstrate that the fractional-order definitions between [9] and EFOGV-PMD are identical when $\alpha = 1$.

However, the resulting images of PMD and RPMD are quite different to the images denoised by FOPMD and EFOGV-PMD. That is, the images processed by PMD and RPMD are smoother than the images processed by FOPMD and EFOGV-PMD. Different discretization schemes, PMD and RPMD adopt half-point central difference while FOPMD and EFOGV-PMD adopt integer-point unilateral difference, leading to this interesting result.

Since two FOMD schemes provide more satisfying results, we only compare two FOPMD methods with different fractional orders (see Figure 2) and different iteration numbers (see Figure 3).

In order to compare denoised results of two FOPMD schemes with different fractional orders, two original LDCT images in Figures 1(b) and 1(d) are used with iteration number $t = 15$ and fractional order $\alpha = 0.5, \alpha = 0.8$ and $\alpha = 1.2$. From the second and the forth rows of Figure 2, we can conclude that the resulting images of EFOGV-PMD are very satisfied and they become smoother when α becomes bigger, which is coherence with our intuition.

However, denoised images Figures 2(a) and 2(g) with $\alpha = 0.5$ using FOPMD in [9] have many artifacts, which are small black circles in two images. In addition, denoised images Figures 2(c) and 2(i) are very dark compared with the original LDCT images in Figures 1(b) and 1(d). Images in Figures 2(c) and 2(i) also have some isolated artificial white points, which are called speckle effect. It is obvious that resulting images in Figures 2(b) and 2(h) with $\alpha = 0.8$ processed by FOPMD in [9] have the best performance in three image series with different α.

Generally, artifacts in denoised images are oscillations near edges, caused by that the low-passed filtering is not processed correctly near the real edges. That is, some smooth regions near edges are regarded false as edges, which make these error edges preserved. Therefore, improving accuracy of edge detection is a good choice for improving the performance of FOPMD in [9]. This is the start point of our new method proposed in this paper.

From Figure 1, we can see the processed images using FOPMD in [9] with $\alpha = 1$ are very satisfied, which implies that when $\alpha = 1$, FOPMD in [9] can locate edges correctly. In addition, processed images with $\alpha = 0.8$, whose fractional orders are closest to $\alpha = 1$ in three image series, also are best in the three image series. In another words, the processed images with nearer fractional order to 1 have better performance. Therefore, $\alpha = 1$ is the best choice for edge locator.

Although when $\alpha = 1$, the FOPMD in [9] has the best performance for edge detection, impressive characters for fractional-order PMD with well preserved edges and power of suppressing noises are also promising in sinogram restoration of LDCT. Thus we adopt a new scheme to get both advantages of integer-order and fraction-order PMD. That is, the gradient vector in diffusion coefficients is integer-order to ensure correct edge detection while the "external" gradient vector is fractional order to suppressing noise and preserving edges.

Intuitively, processed images with bigger iteration number correspond to smoother images. In order to check the influence of iteration numbers for FOPMD in [9] and EFOGV-PMD, processed image series of two original LDCT images in Figures 1(b) and 1(d) with different iteration numbers 3, 8 and 15 are shown in Figure 3.

The resulting images in the first and the third rows of Figure 3 are the processed images using FOPMD in [9]. Compared with original LDCT images in Figures 1(b) and 1(d), all resulting images with different iteration numbers have less noise. In addition, the smoother images can be obtained as the iteration number becomes bigger. However, the most undesired default for FOPMD in [9] is that resulting images become dark as the iteration number becomes big. Moreover, except for Figure 3(g), the resulting images in the first and the third rows have some isolated white points, which are the speckle effect.

The resulting images in the second and the forth rows of Figure 3 show that EFOGV-PMD with different iteration numbers are very satisfied and they become smoother when the iteration number becomes bigger, which is in coherence with our intuition. Another attractive nature for EFOGV-PMD about iteration is that the smoothing shown in these images is very slow. That is, the resulting images in Figures 3(d) and 3(j) with iteration number 3 are slightly different to the images in Figures 3(f) and 3(l) with iteration number 15. This nature shows that EFOGV-PMD has good stability. Therefore, it is not sensitive to iteration number.

Recall that FOPMD in [9] makes artifacts, dark resulting images, and speckle effects. It should be indicated that although FOPMD in [9] suffers from above disadvantages, it can obtain satisfied resulting images by choosing suitable parameters. In addition, all exiting FOPMD methods at least suffer from speckle effect from the resulting images of these images. Fortunately, EFOGV-PMD can avoid artifacts, dark images, and speckle effect completely, which ensure its applications in sinogram restoration. More important for the new scheme is its stability, which makes it not sensitive to the iteration number.

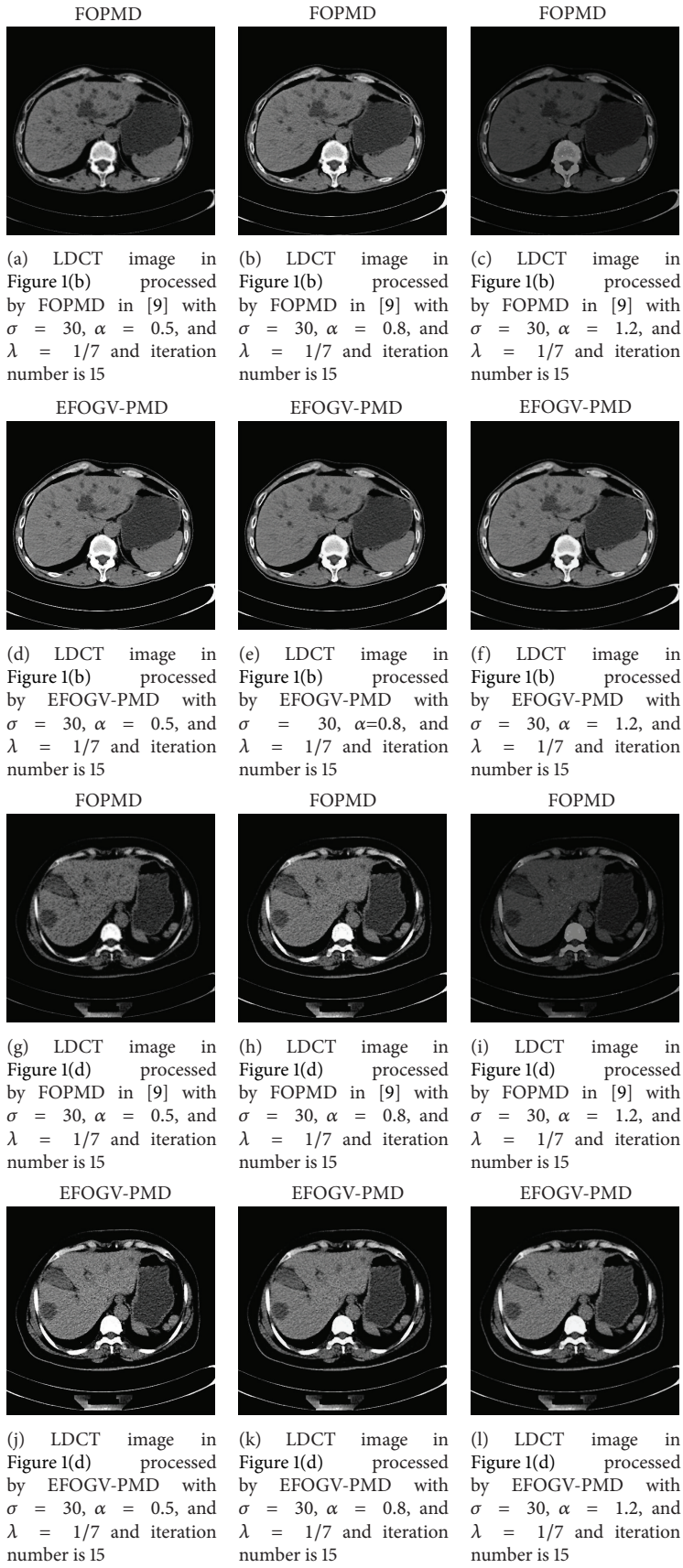

(a) LDCT image in Figure 1(b) processed by FOPMD in [9] with $\sigma = 30$, $\alpha = 0.5$, and $\lambda = 1/7$ and iteration number is 15

(b) LDCT image in Figure 1(b) processed by FOPMD in [9] with $\sigma = 30$, $\alpha = 0.8$, and $\lambda = 1/7$ and iteration number is 15

(c) LDCT image in Figure 1(b) processed by FOPMD in [9] with $\sigma = 30$, $\alpha = 1.2$, and $\lambda = 1/7$ and iteration number is 15

(d) LDCT image in Figure 1(b) processed by EFOGV-PMD with $\sigma = 30$, $\alpha = 0.5$, and $\lambda = 1/7$ and iteration number is 15

(e) LDCT image in Figure 1(b) processed by EFOGV-PMD with $\sigma = 30$, α=0.8, and $\lambda = 1/7$ and iteration number is 15

(f) LDCT image in Figure 1(b) processed by EFOGV-PMD with $\sigma = 30$, $\alpha = 1.2$, and $\lambda = 1/7$ and iteration number is 15

(g) LDCT image in Figure 1(d) processed by FOPMD in [9] with $\sigma = 30$, $\alpha = 0.5$, and $\lambda = 1/7$ and iteration number is 15

(h) LDCT image in Figure 1(d) processed by FOPMD in [9] with $\sigma = 30$, $\alpha = 0.8$, and $\lambda = 1/7$ and iteration number is 15

(i) LDCT image in Figure 1(d) processed by FOPMD in [9] with $\sigma = 30$, $\alpha = 1.2$, and $\lambda = 1/7$ and iteration number is 15

(j) LDCT image in Figure 1(d) processed by EFOGV-PMD with $\sigma = 30$, $\alpha = 0.5$, and $\lambda = 1/7$ and iteration number is 15

(k) LDCT image in Figure 1(d) processed by EFOGV-PMD with $\sigma = 30$, $\alpha = 0.8$, and $\lambda = 1/7$ and iteration number is 15

(l) LDCT image in Figure 1(d) processed by EFOGV-PMD with $\sigma = 30$, $\alpha = 1.2$, and $\lambda = 1/7$ and iteration number is 15

Figure 2: LDCT images in Figures 1(b) and 1(d) processed by FOPMD and EFOGV-PMD with different fractional-orders and iteration number is set to 15. The first column: $\alpha = 0.5$; the second column: $\alpha = 0.8$, the third column: $\alpha = 1.2$. The first row: Figure 1(b) processed by FOPMD; the second row: Figure 1(b) processed by EFOGV-PMD; the third row: Figure 1(d) processed by FOPMD; the fourth row: Figure 1(d) processed by EFOGV-PMD.

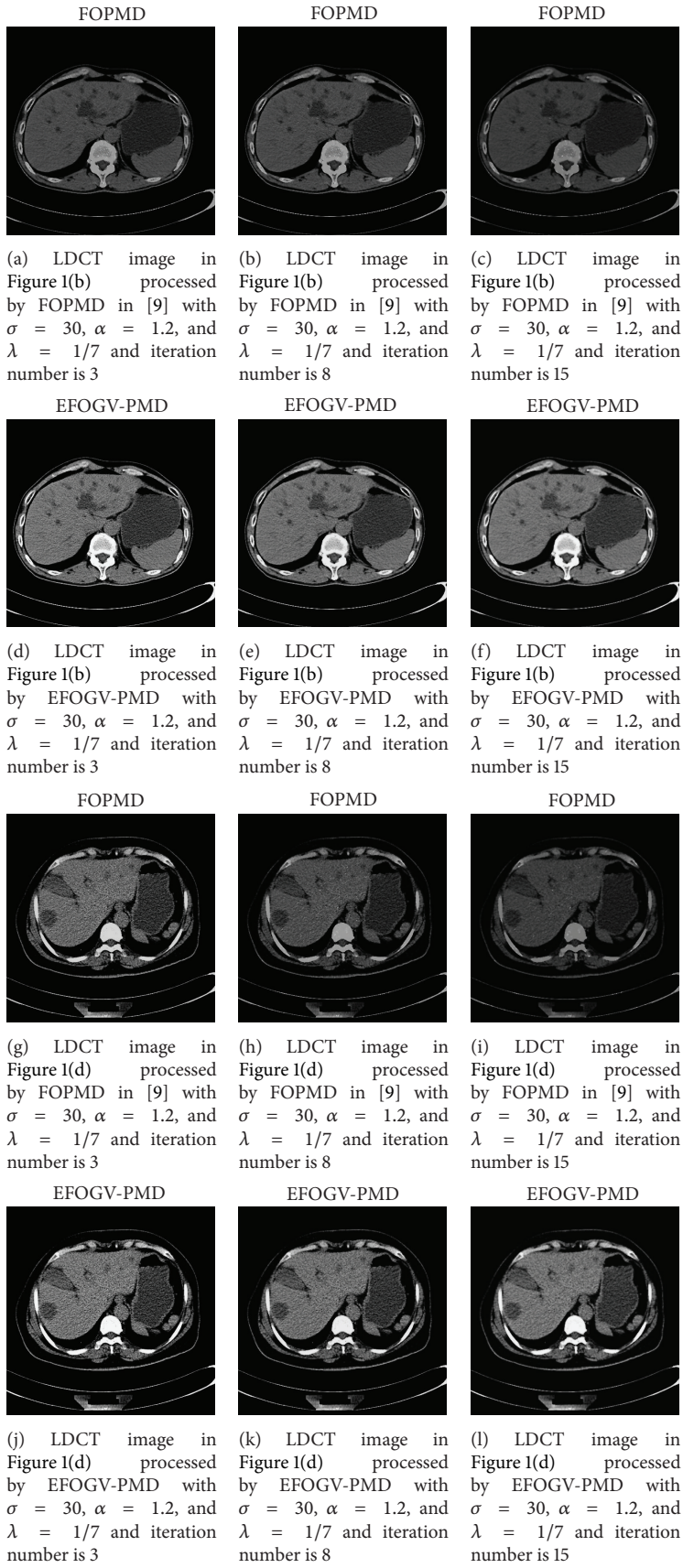

(a) LDCT image in Figure 1(b) processed by FOPMD in [9] with $\sigma = 30$, $\alpha = 1.2$, and $\lambda = 1/7$ and iteration number is 3

(b) LDCT image in Figure 1(b) processed by FOPMD in [9] with $\sigma = 30$, $\alpha = 1.2$, and $\lambda = 1/7$ and iteration number is 8

(c) LDCT image in Figure 1(b) processed by FOPMD in [9] with $\sigma = 30$, $\alpha = 1.2$, and $\lambda = 1/7$ and iteration number is 15

(d) LDCT image in Figure 1(b) processed by EFOGV-PMD with $\sigma = 30$, $\alpha = 1.2$, and $\lambda = 1/7$ and iteration number is 3

(e) LDCT image in Figure 1(b) processed by EFOGV-PMD with $\sigma = 30$, $\alpha = 1.2$, and $\lambda = 1/7$ and iteration number is 8

(f) LDCT image in Figure 1(b) processed by EFOGV-PMD with $\sigma = 30$, $\alpha = 1.2$, and $\lambda = 1/7$ and iteration number is 15

(g) LDCT image in Figure 1(d) processed by FOPMD in [9] with $\sigma = 30$, $\alpha = 1.2$, and $\lambda = 1/7$ and iteration number is 3

(h) LDCT image in Figure 1(d) processed by FOPMD in [9] with $\sigma = 30$, $\alpha = 1.2$, and $\lambda = 1/7$ and iteration number is 8

(i) LDCT image in Figure 1(d) processed by FOPMD in [9] with $\sigma = 30$, $\alpha = 1.2$, and $\lambda = 1/7$ and iteration number is 15

(j) LDCT image in Figure 1(d) processed by EFOGV-PMD with $\sigma = 30$, $\alpha = 1.2$, and $\lambda = 1/7$ and iteration number is 3

(k) LDCT image in Figure 1(d) processed by EFOGV-PMD with $\sigma = 30$, $\alpha = 1.2$, and $\lambda = 1/7$ and iteration number is 8

(l) LDCT image in Figure 1(d) processed by EFOGV-PMD with $\sigma = 30$, $\alpha = 1.2$, and $\lambda = 1/7$ and iteration number is 15

Figure 3: LDCT images in Figures 1(b) and 1(d) processed by FOPMD and EFOGV-PMD with different iteration numbers and the fractional-order $\alpha = 1.2$. The first column: iteration number is 3; the second column: iteration number is 8 and the third column: iteration number is 15. The first row: Figure 1(b) processed by FOPMD; the second row: Figure 1(b) processed by EFOGV-PMD; the third row: Figure 1(d) processed by FOPMD and the fourth row: Figure 1(d) processed by EFOGV-PMD.

5. Conclusions

In this paper, we propose a new FOPMD, EFOGV-PMD for LDCT sinogram imaging based on G-L fractional-order derivative definition. EFOGV-PMD not only has good ability to preserving edges while denoising, it also can avoid artifacts, dark images and speckle effects of FOPMD in [9] and other existing FOPMD schemes completely by correctly located edges, which ensures that EFOGV-PMD can be used for sinogram restoration of LDCT. More importantly, EFOGV-PMD has good stability for iteration numbers, which leads to it is not sensitive to the iteration number choice. Having so many advantages for EFOGV-PMD, it should become an promising candidate method for sinogram restoration of LDCT.

Acknowledgments

This paper is supported by the National Natural Science Foundation of China (no 60873102), the Major State Basic Research Development Program (no. 2010CB732501), and the Open Foundation of Visual Computing and Virtual Reality Key Laboratory Of Sichuan Province (no. J2010N03). This work was supported by a Grant from the National High Technology Research and Development Program of China (no. 2009AA12Z140).

References

[1] P. Perona and J. Malik, "Scale-space and edge detection using anisotropic diffusion," *IEEE Transactions on Pattern Analysis and Machine Intelligence*, vol. 12, no. 7, pp. 629–639, 1990.

[2] F. Catté, P.-L. Lions, J.-M. Morel, and T. Coll, "Image selective smoothing and edge detection by nonlinear diffusion," *SIAM Journal on Numerical Analysis*, vol. 29, no. 1, pp. 182–193, 1992.

[3] Y.-L. You and M. Kaveh, "Fourth-order partial differential equations for noise removal," *IEEE Transactions on Image Processing*, vol. 9, no. 10, pp. 1723–1730, 2000.

[4] T. F. Chan, S. Esedoglu, and F. E. Park, "A fourth order dual method for staircase reduction in texture extraction and image restoration problems," http://basilo.kaist.ac.kr/preprint/uclam/cam05-28.pdf.

[5] T. Chan, A. Marquina, and P. Mulet, "High-order total variation-based image restoration," *SIAM Journal on Scientific Computing*, vol. 22, no. 2, pp. 503–516, 2000.

[6] J. Bai and X.-C. Feng, "Fractional-order anisotropic diffusion for image denoising," *IEEE Transactions on Image Processing*, vol. 16, no. 10, pp. 2492–2502, 2007.

[7] J. Zhang and Z. Wei, "A class of fractional-order multi-scale variational models and alternating projection algorithm for image denoising," *Applied Mathematical Modelling*, vol. 35, no. 5, pp. 2516–2528, 2011.

[8] M. Janev, S. Pilipović, T. Atanacković, R. Obradović, and N. Ralević, "Fully fractional anisotropic diffusion for image denoising," *Mathematical and Computer Modelling*, vol. 54, no. 1-2, pp. 729–741, 2011.

[9] S. Hu, Z. Liao, and W. Chen, "Sinogram restoration for low-dosed X-ray computed tomography using fractional-order Perona-Malik diffusion," *Mathematical Problems in Engineering*, vol. 2012, Article ID 391050, 13 pages, 2012.

[10] M. Li, "Approximating ideal filters by systems of fractional order," *Computational and Mathematical Methods in Medicine*, vol. 2012, Article ID 365054, 6 pages, 2012.

[11] M. Li, S. C. Lim, C. Cattani, and M. Scalia, "Characteristic roots of a class of fractional oscillators," *Advances in High Energy Physics*, vol. 2013, Article ID 853925, 2013.

[12] M. Li and W. Zhao, "On $1/f$ noise," *Mathematical Problems in Engineering*, vol. 2012, Article ID 673648, 23 pages, 2012.

[13] M. Li and W. Zhao, "Solving Abel's type integral equation with Mikusinski's operator of fractional order," *Advances in Mathematical Physics*, vol. 2013, Article ID 806984, 4 pages, 2013.

[14] D. J. Brenner and E. J. Hall, "Computed tomography—an increasing source of radiation exposure," *The New England Journal of Medicine*, vol. 357, no. 22, pp. 2277–2284, 2007.

[15] L. Yu, "Radiation dose reduction in computed tomography: techniques and future perspective," *Imaging in Medicine*, vol. 1, no. 1, pp. 65–84, 2009.

[16] J. Weidemann, G. Stamm, M. Galanski, and M. Keberle, "Comparison of the image quality of various fixed and dose modulated protocols for soft tissue neck CT on a GE Lightspeed scanner," *European Journal of Radiology*, vol. 69, no. 3, pp. 473–477, 2009.

[17] M. K. Kalra, M. M. Maher, M. A. Blake et al., "Detection and characterization of lesions on low-radiation-dose abdominal CT images postprocessed with noise reduction filters," *Radiology*, vol. 232, no. 3, pp. 791–797, 2004.

[18] J. C. R. Giraldo, Z. S. Kelm, L. S. Guimaraes et al., "Comparative study of two image space noise reduction methods for computed tomography: bilateral filter and nonlocal means," *Proceedings of the Annual International Conference of the IEEE Engineering in Medicine and Biology Society*, vol. 1, pp. 3529–3532, 2009.

[19] A. Manduca, L. Yu, J. D. Trzasko et al., "Projection space denoising with bilateral filtering and CT noise modeling for dose reduction in CT," *Medical Physics*, vol. 36, no. 11, pp. 4911–4919, 2009.

[20] N. Mail, D. J. Moseley, J. H. Siewerdsen, and D. A. Jaffray, "The influence of bowtie filtration on cone-beam CT image quality," *Medical Physics*, vol. 36, no. 1, pp. 22–32, 2009.

[21] Z. Liao, S. Hu, and W. Chen, "Determining neighborhoods of image pixels automatically for adaptive image denoising using nonlinear time series analysis," *Mathematical Problems in Engineering*, vol. 2010, Article ID 914564, 14 pages, 2010.

[22] H. Lu, I.-T. Hsiao, X. Li, and Z. Liang, "Noise properties of low-dose CT projections and noise treatment by scale transformations," in *Proceedings of IEEE Nuclear Science Symposium Conference Record*, vol. 3, pp. 1662–1666, November 2001.

[23] J. Xu and B. M. W. Tsui, "Electronic noise modeling in statistical iterative reconstruction," *IEEE Transactions on Image Processing*, vol. 18, no. 6, pp. 1228–1238, 2009.

[24] I. A. Elbakri and J. A. Fessler, "Statistical image reconstruction for polyenergetic X-ray computed tomography," *IEEE Transactions on Medical Imaging*, vol. 21, no. 2, pp. 89–99, 2002.

[25] J. Wang, H. Lu, J. Wen, and Z. Liang, "Multiscale penalized weighted least-squares sinogram restoration for low-dose X-ray computed tomography," *IEEE Transactions on Biomedical Engineering*, vol. 55, no. 3, pp. 1022–1031, 2008.

[26] J. Wang, T. Li, H. Lu, and Z. Liang, "Penalized weighted least-squares approach to sinogram noise reduction and image reconstruction for low-dose X-ray computed tomography,"

IEEE Transactions on Medical Imaging, vol. 25, no. 10, pp. 1272–1283, 2006.

[27] Y. Chen, W. Chen, X. Yin et al., "Improving low-dose abdominal CT images by weighted intensity averaging over large-scale neighborhoods," *European Journal of Radiology*, vol. 80, no. 2, pp. e42–e49, 2011.

Hindawi Publishing Corporation
Advances in Mathematical Physics
Volume 2013, Article ID 825861, 9 pages
http://dx.doi.org/10.1155/2013/825861

Research Article

Geometric Distribution Weight Information Modeled Using Radial Basis Function with Fractional Order for Linear Discriminant Analysis Method

Wen-Sheng Chen,[1,2] Chu Zhang,[2] and Shengyong Chen[3]

[1] *College of Mathematics and Computational Science, Shenzhen University, Shenzhen 518160, China*
[2] *College of Computer Science and Software Engineering, Shenzhen University, Shenzhen 518160, China*
[3] *College of Computer Science and Technology, Zhejiang University of Technology, Hangzhou 310023, China*

Correspondence should be addressed to Wen-Sheng Chen; chenws@szu.edu.cn

Received 20 September 2013; Accepted 24 September 2013

Academic Editor: Ming Li

Fisher linear discriminant analysis (FLDA) is a classic linear feature extraction and dimensionality reduction approach for face recognition. It is known that geometric distribution weight information of image data plays an important role in machine learning approaches. However, FLDA does not employ the geometric distribution weight information of facial images in the training stage. Hence, its recognition accuracy will be affected. In order to enhance the classification power of FLDA method, this paper utilizes radial basis function (RBF) with fractional order to model the geometric distribution weight information of the training samples and proposes a novel geometric distribution weight information based Fisher discriminant criterion. Subsequently, a geometric distribution weight information based LDA (GLDA) algorithm is developed and successfully applied to face recognition. Two publicly available face databases, namely, ORL and FERET databases, are selected for evaluation. Compared with some LDA-based algorithms, experimental results exhibit that our GLDA approach gives superior performance.

1. Introduction

Over the past two decades, face recognition (FR) has made great progress with the increasing computational power of computers and has become one of the most important biometric-based authentication technologies. The key issue of FR algorithm is dimensionality reduction for facial feature extraction. According to different processes of facial feature extraction, face recognition algorithms can be generally divided into two classes, namely, (local) geometric feature based and (holistic) appearance based [1]. The geometric feature-based approach is based on the shape and the location of facial components (such as eyes, eyebrows, nose, and mouth), which are extracted to represent a face geometric feature vector. However, for the appearance-based approach, it depends on the global facial pixel features, which are exploited to form a whole facial feature vector for face classification. Principle component analysis (PCA) [2] and linear discriminant analysis (LDA) [3] are two famous appearance-based approaches for linear feature extraction and dimensionality reduction. They are also called Eigenface method and Fisherface method in face recognition, respectively. The objective of PCA is to find the orthogonal principle component (PC) directions and preserve the maximum variance information of the training data along PC directions. PCA can reconstruct each facial image using all Eigenfaces. Since PCA takes no account of the discriminant information, it is unsuitable for classification tasks. LDA is a supervised learning method and seeks the optimal projection mapping under Fisher criterion such that the ratio of interdistance to intradistance attains the maximum. Therefore, from the classification point of view, LDA should give better performance than PCA. LDA is theoretically sound. However, it still has two issues. For one thing, LDA often encounters a small sample size (3S) problem, which always occurs when the dimension of the input sample space is greater than the

number of training facial images. Under this situation, LDA cannot be performed directly. To solve the 3S problem, a large number of LDA-based approaches have been proposed [4–16]. Among them, Fisher linear discriminant analysis (FLDA) method, also called Fisherface method in FR, is a two-stage algorithm. It first employs PCA for dimensionality reduction to guarantee that the between-class scatter matrix is full rank, and then LDA can be implemented in the PCA-mapped low dimensional feature space. Direct LDA [6] (DLDA) is another LDA-based approach which uses simultaneous diagonalization technique [17] to solve 3S problem. The basic idea of DLDA is to previously discard the null space of between-class scatter matrix S_b and then keep the null space of within-class scatter matrix S_w. Although DLDA is computationally efficient, it suffers from the performance limitation especially when the number of training images increases. This is because discarding the null space of S_b would also discard the null space of S_w indirectly. Literature [5] shows that the null space of S_w contains the most discriminant information. For another thing, these LDA-based methods are based on the classic Fisher criterion, which does not consider the geometric distribution weight information of the training data. So, their recognition performances will be degraded.

To enhance the discriminant power of LDA-based approach, this paper presents a novel Fisher criterion by taking into account the geometric distribution weight information of the training facial data. It is natural to think that the intradata nearby its class center is more important to represent the feature of the class. So, the proposed method attempts to impose a penalty weight (small weight) on the intradata if the intradata is far from its own class center. In the meanwhile, if two different class centers are close to each other, they will be given a small weight as well. To this end, we should extract the geometric distribution weight information of the training data. In recent years, lots of fractional order based methods [18–25] have been proposed in the area of dynamic systems, image processing, face recognition, and so on. This paper will adopt radial basis function (RBF) with fractional order [21–23] to model the geometric distribution weight information of the training samples, and thus we are able to establish a new Fisher criterion incorporated with data geometric distribution weight information. Based on the modified Fisher discriminant criterion, a geometric distribution weight information based linear discriminant analysis (GLDA) method is proposed for face recognition. Our GLDA approach is tested on two face databases, namely, ORL database and FERET database. Compared with FLDA method and DLDA method, experimental results show that the proposed GLDA method outperforms FLDA and DLDA methods.

The rest of this paper is organized as follows. Section 2 briefly introduces the related works. In Section 3, RBF with fractional order is exploited to model the data geometric distribution weight information. The new Fisher criterion is then established using geometric distribution weight information of the training data, and GLDA algorithm is designed. Experimental results on two face databases are reported in Section 4. Finally, Section 5 draws the conclusions.

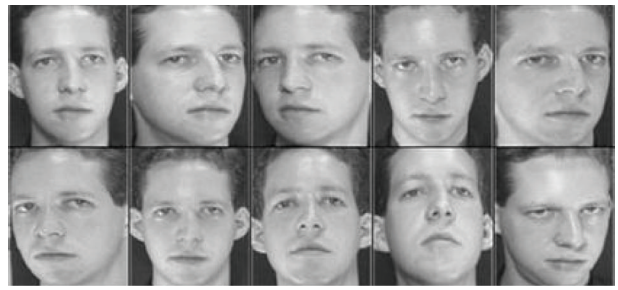

Figure 1: Images of one person from ORL database.

Figure 2: Images of two persons from FERET database.

2. Related Works

In this section, we will introduce some related linear feature extraction and dimensionality reduction algorithms for face recognition.

2.1. Some Notations. Let d be the dimension of the original sample space and let C be the number of the sample classes. The ith class $C_i = \{x_1^{(i)}, x_2^{(i)}, \ldots, x_{Ni}^{(i)}\}$ contains N_i $(1 \le i \le C)$ training samples, and the total number of all training data is $N = \sum_{i=1}^{C} N_i$, where $x_j^{(i)} \in R^d$ denotes the jth samples in class C_i. Assume μ_i is the center of class i; that is, $\mu_i = (1/N_i)\sum_{j=1}^{N_i} x_j^{(i)}$, and the entire mean $\mu = (1/C)\sum_{i=1}^{C} \mu_i$. In PCA algorithm, total scatter matrix S_t, also called covariance matrix, is defined by

$$S_t = \frac{1}{N}\sum_{i=1}^{C}\sum_{j=1}^{N_i}\left(x_j^{(i)} - \mu\right)\left(x_j^{(i)} - \mu\right)^T. \tag{1}$$

In LDA algorithm, within-class scatter matrix S_w and between-class scatter matrix S_b are defined, respectively, as follows:

$$\begin{aligned} S_w &= \frac{1}{N}\sum_{i=1}^{C}\sum_{j=1}^{N_i}\left(x_j^{(i)} - \mu_i\right)\left(x_j^{(i)} - \mu_i\right)^T, \\ S_b &= \frac{1}{N}\sum_{i=1}^{C} N_i\left(\mu_i - \mu\right)\left(\mu_i - \mu\right)^T. \end{aligned} \tag{2}$$

The radial basis function $K_\alpha(x)$ with fractional order α is given as follows

$$K_\alpha(x) = \exp\left(-\|x\|^\alpha\right). \tag{3}$$

The previous RBF can be viewed as the normalized radial kernel of fractional order α.

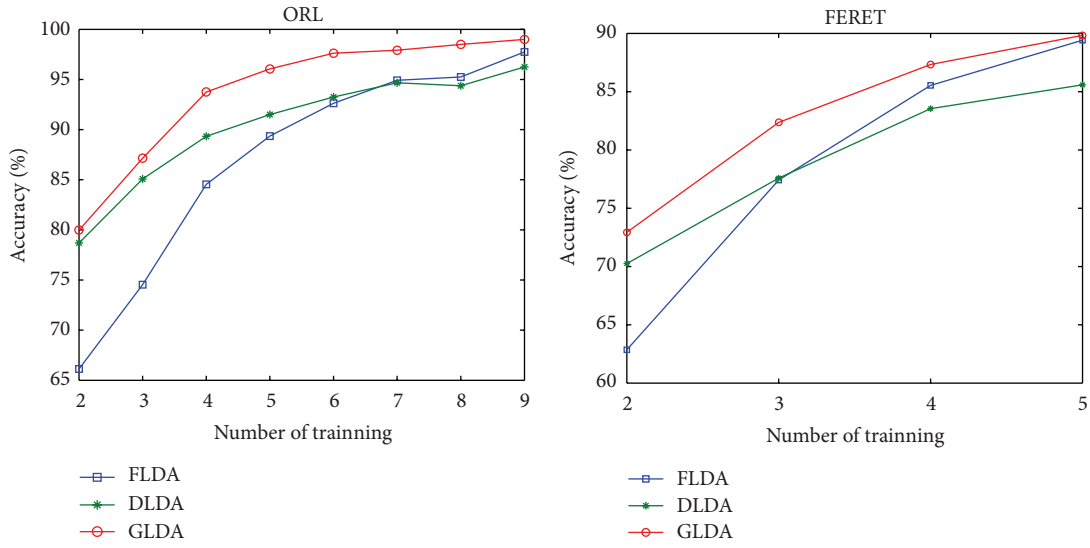

Figure 3: Rank 1 accuracy versus training number on the ORL face database (b) and FERET face database (a).

Table 1: Recognition rates on ORL database.

TN	2	3	4	5	6	7	8	9
FLDA	66.13%	74.54%	84.54%	89.35%	92.63%	94.92%	95.25%	97.75%
DLDA	78.69%	85.07%	89.33%	91.50%	93.25%	94.67%	94.38%	96.25%
GLDA	79.98%	87.14%	93.75%	96.05%	97.63%	97.92%	98.50%	99.00%

Table 2: Recognition rates on FERET database.

TN	2	3	4	5
FLDA	62.85%	77.42%	85.54%	89.42%
DLDA	70.25%	77.58%	83.54%	85.58%
GLDA	72.94%	82.36%	87.33%	89.83%

2.2. PCA. Principal component analysis algorithm is also known as Karhunen-Loeve transformation. It aims to find orthogonal principal component directions such that the scatter of all projected samples on large principal component direction is maximal. PCA is theoretically based on total scatter matrix S_t which can be calculated via formula (1). The PCA projection matrix W_{PCA} is determined by the following criterion:

$$W_{\mathrm{PCA}} = \arg\max_{W} \left| W^T S_t W \right|, \tag{4}$$

where $W \in R^{d\times m}$ and $m \ll d$.

Problem (4) is equivalent to solving the eigen-system: $S_t W = W\Lambda$, where $\Lambda = \mathrm{diag}\{\lambda_1, \lambda_2, \ldots, \lambda_\tau, 0, \ldots, 0\}$ with $\lambda_1 \geq \lambda_2 \geq \cdots \geq \lambda_\tau > 0$ and $W = [w_1, w_2, \ldots, w_d]$. The PCA projection matrix W_{PCA} can be chosen as $W_{\mathrm{PCA}} = [w_1, w_2, \ldots, w_m]$ ($m \ll d$). The column vectors w_i ($i = 1, 2, \ldots, m$) are called the eigenfaces in face recognition. It can be seen that PCA does not use the class label information. So, PCA is an unsupervised learning method, and its performance is not good in classification tasks.

2.3. Fisher LDA. The goal of linear discriminant analysis is to find a low dimensional feature space in which the intradata are tightly clustered and the interdata are far from each other. Therefore, LDA should acquire an optimal projection matrix W_{LDA} to maximize the ratio of between-class scatter and the within-class scatter; namely,

$$W_{\mathrm{LDA}} = \arg\max_{W} \frac{\left| W^T S_b W \right|}{\left| W^T S_w W \right|}. \tag{5}$$

The previous problem is equivalent to solving the following eigen-system:

$$S_w^{-1} S_b W = W\Lambda, \tag{6}$$

where Λ is a $d \times d$ diagonal eigenvalue matrix with its eigenvalues sorted in decreasing order. The projection matrix W_{LDA} is formed with the eigenvectors corresponding to the largest $C - 1$ eigenvalues. In face recognition, the column vectors of W_{LDA} are called Fisherfaces as well. However, LDA often suffers from small sample size problem when the number of training samples is smaller than the dimension of the sample vector. Under this situation, the within-class scatter matrix is invertible, and the eigensystem (6) cannot be solved. This means that LDA cannot be performed

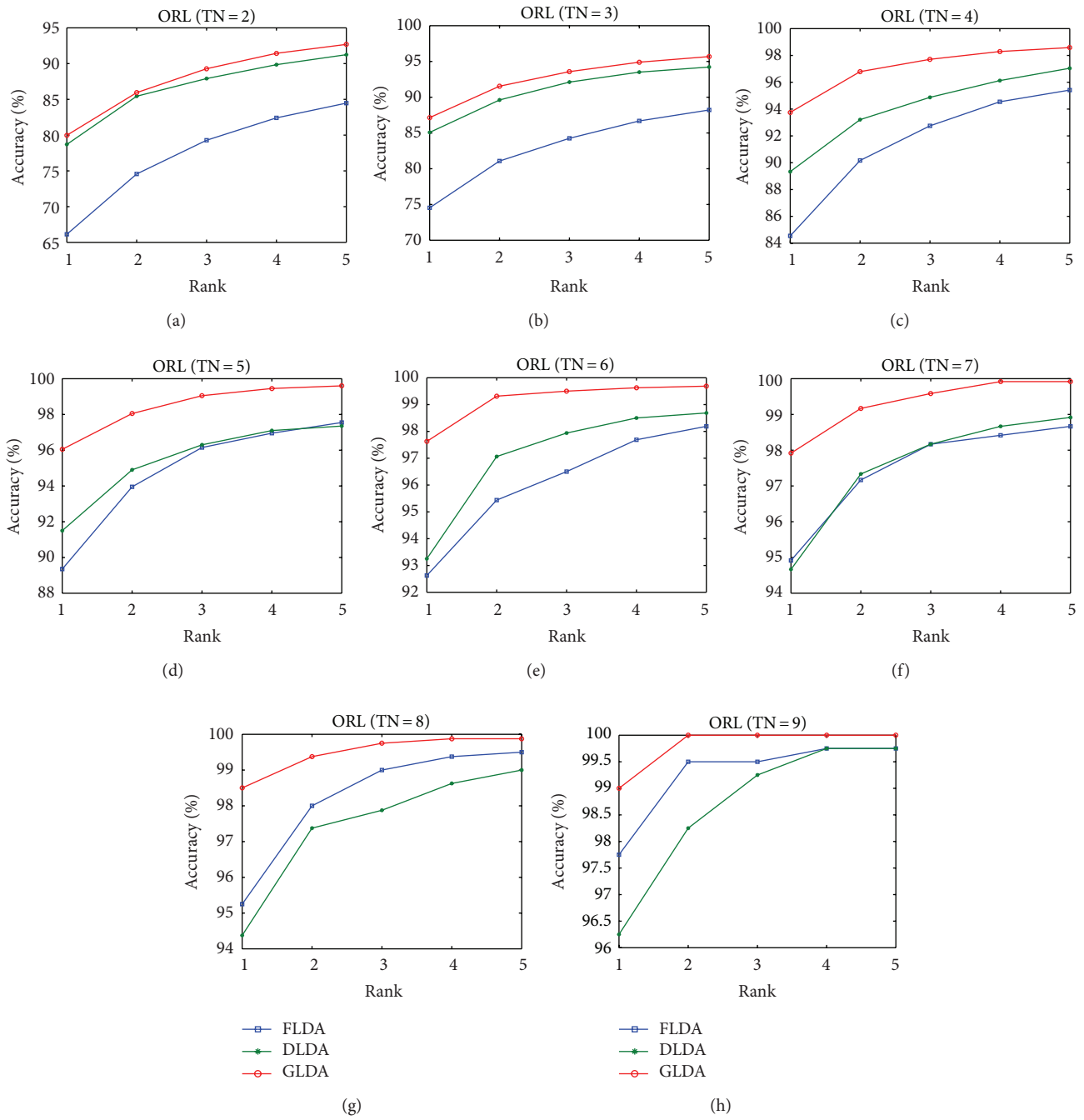

FIGURE 4: CMC curve comparisons on the ORL database.

directly. So, Fisher LDA (FLDA) uses PCA for dimensionality reduction in advance.

2.4. Direct LDA. Yu and Yang [6] proposed a direct LDA (DLDA) approach using simultaneous diagonalization technique [17]. Direct LDA is actually a subspace approach to overcome 3S problem of LDA. It attempts to obtain the optimal projection matrix W in the subspace $N(S_w) \cap \overline{N(S_b)}$ and satisfies the following equations:

$$WS_bW^T = I, \qquad WS_wW^T = \Lambda, \tag{7}$$

where $N(S_w)$ means the null space of S_w, $\overline{N(S_b)}$ denotes the complement subspace of $N(S_b)$, and I is an identity matrix. Diagonal matrix Λ may contain 0s and some small eigenvalues in its diagonal. Details can be found in [6].

We can see that some useful discriminant information will be discarded in the intermediate PCA stage of FLDA or simultaneous diagonalization stage of DLDA. Moreover, both

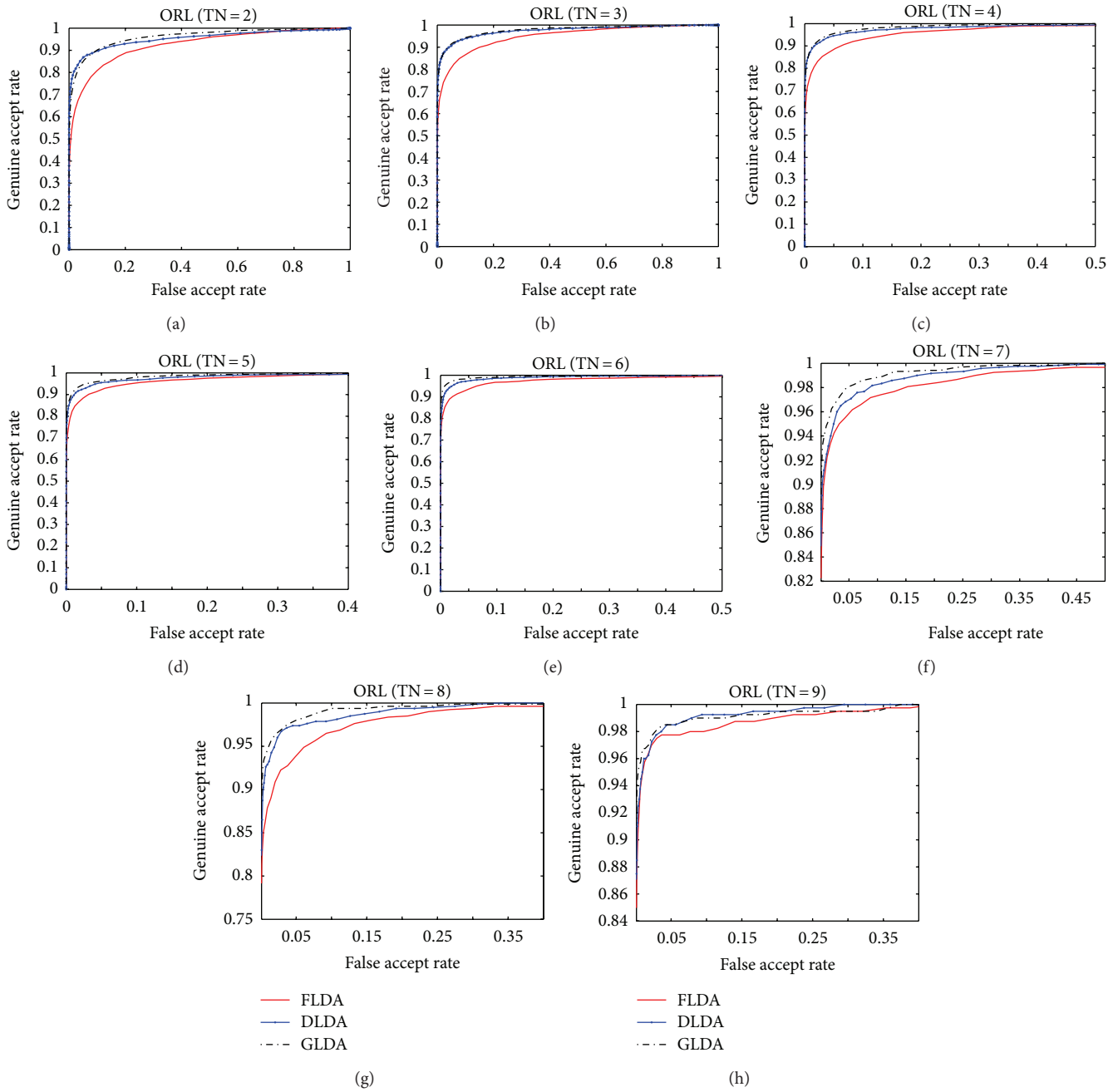

Figure 5: ROC curve comparisons on the ORL database.

FLDA method and DLDA method do not exploit the geometric distribution weight information of the training samples. These factors will affect their recognition performance.

3. Proposed GLDA Method

This section will propose a novel discriminant criterion, which will use the geometric distribution weight information of the training samples. Based on the new discriminant criterion, our GLDA method is proposed. Details are discussed as follows.

3.1. Proposed Discriminant Criterion. To take advantage of geometric distribution weight information of face pattern space, we redefine the within-class scatter matrix $\widetilde{S}_w$ and between-class scatter matrix $\widetilde{S}_b$, respectively, as follows:

$$\widetilde{S}_w = \frac{1}{N}\sum_{i=1}^{C}\sum_{j=1}^{N_i}\left(x_j^{(i)}-\mu_i\right)\left(x_j^{(i)}-\mu_i\right)^T\cdot K_{\alpha_w}\left(x_j^{(i)}-\mu_i\right),$$
$$\widetilde{S}_b = \frac{1}{N}\sum_{i=1}^{C}N_i\left(\mu_i-\mu\right)\left(\mu_i-\mu\right)^T\cdot\left[1-K_{\alpha_b}\left(\mu_i-\mu\right)\right], \quad (8)$$

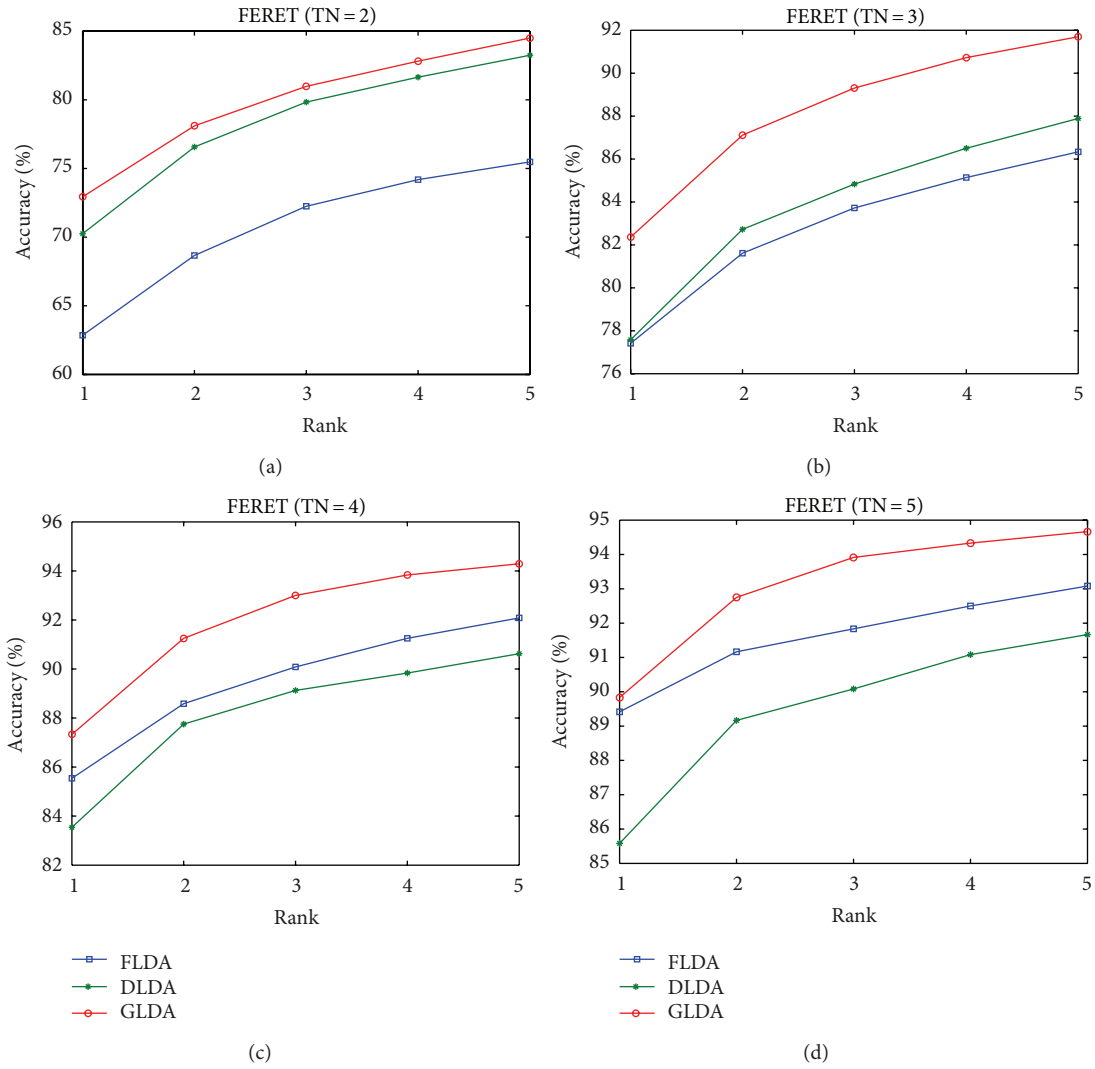

Figure 6: CMC curve comparisons on the FERET database.

where $K_{\alpha_w}(x_j^{(i)} - \mu_i)$ and $K_{\alpha_b}(\mu_i - \mu)$ are radial basis functions defined by (3). α_w and α_b are fractional order parameters, which can be more flexibly adjusted to obtain the optimal parameters. It can be seen from (8) that if the distance between the samples x_i^j and μ_i is large, it will impose a penalty weight. Similarly, if the class center μ_i is nearby the center μ, then we also give it a small weight. Otherwise, it will have a large weight.

Based on the previous analysis, our geometric distribution weight information based Fisher criterion function $J(W)$ is defined by

$$J(W) = \frac{\left|W^T \widetilde{S}_b W\right|}{\left|W^T \widetilde{S}_w W\right|}. \tag{9}$$

To obtain the following optimal projection matrix:

$$W_{\mathrm{GLDA}} = \arg\max_w J(W), \tag{10}$$

we can equivalently solve the following eigensystem:

$$\widetilde{S}_w^{-1} \widetilde{S}_b W = W\Lambda, \tag{11}$$

where Λ is a diagonal eigenvalue matrix with its eigenvalues sorted in decreasing order. The projection matrix W_{GLDA} is formed with eigenvectors corresponding to the largest $C - 1$ eigenvalues.

3.2. Algorithm Design. This subsection will develop our GLDA algorithm based on geometric distribution weight information Fisher discriminant criterion (9). Details are as follows.

It is easily seen that two scatter matrices $\widetilde{S}_w$ and $\widetilde{S}_b$ can be rewritten in the following forms, respectively:

$$\widetilde{S}_w = \widetilde{\Phi}_w \widetilde{\Phi}_w^T \in R^{d \times d}, \tag{12}$$

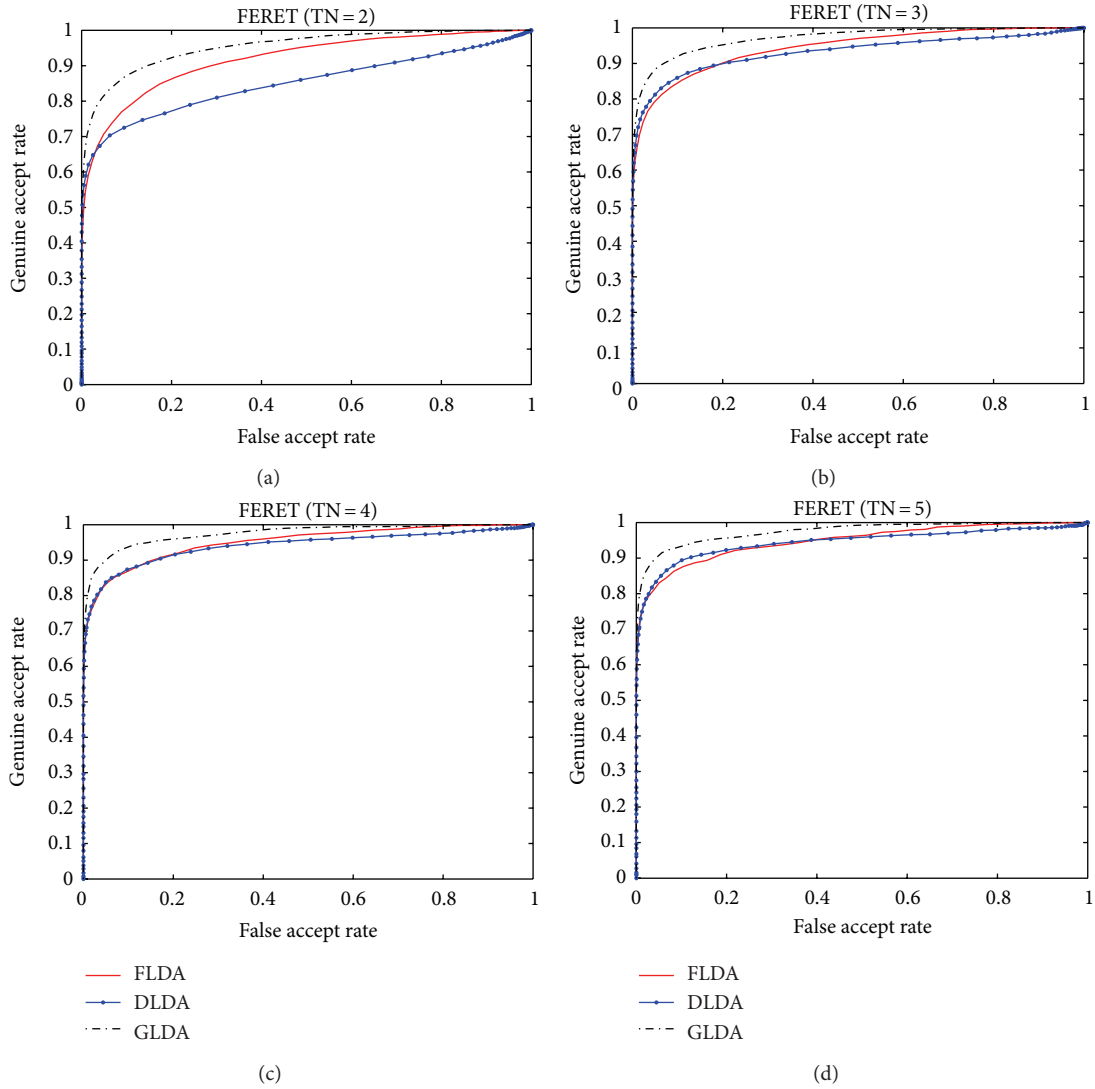

Figure 7: ROC curve comparisons on the FERET database.

where

$$\widetilde{\Phi}_w = \left[\left(x_1^{(1)} - \mu_1\right) \cdot w_1^{(1)} \mid \cdots \mid \left(x_{N_C}^{(C)} - \mu_C\right) \cdot w_{N_C}^{(C)}\right] \in R^{d \times N},$$
$$w_j^{(i)} = \frac{1}{\sqrt{N}} \cdot K_{\alpha_w/2}\left(x_j^{(i)} - \mu_i\right),$$
$$\widetilde{S}_b = \widetilde{\Phi}_b \widetilde{\Phi}_b^T \in R^{d \times d}, \tag{13}$$

where

$$\widetilde{\Phi}_b = \left[(\mu_1 - \mu) \cdot \tau_1 \mid (\mu_2 - \mu) \cdot \tau_2 \mid \cdots \mid (\mu_C - \mu) \cdot \tau_C\right] \in R^{d \times C},$$
$$\tau_i = \sqrt{\frac{N_i}{N} \cdot \left[1 - K_{\alpha_b}\left(\mu_i - \mu\right)\right]}. \tag{14}$$

Since the total scatter matrix $\widetilde{S}_t = \widetilde{S}_w + \widetilde{S}_b$, if we define $\widetilde{\Phi}_t = [\widetilde{\Phi}_w, \widetilde{\Phi}_b] \in R^{d \times (N+C)}$, then $\widetilde{S}_t$ can be written as

$$\widetilde{S}_t = \widetilde{\Phi}_t \widetilde{\Phi}_t^T \in R^{d \times d}. \tag{15}$$

To solve the problem of eigensystem (11) and compare the proposed GLDA with FLDA algorithm under the same conditions, this paper will also use PCA for dimensionality reduction and guarantee that the geometric information based within scatter matrix $\widetilde{S}_w$ is nonsingular. This means that GLDA can be carried out in the PCA-transformed low dimensional feature space. Thereby, our GLDA algorithm is designed as follows.

Step 1. Performing singular value decomposition on $\widetilde{\Phi}_t^T \widetilde{\Phi}_t \in R^{(N+C) \times (N+C)}$, we have $\widetilde{\Phi}_t^T \widetilde{\Phi}_t \overset{\text{svd}}{=} U \Lambda U^T$, where U is an orthonormal matrix, $\Lambda = \text{diag}\{\lambda_1, \lambda_2, \ldots, \lambda_\tau, 0, \ldots, 0\}$ with $\lambda_1 \geq \lambda_2 \geq \cdots \geq \lambda_\tau > 0$. Denote $\Lambda_t = \text{diag}\{\lambda_1, \lambda_2, \ldots, \lambda_\tau\}$, $U_t = U(:, 1 : \tau) \in R^{(N+C) \times \tau}$, and then let $W_t = \widetilde{\Phi}_t U_t \Lambda_t^{-1/2} \in R^{d \times \tau}$.

Step 2. Perform singular value decomposition

$$W_t^T \widetilde{\Phi}_w \overset{\text{svd}}{=} U_w \begin{pmatrix} \Sigma_w & 0 \\ 0 & 0 \end{pmatrix} V_w^T \in R^{\tau \times N}, \tag{16}$$

where $U_w \in R^{\tau \times \tau}$ and $V_w \in R^{N \times N}$ are orthonormal matrices, $\Sigma_w = \text{diag}\{\sigma_1, \ldots, \sigma_r\}$ with $\sigma_1 \geq \cdots \geq \sigma_r > 0$ and $r \leq \tau$.

Step 3. If $r = \tau$, then let $Y = \Sigma_w^{-1} U_w^T W_t^T \in R^{\tau \times d}$, and $\widehat{S}_b = Y \widetilde{S}_b Y^T \in R^{\tau \times \tau}$, and go to Step 4. Otherwise, update W_t according to the rule $W_t = W_t(:, 1 : \tau - 1)$, let $\tau = \tau - 1$, and go to Step 2.

Step 4. Perform an eigenvalue decomposition $\widehat{S}_b = U_b \Lambda_b U_b^T$, where Λ_b is a diagonal eigenvalue matrix of $\widehat{S}_b$ with its diagonal elements in a decreasing order and U_b is an orthonormal eigenvector matrix. Let $W_b = U_w \Lambda_w^{-1} U_b$.

Step 5. The final GLDA optimal projection matrix is

$$W_{\mathrm{GLDA}} = W_t W_b. \tag{17}$$

4. Experimental Results

This section will evaluate the performance of the proposed GLDA method for face recognition. Two LDA-based algorithms, namely FLDA [3] and DLDA [6] algorithms, are chosen for comparisons under the same experimental conditions. In the following experiments, the values of fractional order parameters are given as $\alpha_w = 0.25$ and $\alpha_b = 0.0125$. They are manually determined using full search method.

4.1. Human Face Image Databases. Two popular and publicly available databases, namely, ORL database and FERET database, are selected for the evaluation. In ORL database, there are 40 persons and each person consists of 10 images with different facial expressions, small variations in scales, and orientations. The resolution of each image is 112×92 and with 256 gray levels per pixel. Image variations of one person in the database are shown in Figure 1. For FERET database, we select 120 people, 6 images for each individual. The six images are extracted from 4 different sets, namely, Fa, Fb, Fc, and duplicate. Fa and Fb are sets of images taken with the same camera at the same day but with different facial expressions. Fc is a set of images taken with different cameras at the same day. Duplicate is a set of images taken around 6–12 months after the day the Fa and Fb photos were taken. Details of the characteristics of each set can be found in [26]. All images are aligned by the centers of eyes and mouth and then normalized with resolution 112×92. This resolution is the same as that in ORL database. Images from two individuals are shown in Figure 2. For all facial images, the following preprocessing steps are preformed.

(i) All images are aligned with the centers of eyes and mouth. The orientation of face is adjusted (on-the-plane rotation) such that the line joining the centers of eyes is parallel with x-axis.

(ii) The dimension of the images is reduced by one-fourth using Daubechies' D4 wavelet filter. The resolution for all images in the following experiments is 30×25.

(iii) For each facial image sample $x \in R^d$, it is normalized using the following formula:

$$x^* = (x - \mathrm{mean}(x)) / \mathrm{std}(x). \tag{18}$$

In the recognition stage, the nearest neighbor approach is employed for face classification, which is base on Euclidian distance measurement between the testing image and the class center.

4.2. Comparisons on ORL Database. The experimental setting on ORL database is as follows. We randomly selected n ($n = 2, 3, \ldots, 9$) images from each individual for training and the rest ($10 - n$) of the images are for testing. In order to have a fair comparison, all methods use the same training and testing facial images. Moreover, the experiments are repeated 10 times, and the average accuracies are then calculated to avoid the statistical variations. The average accuracies are recorded and tabulated in Table 1 and plotted in Figure 3. TN in Table 1 means the numbers of training samples. It can be seen that the recognition accuracy of each approach ascends when the number of training images increases. The recognition accuracy of GLDA method increases from 79.98% with 2 training images to 99.00% with 9 training images. However, for FLDA and DLDA methods, their accuracies increase from 66.13% and 78.69% with 2 training images to 97.75% and 96.25% with 9 training images, respectively. Experimental results show that our GLDA method gives the best performance on ORL database.

We would also like to see the detailed performance of every method, which is graphically illustrated using the cumulative match characteristic (CMC) curve and the receiver operating characteristic (ROC) curve. The CMC curve shows the recognition accuracy against the rank, and the ROC curve displays the false acceptance rate (FAR) versus the genuine acceptance rate (GAR). High accuracy or high GAR with low FAR means good performance.

For each number of training images, the CMC curves and the ROC curves are plotted in Figure 4 ((TN = 2)–(TN = 9)) and Figure 5 ((TN = 2)–(TN = 9)), respectively. It can be seen that our method gives the best performance for all cases.

4.3. Comparisons on FERET Database. The experimental setting for the FERET database is similar with that of ORL database. As the number of images for each person is 6, the number of training images ranges from 2 to 5. The experiments are repeated 10 times and the average accuracy is then calculated. The average accuracy is recorded and tabulated in Table 2 and plotted in Figure 3, respectively. When 2 training images is used for testing, the recognition rate of our method is 72.94%, while those of FLDA and DLDA methods are 62.85% and 70.25%, respectively. The performance for each method is also improved when the number of training images increases. When the number of training images is equal to 5, the accuracy for GLDA method is increased to 89.83% while those for FLDA method and DLDA method are 89.42% and 85.58%, respectively. It can be seen that the proposed method outperforms FLDA method and DLDA method on FERET database as well.

Like the ORL database, the detailed performance of each approach is shown using CMC and ROC curves. They are plotted in Figure 6 and Figure 7, respectively, with the number of training images ranging from 2 to 5.

Figures 6 and 7 demonstrate that our GLDA method has superior performance on the FERET database.

5. Conclusions

In order to enhance the discriminant power of the traditional LDA-based FR algorithms, this paper proposed to integrate the geometric distribution weight information of the training samples into Fisher criterion and developed a novel geometric distribution weight information based LDA (GLDA) face recognition approach. The geometric distribution weight information is learnt using radial basis function with fractional order. The proposed GLDA method is tested using two face databases, namely, ORL and FERET face databases. Compared with FLDA method, experimental results demonstrate that our GLDA method has the best performance.

Acknowledgments

This paper is partially supported by the NSFC (61272252) and the Science & Technology Planning Project of Shenzhen City (JC201105130447A, JCYJ20130326111024546). The authors would like to thank the Olivetti Research Laboratory and the Amy Research Laboratory for providing the face image databases.

References

[1] R. Brunelli and T. Poggio, "Face recognition: features versus templates," *IEEE Transactions on Pattern Analysis and Machine Intelligence*, vol. 15, no. 10, pp. 1042–1052, 1993.

[2] M. A. Turk and A. P. Pentland, "Face recognition using eigenfaces," in *Proceedings of the IEEE Computer Society Conference on Computer Vision and Pattern Recognition*, pp. 586–591, June 1991.

[3] P. N. Belhumeur, J. P. Hespanha, and D. J. Kriegman, "Eigenfaces vs. fisherfaces: recognition using class specific linear projection," *IEEE Transactions on Pattern Analysis and Machine Intelligence*, vol. 19, no. 7, pp. 711–720, 1997.

[4] A. M. Martinez and A. C. Kak, "PCA versus LDA," *IEEE Transactions on Pattern Analysis and Machine Intelligence*, vol. 23, no. 2, pp. 228–233, 2001.

[5] L.-F. Chen, H.-Y. M. Liao, M.-T. Ko, J.-C. Lin, and G.-J. Yu, "New LDA-based face recognition system which can solve the small sample size problem," *Pattern Recognition*, vol. 33, no. 10, pp. 1713–1726, 2000.

[6] H. Yu and J. Yang, "A direct LDA algorithm for high-dimensional data-with application to face recognition," *Pattern Recognition*, vol. 34, no. 10, pp. 2067–2070, 2001.

[7] W.-S. Chen, P. C. Yuen, and J. Huang, "A new regularized linear discriminant analysis method to solve small sample size problems," *International Journal of Pattern Recognition and Artificial Intelligence*, vol. 19, no. 7, pp. 917–935, 2005.

[8] P. Howland, J. Wang, and H. Park, "Solving the small sample size problem in face recognition using generalized discriminant analysis," *Pattern Recognition*, vol. 39, no. 2, pp. 277–287, 2006.

[9] W. S. Chen, P. C. Yuen, J. Huang, and B. Fang, "Two-step single parameter regularization fisher discriminant method for face recognition," *International Journal of Pattern Recognition and Artificial Intelligence*, vol. 20, no. 2, pp. 189–208, 2006.

[10] J. D. Tebbens and P. Schlesinger, "Improving implementation of linear discriminant analysis for the high dimension/small sample size problem," *Computational Statistics & Data Analysis*, vol. 52, no. 1, pp. 423–437, 2007.

[11] K. Das and Z. Nenadic, "An efficient discriminant-based solution for small sample size problem," *Pattern Recognition*, vol. 42, no. 5, pp. 857–866, 2009.

[12] H. Hu, P. Zhang, and F. De la Torre, "Face recognition using enhanced linear discriminant analysis," *IET Computer Vision*, vol. 4, no. 3, pp. 195–208, 2010.

[13] D. Chu and G. S. Thye, "A new and fast implementation for null space based linear discriminant analysis," *Pattern Recognition*, vol. 43, no. 4, pp. 1373–1379, 2010.

[14] W.-S. Chen, P. C. Yuen, and X. Xie, "Kernel machine-based rank-lifting regularized discriminant analysis method for face recognition," *Neurocomputing*, vol. 74, no. 17, pp. 2953–2960, 2011.

[15] A. Sharma and K. K. Paliwal, "A two-stage linear discriminant analysis for face-recognition," *Pattern Recognition Letters*, vol. 33, no. 9, pp. 1157–1162, 2012.

[16] F. Dornaika and A. Bosaghzadeh, "Exponential local discriminant embedding and its application to face recognition," *IEEE Transactions on Cybernetics*, vol. 43, no. 3, pp. 921–934, 2013.

[17] K. Fukunaga, *Introduction to Statistical Pattern Recognition*, Computer Science and Scientific Computing, Academic Press, Boston, Mass, USA, 2nd edition, 1990.

[18] C. Liu, "Gabor-based kernel PCA with fractional power polynomial models for face recognition," *IEEE Transactions on Pattern Analysis and Machine Intelligence*, vol. 26, no. 5, pp. 572–581, 2004.

[19] C. Cattani and A. Ciancio, "Separable transition density in the hybrid model for tumor-immune system competition," *Computational and Mathematical Methods in Medicine*, vol. 2012, Article ID 610124, 6 pages, 2012.

[20] C. Cattani, A. Ciancio, and B. Lods, "On a mathematical model of immune competition," *Applied Mathematics Letters*, vol. 19, no. 7, pp. 678–683, 2006.

[21] M. Li and W. Zhao, "Representation of a stochastic traffic bound," *IEEE Transactions on Parallel and Distributed Systems*, vol. 21, no. 9, pp. 1368–1372, 2010.

[22] M. Li, "Approximating ideal filters by systems of fractional order," *Computational and Mathematical Methods in Medicine*, vol. 2012, Article ID 365054, 6 pages, 2012.

[23] M. Li, W. Zhao, and C. Cattani, "Delay bound: fractal traffic passes through servers," *Mathematical Problems in Engineering*. In press.

[24] S. X. Hu, Z. W. Liao, and W. F. Chen, "Sinogram restoration for low-dosed X-ray computed tomography using fractional-order perona-Malik Diffusion," *Mathematical Problems in Engineering*, vol. 2012, Article ID 391050, 13 pages, 2012.

[25] S. X. Hu, "External fractional-order gradient vector Perona-Malik Diffusion for sinogram restoration of low-dosed X-ray computed tomography," *Advances in Mathematical Physics*, vol. 2013, Article ID 516919, 14 pages, 2013.

[26] P. J. Phillips, H. Moon, S. A. Rizvi, and P. J. Rauss, "The FERET evaluation methodology for face-recognition algorithms," *IEEE Transactions on Pattern Analysis and Machine Intelligence*, vol. 22, no. 10, pp. 1090–1104, 2000.

Hindawi Publishing Corporation
Advances in Mathematical Physics
Volume 2013, Article ID 482083, 12 pages
http://dx.doi.org/10.1155/2013/482083

Research Article

Chebyshev Wavelets Method for Solution of Nonlinear Fractional Integrodifferential Equations in a Large Interval

M. H. Heydari,[1] M. R. Hooshmandasl,[1] F. M. Maalek Ghaini,[1] and Ming Li[2]

[1] *Faculty of Mathematics, Yazd University, Yazd 89195741, Iran*
[2] *School of Information Science & Technology, East China Normal University, Shanghai 200241, China*

Correspondence should be addressed to M. R. Hooshmandasl; hooshmandasl@yazd.ac.ir

Received 27 August 2013; Accepted 19 September 2013

Academic Editor: Carlo Cattani

An efficient Chebyshev wavelets method for solving a class of nonlinear fractional integrodifferential equations in a large interval is developed, and a new technique for computing nonlinear terms in such equations is proposed. Existence of a unique solution for such equations is proved. Convergence and error analysis of the proposed method are investigated. Moreover in order to show efficiency of the proposed method, the new approach is compared with some numerical methods.

1. Introduction

Fractional integrodifferential equations (FIDEs) arise in modelling processes in applied sciences such as physics, engineering, and biology. The nonlinear fractional integro-differential equation (NFIDE) of the type

$$D_*^\alpha y(x) = g(x, y(x)) + \lambda \int_0^x K(x, t, y(t))\, dt, \quad 0 < \alpha \le 1, \quad x \in [0, b], \quad y(0) = c, \tag{1}$$

where D_*^α is Caputo fractional derivative, α is a parameter describing the order of the fractional derivative, λ, c, and b are fixed constants, and g is a nonlinear continuous function, arise in the mathematical modelling of various physical phenomena, such as heat conduction in materials with memory. Moreover, these equations are encountered in combined conduction, convection, and radiation problems [1–3]. Therefore in recent years, numerous works have been focusing on the solution of these problems. Some of these methods are Adomian decomposition method (ADM) [4], fractional differential transform method (FDTM) [5], and the collocation method [6]. Most of these methods have been utilized in linear problems, and a few number of works have considered nonlinear problems. In [7] Rawashdeh applied Legendre wavelet method for solving fractional Voltera integro-differential equations in the form

$$D_*^\alpha y(x) = f(x) + p(x)\, y(x) + \lambda \int_0^x K(x, t)\, y(t)\, dt, \quad 0 < \alpha \le 1, \quad x \in [0, 1]. \tag{2}$$

Also in [8] Awawdeh et al. applied homotopy analysis method (HAM) for solution of (2). Mittal and Nigam [9] applied the ADM for (1) in the form

$$D_*^\alpha y(x) = f(x) + p(x)\, y(x) + \lambda \int_0^x K(x, t) [y(t)]^n dt, \quad 0 < \alpha \le 1, \quad x \in [0, 1], \quad n \ge 1. \tag{3}$$

In view of successful application of wavelets in approximation theory [10–17], we will use the Chebyshev wavelets for solving a generalized form of the previous described equations of the form

$$D_*^\alpha y(x) = f(x) + p(x) F(y(x)) + \lambda \int_0^x K(x, t) G(y(t))\, dt, \quad 0 < \alpha \le 1, \quad x \in [0, b], \quad b > 1, \tag{4}$$

with high nonlinearity in a large interval under the initial condition $y(0) = c$.

Here, for simplicity, we assume that f and p are continuous functions on $[0, b]$, $K(x, t)$ is continuous on $0 \le t \le x \le b$, and also F and G are analytic functions.

The method is based on reducing the equation to a system of nonlinear algebraic equations by expanding the solution as Chebyshev wavelet bases with unknown coefficients. We note that, for $\alpha = 1$, (4) is an ordinary integro-differential equation and the method can be easily applied to it. Also the method is fast and mathematically simple and guarantees the necessary accuracy for a small number of basic functions. Moreover in order to show the efficiency of the proposed method the new approach is compared with the ADM, VIM [18–21] and ITM which has been proposed by Daftardar-Gejji and Jafari in 2006 [22, 23].

The outline of this paper is as follows: in Section 2, some basic definitions of the fractional calculus, Chebyshev wavelets, functional approximation, and operational matrix of fractional integration are described. In Section 3 the existence of a unique solution for the problem is established. In Section 4, Chebyshev wavelets method and error investigation are described. In Section 5, some numerical examples are solved by applying the methods of this article. Finally a conclusion is drawn in Section 6.

2. Basic Definitions

2.1. Fractional Calculus. Here, we give some basic definitions and properties of the fractional calculus theory which will be used further in this paper.

Definition 1. A real function $f(t)$, $t > 0$, is said to be in the space C_μ, $\mu \in \mathbb{R}$, if there exists a real number $p\ (> \mu)$ such that $f(t) = t^p f_1(t)$, where $f_1(t) \in C[0, \infty]$ and it is said to be in the space C_μ^n if $f^{(n)} \in C_\mu$, $n \in \mathbb{N}$.

Definition 2. The Riemann-Liouville fractional integration operator of order $\alpha \ge 0$ of a function $f \in C_\mu$, $\mu \ge -1$, is defined as

$$\left(I^\alpha f\right)(t) = \begin{cases} \dfrac{1}{\Gamma(\alpha)} \displaystyle\int_0^t (t-\tau)^{\alpha-1} f(\tau)\, d\tau, & \alpha > 0, \\ f(t), & \alpha = 0. \end{cases} \tag{5}$$

It has the following properties:

$$\begin{aligned} &\text{(i)}\ \ I^\alpha I^\beta = I^{\alpha+\beta}, \\ &\text{(ii)}\ \ I^\alpha I^\beta = I^\beta I^\alpha, \\ &\text{(iii)}\ \ \left(I^\alpha I^\beta f\right)(t) = \left(I^\beta I^\alpha f\right)(t), \\ &\text{(iv)}\ \ I^\alpha t^\vartheta = \frac{\Gamma(\vartheta+1)}{\Gamma(\alpha+\vartheta+1)} t^{\alpha+\vartheta}, \end{aligned} \tag{6}$$

where $\alpha, \beta \ge 0$, $t > 0$, and $\vartheta > -1$.

Riemann-Liouville fractional derivative operator of order $\alpha > 0$ is defined as

$$D^\alpha f(t) = \left(\frac{d}{dt}\right)^n I^{n-\alpha} f(t), \quad (n-1 < \alpha \le n), \tag{7}$$

where n is an integer and $f \in C_1^n$.

The Riemann-Liouville derivatives have certain disadvantages when trying to model real-world phenomena with fractional differential equations. Therefore, we will now introduce a modified fractional differential operator D_*^α proposed by Caputo [24].

Definition 3. The fractional derivative operator of order $\alpha > 0$ in the Caputo sense is defined as

$$D_*^\alpha f(t) = \frac{1}{\Gamma(n-\alpha)} \int_0^t (t-\tau)^{n-\alpha-1} f^{(n)}(\tau)\, d\tau, \quad (n-1 < \alpha \le n), \tag{8}$$

where n is an integer, $t > 0$, and $f \in C_1^n$.

The Riemann-Liouville and Caputo operators have a useful property as

$$I^\alpha D_*^\alpha f(t) = f(t) - \sum_{k=0}^{n-1} f^{(k)}\left(0^+\right) \frac{t^k}{k!}, \quad (n-1 < \alpha \le n), \tag{9}$$

where n is an integer, $t > 0$, and $f \in C_1^n$.

For more details on the mathematical properties of fractional derivatives and integrals see [24].

2.2. Chebyshev Wavelets. Chebyshev wavelets $\psi_{pq}(t) = \psi(k, \widehat{p}, q, t)$ have four arguments; $k \in \mathbb{N}$, $p = 1, 2, \ldots, 2^{k-1}$, and $\widehat{p} = 2p - 1$; moreover q is the degree of the Chebyshev polynomial of the first kind and t is the normalized time, that is, $t \in [0, 1]$. They are defined on the interval $[0, 1]$ as [25]

$$\psi_{pq}(t) = \begin{cases} 2^{k/2} \widetilde{T}_q\left(2^k t - \widehat{p}\right), & \dfrac{\widehat{p}-1}{2^k} \le t \le \dfrac{\widehat{p}+1}{2^k}, \\ 0, & \text{otherwise}, \end{cases} \tag{10}$$

where

$$\widetilde{T}_q(t) = \begin{cases} \dfrac{1}{\sqrt{\pi}}, & q = 0 \\ \sqrt{\dfrac{2}{\pi}} T_q(t), & q > 0 \end{cases}, \tag{11}$$

$q = 0, 1, \ldots, M-1$, and M is a fixed positive integer. The coefficients in (11) are used for orthonormality of the system. Here, $\{T_q(t),\ q \in \mathbb{N} \cup \{0\}\}$ is the set of well-known Chebyshev polynomials of degree m which are orthogonal with respect to the weight function $w(t) = 1/\sqrt{1-t^2}$ on the interval $[-1, 1]$ and satisfy the following recursive formula:

$$\begin{aligned} T_0(t) &= 1, \qquad T_1(t) = t, \\ T_{q+1}(t) &= 2tT_q(t) - T_{q-1}(t), \quad q = 1, 2, 3 \ldots. \end{aligned} \tag{12}$$

We should note that in dealing with Chebyshev polynomials the weight function $\widetilde{w}(t) = w(2t-1)$ has to be dilated and translated as $w_p(t) = w(2^k t - \widehat{p})$, to get orthogonal wavelets.

2.3. Function Approximation. An arbitrary function $f(t) \in L^2(R)$ defined over $[0,1]$ may be expanded into Chebyshev wavelet basis as

$$f(t) = \sum_{p=1}^{\infty} \sum_{q=0}^{\infty} c_{pq} \psi_{pq}(t), \tag{13}$$

where $c_{pq} = (f(t), \psi_{pq}(t))$ in which (,) denotes the inner product.

If the infinite series in (13) is truncated, then (13) can be written as

$$f(t) \simeq \sum_{p=1}^{2^{k-1}M-1} \sum_{q=0} c_{pq} \psi_{pq}(t) = C^T \Psi(t), \tag{14}$$

where C and $\Psi(t)$ are $2^{k-1}M \times 1$ matrices given by

$$\begin{aligned} C &= [c_{10}, c_{11}, \ldots, c_{1M-1}, c_{20}, \ldots, \\ &\quad c_{2M-1}, \ldots, c_{2^{k-1}0}, \ldots, c_{2^{k-1}M-1}]^T, \\ \Psi(t) &= [\psi_{10}(t), \psi_{11}(t), \ldots, \psi_{1M-1}(t), \psi_{20}(t), \ldots, \\ &\quad \psi_{2M-1}(t), \ldots, \psi_{2^{k-1}0}(t), \ldots, \psi_{2^{k-1}M-1}(t)]^T. \end{aligned} \tag{15}$$

Taking the collocation points

$$t_i = \frac{(2i-1)}{2^k M}, \quad i = 1, 2, \ldots, m, \tag{16}$$

where $m = 2^{k-1}M$, we define the wavelet matrix $\Phi_{m\times m}$ as:

$$\Phi_{m\times m} = \left[\Psi\left(\frac{1}{2m}\right), \Psi\left(\frac{3}{2m}\right), \ldots, \Psi\left(\frac{2m-1}{2m}\right)\right]. \tag{17}$$

Indeed $\Phi_{m\times m}$ has a diagonal form (see [15]).

2.4. The Operational Matrix of Fractional Integration. The fractional integration of order α of the vector function $\Psi(t)$ defined in (15) can be expressed as

$$(I^\alpha \Psi)(t) = P^\alpha \Psi(t), \tag{18}$$

where P^α is the $m \times m$ operational matrix of fractional integration of order α. In [25] it is shown that the matrix P^α can be approximated as

$$P^\alpha \simeq P^\alpha_{m\times m} = \Phi_{m\times m} P^\alpha_B \Phi^{-1}_{m\times m}, \tag{19}$$

where P^α_B is the operational matrix of fractional integration of order α of the Block Pulse functions (BPFs) that has the following form [26]:

$$P^\alpha_B = \frac{1}{m^\alpha} \frac{1}{\Gamma(\alpha+2)} \begin{pmatrix} 1 & \xi_1 & \xi_2 & \cdots & \xi_{m-1} \\ 0 & 1 & \xi_1 & \cdots & \xi_{m-2} \\ 0 & 0 & 1 & \cdots & \xi_{m-3} \\ 0 & 0 & 0 & \ddots & \vdots \\ 0 & 0 & 0 & 0 & 1 \end{pmatrix}, \tag{20}$$

where $\xi_i = (i+1)^{\alpha+1} - 2i^{\alpha+1} + (i-1)^{\alpha+1}$.

In Appendix A, some important properties of BPFs are listed. In [15], it is shown that $P^\alpha_{m\times m}$ is an upper trigonometric matrix. Also, from (14) and (19) it is concluded that for a function $f \in C_\mu$, $\mu \geq -1$, we have

$$(I^\alpha f)(t) \simeq C^T \Phi_{m\times m} P^\alpha_B B_m(t). \tag{21}$$

3. Existence and Uniqueness

For investigating existence of a unique solution for initial value problem (4), we reconsider this equation in the following operator form:

$$\mathscr{D}^\alpha_* y(x) = f(x) + p(x) \mathscr{F} y(x) + \mathscr{K}\mathscr{G} y(x), \tag{22}$$

where we define

$$\mathscr{K} y(x) = \lambda \int_0^x K(x,t)\, y(t)\, dt. \tag{23}$$

Applying operator $\mathscr{I}^\alpha$, the inverse of $\mathscr{D}^\alpha_*$, on both sides of (22), and considering initial condition yield

$$y(x) = c + \mathscr{I}^\alpha \left(f(x) + p(x) \mathscr{F} y(x) + \mathscr{K}\mathscr{G} y(x)\right). \tag{24}$$

Equation (24), can be written as a fixed point equation $\mathscr{A} y = y$, where the map $\mathscr{A}$ is defined as

$$\mathscr{A} y(x) = c + \mathscr{I}^\alpha \left(f(x) + p(x) \mathscr{F} y(x) + \mathscr{K}\mathscr{G} y(x)\right), \tag{25}$$

Now let $(C[J], \|\cdot\|_\infty)$ be the Banach space of all continues functions on $J = [0,b]$, $b > 1$, with the norm $\|f\|_\infty = \max_{t\in J} |f(t)|$. Moreover, suppose that the nonlinear terms $\mathscr{F}$ and $\mathscr{G}$ satisfy Lipschitz conditions on $[0,b]$ as

$$\begin{aligned} \left|\mathscr{F}\hat{y}_m(x) - \mathscr{F} y(x)\right| &\leq L_1 \left|\hat{y}_m(x) - y(x)\right|, \\ \left|\mathscr{G}\hat{y}_m(x) - \mathscr{G} y(x)\right| &\leq L_2 \left|\hat{y}_m(x) - y(x)\right|, \end{aligned} \tag{26}$$

where L_1 and L_2 are fixed positive constants. Then we have the following.

Theorem 4. *If $L_1\|p\|_\infty + L_2\|\mathscr{K}\|_\infty < \Gamma(\alpha+1)/b^\alpha$, then the initial value problem* (4) *has a unique solution $y \in C[J]$.*

Proof. There are different approaches in applying the Banach fixed point theorem to prove the existence of a unique solution for (4). We give a sketch of two approaches below. For this purpose we define the nonlinear integral operator

$$\begin{aligned} &\mathscr{A} : C[J] \longrightarrow C[J], \\ &\mathscr{A} y(x) \equiv c + \frac{1}{\Gamma(\alpha)} \\ &\qquad \times \int_0^x (x-t)^{\alpha-1} \left(f(t) + p(t) \mathscr{F} y(t) + \mathscr{K}\mathscr{G} y(t)\right) dt. \end{aligned} \tag{27}$$

□

Approach 1. Let $\widetilde{y}, y \in C[J]$, then we have

$$\begin{aligned}\mathscr{A}\widetilde{y}(x) - \mathscr{A}y(x) = {} & \frac{1}{\Gamma(\alpha)} \\ & \times \int_0^x (x-t)^{\alpha-1} \\ & \times \left(p(t)\left[\mathscr{F}\widetilde{y}(t) - \mathscr{F}y(t)\right]\right. \\ & \left. + \mathscr{K}\left[\mathscr{G}\widetilde{y}(t) - \mathscr{G}y(t)\right]\right) dt.\end{aligned} \tag{28}$$

Then for $x > 0$ we have

$$\begin{aligned}&\left|\mathscr{A}\widetilde{y}(x) - \mathscr{A}y(x)\right| \\ &\quad \le \frac{1}{\Gamma(\alpha)} \\ &\qquad \times \int_0^x (x-t)^{\alpha-1} \left(L_1 \left|p(t)\right| \left|\widetilde{y}(t) - y(t)\right|\right. \\ &\qquad\qquad \left. + L_2 \left|\mathscr{K}\right| \left|\widetilde{y}(t) - y(t)\right|\right) dt, \\ &\left|\mathscr{A}\widetilde{y}(x) - \mathscr{A}y(x)\right| \\ &\quad \le \left(L_1 \left\|p\right\|_\infty + L_2 \left\|\mathscr{K}\right\|_\infty\right) \\ &\qquad \times \left\|\widetilde{y} - y\right\|_\infty \frac{1}{\Gamma(\alpha)} \\ &\qquad \times \int_0^x (x-t)^{\alpha-1} dt \\ &\quad \le \left(L_1 \left\|p\right\|_\infty + L_2 \left\|\mathscr{K}\right\|_\infty\right) \\ &\qquad \times \left\|\widetilde{y} - y\right\|_\infty \frac{b^\alpha}{\Gamma(\alpha+1)}.\end{aligned} \tag{29}$$

Therefore,

$$\left\|\mathscr{A}\widetilde{y} - \mathscr{A}y\right\|_\infty \le \Omega_{L_1,L_2,p,\mathscr{K},\alpha} \left\|\widetilde{y} - y\right\|_\infty, \tag{30}$$

where $\Omega_{L_1,L_2,p,\mathscr{K},\alpha} = \left(L_1 \left\|p\right\|_\infty + L_2 \left\|\mathscr{K}\right\|_\infty\right) \left(b^\alpha/\Gamma(\alpha+1)\right)$.

Since $\Omega_{L_1,L_2,p,\mathscr{K},\alpha} < 1$, by contraction mapping theorem, the initial value problem (4) has a unique solution in $C[J]$.

Approach 2. Let us introduce the norm

$$\left\|\left|f(t)\right|\right\| = \max_{t\in J} e^{-\beta t} \left|f(t)\right|, \tag{31}$$

on the space $C[J]$, which is equivalent to the standard norm $\left\|f\right\|_\infty$ on $C[J]$. The parameter β is chosen to satisfy $\beta^\alpha > \Gamma(\alpha+1)/b^\alpha$. Then for $x > 0$ we have

$$\begin{aligned}& e^{-\beta x} \left|\mathscr{A}\widetilde{y}(x) - \mathscr{A}y(x)\right| \\ &\quad \le \frac{e^{-\beta x}}{\gamma(\alpha)} \int_0^x (x-t)^{\alpha-1} e^{\beta t} e^{-\beta t} \\ &\qquad \times \left(\left|p(t)\right| \left|\mathscr{F}\widetilde{y} - \mathscr{F}y\right| + \left|\mathscr{K}\right| \left|\mathscr{G}\widetilde{y} - \mathscr{G}y\right|\right) dt \\ &\quad \le \left(L_1 \left\|\left|p\right|\right\| + L_2 \left\|\left|\mathscr{K}\right|\right\|\right) \left\|\left|\widetilde{y} - y\right|\right\| \\ &\qquad \times \frac{e^{-\beta x}}{\Gamma(\alpha)} \int_0^x (x-t)^{\alpha-1} e^{\beta t} dt \\ &\quad = \left(L_1 \left\|\left|p\right|\right\| + L_2 \left\|\left|\mathscr{K}\right|\right\|\right) \left\|\left|\widetilde{y} - y\right|\right\| \\ &\qquad \times \frac{e^{-\beta x} e^{\beta x}}{\Gamma(\alpha)} \int_0^x t^{\alpha-1} e^{-\beta t} dt \\ &\quad = \left(L_1 \left\|\left|p\right|\right\| + L_2 \left\|\left|\mathscr{K}\right|\right\|\right) \left\|\left|\widetilde{y} - y\right|\right\| \\ &\qquad \times \frac{1}{\Gamma(\alpha)} \frac{1}{\beta^\alpha} \int_0^{\beta x} t^{\alpha-1} e^{-t} dt \\ &\quad \le \left(L_1 \left\|\left|p\right|\right\| + L_2 \left\|\left|\mathscr{K}\right|\right\|\right) \left\|\left|\widetilde{y} - y\right|\right\| \\ &\qquad \times \frac{1}{\Gamma(\alpha)} \frac{1}{\beta^\alpha} \int_0^{\infty} t^{\alpha-1} e^{-t} dt \\ &\quad = \left(L_1 \left\|\left|p\right|\right\| + L_2 \left\|\left|\mathscr{K}\right|\right\|\right) \left\|\left|\widetilde{y} - y\right|\right\| \frac{1}{\beta^\alpha}.\end{aligned} \tag{32}$$

Then,

$$\left\|\left|\mathscr{A}\widetilde{y} - \mathscr{A}y\right|\right\| \le \Omega_{L_1,L_2,p,\mathscr{K},\alpha} \left\|\left|\widetilde{y} - y\right|\right\|, \tag{33}$$

where $\Omega_{L_1,L_2,p,\mathscr{K},\alpha} = \left(L_1 \left\|\left|p\right|\right\| + L_2 \left\|\left|\mathscr{K}\right|\right\|\right)\left(b^\alpha/\Gamma(\alpha+1)\right)$.

Therefore, the operator $\mathscr{A}$ is a contraction on the Banach space $(C[J], \left\|\left|\cdot\right|\right\|)$, and so the initial value problem (4) has a unique solution in $C[J]$.

4. Chebyshev Wavelets Method

Here, the Chebyshev wavelets expansion together with their operational matrices of fractional order integration are used for numerical solution of nonlinear NFIDE (4). For solving this problem we assume that

$$D_*^\alpha y(x) = K_m^T \Psi_m(x), \tag{34}$$

where K_m^T is an unknown vector and $\Psi_m(x)$ is the expansion of (15) by BPFs, that is, $\Psi_m = \Phi_{m\times m} B_m(x)$, and $B_m(x)$ is defined in Appendix A. By using initial conditions and (9), we have

$$y(x) = K_m^T P_{m\times m}^\alpha \Psi_m(x) + c. \tag{35}$$

From (35) we have

$$y(x) = \left[K_m^T P_{m\times m}^\alpha \Phi_{m\times m} + [c, c, \ldots, c]\right] B_m(x). \tag{36}$$

This equation can also be written as

$$y(x) = \left[K_m^T P_{m\times m}^{\alpha} \Phi_{m\times m} + [c, c, \ldots, c]\right] \times B_m(x) = [a_1, a_2, \ldots, a_m] B_m(x), \tag{37}$$

and from Appendix B, we have

$$F(y(x)) = [F(a_1), F(a_2), \ldots, F(a_m)] B_m(x),$$
$$\int_0^x K(x,t) G(y(t))\, dt = [G(a_1), G(a_2), \ldots, G(a_m)] \times \int_0^x K(x,t) B_m(t)\, dt, \tag{38}$$

where

$$\int_0^x K(x,t) B_m(t)\, dt = \left[\int_0^x K(x,t) b_0(t)\, dt, \int_0^x K(x,t) b_1(t)\, dt, \ldots, \int_0^x K(x,t) b_{m-1}(t)\, dt\right]^T. \tag{39}$$

By substituting (34) and (38) into (4), we obtain

$$K_m^T \Phi_{m\times m} B_m(x) = f(x) + p(x)[F(a_1), F(a_2), \ldots, F(a_m)] B_m(x) + [G(a_1), \ldots, G(a_m)] \int_0^x K(x,t) B_m(t)\, dt. \tag{40}$$

Now, from (37) and (40) we have

$$[a_1 - c, a_2 - c, \ldots, a_m - c] (P_B^{\alpha})^{-1} B_m(x) = f(x) + p(x)[F(a_1), F(a_2), \ldots, F(a_m)] B_m(x) + [G(a_1), \ldots, G(a_m)] \int_0^x K(x,t) B_m(t)\, dt. \tag{41}$$

This is a nonlinear algebraic equation. Now, by taking collocation points, expressed in (16), this equation is transformed into a nonlinear system of algebraic equations with m unknowns a_i $(i = 1, 2, \ldots, m)$. By solving this system and determining a_i, we get the numerical solution of problem (4).

4.1. Error Investigation of the Chebyshev Wavelets Method. In this section we investigate error of the Chebyshev wavelets method. The representation error can be obtained when a function $f(t)$ is presented on interval $[0, 1]$.

Theorem 5 (see [27]). *A function $f(t)$ defined on $[0, 1)$ with bounded second derivative, say $|f''(t)| \le \widehat{M}$, can be expanded as an infinite sum of Chebyshev wavelets, and the series converges uniformly to $f(t)$, that is*

$$f(t) = \sum_{p=1}^{\infty} \sum_{q=0}^{\infty} c_{pq} \psi_{pq}(t), \tag{42}$$

where c_{pq}'s are defined in (13).

Theorem 6 (see [27]). *Let $f(t)$ be a continuous function defined on $[0, 1)$, with bounded second derivative $|f''(t)| \le \widehat{M}$, and let $\sum_{p=1}^{2^{k-1}} \sum_{q=0}^{M-1} c_{pq}\psi_{pq}(t)$ be the approximate solution using Chebyshev wavelets method, respectively. Then for the error bound one has:*

$$\sigma_{k,M} < \frac{\sqrt{\pi}\widehat{M}}{8} \left(\sum_{p=2^{k-1}+1}^{\infty} \frac{1}{p^5} \sum_{q=M}^{\infty} \frac{1}{(q-1)^4} \right)^{1/2}, \tag{43}$$

where

$$\sigma_{k,M} = \left(\int_0^1 \left(f(t) - \sum_{p=1}^{2^{k-1}} \sum_{q=0}^{M-1} c_{pq} \psi_{pq}(t) \right)^2 w_p(t)\, dt \right)^{1/2}. \tag{44}$$

Lemma 7. *Suppose that $f(t)$ is approximated on $[0, 1)$ by*

$$f_m(t) = \sum_{p=1}^{2^{k-1}} \sum_{q=0}^{M-1} c_{pq} \psi_{pq}(t), \tag{45}$$

and moreover suppose that by solving some problems one has found $\widehat{c}_{pq}$ as an approximation of c_{pq} and put:

$$\widehat{f}_m(t) = \sum_{p=1}^{2^{k-1}} \sum_{q=0}^{M-1} \widehat{c}_{pq} \psi_{pq}(t). \tag{46}$$

Then for each $t \in [0, 1)$ one has

$$\left\| \widehat{f}_m(t) - f_m(t) \right\| \le m \left\| \widehat{f}_m(t) - f(t) \right\|_{\infty}. \tag{47}$$

Proof. We have

$$\begin{aligned} \left\| \widehat{f}_m(t) - f_m(t) \right\| &= \left(\int_0^1 \left[\sum_{p=1}^{2^{k-1}} \sum_{q=0}^{M-1} \widehat{c}_{pq} \psi_{pq}(t) - \sum_{p=1}^{2^{k-1}} \sum_{q=0}^{M-1} c_{pq} \psi_{pq}(t) \right]^2 \times w_q(t)\, dt \right)^{1/2} \\ &= \left(\int_0^1 \sum_{p=1}^{2^{k-1}} \sum_{q=0}^{M-1} \left[\widehat{c}_{pq} - c_{pq}\right]^2 \left[\psi_{pq}(t)\right]^2 w_q(t)\, dt \right)^{1/2} \\ &= \sum_{p=1}^{2^{k-1}} \sum_{q=0}^{M-1} \left|\widehat{c}_{pq} - c_{pq}\right| \left(\int_0^1 \left[\psi_{pq}(t)\right]^2 w_q(t)\, dt \right)^{1/2} \\ &= \sum_{p=1}^{2^{k-1}} \sum_{q=0}^{M-1} \left|\widehat{c}_{pq} - c_{pq}\right| \le \sum_{p=1}^{2^{k-1}} \sum_{q=0}^{M-1} \left\| \widehat{f}_m(t) - f(t) \right\|_{\infty} \\ &= m \left\| \widehat{f}_m(t) - f(t) \right\|_{\infty}. \end{aligned} \tag{48}$$

This completes the proof. □

Corollary 8. *Suppose that by solving some problems one obtains $\widehat{f}_m(t)$ as the approximation of $f(t)$. Then one has:*

$$\left\|\widehat{f}_m(t) - f(t)\right\| \le \sigma_{k,M} + m\left\|\widehat{f}_m(t) - f(t)\right\|_\infty. \tag{49}$$

Proof. For every $t \in [0,1)$ we have

$$\begin{aligned}\left\|\widehat{f}_m(t) - f(t)\right\| &= \left\|\widehat{f}_m(t) - f(t) - f_m(t) + f_m(t)\right\| \\ &\le \left\|f_m(t) - f(t)\right\| + \left\|\widehat{f}_m(t) - f_m(t)\right\|.\end{aligned} \tag{50}$$

Now from Theorem 6 and Lemma 7 we have

$$\left\|\widehat{f}_m(t) - f(t)\right\| \le \sigma_{k,M} + m\left\|\widehat{f}_m(t) - f(t)\right\|_\infty. \tag{51}$$

This completes the proof. □

In real problems, we often tend to solve equations with unknown exact solutions. Hence, when we apply our method to these problems, we cannot say that this approximate solution is good or bad unless we are able to calculate the error function $\widehat{e}_m(x) = \widehat{f}_m(x) - f(x)$. Then it is necessary to introduce a process for estimating the error function when the exact solution is unknown [28]. Here, we introduce a method to estimate the error function. Let $\widehat{y}_m(x)$ be an approximate solution of (4). Then from (24), it is concluded that $\widehat{y}_m(x)$ satisfies the following equation:

$$\begin{aligned}\widehat{y}_m(x) &= c + \frac{1}{\Gamma(\alpha)}\int_0^x (x-t)^{\alpha-1} f(t)\,dt \\ &\quad + \frac{1}{\Gamma(\alpha)}\int_0^x (x-t)^{\alpha-1} p(t) F\left(\widehat{y}_m(t)\right) dt \\ &\quad + \frac{\lambda}{\Gamma(\alpha+1)}\int_0^x (x-t)^{\alpha} K(x,t)\, G\left(\widehat{y}_m(t)\right) dt + r_m(x),\end{aligned} \tag{52}$$

where $r_m(x)$ is the perturbation function that depends only on $\widehat{y}_m(x)$ and can be obtained by substituting the computed solution $\widehat{y}_m(x)$ into the equation

$$\begin{aligned}r_m(x) &= \widehat{y}_m(x) - c - \frac{1}{\Gamma(\alpha)}\int_0^x (x-t)^{\alpha-1} f(t)\,dt \\ &\quad - \frac{1}{\Gamma(\alpha)}\int_0^x (x-t)^{\alpha-1} p(t) F\left(\widehat{y}_m(t)\right) dt \\ &\quad - \frac{\lambda}{\Gamma(\alpha+1)}\int_0^x (x-t)^{\alpha-1} K(x,t)\, G\left(\widehat{y}_m(t)\right) dt.\end{aligned} \tag{53}$$

Subtracting (53) from (24), we obtain

$$\begin{aligned}\widehat{e}_m(x) &= \frac{1}{\Gamma(\alpha)}\int_0^x (x-t)^{\alpha-1} p(t)\left[F\left(\widehat{y}_m(t)\right) - F\left(y(t)\right)\right] \\ &\quad + \frac{\lambda}{\Gamma(\alpha+1)}\int_0^x (x-t)^{\alpha} K(x,t) \\ &\qquad \times \left[G\left(\widehat{y}_m(t)\right) - G\left(y(t)\right)\right] dt \\ &\quad + r_m(x),\end{aligned} \tag{54}$$

in which we define $\widehat{e}_m(x) = \widehat{y}_m(x) - y(x)$ as the error function. Since F and G are analytic functions, then we can write

$$\begin{aligned}&F\left(\widehat{y}_m(x)\right) - F\left(y(x)\right) \\ &\quad = F\left(\widehat{y}_m(x)\right) - F\left(\widehat{y}_m(x) - \widehat{e}_m(x)\right) \\ &\quad = F'\left(\widehat{y}_m(x)\right)\widehat{e}_m(x) - \frac{1}{2}F''\left(w_m(x)\right)\left[\widehat{e}_m(x)\right]^2,\end{aligned} \tag{55}$$

and similarly

$$\begin{aligned}G\left(\widehat{y}_m(t)\right) - G\left(y(t)\right) &= G'\left(\widehat{y}_m(t)\right)\widehat{e}_m(t) \\ &\quad - \frac{1}{2}G''\nu_m(t)\left[\widehat{e}_m(t)\right]^2,\end{aligned} \tag{56}$$

where, by Taylor's Theorem, $w_m(t) = \widehat{y}_m(t) - \theta\widehat{e}_m(t)$, $\theta \in (0,1)$, and $\nu_m(t) = \widehat{y}_m(t) - \delta\widehat{e}_m(t)$, $\delta \in (0,1)$. Thus, by substituting (55), and (56) in the error equation (54), we get a nonlinear fractional integral equation in which the error function $\widehat{e}_m(t)$ is unknown. Obviously, we can apply the proposed method for this equation to find an approximation of the error function $\widehat{e}_m(x)$.

5. Numerical Examples

In this section, for the sake of comparison, we have selected some examples that their exact solutions exist, which will ultimately show the simplicity, effectiveness, and exactness of the proposed method. All programs are performed by Maple 15 and digits 20. We consider the following test problems.

Example 1. Let us first consider the following NFIDE:

$$\begin{aligned}D_*^\alpha y(x) &= f(x) + y(x) + \int_0^x xt \arcsin\left(y(t)\right) dt, \\ y(0) &= 0 \quad x \in [0,2],\end{aligned} \tag{57}$$

where

$$f(x) = \cos(x) - \sin(x) - \frac{1}{3}x^4. \tag{58}$$

The exact solution of this problem for $\alpha = 1$ is $y(x) = \sin(x)$. Figure 1 shows the behavior of the numerical solution for $m = 128$ ($M = 4$, $k = 6$). From Figure 1, it is seen that the numerical solution is in a very good agreement with the exact solution for $\alpha = 1$. Therefore, we hold that the solutions

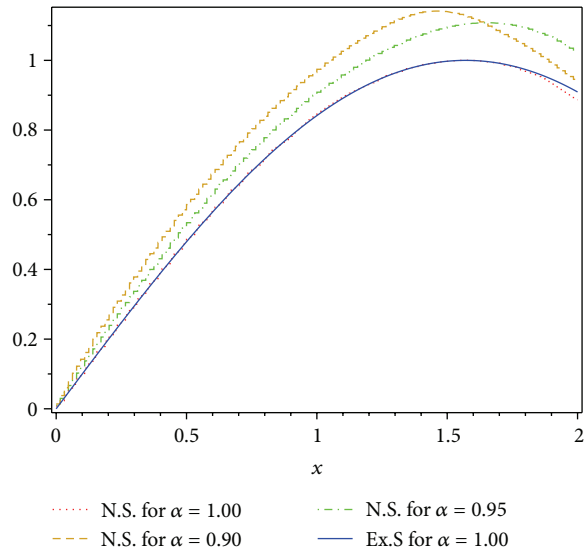

Figure 1: Numerical solution (N.S.) and exact solution (Ex.S).

for $\alpha = 0.90$ and $\alpha = 0.95$ are also credible. Figure 1 also shows that as $\alpha \to 1$, the approximate solution tends to $y(x) = \sin(x)$, which is the exact solution of this equation in the case $\alpha = 1$.

Example 2. Consider the following NFIDE:

$$D_*^{\alpha} y(x) = f(x) + e^{y(x)} + \int_0^x t[y(t)]^2 dt, \quad y(0) = 0, \quad x \in [0,5], \tag{59}$$

where

$$f(x) = \frac{6x^{3-\alpha}}{\Gamma(4-\alpha)} - \frac{15\sqrt{\pi}x^{3/2-\alpha}}{2\Gamma(5/2-\alpha)} - 20x^5 + \frac{40}{13}x^{13/2} - \frac{1}{8}x^8 + e^{x^3-10x^{3/2}}. \tag{60}$$

The exact solution of this problem is $y(x) = x^3 - 10x^{3/2}$.

This NFIDE is now solved by the Chebyshev wavelet method for $\alpha = 0.75$. Numerical solutions of this problem for some values of m are shown in Figure 2. It is obviously seen that computing $y_0(x)$ via the standard ADM and ITM is very difficult because analytic computation of $\int_0^x e^{t^3-10t^{3/2}} dt$ is impossible. Also computing other components $y_i(x)$ $(i \geq 1)$, via the standard ADM, VIM, and ITM, is very difficult in each iteration and also requires a large amount of computational work. We can avoid such integrations by taking the truncated Maclaurin expansion for the exponential term in (59), that is, $e^x = 1 + x + (1/2!)x^2 + \cdots + (1/5!)x^5$. In order to show efficiency of the proposed method, a comparison between the numerical solution given by the proposed method for $m = 128$, $y_4(x)$ of the ADM, ITM, and VIM, and the exact solution is performed in Figure 3. From Figure 3, it can be concluded that the Chebyshev wavelet method for the numerical solution of this problem is very efficient and accurate in comparison with other presented numerical methods.

Example 3. Consider the following NFIDE:

$$D_*^{\alpha} y(x) = f(x) - [y(x)]^2 + x\int_0^x [y(t)]^3 dt, \quad y(0) = 1, \quad x \in [0,4.5], \tag{61}$$

where

$$f(x) = -\frac{2x^{2-\alpha}}{\Gamma(3-\alpha)} + \frac{3x^{1-\alpha}}{\Gamma(2-\alpha)} - \frac{1}{7}x^8 + \frac{3}{2}x^7 - \frac{24}{5}x^6 + \frac{9}{4}x^5 + 9x^4 + 8x^2 + 6x + 1. \tag{62}$$

The exact solution of this problem is $y(x) = 1 + 3x - x^2$.

This problem is now solved by the Chebyshev wavelet method for $\alpha = 0.85$. Numerical solutions of this problem for some values of m are shown in Figure 4. A comparison between the numerical solution given by the proposed method for $m = 128$, $y_4(x)$ of the ADM and ITM and $y_3(x)$ of the VIM and the exact solution is performed in Figure 5. From Figure 5, it can be concluded that the Chebyshev wavelet method for the numerical solution of this problem is very efficient and accurate in comparison with other presented numerical methods. Moreover, the solution has been derived in a large domain. It can be mentioned that computing the components $y_i(x)$ via the ADM, VIM and ITM require a large amount of computational work and memory, such that computing other components for $i > 4$ is very difficult.

Example 4. Finally, consider the following NFIDE:

$$D_*^{\alpha} y(x) = f(x) + \int_0^x e^{-t}[y(t)]^2 dt, \quad y(0) = 0, \quad x \in [0,5], \tag{63}$$

where

$$f(x) = \frac{6x^{3-\alpha}}{\Gamma(4-\alpha)} - \frac{12x^{2-\alpha}}{\Gamma(3-\alpha)} + \frac{8x^{1-\alpha}}{\Gamma(2-\alpha)} + e^{-x} \times \left(80 + 80x + 40x^2 - 8x^3 + 22x^4 - 6x^5 + x^6\right). \tag{64}$$

The exact solution of this problem is $y(x) = x^3 - 6x^2 + 8x$.

This NFIDE is now solved by the proposed method for $\alpha = 0.80$. Numerical solutiones of this problem for some selected values of m are shown in Figure 6. It is clearly seen that computing the components $y_i(x)$ via the standard ADM, VIM, and ITM is very difficult and also requires a large amount of computational work. We can avoid such fractional integrations by taking the truncated Maclaurin expansion

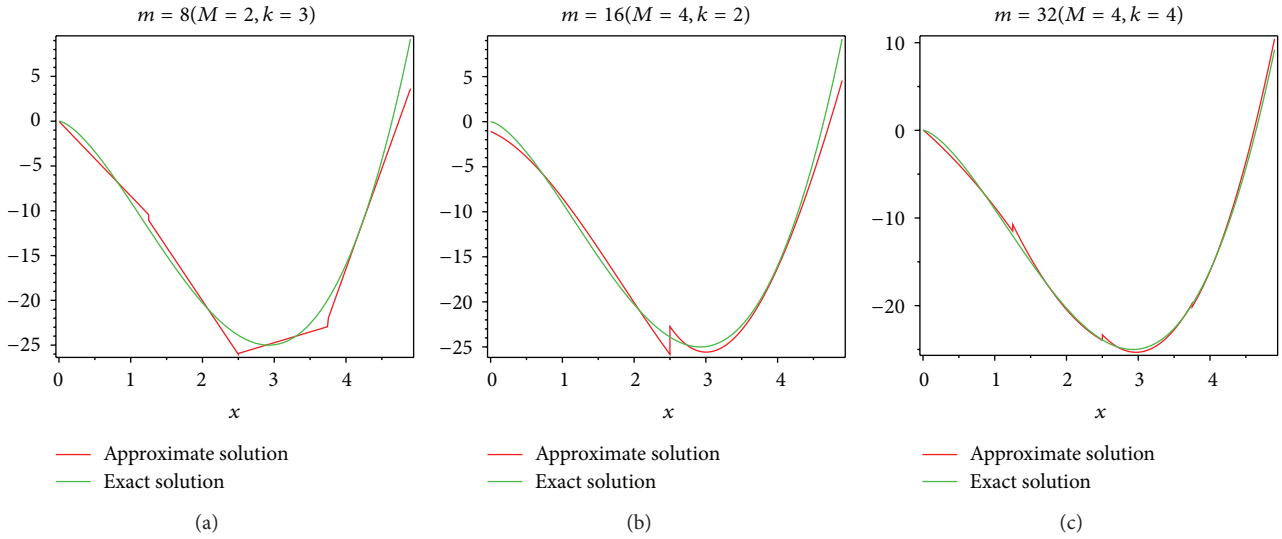

Figure 2: Numerical solutions of Example 1, for some values of m.

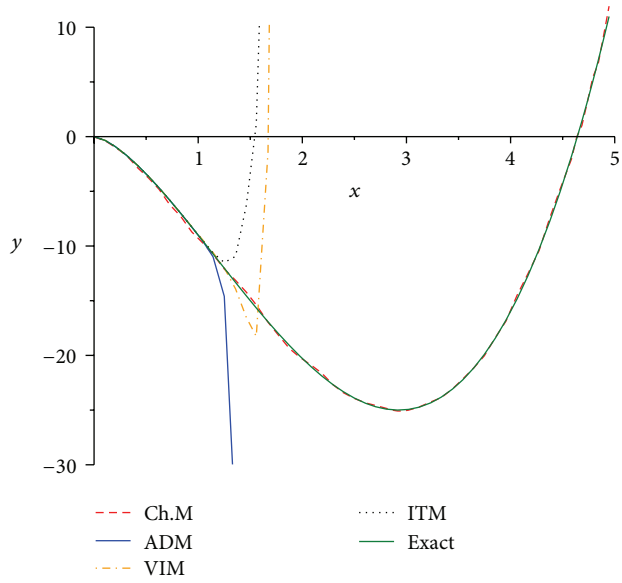

Figure 3: Numerical solutions of Example 1 for $\alpha = 0.75$.

for the exponential term in (63). A comparison between the numerical solution given by the proposed method for $m = 128$, $y_4(x)$ of the ADM, ITM, and VIM for $\alpha = 0.80$ and $\alpha = 0.90$ and the exact solution is performed in Figure 7. From Figure 7, it can be concluded that the Chebyshev wavelet method for the numerical solution of this problem is very efficient and accurate in comparison with the ADM, VIM, and ITM.

6. Discussion and Conclusions

In this paper, we proposed the Chebyshev wavelets method for the numerical solution of nonlinear fractional integro-differential equations in a large interval. Existence of a unique solution for such equations is proved. Convergence and error analysis of the Chebyshev wavelets expansion is discussed. Efficient approximate solutions have derived for NFIDEs, and the results have been shown remarkable performance. Moreover the new approach has been compared with the ADM, VIM, and ITM in solving various nonlinear fractional integro-differential equations. There are five important points to be noted here.

(1) The proposed method uses a new technique for computation of nonlinear terms in such equations.

(2) The proposed approach can provide the suitable approximate solution in a large interval by using only a few number of collocation points, as shown in the solved examples.

(3) The proposed method is very simple and requires less computational work in comparison with ADM, VIM, and ITM.

(4) The proposed method overcomes the probable difficulties arising in calculating integrals.

(5) The proposed method does not need to use Adomian polynomials and also has no need for the Lagrange multiplier, correction functional, stationary conditions, the variational theory, and so forth, which eliminates the complications that exist in VIM.

So in comparison with the ADM, VIM, and ITM, the proposed method is proved to be simpler in principle and more convenient for computer algorithms.

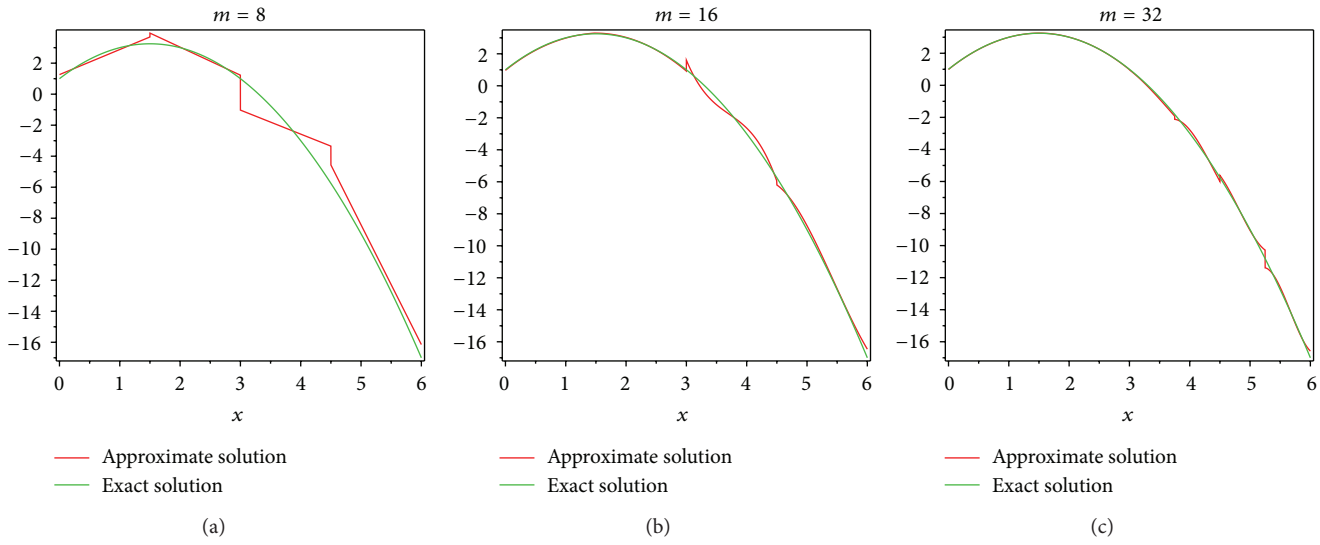

Figure 4: Numerical solutions of Example 2, for some values of m.

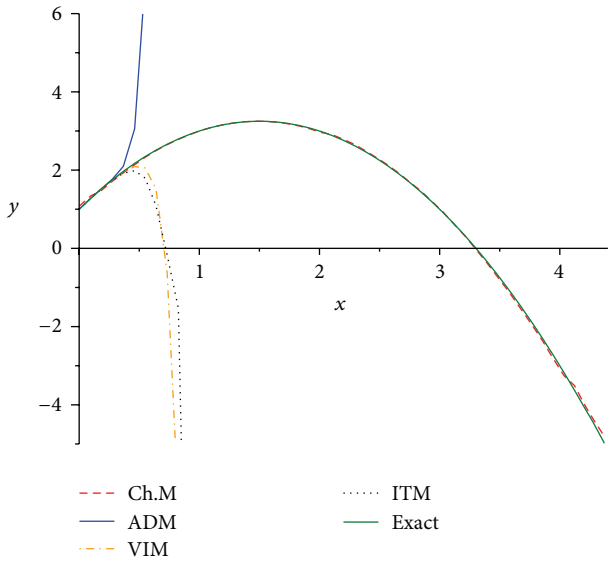

Figure 5: Numerical solutions of Example 2 for $\alpha = 0.85$.

Appendix

A. Some Properties of BPFs

An m-set of BPFs is defined as

$$b_i(t) = \begin{cases} 1, & \frac{i}{m} \le t < \frac{(i+1)}{m}, \\ 0, & \text{otherwise}, \end{cases} \tag{A.1}$$

where $i = 0, 1, 2, \ldots, (m-1)$.

The most important properties of BPFs are disjointness, orthogonality, and completeness.

Disjointness. This property can be clearly obtained from the definition of BPFs as follows:

$$b_i(t)\, b_j(t) = \begin{cases} b_i(t), & i = j, \\ 0, & i \ne j. \end{cases} \tag{A.2}$$

Orthogonality. It is clear that

$$\int_0^1 b_i(\tau)\, b_j(\tau)\, d\tau = \frac{1}{m}\delta_{ij}, \tag{A.3}$$

where δ_{ij} is the Kroneker delta.

Completeness. The sequence $\{b_i(t)\}_{i\in I}$ is complete in $L^2[0,1)$, namely, $f \in L^2[0,1)$, and $\int_0^1 b_i(t) f(t) dt = 0, i \in I$, results in $f(t) = 0$ almost everywhere. Because of completeness of $\{b_i(t)\}_{i\in I}$, Parseval's identity holds; that is, we have $\int_0^1 [f(t)]^2 dt = \sum_{i\in I} f_i^2 \|b_i(t)\|^2$, for every real bounded function $f \in L^2[0,1)$, and

$$f_i = m \int_0^1 b_i(t)\, f(t)\, dt = m \int_{i/m}^{(i+1)/m} b_i(t)\, f(t)\, dt. \tag{A.4}$$

Consider the first m-terms of BPFs and write them concisely as the m-vector as follows:

$$B_m(t) = \left[b_0(t), b_1(t), \ldots, b_i(t), \ldots, b_{m-1}(t)\right]^T, \quad t \in [0, T). \tag{A.5}$$

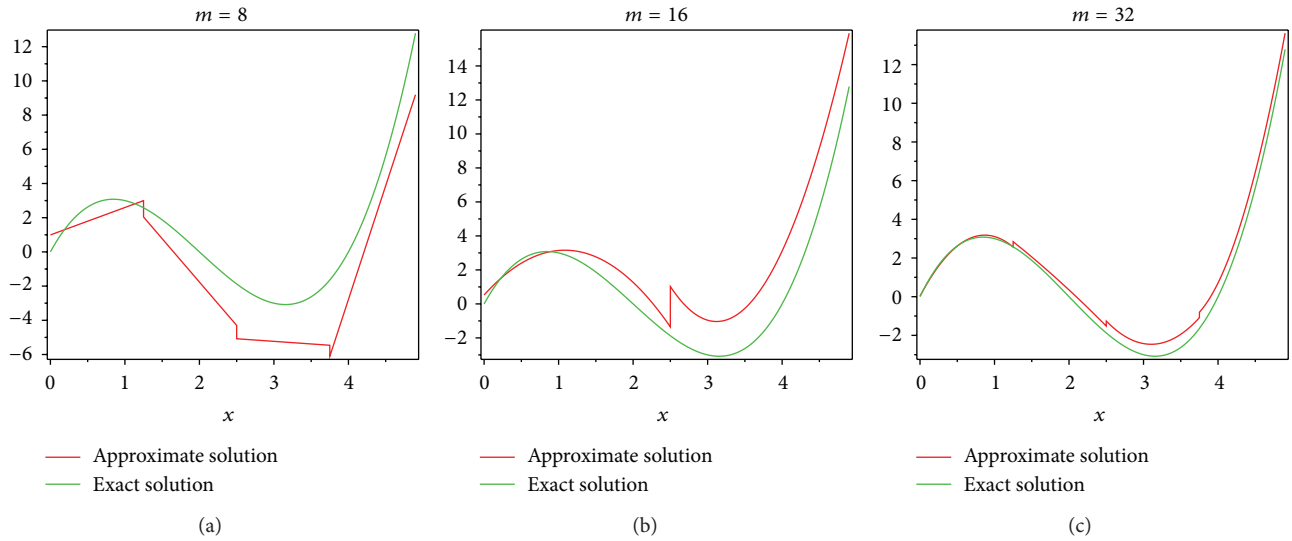

FIGURE 6: Numerical solutions of Example 3, for some values of m.

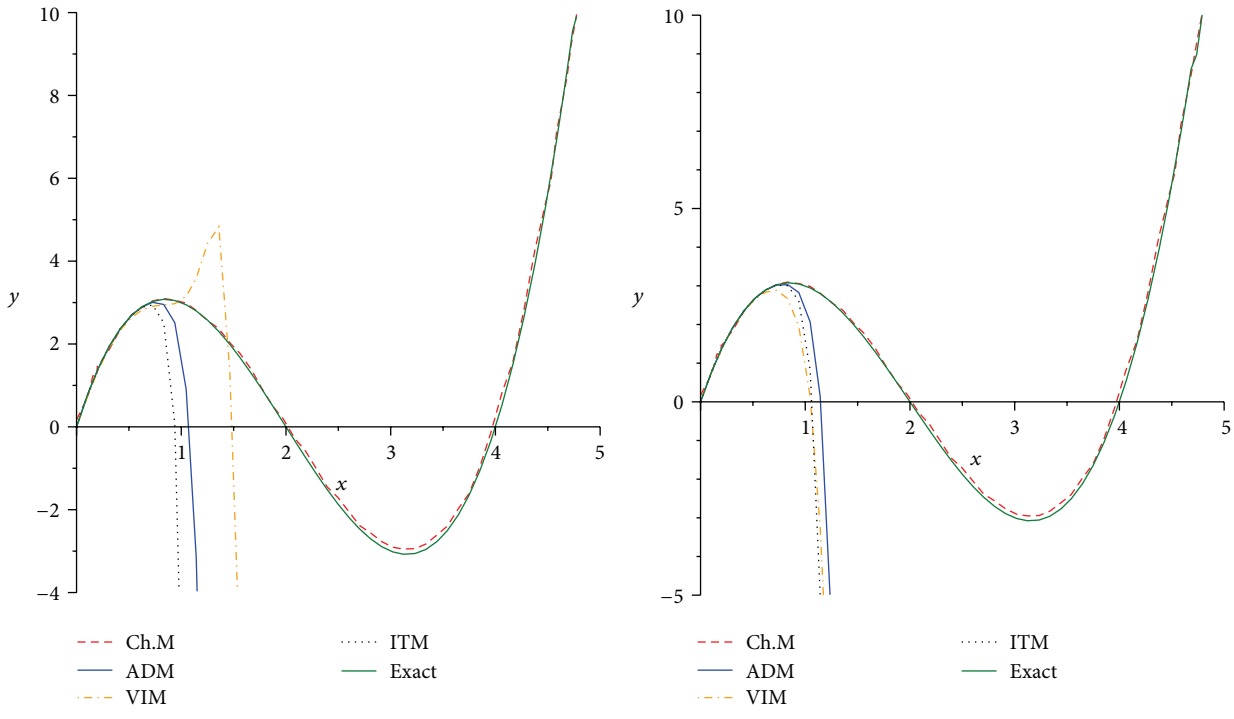

FIGURE 7: Numerical solutions of Example 3, for $\alpha = 0.80$ (a) and $\alpha = 0.90$ (b).

Then from the above representation and the disjointness property, it follows that

$$B_m(t)\,B_m^T(t) = \begin{pmatrix} b_0(t) & 0 & \dots & 0 \\ 0 & b_1(t) & \dots & 0 \\ \vdots & \vdots & \ddots & \vdots \\ 0 & 0 & \dots & b_{m-1}(t) \end{pmatrix}. \quad \text{(A.6)}$$

B. Expanding the Nonlinear Terms via Chebyshev Wavelet Bases

From (37) and (A.6), we have

$$\begin{aligned} [y(x)]^2 &= y(x)\,y(x)^T \\ &= [a_1, a_2, \dots, a_m]\,B_m(x)\,B_m(x)^T [a_1, a_2, \dots, a_m]^T \end{aligned}$$

$$
\begin{aligned}
&= \left[a_1, a_2, \ldots, a_m\right] \\
&\quad \times \begin{pmatrix} b_0(x) & 0 & \ldots & 0 \\ 0 & b_1(x) & \ldots & 0 \\ \vdots & \vdots & \ddots & \vdots \\ 0 & 0 & \ldots & b_{m-1}(x) \end{pmatrix} \\
&\quad \times \left[a_1, a_2, \ldots, a_m\right]^T \\
&= a_1^2 b_0(x) + a_2^2 b_1(x) + \cdots + a_m^2 b_{m-1}(x) \\
&= \left[a_1^2, a_2^2, \ldots, a_m^2\right] B_m(x),
\end{aligned} \tag{B.1}
$$

and in general by induction we have

$$
\left[y(x)\right]^q = \left[a_1^q, a_2^q, \ldots, a_m^q\right] B_m(x), \quad q \geq 2. \tag{B.2}
$$

For an analytic function g, by Maclaurin's expansion, $g(x) = \sum_{n=0}^{\infty} (g^{(n)}(0)/n!) x^n$, we have

$$
g(y) = \sum_{n=0}^{\infty} \frac{g^{(n)}(0)}{n!} y^n, \tag{B.3}
$$

and from (B.2) and (B.3) we have

$$
\begin{aligned}
g(y) &= \sum_{n=0}^{\infty} \frac{g^{(n)}(0)}{n!} \left[a_1^n, \ldots, a_m^n\right] B_m(x) \\
&= \left[\sum_{n=0}^{\infty} \frac{g^{(n)}(0)}{n!} a_1^n, \ldots, \sum_{n=0}^{\infty} \frac{g^{(n)}(0)}{n!} a_m^n\right] B_m(x).
\end{aligned} \tag{B.4}
$$

Since the series in the left hand side is absolutely and uniformly convergent to $g(y)$, each series in the right hand side is also absolutely convergent to the corresponding $g(a_i)$; that is,

$$
\left[\sum_{n=0}^{\infty} \frac{g^{(n)}(0)}{n!} a_1^n, \ldots, \sum_{n=0}^{\infty} \frac{g^{(n)}(0)}{n!} a_m^n\right] = \left[g(a_1), \ldots, g(a_m)\right]. \tag{B.5}
$$

Now, from (B.4) and (B.5), we have

$$
g(y) = \left[g(a_1), g(a_2), \ldots, g(a_m)\right] B_m(x). \tag{B.6}
$$

Acknowledgments

This work was supported in part by the National Natural Science Foundation of China under the Project Grant nos. 61272402, 61070214, and 60873264.

References

[1] M. Caputo, "Linear models of dissipation whose q is almost frequency independent-ii," *Geophysical Journal of the Royal Astronomical Society*, vol. 13, pp. 529–539, 1967.

[2] W. E. Olmstead and R. A. Handelsman, "Diffusion in a semi-infinite region with nonlinear surface dissipation," *SIAM Review*, vol. 18, no. 2, pp. 275–291, 1976.

[3] F. Mainardi, "Fractional calcauls: some basic problems in continument and statistical mechanics," *Fractals and Fractional Calulus in Continuum Mechanics*, pp. 291–348, 1976.

[4] S. Momani and R. Qaralleh, "An efficient method for solving systems of fractional integro-differential equations," *Computers and Mathematics with Applications*, vol. 52, no. 3-4, pp. 459–470, 2006.

[5] D. Nazari and S. Shahmorad, "Application of the fractional differential transform method to fractional-order integro-differential equations with nonlocal boundary conditions," *Journal of Computational and Applied Mathematics*, vol. 234, no. 3, pp. 883–891, 2010.

[6] E. A. Rawashdeh, "Numerical solution of fractional integro-differential equations by collocation method," *Applied Mathematics and Computation*, vol. 176, no. 1, pp. 1–6, 2006.

[7] E. A. Rawashdeh, "Legendre wavelets method for fractional integro-differential equations," *Applied Mathematical Sciences*, vol. 5, no. 49-52, pp. 2467–2474, 2011.

[8] F. Awawdeh, E. A. Rawashdeh, and H. M. Jaradat, "Analytic solution of fractional integro-differential equations," *Annals of the University of Craiova, Mathematics and Computer Science Series*, vol. 38, no. 1, pp. 1–10, 2011.

[9] R. C. Mittal and R. Nigam, "Solution of fractional integro-differential equations by adomian decomposition method," *Appl Math Comput*, vol. 4, no. 2, pp. 87–94, 2008.

[10] C. Cattani, "Fractional calculus and shannon wavelets," *Mathematical Problems in Engineering*, vol. 2012, Article ID 502812, 25 pages, 2012.

[11] C. Cattani, "Shannon wavelets for the solution of integro-differential equations," *Mathematical Problems in Engineering*, vol. 2010, Article ID 408418, 22 pages, 2010.

[12] C. Cattani and A. Kudreyko, "Harmonic wavelet method towards solution of the Fredholm type integral equations of the second kind," *Applied Mathematics and Computation*, vol. 215, no. 12, pp. 4164–4171, 2010.

[13] C. Cattani, "Shannon wavelets theory," *Mathematical Problems in Engineering*, vol. 2008, Article ID 164808, 24 pages, 2008.

[14] M. H. Heydari, M. R. Hooshmandasl, F. M. M. Ghaini, and F. Fereidouni, "Two-dimensionallegendre wavelets forsolving fractional poisson equation with dirichlet boundary conditions," *Engineering Analysis with Boundary Elements*, vol. 37, pp. 1331–1338, 2013.

[15] M. H. Heydari, M. R. Hooshmandasl, F. M. Maalek Ghaini, and F. Mohammadi, "Wavelet collocation method for solving multiorder fractional differential equations," *Journal of Applied Mathematics*, vol. 2012, Article ID 542401, 19 pages, 2012.

[16] M. H. Heydari, M. R. Hooshmandasl, F. Mohammadi, and C. Cattani, "Wavelets method for solving systems of nonlinear singular fractional volterra integro-differential equations," *Communications in Nonlinear Science and Numerical Simulation*, vol. 19, no. 1, pp. 37–48, 2014.

[17] M. R. Hooshmandasl, M. H. Heydari, and F. M. M. Ghaini, "Numerical solution of the one dimensional heat equation by using chebyshev wavelets method," *Applied & Computational Mathematics*, vol. 1, no. 6, pp. 1–7, 2012.

[18] J.-H. He, "Approximate analytical solution for seepage flow with fractional derivatives in porous media," *Computer Methods in Applied Mechanics and Engineering*, vol. 167, no. 1-2, pp. 57–68, 1998.

[19] J. He, "A new approach to nonlinear partial differential equations," *Communications in Nonlinear Science and Numerical Simulation*, vol. 2, no. 4, pp. 230–235, 1997.

[20] S. Momani and Z. Odibat, "Numerical comparison of methods for solving linear differential equations of fractional order," *Chaos, Solitons and Fractals*, vol. 31, no. 5, pp. 1248–1255, 2007.

[21] Z. Odibat and S. Momani, "Numerical solution of Fokker-Planck equation with space- and time-fractional derivatives," *Physics Letters A*, vol. 369, no. 5-6, pp. 349–358, 2007.

[22] V. Daftardar-Gejji and H. Jafari, "An iterative method for solving nonlinear functional equations," *Journal of Mathematical Analysis and Applications*, vol. 316, no. 2, pp. 753–763, 2006.

[23] S. Bhalekar and V. Daftardar-Gejji, "New iterative method: application to partial differential equations," *Applied Mathematics and Computation*, vol. 203, no. 2, pp. 778–783, 2008.

[24] I. Podlubny, *Fractional Differential Equations*, Academic Press, San Diego, Calif, USA, 1999.

[25] Y. LI, "Solving a nonlinear fractional differential equation using Chebyshev wavelets," *Communications in Nonlinear Science and Numerical Simulation*, vol. 15, no. 9, pp. 2284–2292, 2010.

[26] A. Kilicman and Z. A. A. Al Zhour, "Kronecker operational matrices for fractional calculus and some applications," *Applied Mathematics and Computation*, vol. 187, no. 1, pp. 250–265, 2007.

[27] S. Sohrabi, "Comparison Chebyshev wavelets method with BPFs method for solving Abel's integral equation," *Ain Shams Engineering Journal*, vol. 2, no. 3-4, pp. 249–254, 2011.

[28] H. Saeedi, N. Mollahasani, M. Moghadam, and G. Chuev, "An operational haar wavelet method for solving fractional volterra integral equations," *International Journal of Applied Mathematics and Computer Science*, vol. 21, no. 3, pp. 535–547, 2011.

Hindawi Publishing Corporation
Advances in Mathematical Physics
Volume 2013, Article ID 879651, 12 pages
http://dx.doi.org/10.1155/2013/879651

Research Article

Distance-Based Routing Strategy for Traffic Transport in Spatial Networks

Wei Huang, Xiang Pan, Xi Yang, and Jianhua Zhang

College of Computer Science, Zhejiang University of Technology, Hangzhou 310023, China

Correspondence should be addressed to Wei Huang; huangwei@zjut.edu.cn

Received 1 August 2013; Accepted 20 September 2013

Academic Editor: Ming Li

It is well known that routing strategies based on global topological information is not a good choice for the enhancement of traffic throughput in large-scale networks due to the heavy communication cost. On the contrary, acquiring spatial information, such as spatial distances among nodes, is more feasible. In this paper, we propose a novel distance-based routing strategy in spatial scale-free networks, called LDistance strategy. The probability of establishing links among nodes obeys the power-law in the spatial network under study. Compared with the LDegree strategy (Wang et al., 2006) and the mixed strategy (a strategy combining both greedy routing strategy and random routing strategy), results show that our proposed LDistance strategy can further enhance traffic capacity. Besides, the LDistance strategy can also achieve a much shorter delivering time than the LDegree strategy. Analyses reveal that the superiority of our strategy is mainly due to the interdependent relationship between topological and spatial characteristics in spatial scale-free networks. Furthermore, along transporting path in the LDistance strategy, the spatial distance to destination decays more rapidly, and the degrees of routers are higher than those in the LDegree strategy.

1. Introduction

In the last few years, the analysis and modelling of dynamics in networked systems have attracted much attention in the field of theoretic physics [1–3]. Such networked systems include the Internet, high-way networks, airline networks, and social, biology, and some other infrastructure networks. In some real networks such as the Internet [4], electric-power grid [5], and airline networks [6], each node has its individual precise position in the space and the spatial distances among nodes cannot be arbitrarily neglected. Moreover, the spatial distances among nodes are not identical. In such networks, the network is embedded into a space with some (e.g., Euclidean) metric. This is why people usually call these networks spatial networks [7].

Until now, most previous work only focused on the effects of topological characteristics on dynamical occurring in networks, while the effects of spatial characteristics begin to attract much attention only in recent years. It has been reported that in real networks, the topological and spatial characteristics are closely related [8]. Two nodes close to each other are likely to be connected even though both nodes have low degrees, whereas there may not exist any link between two high-degree nodes far away from each other. For example, in an airline network, nodes represent cities, and two nodes are connected by a link if there is at least one airline between cities corresponding to the two nodes. Two big cities, such as *Beijing* and *New York*, even though they are far away from each other, they are still connected with each other. However, it is unlikely that two small cities are connected, unless they are close enough. Empirical studies [8] revealed that the effects of spatial characteristics can play an important role in affecting dynamics on networks [9]. Exploring the effect of spatial characteristics on dynamics may reveal some new and interesting features which cannot be observed when only studying the effect of topological characteristics.

Among different kinds of dynamics on networked systems, transport is a typical kind of dynamics that can be universally observed in real systems. Typical examples include the delivery of information packets in the Internet and airplane flights in airline networks. Much effort has been dedicated to designing efficient routing strategies. Efficient routing strategy can alleviate traffic congestion and enhance transport efficiency [10, 11]. By now, most studies

for designing efficient routing strategy are mainly based on topological information or dynamical information in the network (e.g., the number of packets on nodes). Such typical routing strategies include the shortest path routing strategy [12], the local routing strategy based on nodes' degrees [13], the routing strategy integrating both static topological information and dynamical traffic information [14–17], the routing strategy integrating both local and global topological information [18, 19], the routing strategy aiming to minimize the maximal node betweenness [20, 21], and the routing strategy aiming to find the so-called *efficient path* [22].

Although routing strategies based on topological information have been extensively studied, routing strategies based on spatial information have so far rarely been considered. Actually, in real communication networks, utilizing global topological information, for example, the shortest path between two nodes, needs to consume much communication cost or even cannot be accessed. For example, in the Internet at autonomous system (AS) level, the shortest path between two nodes may be illegal due to complicated relationship of commercial benefit among internet service providers (ISP). On the contrary, spatial distances among nodes are comparably convenient to obtain. The position of each packet's destination node can be affiliated on the packet itself. Since inquiring neighbors' position in the geographical space does not consume much communication cost for each node, when a packet arrives at a node, the spatial distance between each neighbor and the packet can be easily calculated without consuming much communication cost. It is worth noting that the spatial information can be used for searching a destination node from a source node without global topological information in large-size networks [23]. In [23], the authors performed the greedy searching strategy in scale-free networks. In the greedy searching strategy, each node uses the information of spatial distance to select, as the next hop, closest to the destination in the network. The authors claimed that the most navigable topologies are with small degree exponent of the degree distribution and with strong clustering. Moreover in [24], the authors pointed out that the greedy searching in scale-free networks with strong clustering and power-law node degree distribution $\gamma < 3$ find its path with the average scaling as $\ln \ln N$, which is the same as the shortest path length. These reports validate that the information of spatial distance can effectively improve searching efficiency in spatial scale-free networks. In addition, there have also been some reports on the study of spatial ingredients in the fields of communication and computer networks [25–27].

Therefore, in this paper, we propose a novel routing strategy based on the information of spatial distance, to enhance transport efficiency in spatial scale-free networks. Global topological information is not required, and only the local topological information is utilized in our strategy. Therefore, we call our strategy the LDistance (local and based on the information of spatial distance) strategy. To highlight the advantage of spatial information in enhancing transport efficiency, we compare our proposed routing strategy with the local routing strategy based on nodes' degrees [13] (we call it the LDegree strategy in our paper) and the mixed strategy, which is a combination of greedy routing strategy and random routing strategy. Extensive simulations are performed in spatial networks with scale-free structure. Results show that the proposed LDistance routing strategy shows strong superiority over the LDegree strategy and the mixed strategy. Besides, results also show that our proposed LDistance strategy can also achieve a shorter delivering time than the LDegree strategy.

This paper is organized as follows. In Section 2, we present some preliminary work, including the model of spatial networks with scale-free network structure, some backgrounds of our study on traffic problems, and the LDegree strategy proposed in [13]. Then, we present our proposed LDistance routing strategy in spatial networks with scale-free structure. In Section 3, simulation results are presented, followed by detailed analyses and discussions. Finally, conclusions are drawn in Section 4.

2. Model Description

In our study, the modelling of traffic transport is based on the spatial network model proposed in [8]. This model reproduces several important features that can be observed in real communication networks, such as the Internet at the autonomous system level and the USA airline network [23]. These features include small-world, scale-free, and strong clustering. It should be mentioned that strong clustering means that spatial information is highly related to the underlying topological information. In this model, the nodes are placed on a circle. Each node is assigned with a random variable representing the node's polar angle, which is evenly distributed in $[0, 2\pi)$. To keep the density of nodes on the circle fixed to 1, the total number of nodes is proportional to the circle radius R. Each node is then assigned with an expected degree k, which is drawn from a power-law degree distribution $P(k) \sim k^{-\gamma}$. Then we connect each of the two nodes with the probability $r(d; k, k')$ that depends on the geodesic distance d between the two nodes and the nodes' assigned degrees k and k'. The probability $r(d; k, k')$ takes the form:

$$r\left(d; k, k'\right) = \left(1 + \frac{d}{d_c}\right)^{-\lambda} = \left(1 + \frac{d}{\mu k k'}\right)^{-\lambda}, \qquad \mu = \frac{(\lambda - 1)}{2\langle k \rangle}, \tag{1}$$

where $\langle k \rangle$ denotes the average expected degree. Note that the probability follows the power-law and is heavy-tailed [28, 29], which is rather critical in computer networks [30]. With this form of connection probability, long-range links are discouraged and short-range links are favored, as we have mentioned in Section 1. Moreover, the parameter λ, called clustering strength, controls the significance of spatial distance for establishing new links among nodes. The increasing of λ can strengthen the tendency of establishing a new link between two nodes that are close to each other. Therefore, in a network with large λ, connections appear more frequently among the nodes that are close to each other in the spatial

space. It can be inferred consequently that strong clustering can easily form in the network with large λ. The stronger the influence of spatial information on underlying network topology, the more strongly nodes are clustered.

Next, we will describe the model of traffic transport on spatial networks. For simplicity, we treat all nodes in the network as both hosts and routers for generating and delivering packets. At each time step, M packets are generated in the network with randomly chosen sources and destinations (we denote M as the packet generation rate). Note that for each packet, the source node and the destination node must be different. A packet, if its destination is rightly one of the neighbors of the current node where the packet is located, the packet will be directly forwarded to the destination node. Otherwise, the packet is forwarded from one node to another following a given routing strategy. Each node i is assigned with a given delivering capacity C_i, that is, the maximal number of packets each node can deliver at one time step. Without loss of generosity, we set the delivering capacity for each node equal to 5 in our study. An arrived packet will be placed at the end of the queue if this node already has some packets to be delivered to their respective destinations. Packets in queue work on a FIFO (first in first out) basis. Finally, a packet will be removed from the network once it reaches its destination.

In this study, we focus on the traffic capacity [31] and the average delivering time, to evaluate the efficiency of traffic transport in spatial networks with scale-free structure. The traffic capacity can be defined as the critical value M_c of the packet generation rate M and is usually described by an order parameter [31]:

$$\eta(M) = \lim_{t \to +\infty} \frac{\langle \Delta W \rangle}{M \Delta t}, \tag{2}$$

where $\langle \Delta W \rangle = W(t+\Delta t) - W(t)$, and $\langle \cdots \rangle$ is the average over time windows of width Δt. $W(t)$ denotes the total number of packets in the network at time step t. The network undergoes a phase transition from a free-flow state to congested state at $M = M_c$. Under the condition $M < M_c$, $W(t) = 0$ and $\eta = 0$, this indicates that the number of generated and removed packets is kept balanced and the network is under free-flow state. On the other hand, when $M > M_c$, for packets, the generation rate exceeds the removing rate statistically. Therefore, packets are becoming congested with the elapsing of time steps. Under this condition, η is above zero. The designed routing strategy in communication networks should try to maximize the traffic capacity and minimize the average delivering time of packets.

In the LDegree strategy, each node performs a local search among all its direct neighbors. If the packet's destination is found to be not among the neighbors of current node, the packet is delivered to node i, one of the neighbors of current node, with probability:

$$\prod_i = \frac{k_i^\alpha}{\sum_j k_j^\alpha}, \tag{3}$$

where the sum runs over all neighbors of the current node, k_i is the degree of node i, and α is a tunable parameter. The authors of [13] found that the optimal parameter $\alpha = -1$ can achieve the maximal traffic capacity when the delivering capacity is identical for each node.

In this paper, we shall first compare our proposed LDistance strategy with the LDegree strategy. Based on the spatial network model in [8], when any node receives a packet, the node should easily know the distance between any of its neighbors and the packet's destination node, as we have stated in Section 1. Any global topological information is not needed in our strategy. Let us assume a packet's destination is node t. If the packet's destination t is found to be not among the neighbors of current node, the packet is forwarded to the nodes i, one of the neighbors of current node, with probability:

$$\prod_i = \frac{d_{i,t}^\beta}{\sum_j d_{j,t}^\beta}, \tag{4}$$

where the sum runs over all neighbors of the current node, and $d_{i,t}$ denotes the geodesic distance between node i and t, and β is a tunable parameter. If $\beta < 0$, it means that packets are inclined to be forwarded to the neighbor with relatively short distance to destination. If $\beta > 0$, packets are more likely to be forwarded to the neighbor with relatively long distance to destination. Obviously when $\beta \to -\infty$, the proposed routing strategy is recovered to the greedy routing strategy; that is, each packet is always forwarded to the neighbor with the smallest geodesic distance to destination.

To further validate the high efficiency of the LDistance strategy, we will also compare the proposed LDistance strategy with another kind of distance-based routing strategy, called the mixed strategy in this paper. The mixed strategy is a mixture of the greedy routing strategy and the random routing strategy. In this mixed strategy, at each time step, we choose the neighbor closest to destination as the next hop with probability $1 - \sigma$ and randomly choose a neighbor with probability σ. It is obvious that when $\sigma = 0$, the mixed strategy is recovered to the LDistance strategy with $\beta = -\infty$, that is, the greedy routing strategy. When $\sigma = 1$, the mixed strategy becomes a purely random routing strategy.

3. Result, Analysis, and Relevant Discussions

In our study, all experiments were performed in the spatial scale-free network model introduced in Section 2 with the average degree $\langle k \rangle = 13$ and the network size $N = 500$. Different values of clustering exponent λ and degree exponent γ are assigned for the network model under study. We mainly focus on the traffic capacity M_c and the average delivering time T_{ave}. High traffic capacity and low delivering time are favored. Note that the delivering time mainly consists of two parts: the first part is the time consumed on transporting path and the second part is the waiting time on routers. Extensive numerical simulations are performed. Each realization of numerical simulations is terminated when transporting dynamics goes into the steady state; that is, the number of total packets becomes constant or only slightly fluctuate with the elapsing of time steps. According to the

model and relevant parameter settings in our study, the time step $t_{\text{elapse}} = 5000$ is enough to ensure that transporting dynamics have been under the steady state for considerable time steps. Each result is the average over 50 different network configurations and 20 different realizations of transporting dynamics for each network configuration.

Figure 1 demonstrates the traffic capacity M_c for both LDegree strategy and LDistance strategy under different parameter settings. As we have stated in Section 2, when $\beta < 0$, packets are inclined to be forwarded to the neighbor with short distance to destination, which is usually favored in real networks. However, if the value of β is set to be too small, for example, when $\beta \to -\infty$, the LDistance strategy is recovered to the greedy routing strategy. As [24] pointed out, the average length of greedy routing path scales as $\ln \ln N$, which indicates that the greedy routing path does not deviate much from the shortest path. On other hand, it is well known the shortest path routing strategy can supply even lower transport efficiency than the LDegree strategy. Moreover, in the greedy routing strategy, the packet can easily get stuck at nodes without neighbors closer to the destination than themselves, which finally causes an unsuccessful transport, and transport efficiency is heavily affected. Therefore, the value of β should be set to be a proper value in the range $\beta < 0$ so that transport efficiency has chances to be enhanced maximally.

For each given clustering exponent and degree exponent, the traffic capacity of the LDistance strategy is higher than that of the LDegree strategy, which indicates that utilizing the information of geodesic distance is beneficial for enhancing traffic capacity in spatial scale-free networks. It is well known that the LDegree strategy has proved to show strong superiority over the shortest path routing strategy [13] in enhancing traffic capacity. The LDistance strategy, on the other hand, provides a novel way of enhancing traffic capacity. The superiority of LDistance strategy over LDegree strategy in enhancing traffic capacity can be explained by virtue of two auxiliary figures, that is, Figures 2 and 3. Figure 2 illustrates the relationship between the topological shortest path length h and the resized distance d_n between any two distinct nodes for both the spatial network model proposed in [8] and its null model. The null model, which has the same degree distribution as the spatial network model in [8], is generated following the switching algorithm in [32]. In this switching algorithm, starting from the network model in [8], we carry a series of Monte Carlo switching steps whereby a pair of links (A-B and C-D) are chosen randomly, and then the ends are exchange to give (A-D and B-C). Note that the exchanged is performed only when no multilinks or self-links are generated. For the spatial network model in [8], as shown in Figure 2(a), the topological shortest path length monotonously increases with the spatial distance. In the LDistance strategy, choosing the neighbor with shorter distance to the destination means that the chosen neighbor also has a smaller topological shortest path length from the destination. Vice versa, if the neighbor with relatively long distance to the destination is favored to be chosen, then the packets would have to travel over more routers to find their destinations. However, for the null model, as shown in Figure 2(b), we cannot observe any explicit relationship between the topological shortest path length h and the resized distance d_n between any two distinct nodes. Forwarding packets to the neighbor with relatively short distance to destination cannot essentially reduce the topological shortest path length to destination in the null model.

Figure 3 illustrates the relationship between the traffic capacity M_c and the parameter σ under the mixed routing strategy. We only demonstrate the case of $\gamma = 3$, but cases with other degree exponents can still lead to much of the same result as Figure 3. Given the fixed γ and λ, the maximal traffic capacity among different values of tunable parameter (α for the LDegree strategy, β for the LDistance strategy, and σ for the mixed strategy) is denoted as $M_{c\max}$. To compare the LDegree strategy, the LDistance strategy, and the mixed strategy, we label $M_{c\max}$ of LDistance strategy and LDegree strategy on the M_c-axis in each panel of Figure 3. Results show explicitly that in the mixed strategy, $M_{c\max}$ can be achieved at some proper point of σ. More importantly, it can be observed that for any clustering strength λ, the mixed strategy cannot supply a higher $M_{c\max}$ than our proposed LDistance strategy.

Now we can give a justification that our proposed strategy has its unique advantage in achieving a higher traffic capacity according to both Figures 2 and 3. Firstly, we have mentioned that in the greedy routing strategy, that is, $\beta \to -\infty$ in the LDistance strategy, packets can easily get stuck on low-degree nodes. To avoid packets getting stuck on low-degree nodes, packets cannot always choose routers closest to destination in the geographical space. Therefore, by appropriately increasing β, we can choose the router with the distance to destination a little longer than the minimal distance to destination to escape from getting stuck on low-degree nodes. From the relationship between the topological shortest path length h and the resized distance d_n illustrated in Figure 2, we can further conjecture that the topological shortest path length from the chosen router to destination also becomes more accordingly. Although the little increment of distance to destination increases some more hops on transporting path, the chance of getting stuck on low-degree nodes can be reduced, and therefore, traffic capacity can be enhanced. However, if the value of β is increased excessively, the router with the distance to destination much longer than the minimal distance to destination is likely to be chosen. Consequently, the topological shortest path length from the chosen router to destination can hardly decay along transporting path and therefore traffic capacity can hardly be enhanced. Secondly, the LDegree strategy is distance-agnostic. Along transporting path of LDegree strategy, the distance to destination can hardly decay as fast as that of LDistance strategy, which will be validated in the following part of this paper. Thirdly, in the mixed strategy, to reduce the chance of getting stuck on low-degree nodes, random strategy is involved in the mixed strategy. However, although the incorporating of random strategy can somewhat reduce the chance of getting stuck, the random strategy evidently has more chances to forward packets to the neighbor with rather long distance to destination than our proposed LDistance strategy with optimal β. We will verify it in the following

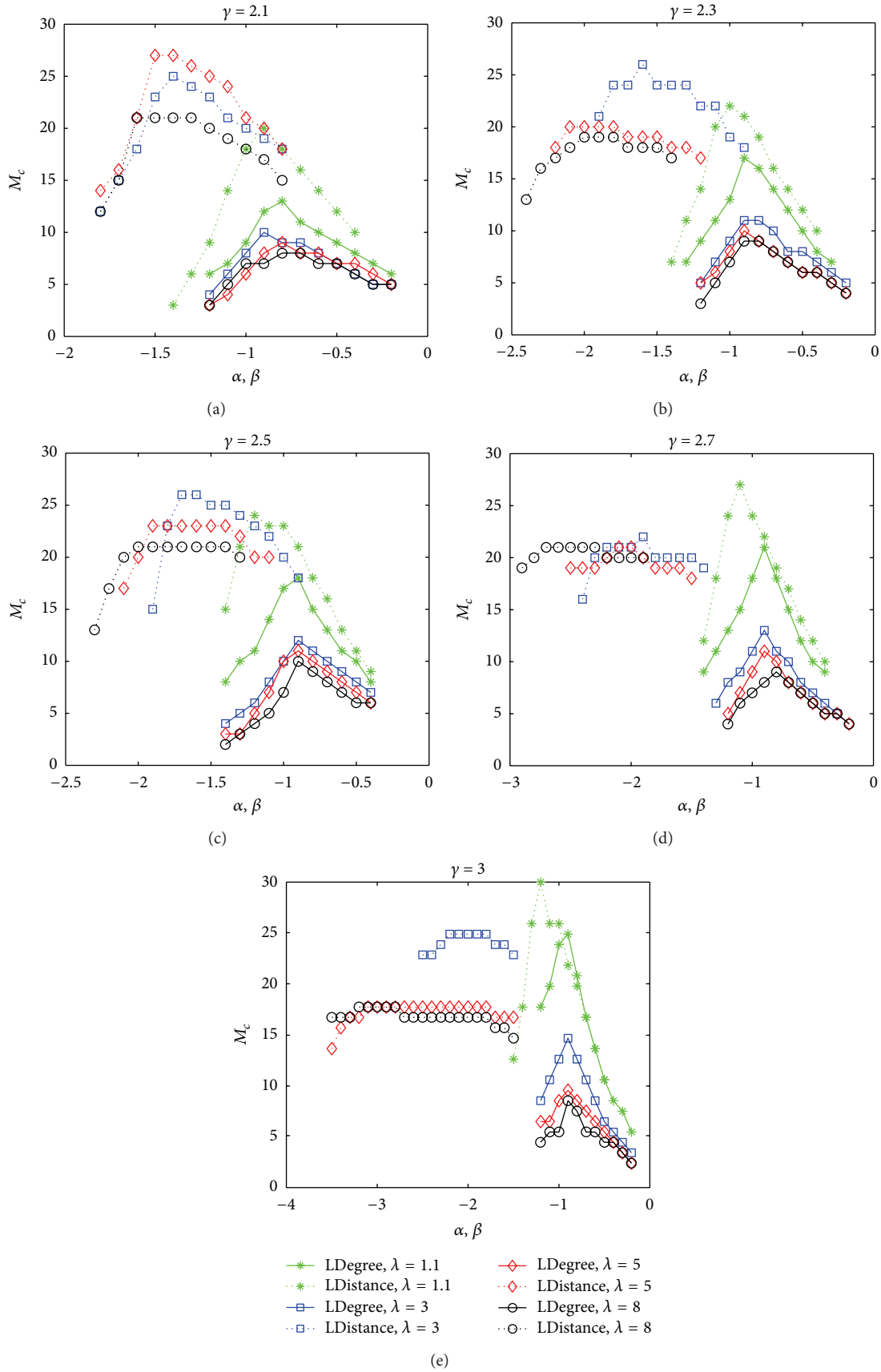

Figure 1: (Color online) The relationship between traffic capacity M_c and tunable parameters (α for LDegree strategy and β for LDistance strategy) under networks with different degree exponent γ and clustering strength λ.

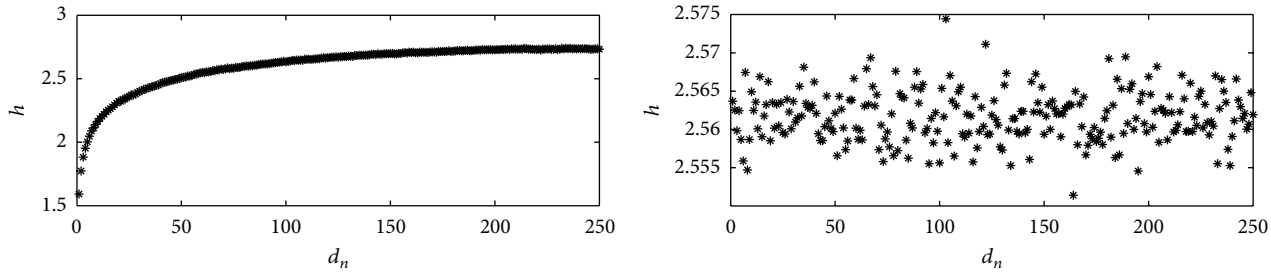

(a) Spatial network model

(b) Null model of spatial network model

FIGURE 2: (Color online) The relationship between the topological shortest path length h versus the resized distance d_n between any two nodes for both the spatial network model in [8] and its null model. Here, in the resized distance $d_n = d/d_{\text{nei}}$, d denotes the actual geodesic distance and d_{nes} denotes the geodesic distance between two neighboring nodes in the geographical space. The degree exponent is set to 3 and the clustering strength in the spatial network model in [8] is set to 1.1.

part of this paper. Therefore, in the mixed strategy, it is still likely that packets have to travel over more routers to arrive at destinations, which is of course not beneficial for the enhancement of traffic capacity.

By now, we can conjecture that, due to the interdependent relationship between network topology and underlying geographical space, we can only utilize spatial information to achieve high traffic capacities. Note that the acquisition of spatial information is comparably easier and more convenient than that of global topological information, especially in large-size networks. Therefore, our strategy is practically useful in real large-size networks because strategies based on global topological information are inconvenient, or even impossible, to be put into use in real large-size networks.

We have also studied the effect of clustering strength λ on traffic capacity for the LDistance strategy. From Figure 1, we can observe that the value of β at which $M_{c\max}$ is achieved is decreased with the enhancement of λ. For example, when $\gamma = 3$, the value of β at which $M_{c\max}$ is achieved is decreased from -1.1 to around -3 when λ rises up to 8 from 1.1. This observed result can be explained as follows. In [23], the authors studied the navigability problem in the spatial scale-free network model proposed in [8]. In their study, they introduced an important navigability parameter, the success ratio p_s, defined as the percentage of successful paths. Here, unsuccessful paths are those that get stuck on nodes without neighbors closer to destination in the space than themselves, which indicates that packets can hardly arrive at their destinations. The authors pointed out in [23] that, give the fixed degree exponent γ, p_s increases with networks' clustering strength λ, which indicates that packets are more likely to get stuck on low-degree nodes in networks with weaker clustering. Therefore, in networks with weaker clustering, to reduce the chance of getting stuck along transporting path, the stringency of packets being forwarded to nodes closest to destinations in the geographical space should be loosened; that is, β should be increased. As a result, the success ratio p_s can be increased, and therefore, $M_{c\max}$ can be enhanced.

Next, we will concerned with the average delivering time of packets for all strategies under study. Figure 4 illustrates the average delivering time T_{ave} with the packet generation rate equal to traffic capacity. We only present the case with the degree exponent $\gamma = 3$, but the results from cases with other values of γ do not deviate too much from the case of $\gamma = 3$. Figure 4(a) illustrates the delivering time for both LDistance and LDegree strategies, and the case of LDistance strategy is zoomed in in Figure 4(b). Moreover, the result of the mixture strategy is also shown in the subgraph of Figure 4(b). It can be observed that the minimal T_{ave} (for a fixed clustering strength λ) achieved from the LDistance strategy does not deviate too much from the mixed strategy under each given clustering strength. However, as Figure 4 shows, both of the two distance-based strategies deliver a much shorter delivering time than the LDegree strategy, which provides another evidence that the performance of our proposed strategy is superior the the LDegree strategy. Moreover, for both the LDistance and the mixed strategies, we find that the impact of clustering strength λ on the average delivering time T_{ave} is not so obvious. However, in the LDegree strategy, T_{ave} shows strong dependence on λ. From Figure 4, we have observed that weak clustering induces shorter delivering time. Recalling that the traffic capacities of networks with weak clustering are generally large in the LDegree strategy, we can thus conclude that in the LDegree strategy, transport of packets is more efficient in networks with weak clustering.

From the above analysis, we have found that, as compared to the LDegree strategy, our proposed LDistance strategy can further enhance traffic capacity and shorten average delivering time. To further explore the differences of LDegree and LDistance strategies, we will next compare the structural and spatial characteristics of routers along transporting path for both routing strategies. Figure 5 shows the average resized distance d_n to destination and the average degree k of routers along transporting path under the optimal condition; that is, the traffic capacity achieves its maximal value given the predefined γ and λ for the LDegree strategy, the LDistance strategy, and the mixed strategy. We only demonstrate the case of networks with ($\gamma = 3, \lambda = 1.1$), but similar conclusions can also be drawn from other cases with different γ and λ. Figures 5(a) and 5(b) clearly illustrate that, under the optimal condition with the traffic capacity maximized, the length of transporting path in the LDistance strategy is far less than

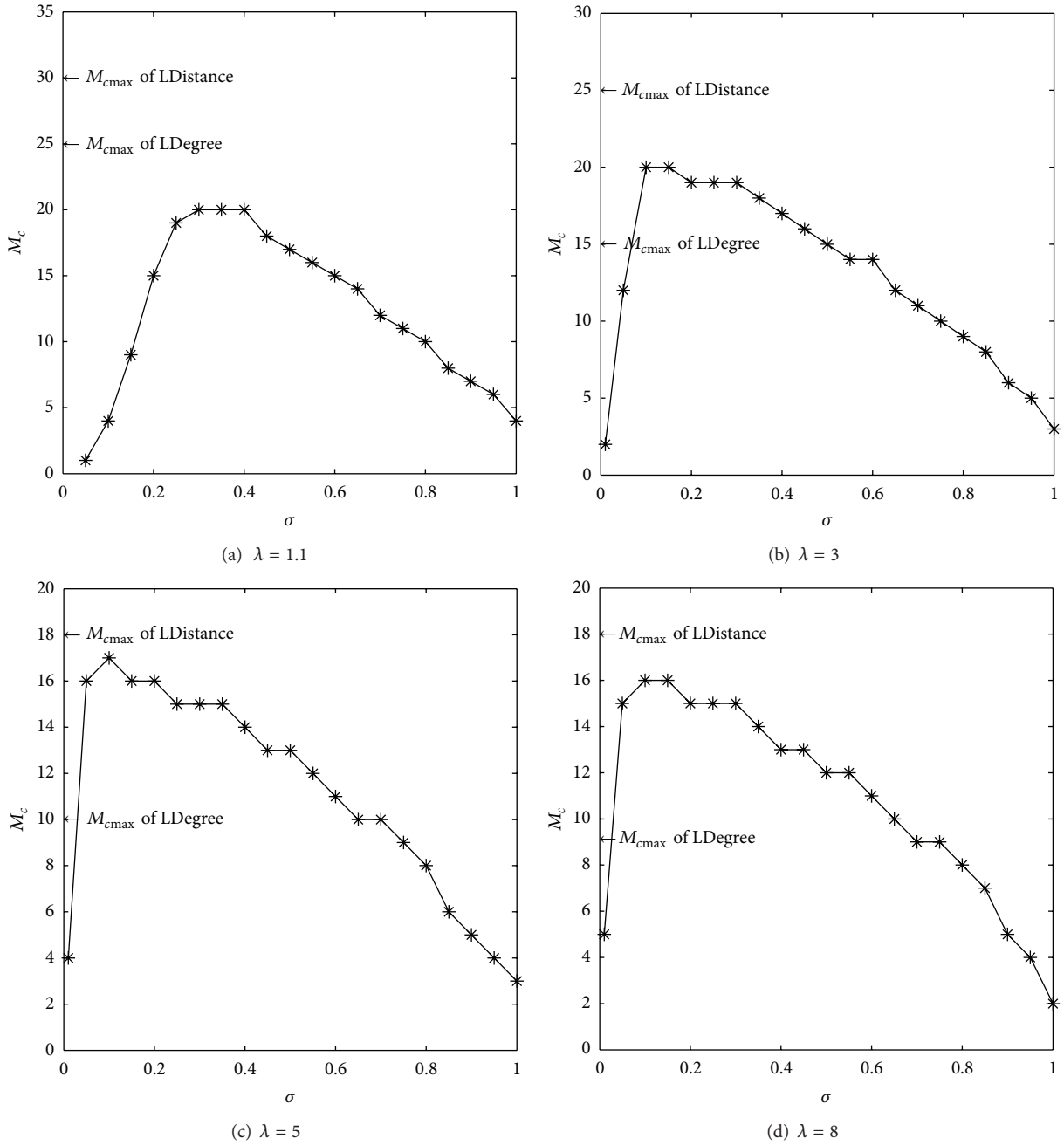

FIGURE 3: The relationship between traffic capacity M_c and tunable parameters σ for the mixed strategy under networks with fixed degree exponent $\gamma = 3$ and different clustering strength λ.

that in the LDegree strategy and is slightly less than that in the mixed strategy. We can see under the network with $\gamma = 3$ and $\lambda = 1.1$ that the average length of transporting path is around 9 under the optimal $\beta_c = -1.2$ with the traffic capacity maximized in the LDistance strategy. The average length of transporting path increases to 10 under the optimal condition $\sigma = 0.45$ in the mixed strategy. However, in the LDegree strategy, the average length of transporting path rises up to 60 under the optimal condition $\alpha_c = -0.9$ with the traffic capacity maximized. We have pointed out that compared to our proposed strategy, the mixed strategy has more chance to forward packets to the neighbor with very long distance to destination. Therefore, in the mixed strategy, the transporting path is longer than that in the LDistance strategy, which is clearly illustrated in Figure 5(a).

Moreover, from Figure 5(a), we can observe that in the LDegree strategy, along transporting path towards destination, the distances of most routers to destination are long and keep almost unchanged. Only at the end of transporting path, the distance to destination decays rapidly until packets finally find their destinations. This result reveals that in the LDegree strategy, except those at the end of transporting path, most deliveries seem not to be as effective as we regarded previously. On the contrary, in the LDistance strategy, the

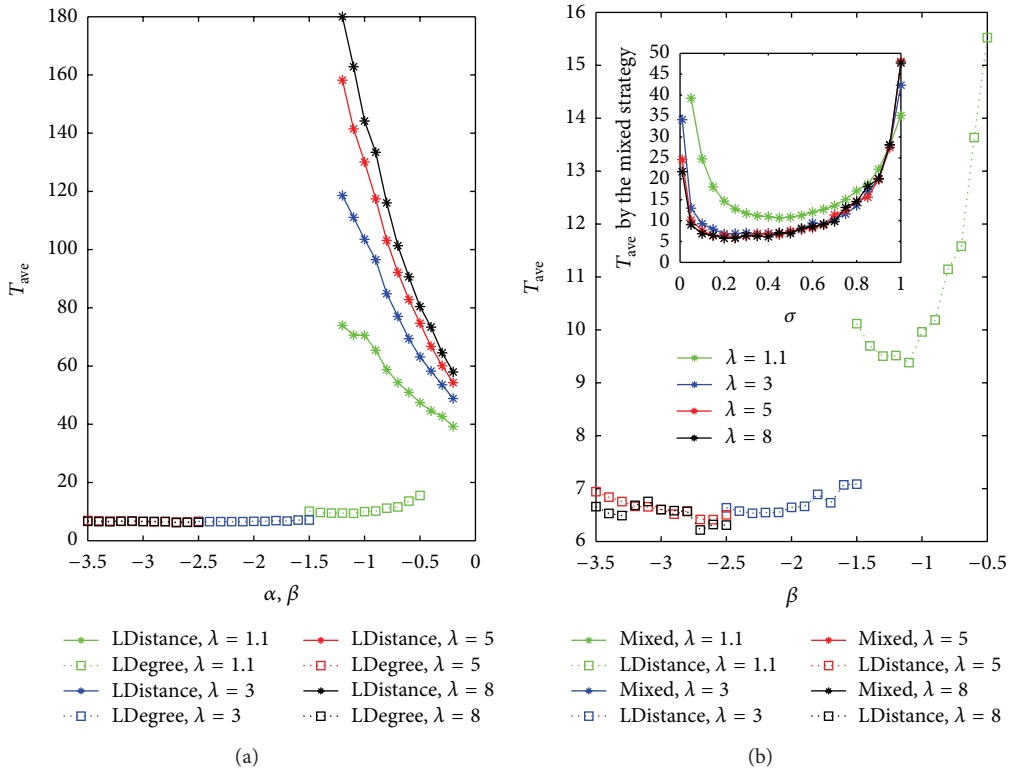

FIGURE 4: (Color online) (a) The relationship between average delivering time T_{ave} and tunable parameters (α for LDegree strategy and β for LDistance strategy) under different clustering strengths on networks with degree exponent $\gamma = 3$. For each fixed network, the packet generation rate is set to the same value as the traffic capacity. (b) The case of LDistance strategy is zoomed in. The subgraph of (b) illustrates the average delivering time for the mixed strategy.

distance of routers to destination keeps on decreasing from the beginning of transporting path, which indicates that in the LDistance strategy, each delivery can be considered to be "valuable" for packets being forwarded towards destinations. On the other hand, as can be observed from Figure 5(b), the routers along transporting path in the LDistance strategy evidently have larger degrees than those in the LDegree strategy. In the LDegree strategy, most routers on transporting path have relatively low degrees, except that when the packet arrives at one neighbor of destination. Figure 5(b) reveals that this neighbor usually has very high degrees. In the LDistance strategy, along transporting path, the degrees of routers firstly rise up to rather high values. These high-degree nodes encountered on the transporting path are due to the relationship between a node's characteristics distance scale and the nodes' spatial distance to destination [24]. The closer the chosen nodes' spatial distance to destination, the higher the nodes' degree is. After travelling over these high-degree nodes, the degrees of routers along the following transporting path decrease. At last, the packet arrives at one neighbor (with large degree) of destination once again. The existing LDegree strategy aims to reduce packets' accumulation on high-degree node by dispersing more packets on low-degree nodes. However, our proposed LDistance strategy indicates that the way of dispersing packets on low-degree nodes in the LDegree strategy is far from optimal. The degrees of routers on transporting path need not be so mall as in the LDegree strategy. Increasing the degree of routers on transporting path, as in our proposed LDistance strategy, can help packets find their destinations more quickly.

To further reveal the topological and spatial characteristics of routers on transporting path in the LDistance strategy, we have performed the same simulations as Figure 5, but with different settings of β. First, Figure 6(a) illustrates the relationship between the average number of hops of transporting path and β. It shows clearly that the transporting path with the least number of hops is achieved around $\beta \approx -0.9$. Above $\beta \approx -0.9$, transporting paths are potentially analogous to those of random search, and therefore, the lengths of transporting paths are lengthened. Figures 6(b) and 6(c) repeat the simulations of Figure 5 for the LDistance strategy, but with different values of β above $\beta \approx -0.9$. It can be observed that when β gets close to $\beta \approx -0.9$, the distance to destination decays more sharply, but the degrees of routers along transporting path do not deviate from each other for different β. Once again, in Figures 6(d) and 6(e), the simulations of Figure 5 for the LDistance strategy are repeated again with the β below -0.9. When β moves away from -0.9 towards $-\infty$, the LDistance strategy is more like the greedy routing strategy, and the interdependence between a nodes' degree and the characteristics scale of spatial distances that the node covers by its connections also becomes stronger. In Figure 6(e), we find that as β decreases towards $-\infty$ from $\beta \approx -0.9$, the degree of the

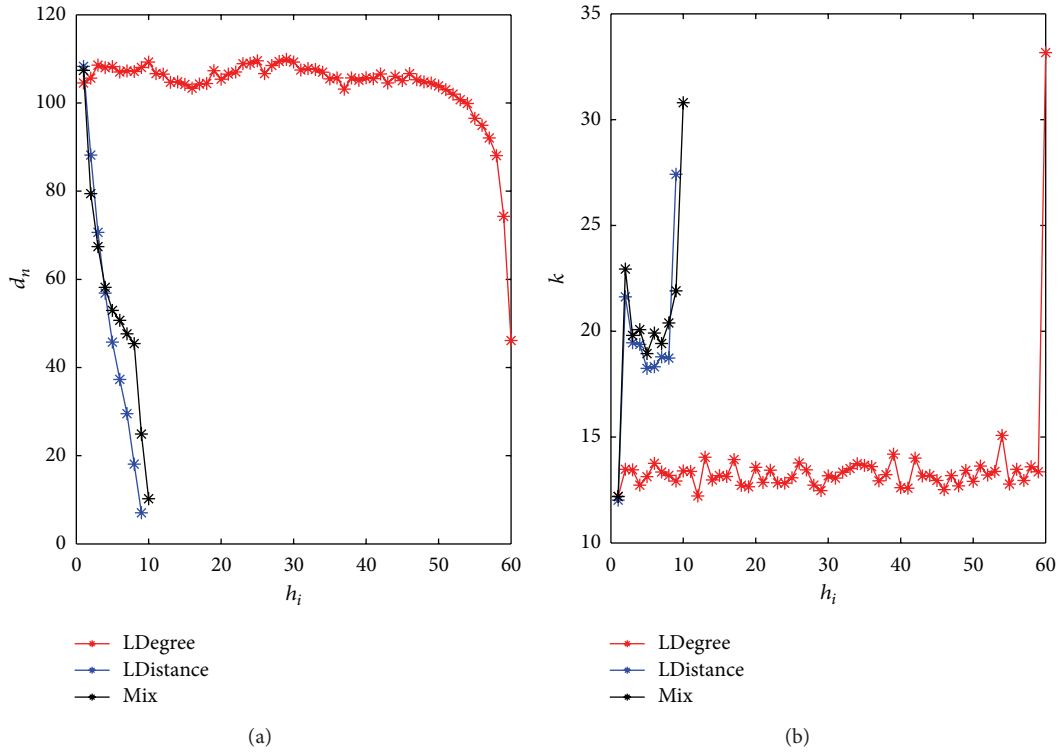

FIGURE 5: (Color online) Resized distance d_n to destination (a) and degree k (b) along transporting path for the LDegree strategy, the LDistance strategy and the mixed strategy. The horizontal axis labels the index h_i of routers along transporting path. The tunable parameters are set to $\alpha_c = -0.9$ in the LDegree strategy, $\beta_c = -1.2$ in the LDistance strategy, and $\sigma = 0.45$ because traffic capacities are maximized at these values under the given values of degree exponent $\gamma = 3$ and clustering strength $\lambda = 1.1$.

first encountered node from the source node becomes higher. Consequently, more packets can accumulate on high-degree nodes and block free flowing of traffic transport. This might be another reason why the traffic capacity becomes decreased as β decreases towards minus infinity from $\beta \approx -0.9$, as illustrated in Figure 1(a). Besides, Figure 6(d) also reveals an interesting observation. As β decreases towards minus infinity, spatial distance to destination along transporting path decays more sharply. However, under the network with very low β, for example, $\beta = -2$, when packets are delivered to nodes close to destinations in the geographical space, packets can easily get stuck on low-degree nodes. As a result, packets keep on wandering around low-degree nodes for a rather long time, and the total delivering time is heavily lengthened.

4. Discussion

The main motivation of this work stems from the scalability difficulty encountered in real large-size communication networks such as the Internet and the high-way network. Accessing global topological information (e.g., the shortest path between any two nodes) is not an easy task in large-size network due to the rapid growing communication and information processing overhead. Therefore, in current days, it is usually not convenient, or even unfeasible, to design routing strategies based on global topological information. Comparatively, spatial distances among nodes in real networks are relatively easier to be accessed. Then it is feasible and practical to utilize spatial information to design efficient strategies in real large-size communication networks.

In this paper, we propose a novel routing strategy, called the LDistance strategy, which is based on the information of spatial distances among nodes. To evaluate the performances of our proposed LDistance strategy, we compare our proposed LDistance strategy with the local routing strategy based on nodes' degrees proposed in [13] (called the LDegree strategy in this paper) and the mixed strategy, which combines the idea of both greedy routing strategy and random routing strategy. Numerical simulations demonstrate that our proposed LDistance strategy can supply a higher traffic capacity and a shorter delivering time. A reasonable explanation for the superiority of the LDistance strategy over the LDegree strategy is the interdependent relationship between topological and spatial characteristics; that is, the average topological shortest path length between any two nodes increases with the average spatial distance between the two nodes. When a packet is delivered to the neighbor closer to destination in the geographical space, the average shortest path length between the chosen neighbor and destination is also lower. On the other hand, the inclination of packets being forwarded to nodes closest to destination should also not be too strong; otherwise, packets can easily get stuck on low-degree nodes and transport efficiency can be heavily degraded. Due to the incorporating of random strategy in the mixed strategy, packets have more chance to be delivered to the neighbor with longer spatial distance to destination as

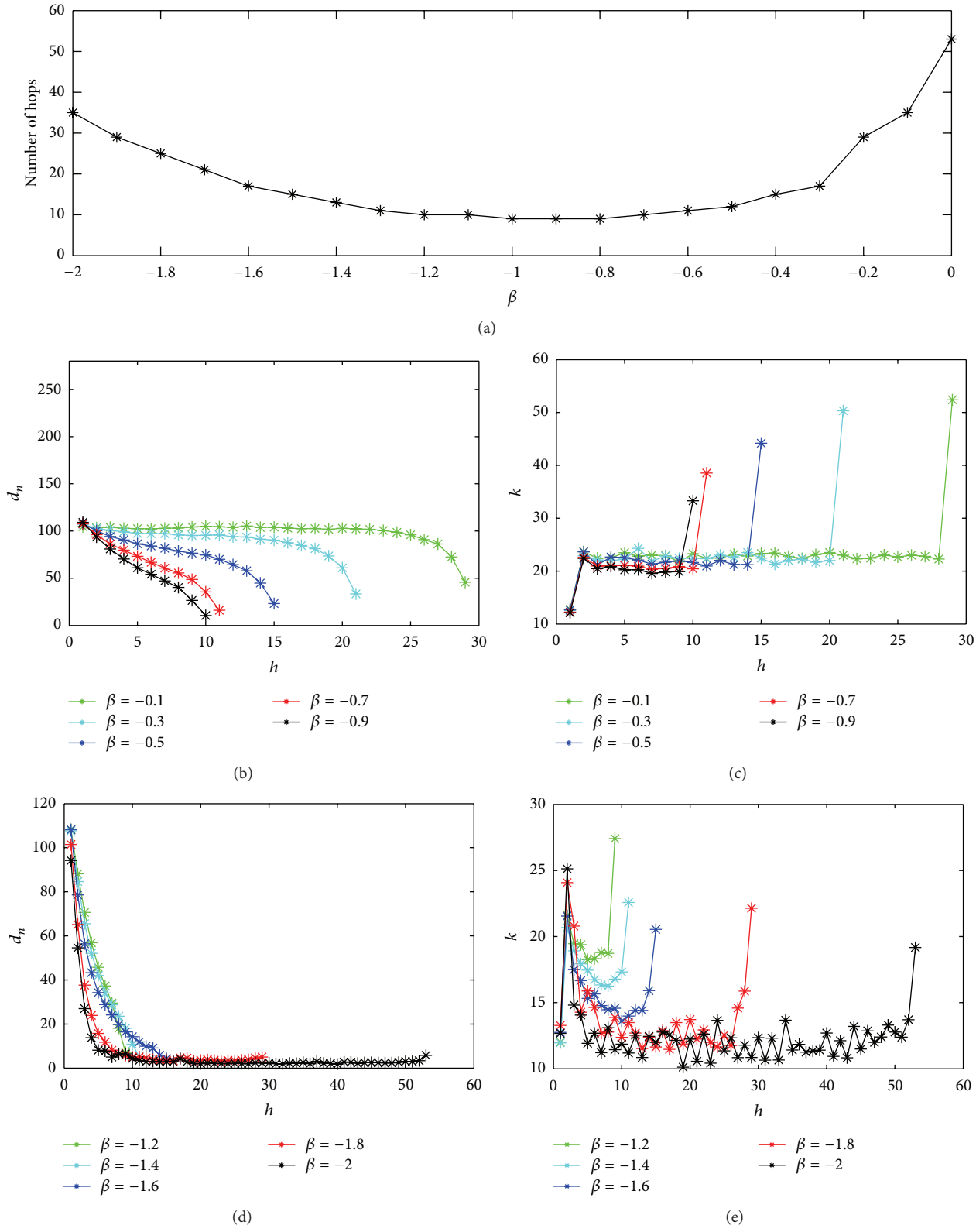

FIGURE 6: (Color online) (a) Number of hops of transporting path versus β in the LDistance strategy. (b) and (c) The changing of d_n and k versus h_i for the LDistance strategy with β above $\beta \approx -0.9$. (d) and (e) The changing of d_n and k versus h_i for the LDistance strategy with β below $\beta \approx -0.9$. All simulations were performed in the network with $\gamma = 3$ and $\lambda = 1.1$.

compared to the LDistance strategy, which is not beneficial for the enhancement of traffic capacity. Regarding the easy accessing of spatial information in large-size networks, we can conclude that our proposed LDistance strategy can be put into use in real large-size networks to achieve high transport efficiency.

We have also observed that along transporting path in the LDegree strategy, the spatial distance d to destination and the degree k keep almost did not change on most routers before packets arrive at the node very close to their destinations. Therefore, most deliveries are not so *valuable* for successful transport of packets to destination because spatial distance to destination does not show evident decrease on most routers along transporting path. On the contrary, in the LDistance strategy, along transporting path, the spatial distance to destination monotonously decreases, which means that each time of delivery is *valuable* for packets approaching destination. Furthermore, we have also noticed that, given the fixed network structure, when the maximal traffic capacities are achieved for both LDegree and LDistance strategies, the degrees of routers along transporting path in the LDistance strategy are higher than those in the LDegree strategy. This result indicates that, to enhance traffic capacity, the way of disseminating packets on low-degree nodes cannot deliver so nice performances as was evaluated previously in the LDegree strategy. Choosing routers with degrees higher than the degrees of chosen routers in the LDegree strategy can actually further improve transport efficiency.

There still remains much room for further studying traffic problems in spatial networks. For example, considering that the theory of network calculus and the technology of leaky bucket have similar goal as our study, we are about to take into account the traffic bound [33] and the bound of packet delay [34] in our further work. We believe that this study is of great importance in real large-size networks, especially in current society with system size increasing explosively. Furthermore, the utilizing of spatial information for designing routing strategies in transport systems can provide more hints for other applications such as information navigation and virus spreading in spatial networks.

Acknowledgments

This work was supported by the Natural Science Foundation of Zhejiang University of Technology (11011119021408, R1110679), the National Natural Science Foundation of China under Grant nos. 61201074 and 61173096, the Qianjiang Talents Project (QJD1202010), and Doctoral Fund of Ministry of Education of China (20113317110001).

References

[1] R. Albert and A.-L. Barabási, "Statistical mechanics of complex networks," *Reviews of Modern Physics*, vol. 74, no. 1, pp. 47–97, 2002.

[2] S. N. Dorogovtsev and J. F. F. Mendes, "Evolution of networks," *Advances in Physics*, vol. 51, no. 4, pp. 1079–1187, 2002.

[3] M. E. J. Newman, "The structure and function of complex networks," *SIAM Review*, vol. 45, no. 2, pp. 167–256, 2003.

[4] R. Pastor-Satorras and A. Vespignani, *Evolution and Structure of the Internet: A Statistical Physics Approach*, Cambridge University Press, Cambridge, UK, 2004.

[5] R. Albert, I. Albert, and G. L. Nakarado, "Structural vulnerability of the North American power grid," *Physical Review E*, vol. 69, no. 2, Article ID 025103, 4 pages, 2004.

[6] R. Guimerà, S. Mossa, A. Turtschi, and L. A. N. Amaral, "The worldwide air transportation network: Anomalous centrality, community structure, and cities' global roles," *Proceedings of the National Academy of Sciences of the United States of America*, vol. 102, no. 22, pp. 7794–7799, 2005.

[7] M. Barthélemy, "Spatial networks," *Physics Reports*, vol. 499, no. 1-3, pp. 1–101, 2011.

[8] M. Ángeles Serrano, D. Krioukov, and M. Boguñá, "Self-similarity of complex networks and hidden metric spaces," *Physical Review Letters*, vol. 100, no. 7, Article ID 078701, 2008.

[9] H. Yang, Y. Nie, A. Zeng, Y. Fan, Y. Hu, and Z. Di, "Scaling properties in spatial networks and their effects on topology and traffic dynamics," *Europhysics Letters*, vol. 89, no. 5, Article ID 58002, 2010.

[10] B.-H. Wang and T. Zhou, "Traffic flow and efficient routing on scale-free networks: a survey," *Journal of the Korean Physical Society*, vol. 50, no. 1 I, pp. 134–141, 2007.

[11] S. Chen, W. Huang, C. Cattani, and G. Altieri, "Traffic dynamics on complex networks: a survey," *Mathematical Problems in Engineering*, vol. 2012, Article ID 732698, 2012.

[12] R. Pastor-Satorras, A. Vázquez, and A. Vespignani, "Dynamical and correlation properties of the internet," *Physical Review Letters*, vol. 87, no. 25, Article ID 258701, pp. 258701/1–258701/4, 2001.

[13] W.-X. Wang, B.-H. Wang, C.-Y. Yin, Y.-B. Xie, and T. Zhou, "Traffic dynamics based on local routing protocol on a scale-free network," *Physical Review E*, vol. 73, no. 2, Article ID 026111, 2006.

[14] Z. Y. Chen and X. F. Wang, "Effects of network structure and routing strategy on network capacity," *Physical Review E*, vol. 73, no. 3, Article ID 036107, 2006.

[15] W. X. Wang, C. Y. Yin, G. Yan, and B. H. Wang, "Integrating local static and dynamic information for routing traffic," *Physical Review E*, vol. 74, no. 1, Article ID 016101, 2006.

[16] P. Echenique, J. Gómez-Gardeñes, and Y. Moreno, "Improved routing strategies for Internet traffic delivery," *Physical Review E*, vol. 70, no. 5, Article ID 056105, pp. 1–56105, 2004.

[17] P. Echenique, J. Gómez-gardeñes, and Y. Moreno, "Dynamics of jamming transitions in complex networks," *Europhysics Letters*, vol. 71, no. 2, pp. 325–331, 2005.

[18] Z. Wu, G. Peng, W. Wong, and K. Yeung, "Improved routing strategies for data traffic in scale-free networks," *Journal of Statistical Mechanics*, Article ID P11002, 2008.

[19] W. Huang and T. W. S. Chow, "Investigation of both local and global topological ingredients on transport efficiency in scale-free networks," *Chaos*, vol. 19, no. 4, Article ID 043124, 2009.

[20] B. Danila, Y. Yu, J. A. Marsh, and K. E. Bassler, "Optimal transport on complex networks," *Physical Review E*, vol. 74, no. 4, Article ID 046106, 2006.

[21] B. Danila, Y. Yu, J. A. Marsh, and K. E. Bassler, "Transport optimization on complex networks," *Chaos*, vol. 17, no. 2, Article ID 026102, 9 pages, 2007.

[22] G. Yan, T. Zhou, B. Hu, Z. Q. Fu, and B. H. Wang, "Efficient routing on complex networks," *Physical Review E*, vol. 73, no. 4, Article ID 046108, 2006.

[23] M. Boguñá, D. Krioukov, and K. C. Claffy, "Navigability of complex networks," *Nature Physics*, vol. 5, no. 1, pp. 74–80, 2009.

[24] M. Boguñá and D. Krioukov, "Navigating ultrasmall worlds in ultrashort time," *Physical Review Letters*, vol. 102, no. 5, Article ID 058701, 2009.

[25] K. Tutschku and P. Tran-Gia, "Spatial traffic estimation and characterization for mobile communication network design," *IEEE Journal on Selected Areas in Communications*, vol. 16, no. 5, pp. 804–811, 1998.

[26] W. Li, M. Canini, A. W. Moore, and R. Bolla, "Efficient application identification and the temporal and spatial stability of classification schema," *Computer Networks*, vol. 53, no. 6, pp. 790–809, 2009.

[27] S. Uhlig, "On the complexity of Internet traffic dynamics on its topology," *Telecommunication Systems*, vol. 43, no. 3-4, pp. 167–180, 2010.

[28] R. J. Adler, R. E. Feldman, and M. S. Taqqu, *Practical Guide to Heavy Tails: Statistical Techniques and Applications*, Birkhäuser, Boston, Mass, USA, 1998.

[29] M. Li and W. Zhao, "On $1/f$ noise," *Mathematical Problems in Engineering*, vol. 2012, Article ID 673648, 23 pages, 2012.

[30] R. G. Clegg, C. Di Cairano-Gilfedder, and S. Zhou, "A critical look at power law modelling of the Internet," *Computer Communications*, vol. 33, no. 3, pp. 259–268, 2010.

[31] A. Arenas, A. Díaz-Guilera, and R. Guimerà, "Communication in networks with hierarchical branching," *Physical Review Letters*, vol. 86, no. 14, pp. 3196–3199, 2001.

[32] M. E. Newman, "Assortative mixing in networks," *Physical Review Letters*, vol. 89, no. 20, Article ID 208701, 2002.

[33] M. Li and W. Zhao, "Representation of a stochastic traffic bound," *IEEE Transactions on Parallel and Distributed Systems*, vol. 21, no. 9, pp. 1368–1372, 2010.

[34] M. Li, W. Zhao, and C. Cattani, "Delay bound: fractal traffic passes through network servers," *Mathematical Problems in Engineering*, vol. 2013, Article ID 157636, 2013.

Hindawi Publishing Corporation
Advances in Mathematical Physics
Volume 2013, Article ID 651357, 7 pages
http://dx.doi.org/10.1155/2013/651357

Research Article

Interval Wavelet Numerical Method on Fokker-Planck Equations for Nonlinear Random System

Li-wei Liu

Department of Mechanical Engineering, North China Institute of Aerospace Engineering, Langfang, Hebei 065000, China

Correspondence should be addressed to Li-wei Liu; liwei_liu@yeah.net

Received 3 August 2013; Accepted 19 September 2013

Academic Editor: Carlo Cattani

The Fokker-Planck-Kolmogorov (FPK) equation governs the probability density function (p.d.f.) of the dynamic response of a particular class of linear or nonlinear system to random excitation. An interval wavelet numerical method (IWNM) for nonlinear random systems is proposed using interval Shannon-Gabor wavelet interpolation operator. An FPK equation for nonlinear oscillators and a time fractional Fokker-Planck equation are taken as examples to illustrate its effectiveness and efficiency. Compared with the common wavelet collocation methods, IWNM can decrease the boundary effect greatly. Compared with the finite difference method for the time fractional Fokker-Planck equation, IWNM can improve the calculation precision evidently.

1. Introduction

The Fokker-Planck equation describes the time evolution of the probability density function of the velocity of a particle, and can be generalized to other observables as well. It is named after Adriaan Fokker and Max Planck and is also known as the Kolmogorov forward equation (diffusion), named after Andrey Kolmogorov, who first introduced it in a 1931 paper. When applied to particle position distributions, it is better known as the Smoluchowski equation. The case with zero diffusion is known in statistical mechanics as Liouville equation. In order to describe subdiffusive behavior of a particle under the combined influence of external nonlinear force field and a Boltzmann thermal heat bath, Metzler et al. introduced a fractional Fokker-Planck equation (FFPE) which was shown to obey generalized Einstein relations, and its stationary solution is the Boltzmann distribution [1].

Many methods for calculating nonlinear random response have been developed by numerous scholars over a long period of time. One type of these methods is the diffuseness process theory method, and the primarily one is Fokker-Planck equation method. In practice, the most difficult problem of using Fokker-Planck equation method is how to solve the equation. For general nonlinear system, it is very difficult to obtain the exact solution. Various numerical methods have been used to solve the Fokker-Planck equation, such as the weighted residual method [2], the finite element method [3], and the path integral method [4] and so on. The Galerkin method for the numerical solution of the stationary Fokker-Planck equation developed by Bhandari and Sherrer is based on taking multiple Hermite polynomial as joint probability density, but the rate of convergence of this method is slow for strong nonlinear system. Based on Galerkin method, a finite element method for Fokker-Planck equation was developed by Langley; this method is more efficient than Galerkin method in computation. The common problem of these three methods is that the error at the tails and peak of the response distribution is larger. As a numerical approach method, the moment equation method, including the non-Gaussian moment-cutting method for nonlinear random vibration, was developed [5].

Recently the wavelet analysis is getting high attention to many authors for the nonlinear dynamic system, not only for the signal analysis but also for developing new numerical methods for calculating the partial difference equations. Bertoluzza and Naldi presented a wavelet collocation method for solving the partial differential equations [6] in 1996. In this method, the autocorrelation function of the Daubechies scaling functions was used as the weight function. The autocorrelation function of the Daubechies wavelet functions possesses interpolation properties due to the orthogonality properties of Daubechies wavelets. Therefore, the numerical

solution of the discrete format of the partial differential equation, which was obtained by wavelet collocation method, is an approximation solution of the partial differential equation. This method is not similar to the wavelet Galerkin method, which needs going back and forth between the space of wavelet coefficients and physical space. On the other hand, the Daubechies scaling functions and the corresponding wavelet function have no explicit expressions, which limit its applications to some extents. Cattani studied the properties of the Shannon wavelet function, which possesses many advantages such as orthogonality, being continuous, and being differentiable. It also has the advantage over the Hermite DAF in that it is an interpolating function, producing matrix equations that have the potential to be relatively sparse. In addition, the second order approximation of a C^2-function, based on Shannon wavelet functions, is given [7]. The approximation is compared with the wavelet reconstruction formula and the error of approximation is explicitly computed [8]. The advantages of the Shannon wavelet have been illustrated in solving PDEs in engineering [9–11]. McWilliam et al. [12] presented a Shannon wavelet collocation method for stationary Fokker-Planck equation. The Shannon scaling function was taken as the weight function in this method, which can avoid the shortcomings of Daubechies wavelet such as the interpolation property. Based on the theory of this method, the specific procedure for solving stationary Fokker-Planck equation, the analysis of the problems existed in this method, and the remedies of the problems were presented in this paper. But the Shannon wavelet has no compact support property which can decrease the efficiency and computational accuracy. Compared with Shannon wavelet function, Shannon-Gabor wavelet [13, 14] possesses better compact support property, which has been widely employed in various mechanical analysis fields [15] including solving the FPK equation [16]. Furthermore, Shi et al. [17] constructed the Shannon-Gabor wavelet defined in the interval based on the Lagrange interpolation theory, which can decrease the boundary effect effectively.

Mei proposed a general construction method of the interval wavelet based on the general variational principle [18] and took the Shannon-Gabor wavelet as example to illustrate its correctness, which has been employed to eliminate the boundary effect in solving PDEs such as the image processing [19], stochastic analysis [20, 21], option pricing [22], hydrodynamics [23–26], and image segmentation [27]. The purpose of this paper is to construct an interval Shannon-Gabor wavelet collocation method on solving Fokker-Planck equation for nonlinear oscillators and a time fractional Fokker-Planck equation describing a subdiffusive behavior of a particle under the combined influence of external nonlinear force field and a Boltzmann thermal heat bath [28].

2. Shannon-Gabor Wavelet Collocation Method

2.1. Construction of the Basis Function. Consider a one dimension function $f(x)$. In order to take Shannon scaling function as basic function, in term of the multiresolution analysis theory, the function $f(x)$ needs to be discretized uniformly in range of [a, b], which is the domain of definition of it. Let the number of the discrete points is $2^j + 1$, $(j \in Z)$, and the definition of the discrete point of variable x is

$$x_i = a + \frac{b-a}{2^j} \cdot i. \tag{1}$$

Then we can obtain the basic function as follows:

$$w_j(x - x_i) = \frac{\sin\left(2^j\pi/(b-a)\right)(x - x_i)}{\left(2^j\pi/(b-a)\right)(x - x_i)} \times \exp\left(-\frac{2^{2j-1}(x - x_i)^2}{r^2(b-a)^2}\right). \tag{2}$$

Using the theory of Fourier transform, it can be proved that the basic function $\omega(x - x_i)$ satisfied the conclusions as follows:

$$w_j(x_i - x_k) = \delta_{ik}, \qquad \delta_{ik} = \begin{cases} 1, & i = k, \\ 0, & i \neq k, \end{cases}$$

$$\int_{-\infty}^{\infty} w_j(x - x_i)\, w_j(x - x_k) = \frac{b-a}{2^j}\delta_{ik}, \tag{3}$$

$$\int_{-\infty}^{\infty} w_j(x - x_i)\frac{d^n w_j(x - x_k)}{dx^n} = \frac{b-a}{2^j}\frac{d^n w_j(x - x_k)}{dx^n}.$$

The two dimension basic function can be expressed by tensor product of the one dimension basic function. In two dimension scaling function space, to each $j \in Z$, V_j can be expressed as $V_j = v_j \otimes v_j$, and so the corresponding basic function is

$$W_{j,n_1,n_2}(x, y) = w_j\left(x - x_{n_1}\right) w_j\left(x - x_{n_2}\right). \tag{4}$$

In a similar way, the basic function of **n** dimension space can be expressed as

$$W_{j,n_1,n_2,\ldots n_n}(x_1, x_2, \ldots, x_n) = \prod_{m=1}^{n} w_j\left(x_m - x_{mn_m}\right). \tag{5}$$

According to the interval interpolation basic functions, the Shannon-Gabor interval wavelet can be obtained as follows:

$$w_{jk} = w\left(2^j x - k\right) + \sum_{n=-N+1}^{-1} a_{nk} w\left(2^j x - n\right), \quad k = 0, \ldots, L,$$

$$w_{jk} = w\left(2^j x - k\right), \quad k = L+1, \ldots, 2^j - L - 1, \tag{6}$$

$$w_{jk} = w\left(2^j x - k\right) + \sum_{n=2^j+1}^{2^j+N-1} b_{nk} w\left(2^j x - n\right), \quad k = 2^j - L, \ldots, 2^j.$$

a_{nk} and b_{nk} could be calculated, respectively, as

$$a_{nk} = l^1_{jk}\left(x_{jn}\right), \qquad b_{nk} = l^2_{jk}\left(x_{jn}\right),$$
$$l^1_{j,k} = \prod_{\substack{i=-L-1 \\ i\neq k}}^{-1} \frac{x - x_{j,i}}{x_{j,k} - x_{j,i}}, \qquad l^2_{j,k} = \prod_{\substack{i=2^j+1 \\ i\neq k}}^{2^j+1+L} \frac{x - x_{j,i}}{x_{j,k} - x_{j,i}}, \tag{7}$$

where L is the number of the external points, and N is the support domain of the wavelet function, that is, $\sup\phi = [-N, N]$.

It is easy to know that the Shannon-Gabor interval wavelet is a linear combination of the Shannon-Gabor scaling function $w_{j,k}(x)$. Therefore, the Shannon-Gabor interval wavelet function possesses all the properties of the Shannon-Gabor scaling function.

It should be noted that the construction method of the interval wavelet function reveals the close relationship between the restricted variational principle and the interval interpolation wavelet.

2.2. Discrete Format of the Fokker-Planck Equation. Consider the following two-dimension stationary Fokker-Planck equation:

$$\frac{\partial\left(a_1 p\right)}{\partial x} + \frac{\partial\left(a_2 p\right)}{\partial y} - \frac{1}{2}\frac{\partial^2\left(b_{11} p\right)}{\partial x^2} - \frac{1}{2}\frac{\partial^2\left(b_{22} p\right)}{\partial y^2} - \frac{1}{2}\frac{\partial^2\left(b_{12} p\right)}{\partial x \partial y} - \frac{1}{2}\frac{\partial^2\left(b_{21} p\right)}{\partial x \partial y} = 0, \tag{8}$$

where

$$a_1 = \lim_{\Delta t\to 0}\frac{1}{\Delta t}E\left[z_1 - x\right],$$
$$a_2 = \lim_{\Delta t\to 0}\frac{1}{\Delta t}E\left[z_2 - y\right],$$
$$b_{12} = b_{21} = \lim_{\Delta t\to 0}\frac{1}{\Delta t}E\left[\left(z_1 - x\right)\left(z_2 - y\right)\right], \tag{9}$$
$$b_{11} = \lim_{\Delta t\to 0}\frac{1}{\Delta t}E\left[\left(z_1 - x\right)^2\right],$$
$$b_{22} = \lim_{\Delta t\to 0}\frac{1}{\Delta t}E\left[\left(z_2 - y\right)^2\right].$$

The unknown quantity p denotes transitional probability density function $p(x, y)$, which can be expressed as

$$p\left(x, y\right) \approx p_j\left(x, y\right) = \sum_{n_1=0}^{2^j}\sum_{n_2=0}^{2^j} p_j\left(x_{n_1}, y_{n_2}\right) w_j\left(x - x_{n_1}\right) w_j\left(y - y_{n_2}\right). \tag{10}$$

In general, $a_1, a_2, b_{11}, b_{12}, b_{21}, b_{22}$ are the known function on the variables x and y. To avoid having to perform the complicated integration presented in the collocation method, those aforementioned known functions can be expressed as a sum of shape functions, such that

$$\begin{aligned} a_m\left(x, y\right)\cdot p\left(x, y\right) &\approx a_{jm}\left(x, y\right) p_j\left(x, y\right) \\ &= \sum_{n_1=0}^{2^j}\sum_{n_2=0}^{2^j} a_{jm}\left(x_{n_1}, y_{n_2}\right) p_j\left(x_{n_1}, y_{n_2}\right) \\ &\qquad \times w_j\left(x - x_{n_1}\right) w_j\left(y - y_{n_2}\right) \\ b_{mn}\left(x, y\right)\cdot p\left(x, y\right) &\approx b_{jmn}\left(x, y\right) p_j\left(x, y\right) \\ &= \sum_{n_1=0}^{2^j}\sum_{n_2=0}^{2^j} b_{jmn}\left(x_{n_1}, y_{n_2}\right) p_j\left(x_{n_1}, y_{n_2}\right) \\ &\qquad \times w_j\left(x - x_{n_1}\right) w_j\left(y - y_{n_2}\right), \end{aligned} \tag{11}$$

where $m = 1, n = 2$.

In terms of the theory of collocation method, substituting (11) into (8), we can obtain the system of equations as follows:

$$\int W_{j,k_1,k_2}\left[\frac{\partial\left(a_{j1} p_j\right)}{\partial x} + \frac{\partial\left(a_{j2} p_j\right)}{\partial y} - \frac{1}{2}\frac{\partial^2\left(b_{j11} p_j\right)}{\partial x^2} - \frac{1}{2}\frac{\partial^2\left(b_{j22} p_j\right)}{\partial y^2} - \frac{1}{2}\frac{\partial^2\left(b_{j12} p_j\right)}{\partial x\,\partial y} - \frac{1}{2}\frac{\partial^2\left(b_{j21} p_j\right)}{\partial x \partial y}\right] dx\,dy = 0, \tag{12}$$

where $k_1, k_2 = 0, 1, 2, \ldots, 2^j$.

Using (3) and integrating with respect to (12), the system of equations can be obtained as follows:

$$\sum_{n_1=0}^{2^j}\sum_{n_2=0}^{2^j} p_j\left(x_{n_1}, y_{n_2}\right) \times \left[a_{j1}\left(x_{n1}, y_{n2}\right)\delta_{k_2 n_2}\frac{\partial w\left(x_{k_1} - x_{n_1}\right)}{\partial x} + a_{j2}\left(x_{n1}, y_{n2}\right)\delta_{k_1 n_1}\frac{\partial w\left(y_{k_2} - y_{n_2}\right)}{\partial y} - \frac{1}{2}b_{j11}\left(x_{n1}, y_{n2}\right)\delta_{k_2 n_2}\frac{\partial w^2\left(x_{k_1} - x_{n_1}\right)}{\partial x^2} - \frac{1}{2}b_{j22}\left(x_{n1}, y_{n2}\right)\delta_{k_1 n_1}\frac{\partial w^2\left(y_{k_2} - y_{n_2}\right)}{\partial y^2}$$

$$-b_{j12}\left(x_{n1}, y_{n2}\right)\frac{\partial w\left(x_{k_1}-x_{n_1}\right)}{\partial x}\frac{\partial w\left(y_{k_2}-y_{n_2}\right)}{\partial y}\Bigg] = 0, \tag{13}$$

where, $k_1, k_2 = 0, 1, 2, \ldots, 2^j$.

As the basic function is the Shannon scaling function which possess explicit expression, so it is easy to deduce the first and second derivative of the basic function w as follows:

$$\frac{\partial\left(x_k - x_n\right)}{\partial x} = \begin{cases} 0, & k = n, \\ \dfrac{2^j \cos\left[\pi\left(k-n\right)\right]}{\left(b-a\right)}, & k \neq n, \end{cases} \tag{14}$$

$$\frac{\partial^2\left(x_k - x_n\right)}{\partial x^2} = \begin{cases} -\dfrac{2^{2j+1}\pi^2}{6(b-a)^2}, & k = n, \\ -\dfrac{2^{2j+1}\cos\left[\pi\left(k-n\right)\right]}{(b-a)^2(k-n)^2}, & k \neq n. \end{cases} \tag{15}$$

Instituting (14) and (15) into (13), a system of homogenous algebraic equations can be deduced, such that

$$\mathbf{AP} = 0. \tag{16}$$

This is the discrete format of stationary Fokker-Planck equation in equinoctial points of the domain of definition.

2.3. Solution of the Discrete Format of Fokker-Planck Equation. In the system of (16), **A** is a square matrix; vector **P** contains the values of the j.p.d.f. on the mesh of equinoctial points. Equation (16) can be solved by prescribing the value of $p(x, y)$ at node 1 to be some constant C, whichs lead to

$$\mathbf{A}_1\mathbf{P}_1 = \mathrm{C}\mathbf{V}, \tag{17}$$

where $\mathbf{A}_1$ is the matrix **A** without the first row or column, $\mathbf{P}_1$ is the vector of nodal values from node 2 onwards, and **V** is the first column of **A** with the first entry omitted. This then yields the value of $p(x, y)$ at each node in terms of C. Finally, C can be evaluated by imposing the normalization property

$$\int_{a_1}^{b_1}\int_{a_2}^{b_2} p\left(x, y\right)dx\,dy = 1, \tag{18}$$

where a_1, b_1 and a_2, b_2 are numeric area of the variables x and y. So we should firstly evaluate the value of a_1, b_1 and a_2, b_2. They can be obtained approximately from the solution of the random vibration differential equation by using the equivalent linear linearization method. Based on the equivalent linearization results, the numeric area of the variables x and y can be evaluated.

3. Numerical Experiments

Example 1. In this section the method was applied to the random vibration of a Duffing oscillator, the equation of motion for which is [2]

$$\ddot{x} + 2\beta\omega_n\dot{x} + {\omega_n}^2\left(1 + \gamma x^2\right)x = F\left(t\right), \tag{19}$$

where $F(t)$ is Gaussian white noise, taken here to have a spectral density of $(1/\pi)$. Putting $z_1 = x$, $z_2 = \dot{x}$, (19) is deduced to

$$\begin{pmatrix}\dot{z}_1 \\ \dot{z}_2\end{pmatrix} = \begin{pmatrix} z_2 \\ -2\beta\omega_n z_2 - {\omega_n}^2\left(z_1 + \gamma {z_1}^3\right)\end{pmatrix} + \begin{pmatrix}0 & 0 \\ 0 & \pi^{1/2}\end{pmatrix}\begin{pmatrix}0 \\ W\left(t\right)\end{pmatrix}, \tag{20}$$

and so we obtain the Fokker-Planck equation as follows:

$$\frac{\partial}{\partial z_1}\left(z_2 p\right) - \frac{\partial}{\partial z_2}\left\{\left[2\beta\omega_n z_2 + {\omega_n}^2\left(z_1 + \gamma {z_1}^3\right)\right]p\right\} - \frac{\partial^2 p}{\partial {z_2}^2} = 0. \tag{21}$$

The exact analytical solution of (21) is

$$p\left(z_1, z_2\right) = C\exp\left[-2\beta\omega_n\left(\frac{1}{2}{z_2}^2 + \frac{1}{2}{\omega_n}^2{z_1}^2 + \frac{1}{4}{\omega_n}^2\gamma {z_1}^4\right)\right], \tag{22}$$

where C is chosen to satisfy the normalization condition, (14).

For the case $\omega_n = 1$, $\beta = 0.5$, $\gamma = 0.1$, the r.m.s. values of the response of displacement and velocity are $\sigma_x = 0.7407$ and $\sigma_{\dot{x}} = 1.0$, which were obtained from the equivalent linear linearization method. Based on this result, a finite region of $-3 \le x \le 3$, $-6 \le y \le 6$ was chosen for the wavelet collocation method.

The numerical results $p_j(x, 0)$, $p_j(0, y)$ and exact result $p_{je}(x, 0)$, $p_{je}(0, y)$ are plotting in Figure 1. It can be seen that the proposed method gives excellent agreement with the exact result, both over the main body of the curve and up to the tails.

The comparison between the wavelet and interval wavelet collocation method for FPK equation is shown in Figure 2. It is easy to see that the error of the interval wavelet collocation method is smaller evidently than the common wavelet method in solving the FPK equation. It is not difficult to understand that the boundary effect of the common wavelet numerical method enlarges the error in the whole definition domain. This illustrates the effect of the interval wavelet numerical method to some extent.

Example 2. Time fractional Fokker-Planck equations have been recently treated by a number of authors and are found to be a useful approach for the description of transport dynamics in complex systems that are governed by anomalous diffusion and nonexponential relaxation patterns. Fractional derivatives play a key role in modeling particle transport in anomalous diffusion. Wei [14] introduced a time fractional extension of the FPK equation, namely, the time-fractional Fokker-Planck equations as follows:

$$\frac{\partial u\left(x,t\right)}{\partial t} = {}_0D_t^{1-\alpha}\left[\frac{\partial}{\partial x}\left(-1\right) + \frac{\partial^2}{\partial x^2}\right]u\left(x,t\right), \quad 0 \le x \le 1,\ t > 0 \tag{23}$$

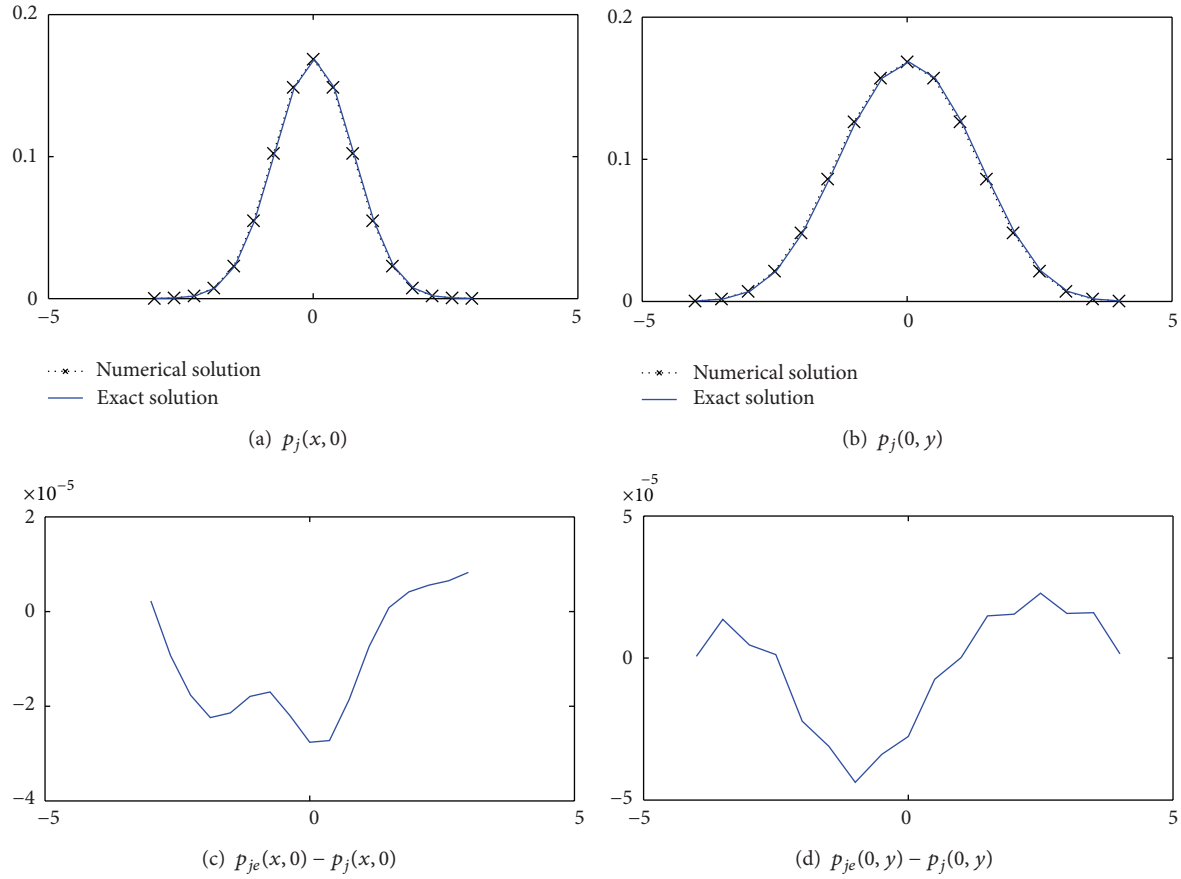

Figure 1: The comparison between numerical solution and exact solution.

with initial condition

$$u(x,0) = x(1-x), \quad 0 \le x \le 1, \tag{24}$$

and boundary conditions

$$\begin{aligned} u(0,t) &= -\frac{3t^{\alpha}}{\Gamma(1+\alpha)} - \frac{2t^{2\alpha}}{\Gamma(1+2\alpha)}, \quad t > 0, \\ u(1,t) &= -\frac{t^{\alpha}}{\Gamma(1+\alpha)} - \frac{2t^{2\alpha}}{\Gamma(1+2\alpha)}, \quad t > 0. \end{aligned} \tag{25}$$

The exact analytical solution of the time-fractional Fokker-Planck equation can be expressed as

$$u(x,t) = x(1-x) + (2x-3)\frac{t^{\alpha}}{\Gamma(1+\alpha)} - \frac{2t^{2\alpha}}{\Gamma(1+2\alpha)}. \tag{26}$$

As mentioned above, the solution of (23) can be expressed approximately as

$$u(x) \approx u_j(x) = \sum_{n=0}^{2^j} u_j(x_n)\, w_j(x - x_n). \tag{27}$$

Substituting (27) into (23), we can obtain

$$\begin{aligned} &{}_0D_t^{1-\alpha}\left(\sum_{n=0}^{2^j} u_j(x_n,t)\left[\omega''(x_k - x_n) - \omega'(x_k - x_n)\right]\right) \\ &\quad = \frac{du_j(x_k,t)}{dt}, \end{aligned} \tag{28}$$

where $k = 0, 1, 2, \ldots, 2^j$. Let

$$\begin{aligned} \mathbf{U}(t) &= \left(u_j(x_0,t), u_j(x_1,t), \ldots, u_j(x_{2^j},t)\right)^T, \\ \mathbf{W}_1 &= \begin{bmatrix} \omega'(x_0 - x_0) & \omega'(x_0 - x_1) & \cdots & \omega'(x_0 - x_{2^j}) \\ \omega'(x_1 - x_0) & \omega'(x_1 - x_1) & \cdots & \omega'(x_1 - x_{2^j}) \\ \vdots & \vdots & \ddots & \vdots \\ \omega'(x_{2^j} - x_0) & \omega'(x_{2^j} - x_1) & \cdots & \omega'(x_{2^j} - x_{2^j}) \end{bmatrix}, \\ \mathbf{W}_2 &= \begin{bmatrix} \omega''(x_0 - x_0) & \omega''(x_0 - x_1) & \cdots & \omega''(x_0 - x_{2^j}) \\ \omega''(x_1 - x_0) & \omega''(x_1 - x_1) & \cdots & \omega''(x_1 - x_{2^j}) \\ \vdots & \vdots & \ddots & \vdots \\ \omega''(x_{2^j} - x_0) & \omega''(x_{2^j} - x_1) & \cdots & \omega''(x_{2^j} - x_{2^j}) \end{bmatrix}, \\ \mathbf{M} &= \mathbf{W}_2 - \mathbf{W}_1. \end{aligned} \tag{29}$$

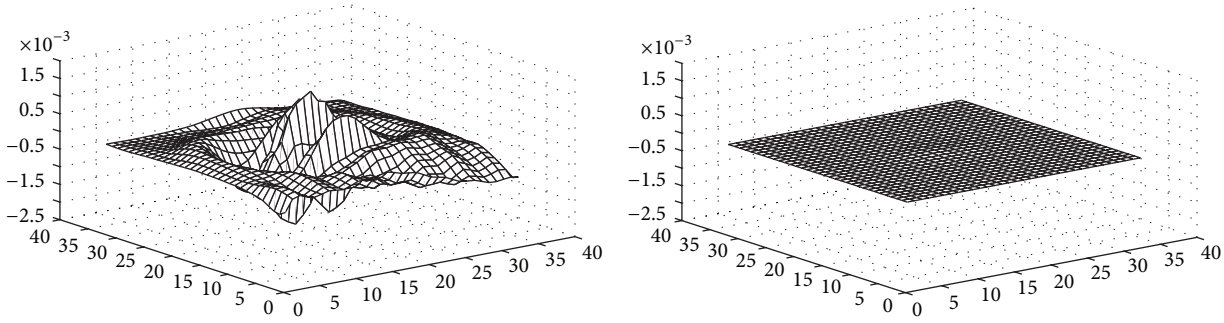

(a) Shannon-Gabor wavelet numerical method (the maximum of the absolute error is 2.2470×10^{-3})

(b) Interval Shannon-Gabor wavelet numerical method (the maximum of the absolute error is 4.1769×10^{-6})

Figure 2: Error comparison between the wavelet and the interval wavelet numerical methods for FPK equation.

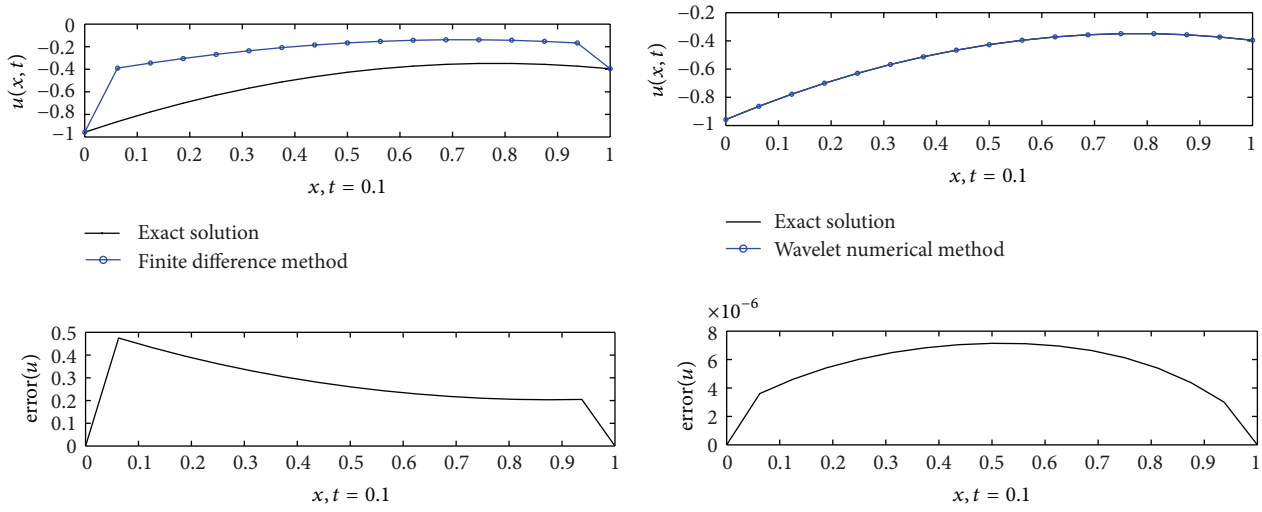

(a) Finite difference method

(b) Wavelet numerical method

Figure 3: Comparison between the finite difference method and the wavelet numerical method in solving the time fractional FPK equation ($\alpha = 0.6$, $t = 0.1$, $\tau = 0.0001$, $j = 4$).

We can obtain the discretized format to solve the time-fractional FPK equations as follows:

$$\mathbf{MU}\left(t_{n+1}\right) = -\sum_{k=1}^{n} g_k \mathbf{U}\left(t_{n-k+1}\right) + \sum_{k=0}^{n} g_k \mathbf{U}\left(t_0\right), \qquad \mathbf{MU}\left(t_1\right) = \mathbf{U}\left(t_0\right). \tag{30}$$

The comparison between the finite difference method and the wavelet numerical method in solving the time fractional FPK equation is shown in Figure 3. Although the iteration times are only 1000, the error of the numerical solution obtained by the finite difference method becomes larger evidently than one obtained by the wavelet numerical method. It should be noticed that the effect of the interval wavelet is limited as the explicit boundary condition in this example.

4. Conclusions

Compared with the finite difference method, the Shannon-Gabor wavelet numerical method possesses more excellent numerical properties in solving the FPK equations, which has been illustrated in solving the time-fractional FPK equations. Based on the interpolation properties of the Shannon-Gabor wavelet, the interval interpolation wavelet collocation method based on the wavelet interpolation technique has been developed to solve the two dimension Fokker-Planck equation in a finite domain in this paper. This new method can decrease the boundary effect evidently and then decrease the numerical error in the whole in the definition domain greatly. We believe that the method can be easily generalized to rectangular higher dimension case. The comparisons with other numerical algorithms show that the method is competitive and efficient. Furthermore, it should be noted that the method can also be used to solve general partial differential equation.

References

[1] R. Metzler, E. Barkai, and J. Klafter, "Anomalous diffusion and relaxation close to thermal equilibrium: a fractional Fokker-Planck equation approach," *Physical Review Letters*, vol. 82, no. 18, pp. 3563–3567, 1999.

[2] R. G. Bhandari and R. E. Sheerer, "Random vibrations in discrete nonlinear dynamic systems," *Journal Mechanical Engineering Science*, vol. 10, no. 2, pp. 168–174, 1968.

[3] R. S. Langley, "A finite element method for the statistics of nonlinear random vibration," *Journal of Sound and Vibration*, vol. 101, no. 1, pp. 41–54, 1985.

[4] M. F. Wehner and W. G. Wolfer, "Numerical evaluation of path-integral solutions to Fokker-Planck equations," *Physical Review A*, vol. 27, no. 5, pp. 2663–2670, 1983.

[5] Z. Senwen, C. Quifu, and Z. Honghui, "Random responses of a two-degree-of-freedom structure with strongly nonlinear coupling and parametric interaction," *Acta Mechanica Sinica*, vol. 9, no. 3, pp. 240–250, 1993.

[6] S. Bertoluzza and G. Naldi, "A wavelet collocation method for the numerical solution of partial differential equations," *Applied and Computational Harmonic Analysis*, vol. 3, no. 1, pp. 1–9, 1996.

[7] C. Cattani and L. M. S. Ruiz, "Discrete differential operators in multidimensional haar wavelet spaces," *International Journal of Mathematics and Mathematical Sciences*, vol. 2004, no. 44, pp. 2347–2355, 2004.

[8] C. Cattani, "Harmonic wavelets towards the solution of nonlinear PDE," *Computers and Mathematics with Applications*, vol. 50, no. 8-9, pp. 1191–1210, 2005.

[9] C. Cattani, "Connection coefficients of Shannon wavelets," *Mathematical Modelling and Analysis*, vol. 11, no. 2, pp. 117–132, 2006.

[10] C. Cattani, "Shannon wavelets theory," *Mathematical Problems in Engineering*, vol. 2008, Article ID 164808, 24 pages, 2008.

[11] C. Cattani, "Shannon wavelets for the solution of integrodifferential equations," *Mathematical Problems in Engineering*, vol. 2010, Article ID 408418, 22 pages, 2010.

[12] S. McWilliam, D. J. Knappett, and C. H. J. Fox, "Numerical solution of the stationary FPK equation using Shannon wavelets," *Journal of Sound and Vibration*, vol. 232, no. 2, pp. 405–430, 2000.

[13] D. K. Hoffman, G. W. Wei, D. S. Zhang, and D. J. Kouri, "Shannon-Gabor wavelet distributed approximating functional," *Chemical Physics Letters*, vol. 287, no. 1-2, pp. 119–124, 1998.

[14] G. W. Wei, "Quasi wavelets and quasi interpolating wavelets," *Chemical Physics Letters*, vol. 296, no. 3-4, pp. 215–222, 1998.

[15] G. W. Wei, "A new algorithm for solving some mechanical problems," *Computer Methods in Applied Mechanics and Engineering*, vol. 190, no. 15–17, pp. 2017–2030, 2001.

[16] G. W. Wei, "A unified approach for the solution of the Fokker-Planck equation," *Journal of Physics A*, vol. 33, no. 27, pp. 4935–4953, 2000.

[17] Z. Shi, G. W. Wei, D. J. Kouri, D. K. Hoffman, and Z. Bao, "Lagrange wavelets for signal processing," *IEEE Transactions on Image Processing*, vol. 10, no. 10, pp. 1488–1508, 2001.

[18] S.-L. Mei, H.-L. Lv, and Q. Ma, "Construction of interval wavelet based on restricted variational principle and its application for solving differential equations," *Mathematical Problems in Engineering*, vol. 2008, Article ID 629253, 14 pages, 2008.

[19] L. Zhang, Y. Yang, and S. Mei, "Wavelet precise integration method on image denoising," *Transactions of the Chinese Society of Agricultural Machinery*, vol. 37, no. 7, pp. 109–112, 2006.

[20] S.-L. Mei, C.-J. Du, and S.-W. Zhang, "Linearized perturbation method for stochastic analysis of a rill erosion model," *Applied Mathematics and Computation*, vol. 200, no. 1, pp. 289–296, 2008.

[21] S.-L. Pang, "Wavelet numerical method for nonlinear random system," *Transactions of the Chinese Society of Agricultural Machinery*, vol. 38, no. 3, pp. 168–170, 2007.

[22] H.-H. Yan, "Adaptive wavelet precise integration method for nonlinear Black-Scholes model based on variational iteration method," *Abstract and Applied Analysis*, vol. 2013, Article ID 735919, 6 pages, 2013.

[23] X. Ruyi, "Wavelet-based homotopy analysis method for nonlinear matrix system and its application in burgers equation," *Mathematical Problems in Engineering*, vol. 2013, Article ID 982810, 7 pages, 2013.

[24] S.-L. Mei, "HAM-based adaptive multi-scale meshless method for burgers equation," *Journal of Applied Mathematics*, vol. 2013, Article ID 248246, 10 pages, 2013.

[25] S.-L. Mei, C.-J. Du, and S.-W. Zhang, "Asymptotic numerical method for multi-degree-of-freedom nonlinear dynamic systems," *Chaos, Solitons and Fractals*, vol. 35, no. 3, pp. 536–542, 2008.

[26] S.-L. Mei and S.-W. Zhang, "Coupling technique of variational iteration and homotopy perturbation methods for nonlinear matrix differential equations," *Computers and Mathematics with Applications*, vol. 54, no. 7-8, pp. 1092–1100, 2007.

[27] S.-L. Mei, "Construction of target controllable image segmentation model based on homotopy perturbation technology," *Abstract and Applied Analysis*, vol. 2013, Article ID 131207, 8 pages, 2013.

[28] R. Metzler and J. Klafter, "The random walk's guide to anomalous diffusion: a fractional dynamics approach," *Physics Report*, vol. 339, no. 1, pp. 1–77, 2000.

Hindawi Publishing Corporation
Advances in Mathematical Physics
Volume 2013, Article ID 501628, 7 pages
http://dx.doi.org/10.1155/2013/501628

Research Article

A Fast Region-Based Segmentation Model with Gaussian Kernel of Fractional Order

Bo Chen, Qing-Hua Zou, Wen-Sheng Chen, and Yan Li

College of Mathematics and Computational Science, Shenzhen University, Shenzhen 518060, China

Correspondence should be addressed to Wen-Sheng Chen; chenws@szu.edu.cn

Received 11 August 2013; Revised 3 September 2013; Accepted 3 September 2013

Academic Editor: Ming Li

By summarizing some classical active contour models from the view of level set representation, a simple energy function expression with the Gaussian kernel of fractional order is proposed, and then a novel region-based geometric active contour model is established. In this proposed model, the energy function with value of $[-1, 1]$ is built, the local mean and global mean of the inside and outside of the evolution curve are employed, and the segmentation results are obtained by controlling the expansion and contraction of the evolution curve. The model is simple and easy to implement; it can also protect weak edges because of considering more statistical information. Experimental results on synthetic and natural images show that the proposed model is much more effective in dealing with the images with weak or blurred edges, and it takes less time.

1. Introduction

Image segmentation is a basic and important topic in the fields of image processing. Accurate image segmentation can provide more important information for the follow-up application, such as machine vision and motion tracking. However, segmental results are always affected by low contrast and the problems of intensity inhomogeneity. The main idea of image segmentation is to extract the concerned regions and their contours from the whole image. There have been thousands of image segmentation algorithms proposed in recent decades. Some researchers put forward the edge detection based on the gradient, derivatives, or Canny edge detection, and so on. Edge detection is good for simple image but not suitable for the clutter target boundary extraction. The main reasons are as follows. Firstly, edge extracted for complex image is often not corresponding to the target boundary. Secondly, the extracted edge is discontinuous, but the goal often needs closed boundary to separate the object from the whole image. In addition, edge detection is dependent on the local information near pixel; it has advantages sometimes, but in many cases overall appearance of the target is the key, so the concepts of the image segmentation and edge detection are not one and the same.

Regional growth is a simple technique to provide segmental region; the algorithm begins with some seed points and found pixels near the seed which has similar image characteristics, such as gray scale and color characteristics. This algorithm has been applied to Mumford-Shah function [1]. Another region-based method is active contour (AC) model [2]. Active contour model is 2D or 3D surface contour description, which involves the contour evolution under an appropriate energy in order to get a satisfactory segmentation result, such as the target boundary with the closed contour. Over the past decade, researchers have proposed many different active contour models, which are mainly divided into two categories, namely, parametric active contour models and geometric active contour models. In parametric active contour models, the parameter equation of the curve is $C(p) = [x(p), y(p)]$, in which $0 \le p \le 1$. The parametric active contour model essentially depends on the energy function rather than the geometric figures of the contour. Therefore, this model cannot handle topology changes when it detects multiple targets, but geometric active contour model can deal with topological changes, because it uses the structure of level set, in which the curve C is zero level set function $\phi(x, t) : R^n \times [0, \infty) \to R, n = \{2, 3\}$; for example, $C = \{x \in R^n : \phi(x, t) = 0\}$. The first type of geometric active contour model

is introduced by Caselles et al. [3]; its main idea is to use curvature and normal direction forcing curve movement, so that it stops on the edge with the edge function $g(x) = g(|\nabla I|^2)$, where ∇I means the gradient of the given image I, which has a property; that, it equals zero on the border, and others equal one. For example, $g(x) = e^{-(1/\sigma_e^2)}|\nabla G_\sigma * I(x)|^2$, where σ_e is a scale factor, $G_\sigma = (1/\sqrt{2\pi}\sigma)e^{-((x-\mu)^2/\sigma^2)}$ is a Gaussian kernel, in which σ denotes the standard deviation of the given image, and μ denotes the expectation of the given image. Another type of geometric active contour model is the Geodesic active contour model [4], which can search for the minimum length of the edge weights under the energy function. This model is similar to the former geometric model, but there is a big difference, a vector filed term is employed in Geodesic active contour model to stop the motion curve on the weak edges. Paragios et al. put forward the famous gradient vector flow (GVF) instead of ∇g to increase the range of results, called GVF geometric AC [5]. Chan and Vese [6] proposed a new model CV AC, and Li et al. [7] proposed a new model (LBF) which uses energy function to overcome the problem of nonhomogeneity. LBF model can deal with the image of different gray levels by adding the kernel function, and it can employ local gray level information effectively.

Many structures of different level set evolution models have been summarized before. The level set evolution of the above energy functions [8] can be represented as

$$\frac{\partial \phi}{\partial t} = \alpha_k K \left|\nabla \phi\right| + V_N \left|\nabla \phi\right| + \vec{N} \cdot \nabla \phi, \tag{1}$$

where K is the Euclidean curvature and α_k, V_N, and $\vec{N}$ are three parameters, which decide the speed and direction of the evolution. The term based on curvature vector is used to smooth the curve. The normal direction is used to control shrinkage and expansion of the curve and force the curve to move along the direction vector. Details are shown in Table 1, where η, μ, λ_1, and λ_2 are constant, $[\widehat{u}, \widehat{v}]$ is the GVF, and $k(x)$ is a function based on the normal curvature and GVF [9]. At the same time, $I(x)$ in Table 1 is original gray level image, C_{in} and C_{out} are average gray values of $I(x)$ inside and outside of curve, and e_1 and e_2 are the weighted average gray values of $I(x)$ inside and outside of curve in the Gaussian window.

The rest of the paper is organized as follows: in the next two sections, we will review classical existing geometric models, Chan-Vese model and LBF model. The new model is introduced in Section 4. Some experimental results are shown in Section 5. We conclude the paper in Section 6.

2. Chan-Vese Model

In Chan-Vese (CV) model, we considered the simplest type of segmentation, which divided the image into the target and the background, and the distributions of the gray values of target and background are approximately constant values. CV model is based on the evolution of the level set and can deal with curve topology changes better for the curve which is

Table 1: The analysis table of energy function model.

Model	α_k	V_N	$\vec{N}$
Geometric AC [3]	$g(x)$	$rg(x)$	$\vec{0}$
Geodesic AC [4]	$g(x)$	$rg(x)$	$\nabla g(x)$
GVF Geo. AC [5]	$g(x)$	$rk(x)g(x)$	$g(x)\,(1 - \lvert k\,(x)\rvert\,[\widehat{u}, \widehat{v}])$
CV AC [6]	η	$\mu + (I - c_{\text{in}})^2 - (I - c_{\text{out}})^2$	$\vec{0}$
LBF AC [7]	η	$\lambda_1 e_1 - \lambda_2 e_2$	$\vec{0}$

expressed by the level set function. The energy function of CV model is

$$\begin{aligned} E\,(C, c_1, c_2) = {} & \mu_0 \text{Length}\,(C) \\ & + \lambda_1 \int_{\text{inside}(C)} \left|u_0\,(x, y) - c_1\right|^2 dx\, dy \\ & + \lambda_2 \int_{\text{outside}(C)} \left|u_0\,(x, y) - c_2\right|^2 dx\, dy, \end{aligned} \tag{2}$$

where u_0 is the given image, C is the evolution curve, $C(s) : [0, 1] \rightarrow R$ is a parameter evolution curve, and μ_0 is the weight coefficient. In the energy function, the first item is the length of the curve evolution and it can regularize the curve. The last two items are global binary fitting items. The basic idea of the model is to minimize the fitting item $F_1 + F_2$, where

$$\begin{aligned} F_1 &= \int_{\text{inside}(C)} \left|u_0 - c_1\right|^2 dx\, dy, \\ F_2 &= \int_{\text{outside}(C)} \left|u_0 - c_2\right|^2 dx\, dy. \end{aligned} \tag{3}$$

The level set function ϕ is defined as

$$\begin{aligned} \phi\,(x, y) > 0, &\quad (x, y) \in \text{in}\,(C), \\ \phi\,(x, y) < 0, &\quad (x, y) \in \text{out}\,(C), \\ \phi\,(x, y) = 0, &\quad (x, y) \in (C). \end{aligned} \tag{4}$$

The following are Dirac function and Heaviside function, respectively:

$$\begin{aligned} \delta\,(\phi) &= \frac{dH\,(\phi)}{d\phi}, \\ H\,(\phi) &= \begin{cases} 1, & \phi \geq 0, \\ 0, & \phi < 0. \end{cases} \end{aligned} \tag{5}$$

Because function $H(\phi)$ cannot directly take the derivative of ϕ, we can replace H with $H_\varepsilon(\phi)$ in the CV model, where

$$H_\varepsilon\,(\phi) = \frac{1}{2}\left(1 + \frac{2}{\pi}\arctan\left(\frac{\phi}{\varepsilon}\right)\right). \tag{6}$$

The level set function of the CV model is:

$$E(\phi, c_1, c_2) = \mu \int_\Omega \delta_\varepsilon(\phi) |\nabla\phi| \, dx\, dy + \lambda_1 \int_\Omega |u_0(x,y) - c_1|^2 H_\varepsilon(\phi) \, dx\, dy + \lambda_2 \int_\Omega |u_0(x,y) - c_2|^2 (1 - H_\varepsilon(\phi)) \, dx\, dy, \tag{7}$$

where

$$\delta_\varepsilon(\phi) = H'_\varepsilon(\phi) = \frac{1}{\pi} \frac{\varepsilon}{\varepsilon^2 + \pi^2}. \tag{8}$$

From the definition of the level set function ϕ, expressions of c_1, c_2 are, respectively, as follows:

$$c_1 = \frac{\int_\Omega u_0(x,y) H(\phi(x,y)) \, dx\, dy}{\int_\Omega H(\phi(x,y)) \, dx\, dy}, \qquad c_2 = \frac{\int_\Omega u_0(x,y) (1 - H(\phi(x,y))) \, dx\, dy}{\int_\Omega (1 - H(\phi(x,y))) \, dx\, dy}. \tag{9}$$

According to Euler-Lagrange equation, the level set expression of CV model is obtained as

$$\frac{\partial\phi}{\partial t} = \delta(\phi) \left[\mu \operatorname{div}\left(\frac{\nabla\phi}{|\nabla\phi|} \right) - \lambda_1 (u_0 - c_1)^2 + \lambda_2 (u_0 - c_2)^2 \right]. \tag{10}$$

3. LBF Model

LBF model defines a local binary fitting energy item, which is actually a kernel function; the model is as follows:

$$E(C, f_1, f_2) = \lambda_1 \int_\Omega \int_{\text{inside}(C)} K_\sigma(x - y) |I(y) - f_1(x)|^2 dy\, dx + \lambda_2 \int_\Omega \int_{\text{outside}(C)} K_\sigma(x - y) |I(y) - f_2(x)|^2 dy\, dx, \tag{11}$$

where $I : \Omega \to R$ is the original image, $(x, y) \in \Omega$, $K_\sigma = (1/2\pi\sigma^2) e^{-((x-\mu_x)^2 + (y-\mu_y)^2/\sigma^2)}$ and is a Gaussian kernel function, μ_x and μ_y are its expectancies, and σ is its standard deviation. f_1 and f_2 are the image fitting function of the local gray level inside and outside of the contour.

The variational level set function of (11) which is got by Euler-Lagrange equation is as follows:

$$\frac{\partial\phi}{\partial t} = -\delta(\phi) (\lambda_1 e_1 - \lambda_2 e_2). \tag{12}$$

By introducing a sign distance constraint and length constraint item, the level set evolution equation is

$$\frac{\partial\phi}{\partial t} = \mu \left(\Delta\phi - \operatorname{div}\left(\frac{\nabla\phi}{|\nabla\phi|} \right) \right) + \nu\delta(\phi) \operatorname{div}\left(\frac{\nabla\phi}{|\nabla\phi|} \right) - \delta(\phi) (\lambda_1 e_1 - \lambda_2 e_2), \tag{13}$$

where functions e_1, e_2 and f_1, f_2 are as follows, respectively:

$$e_1(x) = \int_\Omega K_\sigma(y - x) |I(x) - f_1(y)|^2 dy, \qquad e_2(x) = \int_\Omega K_\sigma(y - x) |I(x) - f_2(y)|^2 dy, \tag{14}$$

$$f_1 = \frac{K_\sigma * [H(\phi) I(x)]}{K_\sigma * H(\phi)}, \qquad f_2 = \frac{K_\sigma * [(1 - H(\phi)) I(x)]}{K_\sigma * ((1 - H(\phi)))}. \tag{15}$$

Equation (15) shows that f_1 and f_2 are the weighted average gray values with the Gaussian window inside and outside of contour. Obviously, they share the local characteristics, so that the segmentation of original image by LBF model is more accurate.

4. Proposed Region-Based Model with Gaussian Kernel of Fractional Order

In order to get better image segmentation results effectively and construct a fast region-based segmentation model, we should keep the energy functional as simple as possible, and energy information must be used effectively. Based on the law of some classical energy function expressions of active contour models summarized in Table 1, we know that the term V_N in energy function is very important, and many models made a breakthrough on it. At the same time, the item $\vec{N}$ of the models is often set as $\vec{0}$, and item α_k is only ordinary parameters. Therefore, only keeping item V_N in the new model will simplify the expression of energy function.

In order to avoid jumping internally, level set function initialized by symbolic distance function (SDF) in the traditional level set method, but it usually needs to be reinitialized. This will lead to the fact that it is hard to decide when to reinitialize and how to reinitialize, as it is hard to find boundary when the zero level set is away from the inner region. So reinitialization is a very complex operation problem. To solve this problem, we propose a new level set method. At the same time, fractional systems [10, 11] gain increasing attention in applied sciences, and functions of fractional order are more flexible, so the new method uses a Gaussian filter with fractional order to regularize binary level set function. The traditional level set method uses curvature item $\operatorname{div}(\nabla\phi/|\nabla\phi|)|\nabla\phi|$ to regularize the level set function, and letting $|\nabla\phi| = 1$ [12], it can replace the regular items with Laplacian. Based on scale space theory in [13], a function with the Laplacian evolution is equivalent to using a Gaussian filter. Then, we filter the initial conditions of the level set function with Gaussian kernel filters of the level set function, and σ controls the regular strength, similar to the item η in Table 1. With Gaussian kernel function, the item $\operatorname{div}(\nabla\phi/|\nabla\phi|)|\nabla\phi|$ (similar to the item α_k in Table 1) can be removed, so the key of whole model is the choice of item V_N.

From the view of level set function, we need to find a function that can adjust the pressure inside and outside of the interest areas. It drives the curve to contract when the curve

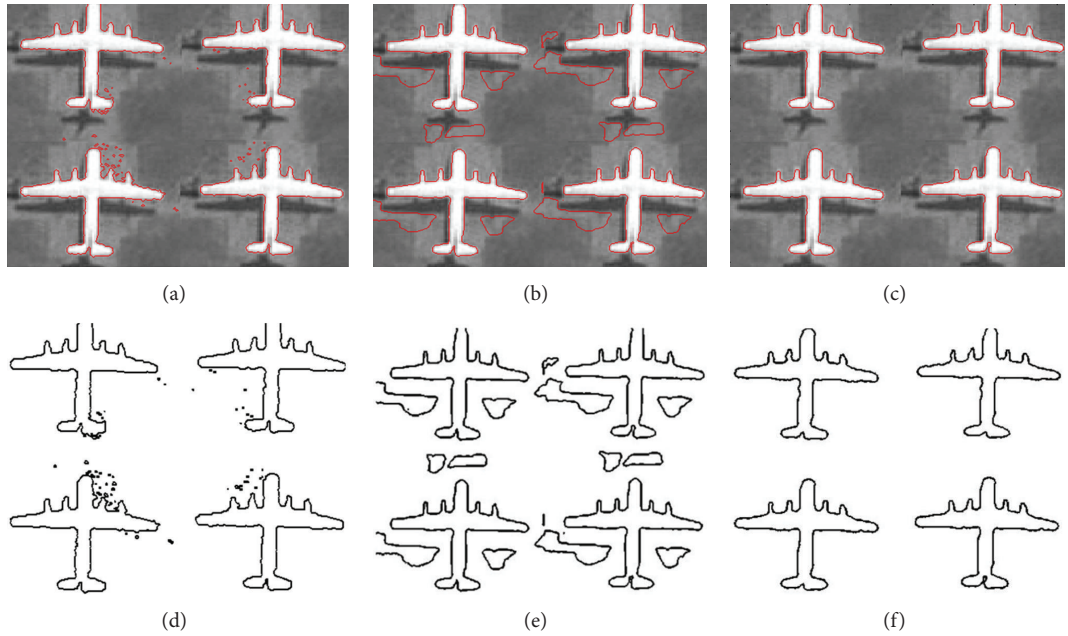

FIGURE 1: The segmentation results of the aircraft composite image: (a) and (d) results using CV model, (b) and (e) results using LBF model, and (c) and (f) results using the new model.

is outside the target and expands when the curve is within the target. Based on SPF function with value of $[-1, 1]$ defined in [14], we can construct a function as follow:

$$f(I(x)) = \frac{(c_1 + c_2 + f_1 + f_2)/4 - I(x)}{\max\left(\left|(c_1 + c_2 + f_1 + f_2)/4 - I(x)\right|\right)}, \quad x \in \Omega, \tag{16}$$

where

$$\begin{aligned} &\operatorname{Min}(I(x)) \le c_1, c_2, f_1, f_2 \le \operatorname{Max}(I(x)), \\ &\operatorname{Min}(I(x)) \le \frac{(c_1 + c_2 + f_1 + f_2)}{4} \le \operatorname{Max}(I(x)), \end{aligned} \tag{17}$$

$$\begin{aligned} f_1 &= \frac{K_\sigma * [H(\phi) I(x)]}{K_\sigma * H(\phi)}, \\ f_2 &= \frac{K_\sigma * [(1 - H(\phi)) I(x)]}{K_\sigma * (1 - H(\phi))}, \end{aligned} \tag{18}$$

$$K_\sigma(\alpha) = \frac{1}{2\pi\sigma^2} e^{-(\|x-\mu\|^\alpha/\sigma^2)}, \tag{19}$$

where $K_\sigma(\alpha)$ is the Gaussian kernel of fractional order α. It takes the ordinary Gaussian kernel as its special case when $\alpha = 2$. Thus, it is more flexible than the ordinary one. We must emphasize that the parameter α may be different from fractal parameters [15, 16]. In this paper, we call α, likely informal, the fractional order of the Gaussian kernel expressed by (19). In the following experiments, we try different values of the fractal order α in the evolution level set function. The value of the function is between -1 and 1. It drives curve to contract externally the target and expands when the curve is within the target. According to the summary of the classic model of general expression (1), we only keep item V_N, so we obtain the corresponding variational level set formulation as follows:

$$\frac{\partial \phi}{\partial t} = f(I(x)) |\nabla \phi|, \quad x \in \Omega. \tag{20}$$

By adding a parameter, the final level set equation of the new model is

$$\frac{\partial \phi}{\partial t} = \eta f(I(x)) |\nabla \phi|, \quad x \in \Omega. \tag{21}$$

The main algorithm of the new model is as follows.

Step 1: initialize the level set function ϕ.

Step 2: compute the mean and the weighted average values of inside and outside of the curve c_1, c_2, f_1, and f_2.

Step 3: compute the evolution of level set function by (21).

Step 4: use Gaussian filter to regularize level set function, $\phi = \phi * G_\sigma$.

Step 5: repeat Steps 2 to 4 until convergence.

5. Experimental Results

In this section, we will show some experimental results of the proposed model on synthetic image and nature image; the results also will be compared with those got by the conventional CV model and LBF model. Our algorithm is implemented in Windows 7 Operating System, i3 Dual Core CPU 2.13 GHz and 2 GB RAM. The initial value and parameters such as time step take different values in the specific experiments in this paper.

Figures 1(d)–1(f) got with 2000, 1500, 40 iterations separately and consume time $t = 217.6$ s, 232.6 s, 13.8 s in turn. We can see that Chan-Vese model and LBF model cannot get

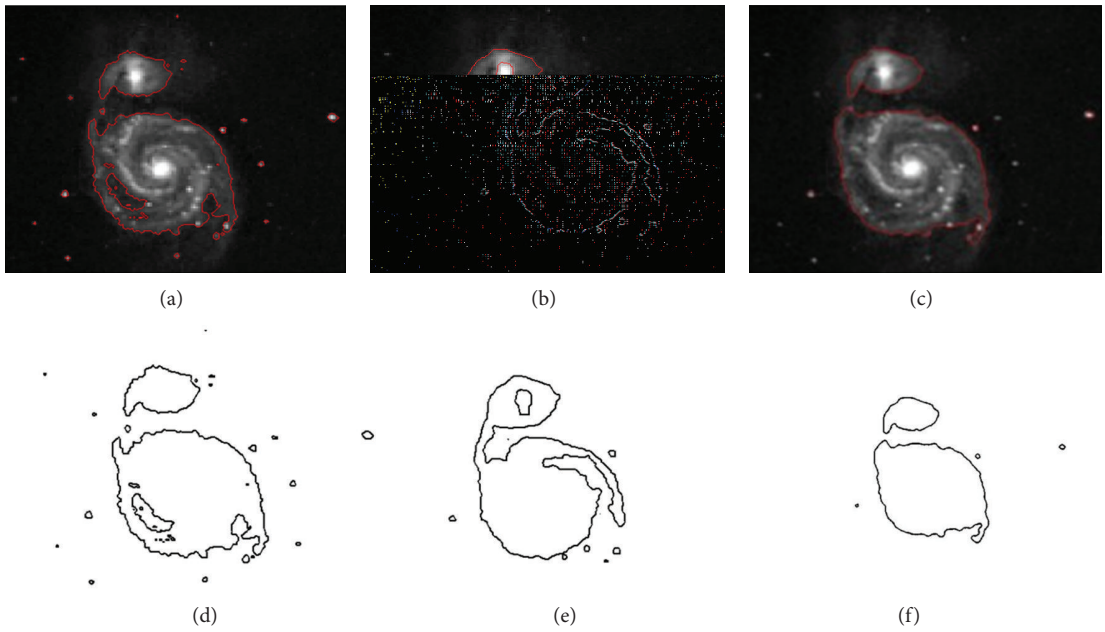

Figure 2: The segmentation results of the natural image: (a) and (d) results using CV model, (b) and (e) results using LBF model, and (c) and (f) results using the new model.

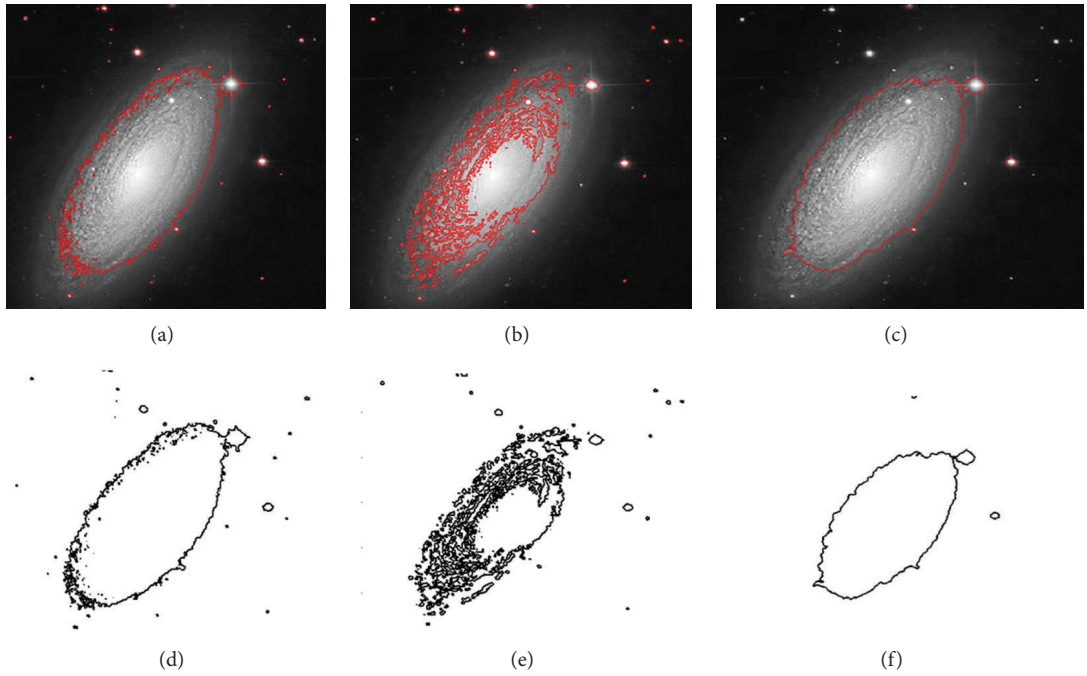

Figure 3: The segmentation results of the natural image: (a) and (d) results using CV model, (b) and (e) results using LBF model, and (c) and (f) results using the new model.

satisfactory result. While here the proposed model gets satisfactory result, meanwhile the proposed model costs less time.

Figure 2 shows the experimental results of natural figure with objects having inhomogeneous background. CV model, LBF model, and the proposed model share the same environment of the initial value. We can find that the gray level of the natural star figure is extremely inhomogeneous easily. The first line shows the segmentation result of CV model. The second line shows the segmentation result of LBF model. The third line shows the segmentation result of new model. The segmentation images reveal that the proposed model gets the most ideal segmentation result.

Figure 3 shows the experimental results of natural figure with CV model, LBF model, and the proposed model; gray

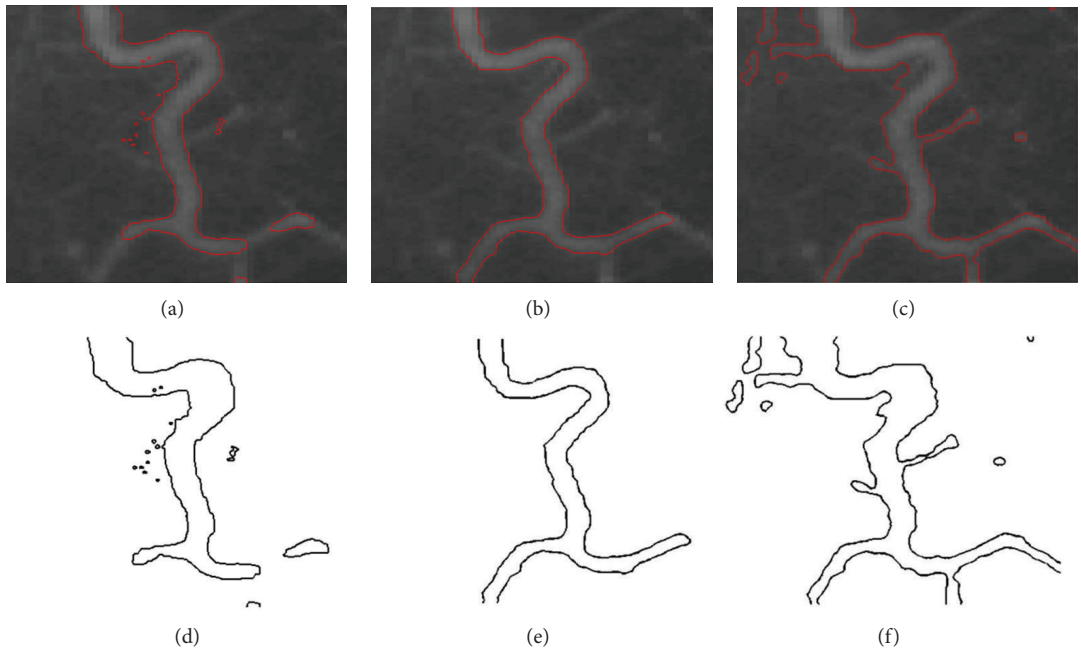

Figure 4: The segmentation results of the blood vessels image: (a) and (d) results using CV model, (b) and (e) results using LBF model, and (c) and (f) results using the new model.

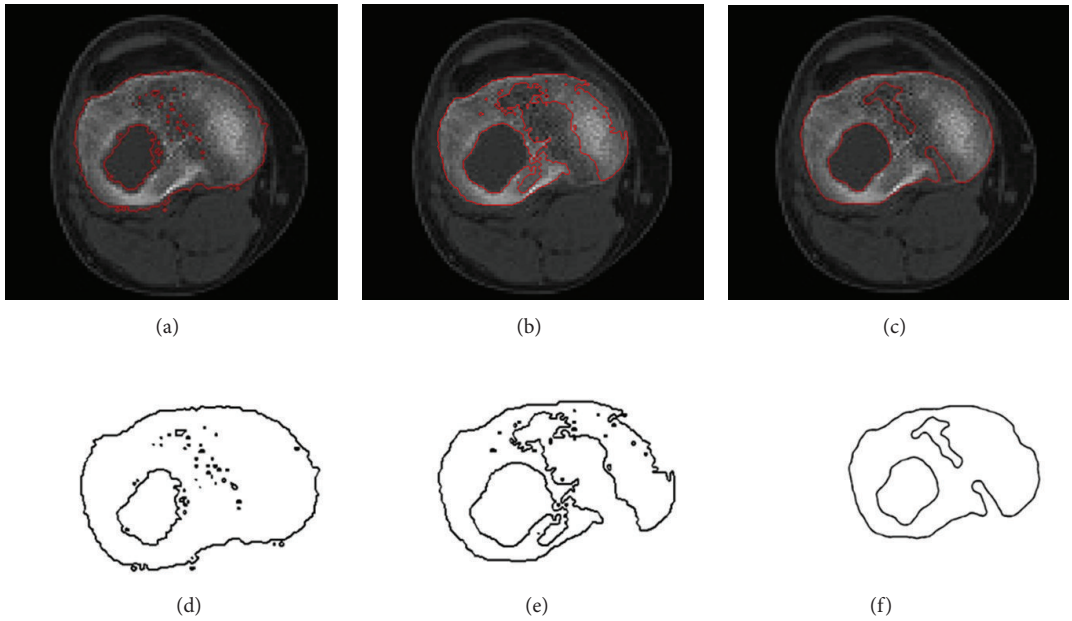

Figure 5: The segmentation results of the CT image: (a) and (d) results using CV model, (b) and (e) results using LBF model, and (c) and (f) results using the new model.

level of the image is extremely inhomogeneous. The three models share the same initial value. Figures 3(a) and 3(d) show the segmentation result of CV model; Figures 3(b) and 3(e) show the segmentation result of LBF model; Figures 3(c) and 3(f) show the segmentation result of the new model. The segmentation results show that the proposed model gets the satisfactory complete result, while the CV model and LBF model have some redundant and inaccurate segmentation.

In Figure 4, the experiment shows the segmentation results of a gray matter blood vessels image. The first column shows the segmentation results of Chan-Vese model. The second column shows the results of LBF model. The third column shows the result of proposed model. Figures 4(d)–4(f) got with 1000, 5000, 40 iterations separately and consume time $t = 79.2$ s, 174.2 s, 6.1 s in turn. Because the mean information of Chan-Vese model is very sensitive to inhomogeneity

image, it fails to extract the accurate contour. The LBF model is better than Chan-Vese model, but it gets many iterations and it is very sensitive to initial value. As shown in the low left of the segmental contour, the proposed model got a better segmentation result.

In Figure 5, experimental results show the segmentation results of CT bone images. The initialization is a single circle. The first column shows the segmentation result of Chan-Vese model. The second column shows the result of the LBF model. The third row shows the result of proposed model. Figures 5(d)–5(f) are the corresponding contours to Figures 5(a)–5(c). Figures 5(d)–5(f) got with 50, 1000, 80 iterations separately and consume time $t = 4.0$ s, 34.6 s, 12.5 s in turn. As seen from Figure 5, the new method can get more complete contour than Chan-Vese model and the LBF model and take less time.

6. Conclusion

Inspired by the idea of some classical energy function expressions of active contour model, from the view of level set representation, a novel fast region-based segmentation model with Gaussian kernel of fractional order is proposed. The model is simple and easy to be implementated, and it can protect weak edges because of considering more statistical information. The experimental results on synthetic images and natural images show that the proposed model is superior to the traditional methods. The new model is much more effective in dealing with the images with weak or blurred edges, and it takes less time.

Acknowledgments

This paper is partially supported by NSFC (61272252) and Science and Technology Planning Project of Shenzhen City (JC201105130461A, JCYJ20120613102415154, ZYC201105130115A, and JCYJ20130326111024546). The authors also would like to thank the Key Laboratory of Medical Image Processing in Southern Medical University for providing original medical images for experiment.

References

[1] D. Mumford and J. Shah, "Optimal approximations by piecewise smooth functions and associated variational problems," *Communications on Pure and Applied Mathematics*, vol. 42, no. 5, pp. 577–685, 1989.

[2] M. Kass, A. Witkin, and D. Terzopoulos, "Snakes: active contour models," *International Journal of Computer Vision*, vol. 1, no. 4, pp. 321–331, 1988.

[3] V. Caselles, F. Catté, T. Coll, and F. Dibos, "A geometric model for active contours in image processing," *Numerische Mathematik*, vol. 66, no. 1, pp. 1–31, 1993.

[4] V. Caselles, R. Kimmel, and G. Sapiro, "Geodesic active contours," *International Journal of Computer Vision*, vol. 22, no. 1, pp. 61–79, 1997.

[5] N. Paragios, O. Mellina-Gottardo, and V. Ramesh, "Gradient vector flow fast geometric active contours," *IEEE Transactions on Pattern Analysis and Machine Intelligence*, vol. 26, no. 3, pp. 402–407, 2004.

[6] T. F. Chan and L. A. Vese, "Active contours without edges," *IEEE Transactions on Image Processing*, vol. 10, no. 2, pp. 266–277, 2001.

[7] C. Li, C.-Y. Kao, J. C. Gore, and Z. Ding, "Implicit active contours driven by local binary fitting energy," in *Proceedings of the IEEE Computer Society Conference on Computer Vision and Pattern Recognition (CVPR '07)*, Minneapolis, Minn, USA, June 2007.

[8] P. T. H. Truc, T.-S. Kim, S. Lee, and Y.-K. Lee, "Homogeneity- and density distance-driven active contours for medical image segmentation," *Computers in Biology and Medicine*, vol. 41, no. 5, pp. 292–301, 2011.

[9] A. Vasilevskiy and K. Siddiqi, "Flux maximizing geometric flows," *IEEE Transactions on Pattern Analysis and Machine Intelligence*, vol. 24, no. 12, pp. 1565–1578, 2002.

[10] M. Li, "Approximating ideal filters by systems of fractional order," *Computational and Mathematical Methods in Medicine*, vol. 2012, Article ID 365054, 6 pages, 2012.

[11] M. Li, S. C. Lim, and S. Chen, "Exact solution of impulse response to a class of fractional oscillators and its stability," *Mathematical Problems in Engineering*, vol. 2011, Article ID 657839, 9 pages, 2011.

[12] S. Osher and R. Fedkiw, *Level Set Methods and Dynamic Implicit Surfaces*, vol. 153 of *Applied Mathematical Sciences*, Springer, New York, NY, USA, 2003.

[13] P. Perona and J. Malik, "Scale-space and edge detection using anisotropic diffusion," *IEEE Transactions on Pattern Analysis and Machine Intelligence*, vol. 12, no. 7, pp. 629–639, 1990.

[14] K. Z. Zhang, L. Zhang, H. H. Song, and W. G. Zhou, "Active contours with selective local or global segmentation: a new formulation and level set methed," *Image and Vision Computing*, vol. 28, no. 4, pp. 668–676, 2010.

[15] M. Li and W. Zhao, "Quantitatively investigating locally weak stationarity of modified multifractional Gaussian noise," *Physica A*, vol. 391, no. 24, pp. 6268–6278, 2012.

[16] M. Li and W. Zhao, "On $1/f$ noise," *Mathematical Problems in Engineering*, vol. 2012, Article ID 673648, 23 pages, 2012.

Hindawi Publishing Corporation
Advances in Mathematical Physics
Volume 2013, Article ID 315979, 3 pages
http://dx.doi.org/10.1155/2013/315979

Research Article

Power Spectrum of Generalized Fractional Gaussian Noise

Ming Li

School of Information Science & Technology, East China Normal University, No. 500 Dong-Chuan Road, Shanghai 200241, China

Correspondence should be addressed to Ming Li; ming_lihk@yahoo.com

Received 29 August 2013; Accepted 10 September 2013

Academic Editor: Wen-Sheng Chen

Recently, we introduced a type of autocorrelation function (ACF) to describe a long-range dependent (LRD) process indexed with two parameters, which takes standard fractional Gaussian noise (fGn for short) as a special case. For simplicity, we call it the generalized fGn (GfGn). This short paper gives the power spectrum density function (PSD) of GfGn.

1. Introduction

LRD time series increasingly gains applications to many fields of science and technologies; see, for example, Mandelbrot [1] and references therein. In this regard, standard fGn introduced by Mandelbrot and van Ness is a widely used tool for modeling LRD time series; see, for example, Beran [2], Abuzeid et al. [3, 4], and Liao et al. [5]. Following [1, H11], [2], its ACF is given by

$$\begin{aligned}\rho(\tau) &= r(\tau; H) \\ &= \frac{\sigma^2}{2}\left[(|\tau|+1)^{2H} - 2|\tau|^{2H} + ||\tau|-1|^{2H}\right],\end{aligned} \tag{1}$$

where H is the Hurst parameter and $\sigma^2 = \Gamma(1-2H)\cos(H\pi)/H\pi$. It implies three families of time series. In the case of $H \in (0.5, 1)$, ρ is nonintegrable, and a corresponding series is LRD. For $H \in (0, 0.5)$, r is integrable, and a corresponding series is short-range dependent (SRD). The case of $H = 0.5$ corresponds to white noise. Note that statistics of LRD series substantially differ from SRD ones. From a practice view, SRD fGn may be less interesting in applications as can be seen from [1, 2]. This paper only considers LRD series unless otherwise stated.

Li [6] recently introduced an ACF form that is a generalization of ACF of fGn. Since ACF is an even function, we write ACF of GfGn by

$$\begin{aligned}C(\tau) &= C(\tau; H, \alpha) \\ &= 0.5\sigma^2\left((|\tau|^\alpha + 1)^{2H} - 2(|\tau|^\alpha)^{2H} + \left||\tau|^\alpha - 1\right|^{2H}\right),\end{aligned} \tag{2}$$

where $H \in (0.5, 1)$ and $\alpha \in (0, 1]$. We call a process whose ACF follows (2) GfGn for simplicity because it takes fGn as a special case of $C(\tau; H, 1) = \rho(\tau; H)$. Without loss of generality, the following considers the normalized ACF by letting $r(\tau) = C(\tau)/\sigma^2$. This paper aims at giving PSD of GfGn. The Fourier transform (FT) of $r(\tau)$ is treated as a generalized function over Schwartz space of test functions since $r(\tau)$ is nonintegrable.

2. PSD of GfGn

Denote

$$r(\tau) = 0.5\left[r_1(\tau) - 2r_2(\tau) + r_3(\tau)\right], \tag{3}$$

where $r_1 = (|\tau|^a + 1)^{2H}$, and $r_2 = (|\tau|^\alpha)^{2H}$, $r_3 = ||\tau|^a - 1|^{2H}$. Denote $S_m(\omega) = F(r_m)$, where F means FT and $m = 1, 2, 3$. Then, FT of $r(\tau)$ is given by

$$S(\omega) = 0.5\left[S_1(\omega) - 2S_2(\omega) + S_3(\omega)\right]. \tag{4}$$

Lemma 1 (see [7] or Gelfand and Vilenkin [8, Chapter 2]). *FT of $|t|^\lambda$ is expressed by*

$$F\left[|t|^\lambda\right] = -\sin\left(\frac{\lambda\pi}{2}\right)\Gamma(\lambda+1)\,|\omega|^{-\lambda-1}, \tag{5}$$

where $\lambda \neq -1, -3, \ldots$.

Corollary 2. *$S_2(\omega)$ equals $-\sin(H\alpha\pi)\Gamma(2H\alpha+1)|\omega|^{-2H\alpha-1}$.*

Proof. Note $2H\alpha \neq -1, -3, \ldots$. Thus, doing $F(|\tau|^{2H\alpha})$ with (5) yields Corollary 2. □

Lemma 3 (binomial series). *$(1+x)^{\nu}$ and $(1-x)^{\nu}$ can be expanded as*

$$\begin{aligned}(1+x)^{\nu} &= \sum_{k=0}^{\infty}\binom{\nu}{k}x^{k} \\ &= \sum_{k=0}^{\infty}\frac{\Gamma(\nu+k)}{\Gamma(\nu)\Gamma(1+k)}x^{k} \quad for\ \ |x|<1,\end{aligned} \tag{6a}$$

$$\begin{aligned}(1-x)^{\nu} &= \sum_{k=0}^{\infty}\binom{\nu}{k}(-x)^{k} \\ &= \sum_{k=0}^{\infty}\frac{(-1)^{k}\Gamma(\nu+k)}{\Gamma(\nu)\Gamma(1+k)}x^{k} \quad for\ \ |x|<1,\end{aligned} \tag{6b}$$

where x and ν are real number, and $\binom{\nu}{k}$ is binomial coefficient [9].

Corollary 4. *$r_1(\tau)$ and $r_3(\tau)$ for $|\tau|<1$ can be expanded as*

$$\begin{aligned}\left(1+|\tau|^{\alpha}\right)^{2H} &= \sum_{k=0}^{\infty}\binom{2H}{k}|\tau|^{\alpha k} \\ &= \sum_{k=0}^{\infty}\frac{\Gamma(2H+k)}{\Gamma(2H)\Gamma(1+k)}|\tau|^{\alpha k},\end{aligned} \tag{7a}$$

$$\begin{aligned}\left(1-|\tau|^{\alpha}\right)^{2H} &= \sum_{k=0}^{\infty}(-1)^{k}\binom{2H}{k}|\tau|^{\alpha k} \\ &= \sum_{k=0}^{\infty}\frac{(-1)^{k}\Gamma(2H+k)}{\Gamma(2H)\Gamma(1+k)}|\tau|^{\alpha k}.\end{aligned} \tag{7b}$$

Proof. This corollary is straightforward from Lemma 3. □

Corollary 5. *For $|\tau|^{\alpha}>1$, $r_1(\tau)$ and $r_3(\tau)$ can be expanded as*

$$\begin{aligned}\left(1+|\tau|^{\alpha}\right)^{2H} &= |\tau|^{2H\alpha}\sum_{k=0}^{\infty}\binom{2H}{k}|\tau|^{-\alpha k} \\ &= \sum_{k=0}^{\infty}\frac{\Gamma(2H+k)}{\Gamma(2H)\Gamma(1+k)}|\tau|^{\alpha(2H-k)},\end{aligned} \tag{8a}$$

$$\begin{aligned}\left||\tau|^{a}-1\right|^{2H} &= |\tau|^{2H\alpha}\sum_{k=0}^{\infty}(-1)^{k}\binom{2H}{k}|\tau|^{-\alpha k} \\ &= \sum_{k=0}^{\infty}\frac{(-1)^{k}\Gamma(2H+k)}{\Gamma(2H)\Gamma(1+k)}|\tau|^{\alpha(2H-k)}.\end{aligned} \tag{8b}$$

Proof. Since $\left(1+|\tau|^{\alpha}\right)^{2H} = |\tau|^{2H\alpha}\left(1+|\tau|^{-\alpha}\right)^{2H}$, according to (7a), (8a) results. Similarly, (8b) follows due to $\left||\tau|^{a}-1\right|^{2H} = |\tau|^{2H\alpha}\left|1-|\tau|^{-\alpha}\right|^{2H}$ and (7b). □

Corollary 6. *For $|\tau|<1$, S_1 and S_3 are given by (6), respectively,*

$$\begin{aligned}S_1(\omega) &= \sum_{k=0}^{\infty}\frac{-\Gamma(2H+k)\Gamma(\alpha k+1)}{\Gamma(2H)\Gamma(1+k)} \\ &\qquad\times\sin\left(\frac{\alpha k\pi}{2}\right)|\omega|^{-\alpha k-1}, \\ S_3(\omega) &= \sum_{k=0}^{\infty}\frac{(-1)^{k+1}\Gamma(2H+k)\Gamma(\alpha k+1)}{\Gamma(2H)\Gamma(1+k)} \\ &\qquad\times\sin\left(\frac{\alpha k\pi}{2}\right)|\omega|^{-\alpha k-1}.\end{aligned} \tag{6}$$

Proof. Doing $F[|\tau|^{\alpha k}]$ term by term for (7a) and (7b) with Lemma 1 yields (6), respectively. □

Corollary 7. *For $|\tau|^{\alpha}>1$, S_1 and S_3 are given by (7), respectively,*

$$\begin{aligned}S_1(\omega) &= \sum_{k=0}^{\infty}\frac{-\Gamma(2H+k)\Gamma[(\alpha(2H-k)+1]}{\Gamma(2H)\Gamma(1+k)} \\ &\qquad\times\sin\left[\frac{\alpha(2H-k)\pi}{2}\right]|\omega|^{-\alpha(2H-k)-1}, \\ S_3(\omega) &= \sum_{k=0}^{\infty}\frac{(-1)^{k+1}\Gamma(2H+k)\Gamma[\alpha(2H-k)+1]}{\Gamma(2H)\Gamma(1+k)} \\ &\qquad\times\sin\left[\frac{\alpha(2H-k)\pi}{2}\right]|\omega|^{-\alpha(2H-k)-1}.\end{aligned} \tag{7}$$

Proof. Doing FTs for (8a) and (8b) based on Lemma 1 results in (7). □

The following proposition is a consequence of Corollaries 2, 6, and 7.

Proposition 8. *PSD of GfGn is given by*

$$\begin{aligned}&S(\omega) \\ &= \begin{cases}\sin(H\alpha\pi)\Gamma(2H\alpha+1)|\omega|^{-2H\alpha-1} \\ \quad +0.5\displaystyle\sum_{k=0}^{\infty}\frac{\left[(-1)^{k+1}-1\right]\Gamma(2H+k)\Gamma(\alpha k+1)}{\Gamma(2H)\Gamma(1+k)} \\ \qquad\times\sin\left(\frac{\alpha k\pi}{2}\right)|\omega|^{-\alpha k-1}, \quad |\tau|<1, \\ \sin(H\alpha\pi)\Gamma(2H\alpha+1)|\omega|^{-2H\alpha-1} \\ \quad +0.5\displaystyle\sum_{k=0}^{\infty}\frac{\left[(-1)^{k}-1\right]\Gamma(2H+k)\Gamma[\alpha(2H-k)+1]}{\Gamma(2H)\Gamma(1+k)} \\ \qquad\times\sin\left[\frac{\alpha(2H-k)\pi}{2}\right]|\omega|^{-\alpha(2H-k)-1}, \\ \qquad\qquad |\tau|^{\alpha}>1.\end{cases}\end{aligned} \tag{8}$$

Considering the leading term of (8) results in the following proposition.

Proposition 9. *PSD of GfGn has the following approximate value:*

$$S(\omega) \approx \sin(H\alpha\pi)\,\Gamma(2H\alpha+1)\,|\omega|^{-2H\alpha-1}. \quad (9)$$

From (9), we can easily get the two notes below.

Note 1. $S(\omega)$ is divergent at the origin for $0 < 2H\alpha + 1 < 1$, which is the LRD condition. This is the basic feature of LRD process.

Note 2. Recall $2H\alpha + 1 > 0$. Then, the cases of $2H\alpha + 1 < 1$ and $H \in (0.5, 1)$ imply $\alpha \in (0, 1]$. This explains the range of α for GfGn from a view in the frequency domain.

3. Conclusions

We have derived PSD of GfGn. Its approximate expression has been given. The range of α has been explained from a spectral view.

Acknowledgments

This work was supported in part by the National Natural Science Foundation of China under the Project Grant nos. 61272402, 61070214, and 60873264, and by the 973 Plan under the Project Grant no. 2011CB302800.

References

[1] B. B. Mandelbrot, *Gaussian Self-Affinity and Fractals*, Springer, 2001.

[2] J. Beran, *Statistics For Long-Memory Processes*, Chapman & Hall, New York, NY, USA, 1994.

[3] O. M. Abuzeid, A. N. Al-Rabadi, and H. S. Alkhaldi, "Recent advancements in fractal geometric-based nonlinear time series solutions to the micro-quasistatic thermoviscoelastic creep for rough surfaces in contact," *Mathematical Problems in Engineering*, vol. 2011, Article ID 691270, 29 pages, 2011.

[4] O. M. Abuzeid, A. N. Al-Rabadi, and H. S. Alkhaldi, "Fractal geometry-based hypergeometric time series solution to the hereditary thermal creep model for the contact of rough surfaces using the Kelvin-Voigt medium," *Mathematical Problems in Engineering*, vol. 2010, Article ID 652306, 22 pages, 2010.

[5] Z. Liao, S. Hu, M. Li, and W. Chen, "Noise estimation for single-slice sinogram of low-dose X-ray computed tomography using homogenous patch," *Mathematical Problems in Engineering*, vol. 2012, Article ID 696212, 16 pages, 2012.

[6] M. Li, "Modeling autocorrelation functions of long-range dependent teletraffic series based on optimal approximation in Hilbert space-A further study," *Applied Mathematical Modelling*, vol. 31, no. 3, pp. 625–631, 2007.

[7] S. Samko, A. A. Kilbas, and D. I. Maritchev, *Integrals and Derivatives of the Fractional Order and Some of Their Applications*, Gordon and Breach, Armsterdam, The Netherlands, 1993.

[8] I. M. Gelfand and K. Vilenkin, *Generalized Functions*, vol. 1, Academic Press, New York, NY, USA, 1964.

[9] G. Arfken, *Mathematical Methods For Physicists*, Academic Press, Orlando, Fla, USA, 3rd edition, 1985.

Hindawi Publishing Corporation
Advances in Mathematical Physics
Volume 2013, Article ID 869484, 6 pages
http://dx.doi.org/10.1155/2013/869484

Research Article

The Periodic Solution of Fractional Oscillation Equation with Periodic Input

Jun-Sheng Duan[1,2]

[1] *School of Sciences, Shanghai Institute of Technology, Shanghai 201418, China*
[2] *School of Mathematics and Information Sciences, Zhaoqing University, Zhaoqing, Guangdong 526061, China*

Correspondence should be addressed to Jun-Sheng Duan; duanjssdu@sina.com

Received 5 July 2013; Revised 14 August 2013; Accepted 15 August 2013

Academic Editor: Ming Li

The periodic solution of fractional oscillation equation with periodic input is considered in this work. The fractional derivative operator is taken as ${}_{-\infty}D_t^{\alpha}$, where the initial time is $-\infty$; hence, initial conditions are not needed in the model of the present fractional oscillation equation. With the input of the harmonic oscillation, the solution is derived to be a periodic function of time t with the same circular frequency as the input, and the frequency of the solution is not affected by the system frequency c as is affected in the integer-order case. These results are similar to the case of a damped oscillation with a periodic input in the integer-order case. Properties of the periodic solution are discussed, and the fractional resonance frequency is introduced.

1. Introduction

Fractional calculus has been used in the mathematical description of real problems arising in different fields of science. It covers the fields of viscoelasticity, anomalous diffusion, analysis of feedback amplifiers, capacitor theory, fractances, generalized voltage dividers, electrode-electrolyte interface models, fractional multipoles, fitting of experimental data, and so on [1–5]. Scientists and engineers became aware of the fact that the description of some phenomena is more accurate when the fractional derivative is used. In recent years, even fractional-order models of happiness [6] and love [7] have been developed, and they are claimed to give a better representation than the integer-order dynamical systems approach.

The fractional differential and integral operators have been extensively applied to the field of viscoelasticity [8]. The use of fractional calculus for the mathematical modelling of viscoelastic materials is quite natural. The main reasons for the theoretical development are the wide use of polymers in various fields of engineering.

The theorem of existence and uniqueness of solutions for fractional differential equations has been presented in [1, 2, 9, 10]. The theory and applications of fractional differential equations are much involved [1–5, 11–17]. Fractional oscillation equations were introduced and discussed by Caputo [18], Bagley and Torvik [19], Beyer and Kempfle [20], Mainardi [21], Gorenflo and Mainardi [22], and others.

Fractional oscillators and fractional dynamical systems were investigated in [23–28]. Achar et al. [23] and Al-rabtah et al. [24] studied the response characteristics of the fractional oscillator. Li et al. [25] considered the impulse response and the stability behavior of a class of fractional oscillators. Lim et al. [26] established the relationship between fractional oscillator processes and the corresponding fractional Brownian motion processes. Lim and Teo [27] introduced a fractional oscillator process as a solution of a stochastic differential equation with two fractional orders. Li [28] proposed an approach to approximate ideal filters by using frequency responses of fractional order.

Let $f(t)$ be piecewise continuous on $(a, +\infty)$ and integrable on any subinterval (a, t). Then, the Riemann-Liouville fractional integral of $f(t)$ is defined as [1–4]

$$ {}_aJ_t^{\alpha} f(t) := \int_a^t \frac{(t-s)^{\alpha-1}}{\Gamma(\alpha)} f(s)\, ds, \quad \alpha > 0, \tag{1} $$

where $\Gamma(\cdot)$ is Euler's gamma function.

Let $f^{(n)}(t)$ be piecewise continuous on $(a, +\infty)$ and integrable on any subinterval (a, t). Then, the Caputo fractional derivative of $f(t)$ of order α, $n-1 < \alpha < n$, is defined as [1–4]

$$ {}_aD_t^{\alpha} f(t) := {}_aJ_t^{n-\alpha} f^{(n)}(t), \quad n-1 < \alpha < n,\ n \in \mathbb{N}^+. \quad (2) $$

It is well-known that the fractional oscillation equation

$$ \begin{aligned} {}_0D_t^{\alpha} x(t) + c^{\alpha} x(t) &= 0, \quad 1 < \alpha < 2, \\ x(0) = c_0, &\qquad x'(0) = c_1 \end{aligned} \quad (3) $$

does not have a periodic solution [21, 22, 29, 30]. The existence of periodic solutions is often a desired property in dynamical systems, constituting one of the most important research directions in the theory of dynamical systems. The existence of weighted pseudo-almost periodic solutions of fractional-order differential equations has been investigated in [31].

In this work, we consider the fractional oscillation equation with periodic input using the fractional derivative operator ${}_{-\infty}D_t^{\alpha}$. We will derive a periodic solution for this equation and discuss its properties. Since we do not consider the effect of initial values, so the periodic solution can be regarded as an asymptotic steady-state solution for a fractional oscillation with initial conditions.

For a classic undamped oscillation with the periodic input

$$ \begin{aligned} x''(t) + c^2 x(t) &= b\cos(\lambda t), \quad c > 0,\ b > 0,\ \lambda > 0, \\ x(0) = c_0, &\qquad x'(0) = c_1, \end{aligned} \quad (4) $$

we list their solutions as follows.

(i) If $\lambda \neq c$,

$$ x(t) = c_0 \cos(ct) + c_1 \frac{\sin(ct)}{c} + \frac{b(\cos(\lambda t) - \cos(ct))}{c^2 - \lambda^2}. \quad (5) $$

(ii) If $\lambda = c$,

$$ x(t) = c_0 \cos(ct) + c_1 \frac{\sin(ct)}{c} + \frac{bt \sin(ct)}{2c}. \quad (6) $$

In the next section, as a comparison we solve the fractional oscillation equation using the fractional derivative operator ${}_0D_t^{\alpha}$ with the periodic input and initial conditions. In Section 3, we consider the fractional oscillation equation using the fractional derivative operator ${}_{-\infty}D_t^{\alpha}$ with the periodic input.

We consider the periodic problem of linear fractional differential system. For nonlinear fractional differential system, the problem is more challenging and some contributions have been made. For example, Li and Ma [32] gave the linearization and stability theorems of the nonlinear fractional system.

2. Fractional Oscillation Equation with Periodic Input and Initial Conditions

In this section, we solve the fractional oscillation equation with the periodic input and initial conditions

$$ \begin{aligned} {}_0D_t^{\alpha} x(t) + c^{\alpha} x(t) &= b\cos(\lambda t), \\ c > 0, \quad b > 0, \quad \lambda > 0, &\quad 1 < \alpha < 2, \end{aligned} \quad (7) $$

$$ x(0) = c_0, \qquad x'(0) = c_1. \quad (8) $$

The Laplace transform of (7) gives

$$ s^{\alpha} \tilde{x}(s) + c^{\alpha} \tilde{x}(s) = c_0 s^{\alpha-1} + c_1 s^{\alpha-2} + b\mathscr{L}[\cos(\lambda t)], \quad (9) $$

where $\mathscr{L}$ denotes the Laplace transform

$$ \mathscr{L}[x(t)] = \tilde{x}(s) := \int_0^{\infty} e^{-st} x(t)\, dt. \quad (10) $$

Solving for $\tilde{x}(s)$ yields

$$ \tilde{x}(s) = c_0 \frac{s^{\alpha-1}}{c^{\alpha} + s^{\alpha}} + c_1 \frac{s^{\alpha-2}}{c^{\alpha} + s^{\alpha}} + b \frac{1}{c^{\alpha} + s^{\alpha}} \mathscr{L}[\cos(\lambda t)]. \quad (11) $$

Upon applying the inverse Laplace transform, we obtain

$$ \begin{aligned} x(t) = {} & c_0 E_{\alpha,1}\left(-(ct)^{\alpha}\right) + c_1 t E_{\alpha,2}\left(-(ct)^{\alpha}\right) \\ & + b\left(t^{\alpha-1} E_{\alpha,\alpha}\left(-(ct)^{\alpha}\right)\right) * \cos(\lambda t), \end{aligned} \quad (12) $$

where $E_{\alpha,\beta}(\cdot)$ denotes the Mittag-Leffler function [1, 21, 22]

$$ E_{\alpha,\beta}(z) = \sum_{k=0}^{\infty} \frac{z^k}{\Gamma(\alpha k + \beta)} \quad (13) $$

and $*$ denotes the Laplace convolution

$$ \begin{aligned} & \left(t^{\alpha-1} E_{\alpha,\alpha}\left(-(ct)^{\alpha}\right)\right) * \cos(\lambda t) \\ & \quad = \int_0^t \tau^{\alpha-1} E_{\alpha,\alpha}\left(-(c\tau)^{\alpha}\right) \cos(\lambda(t-\tau))\, d\tau, \end{aligned} \quad (14) $$

and where the Laplace transform formula [1]

$$ \mathscr{L}\left[t^{\alpha-\beta-1} E_{\alpha,\alpha-\beta}\left(-ct^{\alpha}\right)\right] = \frac{s^{\beta}}{c + s^{\alpha}} \quad (15) $$

is used. Since

$$ \mathscr{L}[\cos(\lambda t)] = \frac{s}{\lambda^2 + s^2}, \quad (16) $$

the convolution in (14) can also be expressed as the following inverse Laplace transform:

$$ \begin{aligned} Y(t) := {} & \left(t^{\alpha-1} E_{\alpha,\alpha}\left(-(ct)^{\alpha}\right)\right) * \cos(\lambda t) \\ & = \mathscr{L}^{-1}\left[\frac{s}{(c^{\alpha} + s^{\alpha})(\lambda^2 + s^2)}\right]. \end{aligned} \quad (17) $$

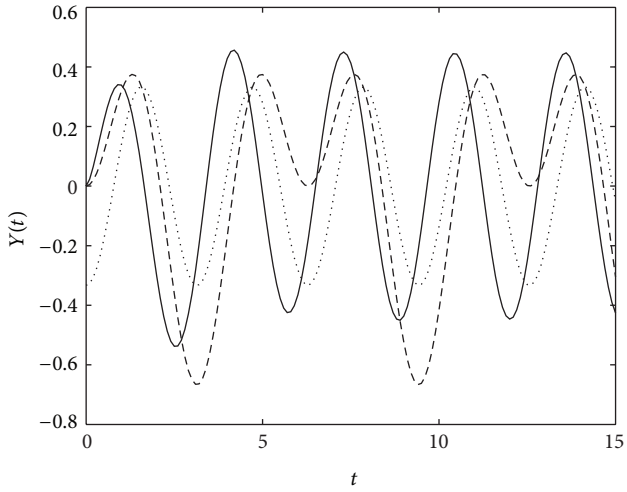

Figure 1: Solid line: $Y(t)$ versus t on interval $0 \le t \le 15$ for $c = 1$, $\lambda = 2$, and $\alpha = 1.5$; dashed line: $(\cos(2t) - \cos(t))/-3$ versus t; doted line: $\cos(2t)/-3$ versus t.

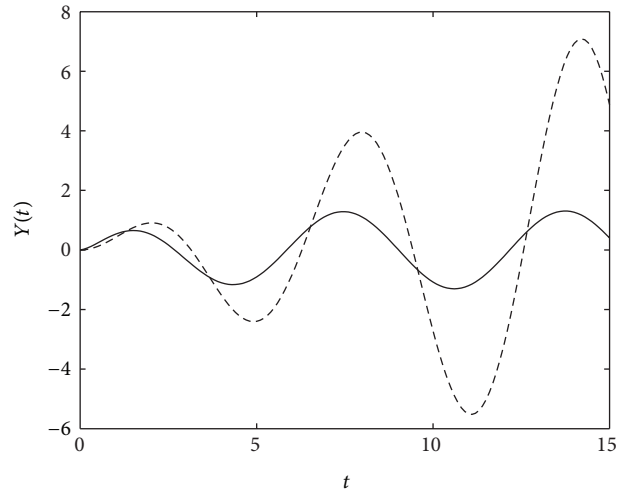

Figure 2: Solid line: $Y(t)$ versus t on interval $0 \le t \le 15$ for $c = 1, \lambda = 1$, and $\alpha = 1.5$; dashed line: $t\sin(t)/2$ versus t.

In Figure 1, the curve of $Y(t)$ versus t on interval $0 \le t \le 15$ for $c = 1$, $\lambda = 2$, and $\alpha = 1.5$ is plotted. In order to compare with the case of $\alpha = 2$ in (5), we also plot the curves of $(\cos(\lambda t) - \cos(ct))/(c^2 - \lambda^2)$ versus t and $\cos(\lambda t)/(c^2 - \lambda^2)$ versus t for $c = 1$ and $\lambda = 2$ in Figure 1. We observe that with the increasing of t, the fractional oscillation $Y(t)$ is more relative to the function $\cos(\lambda t)/(c^2 - \lambda^2)$ than to the function $(\cos(\lambda t) - \cos(ct))/(c^2 - \lambda^2)$. This means that in the fractional case, the effect of the natural frequency c of the system dies out with the passage of time, which displays a damping feature and is different from the integer-order case in (5).

In Figure 2, the curve of $Y(t)$ versus t on interval $0 \le t \le 15$ for $c = 1$, $\lambda = 1$ and $\alpha = 1.5$ is plotted. In order to compare with the case of $\alpha = 2$ in (6), we also plot the curve of $t\sin(ct)/2c$ versus t for $c = 1$ in Figure 2.

The Mittag-Leffler functions in (12) have the following asymptotic behaviour [1]:

$$E_{\alpha,1}\left(-(ct)^{\alpha}\right) \sim \frac{(1-\alpha)\,c^{-\alpha}}{\Gamma(2-\alpha)}t^{-\alpha}, \quad t \longrightarrow +\infty,$$

$$tE_{\alpha,2}\left(-(ct)^{\alpha}\right) \sim \frac{c^{-\alpha}}{\Gamma(2-\alpha)}t^{-(\alpha-1)}, \quad t \longrightarrow +\infty, \tag{18}$$

$$t^{\alpha-1}E_{\alpha,\alpha}\left(-(ct)^{\alpha}\right) \sim \frac{\alpha(1-\alpha)\,c^{-2\alpha}}{\Gamma(2-\alpha)}t^{-(\alpha+1)}, \quad t \longrightarrow +\infty.$$

None of the three Mittag-Leffler functions in (12) are periodic. Numerical simulation displays that the convolution $Y(t)$ in (17) is not periodic, either.

If $\alpha = 2$, the Mittag-Leffler functions in (12) become

$$E_{2,1}\left(-(ct)^2\right) = \cos(ct), \qquad tE_{2,2}\left(-(ct)^2\right) = \frac{\sin(ct)}{c}. \tag{19}$$

In this case, calculating the convolution $\sin(ct) * \cos(\lambda t)$ for the two cases $\lambda \neq c$ and $\lambda = c$, we obtain the classical results (5) and (6) from (12).

But for the fractional case, $1 < \alpha < 2$, the Mittag-Leffler function $t^{\alpha-1}E_{\alpha,\alpha}(-(ct)^{\alpha})$ in (17) approaches asymptotically $t^{-\alpha-1}$ as $t \to +\infty$, so $Y(t)$ is dominated by $\cos(\lambda t)$ as $t \to +\infty$.

We note that it is possible to obtain exact periodic solutions in impulsive fractional-order dynamical systems by choosing the correct impulses at the right moments of time [29].

3. Derivation of the Periodic Solutions for Fractional Oscillation Equation

We consider the fractional oscillation equation using the fractional derivative operator ${}_{-\infty}D_t^{\alpha}$:

$$\begin{gathered} {}_{-\infty}D_t^{\alpha}x(t) + c^{\alpha}x(t) = b\cos(\lambda t), \\ c > 0, \quad b > 0, \quad \lambda > 0, \quad 1 < \alpha < 2. \end{gathered} \tag{20}$$

Equation (20) does not need to subject to initial conditions, and its solution is steady-state.

We use the following Fourier transform and its inverse:

$$\begin{aligned} \mathcal{F}\left[g(t);\omega\right] &= G(\omega) := \int_{-\infty}^{\infty} g(t)\,e^{i\omega t}dt, \\ \mathcal{F}^{-1}\left[G(\omega);t\right] &= g(t) := \frac{1}{2\pi}\int_{-\infty}^{\infty} G(\omega)\,e^{-i\omega t}d\omega, \end{aligned} \tag{21}$$

and the Fourier transform formulas [1, 33]

$$\begin{aligned} \mathcal{F}\left[{}_{-\infty}D_t^{\alpha}x(t);\omega\right] &= (-i\omega)^{\alpha}X(\omega), \\ \mathcal{F}\left[e^{i\lambda t};\omega\right] &= 2\pi\delta(\omega+\lambda), \end{aligned} \tag{22}$$

where $\delta(\cdot)$ is the Dirac's delta function.

We rewrite the right hand side of (20) as a complex exponential function and first solve the equation

$${}_{-\infty}D_t^{\alpha}x(t) + c^{\alpha}x(t) = be^{i\lambda t}. \tag{23}$$

The real part of the solution of (23) is the solution of (20). Applying the Fourier transform to (23) we obtain

$$(-i\omega)^{\alpha} X(\omega) + c^{\alpha} X(\omega) = 2\pi b\delta(\omega + \lambda), \tag{24}$$

from which we solve, for $X(\omega)$,

$$X(\omega) = \frac{2\pi b\delta(\omega + \lambda)}{c^{\alpha} + (-i\omega)^{\alpha}}. \tag{25}$$

Calculating the inverse Fourier transform leads to

$$x(t) = \mathcal{F}^{-1}\left[\frac{2\pi b\delta(\omega + \lambda)}{c^{\alpha} + (-i\omega)^{\alpha}}; t\right] = \frac{be^{i\lambda t}}{c^{\alpha} + (i\lambda)^{\alpha}}. \tag{26}$$

Then, we take the real part of (26) and obtain the solution of (20):

$$x(t) = b\frac{\left(c^{\alpha} + \lambda^{\alpha}\cos(\alpha\pi/2)\right)\cos(\lambda t) + \lambda^{\alpha}\sin(\alpha\pi/2)\sin(\lambda t)}{\left(c^{\alpha} + \lambda^{\alpha}\cos(\alpha\pi/2)\right)^2 + \lambda^{2\alpha}\sin^2(\alpha\pi/2)}. \tag{27}$$

Obviously, (27) represents a periodic solution with the same circular frequency as the input $b\cos(\lambda t)$. Furthermore, (27) can be rewritten as the form

$$x(t) = \frac{b\cos(\lambda t - C)}{\sqrt{\left(c^{\alpha} + \lambda^{\alpha}\cos(\alpha\pi/2)\right)^2 + \lambda^{2\alpha}\sin^2(\alpha\pi/2)}}, \tag{28}$$

where the phase angle is

$$C = \tan^{-1}\frac{\lambda^{\alpha}\sin(\alpha\pi/2)}{c^{\alpha} + \lambda^{\alpha}\cos(\alpha\pi/2)}, \tag{29}$$

and the amplitude is

$$A = A(\alpha, \lambda) = \frac{b}{\sqrt{\left(c^{\alpha} + \lambda^{\alpha}\cos(\alpha\pi/2)\right)^2 + \lambda^{2\alpha}\sin^2(\alpha\pi/2)}}. \tag{30}$$

The curves of $x(t)$ versus t for $b = 1$, $c = 1$, $\lambda = 1.5$, and different α and the curves of $x(t)$ versus t for $b = 1, c = 1$, $\alpha = 1.5$ and different λ are plotted in Figures 3 and 4, respectively.

The effects of the order α and the input circular frequency λ on the amplitude A are interesting. The curves of A versus α for $b = 1$, $c = 1$ and, different λ and the curves of A versus λ for $b = 1$, $c = 1$, and different α are plotted in Figures 5 and 6, respectively.

Similar to a damped oscillation with a periodic input in an integer-ordered case, we observe that the curves of A versus λ have a peak value. Furthermore, the derivative of the amplitude with respective to the frequency λ is calculated to be

$$\frac{dA}{d\lambda} = -\frac{\alpha b\lambda^{\alpha-1}\left(\lambda^{\alpha} + c^{\alpha}\cos(\pi\alpha/2)\right)}{\left(\lambda^{2\alpha} + c^{2\alpha} + 2c^{\alpha}\lambda^{\alpha}\cos(\pi\alpha/2)\right)^{3/2}}. \tag{31}$$

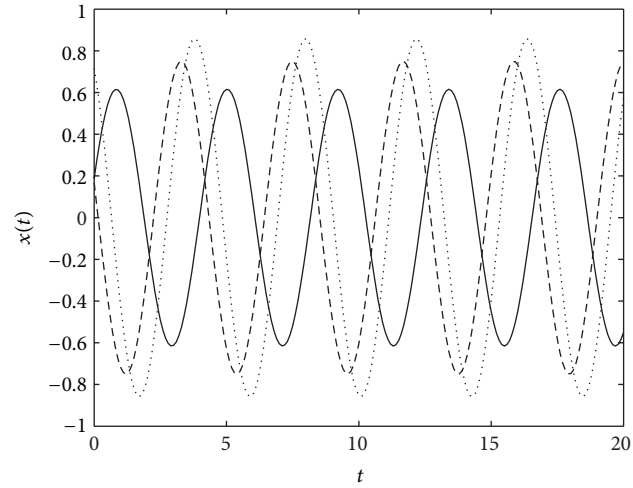

Figure 3: Curves of $x(t)$ versus t for $b = 1$, $c = 1$, and $\lambda = 1.5$ and for $\alpha = 1.2$ (solid line), $\alpha = 1.5$ (dashed line), and $\alpha = 1.8$ (doted line).

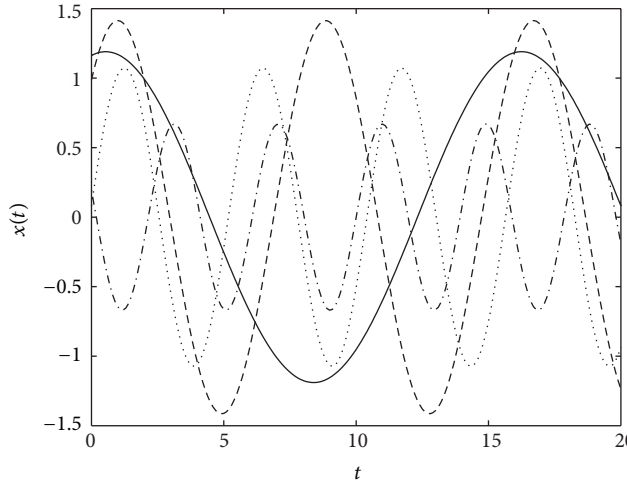

Figure 4: Curves of $x(t)$ versus t for $b = 1$, $c = 1$, and $\alpha = 1.5$ and for $\lambda = 0.4$ (solid line), $\lambda = 0.8$ (dashed line), $\lambda = 1.2$ (doted line), and $\lambda = 1.6$ (doted-dashed line).

Letting $dA/d\lambda = 0$, we obtain

$$\lambda^{*} = c\left(-\cos\left(\frac{\pi\alpha}{2}\right)\right)^{1/\alpha}. \tag{32}$$

For each specified α, $1 < \alpha < 2$, the amplitude $A = A(\alpha, \lambda)$ takes the maximum $A_{\max}(\alpha)$, when $\lambda = \lambda^{*}$. We call λ^{*} the fractional resonance frequency. From (32) the resonance frequency λ^{*} increases monotonically from 0 to c with increasing of α from 1 to 2. The curve of λ^{*} versus α for $c = 1$ is plotted in Figure 7.

The maximum amplitude is calculated to be

$$A_{\max}(\alpha) = A(\alpha, \lambda^{*}) = \frac{b}{c^{\alpha}\sin(\pi\alpha/2)}. \tag{33}$$

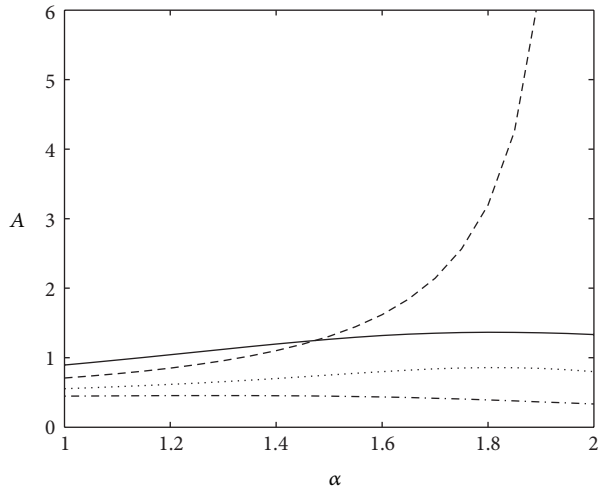

Figure 5: Curves of A versus α for $b = 1$ and $c = 1$ and for $\lambda = 0.5$ (solid line), $\lambda = 1$ (dashed line), $\lambda = 1.5$ (doted line), and $\lambda = 2$ (doted-dashed line).

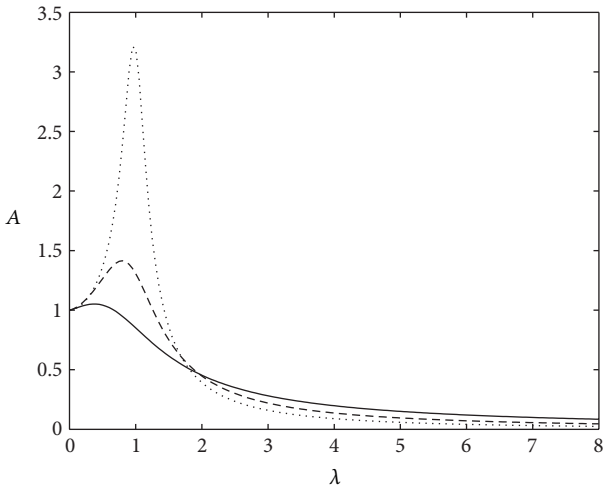

Figure 6: Curves of A versus λ for $b = 1$ and $c = 1$ and for $\alpha = 1.2$ (solid line), $\alpha = 1.5$ (dashed line), and $\alpha = 1.8$ (doted line).

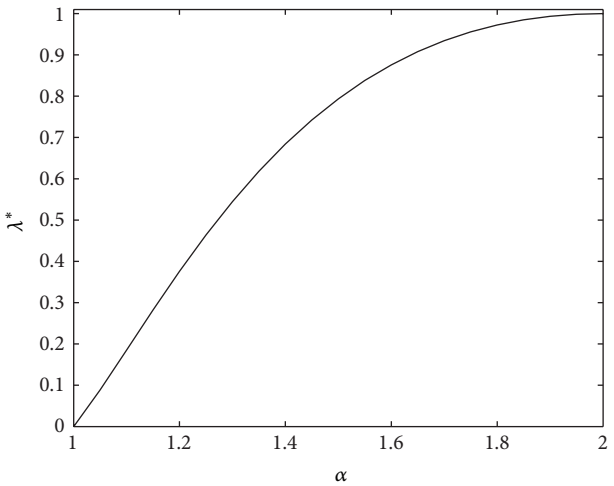

Figure 7: Curve of λ^* versus α for $c = 1$.

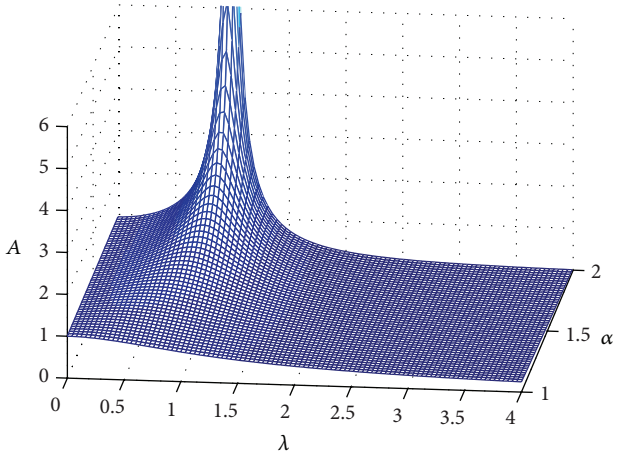

Figure 8: Surface of amplitude $A(\alpha, \lambda)$ for $b = c = 1$.

It follows from (33) that

$$A_{\max}(\alpha) \longrightarrow \frac{b}{c^{\alpha}}, \quad \alpha \longrightarrow 1^{+},$$
$$A_{\max}(\alpha) \longrightarrow +\infty, \quad \alpha \longrightarrow 2^{-}. \tag{34}$$

The surface of the amplitude $A(\alpha, \lambda)$ for $b = c = 1$ is shown in Figure 8.

4. Conclusions

The fractional oscillation equations with a harmonic periodic input are considered for the fractional derivative operators ${}_0D_t^{\alpha}$ and ${}_{-\infty}D_t^{\alpha}$, respectively. For the latter fractional oscillation equation, the periodic solution with the same circular frequency as the input function is derived. The solution is similar to the case of a damped oscillation with a periodic input in the integer-order case, and a fractional resonance frequency occurs. The frequency of the solution of the fractional oscillation equation is not affected by the system frequency c. The results show that the fractional oscillation equations represent the damping feature. We give a detailed analysis for the effects of the order α and the input circular frequency λ on the oscillation amplitude A. The periodic solution can be regarded as an asymptotic steady-state solution for a fractional oscillation with initial conditions.

Acknowledgment

This work was supported by the National Natural Science Foundation of China (no. 11201308) and the Innovation Program of Shanghai Municipal Education Commission (no. 14ZZ161).

References

[1] I. Podlubny, *Fractional Differential Equations*, vol. 198 of *Mathematics in Science and Engineering*, Academic Press, San Diego, Calif, USA, 1999.

[2] A. A. Kilbas, H. M. Srivastava, and J. J. Trujillo, *Theory and Applications of Fractional Differential Equations*, vol. 204 of *North-Holland Mathematics Studies*, Elsevier Science, Amsterdam, The Netherlands, 2006.

[3] F. Mainardi, *Fractional Calculus and Waves in Linear Viscoelasticity*, Imperial College Press, London, UK, 2010.

[4] D. Băleanu, K. Diethelm, E. Scalas, and J. J. Trujillo, *Fractional Calculus Models and Numerical Methods*, vol. 3 of *Series on Complexity, Nonlinearity and Chaos*, World Scientific Publishing, Hackensack, NJ, USA, 2012.

[5] J. T. Machado, V. Kiryakova, and F. Mainardi, "Recent history of fractional calculus," *Communications in Nonlinear Science and Numerical Simulation*, vol. 16, no. 3, pp. 1140–1153, 2011.

[6] L. Song, S. Xu, and J. Yang, "Dynamical models of happiness with fractional order," *Communications in Nonlinear Science and Numerical Simulation*, vol. 15, no. 3, pp. 616–628, 2010.

[7] R. Gu and Y. Xu, "Chaos in a fractional-order dynamical model of love and its control," in *Nonlinear Mathematics for Uncertainty and Its Applications*, S. Li, X. Wang, Y. Okazaki, J. Kawabe, T. Murofushi, and L. Guan, Eds., vol. 100 of *Advances in Intelligent and Soft Computing*, pp. 349–356, Springer, Berlin, Germany, 2011.

[8] Y. A. Rossikhin and M. V. Shitikova, "Applications of fractional calculus to dynamic problems of linear and nonlinear hereditary mechanics of solids," *Applied Mechanics Reviews*, vol. 50, no. 1, pp. 15–67, 1997.

[9] D. Băleanu, O. G. Mustafa, and R. P. Agarwal, "An existence result for a superlinear fractional differential equation," *Applied Mathematics Letters*, vol. 23, no. 9, pp. 1129–1132, 2010.

[10] D. Băleanu and O. G. Mustafa, "On the global existence of solutions to a class of fractional differential equations," *Computers & Mathematics with Applications*, vol. 59, no. 5, pp. 1835–1841, 2010.

[11] J.-S. Duan, "Time- and space-fractional partial differential equations," *Journal of Mathematical Physics*, vol. 46, no. 1, Article ID 013504, pp. 13504–13511, 2005.

[12] V. Daftardar-Gejji and H. Jafari, "An iterative method for solving nonlinear functional equations," *Journal of Mathematical Analysis and Applications*, vol. 316, no. 2, pp. 753–763, 2006.

[13] G. Wu, "A fractional characteristic method for solving fractional partial differential equations," *Applied Mathematics Letters*, vol. 24, no. 7, pp. 1046–1050, 2011.

[14] H. Jafari, C. M. Khalique, and M. Nazari, "An algorithm for the numerical solution of nonlinear fractional-order Van der Pol oscillator equation," *Mathematical and Computer Modelling*, vol. 55, no. 5-6, pp. 1782–1786, 2012.

[15] H. Jafari, M. Nazari, D. Baleanu, and C. M. Khalique, "A new approach for solving a system of fractional partial differential equations," *Computers & Mathematics with Applications*, vol. 66, no. 5, pp. 838–843, 2013.

[16] J.-S. Duan, T. Chaolu, and R. Rach, "Solutions of the initial value problem for nonlinear fractional ordinary differential equations by the Rach-Adomian-Meyers modified decomposition method," *Applied Mathematics and Computation*, vol. 218, no. 17, pp. 8370–8392, 2012.

[17] J. S. Duan, R. Rach, D. Baleanu, and A. M. Wazwaz, "A review of the Adomian decomposition method and its applications to fractional differential equations," *Communications in Fractional Calculus*, vol. 3, pp. 73–99, 2012.

[18] M. Caputo, "Linear models of dissipation whose Q is almost frequency independent—part II," *Geophysical Journal of the Royal Astronomical Society*, vol. 13, no. 5, pp. 529–539, 1967.

[19] R. L. Bagley and P. J. Torvik, "A generalized derivative model for an elastomer damper," *The Shock and Vibration Bulletin*, vol. 49, no. 2, pp. 135–143, 1979.

[20] H. Beyer and S. Kempfle, "Definition of physically consistent damping laws with fractional derivatives," *Zeitschrift für Angewandte Mathematik und Mechanik*, vol. 75, no. 8, pp. 623–635, 1995.

[21] F. Mainardi, "Fractional relaxation-oscillation and fractional diffusion-wave phenomena," *Chaos, Solitons & Fractals*, vol. 7, no. 9, pp. 1461–1477, 1996.

[22] R. Gorenflo and F. Mainardi, "Fractional calculus: integral and differential equations of fractional order," in *Fractals and Fractional Calculus in Continuum Mechanics*, A. Carpinteri and F. Mainardi, Eds., vol. 378 of *CISM Courses and Lectures*, pp. 223–276, Springer, New York, NY, USA, 1997.

[23] B. N. N. Achar, J. W. Hanneken, and T. Clarke, "Response characteristics of a fractional oscillator," *Physica A*, vol. 309, no. 3-4, pp. 275–288, 2002.

[24] A. Al-rabtah, V. S. Ertürk, and S. Momani, "Solutions of a fractional oscillator by using differential transform method," *Computers & Mathematics with Applications*, vol. 59, no. 3, pp. 1356–1362, 2010.

[25] M. Li, S. C. Lim, and S. Chen, "Exact solution of impulse response to a class of fractional oscillators and its stability," *Mathematical Problems in Engineering*, vol. 2011, Article ID 657839, 9 pages, 2011.

[26] S. C. Lim, L. Ming, and L. P. Teo, "Locally self-similar fractional oscillator processes," *Fluctuation and Noise Letters*, vol. 7, no. 2, pp. L169–L179, 2007.

[27] S. C. Lim and L. P. Teo, "The fractional oscillator process with two indices," *Journal of Physics A*, vol. 42, no. 6, Article ID 065208, 34 pages, 2009.

[28] M. Li, "Approximating ideal filters by systems of fractional order," *Computational and Mathematical Methods in Medicine*, vol. 2012, Article ID 365054, 6 pages, 2012.

[29] E. Kaslik and S. Sivasundaram, "Non-existence of periodic solutions in fractional-order dynamical systems and a remarkable difference between integer and fractional-order derivatives of periodic functions," *Nonlinear Analysis: Real World Applications*, vol. 13, no. 3, pp. 1489–1497, 2012.

[30] J.-S. Duan, Z. Wang, Y.-L. Liu, and X. Qiu, "Eigenvalue problems for fractional ordinary differential equations," *Chaos, Solitons & Fractals*, vol. 46, pp. 46–53, 2013.

[31] R. P. Agarwal, B. de Andrade, and C. Cuevas, "Weighted pseudo-almost periodic solutions of a class of semilinear fractional differential equations," *Nonlinear Analysis: Real World Applications*, vol. 11, no. 5, pp. 3532–3554, 2010.

[32] C. Li and Y. Ma, "Fractional dynamical system and its linearization theorem," *Nonlinear Dynamics*, vol. 71, no. 4, pp. 621–633, 2013.

[33] B. Davies, *Integral Transforms and Their Applications*, Springer, New York, NY, USA, 3rd edition, 2001.

Hindawi Publishing Corporation
Advances in Mathematical Physics
Volume 2013, Article ID 293706, 10 pages
http://dx.doi.org/10.1155/2013/293706

Research Article

Maximum Norm Error Estimates of ADI Methods for a Two-Dimensional Fractional Subdiffusion Equation

Yuan-Ming Wang[1,2]

[1] *Department of Mathematics, East China Normal University, Shanghai 200241, China*
[2] *Scientific Computing Key Laboratory of Shanghai Universities, Division of Computational Science, E-Institute of Shanghai Universities, Shanghai Normal University, Shanghai 200234, China*

Correspondence should be addressed to Yuan-Ming Wang; ymwang@math.ecnu.edu.cn

Received 25 June 2013; Accepted 8 July 2013

Academic Editor: Ming Li

This paper is concerned with two alternating direction implicit (ADI) finite difference methods for solving a two-dimensional fractional subdiffusion equation. An explicit error estimate for each of the two methods is provided in the discrete maximum norm. It is shown that the methods have the same order as their truncation errors with respect to the discrete maximum norm. Numerical results are given to confirm the theoretical analysis results.

1. Introduction

Fractional differential equations and fractional calculus arise in various application problems in science and engineering [1–16]. Various numerical methods have been developed for the computation of fractional differential equations [17–34]. Fractional subdiffusion equations describe a special type of anomalous diffusion [35], and it is a more difficult task to solve this kind of equation numerically.

Numerical works for fractional subdiffusion equations are mostly focused on one-dimensional problems due to the memory effect in fractional derivatives; see, for example, [19, 20, 20–26, 31–33, 36–42]. A two-dimensional anomalous subdiffusion equation was numerically treated in [43, 44], where explicit and implicit finite difference schemes were proposed. Chen et al. [28] extended their work in [43] to a variable-order subdiffusion equation. Liu et al. [45] developed an implicit meshless approach based on the radial basis function for the numerical simulation of a two-dimensional subdiffusion problem. Chen and Liu [18] considered an implicit difference scheme for a three-dimensional fractional advection-diffusion equation, and a Richardson extrapolation was applied to improve the accuracy.

The complexity of the fractional differential equations comes from the involving fractional derivatives that are nonlocal and have the character of history dependence and universal mutuality. This means that the computations would be costly if the implicit schemes were applied, especially for solving multidimensional problems [43, 44]. Some researchers have explored some techniques for reducing this cost. These techniques include the adaptive technique [46] and the matrix transfer technique [47, 48]. It is well known that alternating direction implicit (ADI) methods are unconditionally stable as the traditional implicit methods. On the other hand, they reduce a multidimensional problem to a series of independent one-dimensional problems, and thus the computational complexities and the computational cost can be greatly reduced. Therefore, ADI methods for fractional differential equations have the potential to significantly reduce the computational cost, while maintaining the stability of the numerical methods. The works in [29, 49–53] treated ADI finite difference methods for space fractional diffusion equations, and the work in [54] discussed ADI finite difference methods for fractional diffusion wave equations. Recently, Cui [55] derived an ADI compact finite difference scheme for a two-dimensional fractional subdiffusion equation, where the Grünwald formula is used to approximate the temporal Riemann-Liouville fractional derivative, and the spatial derivatives are approximated by a compact finite difference scheme. Another way to treat fractional subdiffusion

problem is to transform the original subdiffusion equation into an equivalent equation by replacing the temporal Riemann-Liouville fractional derivative by the temporal Caputo fractional derivative; see, for example, [40, 42, 56]. An advantage of this approach is that the L_1 approximation (see [1, 24, 25, 40, 57, 58]) can be used to deal with the temporal fractional derivative, and so the resulting scheme has the better temporal accuracy than the first order without the Crank-Nicolson technique (see [25, 40–42]). Based on the previous approach, Zhang and Sun [59] constructed two ADI finite difference schemes, called L_1-ADI and BD-ADI schemes, for the following two-dimensional problem of subdiffusion equation with the temporal Caputo fractional derivative:

$$\begin{aligned} {}_0^C\mathscr{D}_t^\alpha u(x,y,t) &= \Delta u(x,y,t) + f(x,y,t), \\ &\qquad (x,y) \in \Omega, \quad t \in (0,T], \\ u(x,y,t) &= \varphi(x,y,t), \quad (x,y) \in \partial\Omega, \ t \in (0,T], \\ u(x,y,0) &= \psi(x,y), \quad (x,y) \in \overline{\Omega}, \end{aligned} \tag{1}$$

where $\Omega = (0,l_1) \times (0,l_2)$, $\overline{\Omega} = \Omega \cup \partial\Omega$, $\partial\Omega$ is the boundary of Ω, T is a positive constant, Δ is the two-dimensional Laplacian, and ${}_0^C\mathscr{D}_t^\alpha$ denotes the temporal Caputo fractional derivative operator defined as

$$\begin{aligned} &{}_0^C\mathscr{D}_t^\alpha u(x,y,t) \\ &\quad = \frac{1}{\Gamma(1-\alpha)} \int_0^t \frac{\partial u(x,y,s)}{\partial s} (t-s)^{-\alpha} \mathrm{d}s, \quad 0 < \alpha < 1. \end{aligned} \tag{2}$$

The main concern in that paper is the construction of the schemes and error estimates in the discrete H^1-norm. Since H^1-norm error estimates do not provide immediate insight on the phase error occurring during the time evolution, it is more preferable to give error estimates in the discrete maximum norm when we measure computation errors in practice. In this paper, we continue the investigation of the paper [59], by establishing a maximum norm error estimate for the ADI discretizations. It is known that an H^1-norm error estimate does not imply a maximum norm error estimate for two-dimensional problems. We here present a technique of H^2 discrete energy analysis in order to obtain an explicit maximum norm error estimate.

The outline of the paper is as follows. In Section 2, we derive ADI finite difference schemes for (1) and present our main results of the maximum norm error estimates. The proof of the main error results is given in Section 3. In Section 4, we give some numerical results demonstrating the accuracy of the schemes in the discrete maximum norm. Section 5 contains some concluding remarks.

2. ADI Schemes and Maximum Norm Error Estimates

We partition Ω with nonisotropic uniform mesh sizes h_1 and h_2 in the x and y directions, respectively. The integers $M_1 = l_1/h_1$ and $M_2 = l_2/h_2$. The mesh points $(x_i, y_j) = (ih_1, jh_2)$ $(0 \le i \le M_1, 0 \le j \le M_2)$. Let Ω_h and $\partial\Omega_h$ be the sets of mesh points lying in Ω and on $\partial\Omega$, respectively, and let $\overline{\Omega}_h = \Omega_h \cup \partial\Omega_h$. For any grid function $v = \{v_{i,j} \mid 0 \le i \le M_1, 0 \le j \le M_2\}$, we denote

$$\begin{aligned} \delta_x v_{i,j} &= \frac{\left(v_{i+1,j} - v_{i,j}\right)}{h_1}, \qquad \delta_y v_{i,j} = \frac{\left(v_{i,j+1} - v_{i,j}\right)}{h_2}, \\ \delta_x^2 v_{i,j} &= \frac{\left(\delta_x v_{i,j} - \delta_x v_{i-1,j}\right)}{h_1}, \qquad \delta_y^2 v_{i,j} = \frac{\left(\delta_y v_{i,j} - \delta_y v_{i,j-1}\right)}{h_2}, \\ \Delta_h v_{i,j} &= \delta_x^2 v_{i,j} + \delta_y^2 v_{i,j}. \end{aligned} \tag{3}$$

For a positive integer N, we let $\tau = T/N$ be the time step. Define $t_n = n\tau$ and

$$\begin{aligned} U_{i,j}^n &= u\left(x_i, y_j, t_n\right), \qquad f_{i,j}^n = f\left(x_i, y_j, t_n\right), \\ \varphi_{i,j}^n &= \varphi\left(x_i, y_j, t_n\right), \qquad \psi_{i,j} = \psi\left(x_i, y_j\right). \end{aligned} \tag{4}$$

For the temporal approximation, we introduce the operators

$$\begin{aligned} \delta_t U_{i,j}^n &= \frac{1}{\tau}\left(U_{i,j}^{n+1} - U_{i,j}^n\right), \\ D_t^\alpha U_{i,j}^n &= \frac{1}{\mu}\left(U_{i,j}^n - \sum_{k=1}^{n-1} \left(a_{n-k-1} - a_{n-k}\right) U_{i,j}^k - a_{n-1} U_{i,j}^0\right), \end{aligned} \tag{5}$$

where $\mu = \tau^\alpha \Gamma(2-\alpha)$ and $a_k = (k+1)^{1-\alpha} - k^{1-\alpha}$.

Using the Taylor expansion and the L_1 approximation of ${}_0^C\mathscr{D}_t^\alpha u(x,y,t)$ (see [25, 58, 59]), we have

$$\begin{aligned} {}_0^C\mathscr{D}_t^\alpha u\left(x_i, y_j, t_n\right) &= D_t^\alpha U_{i,j}^n + \left(R_t\right)_{i,j}^n, \\ \Delta u\left(x_i, y_j, t_n\right) &= \Delta_h U_{i,j}^n - \left(R_x\right)_{i,j}^n - \left(R_y\right)_{i,j}^n, \\ &\qquad \left(x_i, y_j\right) \in \Omega_h, \quad 1 \le n \le N, \end{aligned} \tag{6}$$

where

$$\begin{aligned} \left(R_x\right)_{i,j}^n &= \frac{h_1^2}{6} \int_0^1 \left(\frac{\partial^4 u}{\partial x^4}\left(x_i + sh_1, y_j, t_n\right) \right. \\ &\qquad \left. + \frac{\partial^4 u}{\partial x^4}\left(x_i - sh_1, y_j, t_n\right) \right) (1-s)^3 \mathrm{d}s, \\ \left(R_y\right)_{i,j}^n &= \frac{h_2^2}{6} \int_0^1 \left(\frac{\partial^4 u}{\partial y^4}\left(x_i, y_j + sh_2, t_n\right) \right. \\ &\qquad \left. + \frac{\partial^4 u}{\partial y^4}\left(x_i, y_j - sh_2, t_n\right) \right) (1-s)^3 \mathrm{d}s. \end{aligned} \tag{7}$$

There exists a positive constant $C(\alpha)$ independent of τ, h_1, h_2 and the time level n such that

$$\left|\left(R_t\right)_{i,j}^n\right| \le C(\alpha) \max_{0\le t\le t_n}\left|\frac{\partial^2 u}{\partial t^2}\left(x_i, y_j, t\right)\right| \tau^{2-\alpha}. \tag{8}$$

Substituting (6) into (1), we obtain

$$\begin{aligned} D_t^\alpha U_{i,j}^n &= \Delta_h U_{i,j}^n + f_{i,j}^n - \left(R_t\right)_{i,j}^n - \left(R_x\right)_{i,j}^n - \left(R_y\right)_{i,j}^n, \\ &\left(x_i, y_j\right) \in \Omega_h, \quad 1 \le n \le N. \end{aligned} \tag{9}$$

2.1. Construction of L_1-ADI and BD-ADI Schemes. In order to construct an ADI scheme, we add the term $\mu^2 D_t^\alpha \delta_x^2 \delta_y^2 U_{i,j}^n$ to (9). This yields

$$\begin{aligned} D_t^\alpha\left(U_{i,j}^n + \mu^2 \delta_x^2 \delta_y^2 U_{i,j}^n\right) &= \Delta_h U_{i,j}^n + f_{i,j}^n + \left(R_1\right)_{i,j}^n, \\ &\left(x_i, y_j\right) \in \Omega_h, \quad 1 \le n \le N, \end{aligned} \tag{10}$$

where

$$\left(R_1\right)_{i,j}^n = \mu^2 D_t^\alpha \delta_x^2 \delta_y^2 U_{i,j}^n - \left(R_t\right)_{i,j}^n - \left(R_x\right)_{i,j}^n - \left(R_y\right)_{i,j}^n. \tag{11}$$

It was shown in [59] that $|\mu^2 D_t^\alpha \delta_x^2 \delta_y^2 U_{i,j}^n| \le C_L(\alpha)\tau^{2\alpha}$ for a positive constant $C_L(\alpha)$ independent of τ, h_1, h_2 and the time level n. Thus, there exists a positive constant C_1 independent of τ, h_1, h_2 and the time level n such that

$$\left|\left(R_1\right)_{i,j}^n\right| \le C_1\left(\tau^{\min\{2\alpha, 2-\alpha\}} + h_1^2 + h_2^2\right). \tag{12}$$

Denote by $u_{i,j}^n$ the finite difference approximation to $U_{i,j}^n$, and let $b_{n,k} = a_{n-k-1} - a_{n-k}$. After multiplying (10) by μ and then dropping the term $\mu(R_1)_{i,j}^n$, we derive a finite difference scheme as follows:

$$\begin{aligned} \left(I - \mu\delta_x^2\right)\left(I - \mu\delta_y^2\right) u_{i,j}^n &= \sum_{k=1}^{n-1} b_{n,k}\left(u_{i,j}^k + \mu^2 \delta_x^2 \delta_y^2 u_{i,j}^k\right) \\ &\quad + a_{n-1}\left(u_{i,j}^0 + \mu^2 \delta_x^2 \delta_y^2 u_{i,j}^0\right) + \mu f_{i,j}^n, \\ &\quad \left(x_i, y_j\right) \in \Omega_h, \quad 1 \le n \le N, \\ u_{i,j}^n &= \varphi_{i,j}^n, \quad \left(x_i, y_j\right) \in \partial\Omega_h, \ 1 \le n \le N, \\ u_{i,j}^0 &= \psi_{i,j}, \quad \left(x_i, y_j\right) \in \overline{\Omega}_h. \end{aligned} \tag{13}$$

By introducing the intermediate variable $v_{i,j}^n$, we obtain the following L_1-ADI scheme (see [59]):

$$\begin{aligned} \left(I - \mu\delta_x^2\right) v_{i,j}^n &= \sum_{k=1}^{n-1} b_{n,k}\left(u_{i,j}^k + \mu^2 \delta_x^2 \delta_y^2 u_{i,j}^k\right) \\ &\quad + a_{n-1}\left(u_{i,j}^0 + \mu^2 \delta_x^2 \delta_y^2 u_{i,j}^0\right) + \mu f_{i,j}^n, \\ &\quad \left(x_i, y_j\right) \in \Omega_h, \quad 1 \le n \le N, \\ v_{0,j}^n &= \left(I - \mu\delta_y^2\right)\varphi_{0,j}^n, \qquad v_{M_1,j}^n = \left(I - \mu\delta_y^2\right)\varphi_{M_1,j}^n, \\ &\quad 0 \le j \le M_2, \quad 1 \le n \le N, \\ u_{i,j}^0 &= \psi_{i,j}, \quad \left(x_i, y_j\right) \in \overline{\Omega}_h, \\ \left(I - \mu\delta_y^2\right) u_{i,j}^n &= v_{i,j}^n, \quad \left(x_i, y_j\right) \in \Omega_h, \ 1 \le n \le N, \\ u_{i,0}^n &= \varphi_{i,0}^n, \qquad u_{i,M_2}^n = \varphi_{i,M_2}^n, \\ &\quad 0 \le i \le M_1, \quad 1 \le n \le N. \end{aligned} \tag{14}$$

Adding the term $\tau\mu\delta_x^2\delta_y^2\delta_t U_{i,j}^n$ to (9), we have

$$D_t^\alpha U_{i,j}^n + \tau\mu\delta_x^2\delta_y^2\delta_t U_{i,j}^n = \Delta_h U_{i,j}^n + f_{i,j}^n + \left(R_2\right)_{i,j}^n, \tag{15}$$

where

$$\left(R_2\right)_{i,j}^n = \tau\mu\delta_x^2\delta_y^2\delta_t U_{i,j}^n - \left(R_t\right)_{i,j}^n - \left(R_x\right)_{i,j}^n - \left(R_y\right)_{i,j}^n. \tag{16}$$

Since $|\tau\mu\delta_x^2\delta_y^2\delta_t U_{i,j}^n| \le C_{BD}(\alpha)\tau^{1+\alpha}$ for a positive constant $C_{BD}(\alpha)$ independent of τ, h_1, h_2 and the time level n (see [59]), there exists a positive constant C_2 independent of τ, h_1, h_2 and the time level n such that

$$\left|\left(R_2\right)_{i,j}^n\right| \le C_2\left(\tau^{\min\{1+\alpha, 2-\alpha\}} + h_1^2 + h_2^2\right). \tag{17}$$

By (15), we obtain the following finite difference scheme:

$$\begin{aligned} \left(I - \mu\delta_x^2\right)\left(I - \mu\delta_y^2\right) u_{i,j}^n &= \mu^2 \delta_x^2 \delta_y^2 u_{i,j}^{n-1} + \sum_{k=1}^{n-1} b_{n,k} u_{i,j}^k \\ &\quad + a_{n-1} u_{i,j}^0 + \mu f_{i,j}^n, \\ &\quad \left(x_i, y_j\right) \in \Omega_h, \quad 1 \le n \le N, \\ u_{i,j}^n &= \varphi_{i,j}^n, \quad \left(x_i, y_j\right) \in \partial\Omega_h, \ 1 \le n \le N, \\ u_{i,j}^0 &= \psi_{i,j}, \quad \left(x_i, y_j\right) \in \overline{\Omega}_h. \end{aligned} \tag{18}$$

It is equivalent to the following BD-ADI scheme (see [59]):

$$\begin{aligned}
&\left(I-\mu\delta_x^2\right)v_{i,j}^n=\mu^2\delta_x^2\delta_y^2u_{i,j}^{n-1}+\sum_{k=1}^{n-1}b_{n,k}u_{i,j}^k\\
&\qquad+a_{n-1}u_{i,j}^0+\mu f_{i,j}^n,\\
&\left(x_i,y_j\right)\in\Omega_h,\quad 1\le n\le N,\\
&v_{0,j}^n=\left(I-\mu\delta_y^2\right)\varphi_{0,j}^n,\qquad v_{M_1,j}^n=\left(I-\mu\delta_y^2\right)\varphi_{M_1,j}^n,\\
&\qquad 0\le j\le M_2,\quad 1\le n\le N,\\
&u_{i,j}^0=\psi_{i,j},\quad \left(x_i,y_j\right)\in\overline{\Omega}_h,\\
&\left(I-\mu\delta_y^2\right)u_{i,j}^n=v_{i,j}^n,\quad \left(x_i,y_j\right)\in\Omega_h,\ 1\le n\le N,\\
&u_{i,0}^n=\varphi_{i,0}^n,\qquad u_{i,M_2}^n=\varphi_{i,M_2}^n,\\
&\qquad 0\le i\le M_1,\quad 1\le n\le N.
\end{aligned}\tag{19}$$

2.2. Maximum Norm Error Estimates. For any grid function $v=\{v_{i,j}\mid 0\le i\le M_1, 0\le j\le M_2\}$, we define its maximum norm $\|v\|_\infty$ by

$$\|v\|_\infty=\max_{0\le i\le M_1,0\le j\le M_2}\left|v_{i,j}\right|.\tag{20}$$

Let $U_{i,j}^n$ be the value of the solution of (1) at the mesh point (x_i,y_j,t_n), and let $u_{i,j}^n$ be the solution of the L_1-ADI scheme (14) or the BD-ADI scheme (19). We now present our main results of the maximum norm estimate for the error $e_{i,j}^n=U_{i,j}^n-u_{i,j}^n$ in the following two theorems. Their proofs will be given in the next section.

Theorem 1. *Assume that the solution $u(x,y,t)$ of (1) is sufficiently smooth, and let $u_{i,j}^n$ be the solution of the L_1-ADI scheme (14). Then*

$$\left(\tau\sum_{l=1}^{n}\left\|U^l-u^l\right\|_\infty\right)^{1/2}\le C_1^*\left(\tau^{\min\{2\alpha,2-\alpha\}}+h_1^2+h_2^2\right),\qquad 1\le n\le N,\tag{21}$$

where $C_1^*=(l_0^2/2)\sqrt{T}C_1$ and $l_0=\max\{l_1,l_2\}$.

Theorem 2. *Assume that the solution $u(x,y,t)$ of (1) is sufficiently smooth, and let $u_{i,j}^n$ be the solution of the BD-ADI scheme (19). Then*

$$\left(\tau\sum_{l=1}^{n}\left\|U^l-u^l\right\|_\infty\right)^{1/2}\le C_2^*\left(\tau^{\min\{1+\alpha,2-\alpha\}}+h_1^2+h_2^2\right),\qquad 1\le n\le N,\tag{22}$$

where $C_2^*=(l_0^2/2)\sqrt{T}C_2$ and $l_0=\max\{l_1,l_2\}$.

Theorems 1 and 2 show that the ADI difference solution $u_{i,j}^n$ from (14) or (19) converges to the analytical solution $U_{i,j}^n$ of (1) in the discrete maximum norm. We also see from the estimates (12), (17), (21), and (22) that the L_1-ADI scheme (14) and the BD-ADI scheme (19) have the same order as their truncation error with respect to the discrete maximum norm.

3. Proof of the Main Results

Let $\mathscr{V}_h$ be the set of all grid functions $v=\{v_{i,j}\mid 0\le i\le M_1, 0\le j\le M_2\}$ defined in $\overline{\Omega}_h$ and vanishing on $\partial\Omega_h$. For arbitrary $v,w\in\mathscr{V}_h$, we define the following inner products:

$$\begin{aligned}
&(v,w)=h_1h_2\sum_{i=1}^{M_1-1}\sum_{j=1}^{M_2-1}v_{i,j}w_{i,j},\\
&\left(\delta_xv,\delta_xw\right)_x=h_1h_2\sum_{i=0}^{M_1-1}\sum_{j=1}^{M_2-1}\left(\delta_xv_{i,j}\right)\left(\delta_xw_{i,j}\right),\\
&\left(\delta_yv,\delta_yw\right)_y=h_1h_2\sum_{i=1}^{M_1-1}\sum_{j=0}^{M_2-1}\left(\delta_yv_{i,j}\right)\left(\delta_yw_{i,j}\right).
\end{aligned}\tag{23}$$

For any $v\in\mathscr{V}_h$, we introduce the following norms:

$$\begin{aligned}
&\|v\|=(v,v)^{1/2},\quad \left\|\delta_\nu v\right\|_\nu=\left(\delta_\nu v,\delta_\nu v\right)_\nu^{1/2}\quad(\nu=x,y),\\
&|v|_1=\left(\left\|\delta_xv\right\|_x^2+\left\|\delta_yv\right\|_y^2\right)^{1/2},\\
&\left\|\delta_x\delta_y^2v\right\|_x=\left(\delta_x\delta_y^2v,\delta_x\delta_y^2v\right)_x^{1/2},\\
&\left\|\delta_y\delta_x^2v\right\|_y=\left(\delta_y\delta_x^2v,\delta_y\delta_x^2v\right)_y^{1/2}.
\end{aligned}\tag{24}$$

Using a simple calculation, we have that for arbitrary $v,w\in\mathscr{V}_h$,

$$\left(\delta_\nu^2v,w\right)=-\left(\delta_\nu v,\delta_\nu w\right)_\nu,\quad \nu=x,y.\tag{25}$$

Before proving Theorems 1 and 2, we first introduce the following embedding theorem from [60, page 281].

Lemma 3. *For any $v\in\mathscr{V}_h$, one has*

$$\|v\|_\infty\le l_0^2\left(2\sqrt{l_1l_2}\right)^{-1}\left\|\Delta_hv\right\|_\infty,\quad l_0=\max\{l_1,l_2\}.\tag{26}$$

Proof of Theorem 1. Let $e_{i,j}^n=U_{i,j}^n-u_{i,j}^n$. Then by (10) and (13),

$$\begin{aligned}
&e_{i,j}^n-\mu\Delta_he_{i,j}^n+\mu^2\delta_x^2\delta_y^2e_{i,j}^n=w_{i,j}^{n-1}+\mu^2\delta_x^2\delta_y^2w_{i,j}^{n-1}+\mu\left(R_1\right)_{i,j}^n,\\
&\qquad\left(x_i,y_j\right)\in\Omega_h,\quad 1\le n\le N,\\
&e_{i,j}^n=0,\quad \left(x_i,y_j\right)\in\partial\Omega_h,\ 1\le n\le N,\\
&e_{i,j}^0=0,\quad \left(x_i,y_j\right)\in\overline{\Omega}_h,
\end{aligned}\tag{27}$$

where

$$w_{i,j}^{n-1}=\sum_{k=1}^{n-1}b_{n,k}e_{i,j}^k+a_{n-1}e_{i,j}^0.\tag{28}$$

This implies that $e^n = \{e^n_{i,j} \mid 0 \le i \le M_1, 0 \le j \le M_2\} \in \mathcal{V}_h$ for each n. Taking the inner product of the first equation in (27) and $-\Delta_h e^n$, we get

$$\begin{aligned}&\left(e^n + \mu^2\delta_x^2\delta_y^2 e^n, -\Delta_h e^n\right) + \left(-\mu\Delta_h e^n, -\Delta_h e^n\right)\\ &\quad = \left(w^{n-1} + \mu^2\delta_x^2\delta_y^2 w^{n-1}, -\Delta_h e^n\right) + \left(\mu(R_1)^n, -\Delta_h e^n\right),\\ &\qquad\qquad 1 \le n \le N.\end{aligned} \tag{29}$$

It follows from (25) that

$$\left(e^n + \mu^2\delta_x^2\delta_y^2 e^n, -\Delta_h e^n\right) = \left|e^n\right|_1^2 + \mu^2\left(\left\|\delta_y\delta_x^2 e^n\right\|_y^2 + \left\|\delta_x\delta_y^2 e^n\right\|_x^2\right). \tag{30}$$

Similarly,

$$\begin{aligned}&\left(w^{n-1} + \mu^2\delta_x^2\delta_y^2 w^{n-1}, -\Delta_h e^n\right)\\ &= \sum_{k=1}^{n-1} b_{n,k}\left(\left(\delta_x e^k, \delta_x e^n\right)_x + \left(\delta_y e^k, \delta_y e^n\right)_y\right.\\ &\qquad \left.+\mu^2\left(\delta_y\delta_x^2 e^k, \delta_y\delta_x^2 e^n\right)_y + \mu^2\left(\delta_x\delta_y^2 e^k, \delta_x\delta_y^2 e^n\right)_x\right).\end{aligned} \tag{31}$$

Since

$$b_{n,k} = a_{n-k-1} - a_{n-k} > 0, \quad \sum_{k=1}^{n-1} b_{n,k} \le 1, \tag{32}$$

we have from Cauchy-Schwarz inequality that

$$\begin{aligned}&\left(w^{n-1} + \mu^2\delta_x^2\delta_y^2 w^{n-1}, -\Delta_h e^n\right)\\ &\quad \le \frac{1}{2}\sum_{k=1}^{n-1} b_{n,k}\left(\left|e^k\right|_1^2 + \mu^2\left(\left\|\delta_y\delta_x^2 e^k\right\|_y^2 + \left\|\delta_x\delta_y^2 e^k\right\|_x^2\right)\right)\\ &\qquad + \frac{1}{2}\left(\left|e^n\right|_1^2 + \mu^2\left(\left\|\delta_y\delta_x^2 e^n\right\|_y^2 + \left\|\delta_x\delta_y^2 e^n\right\|_x^2\right)\right),\\ &\left(\mu(R_1)^n, -\Delta_h e^n\right) \le \frac{\mu}{2}\left(\left\|(R_1)^n\right\|^2 + \left\|\Delta_h e^n\right\|^2\right).\end{aligned} \tag{33}$$

Substituting (30) and (33) into (29) gives the following:

$$\mu\left\|\Delta_h e^n\right\|^2 + E^n \le E^{n-1} + \mu\left\|(R_1)^n\right\|^2, \quad 1 \le n \le N, \tag{34}$$

where

$$\begin{aligned}E^n &= \sum_{k=1}^{n} a_{n-k}\left(\left|e^k\right|_1^2 + \mu^2\left(\left\|\delta_y\delta_x^2 e^k\right\|_y^2 + \left\|\delta_x\delta_y^2 e^k\right\|_x^2\right)\right),\\ E^0 &= 0.\end{aligned} \tag{35}$$

This implies that

$$\mu\sum_{l=1}^{n}\left\|\Delta_h e^l\right\|^2 + E^n \le \mu\sum_{l=1}^{n}\left\|(R_1)^l\right\|^2, \quad 1 \le n \le N. \tag{36}$$

Since $E^n \ge 0$ and by (12), $\|(R_1)^l\|^2 \le l_1 l_2 C_1^2(\tau^{\min\{2\alpha,2-\alpha\}} + h_1^2 + h_2^2)^2$, the estimate (21) follows from (36) and (26) immediately. □

Proof of Theorem 2. The proof follows from the similar argument as that in the proof of Theorem 1 and we give a sketch. Let $e^n_{i,j} = U^n_{i,j} - u^n_{i,j}$. By (15) and (18),

$$\begin{aligned}e^n_{i,j} - \mu\Delta_h e^n_{i,j} + \mu^2\delta_x^2\delta_y^2 e^n_{i,j} &= \mu^2\delta_x^2\delta_y^2 e^{n-1}_{i,j} + w^{n-1}_{i,j} + \mu(R_2)^n_{i,j},\\ &\left(x_i, y_j\right) \in \Omega_h, \quad 1 \le n \le N,\\ e^n_{i,j} &= 0, \quad \left(x_i, y_j\right) \in \partial\Omega_h, \ 1 \le n \le N,\\ e^0_{i,j} &= 0, \quad \left(x_i, y_j\right) \in \overline{\Omega}_h,\end{aligned} \tag{37}$$

where $w^{n-1}_{i,j}$ is defined by (28). Taking the inner product of the first equation in (37) and $-\Delta_h e^n$, we get

$$\begin{aligned}&\left(e^n, -\Delta_h e^n\right) + \left(-\mu\Delta_h e^n, -\Delta_h e^n\right)\\ &\qquad + \left(\mu^2\delta_x^2\delta_y^2\left(e^n - e^{n-1}\right), -\Delta_h e^n\right)\\ &\quad = \left(w^{n-1}, -\Delta_h e^n\right) + \left(\mu(R_2)^n, -\Delta_h e^n\right), \quad 1 \le n \le N.\end{aligned} \tag{38}$$

Since

$$\begin{aligned}&\left(e^n, -\Delta_h e^n\right) = \left|e^n\right|_1^2, \qquad \left(-\mu\Delta_h e^n, -\Delta_h e^n\right) = \mu\left\|\Delta_h e^n\right\|^2,\\ &\left(\mu^2\delta_x^2\delta_y^2\left(e^n - e^{n-1}\right), -\Delta_h e^n\right)\\ &\quad \ge \frac{\mu^2}{2}\left(\left\|\delta_y\delta_x^2 e^n\right\|_y^2 + \left\|\delta_x\delta_y^2 e^n\right\|_x^2\right.\\ &\qquad \left.-\left\|\delta_y\delta_x^2 e^{n-1}\right\|_y^2 - \left\|\delta_x\delta_y^2 e^{n-1}\right\|_x^2\right),\\ &\left(w^{n-1}, -\Delta_h e^n\right) \le \frac{1}{2}\left(\sum_{k=1}^{n-1} b_{n,k}\left|e^k\right|_1^2 + \left|e^n\right|_1^2\right),\\ &\left(\mu(R_2)^n, -\Delta_h e^n\right) \le \frac{\mu}{2}\left(\left\|(R_2)^n\right\|^2 + \left\|\Delta_h e^n\right\|^2\right),\end{aligned} \tag{39}$$

we obtain that

$$\mu\left\|\Delta_h e^n\right\|^2 + F^n \le F^{n-1} + \mu\left\|(R_2)^n\right\|^2, \quad 1 \le n \le N, \tag{40}$$

where

$$\begin{aligned}F^n &= \sum_{k=1}^{n} a_{n-k}\left|e^k\right|_1^2 + \mu^2\left(\left\|\delta_y\delta_x^2 e^n\right\|_y^2 + \left\|\delta_x\delta_y^2 e^n\right\|_x^2\right),\\ F^0 &= 0.\end{aligned} \tag{41}$$

Table 1: The maximum norm error and the temporal accuracy of $u_{i,j}^n$ for Example 4.

τ	L_1-ADI scheme ($h = \pi/200$)			BD-ADI scheme ($h = \pi/200$)		
	α	error(τ, h)	order(τ)	α	error(τ, h)	order(τ)
1/20	1/2	1.1393833280$e-03$	0.860979	1/3	1.5093973350$e-03$	1.266265
1/40		6.2732035469$e-04$	0.882911		6.2750871863$e-04$	1.285881
1/80		3.4017847773$e-04$	0.910189		2.5735409495$e-04$	1.301046
1/160		1.8101416127$e-04$	0.936057		1.0444249965$e-04$	1.319085
1/320		9.4608749632$e-05$	0.959731		4.1859417673$e-05$	1.351071
1/640		4.8643355059$e-05$			1.6408936533$e-05$	
1/20	2/3	1.2585768427$e-03$	1.260363	1/2	3.6622305737$e-04$	1.463622
1/40		5.2537885652$e-04$	1.288661		1.3278581143$e-04$	1.474131
1/80		2.1505367805$e-04$	1.303399		4.7796268443$e-05$	1.488745
1/160		8.7133397922$e-05$	1.307319		1.7030874694$e-05$	1.514438
1/320		3.5208078966$e-05$	1.297645		5.9613630191$e-06$	1.535827
1/640		1.4322284746$e-05$			2.0559641134$e-06$	
1/20	3/4	2.3004703569$e-03$	1.174836	2/3	1.4653603051$e-03$	1.207510
1/40		1.0189566568$e-03$	1.197125		6.3452327488$e-04$	1.242740
1/80		4.4441136189$e-04$	1.210140		2.6813016026$e-04$	1.264770
1/160		1.9208646006$e-04$	1.216775		1.1158658090$e-04$	1.276115
1/320		8.2643912130$e-05$	1.217031		4.6074754492$e-05$	1.274583
1/640		3.5550691871$e-05$			1.9044750580$e-05$	

Therefore

$$\mu\sum_{l=1}^{n}\left\|\Delta_h e^l\right\|^2 + F^n \le \mu\sum_{l=1}^{n}\left\|\left(R_2\right)^l\right\|^2, \quad 1 \le n \le N. \tag{42}$$

The estimate (22) follows from the previous inequality, (17), and (26) immediately. □

4. Numerical Results

In this section, we give some numerical results to demonstrate the accuracy of the L_1-ADI scheme (14) and the BD-ADI scheme (19) with respect to the discrete maximum norm. Some detailed numerical comparisons of these two ADI schemes with the implicit scheme proposed in [43] can be found in [59]. The dependence of the solution of (1) on the anomalous diffusion exponent α was also exhibited in [59] through some numerical results.

In our numerical computations, we take an equal mesh size in each of the space directions; that is, $h_1 = h_2 = h$. We compute the discrete maximum norm error of the numerical solution $u_{i,j}^n$ by

$$\text{error}\,(\tau, h) = \left(\tau\sum_{l=1}^{N}\left\|U^l - u^l\right\|_\infty\right)^{1/2}, \tag{43}$$

and its convergence orders by

$$\begin{aligned}\text{order}\,(\tau) &= \log_2\left(\frac{\text{error}\,(2\tau, h)}{\text{error}\,(\tau, h)}\right),\\ \text{order}\,(h) &= \log_2\left(\frac{\text{error}\,(\tau, 2h)}{\text{error}\,(\tau, h)}\right),\end{aligned} \tag{44}$$

where $U_{i,j}^n$ represents the value of the exact analytic solution of (1) at (x_i, y_j, t_n).

Example 4. We consider the problem (1) in the domain $\Omega = (0, \pi) \times (0, \pi)$, and let $T = 1/2$. Assume that the solution $u(x, y, t)$ of this problem is $u(x, y, t) = t^2 \sin(x) \sin(y)$. It can be checked that the corresponding known functions are given by

$$\begin{aligned} f\,(x, y, t) &= 2\sin(x)\sin(y)\left(\frac{t^{2-\alpha}}{\Gamma(3-\alpha)} + t^2\right),\\ \varphi\,(x, y, t) &= t^2\sin(x)\sin(y), \qquad \psi\,(x, y) = 0.\end{aligned} \tag{45}$$

In Table 1, we present the maximum norm error error(τ, h) and the temporal convergence order order(τ) of the numerical solution $u_{i,j}^n$ by the L_1-ADI scheme (14) and the BD-ADI scheme (19). We see that the L_1-ADI scheme has the temporal accuracy of $\min\{2\alpha, 2 - \alpha\}$ in the discrete maximum norm, and the best temporal accuracy is attained at $\alpha = 2/3$. It is also seen that the BD-ADI scheme generates the temporal accuracy of $\min\{1 + \alpha, 2 - \alpha\}$ in the discrete maximum norm, and it gets the best temporal accuracy when $\alpha = 1/2$. These observations coincide well with the theoretical analysis.

Table 2 gives the maximum norm error error(τ, h) and the spatial convergence order order(h) of the numerical solution $u_{i,j}^n$ by the L_1-ADI scheme (14) and the BD-ADI scheme (19). As expected from the theoretical analysis, these two schemes have the second-order spatial accuracy.

Table 2: The maximum norm error and the spatial accuracy of $u_{i,j}^n$ for Example 4.

h	L_1-ADI scheme ($\alpha = 2/3, \tau = 1/4000$)		BD-ADI scheme ($\alpha = 1/2, \tau = 1/4000$)	
	error(τ, h)	order(h)	error(τ, h)	order(h)
$\pi/4$	$1.4977394377e-03$	1.994343	$1.8149573747e-03$	2.001730
$\pi/8$	$3.7590600110e-04$	1.989441	$4.5319556650e-04$	2.000950
$\pi/16$	$9.4666844874e-05$	1.960585	$1.1322433260e-04$	2.002088
$\pi/32$	$2.4322216030e-05$	1.844870	$2.8265146732e-05$	2.007753
$\pi/64$	$6.7708311670e-06$		$7.0284169450e-06$	

Table 3: The maximum norm error and the temporal accuracy of $u_{i,j}^n$ for Example 5.

τ	L_1-ADI scheme ($h = 1/200$)			BD-ADI scheme ($h = 1/200$)		
	α	error(τ, h)	order(τ)	α	error(τ, h)	order(τ)
1/20	1/2	$4.6386801902e-03$	0.835782	1/3	$3.0682418814e-03$	1.247710
1/40		$2.5989567998e-03$	0.906370		$1.2920863692e-03$	1.295329
1/80		$1.3866102907e-03$	0.947443		$5.2645185538e-04$	1.315075
1/160		$7.1902789341e-04$	0.970534		$2.1158337290e-04$	1.325682
1/320		$3.6693233527e-04$	0.983962		$8.4413446753e-05$	1.335982
1/640		$1.8551714096e-04$			$3.3438043901e-05$	
1/20	2/3	$1.5621553331e-03$	1.192172	1/2	$1.5491678500e-03$	1.423830
1/40		$6.8366714097e-04$	1.262779		$5.7740819917e-04$	1.463914
1/80		$2.8491177407e-04$	1.297640		$2.0931522211e-04$	1.481554
1/160		$1.1589959988e-04$	1.317329		$7.4956359178e-05$	1.496663
1/320		$4.6507867889e-05$	1.333601		$2.6562452368e-05$	1.524750
1/640		$1.8453234155e-05$			$9.2315064167e-06$	
1/20	3/4	$1.7962917770e-03$	1.063599	2/3	$1.1129679333e-03$	1.112230
1/40		$8.5941268352e-04$	1.128142		$5.1483494465e-04$	1.171085
1/80		$3.9318529135e-04$	1.161548		$2.2863166690e-04$	1.211600
1/160		$1.7576660520e-04$	1.180856		$9.8720772742e-05$	1.239224
1/320		$7.7528818903e-05$	1.191836		$4.1818156321e-05$	1.255314
1/640		$3.3937881480e-05$			$1.7517727276e-05$	

Example 5. We consider the subdiffusion equation

$$\begin{aligned} &u_t(x,y,t) \\ &= {}_0\mathscr{D}_t^{1-\alpha}\left(\Delta u(x,y,t)\right) + e^{x+y}\left((1+\alpha)t^{\alpha} - \frac{2\Gamma(2+\alpha)}{\Gamma(1+2\alpha)}t^{2\alpha}\right), \\ &\qquad (x,y) \in \Omega, \quad t \in [0,1], \end{aligned} \tag{46}$$

with boundary and initial conditions

$$\begin{aligned} u(x,y,t) &= e^{x+y}t^{1+\alpha}, \quad (x,y) \in \partial\Omega, \ t \in (0,1], \\ u(x,y,0) &= 0, \quad (x,y) \in \overline{\Omega}, \end{aligned} \tag{47}$$

where $\Omega = (0,1) \times (0,1)$ and ${}_0\mathscr{D}_t^{1-\alpha}$ denotes the Riemann-Liouville fractional derivative operator defined as

$${}_0\mathscr{D}_t^{1-\alpha} y(t) = \frac{1}{\Gamma(\alpha)}\frac{\mathrm{d}}{\mathrm{d}t}\int_0^t \frac{y(s)}{(t-s)^{1-\alpha}}\mathrm{d}s, \quad 0 < \alpha < 1. \tag{48}$$

Operating Riemann-Liouville fractional derivative operator ${}_0\mathscr{D}_t^{\alpha-1}$ on both sides of (46), we obtain the equivalent problem of the subdiffusion equation with the temporal Caputo fractional derivative [40, 42, 59] as follows:

$$\begin{aligned} {}_0^C\mathscr{D}_t^{\alpha} u(x,y,t) &= \Delta u(x,y,t) + e^{x+y}\left(\Gamma(2+\alpha)t - 2t^{1+\alpha}\right), \\ &\qquad (x,y) \in \Omega, \quad t \in [0,1], \\ u(x,y,t) &= e^{x+y}t^{1+\alpha}, \quad (x,y) \in \partial\Omega, \ t \in (0,1], \\ u(x,y,0) &= 0, \quad (x,y) \in \overline{\Omega}. \end{aligned} \tag{49}$$

We now solve the aforementioned problem by the L_1-ADI scheme (14) and the BD-ADI scheme (19). Tables 3 and 4 give the maximum norm error error(τ, h) and the convergence orders order(τ) and order(h) of the numerical solution $u_{i,j}^n$. It is easily seen that the numerical results confirm the theoretical analysis results.

Table 4: The maximum norm error and the spatial accuracy of $u_{i,j}^n$ for Example 5.

h	L_1-ADI scheme ($\alpha = 2/3, \tau = 1/4000$)		BD-ADI scheme ($\alpha = 1/2, \tau = 1/4000$)	
	error(τ, h)	order(h)	error(τ, h)	order(h)
1/4	$8.9083790169e-04$	1.901804	$9.4164046481e-04$	1.901896
1/8	$2.3839587645e-04$	1.985610	$2.5197489313e-04$	1.974325
1/16	$6.0196414976e-05$	2.072000	$6.4124816806e-05$	2.032967
1/32	$1.4316490746e-05$	2.263270	$1.5669032476e-05$	2.158045
1/64	$2.9821150680e-06$		$3.5107982244e-06$	

5. Conclusions

We have studied two ADI finite difference methods for a two-dimensional fractional subdiffusion equation. An explicit error estimate for each of the two methods has been provided in the discrete maximum norm. It has been shown that the methods have the same order as their truncation errors with respect to the discrete maximum norm. The maximum norm error estimates presented here are more preferable for measuring computation errors in practice, compared to the H^1-norm error estimates in [59]. Numerical results have confirmed the theoretical analysis results.

Acknowledgments

This work was supported in part by E-Institutes of Shanghai Municipal Education Commission no. E03004 and Shanghai Leading Academic Discipline Project no. B407.

References

[1] I. Podlubny, *Fractional Differential Equations*, Academic Press, New York, NY, USA, 1999.

[2] R. Gorenflo, F. Mainardi, D. Moretti, G. Pagnini, and P. Paradisi, "Discrete random walk models for space-time fractional diffusion," *Chemical Physics*, vol. 284, pp. 521–541, 2002.

[3] B. I. Henry and S. L. Wearne, "Fractional reaction-diffusion," *Physica A*, vol. 276, no. 3-4, pp. 448–455, 2000.

[4] M. Giona and H. E. Roman, "Fractional diffusion equation for transport phenomenna in random media," *Physica A*, vol. 185, pp. 87–97, 1992.

[5] T. Kosztolowicz, "Subdiffusion in a system with a thick membrane," *Journal of Membrane Science*, vol. 320, pp. 492–499, 2008.

[6] R. Metzler, E. Barkai, and J. Klafter, "Anomalous diffusion and relaxation close to thermal equilibrium: a fractional Fokker-Planck equation approach," *Physical Review Letters*, vol. 82, pp. 3563–3567, 1999.

[7] R. Metzler and J. Klafter, "The random walk's guide to anomalous diffusion: a fractional dynamics approach," *Physics Reports*, vol. 339, no. 1, p. 77, 2000.

[8] R. Metzler and J. Klafter, "Boundary value problems for fractional diffusion equations," *Physica A*, vol. 278, no. 1-2, pp. 107–125, 2000.

[9] M. Li, "Approximating ideal filters by systems of fractional order," *Computational and Mathematical Methods in Medicine*, vol. 2012, Article ID 365054, 6 pages, 2012.

[10] M. Li, S. C. Lim, and S. Chen, "Exact solution of impulse response to a class of fractional oscillators and its stability," *Mathematical Problems in Engineering*, vol. 2011, Article ID 657839, 9 pages, 2011.

[11] M. Li and W. Zhao, "Essay on fractional Riemann-Liouville integral operator versus Mikusinski's," *Mathematical Problems in Engineering*, vol. 2013, Article ID 635412, 3 pages, 2013.

[12] M. Li and W. Zhao, "Solving the Abel's type integral equation with the Mikusinski's operator of fractional order," *Advances in Mathematical Physics*, vol. 2013, Article ID 806984, 4 pages, 2013.

[13] J. A. Tenreiro MacHado, M. F. Silva, R. S. Barbosa et al., "Some applications of fractional calculus in engineering," *Mathematical Problems in Engineering*, vol. 2010, Article ID 639801, 34 pages, 2010.

[14] H. Sun, Y. Chen, and W. Chen, "Random-order fractional differential equation models," *Signal Processing*, vol. 91, no. 3, pp. 525–530, 2011.

[15] C. Cattani, "Fractional calculus and Shannon wavelet," *Mathematical Problems in Engineering*, vol. 2012, Article ID 502812, 26 pages, 2012.

[16] C. Cattani, G. Pierro, and G. Altieri, "Entropy and multifractality for the myeloma multiple TET 2 gene," *Mathematical Problems in Engineering*, vol. 2012, Article ID 193761, 14 pages, 2012.

[17] B. Baeumer, M. Kovács, and M. M. Meerschaert, "Numerical solutions for fractional reaction-diffusion equations," *Computers & Mathematics with Applications*, vol. 55, no. 10, pp. 2212–2226, 2008.

[18] C.-M. Chen and F. Liu, "A numerical approximation method for solving a three-dimensional space Galilei invariant fractional advection-diffusion equation," *Journal of Applied Mathematics and Computing*, vol. 30, no. 1-2, pp. 219–236, 2009.

[19] C.-M. Chen, F. Liu, I. Turner, and V. Anh, "A Fourier method for the fractional diffusion equation describing sub-diffusion," *Journal of Computational Physics*, vol. 227, no. 2, pp. 886–897, 2007.

[20] C.-M. Chen, F. Liu, V. Anh, and I. Turner, "Numerical schemes with high spatial accuracy for a variable-order anomalous subdiffusion equation," *SIAM Journal on Scientific Computing*, vol. 32, no. 4, pp. 1740–1760, 2010.

[21] C.-m. Chen, F. Liu, and K. Burrage, "Finite difference methods and a Fourier analysis for the fractional reaction-subdiffusion equation," *Applied Mathematics and Computation*, vol. 198, no. 2, pp. 754–769, 2008.

[22] A. Mohebbi, M. Abbaszadeh, and M. Dehghan, "A high-order and unconditionally stable scheme for the modified anomalous fractional sub-diffusion equation with a nonlinear source term," *Journal of Computational Physics*, vol. 240, pp. 36–48, 2013.

[23] G.-H. Gao, Z.-Z. Sun, and Y.-N. Zhang, "A finite difference scheme for fractional sub-diffusion equations on an unbounded domain using artificial boundary conditions," *Journal of Computational Physics*, vol. 231, no. 7, pp. 2865–2879, 2012.

[24] T. A. M. Langlands and B. I. Henry, "The accuracy and stability of an implicit solution method for the fractional diffusion equation," *Journal of Computational Physics*, vol. 205, no. 2, pp. 719–736, 2005.

[25] Y. Lin and C. Xu, "Finite difference/spectral approximations for the time-fractional diffusion equation," *Journal of Computational Physics*, vol. 225, no. 2, pp. 1533–1552, 2007.

[26] F. Liu, C. Yang, and K. Burrage, "Numerical method and analytic technique of the modified anomalous subdiffusion equation with a nonlinear source term," *Journal of Computational and Applied Mathematics*, vol. 231, no. 1, pp. 160–176, 2009.

[27] F. Liu, P. Zhuang, V. Anh, I. Turner, and K. Burrage, "Stability and convergence of the difference methods for the space-time fractional advection-diffusion equation," *Applied Mathematics and Computation*, vol. 191, no. 1, pp. 12–20, 2007.

[28] C.-M. Chen, F. Liu, V. Anh, and I. Turner, "Numerical methods for solving a two-dimensional variable-order anomalous subdiffusion equation," *Mathematics of Computation*, vol. 81, no. 277, pp. 345–366, 2012.

[29] Q. Liu, F. Liu, I. Turner, and V. Anh, "Numerical simulation for the 3D seepage flow with fractional derivatives in porous media," *IMA Journal of Applied Mathematics*, vol. 74, no. 2, pp. 201–229, 2009.

[30] C. Tadjeran, M. M. Meerschaert, and H.-P. Scheffler, "A second-order accurate numerical approximation for the fractional diffusion equation," *Journal of Computational Physics*, vol. 213, no. 1, pp. 205–213, 2006.

[31] S. B. Yuste, "Weighted average finite difference methods for fractional diffusion equations," *Journal of Computational Physics*, vol. 216, no. 1, pp. 264–274, 2006.

[32] S. B. Yuste and L. Acedo, "An explicit finite difference method and a new von Neumann-type stability analysis for fractional diffusion equations," *SIAM Journal on Numerical Analysis*, vol. 42, no. 5, pp. 1862–1874, 2005.

[33] P. Zhuang, F. Liu, V. Anh, and I. Turner, "New solution and analytical techniques of the implicit numerical method for the anomalous subdiffusion equation," *SIAM Journal on Numerical Analysis*, vol. 46, no. 2, pp. 1079–1095, 2008.

[34] P. Zhuang, F. Liu, V. Anh, and I. Turner, "Numerical methods for the variable-order fractional advection-diffusion equation with a nonlinear source term," *SIAM Journal on Numerical Analysis*, vol. 47, no. 3, pp. 1760–1781, 2009.

[35] J.-P. Bouchaud and A. Georges, "Anomalous diffusion in disordered media: statistical mechanisms, models and physical applications," *Physics Reports*, vol. 195, no. 4-5, pp. 127–293, 1990.

[36] P. Zhuang, F. Liu, V. Anh, and I. Turner, "Stability and convergence of an implicit numerical method for the nonlinear fractional reaction-subdiffusion process," *IMA Journal of Applied Mathematics*, vol. 74, no. 5, pp. 645–667, 2009.

[37] Y. T. Gu, P. Zhuang, and F. Liu, "An advanced implicit meshless approach for the non-linear anomalous subdiffusion equation," *Computer Modeling in Engineering & Sciences*, vol. 56, no. 3, pp. 303–333, 2010.

[38] M. Cui, "Compact finite difference method for the fractional diffusion equation," *Journal of Computational Physics*, vol. 228, no. 20, pp. 7792–7804, 2009.

[39] Y.-N. Zhang, Z.-Z. Sun, and H.-W. Wu, "Error estimates of Crank-Nicolson-type difference schemes for the subdiffusion equation," *SIAM Journal on Numerical Analysis*, vol. 49, no. 6, pp. 2302–2322, 2011.

[40] G.-h. Gao and Z.-z. Sun, "A compact finite difference scheme for the fractional sub-diffusion equations," *Journal of Computational Physics*, vol. 230, no. 3, pp. 586–595, 2011.

[41] X. Li and C. Xu, "A space-time spectral method for the time fractional diffusion equation," *SIAM Journal on Numerical Analysis*, vol. 47, no. 3, pp. 2108–2131, 2009.

[42] X. Zhao and Z.-z. Sun, "A box-type scheme for fractional sub-diffusion equation with Neumann boundary conditions," *Journal of Computational Physics*, vol. 230, no. 15, pp. 6061–6074, 2011.

[43] C.-M. Chen, F. Liu, I. Turner, and V. Anh, "Numerical schemes and multivariate extrapolation of a two-dimensional anomalous sub-diffusion equation," *Numerical Algorithms*, vol. 54, no. 1, pp. 1–21, 2010.

[44] P. Zhuang and F. Liu, "Finite difference approximation for two-dimensional time fractional diffusion equation," *Journal of Algorithms & Computational Technology*, vol. 1, no. 1, pp. 1–15, 2007.

[45] Q. Liu, Y. T. Gu, P. Zhuang, F. Liu, and Y. F. Nie, "An implicit RBF meshless approach for time fractional diffusion equations," *Computational Mechanics*, vol. 48, no. 1, pp. 1–12, 2011.

[46] H. Brunner, L. Ling, and M. Yamamoto, "Numerical simulations of 2D fractional subdiffusion problems," *Journal of Computational Physics*, vol. 229, no. 18, pp. 6613–6622, 2010.

[47] Q. Yang, T. Moroney, K. Burrage, I. Turner, and F. Liu, "Novel numerical methods for time-space fractional reaction diffusion equations in two dimensions," *ANZIAM Journal. Electronic Supplement*, vol. 52, pp. C395–C409, 2010.

[48] Q. Yang, I. Turner, F. Liu, and M. Ilić, "Novel numerical methods for solving the time-space fractional diffusion equation in two dimensions," *SIAM Journal on Scientific Computing*, vol. 33, no. 3, pp. 1159–1180, 2011.

[49] Q. X. Liu and F. W. Liu, "Modified alternating direction methods for solving a two-dimensional non-continuous seepage flow with fractional derivatives," *Mathematica Numerica Sinica*, vol. 31, no. 2, pp. 179–194, 2009.

[50] S. Chen and F. Liu, "ADI-Euler and extrapolation methods for the two-dimensional fractional advection-dispersion equation," *Journal of Applied Mathematics and Computing*, vol. 26, no. 1-2, pp. 295–311, 2008.

[51] M. M. Meerschaert, H.-P. Scheffler, and C. Tadjeran, "Finite difference methods for two-dimensional fractional dispersion equation," *Journal of Computational Physics*, vol. 211, no. 1, pp. 249–261, 2006.

[52] H. Wang and K. Wang, "An $O(N\log^2 N)$ alternating-direction finite difference method for two-dimensional fractional diffusion equations," *Journal of Computational Physics*, vol. 230, no. 21, pp. 7830–7839, 2011.

[53] C. Tadjeran and M. M. Meerschaert, "A second-order accurate numerical method for the two-dimensional fractional diffusion equation," *Journal of Computational Physics*, vol. 220, no. 2, pp. 813–823, 2007.

[54] Y.-N. Zhang, Z.-Z. Sun, and X. Zhao, "Compact alternating direction implicit scheme for the two-dimensional fractional diffusion-wave equation," *SIAM Journal on Numerical Analysis*, vol. 50, no. 3, pp. 1535–1555, 2012.

[55] M. Cui, "Compact alternating direction implicit method for two-dimensional time fractional diffusion equation," *Journal of Computational Physics*, vol. 231, no. 6, pp. 2621–2633, 2012.

[56] S. Chen, F. Liu, P. Zhuang, and V. Anh, "Finite difference approximations for the fractional Fokker-Planck equation," *Applied Mathematical Modelling*, vol. 33, no. 1, pp. 256–273, 2009.

[57] W. Deng, "Finite element method for the space and time fractional Fokker-Planck equation," *SIAM Journal on Numerical Analysis*, vol. 47, no. 1, pp. 204–226, 2008/09.

[58] Z.-Z. Sun and X. Wu, "A fully discrete difference scheme for a diffusion-wave system," *Applied Numerical Mathematics*, vol. 56, no. 2, pp. 193–209, 2006.

[59] Y.-N. Zhang and Z.-Z. Sun, "Alternating direction implicit schemes for the two-dimensional fractional sub-diffusion equation," *Journal of Computational Physics*, vol. 230, no. 24, pp. 8713–8728, 2011.

[60] A. A. Samarskii, *The Theory of Difference Schemes*, Marcel Dekker, New York, NY, USA, 2001.

Hindawi Publishing Corporation
Advances in Mathematical Physics
Volume 2013, Article ID 827192, 11 pages
http://dx.doi.org/10.1155/2013/827192

Research Article

The $\mathcal{S}$-Transform of Sub-fBm and an Application to a Class of Linear Subfractional BSDEs

Zhi Wang[1,2] and Litan Yan[3]

[1] *College of Information Science and Technology, Donghua University, 2999 North Renmin Road, Songjiang, Shanghai 201620, China*
[2] *School of Sciences, Ningbo University of Technology, 201 Fenghua Road, Ningbo 315211, China*
[3] *Department of Mathematics, College of Science, Donghua University, 2999 North Renmin Road, Songjiang, Shanghai 201620, China*

Correspondence should be addressed to Litan Yan; litanyan@dhu.edu.cn

Received 28 May 2013; Revised 7 June 2013; Accepted 8 June 2013

Academic Editor: Ming Li

Let S^H be a subfractional Brownian motion with index $0 < H < 1$. Based on the $\mathcal{S}$-transform in white noise analysis we study the stochastic integral with respect to S^H, and we also prove a Girsanov theorem and derive an Itô formula. As an application we study the solutions of backward stochastic differential equations driven by S^H of the form $-dY_t = f(t, Y_t, Z_t)dt - Z_t dS_t^H, t \in [0, T], Y_T = \xi$, where the stochastic integral used in the above equation is Pettis integral. We obtain the explicit solutions of this class of equations under suitable assumptions.

1. Introduction

As an extension of Brownian motion, Bojdecki et al. [1, 2] introduced and studied a rather special class of self-similar Gaussian processes which preserves many properties of the fractional Brownian motion of the Weyl type here and below. This process arises from occupation time fluctuations of branching particle systems with Poisson initial condition. This process is called the *subfractional Brownian motion* (sub-fBm). The so-called sub-fBm with index $H \in (0, 1)$ is a mean zero Gaussian process $S^H = \{S_t^H, t \geq 0\}$ with $S_0^H = 0$ and the covariance

$$E\left[S_t^H S_s^H\right] = s^{2H} + t^{2H} - \frac{1}{2}\left[(s+t)^{2H} + |t-s|^{2H}\right] \quad (1)$$

for all $s, t \geq 0$. For $H = 1/2$, S^H coincides with the standard Brownian motion B. S^H is neither a semimartingale nor a Markov process unless $H = 1/2$. So many of the powerful techniques from stochastic analysis are not available when dealing with S^H. As a Gaussian process, it is possible to construct a stochastic calculus of variations with respect to S^H (see, e.g., Alòs et al. [3] and Nualart [4]). The sub-fBm has properties analogous to those of fractional Brownian motion and satisfies the following estimates:

$$\left[\left(2 - 2^{2H-1}\right) \wedge 1\right](t-s)^{2H} \leq E\left[\left(S_t^H - S_s^H\right)^2\right] \leq \left[\left(2 - 2^{2H-1}\right) \vee 1\right](t-s)^{2H}. \quad (2)$$

Thus, Kolmogorov's continuity criterion implies that subfractional Brownian motion is Hölder continuous of order γ for any $\gamma < H$. But its increments are not stationary. More works for sub-fBm can be found in Bojdecki et al. [5], Liu and Yan [6], Shen and Chen [7], Tudor [8–11], Yan et al. [12–14], and the references therein.

On the other hand, it is well known that general backward stochastic differential equations (BSDEs) driven by a Brownian motion were first studied by Pardoux and Peng [15], where they also gave a probabilistic interpretation for the viscosity solution of semilinear partial differential equations. Because of their important value in various areas including probability theory, finance, and control, BSDEs have been subject to the attention and interest of researchers. A survey and complete literature for BSDEs could be found in Peng [16]. Recently, motivated by stochastic control problems, Biagini et al. [17]

first studied linear BSDEs driven by a fractional Brownian motion, where existence and uniqueness were discussed in order to study a maximum principle. Bender [18] gave explicit solutions for a linear BSDEs driven by a fractional Brownian motion, and Hu and Peng [19] studied the linear and nonlinear BSDEs driven by a fractional Brownian motion using the quasi-conditional expectation. More works for the BSDEs driven by Brownian motion and fractional Brownian motion can be found in Bisumt [20], Geiss et al. [21], Karoui et al. [22], Ma et al. [23], Maticiuc and Nie [24], Peng [25], and the references therein. In this paper, we study the BSDEs driven by a sub-fBm S^H of the form

$$\begin{aligned} -dY_t &= f\left(t, Y_t, Z_t\right) dt - Z_t dS_t^H, \quad t \in [0,T], \\ Y_T &= \xi, \end{aligned} \tag{3}$$

where the stochastic integral used in above equation is Pettis integral.

In recent years, there has been considerable interest in studying fractional Brownian motion due to its applications in various scientific areas including telecommunications, turbulence, image processing, and finance and also due to some of its compact properties such as long-range dependence, self-similarity, stationary increments, and Hölder's continuity (see, e.g., Mandelbrot and van Ness [26], Biagini et al. [27], Hu [28], Mishura [29], Li [30], Li and Zhao [31, 32], and Lim and Muniandy [33]). Moreover, many authors have proposed to use more general self-similar Gaussian processes and random fields as stochastic models. Such applications have raised many interesting theoretical questions about self-similar Gaussian processes and fields in general. Therefore, other generalizations of Brownian motion have been introduced such as sub-fBm, bifractional Brownian motion, and weighted-fractional Brownian motion. However, in contrast to the extensive studies on fractional Brownian motion, there has been little systematic investigation on other self-similar Gaussian processes. The main reason for this is the complexity of dependence structures for self-similar Gaussian processes which do not have stationary increments. The sub-fBm has properties analogous to those of fractional Brownian motion (self-similarity, long-range dependence, Hölder paths, the variation, and the renormalized variation). However, in comparison with fractional Brownian motion, the sub-fBm has nonstationary increments and the increments over nonoverlapping intervals are more either weakly or strongly correlated and their covariance decays polynomially as a higher rate in comparison with fractional Brownian motion (for this reason in Bojdecki et al. [1] is called subfractional Brownian motion). The above mentioned properties make sub-fBm a possible candidate for models which involve long-range dependence, self-similarity, and nonstationary. Thus, it seems interesting to study the BSDEs driven by a sub-fBm.

This paper is organized as follows. Section 2 contains some basic results. In Section 3, we give a definition of subfractional Itô integral based on an $\mathcal{S}$-transform in white noise analysis. As an application we establish a Girsanov theorem for this integral. In Section 4, we give an Itô formula for functionals of a Wiener integral for a sub-fBm. We also discuss the geometric sub-fBm in this section. Section 5 considers the BSDEs (3). Finally, we will conclude the paper in Section 6.

2. Preliminaries

In this section, we briefly recall some basic definitions and results of sub-fBm. Throughout this paper we assume that $0 < H < 1$ is arbitrary but fixed and let $S^H = \{S_t^H, 0 \le t \le T\}$ be a one-dimensional sub-fBm with Hurst index H defined on $(\Omega, \mathcal{F}^H, P)$. To simplify, we denote $\alpha = H - 1/2$, and let $B = \{B_t\}_{t\in\mathbb{R}}$ be a two-sides Brownian motion and

$$1_{(a,b)}(t) = \begin{cases} 1, & \text{if } a \le t < b, \\ -1, & \text{if } b \le t < a, \\ 0, & \text{others.} \end{cases} \tag{4}$$

We also denote

(i) $|f|_2$: the usual $L^2(\mathbb{R})$-norm, and the corresponding inner product is denoted by $(f,g)_2$;

(ii) $S(\mathbb{R})$: the Schwartz space of rapidly decreasing smooth functions of real valued;

(iii) $I(f)$: the Wiener integral $\int_{\mathbb{R}} f(s)dB_s$ of the function $f \in L^2(\mathbb{R})$;

(iv) $\mathcal{G}$: the σ-field generated by $\{I(f), f \in L^2(\mathbb{R})\}$;

(v) $\|\Phi\|_2$: the $L^2(\Omega, \mathcal{G}, P)$-norm.

S^H can be written as a Volterra process with the following moving average representation:

$$S_t^H = C_H^\alpha \int_{\mathbb{R}} \left[(t-s)_+^\alpha + (t+s)_-^\alpha - 2(-s)_+^\alpha\right] dB_s, \tag{5}$$

where $C_H^\alpha = \Gamma(H+1/2)/\sqrt{H \sin \pi H \Gamma(2H)}$, $x_+ = \max(x,0)$, $x_- = \max(-x,0)$. The sub-fBm S^H is also possible to construct a stochastic calculus of variations with respect to the Gaussian process S^H, which will be related to the Malliavin calculus. Some surveys and complete literatures for Malliavin calculus of Gaussian process could be found in Alòs et al. [3], Nualart [4] and Tudor [9, 10], Zähle [34], and the references therein.

Let $0 < \beta < 1$. Consider Weyl's type fractional integrals $I_\pm^\beta$ of order β

$$\begin{aligned} \left(I_-^\beta f\right)(x) &:= \frac{1}{\Gamma(\beta)} \int_x^\infty f(t)(t-x)^{\beta-1} dt, \\ \left(I_+^\beta f\right)(x) &:= \frac{1}{\Gamma(\beta)} \int_{-\infty}^x f(t)(x-t)^{\beta-1} dt, \end{aligned} \tag{6}$$

if the integrals exist for almost all $x \in \mathbb{R}$, and Marchand's type fractional derivatives $D_\pm^\beta$ of order β

$$\left(D_\pm^\beta f\right) := \lim_{\varepsilon \downarrow 0^+} \left(D_{\pm,\varepsilon}^\beta f\right) \tag{7}$$

if the limit exists in $L^p(\mathbb{R})$ for some $p > 1$, where

$$\left(D^{\beta}_{\pm,\varepsilon} f\right)(x) := \frac{\beta}{\Gamma(1-\beta)} \int_{\varepsilon}^{\infty} \frac{f(x) - (x \mp t)}{t^{1+\beta}}\, dt \tag{8}$$

for $\varepsilon > 0$. Define the operator

$$M^{H}_{\pm} f := \begin{cases} C_H D^{-\alpha}_{\pm} f, & \text{if } 0 < H < \frac{1}{2}, \\ f, & \text{if } H = \frac{1}{2}, \\ C_H I^{\alpha}_{\pm} f, & \text{if } \frac{1}{2} < H < 1, \end{cases} \tag{9}$$

where $C_H = \sqrt{2H \sin \pi H \Gamma(2H)}$ and $\Gamma(\cdot)$ denotes the gamma function defined by

$$\Gamma(z) = \int_0^{\infty} t^{z-1} e^{-t}\, dt, \quad z > 0. \tag{10}$$

Recall that we now give a stochastic version of the Hardy-Littlewood theorem as follows.

Theorem 1 (Theorem 2.10 in [35]). *Let $1/2 < H < 1$ and let the operators $M^H_{\pm}$ be defined as above. Then $M^H_{\pm}$ is a continuous operator from $L^p(\mathbb{R};\Omega)$ into $L^q(\mathbb{R};\Omega)$ if $1 < p < 2/(2H-1)$ and $q = 2p/(2 - p(2H-1))$.*

Define the function

$$f^0(x) := \begin{cases} f(x), & x \geq 0, \\ -f(-x), & x < 0 \end{cases} \tag{11}$$

for any Borel function f on $\mathbb{R}_+$. Then the function f^0 is odd, which is called the odd extension of f. Based on the moving average representation (5), we can show the following proposition.

Proposition 2. *Let the operators $M^H_{\pm}$ be defined as above. Then $M^H_{-}(1^0_{[0,t)}) \in L^2(\mathbb{R})$ and S^H admits the following integral representation:*

$$S^H_t = \frac{1}{\sqrt{2}} \int_{\mathbb{R}} M^H_{-}\left(1^0_{[0,t)}\right)(s)\, dB_s \tag{12}$$

for all $t \geq 0$.

We finally recall the $\mathcal{S}$-transform. The $\mathcal{S}$-transform is an important tool in white noise analysis. Here we give a definition and state some results that do not depend on properties of the white noise space. Denote the $\mathcal{S}$-transform of $\Phi \in L^2(\Omega, \mathcal{G}, P)$ (see, e.g., [35, 36] for more details) by

$$\mathcal{S}\Phi(\eta) := E\left[\Phi \cdot : e^{I(\eta)} :\right], \quad \eta \in \mathcal{S}(\mathbb{R}), \tag{13}$$

where the Wick exponential $: e^{I(\eta)} :$ of $I(\eta)$ is given by

$$: e^{I(\eta)} := e^{I(\eta) - (1/2)|\eta|_2^2}. \tag{14}$$

The $\mathcal{S}$-transform has the following important properties.

(A_1) The $\mathcal{S}$-transform is injective; that is, $\mathcal{S}\Phi(\eta) = \mathcal{S}\Psi(\eta)$ for all $\eta \in \mathcal{S}(\mathbb{R})$, implies that $\Phi = \Psi$.

(A_2) Let f_n be a sequence that converges to f in $L^2(\mathbb{R})$; then $: e^{I(f_n)} :$ converges to $: e^{I(f)} :$ in $L^2(\mathbb{R})$.

(A_3) $E[: e^{I(f)} :] = 1$ for $f \in L^2(\mathbb{R})$. Hence it can deduce a probability measure on $\mathcal{F}$ by

$$dQ_f =: e^{I(f)} : dP, \tag{15}$$

especially, for $\eta \in \mathcal{S}(\mathbb{R})$, we can rewrite the $\mathcal{S}$-transform as

$$\mathcal{S}\Phi(\eta) = E^{Q_\eta}[\Phi]. \tag{16}$$

(A_4) Let $X : \mathbb{R} \times \Omega \to \mathbb{R}$ be a progressively measurable process such that

$$E \int_{\mathbb{R}} |X_t|^2 dt < \infty. \tag{17}$$

Then $\int_{\mathbb{R}} X_t\, dB_t$ is the unique element in $L^2(\Omega, \mathcal{G}, P)$ with $\mathcal{S}$-transform given by

$$\int_{\mathbb{R}} (\mathcal{S}X_t)(\eta)\, \eta(t)\, dt. \tag{18}$$

(A_5) The Wiener integral $I(f), f \in L^2(\mathbb{R})$ is the unique element in $L^2(\Omega, \mathcal{G}, P)$ with $\mathcal{S}$-transform given by

$$\int_{\mathbb{R}} f(t)\, \eta(t)\, dt. \tag{19}$$

The following result points out that the operators $M^H_{\pm}$ interchanges with the $\mathcal{S}$-transform.

Lemma 3 (Lemma 2.9 in [35]). *Let $M^H_{\pm} X$ exist for some $X : \mathbb{R} \to L^2(\Omega, \mathcal{G}, P)$. Then one has*

$$E\left[\left(M^H_{\pm} X\right)_t \Psi\right] = M^H_{\pm}\left(E\left[X_t \Psi\right]\right) \tag{20}$$

for all $\Psi \in L^2(\Omega, \mathcal{G}, P)$. In the case $H < 1/2$ the convergence of the fractional derivative on the right-hand side is in the $L^p(\mathbb{R})$ sense, if $M^{-(H-1/2)}_{\pm} X \in L^p(\mathbb{R}; L^2(\Omega, \mathcal{G}, P))$. In particular, the operators $M^H_{\pm}$ interchange with the $\mathcal{S}$-transform.

3. A Subfractional Itô Integral

In this section, based on the $\mathcal{S}$-transform we aim to define the subfractional Itô integral, denoted by $\Phi = \int_a^b X_t\, dS^H_t$ with $0 \leq a < b$, and introduce the Girsanov theorem. To this end, inspired by the Hitsuda-Skorohod integral, we define the subfractional Itô integral as the unique random variable Φ such that

$$\mathcal{S}\Phi(\eta) = \int_a^b \mathcal{S}(X_t)(\eta)\, \frac{d}{dt} \mathcal{S}\left(S^H_t\right)(\eta)\, dt \tag{21}$$

for all $\eta \in \mathcal{S}(\mathbb{R})$, provided the integral exists under suitable conditions. According to (12) and Property (A_5), we have

$$\begin{aligned}
&\frac{d}{dt}\mathcal{S}\left(S_t^H\right)(\eta) \\
&= \frac{1}{\sqrt{2}}\frac{d}{dt}\int_{\mathbb{R}} M_-^H\left(1_{[0,t)}^0\right)\eta(s)\,ds \\
&= \frac{1}{\sqrt{2}}\frac{d}{dt}\int_{\mathbb{R}} \left(1_{[0,t)}^0\right)M_+^H\eta(s)\,ds \\
&= \frac{1}{\sqrt{2}}\frac{d}{dt}\int_0^t M_+^H\eta(s)\,ds - \frac{1}{\sqrt{2}}\frac{d}{dt}\int_{-t}^0 M_+^H\eta(s)\,ds \\
&= \frac{1}{\sqrt{2}}\left[M_+^H\eta(t) - M_+^H\eta(-t)\right].
\end{aligned} \tag{22}$$

Combining this with the fact (A_1) in Section 2, we give the following definition.

Definition 4. Let $M \subset \mathbb{R}^+$ be a Borel set. A mapping $X : M \to L^2(\Omega, \mathcal{G}, P)$ is said to be subfractional Itô integrable on M if

$$(\mathcal{S}X.)(\eta)\left[\left(M_+^H\eta\right)(\cdot) - \left(M_+^H\eta\right)(-\cdot)\right] \in L^1(M) \tag{23}$$

for any $\eta \in \mathcal{S}(\mathbb{R})$, and there is a $\Phi \in L^2(\Omega, \mathcal{G}, P)$ such that

$$\mathcal{S}\Phi(\eta) = \frac{1}{\sqrt{2}}\int_M \mathcal{S}(X_t)(\eta)\left[\left(M_+^H\eta\right)(t) - \left(M_+^H\eta\right)(-t)\right]dt \tag{24}$$

for all $\eta \in S(\mathbb{R})$.

It is important to note that Φ in the above definition is unique because the $\mathcal{S}$-transform is injective, which is called the *subfractional Itô integral of X on M* and we denote it by

$$\Phi = \int_M X_t\,dS_t^H. \tag{25}$$

In this paper, sub-fractional Itô integralalways refers to the $\mathcal{S}$-transform approach proposed in Definition 4.

Proposition 5. *The following statements hold.*

(1) *For any $a < b$ one has*

$$S_b^H - S_a^H = \int_a^b dS_t^H. \tag{26}$$

(2) *Let $X : [a, b] \to L^2(\Omega, \mathcal{G}, P)$ be subfractional Itô integrable for $0 \le a < b$. Then*

$$\begin{aligned}
&\int_a^b X_t dS_t^H = \int_{\mathbb{R}} 1_{[a,b]}(t)\,X_t dS_t^H, \\
&E\left[\int_a^b X_t dS_t^H\right] = 0.
\end{aligned} \tag{27}$$

Proof. These results are some simple examples. □

Recall that the Wick product $F \diamond G$ of $F, G \in L^2(\Omega, \mathcal{G}, P)$ is an element $F \diamond G \in L^2(\Omega, \mathcal{G}, P)$ such that

$$\mathcal{S}(F \diamond G)(\eta) = \mathcal{S}(F)(\eta)\,\mathcal{S}(G)(\eta) \tag{28}$$

for all $\eta \in \mathcal{S}(\mathbb{R})$. The following theorem expresses the relationship between the subfractional Itô integral defined as above and the integral based on Wick product $\diamond$.

Theorem 6. *Let $X : \mathbb{R}^+ \to L^2(\Omega, \mathcal{G}, P)$ and $Y \in L^2(\Omega, \mathcal{G}, P)$; then*

$$Y \diamond \int_{\mathbb{R}^+} X_s\,dS_s^H = \int_{\mathbb{R}^+} Y \diamond X_s\,dS_s^H \tag{29}$$

in the sense that if one side is well defined then so is the other, and both coincide.

We can obtain it by calculating the $\mathcal{S}$-transform of both sides. In particular, for $Y \in L^2(\Omega, \mathcal{G}, P)$, this theorem implies that

$$Y \diamond \left(S_b^H - S_a^H\right) = \int_{\mathbb{R}^+} 1_{(a,b)}(s)\,Y dS_s^H. \tag{30}$$

It means that the subfractional Itô integral is the $L^2(\Omega, \mathcal{G}, P)$-limit of Wick-Riemann sums for some suitable processes. That is,

$$\int_0^T X_s\,dS_s^H = \lim_{|\pi_n|\to 0}\sum_{i=0}^n X_{s_i} \diamond \left(S_{s_{i+1}}^H - S_{s_i}^H\right) \tag{31}$$

for some suitable processes X, where $\pi_n = \{0 = s_0 < s_1 < \cdots < s_{n+1} = T\}$ is a partition of $[0, T]$ with $|\pi_n| := \max\{s_{i+1} - s_i\}$ and the convergence is in $L^2(\Omega, \mathcal{G}, P)$.

Now we calculate the expectation of a subfractional Itô integral under a measure Q_f, $f \in L^2(\mathbb{R})$.

Theorem 7. *Let $0 < H < 1$ and Q_f, $f \in L^2(\mathbb{R})$ be given by (15). If the following assumptions hold:*

(1) *$X : \mathbb{R}^+ \to L^2(\Omega, \mathcal{G}, P)$ is subfractional Itô integrable, and $X \in L^{1/H}(\mathbb{R}^+, L^2(\Omega, \mathcal{G}, P))$;*

(2) *$M_+^H f \in L^{1/(1-H)}$ and $M_-^H X \in L^2(\mathbb{R}^+)$ for $H < 1/2$,*

One then has

$$\begin{aligned}
&E^{Q_f}\left[\int_{\mathbb{R}^+} X_t\,dS_t^H\right] \\
&\quad = \frac{1}{\sqrt{2}}\int_{\mathbb{R}^+} E^{Q_f}[X_t]\left[\left(M_+^H f\right)(t) - \left(M_+^H f\right)(-t)\right]dt.
\end{aligned} \tag{32}$$

Proof. Let $(\eta_n)_{n\in\mathbb{N}} \subset \mathcal{S}(\mathbb{R})$ be given such that η_n converges to f in $L^2(\mathbb{R})$, we have the identity

$$\begin{aligned}
&E^{Q_{\eta_n}}\left[\int_{\mathbb{R}^+} X_t\,dS_t^H\right] \\
&\quad = \frac{1}{\sqrt{2}}\int_{\mathbb{R}^+} E^{Q_{\eta_n}}[X_t]\left[\left(M_+^H\eta_n\right)(t) - \left(M_+^H\eta_n\right)(-t)\right]dt.
\end{aligned} \tag{33}$$

It can be easily obtained that the left-hand side of (33) converges to the same side of (32) by Theorem 1 and (A_2) in Section 2.

Then we just need to prove the right-hand side of (33) converges to (32) correspondingly. By Lemma 3, applying the fractional integration by parts rule, we have

$$\begin{aligned}
&\left|\int_{\mathbb{R}^+} E^{Q_{(\eta_n)}}[X_t]\left[\left(M_+^H\eta_n\right)(t)-\left(M_+^H\eta_n\right)(-t)\right]\right.\\
&\quad\left.-E^{Q_f}[X_t]\left[\left(M_+^Hf\right)(t)-\left(M_+^Hf\right)(-t)\right]dt\right|\\
&=\left|\int_{\mathbb{R}^+} E\left[X_t:e^{I(\eta_n)}:\right]\left[\left(M_+^H\eta_n\right)(t)-\left(M_+^H\eta_n\right)(-t)\right]\right.\\
&\quad\left.-E\left[X_t:e^{I(f)}:\right]\left[\left(M_+^Hf\right)(t)-\left(M_+^Hf\right)(-t)\right]dt\right|
\end{aligned}\tag{34}$$

which is bounded by

$$\begin{aligned}
&\left|\int_{\mathbb{R}^+} E\left[\left(M_-^HX\right)_t:e^{I(\eta_n)}:\right]\eta_n(t)-E\left[\left(M_-^HX\right)_t:e^{I(f)}:\right]f(t)\,dt\right|\\
&+\left|\int_{\mathbb{R}^+} E\left[\left(M_-^HX\right)_t:e^{I(f)}:\right]f(-t)-E\left[\left(M_-^HX\right)_t:e^{I(\eta_n)}:\right]\eta_n(-t)\,dt\right|\\
&\le\left|\int_{\mathbb{R}^+} E\left[\left|\left(M_-^HX\right)_t\left(:e^{I(\eta_n)}:-:e^{I(f)}:\right)\right|\right]|\eta_n(t)|\,dt\right|\\
&\quad+\left|\int_{\mathbb{R}^+} E\left[\left|\left(M_-^HX\right)_t:e^{I(f)}:\right|\right]|\eta_n(t)-f(t)|\,dt\right|\\
&\quad+\left|\int_{\mathbb{R}^+} E\left[\left|\left(M_-^HX\right)_t\left(:e^{I(\eta_n)}:-:e^{I(f)}:\right)\right|\right]|\eta_n(-t)|\,dt\right|\\
&\quad+\left|\int_{\mathbb{R}^+} E\left[\left|\left(M_-^HX\right)_t:e^{I(f)}:\right|\right]|\eta_n(-t)-f(-t)|\,dt\right|\\
&\equiv I_1+I_2+I_3+I_4.
\end{aligned}\tag{35}$$

We can easily show that I_1, I_2, I_3, I_4 converge to zero, as $n\to\infty$, respectively, by Hölder's inequality. This completes the proof. □

Remark 8. Under the assumptions of Theorem 7, $\int_{\mathbb{R}^+}X_t[(M_+^Hf)(t)-(M_+^Hf)(-t)]dt$ exists as a Pettis integral (see Definition 2.3 in [35]). In fact, for all $\Phi\in L^2(\Omega,\mathcal{G},P)$,

$$\begin{aligned}
&\int_{\mathbb{R}^+}\left|E\left[X_t\left[\left(M_+^Hf\right)(t)-\left(M_+^Hf\right)(-t)\right]\Phi\right]\right|dt\\
&\le\left(\int_{\mathbb{R}^+}\left|\left(M_+^Hf\right)(t)-\left(M_+^Hf\right)(-t)\right|^{1/(1-H)}dt\right)^{1-H}\\
&\quad\times\left(\int_{\mathbb{R}^+}E\left[\left|X_t\right|^2\right]^{1/2H}dt\right)^{H}E\left[|\Phi|^2\right]^{1/2}\\
&\le\left[\left(\int_{\mathbb{R}^+}\left|\left(M_+^Hf\right)(t)\right|^{1/(1-H)}dt\right)^{1-H}\right.\\
&\quad\left.+\left(\int_{\mathbb{R}^+}\left|\left(M_+^Hf\right)(-t)\right|^{1/(1-H)}dt\right)^{1-H}\right]\\
&\quad\times\left(\int_{\mathbb{R}^+}E\left[\left|X_t\right|^2\right]^{1/2H}dt\right)^{H}E\left[|\Phi|^2\right]^{1/2}\\
&<\infty.
\end{aligned}\tag{36}$$

Thus, the property of the Pettis integral deduces

$$\begin{aligned}
&E^{Q_f}\left[\int_{\mathbb{R}^+}X_t\,dS_t^H\right]\\
&\quad=\frac{1}{\sqrt{2}}E^{Q_f}\int_{\mathbb{R}^+}X_t\left[\left(M_+^Hf\right)(t)-\left(M_+^Hf\right)(-t)\right]dt.
\end{aligned}\tag{37}$$

Now, we establish a Girsanov theorem for subfractional Itô integral. Consider the measure Q_f, $f\in L^2(\mathbb{R})$, the probability space $(\Omega,\mathcal{F},Q_f)$ carries a two-side Brownian motion given by

$$\widetilde{B}_t=B_t-\int_0^t f(s)\,ds\tag{38}$$

according to the classical Girsanov theorem. On this probability space, we denote $\mathcal{S}_{Q_f}$ the $\mathcal{S}$-transform with respect to the measure Q_f, $f\in L^2(\mathbb{R})$; that is,

$$\left(\mathcal{S}_{Q_f}X\right)(\eta):=E^{Q_f}\left[:e^{I^{\tilde{B}}(\eta)}:X\right],\tag{39}$$

and the following identity holds:

$$:e^{I^{\tilde{B}}(g)}:\cdot:e^{I(f)}:=:e^{I(f+g)}:\tag{40}$$

for all $g\in L^2(\mathbb{R})$.

Theorem 9. *Let the assumptions of Theorem 7 be satisfied, and*

$$\begin{aligned}
&E^{Q_f}\left[\left|\int_{\mathbb{R}^+}X_t\,dS_t^H-\frac{1}{\sqrt{2}}\int_{\mathbb{R}^+}X_t[(M_+^Hf)(t)-(M_+^Hf)(-t)]dt\right|^2\right]\\
&\quad<\infty.
\end{aligned}\tag{41}$$

Then, the identity

$$\begin{aligned}
&\int_{\mathbb{R}^+}X_t\,d\widetilde{S}_t^H\\
&\quad=\int_{\mathbb{R}^+}X_t\,dS_t^H-\frac{1}{\sqrt{2}}\int_{\mathbb{R}^+}X_t\left[\left(M_+^Hf\right)(t)-\left(M_+^Hf\right)(-t)\right]dt
\end{aligned}\tag{42}$$

holds in $L^2(\Omega,\mathcal{F},Q_f)$-almost surely.

Proof. We apply Theorem 7 to $f+\eta, \eta \in \mathcal{S}(\mathbb{R})$. It is easy to check that $M_+^H(f+\eta) \in L^{1/(1-H)}(\mathbb{R})$ according to Lemma 2.5 in [36]. By Theorem 7 and (40), it follows

$$\begin{aligned}
&\mathcal{S}_{Q_f}\left(\int_{\mathbb{R}^+} X_t dS_t^H - \int_{\mathbb{R}^+} X_t\left[\left(M_+^H f\right)(t) - \left(M_+^H f\right)(-t)\right]dt\right)(\eta)\\
&= E^{Q_{f+\eta}}\left[\int_{\mathbb{R}^+} X_t dS_t^H - \int_{\mathbb{R}^+} X_t\left[\left(M_+^H f\right)(t) - \left(M_+^H f\right)(-t)\right]dt\right]\\
&= \frac{1}{\sqrt{2}}\int_{\mathbb{R}^+} E^{Q_{f+\eta}}[X_t]\left[M_+^H(f+\eta)(t) - M_+^H(f+\eta)(-t)\right]dt\\
&\quad - \frac{1}{\sqrt{2}}\int_{\mathbb{R}^+} E^{Q_{f+\eta}}[X_t]\left[\left(M_+^H f\right)(t) - \left(M_+^H f\right)(-t)\right]dt\\
&= \frac{1}{\sqrt{2}}\int_{\mathbb{R}^+} E^{Q_{f+\eta}}[X_t]\left[\left(M_+^H \eta\right)(t) - \left(M_+^H \eta\right)(-t)\right]dt\\
&= \frac{1}{\sqrt{2}}\int_{\mathbb{R}^+} \mathcal{S}_{Q_f} X_t(\eta)\left[\left(M_+^H \eta\right)(t) - \left(M_+^H \eta\right)(-t)\right]dt.
\end{aligned} \tag{43}$$

The second identity based on the fact that $\int_{\mathbb{R}^+} X_t[(M_+^H f)(t) - (M_+^H f)(-t)]dt$ exists as a Pettis integral which is proved in Remark 8. The proof is complete. □

4. An Itô Formula

In this section, we prove an Itô formula for a subfractional Wiener integral using the $\mathcal{S}$-transform approach. An indefinite subfractional Wiener integral is understood as a process

$$X_t = \int_0^t \varphi(s)\, dS_s^H \equiv \int_{\mathbb{R}} 1_{[0,t]}(s)\,\varphi(s)\, dS_s^H \tag{44}$$

for all $0 \le t \le T$ provided φ is a deterministic function such that the above integral exists as a subfractional Itô integral for all $0 \le t \le T$.

Proposition 10. *Assume that $\varphi : [0,T] \to \mathbb{R}$ is continuous for $1/2 \le H < 1$, and λ-Hölder continuous with $\lambda > 1/2 - H$ for $0 < H < 1/2$. Then the indefinite subfractional Wiener integral $\int_0^t \varphi(s) dS_s^H$ exists, and*

$$\int_0^t \varphi(s)\, dS_s^H = \frac{1}{\sqrt{2}} I\left(M_-^H\left(1_{(0,t)}\varphi\right)^0\right). \tag{45}$$

Proof. We should prove that $M_-^H(1_{(0,t)}\varphi)^0 \in L^2(\mathbb{R})$ and $\mathcal{S}(\int_0^t \varphi(s) dS_s^H)(\eta)$ exists.

For $1/2 \le H < 1$, since φ is continuous on $[0,T]$, by Hardy-Littlwood theorem, it is obvious that $M_-^H(1_{(0,t)}\varphi)^0 \in L^2(\mathbb{R})$.

For $0 < H < 1/2$, similar to the argument in Proposition 5.1 in [35], there exists a function $g \in L^2(\mathbb{R})$, such that

$$1_{(0,t)}\varphi = I_-^{1/2-H} g. \tag{46}$$

Hence, $M_-^H(1_{(0,t)}\varphi) \in L^2(\mathbb{R})$, and so is $M_-^H(1_{(0,t)}\varphi)^0 \in L^2(\mathbb{R})$. φ is a deterministic function implies that $\mathcal{S}(\int_0^t \varphi(s) dS_s^H)(\eta)$ exists.

Next, consider the $\mathcal{S}$-transform of the right-hand side in (45), then by (19), we obtain that

$$\begin{aligned}
&\mathcal{S}\left(\frac{1}{\sqrt{2}} I\left(M_-^H\left(1_{(0,t)}\varphi\right)^0\right)\right)(\eta)\\
&= \frac{1}{\sqrt{2}}\int_{\mathbb{R}} M_-^H\left(1_{(0,t)}\varphi\right)^0 \eta\, ds\\
&= \frac{1}{\sqrt{2}}\int_{\mathbb{R}} \left(1_{(0,t)}\varphi\right)^0 M_+^H(\eta)\, ds\\
&= \frac{1}{\sqrt{2}}\int_0^t \varphi(s)\left(M_+^H\eta\right)(s)\, ds + \frac{1}{\sqrt{2}}\int_0^{-t} \varphi(-s)\left(M_+^H\eta\right)(s)\, ds\\
&= \frac{1}{\sqrt{2}}\int_0^t \varphi(s)\left(M_+^H\eta\right)(s)\, ds - \frac{1}{\sqrt{2}}\int_0^t \varphi(s)\left(M_+^H\eta\right)(-s)\, ds\\
&= \mathcal{S}\left(\int_0^t \varphi(s)\, dS_s^H\right)(\eta).
\end{aligned} \tag{47}$$

This completes the proof. □

The following lemma is essential to the proof of our Itô's formula.

Lemma 11. *Let $\varphi : \mathbb{R} \to \mathbb{R}$ be continuous and $H > 1/2$. Then one has*

$$\begin{aligned}
&\left|M_-^H\left(1_{(0,t)}\varphi\right)^0\right|_2^2\\
&\quad = 8\alpha H\int_0^t\int_0^\tau \varphi(s)\varphi(\tau)\left[(\tau - s)^{2\alpha-1} + (s+\tau)^{2\alpha-1}\right]ds\, d\tau.
\end{aligned} \tag{48}$$

In particular,

(1) *for all $t > 0$, $|M_-^H(1_{(0,t)}\varphi)^0|_2^2 \le 3\max_{s\in[0,t]}|\varphi(s)|^2 t^{2H}$;*

(2) *$|M_-^H(1_{(0,t)}\varphi)^0|_2^2$ is differentiable in t, and for all $t \ge 0$, one has*

$$\begin{aligned}
&\frac{d}{dt}\left|M_-^H\left(1_{(0,t)}\varphi\right)^0\right|_2^2\\
&\quad = 8\alpha H\varphi(t)\int_0^t \varphi(s)\left[(t-s)^{2\alpha-1} + (s+t)^{2\alpha-1}\right]ds\\
&\quad \le 4H\max_{s\in[0,t]}\left|\varphi(s)\right|^2 t^{2\alpha}.
\end{aligned} \tag{49}$$

Proof. For $H > 1/2$, the following identity holds:

$$\left|M_-^H\varphi\right|_2^2 = 2\alpha H\iint_{\mathbb{R}} \varphi(s)\varphi(\tau)|s-\tau|^{2\alpha-1} ds\, d\tau. \tag{50}$$

Then,

$$\begin{aligned}
&\left|M_-^H\left(1_{(0,t)}\varphi\right)^0\right|_2^2 \\
&\quad = 2\alpha H\iint_{\mathbb{R}}\left(1_{(0,t)}\varphi\right)^0(s)\left(1_{(0,t)}\varphi\right)^0(\tau)\,|s-\tau|^{2\alpha-1}ds\,d\tau \\
&\quad = 4\alpha H\iint_0^t\varphi(s)\,\varphi(\tau)\,|s-\tau|^{2\alpha-1}ds\,d\tau \\
&\qquad + 4\alpha H\iint_0^t\varphi(s)\,\varphi(\tau)\,|s+\tau|^{2\alpha-1}ds\,d\tau \\
&\quad = 8\alpha H\int_0^t\int_0^\tau\varphi(s)\,\varphi(\tau)\,|s-\tau|^{2\alpha-1}ds\,d\tau \\
&\qquad + 8\alpha H\int_0^t\int_0^\tau\varphi(s)\,\varphi(\tau)\,|s+\tau|^{2\alpha-1}ds\,d\tau.
\end{aligned} \tag{51}$$

Equation (48) easily follows and the other assertions are trivial. □

Remark 12. Since the right of (48) is not hold when $H < 1/2$, there is a lack of a result similar to the above Lemma. Hence, we only consider the case of constant φ, and we have $|M_-^H(1_{(0,t)}\varphi)^0|_2^2 = (2-2^{2H-1})\varphi^2 t^{2H}$.

Now we give the following Itô formula.

Theorem 13. *Let $T > 0$, such that*

(B_1) *X be an indefinite subfractional Wiener integral; that is, for all $0 \le t \le T$, $X_t = \int_0^t \varphi(s)dS_s^H$, where φ is continuous when $H \ge 1/2$, constant when $H < 1/2$;*

(B_2) *$F \in \mathscr{C}^{1,2}([0,T]\times\mathbb{R})$;*

(B_3) *there exists constants $C \ge 0$ and $\lambda \le [2\sqrt{3}T^H \cdot \max_{s\in[0,T]}|\varphi(s)|]^{-2}$ such that*

$$\begin{aligned}
&\max\left\{|F(t,x)|, \left|\frac{\partial}{\partial t}F(t,x)\right|, \left|\frac{\partial}{\partial x}F(t,x)\right|, \left|\frac{\partial^2}{\partial x^2}F(t,x)\right|\right\} \\
&\quad \le Ce^{\lambda x^2}.
\end{aligned} \tag{52}$$

Then the following equality holds in (L^2):

$$\begin{aligned}
&\int_0^T\varphi(t)\,\frac{\partial}{\partial x}F(t,X_t)\,dS_t^H \\
&\quad = F(T,X_T) - F(0,0) - \int_0^T\frac{\partial}{\partial t}F(t,X_t)\,dt \\
&\qquad - \frac{1}{2}\int_0^T\frac{d}{dt}\left|M_-^H\left(1_{(0,t)}\varphi\right)^o\right|_2^2\frac{\partial^2}{\partial x^2}F(t,X_t)\,dt.
\end{aligned} \tag{53}$$

Proof. It suffices to show that both sides have the same $\mathcal{S}$-transform. Indeed, by Definition 4, the integral of the left-hand side has the $\mathcal{S}$-transform given by

$$\begin{aligned}
&\mathcal{S}\left(\int_0^T\varphi(t)\,\frac{\partial}{\partial x}F(t,X_t)\,dS_t^H\right)(\eta) \\
&\quad = \frac{1}{\sqrt{2}}\int_0^T\varphi(t)\left[\left(M_+^H\eta\right)(t) - \left(M_+^H\eta\right)(-t)\right]\mathcal{S} \\
&\qquad \times\left(\frac{\partial}{\partial x}F(t,X_t)\right)(\eta)\,dt.
\end{aligned} \tag{54}$$

Henceforth, we just need to show the right-hand side has the same result. Firstly, we show the integrals of the right-hand side exist in (L^2). Without loss of generality, denote $G = F$, $(\partial/\partial t)F(t,x)$, $(\partial/\partial x)F(t,x)$, $(\partial^2/\partial x^2)F(t,x)$, and $0 \le t \le T$. By the growth condition (52), we obtain

$$\left\|G(t,X_t)\right\|_2^2 \le C^2\left(1-4\lambda\left|\left(M_-^H\left(1_{(0,t)}\varphi\right)^0\right|_2^2\right)^{(-1/2)} \le \text{const.} \tag{55}$$

Consequently, $\int_0^T(\partial/\partial t)F(t,X_t)dt$ exists. For the last one, by Lemma 11 and Remark 12, we have

$$\begin{aligned}
&\int_0^T\left\|\frac{d}{dt}\left|M_-^H\left(1_{(0,t)}\varphi\right)^0\right|_2^2\frac{\partial}{\partial x^2}F(t,X_t)\right\|_2 dt \\
&\quad \le \int_0^T\left|\frac{d}{dt}\left|M_-^H\left(1_{(0,t)}\varphi\right)^0\right|_2^2\right|\left\|\frac{\partial}{\partial x^2}F(t,X_t)\right\|_2 dt \\
&\quad \le \text{const.}\int_0^T t^{2H}dt < \infty.
\end{aligned} \tag{56}$$

Hence, the last integral exists as a Pettis integral in the (L^2)-sense.

On the other hand, denote the heat kernel as follows:

$$g(t,x) := \frac{1}{\sqrt{2\pi t}}\exp\left\{\frac{-x^2}{2t}\right\}. \tag{57}$$

Thanks to the classical Girsanov theorem, for arbitrary $\eta \in \mathcal{S}(\mathbb{R})$, under the measure Q_η, we can easily calculate that X_t is a Gaussian random variable with mean $(1/\sqrt{2})\int_0^t\varphi(s)[(M_+^H\eta)(s) - (M_+^H)\eta(-s)]ds$ and variance $|M_-^H(1_{(0,t)}\varphi)^0|_2^2$. Thus, we obtain

$$\begin{aligned}
&\mathcal{S}\left(F(t,X_t)\right)(\eta) \\
&= E^{Q_\eta}\left[F(t,X_t)\right] \\
&= \int_{\mathbb{R}}F\left(t,u+\frac{1}{\sqrt{2}}\int_0^t\varphi(s)\left[\left(M_+^H\eta\right)(s) - \left(M_+^H\eta\right)(-s)\right]ds\right) \\
&\qquad \times g\left(\left|M_-^H\left(1_{(0,t)}\varphi\right)^0\right|_2^2, u\right)du.
\end{aligned} \tag{58}$$

Moreover, by (B_3), integration and differentiation can be interchanged. Since the heat kernel fulfills $(\partial/\partial t)g = (1/2)(\partial^2/\partial x^2)g$, we have

$$\begin{aligned}
&\frac{d}{dt}\mathcal{S}\left(F\left(t,X_t\right)\right)(\eta)\\
&=\mathcal{S}\left(\frac{\partial}{\partial t}F\left(t,X_t\right)\right)(\eta)\\
&\quad+\frac{1}{\sqrt{2}}\left[\left(M_+^H\eta\right)(t)-\left(M_+^H\eta\right)(-t)\right]\varphi(t)\,\mathcal{S}\left(\frac{\partial}{\partial x}F\left(t,X_t\right)\right)(\eta)\\
&\quad+\frac{1}{2}\frac{d}{dt}\left|M_-^H\left(1_{(0,t)}\varphi\right)^0\right|_2^2\cdot\mathcal{S}\left(\frac{\partial^2}{\partial x^2}F\left(t,X_t\right)\right)(\eta).
\end{aligned}\tag{59}$$

Consequently,

$$\begin{aligned}
&\mathcal{S}\left(F\left(T,X_T\right)-F\left(0,0\right)\right)(\eta)\\
&\quad=\lim_{\varepsilon\to 0}\mathcal{S}\left(F\left(T,X_T\right)-F\left(\varepsilon,X_\varepsilon\right)\right)(\eta)\\
&\quad=\int_0^T\mathcal{S}\left(\frac{\partial}{\partial t}F\left(t,X_t\right)\right)(\eta)\,dt\\
&\qquad+\frac{1}{\sqrt{2}}\int_0^T\left[\left(M_+^H\eta\right)(t)-\left(M_+^H\eta\right)(-t)\right]\varphi(t)\\
&\qquad\qquad\times\mathcal{S}\left(\frac{\partial}{\partial x}F\left(t,X_t\right)\right)(\eta)\,dt\\
&\qquad+\frac{1}{2}\int_0^T\frac{d}{dt}\left|M_-^H\left(1_{(0,t)}\varphi\right)^0\right|_2^2\cdot\mathcal{S}\left(\frac{\partial^2}{\partial x^2}F\left(t,X_t\right)\right)(\eta)\,dt.
\end{aligned}\tag{60}$$

Compared with (54), the proof can be completed. □

The objective of this part is to define the geometric sub-fBm and establish an Itô formula with respect to it.

Definition 14. Let $H\in(0,1)$, $x_0>0$, and $\varphi, r:[0,\infty)\to\mathbb{R}$, Then one calls

$$P_t:=x_0\exp\left\{\int_0^t r(s)\,ds-\frac{1}{2}\left|M_-^H\left(1_{(0,t)}\varphi\right)^0\right|_2^2+\int_0^t\varphi(s)\,dS_s^H\right\}\tag{61}$$

a geometric sub-fBm with coefficients H, x_0, φ, r, provided the right-hand side exists as an element of (L^2) for all $0\le t<\infty$.

Theorem 15. *Let $T>0$, such that*

(i) *P be a geometric sub-fBm with continuous coefficients φ, r, and let φ be a constant when $H<1/2$;*

(ii) *(B_2), (B_3) hold.*

Then the following equality holds in (L^2):

$$\begin{aligned}
&\int_0^T\varphi(t)\,P_t\frac{\partial}{\partial x}F\left(t,P_t\right)dS_t^H\\
&\quad=F\left(T,P_T\right)-F\left(0,x_0\right)-\int_0^T\frac{\partial}{\partial t}F\left(t,P_t\right)dt\\
&\quad-\int_0^T r(t)\,P_t\frac{\partial}{\partial x}F\left(t,P_t\right)dt\\
&\qquad-\frac{1}{2}\int_0^T\frac{d}{dt}\left|M_-^H\left(1_{(0,t)}\varphi\right)^0\right|_2^2P_t^2\frac{\partial^2}{\partial x^2}F\left(t,P_t\right)dt.
\end{aligned}\tag{62}$$

Proof. Let

$$g(t,x):=x_0\exp\left\{\int_0^t r(s)\,ds-\frac{1}{2}\left|M_-^H\left(1_{(0,t)}\varphi\right)^0\right|_2^2+x\right\}.\tag{63}$$

Then, apply Theorem 13 to $F(t,g(t,x))$, and the result is obvious. □

The special case $F(t,x)=x$ yields the following.

Corollary 16. *Let P be a geometric sub-fBm as in Theorem 15; then for all $t\ge 0$,*

$$P_t=x_0+\int_0^t r(s)\,P_s\,ds+\int_0^t\varphi(s)\,P_s\,dS_s^H.\tag{64}$$

For this reason, one calls it "geometric sub-fBm".

5. Explicit Solution of a Class of Linear Subfractional BSDEs

General BSDEs driven by a Brownian motion are usually of the form

$$\begin{aligned}
-dY_t&=f\left(t,Y_t,Z_t\right)dt-Z_t\,dB_t,\quad t\in[0,T],\\
Y_T&=\xi,
\end{aligned}\tag{65}$$

where f,ξ are given. The generator $f(t,y,z)$ is a $\mathcal{G}_t$-adapted process for every pair $(y,z)\in\mathbb{R}^2$, the terminal value ξ is a $\mathcal{G}_T$-measureable random variable, and $\mathcal{G}_t$ denotes the filtration generated by B_t. We say a pair (Y,Z) is a solution of this equation, if the processes Y,Z which are $\mathcal{G}_t$-adapted and satisfy a suitable integrability condition solve the equation P-almost surely.

After these preparations, we now turn to the problems to solve the BSDEs driven by a sub-fBm of the form

$$Y_t=\xi-\int_t^T f\left(s,Y_t,Z_t\right)ds-\int_t^T Z_t\,dS_s^H,\tag{66}$$

where $f,\xi=Y_T$ are given. The generator $f(t,y,z)$ is a $\mathcal{G}_t$-adapted process for every pair $(y,z)\in\mathbb{R}^2$, the terminal value ξ is a $\mathcal{G}_T$-measureable random variable, and $\mathcal{G}_t$ denotes the filtration generated by S_t^H. We say a pair (Y,Z) is a solution of this equation, if the processes Y,Z which are $\mathcal{G}_t$-adapted and

satisfy a suitable integrability condition solve the equation P-almost surely.

Let us recall a result about the following PDE, which is a parabolic partial differential equation solved by the heat equation (see Theorem 9 in [18]). Let the following conditions be satisfied:

(C_1) $S \in \mathscr{C}^1((0,T),\mathbb{R}) \cap \mathscr{C}([0,T],\mathbb{R})$ and S is strictly increasing with $S(0) = 0$ and $S' \in L^1([0,T],\mathbb{R})$;

(C_1) $r, A, f \in \mathscr{C}((0,T],\mathbb{R}) \cap L^1([0,T],\mathbb{R})$;

(C_1) $\phi \in \mathscr{C}(\mathbb{R},\mathbb{R})$ and there exists constant $C \geq 0$ and $\lambda < (8S(T))^{-1}$ such that for all $(t,x) \in [0,T] \times \mathbb{R}$, $|\phi(t,x)| \leq Ce^{\lambda x^2}$.

Then the PDE

$$\begin{aligned}\partial_t u(t,x) = &-\frac{1}{2}S'(t)\,\partial_{xx}u(t,x) + r(t)\,\partial_x u(t,x)\\ &+ A(t)\,u(t,x) + f(t),\\ u(T,x) = &\,\phi(x),\end{aligned} \tag{67}$$

has a classical solution given by

$$\begin{aligned}u(t,x) := &-\int_t^T f(s)\,e^{\int_s^t A(u)du}\,ds\\ &+\frac{e^{-\int_t^T A(s)ds}}{\sqrt{2\pi(S(T)-S(t))}}\\ &\times\int_{\mathbb{R}}\phi(y)\exp\left\{\frac{-\left(x-y-\int_t^T r(s)\,ds\right)^2}{2(S(T)-S(t))}\right\}dy.\end{aligned} \tag{68}$$

Next we give the main result of this paper.

Theorem 17. *Let $\Phi_t = x_0 + b(t) + \int_0^t \varphi(s)dS_s^H$ and $T > 0$. Suppose the following conditions are satisfied:*

(D_1) *$\varphi : [0,T] \to \mathbb{R}^+$ is continuous when $H \geq 1/2$, constant when $H < 1/2$, and there exist constants $0 < K_1 \leq K_2$, such that $K_1 \leq \varphi(t) \leq K_2, t \in [0,T]$;*

(D_2) *$x_0 \in \mathbb{R}, b \in \mathscr{C}^1((0,T),\mathbb{R}) \cap \mathscr{C}([0,T],\mathbb{R})$;*

(D_3) *(C_2) holds with $r(t) = \varphi(t)h(t) - b'(t)$ and $h : [0,T] \to \mathbb{R}$ with φh bounded on $[0,T]$;*

(D_4) *$\phi \in \mathscr{C}(\mathbb{R},\mathbb{R})$ and there exist constants $C \geq 0$, and $\lambda \leq 1/(12T^{2H}\max_{s\in[0,T]}|f(s)|^2)$ such that for all $(t,x) \in [0,T] \times \mathbb{R}$, $|\phi(t,x)| \leq Ce^{\lambda x^2}$.*

Then the BSDEs,

$$\begin{aligned}Y_t = &\,\phi(\Phi_T) - \int_t^T \left[f(s) + A(s)\,Y_s + h(s)\,Z_s\right]ds\\ &-\int_t^T Z_s\,dS_s^H,\end{aligned} \tag{69}$$

have a solution (Y,Z) of the form

$$Y(t) := v(t,\Phi_t), \qquad Z_t := \varphi(t)\,\partial_x v(t,\Phi_t),$$

$$\begin{aligned}&v(t,x)\\ &:= -\int_t^T f(s)\,e^{\int_s^t A(u)du}\,ds\\ &\quad+\frac{e^{-\int_t^T A(s)ds}}{\sqrt{2\pi\left(\left|M_-^H(1_{(0,T)}\varphi)^0\right|_2^2 - \left|M_-^H(1_{(0,t)}\varphi)^0\right|_2^2\right)}}\\ &\quad\times\int_{\mathbb{R}}\phi(y)\exp\left\{\frac{-\left(x-y-\int_t^T(\varphi(s)h(s)-b'(s))\,ds\right)^2}{2\left|M_-^H(1_{(0,T)}\varphi)^0\right|_2^2 - 2\left|M_-^H(1_{(0,t)}\varphi)^0\right|_2^2}\right\}dy.\end{aligned} \tag{70}$$

Proof. Let $S(t) := |M_-^H(1_{(0,t)}\varphi)^0|_2^2$; from Lemma 11 and Remark 12, we have $S(t)$ satisfies (C_1). By the growth condition (D_4), (C_3) is yielded, and (C_2) follows from (D_3). Henceforth, $v(t,x)$ is a classical solution of the PDE

$$\begin{aligned}\partial_t v(t,x) = &-\frac{1}{2}\frac{d}{dt}\left|M_-^H(1_{(0,t)}\varphi)^0\right|_2^2\partial_{xx}v(t,x)\\ &+\left[\varphi(t)h(t) - b'(t)\right]\partial_x v(t,x) + A(t)\,v(t,x)\\ &+ f(t);\quad (t,x) \in ((0,T),\mathbb{R}),\\ v(T,x) = &\,\phi(x),\quad x \in \mathbb{R}.\end{aligned} \tag{71}$$

Moreover, by Lemma 10 and Corollary 11 in [18], suppose that $F(t,x) := v(t, x_0 + b(t) + x)$, which fulfills the conditions of Theorem 13 for all $0 \leq t \leq T - \varepsilon$ and $\varepsilon > 0$. Consequently,

$$\begin{aligned}&v(t,\Phi_t)\\ &= v(T-\varepsilon,\Phi_{T-\varepsilon}) - \int_t^{T-\varepsilon}\varphi(s)\,\partial_x v(s,\Phi_s)\,dS_s^H\\ &\quad-\int_t^{T-\varepsilon} f(s) + A(s)\,v(s,\Phi_s) + h(s)\,\varphi(s)\,\partial_x v(s,\Phi_s)\,ds.\end{aligned} \tag{72}$$

Next, according to Definition 4 and the growth condition, $\int_t^{T-\varepsilon}\varphi(s)\partial_x v(s,\Phi_s)dS_s^H$ exists when ε tends to zero.

On the other hand, similar to (58), we obtain

$$\begin{aligned}&\mathcal{S}\left(v(T-\varepsilon,\Phi_{T-\varepsilon})\right)(\eta)\\ &= \int_{\mathbb{R}} F\left(T-\varepsilon, x\right.\\ &\qquad\left.+\frac{1}{\sqrt{2}}\int_0^{T-\varepsilon}\varphi(s)\left[\left(M_+^H\eta\right)(s) - \left(M_+^H\eta\right)(-s)\right]ds\right)\\ &\qquad\times g\left(\left|M_-^H(1_{(0,T-\varepsilon)}\varphi)^0\right|_2^2, x\right)dx.\end{aligned} \tag{73}$$

By the growth and the continuity conditions of v, we have $\mathcal{S}(v(T-\varepsilon,\Phi_{T-\varepsilon}))(\eta)$ converges to $\mathcal{S}(v(T,\Phi_T))(\eta)$ as ε tends to zero.

Now it remains to show the existence of the last integral of (72). In fact, there exists a constant K, such that

$$\begin{aligned}\int_0^T &\left\| f(s)+A(s)v(s,\Phi_s)+h(s)\varphi(s)\partial_x v(s,\Phi_s)\right\|_2 ds\\ &\le |f|_{L^1([0,T])}+K|A|_{L^1([0,T])}\\ &\quad+K\int_0^T \frac{1}{\sqrt{\left|M_-^H\left(1_{(0,T)}\varphi\right)^0\right|_2^2-\left|M_-^H\left(1_{(0,t)}\varphi\right)^0\right|_2^2}}\,dt.\end{aligned} \tag{74}$$

For $H>1/2$, (48) and (D_1) yield

$$\begin{aligned}&\int_0^T \frac{1}{\sqrt{\left|M_-^H\left(1_{(0,T)}\varphi\right)^0\right|_2^2-\left|M_-^H\left(1_{(0,t)}\varphi\right)^0\right|_2^2}}\,dt\\ &=\int_0^T\left[8\alpha H\int_t^T\int_0^\tau \varphi(s)\varphi(\tau)\left[(\tau-s)^{2\alpha-1}+(s+\tau)^{2\alpha-1}\right]ds\,d\tau\right]^{-1/2}dt\\ &\le\frac{1}{K_1}\int_0^T\left[8\alpha H\int_t^T\int_0^\tau\left[(\tau-s)^{2\alpha-1}+(s+\tau)^{2\alpha-1}\right]ds\,d\tau\right]^{-1/2}dt\\ &=\frac{1}{K_1}\int_0^T\frac{1}{\sqrt{T^{2H}-t^{2H}}}\,dt=\frac{T^{1-H}}{HK_1 2^{H+1}}\frac{\Gamma(1/2)\Gamma(1/2H)}{\Gamma(1/2H+1/2)}.\end{aligned} \tag{75}$$

For $H<1/2$, $|M_-^H(1_{(0,t)}\varphi)^0|_2^2=(2-2^{2H-1})\varphi^2 t^{2H}$, we obtain

$$\begin{aligned}&\int_0^T \frac{1}{\sqrt{\left|M_-^H\left(1_{(0,T)}\varphi\right)^0\right|_2^2-\left|M_-^H\left(1_{(0,t)}\varphi\right)^0\right|_2^2}}\,dt\\ &=\frac{1}{\sqrt{2-2^{2H-1}}\varphi}\int_0^T\frac{1}{\sqrt{T^{2H}-t^{2H}}}\,dt\\ &=\frac{1}{\sqrt{2-2^{2H-1}}f}\frac{T^{1-H}\Gamma(1/2)\Gamma(1/2H)}{2H\Gamma(1/2H+1/2)}.\end{aligned} \tag{76}$$

This means that $\int_0^T f(s)+A(s)v(s,\Phi_s)+h(s)\varphi(s)\partial_x v(s,\Phi_s)ds$ is well defined, which completes the proof. □

The above theorem also holds for geometric sub-fBm as described in the following proposition.

Proposition 18. *Let a geometric sub-fBm $P_t=x_0\exp\{kS_t^H+\mu t-(1/2)(2-2^{2H-1})k^2t^{2H}\}$, and G is continuous and of polynomial growth. Then Theorem 17 holds with the terminal value of the form $G(P_T)$.*

Proof. We just need to apply Theorem 17 with $\Phi(t)=\ln x_0+kS_t^H+\mu t-(1/2)(2-2^{2H-1})k^2t^{2H}$ and $\phi(x)=G(e^x)$. □

The regularity of the obtained solutions is described as follows.

Proposition 19. *Let Y, Z as defined in Theorem 17. Then $Y\in L^2([0,T],(L^2))$. Moreover, $Z\in L^{1/H}([0,T],(L^2))$ when $H>1/4$.*

It is a straightforward result in view of the growth condition of v.

6. Conclusion

We have presented the subfractional Itô integral using the method of the $\mathcal{S}$-transform. A Girsanov theorem with respect to the subfractional Itô integral and an Itô formula for functionals of a subfractional Wiener integral has been established. As an application, we obtain explicit solutions for a class of linear BSDEs driven by a sub-fBm with arbitrary Hurst parameter under suitable assumptions.

Acknowledgments

The Project was sponsored by NSFC (11171062, 40901241), Innovation Program of Shanghai Municipal Education Commission(12ZZ063), the Research Project of Education of Zhejiang Province (Y201326507) and Natural Science Foundation of Zhejiang Province (Y5090377).

References

[1] T. Bojdecki, L. G. Gorostiza, and A. Talarczyk, "Sub-fractional Brownian motion and its relation to occupation times," *Statistics & Probability Letters*, vol. 69, no. 4, pp. 405–419, 2004.

[2] T. Bojdecki, L. G. Gorostiza, and A. Talarczyk, "Some extensions of fractional Brownian motion and sub-fractional Brownian motion related to particle systems," *Electronic Communications in Probability*, vol. 12, pp. 161–172, 2007.

[3] E. Alòs, O. Mazet, and D. Nualart, "Stochastic calculus with respect to Gaussian processes," *The Annals of Probability*, vol. 29, no. 2, pp. 766–801, 2001.

[4] D. Nualart, *The Malliavin Calculus and Related Topics*, Springer, Berlin, Germany, 2nd edition, 2006.

[5] T. Bojdecki, L. G. Gorostiza, and A. Talarczyk, "Fractional Brownian density process and its self-intersection local time of order k," *Journal of Theoretical Probability*, vol. 17, no. 3, pp. 717–739, 2004.

[6] J. Liu and L. Yan, "Remarks on asymptotic behavior of weighted quadratic variation of subfractional Brownian motion," *Journal of the Korean Statistical Society*, vol. 41, no. 2, pp. 177–187, 2012.

[7] G. Shen and C. Chen, "Stochastic integration with respect to the sub-fractional Brownian motion with $H\in(0,1/2)$," *Statistics & Probability Letters*, vol. 82, no. 2, pp. 240–251, 2012.

[8] C. Tudor, "Some properties of the sub-fractional Brownian motion," *Stochastics*, vol. 79, no. 5, pp. 431–448, 2007.

[9] C. Tudor, "Inner product spaces of integrands associated to subfractional Brownian motion," *Statistics & Probability Letters*, vol. 78, no. 14, pp. 2201–2209, 2008.

[10] C. Tudor, "Some aspects of stochastic calculus for the sub-fractional Brownian motion," *Analele Universitatii Bucuresti. Matematica*, vol. 57, no. 2, pp. 199–230, 2008.

[11] C. Tudor, "On the Wiener integral with respect to a sub-fractional Brownian motion on an interval," *Journal of Mathematical Analysis and Applications*, vol. 351, no. 1, pp. 456–468, 2009.

[12] L. Yan, K. He, and C. Chen, "The generalized Bouleau-Yor identity for a sub-fractional Brownian motion," *Science China Mathematics*, 2013.

[13] L. Yan and G. Shen, "On the collision local time of sub-fractional Brownian motions," *Statistics & Probability Letters*, vol. 80, no. 5-6, pp. 296–308, 2010.

[14] L. Yan, G. Shen, and K. He, "Itô's formula for a sub-fractional Brownian motion," *Communications on Stochastic Analysis*, vol. 5, no. 1, pp. 135–159, 2011.

[15] É. Pardoux and S. G. Peng, "Adapted solution of a backward stochastic differential equation," *Systems & Control Letters*, vol. 14, no. 1, pp. 55–61, 1990.

[16] S. Peng, "Backward stochastic differential equations," in *Nonlinear Expectations, Nonlinear Evaluations and Risk Measures*, Lecture Notes in Chinese Summer School in Mathematics Weihai, 2004.

[17] F. Biagini, Y. Hu, B. Øksendal, and A. Sulem, "A stochastic maximum principle for processes driven by fractional Brownian motion," *Stochastic Processes and their Applications*, vol. 100, pp. 233–253, 2002.

[18] C. Bender, "Explicit solutions of a class of linear fractional BSDEs," *Systems & Control Letters*, vol. 54, no. 7, pp. 671–680, 2005.

[19] Y. Hu and S. Peng, "Backward stochastic differential equation driven by fractional Brownian motion," *SIAM Journal on Control and Optimization*, vol. 48, no. 3, pp. 1675–1700, 2009.

[20] J.-M. Bismut, "Conjugate convex functions in optimal stochastic control," *Journal of Mathematical Analysis and Applications*, vol. 44, pp. 384–404, 1973.

[21] C. Geiss, S. Geiss, and E. Gobet, "Generalized fractional smoothness and L_p-variation of BSDEs with non-Lipschitz terminal condition," *Stochastic Processes and their Applications*, vol. 122, no. 5, pp. 2078–2116, 2012.

[22] N. El Karoui, S. Peng, and M. C. Quenez, "Backward stochastic differential equations in finance," *Mathematical Finance*, vol. 7, no. 1, pp. 1–71, 1997.

[23] J. Ma, P. Protter, and J. M. Yong, "Solving forward-backward stochastic differential equations explicitly—a four step scheme," *Probability Theory and Related Fields*, vol. 98, no. 3, pp. 339–359, 1994.

[24] L. Maticiuc and T. Nie, "Fractional backward stochastic differentialequations and fractional backward variational inequalities," http://arxiv.org/abs/1102.3014.

[25] S. G. Peng, "Backward stochastic differential equations and applications to optimal control," *Applied Mathematics and Optimization*, vol. 27, no. 2, pp. 125–144, 1993.

[26] B. B. Mandelbrot and J. W. van Ness, "Fractional Brownian motions, fractional noises and applications," *SIAM Review*, vol. 10, pp. 422–437, 1968.

[27] F. Biagini, Y. Hu, B. Øksendal, and T. Zhang, *Stochastic Calculus for Fractional Brownian Motion and Applications*, Springer, London, UK, 2006.

[28] Y. Hu, "Integral transformations and anticipative calculus for fractional Brownian motions," *Memoirs of the American Mathematical Society*, vol. 175, no. 825, 2005.

[29] Y. S. Mishura, *Stochastic Calculus for Fractional Brownian Motion and Related Processes*, Springer, Berlin, Germany, 2008.

[30] M. Li, "On the long-range dependence of fractional Brownian motion," *Mathematical Problems in Engineering*, vol. 2013, Article ID 842197, 5 pages, 2013.

[31] M. Li and W. Zhao, "On $1/f$ noise," *Mathematical Problems in Engineering*, vol. 2012, Article ID 673648, 23 pages, 2012.

[32] M. Li and W. Zhao, "Quantitatively investigating locally weak stationarity of modified multifractional Gaussian noise," *Physica A*, vol. 391, no. 24, pp. 6268–6278, 2012.

[33] S. C. Lim and S. V. Muniandy, "On some possible generalizations of fractional Brownian motion," *Physics Letters A*, vol. 266, no. 2-3, pp. 140–145, 2000.

[34] M. Zähle, "Integration with respect to fractal functions and stochastic calculus. I," *Probability Theory and Related Fields*, vol. 111, no. 3, pp. 333–374, 1998.

[35] C. Bender, "An S-transform approach to integration with respect to a fractional Brownian motion," *Bernoulli*, vol. 9, no. 6, pp. 955–983, 2003.

[36] C. Bender, "An Itô formula for generalized functionals of a fractional Brownian motion with arbitrary Hurst parameter," *Stochastic Processes and their Applications*, vol. 104, no. 1, pp. 81–106, 2003.

Hindawi Publishing Corporation
Advances in Mathematical Physics
Volume 2013, Article ID 806984, 4 pages
http://dx.doi.org/10.1155/2013/806984

Research Article

Solving Abel's Type Integral Equation with Mikusinski's Operator of Fractional Order

Ming Li[1] and Wei Zhao[2]

[1] *School of Information Science & Technology, East China Normal University, No. 500, Dong-Chuan Road, Shanghai 200241, China*
[2] *Department of Computer and Information Science, University of Macau, Avenida Padre Tomas Pereira, Taipa, Macau*

Correspondence should be addressed to Ming Li; ming_lihk@yahoo.com

Received 21 April 2013; Accepted 10 May 2013

Academic Editor: Carlo Cattani

This paper gives a novel explanation of the integral equation of Abel's type from the point of view of Mikusinski's operational calculus. The concept of the inverse of Mikusinski's operator of fractional order is introduced for constructing a representation of the solution to the integral equation of Abel's type. The proof of the existence of the inverse of the fractional Mikusinski operator is presented, providing an alternative method of treating the integral equation of Abel's type.

1. Introduction

Abel studied a physical problem regarding the relationship between kinetic and potential energies for falling bodies [1]. One of his integrals stated in [1] is expressed in the form

$$f(t) = \int_a^t \frac{g(u)}{\sqrt{t-u}}du, \quad a > 0, \tag{1}$$

where $f(t)$ is known, but $g(t)$ is unknown. The previous expression is in the literature nowadays called Abel's integral equation [2]. In addition to (1), Abel also worked on the integral equation in [1] in the following form:

$$f(t) = \int_a^t \frac{g(u)}{(t-u)^{\lambda}}du, \quad a > 0,\ 0 < \lambda < 1,\ a\ \le t \le b, \tag{2}$$

which is usually termed the integral equation of Abel's type [3] or the generalized Abel integral equation [4]. The function $(t-u)^{-\lambda}$ may be called Abel's kernel. It is seen that (1) is a special case of (2) for $\lambda = 1/2$. This paper is in the aspect of (2). Without generality losing, for the purpose of facilitating the discussions, we multiply the left side of (1) with the constant $1/\Gamma(\lambda)$, and let $a = 0$. That is, we rewrite (2) by

$$f(t) = \frac{1}{\Gamma(\lambda)} \int_0^t \frac{g(u)}{(t-u)^{\lambda}}du, \quad 0 < \lambda < 1,\ 0 \le t \le b. \tag{3}$$

The integral equation of Abel's type attracts the interests of mathematicians and physicists. In mathematics, for example, for solving the integral equation of Abel's type, [5] discusses a transformation technique, [6] gives a method of orthogonal polynomials, [7] adopts the method of integral operators, [8, 9] utilize the fractional calculus, [10] is with the Bessel functions, [11, 12] study the wavelet methods, [13, 14] describe the methods based on semigroups, [15] uses the almost Bernstein operational matrix, and so forth [16, 17], just to mention a few. Reference [18] represents a nice description of the importance of Abel's integral equations in mathematics as well as engineering, citing [19–23] for the various applications of Abel's integral equations.

The above stands for a sign that the theory of Abel's integral equations is developing. New methods for solving such a type of equations are demanded in this field. This paper presents a new method to describe the integral equation of Abel's type from the point of view of the Mikusinski operator of fractional order. In addition, we will give a solution to the integral equation of Abel's type by using the inverse of the Mikusinski operator of fractional order.

The remainder of this article is organized as follows. In Section 2, we shall express the integral equation of the Abel's type using the Mikusinski operator of fractional order and give the solution to that type of equation in the constructive way based on the inverse of the fractional-order Mikusinski

operator. Section 3 consists of two parts. One is the proof of the existence of the inverse of the fractional-order Mikusinski operator. The other is the computation of the solution to Abel's type integral equation. Finally, Section 4 concludes the paper.

2. Constructive Solution Based on Fractional-Order Mikusinski Operator

Denote the operation of Mikusinski's convolution by $\otimes$. Let $\oplus$ be the operation of its inverse. Then, for $a(t), b(t) \in C(0, \infty)$, one has

$$a(t) \otimes b(t) = \int_0^t a(t-\tau)\, b(\tau)\, d\tau = c(t). \tag{4}$$

The inverse of the previous expression is the deconvolution, which is denoted by (see [24–26])

$$c(t) \oplus a(t) = b(t), \qquad c(t) \oplus b(t) = a(t). \tag{5}$$

In (4) and (5), the constraint $a(t), b(t) \in C(0, \infty)$ may be released. More precisely, we assume that $a(t)$ and $b(t)$ may be generalized functions. Therefore, the Diract-δ function in the following is the identity in this convolution system. That is,

$$a(t) \otimes \delta(t) = \delta(t) \otimes a(t) = a(t). \tag{6}$$

Consequently,

$$a(t) \oplus a(t) = \delta(t). \tag{7}$$

Let l be an operator that corresponds to the function $1(t)$ such that

$$la(t) = 1(t) \otimes a(t) = \int_0^t a(\tau)\, d\tau. \tag{8}$$

Therefore, the operator l^2 implies

$$l^2 \Longleftrightarrow 1(t) \otimes 1(t) = \int_0^t d\tau = \frac{t}{1}. \tag{9}$$

For $n = 1, \ldots$, consequently, we have

$$l^n \Longleftrightarrow \frac{t^{n-1}}{(n-1)!}, \tag{10}$$

where $0! = 1$.

The Cauchy integral formula may be expressed by using l^n, so that

$$l^n g(t) = \frac{t^{n-1}}{(n-1)!} \otimes g(t) = \int_0^t \frac{(t-\tau)^{n-1}}{(n-1)!}\, g(\tau)\, d\tau. \tag{11}$$

Generalizing l^n to l^λ in (12) for $\lambda > 0$ yields the Mikusinski operator of fractional order given by

$$l^\tau \Longleftrightarrow \frac{t^{\lambda-1}}{(\lambda-1)!} = \frac{t^{\lambda-1}}{\Gamma(\lambda)}. \tag{12}$$

Thus, taking into account (12), we may represent the integral equation of Abel's type by

$$l^\lambda g(t) = \frac{t^{\lambda-1}}{\Gamma(\lambda)} \otimes g(t) = \int_0^t \frac{(t-\tau)^{\lambda-1}}{\Gamma(\lambda)}\, g(\tau)\, d\tau = f(t). \tag{13}$$

Rewrite the above by

$$l^\lambda g(t) = f(t). \tag{14}$$

Then, the solution to Able's type integral equation (3) may be represented by

$$g(t) = l^{-\lambda} f(t), \tag{15}$$

where $l^{-\lambda}$ is the inverse of l^λ.

There are two questions in the constructive solution expressed by (15). One is whether $l^{-\lambda}$ exists. The other is how to represent its computation. We shall discuss the answers next section.

3. Results

3.1. Existence of the Inverse of Mikusinski's Operator of Order λ. Let $\mathbf{G}$ and $\mathbf{F}$ be two normed spaces for $g(t) \in \mathbf{G}$ and $f(t) \in \mathbf{F}$, respectively. Then, the operator l^λ regarding Able's type integral equation (13) may be expressed by

$$l^\lambda : \mathbf{G} \longrightarrow \mathbf{F}. \tag{16}$$

The operator l^λ is obviously linear. Note that (3) is convergent [1]. Thus, one may assume that

$$m \le \int_0^b \left| \frac{(t-\tau)^{\lambda-1}}{\Gamma(\lambda)}\, g(\tau) \right| d\tau \le M, \tag{17}$$

where

$$m \ge 0, \quad M \ge 0. \tag{18}$$

Define the norm of $f(t)$ by

$$\|f(t)\| = \max_{0<t<b} f(t). \tag{19}$$

Then, we have

$$\left\| l^\lambda g(t) \right\| \le M \|f(t)\|. \tag{20}$$

The above implies that l^λ is bounded. Accordingly, it is continuous [27, 28].

Since

$$\left\| l^\lambda g(t) \right\| \ge m \|f(t)\|, \tag{21}$$

$l^{-\lambda}$ exists. Moreover, the inverse of l^λ is continuous and bounded according to the inverse operator theorem of Banach [27, 28]. This completes the proof of (15).

3.2. Computation Formula. According to the previous analysis, $l^{-\lambda}$ exists. It actually corresponds to the differential of order λ. Thus,

$$g(t) = l^{-\lambda} f(t) = \frac{d^{\lambda} f(t)}{dt^{\lambda}}. \tag{22}$$

In (13), we write $\int_0^t (((t-\tau)^{\lambda-1}/\Gamma(\lambda))g(\tau))d\tau = f(t)$ by

$$\int_0^t (t-\tau)^{\lambda-1} g(\tau)\, d\tau = \Gamma(\lambda)\, f(t). \tag{23}$$

Following [29, p. 13, p. 527], [30], therefore,

$$\begin{aligned} g(t) = l^{-\lambda} f(t) &= \frac{\sin(\pi\lambda)}{\pi} \frac{d}{dt} \int_0^t \frac{\Gamma(\lambda) f(u)}{(t-u)^{1-\lambda}} du \\ &= \frac{\Gamma(\lambda)\sin(\pi\lambda)}{\pi} \left[\frac{f(0)}{t^{1-\lambda}} + \int_0^t \frac{f'(t)\, dt}{(t-u)^{1-\lambda}} \right]. \end{aligned} \tag{24}$$

Since

$$\frac{\sin(\pi\lambda)}{\pi} = \frac{1}{\Gamma(\lambda)\Gamma(1-\lambda)}, \tag{25}$$

we write (24) by

$$g(t) = \frac{1}{\Gamma(1-\lambda)} \left[\frac{f(0)}{t^{1-\lambda}} + \int_0^t \frac{f'(t)\, dt}{(t-u)^{1-\lambda}} \right]. \tag{26}$$

In the solution (26), if $f(0) = 0$, one has

$$g(t) = \frac{1}{\Gamma(1-\lambda)} \int_0^t \frac{f'(t)\, dt}{(t-u)^{1-\lambda}}, \tag{27}$$

which is a result described by Gelfand and Vilenkin in [9, Section 5.5].

Note that Mikusinski's operational calculus is a tool usually used for solving linear differential equations [24–26], but we use it in this research for the integral equation of the Abel's type from a view of fractional calculus. In addition, we suggest that the idea in this paper may be applied to studying other types of equations, for instance, those in [31–50], to make the possible applications of Mikusinski's operational calculus a step further.

4. Conclusions

We have presented the integral equation of Abel's type using the method of the Mikusinski operational calculus. The constructive representation of the solution to Abel's type integral equation has been given with the Mikusinski operator of fractionally negative order, giving a novel interpretation of the solution to Abel's type integral equation.

Acknowledgments

This work was supported in part by the 973 plan under the Project Grant no. 2011CB302800 and by the National Natural Science Foundation of China under the Project Grant nos. 61272402, 61070214, and 60873264.

References

[1] N. H. Abel, "Solution de quelques problèmes à l'aide d'intégrales définies," *Magaziu for Naturvidenskaberue*, Alu-gang I, Bînd 2, Christiania, pp. 11–18, 1823.

[2] R. Gorenflo and S. Vessella, *Abel Integral Equations*, Springer, 1991.

[3] P. P. B. Eggermont, "On Galerkin methods for Abel-type integral equations," *SIAM Journal on Numerical Analysis*, vol. 25, no. 5, pp. 1093–1117, 1988.

[4] A. Chakrabarti and A. J. George, "Diagonalizable generalized Abel integral operators," *SIAM Journal on Applied Mathematics*, vol. 57, no. 2, pp. 568–575, 1997.

[5] J. R. Hatcher, "A nonlinear boundary problem," *Proceedings of the American Mathematical Society*, vol. 95, no. 3, pp. 441–448, 1985.

[6] G. N. Minerbo and M. E. Levy, "Inversion of Abel's integral equation by means of orthogonal polynomials," *SIAM Journal on Numerical Analysis*, vol. 6, no. 4, pp. 598–616, 1969.

[7] J. D. Tamarkin, "On integrable solutions of Abel's integral equation," *The Annals of Mathematics*, vol. 31, no. 2, pp. 219–229, 1930.

[8] D. B. Sumner, "Abel's integral equation as a convolution transform," *Proceedings of the American Mathematical Society*, vol. 7, no. 1, pp. 82–86, 1956.

[9] I. M. Gelfand and K. Vilenkin, *Generalized Functions*, vol. 1, Academic Press, New York. NY, USA, 1964.

[10] C. E. Smith, "A theorem of Abel and its application to the development of a function in terms of Bessel's functions," *Transactions of the American Mathematical Society*, vol. 8, no. 1, pp. 92–106, 1907.

[11] S. Sohrabi, "Comparison Chebyshev wavelets method with BPFs method for solving Abel's integral equation," *Ain Shams Engineering Journal*, vol. 2, no. 3-4, pp. 249–254, 2011.

[12] A. Antoniadis, J. Q. Fan, and I. Gijbels, "A wavelet method for unfolding sphere size distributions," *The Canadian Journal of Statistics*, vol. 29, no. 2, pp. 251–268, 2001.

[13] R. J. Hughes, "Semigroups of unbounded linear operators in Banach space," *Transactions of the American Mathematical Society*, vol. 230, pp. 113–145, 1977.

[14] K. Ito and J. Turi, "Numerical methods for a class of singular integro-differential equations based on semigroup approximation," *SIAM Journal on Numerical Analysis*, vol. 28, no. 6, pp. 1698–1722, 1991.

[15] O. P. Singh, V. K. Singh, and R. K. Pandey, "A stable numerical inversion of Abel's integral equation using almost Bernstein operational matrix," *Journal of Quantitative Spectroscopy and Radiative Transfer*, vol. 111, no. 1, pp. 245–252, 2010.

[16] R. K. Pandey, O. P. Singh, and V. K. Singh, "Efficient algorithms to solve singular integral equations of Abel type," *Computers & Mathematics with Applications*, vol. 57, no. 4, pp. 664–676, 2009.

[17] M. Khan and M. A. Gondal, "A reliable treatment of Abel's second kind singular integral equations," *Applied Mathematics Letters*, vol. 25, no. 11, pp. 1666–1670, 2012.

[18] R. Weiss, "Product integration for the generalized Abel equation," *Mathematics of Computation*, vol. 26, pp. 177–190, 1972.

[19] W. C. Brenke, "An application of Abel's integral equation," *The American Mathematical Monthly*, vol. 29, no. 2, pp. 58–60, 1922.

[20] E. B. Hansen, "On drying of laundry," *SIAM Journal on Applied Mathematics*, vol. 52, no. 5, pp. 1360–1369, 1992.

[21] A. T. Lonseth, "Sources and applications of integral equations," *SIAM Review*, vol. 19, no. 2, pp. 241–278, 1977.

[22] Y. H. Jang, "Distribution of three-dimensional islands from two-dimensional line segment length distribution," *Wear*, vol. 257, no. 1-2, pp. 131–137, 2004.

[23] L. Bougoffa, R. C. Rach, and A. Mennouni, "A convenient technique for solving linear and nonlinear Abel integral equations by the Adomian decomposition method," *Applied Mathematics and Computation*, vol. 218, no. 5, pp. 1785–1793, 2011.

[24] J. Mikusiński, *Operational Calculus*, Pergamon Press, 1959.

[25] T. K. Boehme, "The convolution integral," *SIAM Review*, vol. 10, no. 4, pp. 407–416, 1968.

[26] G. Bengochea and L. Verde-Star, "Linear algebraic foundations of the operational calculi," *Advances in Applied Mathematics*, vol. 47, no. 2, pp. 330–351, 2011.

[27] V. I. Istrăţescu, *Introduction to Linear Operator Theory*, vol. 65, Marcel Dekker, New York, NY, USA, 1981.

[28] M. Li and W. Zhao, *Analysis of Min-Plus Algebra*, Nova Science Publishers, 2011.

[29] A. D. Polyanin and A. V. Manzhirov, *Handbook of Integral Equations*, CRC Press, Boca Raton, Fla, USA, 1998.

[30] http://eqworld.ipmnet.ru/.

[31] C. Cattani and A. Kudreyko, "Harmonic wavelet method towards solution of the Fredholm type integral equations of the second kind," *Applied Mathematics and Computation*, vol. 215, no. 12, pp. 4164–4171, 2010.

[32] C. Cattani, M. Scalia, E. Laserra, I. Bochicchio, and K. K. Nandi, "Correct light deflection in Weyl conformal gravity," *Physical Review D*, vol. 87, no. 4, Article ID 47503, 4 pages, 2013.

[33] C. Cattani, "Fractional calculus and Shannon wavelet," *Mathematical Problems in Engineering*, vol. 2012, Article ID 502812, 26 pages, 2012.

[34] M. Carlini, T. Honorati, and S. Castellucci, "Photovoltaic greenhouses: comparison of optical and thermal behaviour for energy savings," *Mathematical Problems in Engineering*, vol. 2012, Article ID 743764, 10 pages, 2012.

[35] M. Carlini and S. Castellucci, "Modelling the vertical heat exchanger in thermal basin," in *Computational Science and Its Applications*, vol. 6785 of *Lecture Notes in Computer Science*, pp. 277–286, Springer, 2011.

[36] M. Carlini, C. Cattani, and A. Tucci, "Optical modelling of square solar concentrator," in *Computational Science and Its Applications*, vol. 6785 of *Lecture Notes in Computer Science*, pp. 287–295, Springer, 2011.

[37] E. G. Bakhoum and C. Toma, "Mathematical transform of traveling-wave equations and phase aspects of Quantum interaction," *Mathematical Problems in Engineering*, vol. 2010, Article ID 695208, 15 pages, 2010.

[38] E. G. Bakhoum and C. Toma, "Specific mathematical aspects of dynamics generated by coherence functions," *Mathematical Problems in Engineering*, vol. 2011, Article ID 436198, 10 pages, 2011.

[39] C. Toma, "Advanced signal processing and command synthesis for memory-limited complex systems," *Mathematical Problems in Engineering*, vol. 2012, Article ID 927821, 13 pages, 2012.

[40] G. Toma, "Specific differential equations for generating pulse sequences," *Mathematical Problems in Engineering*, vol. 2010, Article ID 324818, 11 pages, 2010.

[41] J. Yang, Y. Chen, and M. Scalia, "Construction of affine invariant functions in spatial domain," *Mathematical Problems in Engineering*, vol. 2012, Article ID 690262, 11 pages, 2012.

[42] J. W. Yang, Z. R. Chen, W.-S. Chen, and Y. J. Chen, "Robust affine invariant descriptors," *Mathematical Problems in Engineering*, vol. 2011, Article ID 185303, 15 pages, 2011.

[43] Z. Jiao, Y.-Q. Chen, and I. Podlubny, "Distributed-Order Dynamic Systems," *Springer*, 2011.

[44] H. Sheng, Y.-Q. Chen, and T.-S. Qiu, *Fractional Processes and Fractional Order Signal Processing*, Springer, 2012.

[45] H. G. Sun, Y.-Q. Chen, and W. Chen, "Random-order fractional differential equation models," *Signal Processing*, vol. 91, no. 3, pp. 525–530, 2011.

[46] S. V. Muniandy, W. X. Chew, and C. S. Wong, "Fractional dynamics in the light scattering intensity fluctuation in dusty plasma," *Physics of Plasmas*, vol. 18, no. 1, Article ID 013701, 8 pages, 2011.

[47] H. Asgari, S. V. Muniandy, and C. S. Wong, "Stochastic dynamics of charge fluctuations in dusty plasma: a non-Markovian approach," *Physics of Plasmas*, vol. 18, no. 8, Article ID 083709, 4 pages, 2011.

[48] C. H. Eab and S. C. Lim, "Accelerating and retarding anomalous diffusion," *Journal of Physics A*, vol. 45, no. 14, Article ID 145001, 17 pages, 2012.

[49] C. H. Eab and S. C. Lim, "Fractional Langevin equations of distributed order," *Physical Review E*, vol. 83, no. 3, Article ID 031136, 10 pages, 2011.

[50] L.-T. Ko, J.-E. Chen, Y.-S. Shieh, H.-C. Hsin, and T.-Y. Sung, "Difference-equation-based digital frequency synthesizer," *Mathematical Problems in Engineering*, vol. 2012, Article ID 784270, 12 pages, 2012.

Hindawi Publishing Corporation
Advances in Mathematical Physics
Volume 2013, Article ID 950289, 8 pages
http://dx.doi.org/10.1155/2013/950289

Research Article

Extraction of Affine Invariant Features Using Fractal

Jianwei Yang,[1] Guosheng Cheng,[1] and Ming Li[2]

[1] *School of Mathematics and Statistics, Nanjing University of Information Science and Technology, Nanjing 210044, China*
[2] *School of Information Science and Technology, East China Normal University, No. 500, Dong-Chuan Road, Shanghai 200241, China*

Correspondence should be addressed to Jianwei Yang; yjianw@hotmail.com

Received 19 March 2013; Accepted 29 April 2013

Academic Editor: Chen Wensheng

An approach based on fractal is presented for extracting affine invariant features. Central projection transformation is employed to reduce the dimensionality of the original input pattern, and general contour (GC) of the pattern is derived. Affine invariant features cannot be extracted from GC directly due to shearing. To address this problem, a group of curves (which are called shift curves) are constructed from the obtained GC. Fractal dimensions of these curves can readily be computed and constitute a new feature vector for the original pattern. The derived feature vector is used in question for pattern recognition. Several experiments have been conducted to evaluate the performance of the proposed method. Experimental results show that the proposed method can be used for object classification.

1. Introduction

The images of an object taken from different viewpoints often suffer from perspective distortions. For this reason, features extracted from the image of an object should be tolerant to an appropriate class of geometric transformation (such as translation, rotation, scaling, and shearing). A perspective transformation between two views can be approximated with an affine transformation if the object is planar and far away from the image plane [1]. Therefore, the extraction of affine invariant features plays a very important role in object recognition and has been found application in many fields such as shape recognition and retrieval [2, 3], watermarking [4], identification of aircrafts [5, 6], texture classification [7], image registration [8], and contour matching [9].

Many algorithms have been developed for affine invariant features extraction [10–12]. Based on whether the features are extracted from the contour only or from the whole shape region, the approaches can be classified into two main categories: region-based methods and contour-based methods. Contour-based methods provide better data reduction [13], but they are inapplicable to objects with several separable components. Region-based methods can achieve high accuracy but usually at the expense of high computational demands, for good overviews of the various techniques refer to [13–16]. Central projection transformation (CPT) [17] can be used to combine contour-based methods and region-based methods together. However, CPT cannot be used to extract affine invariant features directly. In this paper, we extract affine invariant features by integrating CPT and fractal.

The essential advantage of fractal technique descriptor is that it can greatly speed up computation [17]. Fractal, which is introduced by Mandelbrot [18], has been shown to be one of the most important scientific discoveries in the last century. It proposes a powerful tool for human being to explore the complexity. It can be used to model many classes of time-series data as well as images. The fractal dimension (FD) is an important characteristic of fractals; it contains information about their geometrical structure. Many applications of fractal concepts rely on the ability to estimate the FD of objects. In the area of pattern recognition and image processing, the FD has been used for image compression, texture segmentation, feature extraction [19, 20], and so forth. The utility of fractal to extract rotation invariant features has been invested in [17]. CPT is employed to reduce the dimensionality of the original pattern. A discrete wavelet transformation technique transforms the derived pattern into a set of subpatterns. Consequently, its FD is computed and has been used as the feature vectors. A satisfying classification rate has been achieved in the

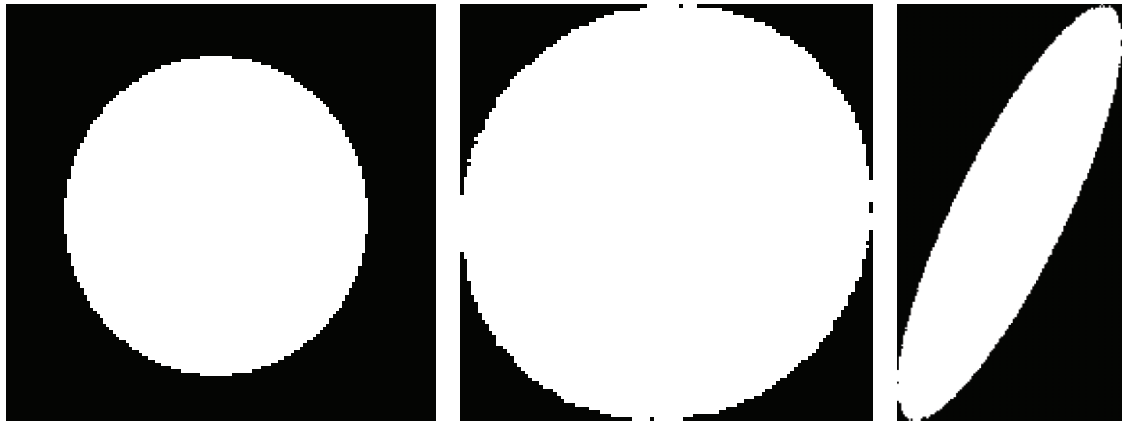

(a) (b) (c)

Figure 1: (a) An image of a circle. (b) A scaled version of circle in Figure 1(a). (c) An affine transformation version of circle in Figure 1(a).

recognition of rotated English letters, Chinese characters, and handwritten signatures. For more details, please refer to those papers.

However, the approach presented in [17] is hard to be used to extract invariant features for general affine transformation. A general affine transformation not only includes rotation, scaling, and translation but also includes shearing. That is to say, a circle may be transformed into an eclipse. Figure 1(a) is an image of a circle. Figure 1(b) is a scale and rotation version of circle in Figure 1(a). Figure 1(c) is an affine transformation version of circle in Figure 1(a). It can be calculated that FD of curve derived from the circle in Figure 1(a) by CPT is $f_1 = 1.4007$, FD of curve derived from the circle in Figure 1(b) by CPT is $f_2 = 1.4012$, while FD of curve derived from the eclipse in Figure 1(c) is $f_3 = 1.4244$. That is to say, FD can not be used to extract affine invariant features directly. To address this problem, a group of curves (which are called shift curves) are constructed from the closed curve derived by CPT in this paper. FDs of these curves can readily be computed and constitute a new feature vector for the original pattern. Several experiments have been conducted to evaluate the performance of the proposed method. Experimental results show that the constructed affine invariant feature vector can be used for object classification.

The rest of the paper is organized as follows. In Section 2, some basic concepts about CPT are introduced. The method for the extraction of affine invariant features is provided in Section 3. The performance of the proposed method is evaluated experimentally in Section 4. Finally, some conclusion remarks are provided in Section 5.

2. CPT and Its Properties

This section is devoted to providing some characteristics of CPT. In CPT, any object can be converted to a closed curve of the object by taking projection along lines from the centroid with different angles. Consequently, any object can be transformed into a single contour. In addition, the derived single contour also has affine property.

2.1. The CPT Method. Firstly, we translate the origin of the reference system to the centroid of the image. To perform CPT, the Cartesian coordinate system should be transformed to polar coordinate system. Hence, the shape $I(x, y)$ can be represented by a function f of r and θ, namely, $I(x, y) = f(r, \theta)$, where $r \in [0, \infty)$ and $\theta \in [0, 2\pi)$. After the transformation of the system, the CPT is performed by computing the following integral:

$$g(\theta) = \int_0^\infty f(r, \theta)\, dr, \tag{1}$$

where $\theta \in [0, 2\pi)$.

Definition 1. For an angle $\theta \in \mathbb{R}$, $g(\theta)$ is given in (1) and $(\theta, g(\theta))$ denotes a point in the plane of $\mathbb{R}^2$. Letting θ go from 0 to 2π, then $\{(\theta, g(\theta)) \mid \theta \in [0, 2\pi)\}$ forms a closed curve. We call this closed curve the general contour (GC) of the object.

For an object $\digamma$, we denote the GC extracted from it by CPT as $\partial\digamma$. The GC of an object has the following properties: single contour, affine invariant.

By (1), an angle $\theta \in [0, 2\pi)$ corresponds to a single value $g(\theta)$. Consequently, GC can be derived from any object by employing CPT. For instance, Figure 2(a) shows the image of Chinese character "Yang", which consists of several components. Figure 2(b) shows the GC of Figure 2(a). The object has been concentrated into an integral pattern, and a single contour has been extracted.

In real life, many objects consist of several separable components (such as Chinese character "Yang" in Figure 2(a)). Contour-based methods are unapplicable to these objects. By CPT, a single closed curve can be derived, and contour-based methods can be applied. Consequently, shape representation based on GC of the object may provide better data reduction than some region-based methods.

2.2. Affine Invariant of GC. An affine transformation $\mathbf{A}$ of coordinates $\mathbf{x} \in \mathbb{R}^2$ is defined as

$$\mathbf{x}' = \mathbf{A}\mathbf{x} + \mathbf{b}, \tag{2}$$

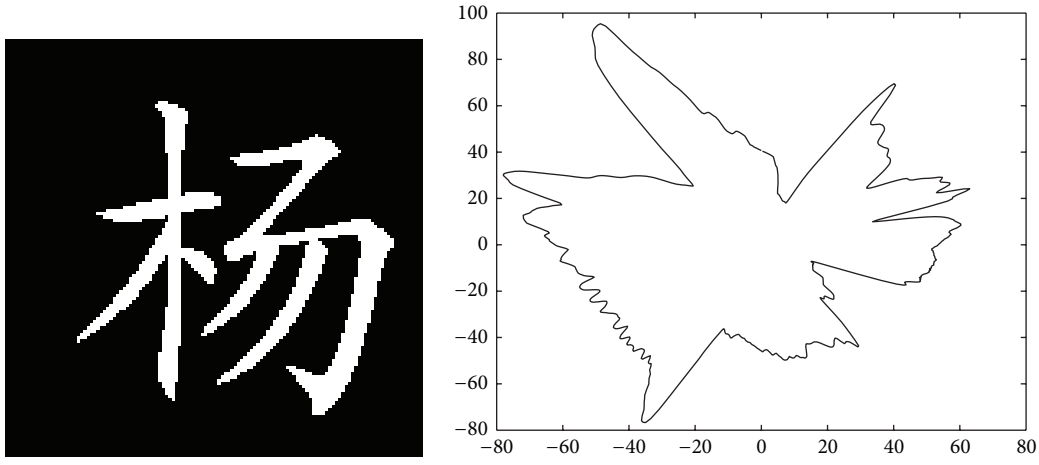

Figure 2: (a) The Chinese character "Hai". (b) GC derived from (a).

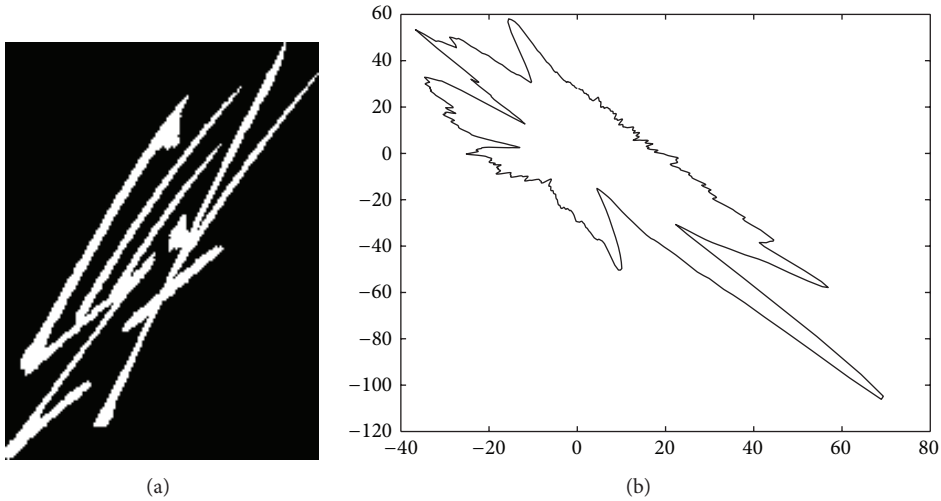

Figure 3: (a) An affine transformation version of Figure 2(a). (b) GC derived from (a).

where $\mathbf{b} = \begin{pmatrix} b_1 \\ b_2 \end{pmatrix} \in \mathbb{R}^2$ and $\mathbf{A} = \begin{pmatrix} a_{11} & a_{12} \\ a_{21} & a_{22} \end{pmatrix}$ is a two-by-two nonsingular matrix with real entries.

Affine transformation maps parallel lines onto parallel lines and intersecting lines into intersecting lines. Based on this fact, it can be shown that the GC extracted from the affine-transformed object by CPT is also an affine-transformed version of GC extracted from the original object.

Consider two objects F and F' are related by an affine transformation $\mathbf{A}$:

$$F' = \left\{ \mathbf{x}' \mid \mathbf{x}' = \mathbf{A}\mathbf{x} + \mathbf{b}, \mathbf{x} \in F \right\}. \tag{3}$$

Then ∂F and $\partial F'$, GCs of F and F', are related by the same affine-transformation $\mathbf{A}$:

$$\partial F' = \left\{ \mathbf{x}' \mid \mathbf{x}' = \mathbf{A}\mathbf{x} + \mathbf{b}, \mathbf{x} \in \partial F \right\}. \tag{4}$$

For example, Figure 3(a) shows an affine transformed version of Figures 2(a) and 3(b) shows the GC derived from Figure 3(a). Observing the two GCs in Figures 2(b) and 3(b), we can see that CPT not only represents the distribution information of the object but also preserves the affine transformation signature.

Therefore, to see whether an object Θ is the affine transform version of F, we just need to check if $\partial\Theta$, the GC of Θ, is the same affine-transformed version of ∂F. We extract affine invariant features using fractal from GC of the object.

3. Extraction of Affine Invariant Features Using Fractal

By CPT, a closed curve can be derived from any object. In order to extract affine invariant features from the derived GC, the GC should firstly be parameterized. Thereafter, shift curves are constructed from the parameterized GC. Consequently, divider dimensions of these curves are computed to form feature vectors.

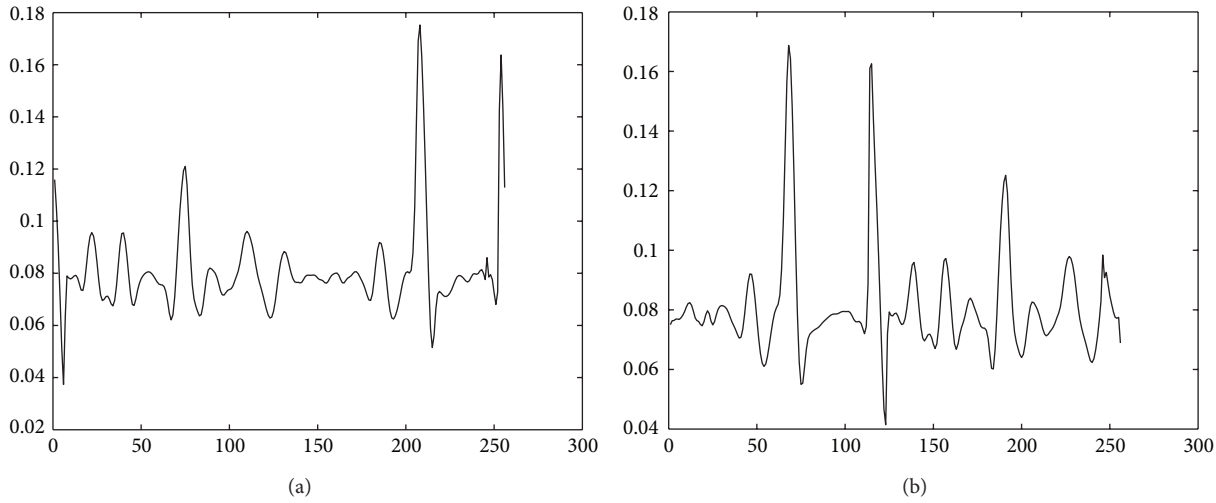

Figure 4: (a) 10-shift curve of the Chinese character given in Figure 2(a). (b) 10-shift curve of the Chinese character given in Figure 3(a).

3.1. Affine Invariant Parameterization. GC should be parameterized to establish one-to-one relation between points on GC of the original object and those on GC of its affine transformed version.

There are two parameters which are linear under an affine transformation: the affine arc length [21], and the enclosed area [22]. These two parameters can be made completely invariant by simply normalizing them with respect to either the total affine arc length or the enclosed area of the contour. In the discrete case, the derivatives can be calculated using finite difference equations. The curve normalization approach used in this paper is the same as the method given in [23]. In the experiments of this paper, GC is normalized and resampled such that $N = 256$.

Suppose that GC of the object has been normalized and resampled. Furthermore, we suppose that the starting point on GC of the original object and that on GC of the affine-transformed version of the original object are identical. Then, a parametric point $\mathbf{x}(\sigma) = [x(\sigma), y(\sigma)]^T$ on GC of the original object and a parametric point $\widetilde{\mathbf{x}}(\widetilde{\sigma}) = [\widetilde{x}(\widetilde{\sigma}), \widetilde{y}(\widetilde{\sigma})]^T$ on GC of its affine transformed version satisfy the following equation:

$$\begin{aligned} \widetilde{x}(\widetilde{\sigma}) &= a_{11}x(\sigma) + a_{12}y(\sigma) + b_1, \\ \widetilde{y}(\widetilde{\sigma}) &= a_{21}x(\sigma) + a_{22}y(\sigma) + b_2. \end{aligned} \tag{5}$$

3.2. Shift Curves. In this part, we will derive invariant features from the normalized GC. Let $[x(\sigma), y(\sigma)]$ and $[\widetilde{x}(\widetilde{\sigma}), \widetilde{y}(\widetilde{\sigma})]$ be the parametric equations of two GCs derived from objects that differ only by an affine transformation. For simplicity, in this subsection, we assume that the starting points on both GCs are identical. After normalizing and resampling, there is a one-to-one relation between σ and $\widetilde{\sigma}$. We use the object centroid as the origin, then translation factor $\mathbf{b}$ is elimated. Equation (2) can be written in matrix form as $\widetilde{\mathbf{x}}(\widetilde{\sigma}) = \mathbf{A}\mathbf{x}(\sigma)$.

Letting γ be an arbitrary positive constant, then $[x(\sigma + \gamma), y(\sigma + \gamma)]$ is a shift version of $[x(\sigma), y(\sigma)]$. We denote M_0 as the zero moment of the object:

$$M_0 = \int\int I(x, y)\, dxdy. \tag{6}$$

We define the following function:

$$C_\gamma(\sigma) = \frac{1}{M_0}\left|x(\sigma)\, y(\sigma + \gamma) - y(\sigma)\, x(\sigma + \gamma)\right|. \tag{7}$$

We call $C_\gamma(\sigma)$ as γ shift curve of the object. Figure 4(a) shows a 10-shift curve of the Chinese character given in Figure 2(a). As a result of normalizing and resampling, $[x(\sigma), y(\sigma)]$, $[\widetilde{x}(\widetilde{\sigma}), \widetilde{y}(\widetilde{\sigma})]$ and $[x(\sigma + \gamma), y(\sigma + \gamma)]$, $[\widetilde{x}(\widetilde{\sigma} + \gamma), \widetilde{y}(\widetilde{\sigma} + \gamma)]$ satisfy the following equation:

$$\begin{aligned} \widetilde{x}(\widetilde{\sigma}) &= a_{11}x(\sigma) + a_{12}y(\sigma), \\ \widetilde{y}(\widetilde{\sigma}) &= a_{21}x(\sigma) + a_{22}y(\sigma), \\ \widetilde{x}(\widetilde{\sigma} + \gamma) &= a_{11}x(\sigma + \gamma) + a_{12}y(\sigma + \gamma), \\ \widetilde{y}(\widetilde{\sigma} + \gamma) &= a_{21}x(\sigma + \gamma) + a_{22}y(\sigma + \gamma). \end{aligned} \tag{8}$$

It follows that

$$\begin{aligned} \widetilde{C}_\gamma(\widetilde{\sigma}) &= \frac{\left|\widetilde{x}(\widetilde{\sigma})\, \widetilde{y}(\widetilde{\sigma} + \gamma) - \widetilde{y}(\widetilde{\sigma})\, \widetilde{x}(\widetilde{\sigma} + \gamma)\right|}{\widetilde{M}_0} \\ &= \frac{\det(\mathbf{A})\left|x(\sigma)\, y(\sigma + \gamma) - y(\sigma)\, x(\sigma + \gamma)\right|}{\det(\mathbf{A})\, M_0} \\ &= C_\gamma(\sigma). \end{aligned} \tag{9}$$

In other words, C_γ given in (7) is affine invariant.

Note that, after affine transformation, the starting point of GC is different. Figure 4(b) shows the 10-shift curve of the affine transformed version Chinese character given in Figure 3(a). We observe that the shift curve of an affine transformation version of the object (see Figure 4(b)) is a translated version of the shift curve of the original object (see Figure 4(a)).

3.3. Computing Divider Dimension of Shift Curves. The FD is a useful method to quantify the complexity of feature details present in an image. In this subsection, we shall discuss the problem of computing the divider dimension of shift curves and, thereafter, use the computed divider dimension to construct a feature vector for the original two-dimensional pattern in question for pattern recognition.

Fractals are mathematical sets with a high degree of geometrical complexity, which can model many classes of time series data as well as images. The FD is an important characteristic of the fractals because it contains information about its geometric structures. When employing fractal analysis researchers typically estimate the dimension from an image. Of the wide variety of FDs in use, the definition of Hausdorff is the oldest and probably the most important. Hausdorff dimension has the advantage of being defined for any set and is mathematically convenient, as it is based on measures, which are relatively easy to manipulate. A major disadvantage is that in many cases it is hard to calculate or estimate by computation methods.

In general, the dimension of a set can be found by the equation

$$D = \frac{\log(N)}{\log(1/r)}, \tag{10}$$

where D is the dimension and N is the number of parts comprising the set, each scaled down by a ratio r from the whole [18].

In what follows, we use the notion of divider dimension of a nonself-intersecting curve (see [24, 25] etc.). Suppose that C is a nonself-intersecting curve and $\delta > 0$. Let $M_\delta(C)$ be the maximum number of ordered sequence of points $x_0, x_1, \ldots, x_M$ on curve C, such that $|x_k - x_{k-1}| = \delta$ for $k = 1, 2, \ldots, M$. The divider dimension $\dim_D C$ of curve C is defined as follows:

$$\dim_D C = \lim_{\delta \to 0} \frac{\log M_\delta(C)}{-\log \delta}, \tag{11}$$

where $|x_k - x_{k-1}|$ represents the magnitude of the difference between two vectors x_k and x_{k-1}.

It should also be mentioned that x_M is not necessarily the end point of curve C, x_T, but $|x_T - x_M| < \delta$. Furthermore, $(M_\delta(C) - 1)\delta$ may be viewed as the length of curve C as measured using a pair of dividers that are set δ distance apart.

Since the divider dimension of nonself-intersecting curves is asymptotic values, we derive their approximations based on the following expression in our experiments:

$$\frac{\log M_\delta(C)}{-\log \delta}, \tag{12}$$

where δ is set small enough.

The divider dimension of shift curve in Figure 4(a) is 1.6168 and that of shift curve in Figure 4(b) is 1.6195. In the experiments of this paper, divider dimensions of shift curves $\gamma = 1, 2, \ldots, 256$ are computed. The feature vector is constituted

$$V_{\text{fea}} = \left(\text{FD}_1, \text{FD}_2, \ldots, \text{FD}_{255}\right)^T. \tag{13}$$

4. Experiment

In this section, we evaluate the discriminate ability of the proposed method. In the first experiment, we examine the proposed method by using some airplane images. Object contours can be derived from these images. In the second experiment, we evaluate the discriminate ability of the proposed method by using some Chinese characters. These characters have several separable components, and contours are not available for these objects.

In the following experiments, the classification accuracy is defined as

$$\eta = \frac{\delta}{\lambda} \times 100\%, \tag{14}$$

where δ denotes the number of correctly classified images and λ denotes the total number of images applied in the test. Affine transformations are generated by the following matrix [5]:

$$A = k \begin{pmatrix} \cos\theta & -\sin\theta \\ \sin\theta & \cos\theta \end{pmatrix} \begin{pmatrix} a & b \\ 0 & \frac{1}{a} \end{pmatrix}, \tag{15}$$

where k, θ denote the scaling and rotation transformation, respectively, and a, b denote the skewing transformation. To each object, the affine transformations are generated by setting the parameters in (15) as follows: $k \in \{0.8, 1.2\}$, $\theta \in \{30^\circ, 90^\circ, 150^\circ, 210^\circ, 270^\circ, 330^\circ\}$, $b \in \{-3/2, -1, -1/2, 0, 1/2, 1, 3/2\}$, and $a \in \{1, 2\}$. Therefore, each image is transformed 168 times.

4.1. Binary Image Classification. In these experiments, we examine the discrimination power of the proposed method using 40 Chinese characters shown in Figure 5. These Chinese characters are with regular script font, and the images have size 128 × 128 in the experiments. We observe that some characters in this database have the same structures, but the number of strokes or the shape of specific stokes may be a little different. Some characters consist of several separable components. As aforementioned, each character image is transformed 140 times. That is to say, the test is repeated 5600 times. Experiments on these Chinese characters in Figure 5 and their affine transformations show that 98.14% accurate classification can be achieved by the proposed method.

The images are sometimes noised for reasons in many real-life recognition situations. The robustness of the proposed method is tested using binary image in this part. We add salt and pepper noise to the transformed binary images. We compare the proposed method with two region-based methods, namely, the AMIs and MSA. The comparative methods are described in [26, 27], and these methods are implemented as discussed in those articles. 3 AMIs and 29 MSA invariants are selected for recognition. The nearest neighbor classifier is applied for AMIs and MSA methods. We firstly add the salt and pepper noise with intensities varying from 0.005 to 0.03 to the transformed images.

Table 1 shows the classification accuracies of all methods in the corresponding noise degree. We can observe that

Figure 5: Test characters used in the second experiments.

Table 1: Classification accuracies of AMIs, MSA, and the proposed method for Chinese characters in case of affine transformation and different intensities of salt and pepper noise.

Noise degree	0	0.005	0.010	0.015	0.020	0.025	0.030
AMIs	91.70%	45.50%	34.82%	28.54%	23.82%	19.89%	17.77%
MSA	94.48%	90.63%	73.57%	53.80%	38.16%	26.86%	19.88%
Our method	98.14%	96.21%	93.48%	89.46%	86.25%	82.07%	77.59%

the classification accuracy of AMIs decreases rapidly from noise-free condition to small noise degree. The classification accuracy decreases from 91.70% to less than 50% when the noise intensity is 0.010. MSA performs much better than AMIs, but the results are not satisfying. To large noise degrees, the proposed method keeps high accuracies all the time.

4.2. Gray Image Classification. In this part, the well-known Columbia Coil-20 database [28], which contains 20 different objects shown in Figure 6, is applied in this experiment. To each object, the affine transformations are generated by setting the parameters in (15) as aforementioned. Therefore, each image is transformed 140 times. That is to say, the test is repeated 2800 times using every method. The classification accuracies of the proposed method, AMIs, and MSA in this situation are 96.00%, 100%, and 95.31%, respectively. The results indicate that AMIs perform best in this test, and the proposed method is similar with MSA.

The effect of adding different kinds of noises is also studied. The noise is added to the affine-transformed images before recognition.

We firstly add the salt and pepper noise with intensities varying from 0.005 to 0.03 to the transformed images. Table 2 shows the classification accuracies of all methods in the corresponding noise degree. We can observe that the classification accuracy of AMIs decreases rapidly from noise-free condition to small noise degree. The classification accuracy decreases from 100% to less than 50% when the noise intensity is 0.010. MSA performs much better than AMIs, but the results are not satisfying. To large noise degrees, the proposed method keeps high accuracies all the time.

In addition, we add the Gaussian noise with zero mean and different variance varying from 0.005 to 0.03 to the transformed images. Table 3 shows the classification accuracies of all methods in the corresponding noise degree. The results indicate that AMIs and MSA are much more sensitive to Gaussian noise than salt and pepper noise. However, the classification accuracies of the proposed method outperform AMIs and MSA in every noise degree.

The experimental results tell us that the proposed method presents better performances in noise situations. The reason may lie in that CPT is robust to noise. It was shown in [29] that Radon transform is quite robust to noise. We can similarly show that GC derived by CPT from the object is robust to additive noise as a result of summing pixel values to generate GC.

Figure 6: Columbia Coil-20 image database.

Table 2: Classification accuracies of AMIs, MSA, and the proposed method for images in Figure 6 in case of affine transformation and different intensities of salt and pepper noise.

Noise degree	0	0.005	0.010	0.015	0.020	0.025	0.030
AMIs	100%	55.04%	43.29%	35.93%	31.96%	26.75%	23.04%
MSA	95.31%	88.10%	74.18%	62.14%	53.74%	47.02%	42.08%
Our method	96.00%	95.07%	93.18%	89.25%	83.32%	77.61%	72.54%

Table 3: Classification accuracies of AMIs, MSA, and the proposed method for images in Figure 6 in case of affine transformation and different intensities of Gaussian noise.

Noise degree	0	0.005	0.010	0.015	0.020	0.025	0.030
AMIs	100%	32.50%	26.04%	21.82%	19.54%	17.64%	16.05%
MSA	95.31%	57.04%	45.82%	40.79%	37.39%	34.78%	32.79%
Our method	96.00%	85.57%	74.89%	63.07%	51.71%	42.89%	34.93%

5. Conclusions

In this paper, affine invariant features are extracted by using fractal. A closed curve, which is called GC, is derived from the original input pattern by employing CPT. Due to shearing, affine invariant features cannot be extracted from GC directly. To address this problem, a group of curves (which are called shift curves) are constructed from the obtained GC. Fractal dimensions of these curves can readily be computed and constitute a new feature vector for the original pattern. The derived feature vector is used for object classification tasks. Several experiments have been conducted to evaluate the performance of the proposed method.

Although satisfying results have been achieved in object classification tasks, some remarks should be made. The performance of CPT depends strongly on the accuracy calculation of the centroid. We are working towards developing

method without the centroid. Furthermore, some characteristics of CPT should be further studied.

Acknowledgments

This work was supported in part by the National Science Foundation under Grant 60973157, and Ming Li thanks the supports in part by the 973 plan under the project Grant no. 2011CB302800 and by the National Natural Science Foundation of China under the project Grant nos. 61272402, 61070214, and 60873264.

References

[1] Q. M. Tieng and W. W. Boles, "Wavelet-based affine invariant representation: a tool for recognizing planar objects in 3D space," *IEEE Transactions on Pattern Analysis and Machine Intelligence*, vol. 19, no. 8, pp. 846–857, 1997.

[2] M. R. Daliri and V. Torre, "Robust symbolic representation for shape recognition and retrieval," *Pattern Recognition*, vol. 41, no. 5, pp. 1799–1815, 2008.

[3] P. L. E. Ekombo, N. Ennahnahi, M. Oumsis, and M. Meknassi, "Applicationof affine invariant fourier descriptor to shape based image retrieval," *International Journal of Computer Science and Network Security*, vol. 9, no. 7, pp. 240–247, 2009.

[4] X. Gao, C. Deng, X. Li, and D. Tao, "Geometric distortion insensitive image watermarking in affine covariant regions," *IEEE Transactions on Systems, Man and Cybernetics C*, vol. 40, no. 3, pp. 278–286, 2010.

[5] M. I. Khalil and M. M. Bayoumi, "A dyadic wavelet affine invariant function for 2D shape recognition," *IEEE Transactions on Pattern Analysis and Machine Intelligence*, vol. 23, no. 10, pp. 1152–1164, 2001.

[6] M. I. Khalil and M. M. Bayoumi, "Affine invariants for object recognition using the wavelet transform," *Pattern Recognition Letters*, vol. 23, no. 1–3, pp. 57–72, 2002.

[7] G. Liu, Z. Lin, and Y. Yu, "Radon representation-based feature descriptor for texture classification," *IEEE Transactions on Image Processing*, vol. 18, no. 5, pp. 921–928, 2009.

[8] R. Matungka, Y. F. Zheng, and R. L. Ewing, "Image registration using adaptive polar transform," *IEEE Transactions on Image Processing*, vol. 18, no. 10, pp. 2340–2354, 2009.

[9] Y. Wang and E. K. Teoh, "2D affine-invariant contour matching using B-spline model," *IEEE Transactions on Pattern Analysis and Machine Intelligence*, vol. 29, no. 10, pp. 1853–1858, 2007.

[10] F. Mai, C. Q. Chang, and Y. S. Hung, "A subspace approach for matching 2D shapes under affine distortions," *Pattern Recognition*, vol. 44, no. 2, pp. 210–221, 2011.

[11] M. Gong, H. Li, and W. Cao, "Moment invariants to affine transformation of colours," *Pattern Recognition Letters*, vol. 34, no. 11, pp. 1240–1251, 2013.

[12] X. Song, D. Muselet, and A. Tremeau, "Affine transforms between image space and color space for invariant local descriptors," *Pattern Recognition*, vol. 46, no. 8, pp. 2376–2389, 2013.

[13] D. Zhang and G. Lu, "Review of shape representation and description techniques," *Pattern Recognition*, vol. 37, no. 1, pp. 1–19, 2004.

[14] E. Rahtu, *A multiscale framework for affine invariant pattern recognitionand registration [Ph.D. thesis]*, University of OULU, Oulu, Finland, 2007.

[15] R. Veltkamp and M. Hagedoorn, "State-of the art in shape matching," Tech. Rep. UU-CS-1999, 1999.

[16] I. Weiss, "Geometric invariants and object recognition," *International Journal of Computer Vision*, vol. 10, no. 3, pp. 207–231, 1993.

[17] Y. Y. Tang, Y. Tao, and E. C. M. Lam, "New method for extractionbased on fractal behavior," *Pattern Recognition*, vol. 35, pp. 1071–1081, 2002.

[18] B. B. Mandelbrot, *The Fractal Geometry of Nature*, W. H. Freeman, San Francisco, Calif, USA, 1982.

[19] B. B. Chaudhuri and N. Sarkar, "Texture segmentation using fractal dimension," *IEEE Transactions on Pattern Analysis and Machine Intelligence*, vol. 17, no. 1, pp. 72–77, 1995.

[20] Y. Y. Tang, J. Liu, H. Ma, and B. Li, "Two-dimensional wavelet transform indocument analysis," in *Proceedings of the 1st International Conferenceon Multimodal Interface*, pp. 274–279, Beijing, China, October 1996.

[21] D. Cyganski and R. F. Vaz, "A linear signal decomposition approach to affineinvariant contour identification," in *Intelligent Robots and Computer Vision X*, vol. 1607 of *Proceedings of SPIE*, pp. 98–109, 1991.

[22] K. Arbter, W. E. Snyder, H. Burkhardt, and G. Hirzinger, "Application of affine-invariant Fourier descriptors to recognition of 3-D objects," *IEEE Transactions on Pattern Analysis and Machine Intelligence*, vol. 12, no. 7, pp. 640–647, 1990.

[23] M. Yang, K. Kpalma, and J. Ronsin, "Affine invariance contour desciptor based on the equal area normalization," *IAENG International Journal of Applied Mathematics*, vol. 36, no. 2, paper 5, p. 6, 2007.

[24] K. Falconer, *Fractal Geometry. Mathematical Foundations and Applications*, John Wiley & Sons, Chichester, UK, 1990.

[25] G. A. Edgar, *Measure, Topology, and Fractal Geometry*, Undergraduate Texts in Mathematics, Springer, New York, NY, USA, 1990.

[26] J. Flusser and T. Suk, "Pattern recognition by affine moment invariants," *Pattern Recognition*, vol. 26, no. 1, pp. 167–174, 1993.

[27] E. Rahtu, M. Salo, and J. Heikkilä, "Affine invariant pattern recognition using multiscale autoconvolution," *IEEE Transactions on Pattern Analysis and Machine Intelligence*, vol. 27, no. 6, pp. 908–918, 2005.

[28] http://www1.cs.columbia.edu/CAVE/software/softlib/coil-20.php.

[29] K. Jafari-Khouzani and H. Soltanian-Zadeh, "Rotation-invariant multiresolution texture analysis using Radon and wavelet transforms," *IEEE Transactions on Image Processing*, vol. 14, no. 6, pp. 783–795, 2005.